

2019-09-20

# Sediment exchange between the beach and the inner shelf

Garcia Valiente, N

<http://hdl.handle.net/10026.1/15150>

---

---

*All content in PEARL is protected by copyright law. Author manuscripts are made available in accordance with publisher policies. Please cite only the published version using the details provided on the item record or document. In the absence of an open licence (e.g. Creative Commons), permissions for further reuse of content should be sought from the publisher or author.*



**UNIVERSITY OF  
PLYMOUTH**

**SEDIMENT EXCHANGE BETWEEN THE  
BEACH AND THE INNER SHELF**

by

**NIEVES GARCIA VALIENTE**

A thesis submitted to University of Plymouth in partial  
fulfilment for the degree of

**DOCTOR OF PHILOSOPHY**

School of Biological and Marine Sciences

**October 2019**



## Abstract

---

**Name:** Nieves G. Valiente

**Title:** Sediment exchange between the beach and the inner shelf

Embayed beaches are often considered closed sediment cells. Contrarily to this widely spread idea, recent studies suggest that the inability of certain embayments to recover to storms is a consequence of significant sediment exchange between the beach and neighbouring areas during extreme wave events; however, the physical coupling is still poorly understood.

The estimation of the depth of closure in relation to the depth in front of the bounding headlands along embayed coastlines allows questioning whether embayments experience more headland bypassing than expected. The macrotidal, embayed and high-energy coastline of SW England was used as a natural field laboratory to identify the 'active' nearshore limits (Depth of Closure, *DoC*, and Depth of Transport, *DoT*) using a multi-method approach that includes observations of shoreface morphology and sedimentology, offshore/inshore wave formulations and bed shear stress computations. Values of *DoC* are c. 10 – 15 m; and the computed *DoT*, represented by the upper-plane bed transition attained under extreme conditions, exceeds 30 m depth in the study area. Even though many headlands appear sufficiently prominent to suggest a closed boundary, significant wave- and tide-driven sediment transport is likely to occur beyond the headland base during extreme events. *DoT* was computed across a broad wave-current parameter space, further highlighting that tidal currents can increase this closure depth estimate by ~10 m along macrotidal coastlines, representing a 30% increase compared to tideless settings.

A combination of LiDAR, UAV photogrammetry, RTK-GNSS, single-beam and multi-beam echosounder surveys, that encompassed the dune system to > 40 m water depth of Perranporth embayment was used to quantify the sediment budget. Inter-annual dynamics and embayment sub-systems response over a 10-year period that included extreme storm erosion and post-storm recovery were evaluated,

demonstrating that Perranporth is neither closed, nor balanced. The very significant net changes, representing a loss of c.  $100 \text{ m}^3 \text{ m}^{-1}$  during the extreme storm epoch (2011 – 2016, period encompassing 2013/14 storms) and a gain of c.  $200 \text{ m}^3 \text{ m}^{-1}$  during the subsequent recovery period (2016 – 2018), indicated that significant sediment transport occurred seaward of the base of the headlands and beyond the morphological depth of closure. It is further demonstrated that the inter-tidal region is partly uncoupled from the sub-tidal region, with the former region dominated by cross-shore sediment fluxes, whereas the sub-tidal region is also significantly affected by longshore sediment fluxes.

The nearshore sediment transport dynamics along a 15-km stretch of coastline encompassing Perranporth beach were investigated using Delft3D. Numerically-modelled wave-driven and tidal currents were used to support interpretation of sediment flux pathways inferred from the morphological observations of Chapter 3. Multi-embayment circulation, mega-rip formation where an alongshore current is deflected offshore ( $0.7 \text{ m s}^{-1}$  at  $> 20 \text{ m}$  depth) in the down-wave sectors and cross-shore exchanges extending to depths that exceed the base of the headlands (c.  $10^4 \text{ m}^3 \text{ day}^{-1}$ ) dominated during extreme events. Accretionary phases over moderate-high swell periods were associated with clockwise intra-embayment circulation with predicted currents inducing redistribution in the long embayments ( $> 10^3 \text{ m}^3 \text{ day}^{-1}$ ) towards the south. This circulation mode is combined with significant bypassing rates around the shallower and wider headlands ( $10^2 - 10^3 \text{ m}^3 \text{ day}^{-1}$ ). A simple empirical parameterisation for sediment bypass based on offshore wave-conditions ( $r > 0.92$ ) is presented, allowing prediction of sediment fluxes on the lower shoreface and sediment budgets over multi-annual time scales.

This work provides new insights on nearshore sediment dynamics at different spatial and temporal scales, with a major focus on headland and cross-embayment bypass. This thesis demonstrates that headland bypassing is more widespread than commonly assumed, leading to a shift in understanding of sediment budgets along exposed and macrotidal embayments, particularly along sediment starved coastlines, while contributing to the knowledge of the processes affecting coastal vulnerability and long-term evolution of embayed beaches.

## Author's declaration

---

At no time during the registration for the degree of Doctor of Philosophy has the author been registered for any other University award without prior agreement of the Doctoral College Quality Sub-Committee.

Work submitted for this research degree at the University of Plymouth has not formed part of any other degree either at the University of Plymouth or at another establishment.

The PhD supervisory team consisted of Prof. Gerd Masselink (Director of Studies), Dr. Tim Scott and Prof. Daniel Conley from the School of Biological and Marine Sciences, University of Plymouth.

This research funding was linked to UK Natural Environment Research Council grant (NE/M004996/1; BLUE-coast project).

Relevant scientific seminars, project meetings and conferences were regularly attended throughout the duration of this thesis at which work was presented, and several papers were prepared for publication.

Word count of main body of thesis: 43,624



Signed.....

Date.....15/11/2019.....



## PhD outputs

---

### Refereed Journal Publications

**N.G. Valiente**, G. Masselink, R.J. McCarroll, T. Scott, M. Wiggins, 2019. Multi-annual embayment sediment dynamics involving headland bypassing and sediment exchange across the depth of closure, *Geomorphology*, 314, 48–64. <https://doi.org/10.1016/j.geomorph.2019.06.020>.

R.J. McCarroll, G. Masselink, M. Wiggins, T. Scott, O. Bilson, D. Conley, **N. G. Valiente**, 2019. High-efficiency gravel longshore sediment transport and headland bypassing over an extreme wave event, *Earth Surface Processes and Landforms*. <https://doi.org/10.1002/esp.4692>.

M. Wiggins, T. Scott, G. Masselink, P. Russell, **N.G. Valiente**, 2019. Regionally coherent embayment rotation; Behavioral response to bi-directional waves and atmospheric forcing, *Journal of Marine Science and Engineering*, 7, 116. <https://doi.org/10.3390/jmse7040116>.

**N.G. Valiente**, G. Masselink, T. Scott, D. Conley, R.J. McCarroll, 2019. Role of waves and tides on depth of closure and potential for headland bypassing, *Marine Geology* 407, 60-75. <https://doi.org/10.1016/j.margeo.2018.10.009>.

R.J. McCarroll, G. Masselink, **N.G. Valiente**, T. Scott, E. King, 2018. Wave and tidal controls on headland bypassing and embayment circulation, *Journal of Marine Science and Engineering* 6 (3), 94. <https://doi.org/10.3390/jmse6030094>.

### Refereed Conference Proceedings

**N.G. Valiente**, R.J. McCarroll, G. Masselink, T. Scott, D. Conley, E. King. Circulation and sediment fluxes on a macrotidal, exposed and embayed coastline. Proceedings Coastal Sediments, ASCE, Florida, USA, May 2019.

**N.G. Valiente**, G. Masselink, T. Scott, D. Conley. Depth of Closure Along an Embayed, Macro-Tidal and Exposed Coast: a Multi-Criteria Approach. Proceedings Coastal Dynamics, ASCE, Helsingor, Denmark, Paper No. 185, 1211-1222, June 2017.

### **Conference presentations**

**N.G. Valiente**, R.J. McCarroll, G. Masselink, T. Scott, D. Conley, E. King. Circulation and sediment fluxes on a macrotidal, exposed and embayed coastline. Proceedings Coastal Sediments, ASCE, Florida, USA, May 2019. Poster.

**N.G. Valiente**, G. Masselink, R.J. McCarroll, T. Scott, D. Conley. Total sediment budget approach to multi-annual morphodynamic response of an exposed, macro-tidal and embayed sandy beach. Ocean Sciences Meeting, AGU, Portland, USA, February 2018 (abstract 311281). Talk.

R.J. McCarroll, **N.G. Valiente**, E. King, G. Masselink, T. Scott, D. Conley. Wave and tidal controls on headland bypassing. Ocean Sciences Meeting, AGU, Portland, USA, February 2018 (abstract MG44B-0346). Poster.

**N.G. Valiente**, G. Masselink, T. Scott, D. Conley. Depth of Closure Along an Embayed, Macro-Tidal and Exposed Coast: a Multi-Criteria Approach. Proceedings Coastal Dynamics, ASCE, Helsingor, Denmark, Paper No. 185, 1211-1222, June 2017.

**N.G. Valiente**, G. Masselink, T. Scott, D. Conley, K. Amoudry. Exploration of Inner shelf dynamics on the North Coast of SW England. Young Coastal Scientists and Engineers Conference (YCSEC), Swansea, UK, March 2016. Award for best poster.

# Contents

---

List of Figures.....	X
List of tables.....	XXI
Acknowledgements.....	XXII
<b>Chapter 1 – Introduction.....</b>	<b>1</b>
1.1 Context.....	1
1.2 Overview of thesis aims .....	2
1.3 Review .....	3
1.3.1 Embayed coastlines.....	4
1.3.2 Morphodynamics along embayed coastlines .....	6
1.3.3 Quantification of sediment exchange between the beach and the inner shelf	16
1.4 Study area regional setting.....	20
1.4.1 Geology and geomorphology .....	20
1.4.2 Hydrodynamics.....	22
1.5 Aims and thesis outline.....	23
<b>Chapter 2 – Role of waves and tides on depth of closure and potential for headland bypassing.....</b>	<b>27</b>
2.1 Introduction.....	27
2.2 Background.....	30
2.3 Study area .....	33
2.4 Methodology .....	39
2.4.1 Observational data .....	39
2.4.2 Numerical modelling data .....	40
2.4.3 Depth of closure methods.....	42
2.5 Results .....	46
2.5.1 Shoreface shape .....	46
2.5.2 Closure depth based on observations: Perranporth case of study ( $DoC_{obs,a-b}$ )	47
2.5.3 Along-coast variability in depth of closure ( $DoC_{param}$ , $DoC_{obs,c}$ ).....	49
2.5.4 DoC determined using bed shear stress maxima ( $DoC_{stress}$ ) .....	52
2.6 Discussion.....	56
2.7 Conclusions.....	62

## **Chapter 3 – New insights into multi-annual embayment scale sediment dynamics 65**

3.1	Introduction .....	65
3.2	Study area and methodology .....	69
3.2.1	Perranporth and Penhale Sands beach .....	69
3.2.2	Multimethod morphological surveys .....	74
3.2.3	DEM creation .....	75
3.2.4	Full embayment volume change computation .....	77
3.3	Quasi full embayment beach response and evolution .....	78
3.3.1	Volume time series .....	78
3.3.2	Outer bar dynamics .....	82
3.4	Full embayment total sediment budget .....	86
3.4.1	Storm response .....	86
3.4.2	Multi-annual beach recovery .....	89
3.4.3	Sub-tidal sediment redistribution .....	93
3.5	Relating wave forcing and morphological change .....	95
3.6	Discussion .....	100
3.6.1	Sediment budget conceptual model .....	100
3.6.2	Multi-annual embayment scale dynamics .....	104
3.6.3	Outer bar dynamics .....	105
3.7	Conclusions .....	106

## **Chapter 4 – Numerical modelling of nearshore sediment transport and headland bypassing.....109**

4.1	Introduction .....	109
4.2	Study area .....	114
4.3	Materials and methods .....	115
4.3.1	Wave and hydrodynamic field observations .....	115
4.3.2	Numerical model setup .....	116
4.3.3	Modelled scenarios .....	121
4.3.4	Transects for transport rates integration .....	122
4.4	Results .....	124
4.4.1	Calibration and validation .....	124
4.4.2	Numerically modelled circulation .....	129
4.4.3	Numerically modelled sediment fluxes .....	131
4.5	Discussion .....	137

4.5.1 Sediment transport mechanisms .....	137
4.5.2 Prediction of bypassing rates and sediment budgets.....	137
4.6 Conclusions .....	142
<b>Chapter 5 – Synthesis and conclusions.....</b>	<b>145</b>
5.1 Synthesis and conclusions .....	146
5.1.1 Potential for headland bypassing in embayed coastlines.....	147
5.1.2 Multi-annual embayment-scale sediment dynamics .....	148
5.1.3 Nature of exposed and macrotidal embayments: open or closed? .....	152
5.1.4 Driving processes and major sediment transport pathways within and between adjacent bays .....	153
5.2 Future work .....	156
5.3 Thesis conclusions .....	157
<b>References.....</b>	<b>159</b>
<b>Appendix A – Model sensitivity analysis.....</b>	<b>A-193</b>
<b>Appendix B – First author papers .....</b>	<b>A-197</b>

## List of Figures

---

**Fig. 1.1** Examples of rocky coastlines in Europe including the study site (red box): (A) W Ireland, (B) N coast of SW England, (C) Brittany coast, (D) N Spain, and (E) S Portugal. White dashed line represents the edge of continental shelf. ....6

**Fig. 1.2** (a) Definition sketch of the parabolic approach to bay shape (after Hsu et al., 1989a). (b) Example of equilibrium bay shape calculated using Eq. 1.1 for variable wave obliquity,  $\beta = 20^\circ$  and  $60^\circ$  (Source: Short and Masselink, 1999). ....8

**Fig. 1.3** Common morphometrics for embayment/headland classification. (a) Non-dimensional embayment scaling factor ( $\delta'$ ) as per Short and Masselink (1999) with width between headlands ( $R_o$ ) and total embayment length, including beach and headlands ( $S$ ). (b) Embayment morphometric parameters as per Fellows et al. (2019). Embayment area ( $A_e$ ), embayment indentation ( $a$ ), headland orientation to beach aspect ( $\theta_h$ ) and shadowed beach length ( $X_{sh}$ ). (c) Schematics of headland geomorphic parameters as per George et al. (2015). Headland perimeter ( $P_e$ ) and apex angle ( $\alpha_{up}$ ,  $\alpha_{dn}$ ). (d) Example of schematic of transects and bathymetry (contours 10 – 60 m depth) used to compute the nearshore bathymetric slope ratio across the headland as per George et al. (2015). A and C are reference transects and B is the headland transect. ....10

**Fig. 1.4** Modes of embayment circulation and rip channel configurations based on Short and Masselink (1999) and Castelle and Coco (2012). Cellular circulation with a rip developing at the centre of the beach (a) and with headland rips (b). (c) Transitional circulation with a rip occurring at one end of the embayment and two additional rips. (d) Normal circulation with rips at both headlands and four additional rips. Preferred flow paths of surf zone exits are indicated by the red arrows. ....11

**Fig. 1.5** Examples of embayment-scale circulation on embayed beaches. Oblique (left panels) and aerial (right panels) images of: (a–b) embayment-cellular rip circulation at Aileens, County Claire, Ireland; (c–d) transitional circulation at Sennen-Gwynver beach, SW England; and (e–f) normal circulation at Porthtowan, SW England. Image sources: Tim Scott, DRIBS project and Goggle Earth. ....13

**Fig. 1.6** Upper panel: Representation of the headland structural impact on shoreface current circulation. (Modified from Short and Masselink (1999)). Bottom

panel: Schematic illustration of headland-attached sand bar/spit bypassing. (A) Updrift accumulation; (B) headland sub-aqueous sand wave; (C) downdrift attached sand bar/spit; (D) advancing of sand wave and erosion rip merges with downdrift beach (extracted from Short and Masselink, 1999)..... 15

**Fig. 1.7** Processes parameterised by coastal models to predict sediment transport and morphological evolution as per Amoudry and Souza (2002). (a) Coastal shelf sediment transport processes and boundaries. Lateral boundaries can be open or closed with the shoreline boundary usually taken to be of the closed type. (b) Near-bed sediment transport processes..... 19

**Fig. 1.8** (a) Offshore 1:250,000 scale seabed sediment distribution and (b) geological setting (modified from: Leveridge and Shail, 2011; May and Hansom, 2013) of SW England based upon BGS maps. Red dots represent the location of the beaches used in this study..... 21

**Fig. 1.9** Littoral sediment cells and subcells for the SW of England with direction of littoral drift (blue arrows) based on a classification conducted by Motyka and Brampton (1993). Cells are numbered clockwise from St. Abb's Head (NE England). Red dots represent the location of the beaches used in this study and pink dot refers to Perranporth beach. .... 22

**Fig. 1.10** Maps of the U.K. with: (a) M2 tidal amplitude (adapted from Proudman and Doodson, 1924); (b) 10% exceedance significant wave height,  $H_{s,10\%}$  (Draper, 1991); and (c) 1-in-50-yr storm surge level (Flather, 1987). Source: Scott, 2009..... 23

**Fig. 2.1** Study area, SW England. Top panel: wave climate variability and tidal range. Wave climate data represent a 4-year record (2013 – 2016) from the MetOffice WW3 model, with cell colour indicating offshore  $H_s$  exceeded 12 hours per year and associated direction. Red circles (A to C) indicate the locations of wave roses. Black solid lines represent mean spring tidal range, adapted from BERR (2008). Bottom panel: location of study areas along the SW (SWAN model domains for *Regions 1 – 6*). Black dots indicate the studied embayments and white circles are MetOffice UK Waters Wave Model nodes used as SWAN input..... 34

**Fig. 2.2** Left panel: Spatial distribution of bottom tidal current velocities and direction during spring tides. Magenta dots with labels (A, B, C) represent locations of

velocity time series shown in the right panels. Right panels: velocity current time series for a neap-spring-neap tidal cycle at the 30-m contour line off the headlands for *Region 6* (upper), *Perranporth-Region 3* (middle) and *Region 1* (lower). Data sourced from FVCOM numerical model (Chen *et al.*, 2003), produced by the UK National Oceanography Centre.....36

**Fig. 2.3** Upper panel (a–f): aerial photography and bathymetry for the six regions of study. Lower panel (g): representative shoreface profiles extracted from the central part of selected LTEs. Bathymetry data were obtained from United Kingdom Hydrographic Office (2011) and aerial photographs were courtesy of Plymouth Coastal Observatory (available at <https://www.channelcoast.org/southwest/>). .....38

**Fig. 2.4** Flow diagram of research methodology of the *DoC* quantification. Underlined criteria correspond with the methods to test. ....39

**Fig. 2.5** Boxplots representing values of *A* (a) and associated *RMSE* (b) at central profiles for each of the six regions (excluding profiles located at headlands). (c) Example of fitted profile for *Region 3*. ....47

**Fig. 2.6** Left panel: observed depth of closure estimated for Perranporth beach, north Cornwall, from the profile envelope ( $DoC_{obs,a}$ ) and from sediment distribution ( $DoC_{obs,b}$ ). Light and dark blue bars represent the median sediment size ( $D_{50}$ ) for winter and summer samples, respectively. The grey lines represent alongshore-average profiles associated with beach survey data collected from 2010 to 2016; the blue line is the mean profile over the survey period; and the red line shows the standard deviation associated with the mean profile. The dashed line represents *DoC* based on the morphological observations. Right panel: topographic and bathymetric survey with 250-m wide section of beach (black box) for alongshore-average profile used in left panel. ....48

**Fig. 2.7** Along-coast variability in depth of closure obtained by applying the wave-based formulations of Hallermeier for *DoC* (light blue) and *DoC-motion* (dark blue), Capobianco (green) and Birkemeier (yellow). Upper panel: *DoC* at each region computed using offshore WW3 wave conditions ( $DoC_{param,a}$ ). Light bars show *DoC* values for  $t = 4$  years and darkest colour bars represent *DoC* ( $t = 1$  years). Bottom panel: bars represent the average *DoC* for each embayment, computed using the modelled inshore wave conditions and forcing the SWAN wave model with  $H_{s,12}$  and  $T_{p,12}$  derived from

the 4-year time series ( $DoC_{param,b}$ ). Minimum and maximum  $DoC$  values for each embayment are represented by the red intervals. Grey bars represent the embayment-averaged depth of the transition between sand and rock. Vertical black dashed lines separate the different regions.....50

**Fig. 2.8** Example of along-embayment variability in depth of closure due to wave transformation for *Region 2* using  $DoC_{param,b}$  (Hallermeier, 1978; Eq. 2.2).....52

**Fig. 2.9** Left panels show wave-induced bed shear stress ( $\tau_w$ ) computed for extreme wave conditions ( $H_{s,12}$  and  $T_{p,12}$ ) and for *Regions 1 – 6* (a, d, g, j, m, p). Middle panels present combined wave- and current-induced bed shear stress ( $\tau_{wc}$ ) computed for extreme wave conditions ( $H_{s,12}$  and  $T_{p,12}$ ) during maximum values of tidal currents (spring tides) and for *Regions 1 – 6* (b, e, h, k, n, q). Magenta line represents the bed shear stress at the transition to upper-plane bed conditions for medium sand ( $D_{50} = 0.3$  mm,  $\tau_{cr} = 4.77$  N m<sup>-2</sup>). Right panels:  $\tau_w$  (blue) and  $\tau_{wc}$  (red) transition depth to upper-plane bed conditions. ....54

**Fig. 2.10** Bed shear stress at the transition to upper-plane bed conditions for medium and coarse sand ( $D_{50} = 0.3$  and  $0.6$  mm), limit for initiation of motion ( $DoC-motion$ ) and depth between sand and rock for *Region 5*. Bed shear stress transition limit is computed using (a) wave-induced bed shear stress ( $\tau_w$ ) and (b) combined wave- and current-induced bed shear stress ( $\tau_{wc}$ ) computed for extreme wave conditions ( $H_{s,12}$  and  $T_{p,12}$ ) and maximum tidal currents (spring tides). (c)  $DoC-motion$  is predicted using Hallermeier (1981; Eq. 2.3), and depth between sand-rock is based on observations. ...55

**Fig. 2.11** Variation of  $DoT$  across a broad wave-current parameter space.  $DoT$  is computed using significant wave height ( $H_s$ ) and tidal current speed ( $U$ ) for medium sand ( $D_{50} = 0.3$  mm) and a constant period ( $T_p$ ) of 10 s (left panel) and 15 s (right panel). Examples of computed  $DoT$  values using extreme significant wave height ( $H_{s,99\%}$ ) and maximum tidal current in the bottom layer are shown as red dots: *GoM* – Gulf of Mexico (Pepper and Gregory, 2004; Ortiz and Ashton, 2016); *NSW* – New South Wales (Kulmar et al., 2005); *MAB* – Middle Atlantic Bight (Wright, 1994); *DaC* – Danish Coast (Aagaard et al., 2010); *DuC* – Dutch Coast (Luijendijk et al., 2017); *EE* – East England (Haskoning, 2005; Leonardi and Platter, 2017); and *PPT* – Perranporth. The range of  $H_s - U$  combinations estimated for the SW (South West England) is also indicated (red box).61

**Fig. 2.12** Plan view of an idealised high-energy and embayed coastline. *DoC* and *DoT* limits are included for both microtidal (dashed lines) and macrotidal settings (solid lines).....62

**Fig. 3.1** Plan view of beach-inner shelf dynamics for a closed cell (left panel), a balanced open system (middle panel) and a non-balanced open system (right panel) using an idealized high-energy, cross-shore dominated and embayed coastal cell section. Red arrows depict sediment fluxes in/out of the embayment with size representing magnitude. ....68

**Fig. 3.2** (a) Location map of Perranporth beach, SW England, physical context and regions used for quasi and full embayment volume time series calculation (red and blue boxes, and black dashed region, respectively). (b) Embayment 3D-view with extension of north and south sectors and aerial photograph of Penhale Sands taken to the north showing north dune system. Bottom right-hand panels show a representation of a vertical profile from the frontal dune system to the inner-shelf for the north (c) and south (d) beach sectors, including the considered sub-systems (sub-tidal, inter-tidal and dunes). ....71

**Fig. 3.3** Monthly statistics of: (a) significant wave height; and (b) peak wave period; and (c) wave direction, computed for the period 2007 – 2018. Wave statistics were derived from the Perranporth directional waverider buoy (refer to Fig. 3.2a for location). In all left panels, bars indicate monthly-averaged values with error bars showing the monthly standard deviation and circles indicating 2013/2014 and years 2016 – 2018 monthly-averaged values. (d) Directional wave rose showing distribution of  $H_s$  and (e) joint probability of  $H_s$  and  $T_p$  with percentage occurrence contours. (f) 11-year time series of alongshore wave power,  $P_y$  (1-day and 8-week running mean) for an averaged orientation of c.  $285^\circ$ . Southward  $P_y$  is negative.....73

**Fig. 3.4** Timeline of the data sources available for analysis. From top: Perranporth beach inter-tidal beach morphology (Inter south), Perranporth beach sub-tidal bathymetry (Bathy south), full embayment dune morphology from LiDAR and UAV (Dunes), full embayment inter-tidal beach morphology (Inter full), full embayment sub-tidal bathymetry (Bathy full) and directional wave rider buoy (DWR).

Grey stripes show years for which LiDAR data are available. Orange dashed line represents winter 2011 reference state. ....75

**Fig. 3.5** South (black) and north (green) Perranporth beach response and evolution. (a) 11-year time series of significant wave height measured at Perranporth wave buoy (30-min and 8-week running mean), wave power  $P$  (Herbich, 2000) and storm events (orange bubbles,  $H_s > H_{s,99\%}$ , minimum of 6 hours duration and a meteorological independence criterion of 24 h between peaks). The size of the bubbles is proportional to storm duration based on  $H_{s,95\%}$  cut-off. Dune (b), inter-tidal (c) and sub-tidal (d) sediment volume ( $\text{m}^3 \text{m}^{-1}$  alongshore-averaged) and associated alongshore standard deviation (bounded area). (e) Total beach sediment volume ( $\text{m}^3 \text{m}^{-1}$  alongshore-averaged, from dune foot to -14.5 m ODN) and associated alongshore standard deviation (bounded area). Dune volume refers to the area above the dune foot ( $z = 5$ ), inter-tidal volume corresponds with the area from the dune foot to  $z = -2$  m ODN and sub-tidal from  $z = -2$  m to -14.5 m ODN. Red (storm) and blue (recovery) squares represent the considered epochs in Section 3.4. ....81

**Fig. 3.6** Upper panels: residual morphology of the full embayment with inner and outer bar systems. Warm colours represent positive values of residual morphology and cool colours represent negative values. The horizontal blue and grey lines show the location of the 2D cross-shore profile (extracted from actual *DEMs*) presented in bottom panels. Magenta and black contours represent *DoC* and low tide water level, respectively. Bar states are included as welded bar (W), crescentic attached bar (CA), crescentic bar (C) and longshore bar (L). ....83

**Fig. 3.7** Alongshore-averaged residual cross-shore profiles for (a) southern and (b) northern part of Perranporth beach. Profile edges are highlighted in blue for summer and red for winter, and circles indicate outer bar crest position. (c) Scatter plot of outer bar volume  $Q_{\text{residual}}$  and bar crest position  $x_c$  for the southern part of Perranporth beach. Colour indicate maximum depth of the bar crest  $z_c$  and numbers represent survey position in the time series (September 2010 to September 2018). Grey line represents the least-squares best fit. ....85

**Fig. 3.8** Storm response total sediment budget. Left panel: full embayment *DoD* from 2011 to 2016. Areas where morphological change is not significant ( $Z_{\text{DEM1}} -$

$Z_{DEM2} \geq \min LoD_{95\%}$ ) are uncoloured. Orange and yellow contours represent the inter-tidal to sub-tidal limit (-2 m, ODN) and  $DoC$  (-14.5 m, ODN) respectively. Right panels: cross-shore and alongshore variability of volume changes for the complete cross-shore profile and the different sub-systems for the domain comprised inside the black box. i–iii highlight offshore areas where morphological change is within the propagated uncertainty. ....88

**Fig. 3.9** Multi-annual recovery total sediment budget. Left panel: full embayment  $DoD$  from 2016 to 2018. Areas where morphological change is not significant ( $Z_{DEM1} - Z_{DEM2} \geq \min LoD_{95\%}$ ) are uncoloured. Orange and yellow contours represent the inter-tidal to sub-tidal limit (-2 m, ODN) and  $DoC$  (-14.5 m, ODN) respectively. Right panels: cross-shore and alongshore variability of volume changes for the complete cross-shore profile and the different sub-systems for the domain comprised inside the black box. i–iii highlight offshore areas where morphological change is within the propagated uncertainty. ....91

**Fig. 3.10** Averaged sub-tidal, inter-tidal and dune volume per beach width ( $m^3 m^{-1}$  alongshore) and associated uncertainty (error bars) for epochs 2011 – 2016 and 2016 – 2018. Alongshore-averaged volumes are presented for north (1400-m alongshore) and south (1400-m alongshore) domains, except for the case of south dunes (100-m alongshore). Dune volume correspond with regions  $> 5$  m ODN, inter-tidal volume from 5 m to -2 m ODN and sub-tidal volume corresponds with the regions from -2 m to -14.5 m ODN. ....92

**Fig. 3.11** Upper panels: 3D variability of Perranporth full embayment where red indicates erosion and blue accretion. Contours are from the first of the beach surveys. In order from 2<sup>nd</sup> to 3<sup>rd</sup> row panels: full embayment erosion (Er.), accretion (Ac.) and net (Net) volumetric change; and volumes for north and south sectors. All volumes are for epochs 2011 – 2016 and seasonal 2016 – 2018. Bottom panels: longshore variation index (LVI) computed using 2-m alongshore-averaged cross-shore profiles (circle) and a low-pass filter with a 400-m span (triangle). ....94

**Fig. 3.12** Time series of wave power and volume observations. (a)  $P_{cum}$  and  $P_{y,cum}$ ; (b)  $P_{cum}$  and  $V_{s,INTER}$ ; (c)  $P_{cum}$  and  $V_{s,TOTAL}$ ; (d)  $P_{y,cum}$  against  $V_{s,TOTAL}$ . For (c, d) grey circles

are the points on wave power time series' interpolated to volume. Southward alongshore wave power is negative..... 99

**Fig. 3.13** Semi-quantitative conceptual sediment budget for Perranporth embayment with volume changes ( $\Delta V_N, \Delta V_S$ ) and cross-shore flux ( $q_{x,N}, q_{x,S}$ ; sed. flux obs.) based on observations. The external flux ( $Q_S, Q_N$ ) refer to both cross- and alongshore contributions.  $Q_S$  and  $Q_M$  are estimated using observations and bypass rate in the northern headland (sed. flux est.). Flux and volume change values are  $\times 10^5 \text{ m}^3$ . + and – symbols refer to magnitude of significant wave height ( $H_s$ ) with (++) for large waves, (-) for low energy wave conditions and (+) for moderate to energetic conditions. Direction ( $Dir$ ) refers to shore normal wave direction ( $Dir \sim 283^\circ$ ) with -S for more southward wave approach (W), and +N to ++N for WNW and NW, respectively..... 103

**Fig. 4.1** (a) Delft3D model grid and transects used for the analysis (thick solid lines). Red dots indicate UK MetOffice Wave Watch III 8 km (WW3) model nodes used as wave input and green dots represent Forecasting Ocean Assimilation Model Shelf Seas Atlantic Margin Model 7 km (FOAM-AMM7) hydrodynamic nodes provided by Copernicus Marine Environment Monitoring Service (CMEMS, 2017). Grid nodes are plotted every 2 points in each direction for clarity. Location A was used for examining boundary conditions for simulated sample cases. (b) Wave rose and (c) joint probability for Perranporth using 11 years of wave buoy data (DWR). (d) Physical context of the study site and instrument positions (squares). Instrument name refers to the location and mooring depth relative ODN, respectively, e.g., AS20 was the ADCP deployed in the south of the bay at 20 m water depth. (e) Oblique Google Earth image of headlands and embayments..... 113

**Fig. 4.2** Example of de-spiking ellipsoid using Goring and Nikora method (2002) for the easting velocity component of the current ( $u$ ) in the bottom bin of AN17.  $\Delta u$  and  $\Delta^2 u$  are the surrogate (not divided by the time step  $\Delta t$ ) of first and second derivative of  $u$  using central differences of  $u$  and  $\Delta u$ , respectively..... 116

**Fig. 4.3** (a) 8-year time series of significant wave height  $H_s$  (30-min and 4-week running mean) and wave power  $P_o$  (Herbich, 2000). Normalised probability of occurrence for  $H_s$  (a), wave direction  $Dir$  (b) and water level WL (d) based on the

complete hindcast from 2011 – 2018, compared to distribution of the selected cases for model runs (dashed boxes in a). (e, f) Distribution of selected cases for the combinations of  $P_o$ , wave direction ( $Dir$ ) and water level ( $WL$ ). All variables correspond to the CMEMS nodes located at the centre of the offshore boundary of the model domain ( $A$  nodes, refer to Fig. 4.1a for location).....122

**Fig. 4.4** Transects (thick coloured straight lines) and contour lines (thick coloured contour lines) used to integrate the longshore and cross-shore sediment fluxes, respectively. ....124

**Fig. 4.5** Wave ADCP observations at AN20 and AS20 compared with Delft3D model output. From top to bottom: significant wave height ( $H_s$ ), peak period ( $T_p$ ), and mean direction ( $Dir_{mean}$ ). Zoomed-in locations of the ADCPs are presented in the small top panels; cf. Fig. 4.1d for large-scale setting of the ADCP locations. ....125

**Fig. 4.6** (a) Water level ( $WL$ ) and flow observations at ADCPs AN20 (a – d) and AN27 (e – g) compared with Delft3D model output over February 2017. Flow observations include: (b, e) northward current component ( $v$ ), (c, f) flow speed and (d, g) direction (current dir.). The observed and modelled current speed and direction are 30-min averages. Low-pass flow speed has a Fourier transform filter applied, with a 25-h cut-off. For reference, observed significant wave height at AN27 (green line in top panel) is presented. Zoomed-in locations of the ADCPs are presented in the small top panel; cf. Fig. 4.1d for large-scale setting of the ADCP locations.....126

**Fig. 4.7** (a) Flow based on observations (black) and model output (red) for a representative tidal cycle at the ADCPs locations. Observations compared with Delf3D model output over February 2017 for (b) water level ( $WL$ ), (c) eastward current component ( $u$ ), (d) northward current component ( $v$ ), and (e) direction at ADCP AS20. The observed and modelled current speed and direction are 30-min averages. Low-pass flow speed has a Fourier transform filter applied, with a 25-h cut-off. For reference, observed significant wave height at AS20 (green line in right top panel) is presented. Zoomed-in location of the ADCP is presented in the small top panel; cf. Fig. 4.1d for large-scale setting of the ADCP location. ....127

**Fig. 4.8** Time-averaged (12.5 h) currents (top panels) with zoom focused on Perranporth embayment (bottom panels) under storm conditions during spring tides. Circulation under moderate-high waves from the W (a, d), WNW (b, e) and extreme waves during storm Hercules, 2013/14 winter (c, f).  $H_s$  and  $Dir$  presented for each scenario correspond with offshore conditions at the A nodes, refer to Fig. 4.1a for location. For reference, embayment names abbreviations are included in first column panels..... 130

**Fig. 4.9** (a) Gross sediment transport (cumulative flux) for the simulated scenarios. Gross longshore fluxes as a function of water depth for T1 – T6 (b – d, f – h) and T-PPT (e)..... 132

**Figure 4.10** Sediment fluxes and transport pathways during major circulation modes (storm conditions during spring tides). Time-averaged (12.5) fluxes (top panels) with zoom focused on Perranporth embayment (bottom panels) under moderate-high waves from the W (a, d), WNW (b, e) and extreme waves during storm Hercules, 2013/14 winter (c, f).  $H_s$  and  $Dir$  presented for each scenario correspond with offshore conditions. The magenta arrows indicate qualitatively major sediment paths. For reference, embayment names abbreviations are included in first column panels. .... 133

**Fig. 4.11** Sediment fluxes during major circulation modes: moderate-high waves from the W, WNW and extreme waves during storm Hercules, 2013/14 winter (bounded areas). Time series of (a, b) significant wave height ( $H_s$ ); (c, d) direction ( $Dir$ ); and (e, f) fluxes integrated around the headland transects ( $Q_{bypass}$ ) and (g, h) over the morphological DoC per embayment/ bay width ( $Q_{cross}$ ). Positive indicates northward and negative represents southward. Bounded areas represent the time period encompassing the scenarios shown in Fig. 4.9. Inset with location of transects and contours used for  $Q_{bypass}$  and  $Q_{cross}$  integration are presented to facilitate interpretation..... 135

**Fig. 4.12** Daily sediment fluxes integrated over two tidal cycles (25 h) versus daily averages of offshore wave forcing parameters ( $Po$  and  $Dir$ ). Upper panels: sediment fluxes integrated over the selected transects (refer to Fig. 4.1 for location) with positive values corresponding to northward fluxes and negative to southward. Bottom panels: sediment fluxes integrated over the 15-m contour line (averaged DoC for the

embayments/bays of study). Positive values represent inflows to the embayment and negative values correspond with outflows. Empty circles represent sea states during neap tides whereas filled markers depict spring tides. ....136

**Fig. 4.13** 8-year cumulative headland bypass volumes ( $Q_{bypass}$ ) for T1 (a) and T3 – T6 (b – e). Positive (negative) values are northward (southward). Grey-patched area indicates cumulative uncertainty bounds (95% confidence based on the statistical model) for the prediction. ....139

**Figure 4.14** (a) Predicted total sediment budgets ( $dQ_{net}/dt$ ) and net headland bypassing ( $Q_{bypass}$ ) and associated uncertainty bounds (95% confidence based on the statistical model). (b) Planform sediment budget model for Chapel Porth, St. Agnes, Perranporth, Hoblyn's Cove and Holywell over 2011 – 2018. Arrows indicate qualitatively net headland bypassing paths. Arrows and circles size represents magnitude. ....141

**Fig. 5.1** Embayment-scale sediment dynamics conceptual model for Perranporth beach based on observations and numerical modelling simulations. Light and dark brown coloured areas correspond to the upper and lower shoreface, respectively.....151

**Fig. 5.2** Conceptual diagram of major alongshore sediment fluxes pathways for a period of (a) mild waves, (b) moderate-high waves and (c) higher than average wave. Arrows (size increases with increasing magnitude) indicate predicted residual fluxes based on model output. Accretion due to cross-shore fluxes is shown in beige. Idealised limits of the active shoreface Depth of Transport ( $DoT$ ) and Depth of Closure ( $DoC$ ) are presented as dot and dashed lines, respectively. ....156

## List of tables

---

<b>Table 2.1</b> Deep-water wave climate statistics for the selected regions using hourly wave model outputs from the MetOffice UK Waters Wave Model, 2013 to 2016. ....	35
<b>Table 2.2</b> Dependence of critical shear stress values ( $\text{N m}^{-2}$ ) with sediment size for the considered scenarios: sediment motion, initiation of vortex ripples, initiation of post-vortex ripples and plane bed.....	53
<b>Table 2.3</b> Summary of results for the predicted shoreface limits along the SW of England. Region-averaged values of <i>DoC</i> , <i>DoC-motion</i> , sand-rock transition depth, <i>DoT</i> and associated along-coast standard deviation ( <i>SD</i> ) using the different formulations are presented.....	58
<b>Table 3.1</b> Component gridded datasets and calculated uncertainty ( $\sigma$ ) included in the 3 full embayment <i>DEMs</i> .....	76
<b>Table 3.2</b> Net volumetric changes ( $\text{m}^3$ ) and associated uncertainty in sub-tidal, inter-tidal and dune sub-systems for epochs 2011 – 2016 and 2016 – 2018. Volumes are presented for north and south domains. Inter-tidal volume corresponds with the area from the dune foot ( $z = 5 \text{ m}$ ) to $-2 \text{ m}$ and sub-tidal volume corresponds with the area from $-14.5$ to $-2 \text{ m}$ , inter- and supratidal from $-2$ to the dune foot ( $z = 5 \text{ m}$ ) and dunes beyond $z = 5 \text{ m}$ .....	92
<b>Table 3.3</b> Correlation coefficients ( $r$ ) for Perranporth southern sector beach volume and cumulative wave power (total and alongshore). Bold values are significant ( $p\text{-value} < 0.01$ ).....	98
<b>Table 4.1</b> Delft3D model settings. ....	120
<b>Table 4.2</b> Model validation coefficients.....	128
<b>Table 4.3</b> Best fitting parameters for Eq. 4.1 based on correlation between modelled sediment fluxes and offshore wave forcing conditions. ....	138

## Acknowledgements

---

Firstly, I would like to give a huge thank you to my Director of Studies Prof. Gerd Masselink who have provided me with a lot of expertise, inspiration and enthusiasm for the research. Thank you for the opportunity and for believing in that Spanish girl with a questionable English. You have been an incredible supervisor and I can only hope to be able to work with you in the near future. I would also like to thank my supervisors Dr. Tim Scott and Prof. Daniel Conley who have also provided me a continued support throughout this PhD. A massive thank you to Dr. Jak McCarroll, my other “half” supervisor who always had a research idea to share. “McCrack”, all the research outputs over the last years would have not been possible without your help. Thank you all.

I also want to thank all my field/office colleagues and now friends Mark (aka Lord Wiggo), Oli, Erin and Olivier. I enjoyed every minute we have spent together driving to Perranporth or Slapton, attending conferences or just having a coffee at Drakes Cafe. This journey would have not been the same without all the beers, dinners and many laughs with you. Many thanks to Hannah, Francesco and Jose, it has been great to get to know you in this Plymothian adventure. Thanks for the support from the distance to my Spanish friends: Laura, Judith, Cristina, Marta, Luis, Jose, Jaime, Maider and Noe. Special mentions to Saruka, Mariona and Alberto; best friends and amazing coaches. You always find time to cheer me up, a million thanks are not enough.

A particularly huge acknowledgement goes to my family. The biggest thanks to my mum and my sister, the strongest women I know. You encourage me to move to another country and pursue my career as a researcher. Thank you for the support, the many visits and your strong belief in my potentials. Mami, todas las gracias que pueda escribir aquí no son suficientes para lo que tú te mereces; lo único que puedo decir es que sin ti todo esto no hubiera sido possible y que te adoro. Calan, recuerdo que tú fuiste principalmente la que me animó a dar el paso de hacer el doctorado y mudarme a Plymouth; muchas gracias por ser la mejor hermana del mundo, cuidar de mamá y ser como eres. Os quiero.

Last but not least, *grazie mille*. This PhD is also yours.



# Chapter 1 – Introduction

---

## 1.1 Context

Embayed beaches constitute a large proportion of the world's rocky coastlines (Inman and Nordstrom, 1971). The north coast of SW England represents an ideal example of this type of setting providing a large variability of embayed sandy beaches. For a beach to be considered embayed, it must be delineated by headlands (or coastal structures), which significantly influence the dynamic processes affecting the beach. Moreover, embayed beaches are often deemed closed sediment cells with headlands acting as barriers to littoral drift and studies focused on the physical coupling between the beach and its outer region, generally considered relatively weak, are relatively scarce.

Recent studies of beach storm response and evolution emphasize that substantial transport occurs to large depths highlighting the potential inability of certain embayments to recover after a cluster of storms. Niedoroda and Swift (1981) showed that sediment may be permanently lost to the inner shelf during storms. Later, Wright et al. (1995) studied the surf zone processes connected to the inner shelf from a morphodynamic point of view, finding that part of the infragravity oscillations contributing to cross-shore transport and reaching the inner shelf area were originated in the surf zone. Additionally, Short (1985) stated that major storm wave events are one of the key drivers to explain headland-attached bar bypassing, allowing sand to be transported well offshore and outside of the headland position. More recent studies of mega-rips and beach response to extreme storm events along embayed coastlines also point in this direction (Gallop et al, 2011; Loureiro et al., 2012a; Castelle and Coco, 2012, 2013), revealing that a significant amount of sediment can be ejected outside the surf zone (Castelle and Coco, 2012, 2013), and between adjacent beaches through headland bypassing (Cudaback, 2005; Vieira da Silva et al., 2016). Despite these latest efforts (e.g., Hendrickson and MacMahan, 2009; Aagaard et al., 2010; Loureiro et al., 2012a; Castelle and Coco, 2012, 2013), key processes (e.g., mega-rips, headland bypassing), driving forces, flux rates and local factors such as headland/embayment morphometric

parameters or sediment availability, influencing the sediment exchange between the beach and adjacent areas (e.g., lower shoreface, neighbouring bays) are still poorly resolved.

Because long-term local beach response along embayed coastlines is often influenced by sediment exchanges with other depositional environments of a larger sediment-sharing system, a better understanding of the physical coupling between the embayments and neighbouring areas is of high value to increase our ability to predict coastal evolution and forecast coastal impacts due to climate change. This study will not only contribute to the knowledge of the processes affecting coastal vulnerability and long-term evolution of embayed beaches worldwide, but ultimately will help informing future management strategies for the high-energy and sediment starved (deficit of sediment offshore and limited natural sediment supply) north coast of SW England.

### **1.2 Overview of thesis aims**

The over-arching aim of this thesis is to improve our understanding of the sediment dynamics and linkages between the surf zone and the inner shelf along embayed coastlines at a decadal scale, implementing a combined approach of morphologic and hydrodynamic field observations, and numerical modelling. Using the north coast of SW England as a test site, approaches followed to address this aim include: (i) estimating the depth of closure in relation to the depth in front of the bounding headlands (Chapter 2); (ii) beach topographic and bathymetric surveys to compute volumetric changes and derive a sediment budget (Chapter 3); and (iii) numerical modelling using a process-based model (Delft3D) to infer the major sediment transport pathways (Chapter 4).

Detailed formulation of the aims and structure of this thesis is described in Section 1.5; here, the aims are briefly introduced to provide the connection to the main points covered by the review in Section 1.3. The first part of the research focuses on the investigation of depth of closure and maximum depth of transport following a multi-criteria approach along six regions of a macrotidal, high-energy and embayed coast (Chapter 2). The aim of this part of the study is to (i) examine the potential for headland

bypassing along different types of rocky coastline. Analysis of multi-annual morphodynamic response on an exposed, macrotidal and embayed sandy beach (Chapter 3) based on field observations is conducted during the second stage of the research. This embayment is located in one of the regions studied in the first part of the investigation and the aims are to (ii) evaluate the inter-annual dynamics over multi-annual time scales, and (iii) investigate whether the coastal cell is open or closed. The last part of the research implements the numerical model Delft3D along a 15-km stretch of coast (Chapter 4), encompassing the monitored embayment, and aims to (iv) infer the major sediment transport pathways between adjacent bays and the embayment of study.

### 1.3 Review

The following section serves as a brief overview and state of the art of different aspects of coastal dynamics in embayed beaches relevant to the thesis topic. The subjects covered are: (i) embayed beaches globally; (ii) embayment morphodynamics with particular emphasis on parameters and mechanisms affecting sediment exchange with neighbouring areas; and (iii) observations and numerical methods to quantify the sediment exchange between the beach and the inner shelf. Further specific overview pertinent for each thesis aim is presented in Chapters 2 – 4.

#### Terminology

A brief review in terminology is required to elucidate some concepts of the coastal system that will be mentioned in the thesis. This terminology mainly concerns the definition of areas (e.g., inner shelf, shoreface) and theoretical concepts (e.g., depth of closure) that have been fully described in the literature but have not always been applied consistently. Therefore, the morphodynamic approach followed in the rest of the study uses the following definitions for the relevant terms:

- Continental shelf – area which controls physical oceanographic processes that drive coastal behaviour (Wright, 1995). This submarine region goes from the surf zone to the shelf edge and can be divided into the shoreface and the inner, mid and outer shelf.

- Inner shelf – area immediately seaward of the surf zone and sub-region of the continental shelf. This area is defined as dynamically, morphologically and sedimentologically contiguous with beaches (Wright, 1995). Hendrickson and MacMahan (2009) suggest that the offshore extent of this area is controlled by the surface bottom stress and the stratification of the water column.
- Shoreface – active littoral zone seaward of the low water line. This area can be divided into upper and lower shoreface. The upper shoreface includes the region where the effects of wave energy dissipation dominate (surf zone), while the lower shoreface is dominated by bed interactions from shoaling waves (Stive and de Vriend, 1995).
- Depth of closure ( $DoC$ ) – or morphological depth of closure is defined as the short-term (1 – 10 years) limit of ‘significant’ bed-level change. This vertical change must be measurable and is thus constrained by survey instrument accuracy, which is  $O(10\text{ cm})$ . Consequently, for dissipative shorefaces, where maximum vertical changes are small, this limit appears too conservative as it represents large amount of sediment when integrated over the shoreface. An extended description of this limit is provided in Chapter 2, Section 2.1.
- Depth of transport ( $DoT$ ) – the maximum water depth for intense bed agitation or transition to flat bed. This limit is described in more detail in Chapter 2, Section 2.1.
- Embayed beach – beach that is delineated by headlands. Hereafter, the term short (long) embayment refers to those beaches with small (large) longshore distances between the bounding headlands. Hence, embayments  $< 1\text{ km}$  long will be considered short and vice versa.
- Low tide embayment ( $LTE$ ) – embayed systems that represent a single embayment at low tide but may be split up into smaller beaches at high tide.
- Coastal/ littoral cell – coastal compartment within which sediment movement is self-contained.
- Up-wave (down-wave) headland – the headland toward (from) which the wave-induced flow would travel.

### 1.3.1 Embayed coastlines

Rocky coastlines are characterised by a wide range of geomorphological settings that cover from cliffs and rocky platforms to pocket and sandy embayments. The latter are common worldwide inspiring a large number of studies focused on the role of the inherited geology in defining the morphodynamic beach response (e.g., Short and Masselink, 1999; Klein et al., 2010; Scott et al., 2011; Castelle and Coco, 2012; McCarroll et al., 2016). Furthermore, recent studies indicate that the range of embayment responses to changes in wave climate are more limited compared to beaches in open coasts (McNinch, 2004; Jackson et al., 2005) as the geological factors (headlands) seem to regulate both sediment source and volume of accommodation space at mid- to long-temporal scale (years to decades). Conversely, embayed beaches appear more dynamic environments at shorter temporal scales (days to season) which often result in the presence of very characteristic morphological patterns such as offshore bars and rips (e.g., Holman et al., 2006; Gallop et al., 2011; McCarroll et al., 2014; Masselink et al., 2014; Scott et al., 2016).

Some examples of sandy embayed coastlines worldwide comprise the W coast of U.S., New South Wales (NSW) and Victoria coast of Australia, and the Atlantic coast of Europe. All these regions occur in a similar geologic setting of alternating sediment-free areas and embayed sectors delineated by sharp headlands, but differ in the sediment availability, degree of embaymentisation and/or the hydrodynamic forcing. Hence, similar embayed coastlines can display different responses to the same wave forcing conditions and vice versa. One of the most studied regions is the coastline in San Diego where, despite that sediment supply brought by river streamflow during wet periods seem to naturally nourish the littoral cells (Inman and Scott, 1998), the large offshore losses at submarine canyons and an extensively modified coastline provoke an imbalance between the sediment gains and losses with a constant loss of sand. Similarly, for the NSW coast of Australia, the net northward sand transport and the offshore sediment deficit result in persistent and ongoing shoreline recession (Kinsela et al., 2017). Consequently, persistent losses of sand in these coastlines constitute potential present and future asset exposure to coastal erosion.

Similar response patterns where local beach dynamics are influenced by sediment exchanges with neighbouring areas are also observed along some stretches of the Atlantic coast of Europe. An example is the bedrock-dominated coast of southwestern Portugal (Fig. 1.1E) where beaches occur generally in narrow bays associated with small streams or in coastal re-entrants along greywacke cliffs (Loureiro et al, 2012b). Despite being a very different geologic setting, this coast showed similar storm response to embayments located in the SW of England (Fig. 1.1B) or the rocky west coast of France (Fig. 1.1C) during extreme winters (Masselink et al., 2016). Conversely, the latter displayed a much faster recovery, possibly due to more energetic waves (e.g., Castle et al., 2017), than the other W Europe sandy beaches, where limited sediment supply plays a major role on beach evolution (Scott et al., 2016; Burvingt et al., 2017).

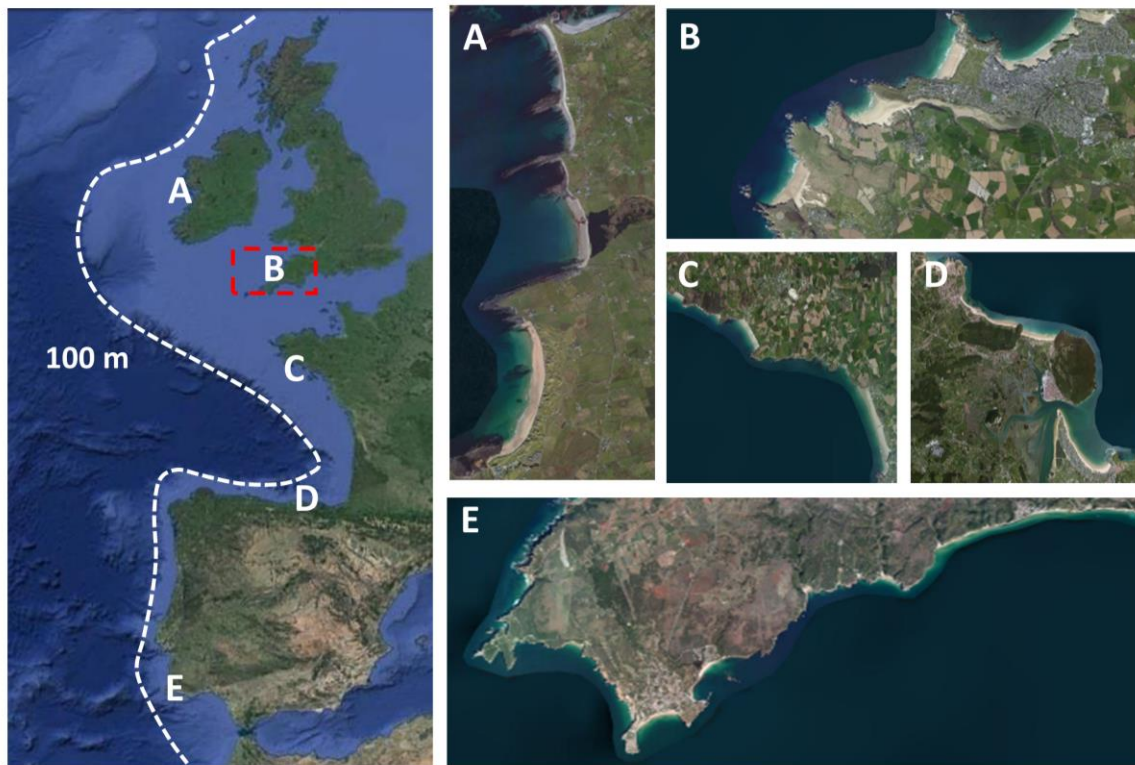


**Fig. 1.1** Examples of rocky coastlines in Europe including the study site (red box): (A) W Ireland, (B) N coast of SW England, (C) Brittany coast, (D) N Spain, and (E) S Portugal. White dashed line represents the edge of continental shelf.

### 1.3.2 Morphodynamics along embayed coastlines

Sediment transport is a dynamic process resulting from a number of coastal hydrodynamic processes, such as currents (tide, wave, density or wind driven), turbulence, wave motions, and their interaction with the sediment particles (Wright, 1995). For geologically constrained coastlines described by different morphometric parameters, headland bypassing and embayment-scale circulation are the main mechanisms responsible for sediment exchange between embayments and their neighbouring areas. Concepts are described here separately, although it is noted that headland bypassing can be a consequence of the hydrodynamic forcing around headlands derived from the different types of embayment-scale circulation.

#### 1.3.2.1 Embayed beach morphometric parameterisation

The orientation and the planform of embayed beaches are controlled by the refraction and diffraction associated with the prevailing swell waves (Davies, 1958). Embayed planform is based on the parabolic shape proposed by Hsu et al. (1989b). The first control point (upcoast) is the diffraction point (headland or coastal structure) around which the incident waves diffract as they propagate into the embayment. Along embayed coastlines, the second control point (downcoast) will be the second headland or, for larger embayments, the straight section where the shoreline is parallel to the incident waves. Hence, the parabolic equation provided by Hsu et al. (1989) derives the ratio between a series of lines with length  $R$  from the diffraction point to the beach at an angle  $\theta$  to the wave crest, and the control line or line connecting the control points of length  $R_0$ :

$$\frac{R}{R_0} = C_0 + C_1 \left( \frac{\beta}{\theta} \right) + C_1 \left( \frac{\beta}{\theta} \right)^2 \quad (1.1)$$

where  $\beta$  is the angle between the wave crests and the control line or wave obliquity and  $C_{0,1,2}$  (-1 – 2.5) are coefficients given in Hsu and Evans (1989a). Fig. 1.2 shows the equilibrium bay shape for a single headland (Fig. 1.2a) and for double-headland (Fig. 1.2b). Whereas the planform parabola proposed by Hsu et al. (1989b) only applies to embayed beaches in static equilibrium with no littoral drift within the bay, embayed

beaches can also be in dynamic equilibrium with the wave climate and the sediment supply. Conversely, cases such as the examples previously discussed along the NSW coast of Australia where the sediment supply of a bay is either reduced or cut off, are in disequilibrium.

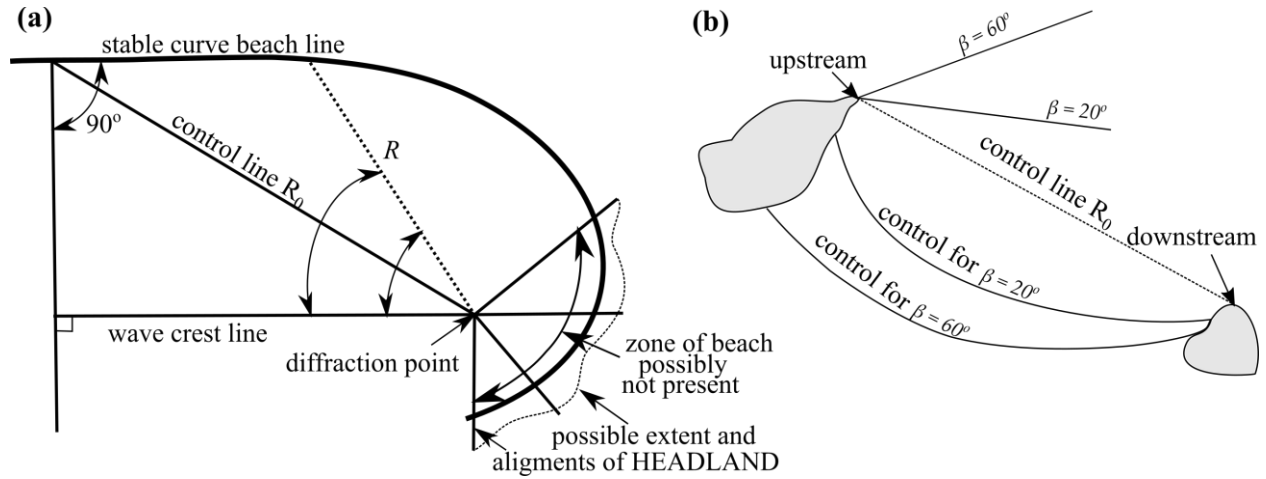


**Fig. 1.2** (a) Definition sketch of the parabolic approach to bay shape (after Hsu et al., 1989a). (b) Example of equilibrium bay shape calculated using Eq. 1.1 for variable wave obliquity,  $\beta = 20^\circ$  and  $60^\circ$  (Source: Short and Masselink, 1999).

For non-parabolic embayment planform shapes, a widely used parameter is the non-dimensional embayment scaling factor ( $\delta'$ ) proposed by Short and Masselink (1999) (Fig. 1.3a) and revised ( $\delta$ ) by Castle and Coco (2012). The main difference between both approaches lie in beaches with pronounced headlands, where  $\delta'$  underestimates headland impact as it assumes equal wave energy distribution along the shoreline. The non-dimensional embayment scaling factor provides a classification for circulation types and is related to the number of surf zone widths ( $X_s$ ) that can fit into the total embayment length ( $S$ ) of the form:

$$\delta' = S^2 / 100 R_0 H_b \quad (1.2)$$

where  $H_b$  is the breaking wave height and  $R_0$  is the control line or distance between headlands. For a beach of length  $L$  with a slope ( $\tan\beta$ ) exposed to waves of significant wave height  $H_s$ , the surf zone width ( $X_s$ ) can be described as  $X_s = H_s / (\gamma_b \tan\beta)$  where  $\gamma_b$  is the breaker index (Battjes and Stive, 1985). Hence, according to Castle and Coco (2012)  $\delta$  can also be parameterised as follows:

$$\delta = \frac{L}{X_s} = L\gamma_b \tan\beta / H_s \quad (1.2)$$

Common morphometric parameters to classify embayed beaches presented in Fig. 1.3b (Fellows et al., 2019) include: headland orientation ( $\theta_h$ ), embayment indentation ( $a$ ), embayment area ( $A_e$ ), alongshore beach length ( $R_0$ ) between the headland boundaries, total embayment length ( $S$ ) and shadowed beach length ( $X_{sh}$ ). Some combinations of these parameters to determine the impact of embaymentisation were also proposed by Fellows et al. (2019), e.g., the embayment morphometric parameter ( $\gamma_e = a/\sqrt{A_e}$ ). Additional parameters based on headland geomorphic and bathymetric characteristics, and used for embayed beach classification, are: headland perimeter ( $P_e$ ; Fig. 1.3c), apex angle ( $\alpha_{up}$ ,  $\alpha_{dn}$ ; Fig. 1.3c) and nearshore bathymetric slope ratio across the headland (George et al., 2015) defined by the ratio of the upstream (transects A and B) to downstream (transects C and B) median (Fig. 1.3d).

Embayment and headlands morphometric parameters are only used as a tool for embayment classification. Although all these parameterisations are not directly applied in this research, their combination with the hydrodynamics affecting the embayment should deliver the broad picture necessary to provide more complex parameterisations (e.g., prediction of bypassing rates) for the morphodynamics along embayed coastlines.

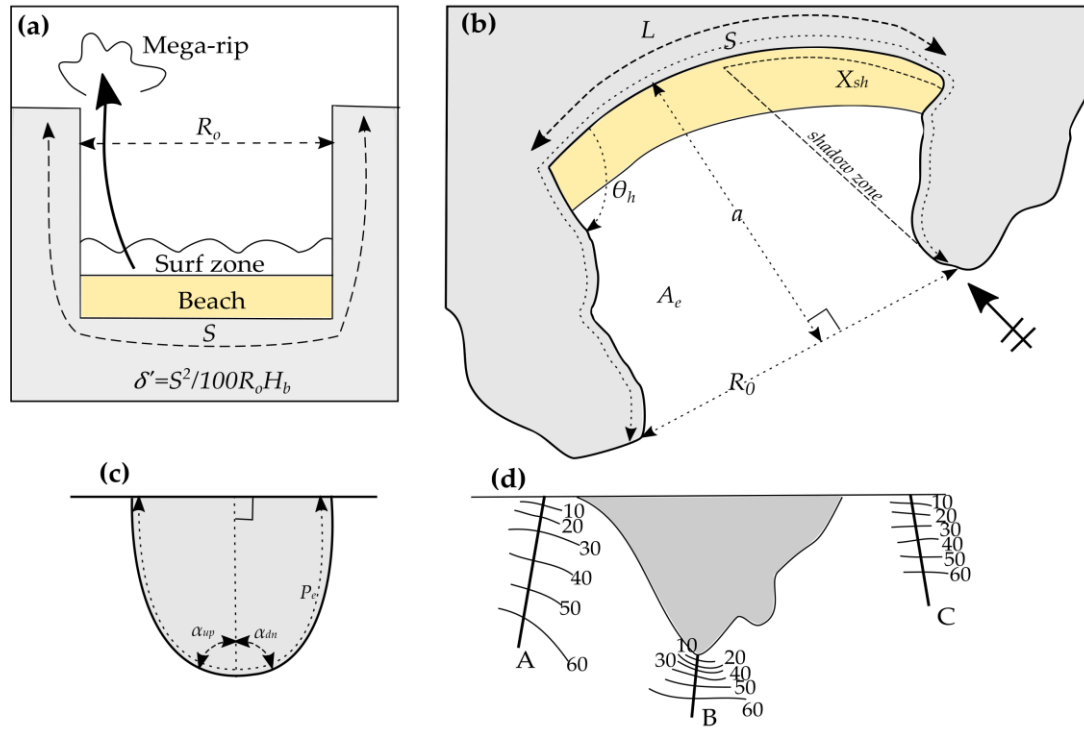


**Fig. 1.3** Common morphometrics for embayment/headland classification. (a) Non-dimensional embayment scaling factor ( $\delta'$ ) as per Short and Masselink (1999) with width between headlands ( $R_0$ ) and total embayment length, including beach and headlands ( $S$ ). (b) Embayment morphometric parameters as per Fellows et al. (2019). Embayment area ( $A_e$ ), embayment indentation ( $a$ ), headland orientation to beach aspect ( $\theta_h$ ) and shadowed beach length ( $X_{sh}$ ). (c) Schematics of headland geomorphic parameters as per George et al. (2015). Headland perimeter ( $P_e$ ) and apex angle ( $\alpha_{up}$ ,  $\alpha_{dn}$ ). (d) Example of schematic of transects and bathymetry (contours 10 – 60 m depth) used to compute the nearshore bathymetric slope ratio across the headland as per George et al. (2015). A and C are reference transects and B is the headland transect.

### 1.3.2.2 Embayment-scale circulation

Embayment-scale circulation can be defined by the degree of headland control on the beach type (Martens et al., 1999; Short and Masselink, 1999): (i) ‘normal’ beach circulation (Eq. 1.1 and 1.2;  $\delta' \geq 20$  or  $\delta \geq 16$ ) on long beaches, with no geological control and rip cells occurring along the beach (Fig. 1.4d); ‘intermediate’ or ‘transitional’ circulation (Eq. 1.1 and 1.2;  $\delta' = 9 - 19$  or  $\delta = 8 - 15$ ) with both along-spaced rip channels and headland rips occurring on embayments with moderate headland control (Fig. 1.4c); and (iii) ‘cellular’ circulation (Eq. 1.1 and 1.2;  $\delta' \leq 8$  or  $\delta \leq 9$ ) normally occurring on short embayments where strong geological control exists and either two large headland rips or one central rip channel (Fig. 1.4a,b) are present. The latter is often described as

mega-rip and can be defined as large-scale erosional rips driven by headland-forced alongshore energy that can reach up to 1 km offshore (Short, 1985).

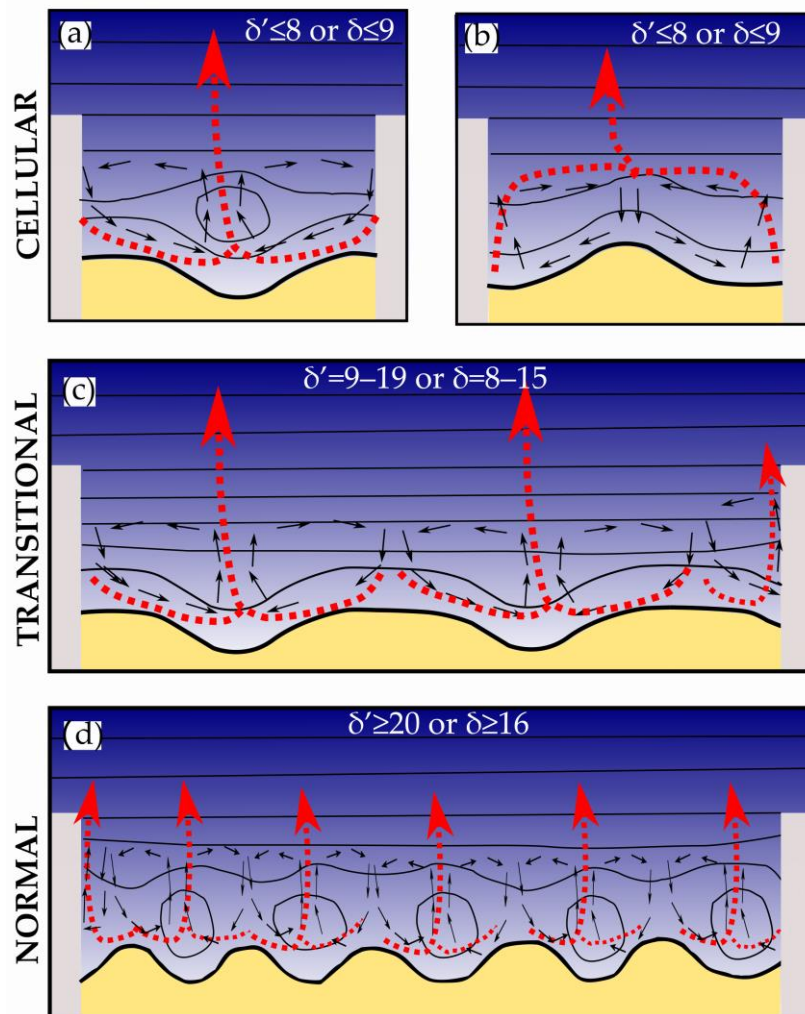


**Fig. 1.4** Modes of embayment circulation and rip channel configurations based on Short and Masselink (1999) and Castelle and Coco (2012). Cellular circulation with a rip developing at the centre of the beach (a) and with headland rips (b). (c) Transitional circulation with a rip occurring at one end of the embayment and two additional rips. (d) Normal circulation with rips at both headlands and four additional rips. Preferred flow paths of surf zone exits are indicated by the red arrows.

Castelle and Coco (2012) reproduced the different circulation patterns observed from field observations in Short and Masselink (1999). Using modelling simulations, they found that 'cellular' circulation in short embayments with small curvature facilitate headland rips, whereas the central rip appears in short embayments with large curvature. Both 'transitional' and 'normal' beach circulation occur in intermediate to long embayments and the major difference between both circulation modes resides in

the wave obliquity and beach length: increasing beach length and/or wave angle results in embayments that tend to behave as an open beach with no geological constraint by the headlands. Recently, McCarroll et al. (2018) found an extra circulation mode of larger spatial-scale: the 'multi-embayment' circulation. This circulation mode occurs in embayments where extreme waves break beyond the shallower headlands and the developed circulation encompass several bays.

Mega-rips are often associated to short (small beach alongshore length) embayments where headland control induces two alongside headland mega-rips on straight beaches or a central mega-rip on curved beaches. Castle and Coco (2013) studied the role of headlands in governing ejection outside the surf zone using simulations of passive tracers. They showed that the surf zone of embayed beaches systematically flushes out more floating material than in open beaches, with most exits occurring through the headland rips. Additionally, they found that for beaches in embayments up to c. 1 km long, a longshore current meandering over the bar and rip patterns develops and is further deflected offshore against the downwave (respect the predominant direction of wave approach) headland. Later in this thesis (Chapter 4), it will be demonstrated that mega-rips are a major process to eject sediment offshore in longer embayments (> 3.5 km).

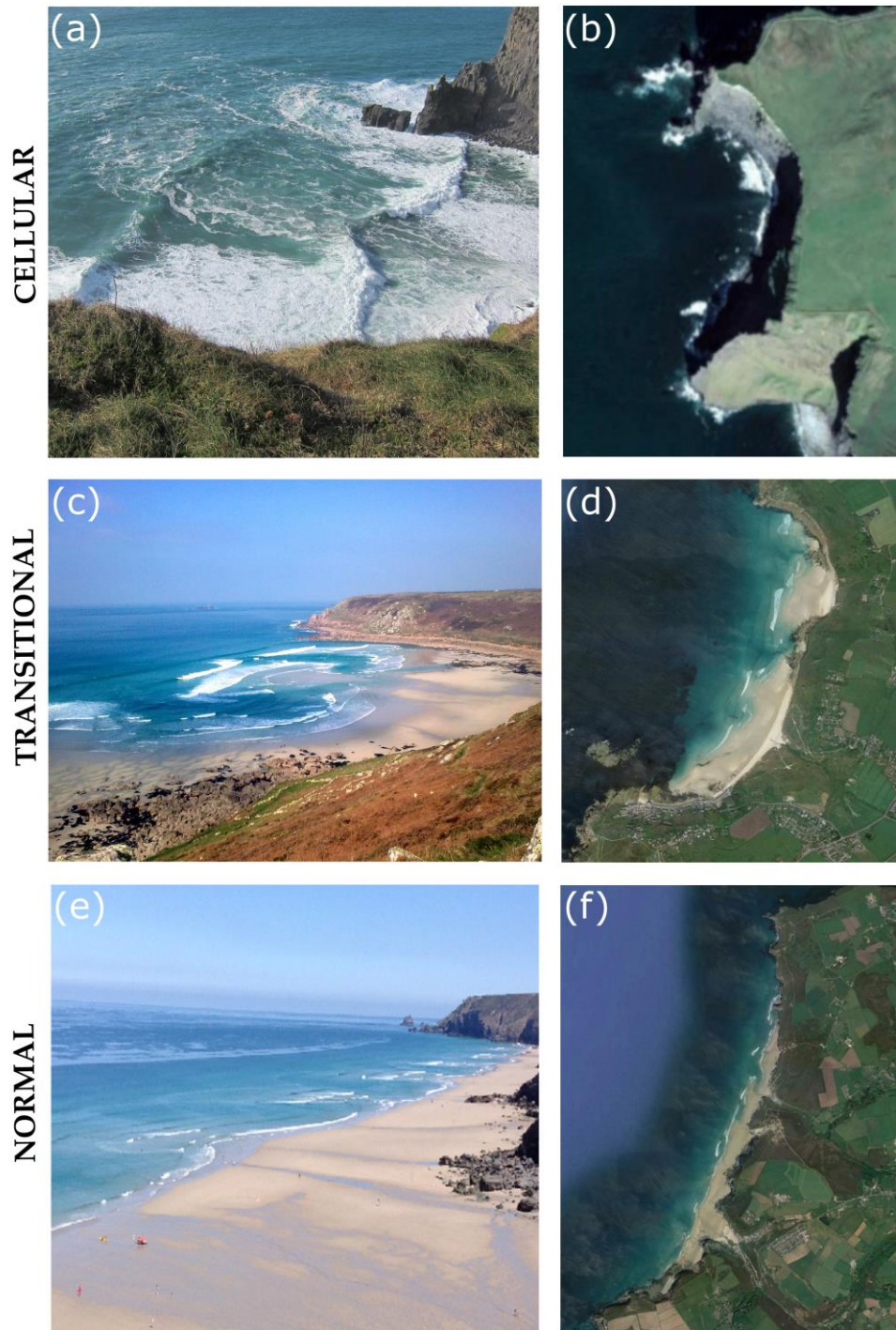


**Fig. 1.5** Examples of embayment-scale circulation on embayed beaches. Oblique (left panels) and aerial (right panels) images of: (a–b) embayment-cellular rip circulation at Aileens, County Claire, Ireland; (c–d) transitional circulation at Sennen-Gwynver beach, SW England; and (e–f) normal circulation at Porthtowan, SW England. Image sources: Tim Scott, DRIBS project and Goggle Earth.

### 1.3.2.3 Bypass mechanisms

Evans (1943) first introduced the concept of sand bypassing around headlands as the process of sediment transport around rigid obstructions induced by waves and mean currents. Headland bypassing was qualitatively described by Short and Masselink (1999): sand is accumulated on the updrift side of the headland (lower panel-Fig. 1.6, situation A); the longshore sediment transport partially assisted by beach rotation pushes sediment to the tip and immediately downdrift of the headland (lower panel-Fig. 1.6, situation B); the accumulated sediment is then moved as an offshore bar along the downdrift side of the headland (lower panel-Fig. 1.6, situation C) until it is attached to the beach (lower panel-Fig. 1.6 situation D). This headland bypass mechanism is also mentioned in Goodwin et al. (2013) as one of the possible mechanisms for bypass: (i) headland attached bars that gradually migrate around the headland in moderate- to high-energy waves (Short and Masselink, 1999); (ii) mega-rip (Fig. 1.6) bypassing during extreme events, with sediment transported by the rip current beyond the headland (McCarroll et al., 2018; Loureiro et al., 2012a); and (iii) across-embayment bypass, where sediment is transported directly across an embayment to deeper water from where sediment may not be transported back onshore. The latter is often associated with 'open beach' rip currents. This rip type occurs on open coastlines and embayed beaches where beach morphology is characterised by alternates of deep channels and shore-connected shoals. These rip currents can be erosional or accretional, depending on the dynamic transitional state: downstate or upstate, respectively (Short, 1985; Austin et al., 2013; Masselink et al., 2014; Poate et al., 2014).

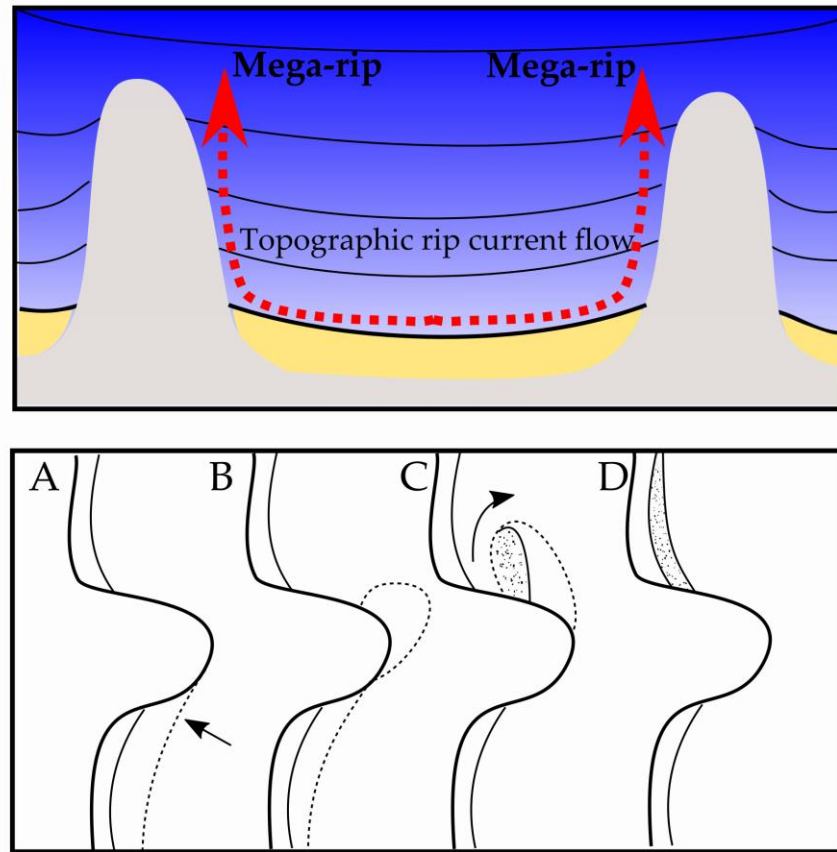


**Fig. 1.6** Upper panel: Representation of the headland structural impact on shoreface current circulation. (Modified from Short and Masselink (1999)). Bottom panel: Schematic illustration of headland-attached sand bar/spit bypassing. (A) Updrift accumulation; (B) headland sub-aqueous sand wave; (C) downdrift attached sand bar/spit; (D) advancing of sand wave and erosion rip merges with downdrift beach (extracted from Short and Masselink, 1999).

Observations of open beach rip currents (or away from the headlands) on multi-bar beaches indicate that different bar transitional states can be identified for the inner-outer bar system. As reported by Masselink et al. (2014), these upstate/ downstate sequences are associated with wave action; therefore, a gradient in wave exposure will lead to a spatially variable state (alongshore variability). The inner-outer bar system generally exhibits an out-of-phase relationship, where the landward pointing horns of the outer bar coincide with the seaward pointing salients of the inner bar system, attributed to the dominance of parallel wave approach (Castelle et al., 2010a,b) and dominant cross-shore sediment transport. Under such conditions, advected sediment from the inter-tidal beach is deposited in the outer bar by the bed return flow currents aided by the rip currents (Scott et al., 2016). Furthermore, under large wave conditions

sediment can be advected further offshore due to mega-rip formation, resulting in large amounts of sediment removed from the beach and transported to the lower shoreface and often outside the embayment limits.

### **1.3.3 Quantification of sediment exchange between the beach and the inner shelf**

This thesis investigates the sediment transport dynamics along embayed coastlines using a combination of morphologic and hydrodynamic observations, complemented by numerical simulations. Hence, a brief state of the art of both in-situ observations and existing models for inferring sediment transport is presented.

#### **1.3.3.1 In-situ observations and beach evolution**

Techniques for making field observations of both the beach morphology and the hydrodynamics are considered an important aspect of this research (Chapter 3 and 4, respectively). Two types of observations can be developed to study sediment transport exchange between the beach and the inner shelf: (1) morphological measurements to derive net sediment fluxes; and (2) in-situ measurements of waves, currents and sediment fluxes.

Beach morphological change is the result of time-integrated sediment transport and consequently estimates of net sediment transport over different epochs can be obtained from morphologic changes in the beach. Direct measurements of beach morphology have been widely employed to infer sediment transport rates from changes in beach volume (e.g., Chesher et al., 1981; Backstrom et al., 2009; Fontan et al., 2012; Goodwin et al., 2013), but often only subaerial changes are assessed. Hence, the approach followed in this thesis to understanding sediment exchanges between the beach and the inner shelf is to monitor the redistribution of sediments within the coastal depositional system using 3-dimensional topo-bathymetric surveys that cover from the dune ( $> 30$  m) to the lower shoreface ( $< 40$  m depth). This seems an easy task for closed systems where sediment losses in a sector will lead to sediment gains within the system. However, for embayments with sediment imbalance or not closed, it is assumed that these depositional environments are connected to adjacent depositional systems, being

part of a larger sediment-sharing area that is more or less contained. Sediment budgets can then be applied as a tool to quantify sediment fluxes within and in/out the system, but need to be assisted by in-situ measurements or numerical modelling to provide additional explanation of sediment pathways and processes responsible for the sediment transport.

In order to interpret sand transport mechanisms from sequential shoreface topobathymetric comparisons for the embayment as a whole over a particular time scale, it is essential to combine different types of instrumentation. A number of techniques have been developed to monitor subaerial coastal morphology such as RTK-GPS (Real-Time Kinematic Global Positioning System) (Scott et al., 2016), LiDAR (Light Detection And Ranging) technology (e.g. Burvingt et al., 2016) or UAV (unmanned aerial vehicle) (e.g., Wiggins et al., 2019). For the sub-tidal realm, single-beam (Masselink et al., 2014; Poate et al., 2015) and multi-beam (e.g., Valiente et al., 2019b) bathymetric techniques are broadly used to extend the spatial coverage of the topographic surveys to the sub-tidal domain. In recent years, the improvement of acoustic tools resulting in multibeam datasets used as cartographic information has also contributed to the accurate interpretation of the seabed configuration (e.g., Goff et al., 2010; Record et al., 2014), helping to identify offshore morphodynamic features and informing of possible linkages between the beach and adjacent areas. This morphology-based method can provide valuable information when combined with morphological measurements and/or in-situ measurements.

Beach evolution is the natural constant change of beaches as nearshore currents and waves move sediments inside, outside and within the nearshore zone (Mentaschi et al., 2018). Consequently, in-situ measurements of the hydrodynamics and sediment fluxes help to better understand the processes inducing beach changes. Several field studies have been conducted in order to measure high frequency hydrodynamic processes near the bed and sediment resuspension (e.g., Storlazzi and Ja, 2002; Warner et al., 2012). However, direct observations of sediment transport using in-situ instrumentation, such as sediment tracers (Duarte et al, 2014), sediment trapping methods (Vieira da Silva et al., 2016) or turbidity data (George et al., 2018), are limited

due to the energetic and hazardous conditions during which sediment transport beyond the beach limits occurs. Although this type of observations provide important information on hydrodynamics (tides, waves, and currents), composition of the bed and suspended sediment transport, the addressed problems will only be on a localised scale (e.g., George et al., 2018) and additional observations and/or numerical simulations will be necessary to infer sediment fluxes in a larger spatial scale (e.g., embayment-scale).

### 1.3.3.2 Modelling of sediment transport

Numerical models are an important tool to investigate the dynamics that drive sediment transport and help interpret and further explore the field observations. Numerical models can be classified as process-based and behaviour-based (Amoudry and Souza, 2011): behaviour-based models (e.g., Plant et al., 1999; Ashton and Murray, 2006a,b; Yates et al., 2009; Davidson et al., 2010; Splinter et al., 2014) are focused on representing long-term (yearly to centennial) response through simple parameterisations of the general behaviour of the morphodynamic system; whereas process-based models (e.g., Brown and Davies, 2009; Vieira da Silva et al., 2018; McCarroll et al., 2018; King et al., 2019) try to represent all the processes driving the sediment transport, being more appropriate for short-term (hours to days) to medium-term (days to months) response.

Sediment transport can be explained as a combination of its cross-shore and longshore component. Cross-shore transport (transversal to shoreface) and longshore gradients in the longitudinal transport cause modifications in the shoreface profile, while longshore transport and its longshore gradients are the responsible of transport between sections, causing planform changes in the shoreface. In this sense, shoreface change can be model evaluating both cross-shore or longshore changes using profile evolution (e.g., Aagaard and Hughes, 2017; Bernabeu et al., 2003; Stive and de Vriend, 1995) and contour line evolution models (e.g., Hurst et al., 2015; Ashton et al, 2001), respectively. These models use simplified versions of the coastline; hence, most of the models are designed for open coasts or within embayments, treating bounding structures of the embayments as barriers to littoral drift.

Overall, sediment transport is a complex, multidimensional, and dynamic process that results from the interactions of coastal hydrodynamics, turbulence, and sediment particles (Fig. 1.7a). Hence, the application of deterministic two-dimensional (2D)-horizontal or three-dimensional (3D) process-based models is necessary to resolve major mechanisms inducing sediment transport in complex systems. Sediment transport in embayed coastlines involves significant wave-current interaction (Grant and Madsen, 1979; Olabarrieta et al., 2010), with wave oscillations stirring bottom sediment and mean currents contributing significantly to transport (Fig. 1.7b). As a subgroup of process-based models, the use of deterministic models to resolve 3D flow structure is increasing (e.g., CSTM-ROMS, Delft3D), although quasi three-dimensional or (2D)-horizontal based on depth averaged equations and using quasi three-dimensional (quasi 3-D) concepts are still the most common.

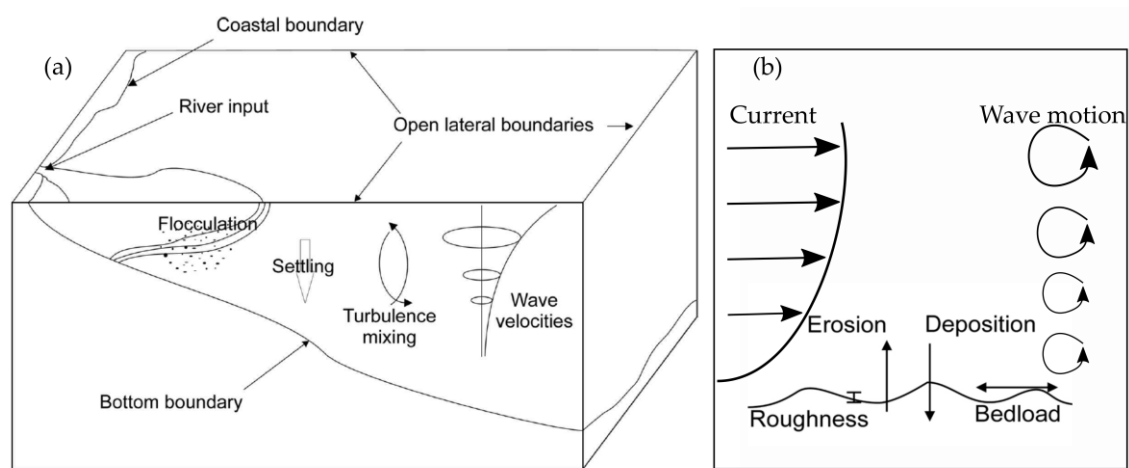


**Fig. 1.7** Processes parameterised by coastal models to predict sediment transport and morphological evolution as per Amoudry and Souza (2002). (a) Coastal shelf sediment transport processes and boundaries. Lateral boundaries can be open or closed with the shoreline boundary usually taken to be of the closed type. (b) Near-bed sediment transport processes.

3D models are able to simulate horizontal and vertical currents, as well as transport of suspended matter. In most cases, the sediment transport processes are part of a modular structure into the hydrodynamic model. As an example, the sediment module in the case of the Delft3D (Delft3D-FLOW), which is the model used in this thesis, applies advection-diffusion equations to obtain suspended sediment concentration and resolve bed load transport based on Van Rijn expressions (Deltares,

2014). Delft3D-FLOW integrates the effects of waves, currents and sediment transport on morphological changes. These models are a good tool to understand transport patterns, but they are still far away from being able to represent sediment fluxes along and across the shoreface accurately over long time scales.

## **1.4 Study area regional setting**

A brief description of the study area is provided in this section. A more extended presentation of the hydrodynamics and beach morphology of the study site is presented in Chapter 2.

### **1.4.1 Geology and geomorphology**

The North coast of Cornwall and Devon is located in the southwest of England (United Kingdom). The physiography of this coast can be considered as highly diverse, combining high hard rock cliffs with relatively short (< 5 km) embayed beaches, often backed by dune systems and cliffs, and separated by rocky headlands and small estuaries (Buscombe and Scott, 2008). The medium resistance to erosion of the cliffs combined with the main phases of transgression have resulted in a large proportion of embayed beaches that cover a wide spectrum from reflective to dissipative morphodynamic conditions. The configuration of the inner shelf is very diverse and includes: (i) large and deep bays with several beaches/embayments with varying orientations; (ii) stretches of coast characterised by a relatively steep and narrow shoreface with shallow and mainly west-facing embayments separated by headlands; and (iii) sections with rocky cliffs fronted by sandy beaches, without any clear embayments.

The coastline is dominated by marine basin sediments (slates, shales, sandstones and limestones) formed in the Devonian and Carboniferous periods, and subsequently altered by highly resistant granite intrusions during the Carboniferous to Permian times (Clayton and Sharnoon, 1998; Fig. 1.8b). After the last glaciation (the Devensian), large quantities of glacial and paraglacial sediments of different sediment sizes (mud to boulders) were left by the retreating glaciers on what is now the continental shelf (Fig. 1.8a). During the post-glacial transgression, the coarser material (gravel and sand)

entered the littoral system and was distributed along the coast and incorporated in dunes, beaches, barriers and estuaries (Anon, 2002). This coastline can be described now as 'sediment-starved' as the offshore sediment source is depleted and coastal sediment supply by natural processes is very limited.

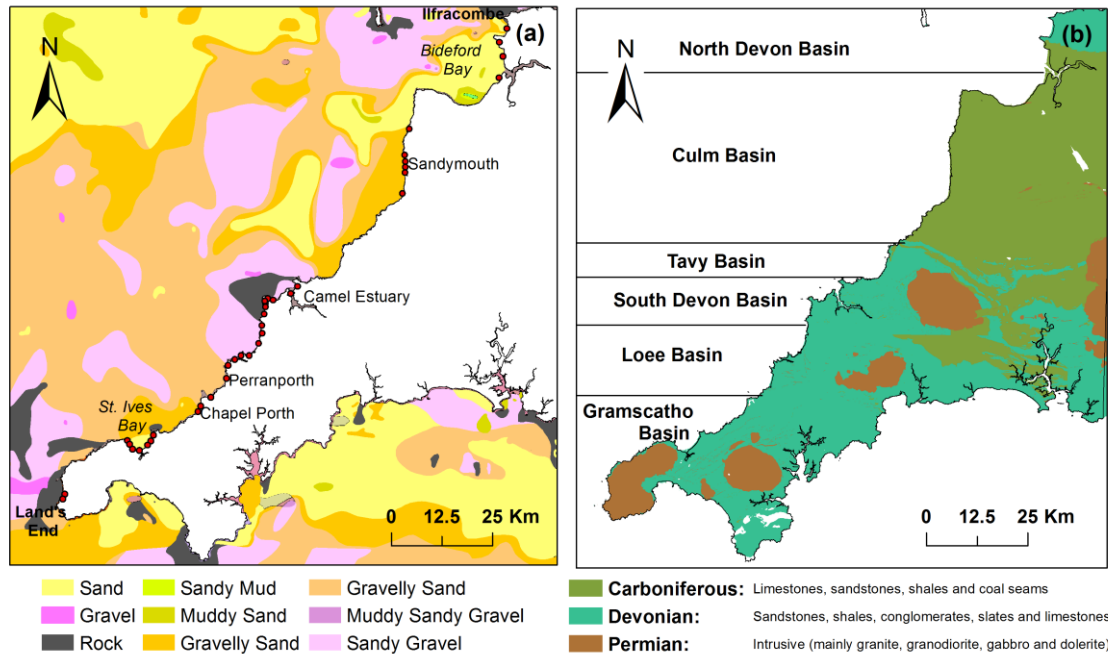


**Fig. 1.8** (a) Offshore 1:250,000 scale seabed sediment distribution and (b) geological setting (modified from: Leveridge and Shail, 2011; May and Hansom, 2013) of SW England based upon BGS maps. Red dots represent the location of the beaches used in this study.

Motyka and Brampton (1993) defined the coastal cell as a coastline section within which any changes along the beaches or nearshore seabed do not affect beaches in adjacent cells. For the particular case of the north coast of the SW, they identified a single cell encompassing the coast from Land's End to the Bristol Channel (Fig. 1.9-cell 7). Likewise, this cell encloses five subcells (Fig. 1.9-subcells 7a–e) separated by large headlands acting as semi-permeable barriers where only little interaction between adjoining stretches is observed. These authors also identified northward drift along the coastline, from Land's End towards the Bristol Channel due to increased tidal currents.

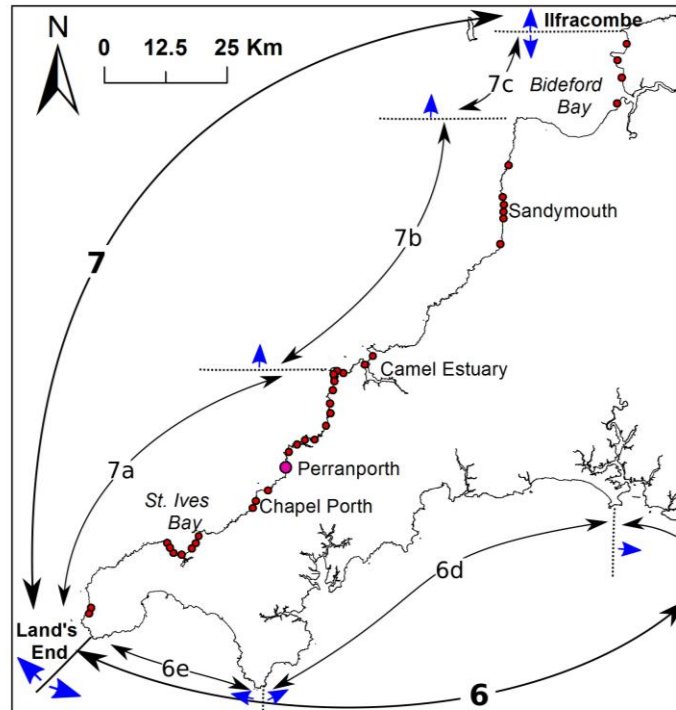


**Fig. 1.9** Littoral sediment cells and subcells for the SW of England with direction of littoral drift (blue arrows) based on a classification conducted by Motyka and Brampton (1993). Cells are numbered clockwise from St. Abb's Head (NE England). Red dots represent the location of the beaches used in this study and pink dot refers to Perranporth beach.

### 1.4.2 Hydrodynamics

The coastline of SW England is macrotidal with the mean spring tidal range varying between 6 m and 11 m (Scott et al., 2011) and the amplitude of the M2 tidal component  $> 1.5$  m (Fig. 1.10a). The tidal range varies along the coast due to the presence of several amphidromic systems and the interactions between the tidal motion and the coastal topography. Tidal currents with values of c.  $0.7 \text{ m s}^{-1}$  have been observed during spring tides near headlands and  $> 1 \text{ m s}^{-1}$  in areas closed to the Bristol Channel.

Wave conditions along the SW are characterized by energetic waves from the W and WNW as a result of a combination of Atlantic swell and local wind waves (Scott, 2009). Wave statistics present a 10% exceedance significant wave height ( $H_{s,10\%}$ ) larger than 3 m (Fig. 1.10b). There is a progressive change in the wave conditions from south to north with decrease in both modal (50% exceedance) and extreme (99% exceedance) wave heights ( $H_{s,50\%} = 1.9 - 1.4 \text{ m}$ ;  $H_{s,99\%} = 7 - 5.1 \text{ m}$ ). The wave period is relatively

constant ( $T_{p,50\%} = 10 - 11$  s;  $T_{p,99\%} = 16 - 17$  s). A strong seasonality in wave climate exists with large summer-winter wave energy variations. Storm surge play a minor role along this coastline and rarely exceeds 1.2 m (Fig. 1.10c).

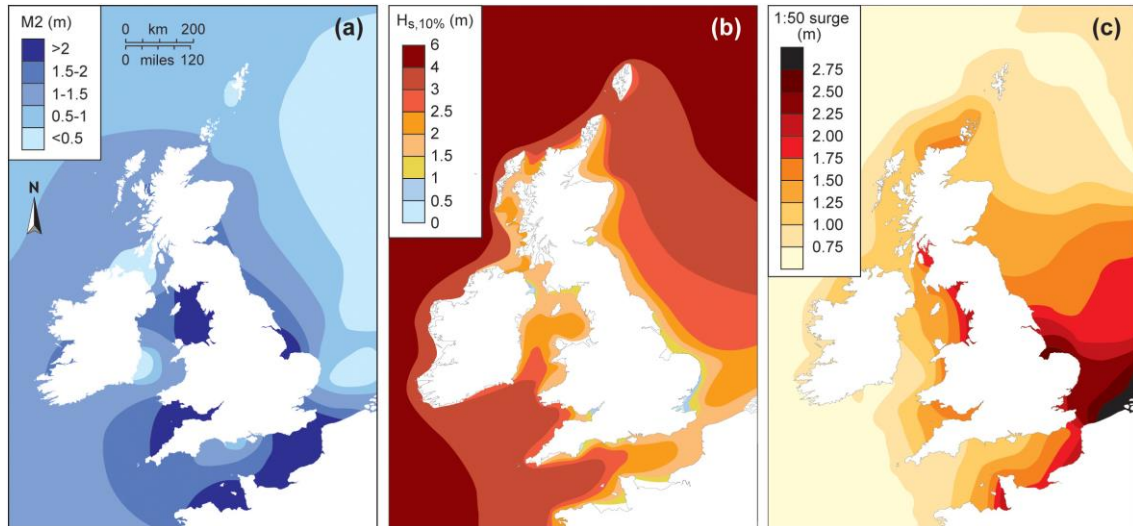


**Fig. 1.10** Maps of the U.K. with: (a) M2 tidal amplitude (adapted from Proudman and Doodson, 1924); (b) 10% exceedance significant wave height,  $H_{s,10\%}$  (Draper, 1991); and (c) 1-in-50-yr storm surge level (Flather, 1987). Source: Scott, 2009.

## 1.5 Aims and thesis outline

The over-arching aim of this thesis is to improve qualitatively and quantitatively our understanding of the physical coupling and sediment dynamics across the beach and the inner shelf along geologically constrained (embayed) coastlines at multi-annual timescale. Using the north coast of SW England as study case, we investigate embayment and inner continental shelf morphodynamics (e.g., maximum depth of transport, sediment fluxes) and possible linkages (e.g., through headland bypassing, cross-embayment bypass) combining field measurements (hydrodynamics and morphological observations) and numerical simulations. This section outlines the structure of the thesis and provides detailed aims.

## **Chapter 2 - Role of waves and tides on depth of closure and potential for headland bypassing**

Depth of closure is a fundamental concept used to define the seaward extent of a morphodynamically active shoreface at a particular temporal scale. The aim of Chapter 2 is to:

- (i) examine the potential for headland bypassing along six different types of rocky coastline using as study site the north coast of SW England.

In order to achieve this aim, we estimate the limit of the 'active' shoreface in relation to the depth in front of the bounding headlands at a decadal scale along a large number of contrasting embayments as it allows questioning whether embayments, often deemed closed sediment cells, experience more headland bypassing than expected. We apply a multi-method approach that includes observations of shoreface morphology and sedimentology, offshore/inshore wave formulations and bed shear stress computations and investigate the role of waves and tides in influencing the depth of closure and maximum depth of transport. We provide a new broad parameter-space for the maximum depth of sediment transport applicable from micro- to macrotidal and exposed coastlines globally.

## **Chapter 3 – New insights into multi-annual embayment scale sediment dynamics**

Predicting coastal system behaviour requires an accurate delineation and understanding of coastal cell boundaries, sediment sources and sinks, and transport pathways. We combine LiDAR, UAV photogrammetry, RTK-GNSS, single-beam and multi-beam echosounder surveys, that encompass the dune system to > 40 m water depth; representing a unique dataset in terms of spatio-temporal coverage. We apply a novel total sediment budget approach based on field observations and spatially-variable uncertainty analysis in order to:

- (ii) evaluate the inter-annual dynamics of Perranporth beach, a sandy, exposed and macrotidal embayment over multi-annual time scales; and
- (iii) investigate the nature ('open' or 'closed') of Perranporth beach, for the period 2011 – 2018.

We provide new insights into multi-annual embayment-scale dynamics by analysing the embayment morphological response and evolution, and its linkages with wave parameters; and by examining the spatio-temporal interdependence between embayment sub-systems (dunes, supra- and inter-tidal, and sub-tidal).

#### **Chapter 4 - Numerical modelling of nearshore sediment transport and headland bypassing**

Using Delft3D morphodynamic model, we examine the sediment transport dynamics along a 15-km stretch of coastline encompassing Perranporth beach. Numerical simulations of a wide range of representative forcing conditions for 2011 – 2018 are used to determine rates of exchange through headland bypassing (along six headlands) and through cross-embayment sediment bypassing (at five embayments). Hence, following the observational study conducted in Chapter 3, the aim of Chapter 4 is to:

- (iv) investigate major sediment transport pathways between adjacent bays and the embayment of study (Perranporth beach) in order to depict a more complete picture of the complex sediment dynamics in the sub-tidal realm of embayed coastlines.

#### **Chapter 5 – Synthesis and conclusions**

Chapter 5 provides a synthesis of the thesis results, conclusions and implications for future work. Major contributions of this thesis include: (i) new broad parameter-space for the closure limit of sediment transport applicable to exposed coastlines globally; (ii) new insights into multi-annual embayment scale dynamics as it is disproved the commonly held understanding that when sediment exits the inter-tidal, it rests undisturbed in the sub-tidal waiting for a period of low-moderate energy to bring it onshore; and (iii) predictability of sediment fluxes along and across high-energy and macrotidal embayed coastlines.

The various themes that have been examined are finally summarised in a conceptual model of multi-embayment-scale dynamics. This includes the different areas of the ‘active’ shoreface, spatio-temporal evolution of embayment sub-systems and

major sediment fluxes at the decadal scale for high-energy and macrotidal embayed coastlines.

## Chapter 2 – Role of waves and tides on depth of closure and potential for headland bypassing

---

This chapter contains work previously presented in the following papers included in Appendix B:

N.G. Valiente, G. Masselink, T. Scott, D. Conley, R.J. McCarroll, 2019. Role of waves and tides on depth of closure and potential for headland bypassing, *Marine Geology*, 407, 60-75. <https://doi.org/10.1016/j.margeo.2018.10.009>.

N.G. Valiente, G. Masselink, T. Scott, D. Conley. Depth of closure along an embayed, macro-tidal and exposed coast: a multi-criteria approach. Proceedings Coastal Dynamics, ASCE, Helsingor, Denmark, Paper No. 185, 1211-1222, June 2017.

### 2.1 Introduction

Delineation of the active shoreface has long been a subject of investigation for coastal scientists and engineers (Hallermeier, 1978; Birkemeier, 1985; Wright et al., 1991; Wright, 1995; Ortiz and Ashton, 2016). The processes leading to sediment exchange across the shoreface, and the estimation of the seaward extent (depth) of those processes, are relevant to a wide range of coastal topics, including evaluation of sediment budgets (Hands and Allison, 1991; Capobianco et al., 2002), investigation of shoreface morphodynamics (Tanaka and Vang To, 1994; Ortiz and Ashton, 2016), identification of the active zone for beach nourishment design (Hinton and Nicholls, 1998; Phillips and Williams, 2007; Aragonés et al., 2016), computation of the long-term stability of beaches (Stive et al., 1992; Marsh et al., 1998), modelling coastal evolution (Hanson and Kraus, 1989; Larson and Kraus, 1992) and assessing the impact of sea-level rise on coasts (Stive et al., 1991; Rosati, Dean and Walton, 2013). Recognising the importance of appropriately framing the shoreface extent affected by intense bed activity, this offshore limit, denoted as ‘depth of closure’, remains a contentious subject in coastal science (Stive et al., 1991; Stive and Devriendt, 1995; Hinton and Nicholls, 1998; Nicholls et al., 1998b; Robertson et al., 2008; Ortiz and Ashton, 2016). Despite the availability of

relatively robust nearshore sediment transport models, driven by appropriate hydrodynamic forcing (waves and tides), the concept also remains relevant, especially where resources to develop such numerical models are not available, for example due to lack of reliable bathymetric data.

The term ‘depth of closure’ is a theoretical concept used to limit two zones of different morphodynamic activity along the beach profile at short- and medium-term time scales (1 – 10 years): the *upper* shoreface is described as the area where significant changes on the beach profile are detected, while the *lower* shoreface is the area extending from the limit of significant change to the wave base where morphological change is negligible (or within the uncertainty limits), but intense bed agitation may occur under energetic wave conditions. The transition between the upper and lower shoreface is known as the morphological depth of closure (*DoC*) and the seaward extent of the lower shoreface is referred to as the maximum depth of significant sediment transport (*DoT*). Hence, *DoC* represents a morphodynamic boundary separating a landward, morphodynamically active region (Hallermeier, 1981; Hinton and Nicholls, 1998; Nicholls et al., 1998b), from a seaward region that is generally considered morphodynamically non-active. In this thesis, *DoT* is defined as the maximum water depth for intense bed agitation; therefore, we consider that significant sediment transport exists when transition to flat bed induced by wave-and tidal-currents occurs. Of course, the definition of ‘significant change’ or ‘significant sediment transport’ is ambiguous and depends on the time scale of consideration and the methods of morphological change detection; thus, different closure criteria may be used to define the corresponding closure points.

Changes in shoreface configuration are controlled by beach intrinsic properties, such as sediment characteristics, as well as by external factors including waves and tidal flows. Together with the depth of closure concept, the study of the shoreface profile shape is a useful tool to investigate beach morphodynamics (Dean, 1991; Aragonés et al., 2016). As presented by Capobianco et al. (1997), Nicholls et al. (1998a) and Inman and Adams (2005), a general predictive approach for *DoC* can be developed using the equilibrium profile concept (EP). Strictly speaking, the EP is a theoretical profile that the

beach reaches when the cross-shore sediment transport average through time is zero (Bernabeu et al., 2003a; Ortiz and Ashton, 2016), and where  $DoC$  is established as the seaward extent. Bruun (1954) and Dean (1977) based the EP expression for the surf zone on the sediment characteristics founded on the assumption that the EP results when the bed shear stress and energy dissipation rate become equal along the profile, resulting in the following beach profile formulation:

$$y(x) = Ax^m \quad (2.1)$$

where  $y(x)$  is water depth,  $x$  is cross-shore distance, and  $A$  and  $m$  are constants (Dean, 1977). The constant  $A$  is a sediment-dependent scale parameter (Moore, 1982; Dean, 1987) and  $m$  is equal to  $2/3$  when turbulence results from uniform wave energy dissipation rate per unit volume (Dean, 1977, 1991).

Embayed beaches are often considered closed systems, but even bounding headlands that appear sufficiently prominent to restrict headland bypassing under modal conditions, can ‘leak’ under extreme storms. Estimating the limit of the active shoreface under storm conditions in front of headlands allows identifying whether related embayments are open or closed sediment cells. Additionally, strong tidal currents associated with macrotidal settings are expected to move the closure limit of the active shoreface seaward. Therefore, where geological controls and strong tidal currents influence shoreface configurations, a re-evaluation of the ‘active’ nearshore limit seems appropriate. Here, we use the embayed, macrotidal and high-energy coasts of north Devon and Cornwall (UK) as a natural field laboratory to identify this limit using a multi-criteria approach that includes: (1) observations of shoreface topography and sedimentology; (2) classic wave-based  $DoC$  parameterisations; and (3) bed shear stress computations. We focus on the investigation of the role of headlands in influencing  $DoC$  and  $DoT$ , and thus the potential for headland bypassing, thereby improving our understanding of shoreface dynamics on wave- and tide-dominated coasts.

The outline of this chapter is as follows. Section 2.2 contextualizes the depth of closure concept and methods for its estimation employed to date. Section 2.3 presents a

regional description of the North coast of Cornwall and Devon (SW England), as well as the prevailing dynamics affecting shoreface configuration along the coast. In Section 2.4, we present the methods for a multicriteria approach used to estimate *DoC* based on observations (Section 2.4.3.1), previously established wave-based parameterisations (Section 2.4.3.2) and modelling of wave- and current-induced bed shear stress (Section 2.4.3.3). In Section 2.5, results from the different approaches are explored. A discussion of the replicability and application of the different approaches for geologically-constrained and macrotidal coastal areas is presented in Section 2.6, followed by the conclusions of this research in Section 2.7.

## 2.2 Background

Several approaches have been pursued over the past four decades to estimate the morphological depth of closure. These can be synthesized in: (1) direct methods based on observations of morphological data (Hinton and Nicholls, 1998; Kraus et al., 1998; Nicholls et al., 1998b; Hartman and Kennedy, 2016); and (2) indirect methods that predict this depth based on wave hydrodynamics (Hallermeier, 1978, 1981; Roy and Thom, 1981; Birkemeier, 1985; Capobianco et al., 1997; Peters and Loss, 2012). Direct estimations are based on morphological data defining an envelope of variation that decreases with depth (Hinton and Nicholls, 1998; Kraus et al., 1998; Nicholls et al., 1998b; Hartman and Kennedy, 2016). Historically, *DoC* has been estimated using profile comparison as it is the most reliable method to estimate the point beyond which no significant changes on the profile are detected, where ‘significant’ generally relates to bed-level change larger than the detection limit. This traditional method requires an extended dataset (collected over several years at least) with repeated surveys along cross-shore transects of the beach, which ultimately makes it time-consuming and relatively expensive to obtain; therefore, direct estimates of *DoC* are only available from a small number of sites.

The challenge in accurately quantifying *DoC* motivated the development of indirect methods of prediction based on wave hydrodynamics and sediment characteristics affecting the shoreface. Examples of such indirect methods include wave-based formulations (Hallermeier, 1978, 1981; Birkemeier, 1985; Capobianco et al., 1997),

energetics-based sediment transport methods (Ortiz and Ashton, 2016) and identification based on observations of sedimentary sequences (Roy and Thom, 1981; Nichols, 1999; Peters and Loss, 2012), as well as of abrupt changes in the textural composition of the seabed (e.g., Potter, 1967; Chesher et al, 1981; Larson, 1991; Work and Dean, 1991; Thielert et al., 2001).

Sedimentological approaches quantify the transition limit of areas with different wave activity as a particular change in the vertical stratigraphic sequence (sedimentary structures and bedforms); for example, hummocky stratification develops below normal fair-weather wave base during conditions analogous to the transition to upper plane-bed in unidirectional flow (Dott and Bourgeois, 1982). Studies of seabed composition often identify clear variations in texture and/or abrupt differences in sediment size along a beach profile (Potter, 1967; Chesher et al, 1981; Larson, 1991; Work and Dean, 1991). Sedimentological changes are more a reflection of the maximum depth of sediment transport ( $DoT$ ) as both bedforms and sediment texture respond to wave-stirring and tidal current forcing, and they are not necessarily associated with morphological change as delimited by  $DoC$ .

Wave-based formulations propose different expressions to quantify limits of shoreface activity under the assumption that only the most energetic (i.e., largest) waves cause morphological change out to the closure depth (Hallermeier, 1981; Birkemeier, 1985; Capobianco et al., 1997). Hallermeier (1978, 1981) developed the first empirical approach to estimate the annual depth of closure ( $DoC$ ) and an offshore limit for maximum depth of bed activity ( $DoC-motion$ ) on microtidal sandy beaches, based on the activity experienced by the seabed using laboratory experiments. According to these early studies,  $DoC$  represents the ‘depth of significant morphological change’, and is estimated as:

$$DoC = 2.28 H_{12,t} - 68.5 \left( \frac{H_{12,t}^2}{gT_t^2} \right) \quad (2.2)$$

where  $DoC$  is the predicted depth of closure over  $t$  years referenced to Mean Low Water (Hinton and Nicholls, 1998),  $H_{12,t}$  is the non-breaking significant wave height that is exceeded for 12 hours per  $t$  years,  $T_t$  is the associated wave period and  $g$  is the

acceleration due to gravity. *DoC-motion* (Hallermeier, 1981) represents the limit for sediment motion and follows the expression:

$$DoC - motion = (\overline{H_{s,t}} - 0.3SD_s)\overline{T_{s,t}}\left(\frac{g}{5000D_{50}}\right)^{0.5} \quad (2.3)$$

where  $\overline{H_{s,t}}$  is the annual mean significant wave height,  $SD_s$  and  $\overline{T_{s,t}}$  are the associated standard deviation and average period of the significant wave height, respectively, and  $D_{50}$  is the median grain size.

Later, Birkemeier (1985), found that the expression for *DoC* (Eq. 2.2) proposed by Hallermeier (1978) over-predicted observations by about 25% (Nicholls et al., 1998a) and proposed an adjusted expression for *DoC* of the form:

$$DoC = 1.75 H_{12,t} - 57.9 \left( \frac{H_{12,t}^2}{gT_t^2} \right) \quad (2.4)$$

Other authors proposed alternative formulations, simplifying the expression proposed by Hallermeier (1978). As an example, Capobianco et al. (1997), suggested an expression for *DoC*, which is only a function of the non-breaking significant wave height exceeded for 12 hours:

$$DoC = KH_{12,t}^{0.67} \quad (2.5)$$

where the constant  $K$  has value 3.4, 2.8 and 2.1 for a maximum vertical variation in the profile of 0.05, 0.1 and 0.2 m, respectively, over annual to medium temporal scale.

Eqs. 2.2, 2.4 and 2.5 have been shown to provide good predictions of the depth of closure on relatively-exposed, microtidal, sandy coasts. Nicholls et al. (1998a, b) compared 12 years of bathymetric data and nearshore wave statistics from Duck, NC. They showed that Eq. 2.2 provided conservative estimates of the annual depth of closure values for different closure criteria (maximum vertical variation of 0.06 m, 0.1 m, and 0.15 m), but successfully predicted the closure limit (*DoC*) during erosional events. Later, Robertson et al. (2008) tested Eqs. 2.2 and 2.5 using observations of measured changes in the peninsula of Florida and showed that Hallermeier's (1978) wave-based formulation best matched the observations of that area. In all mentioned studies, these

formulations were tested on a microtidal coast and they may not necessarily be directly transferable to macrotidal beaches (Nicholls, 1998a). According to Hallermeier (1978), the effect of tidal action on Eq. 2.2 can be accounted for by referencing the depths obtained relative to mean low water (MLW), but this only provides a tidal datum adjustment and does not account for the role of tidal currents.

Although wave-based formulations continue to be a common and widely-accepted approach to predict *DoC*, other approaches are appearing in the literature. Robertson et al. (2008) presented the influence of non-erodible beds or hardgrounds on *DoC* using airborne bathymetric data, and suggested that this method based on observations is a good approach to follow in areas where the presence of bedrock plays an important role in determining the depth of closure. In addition to the mentioned geological control, other authors have also pointed to a clear influence of the tidal currents in the estimation of *DoC* (Hartman and Kennedy, 2016). Following these more recent suggestions, the usefulness of the wave-based formulations is evaluated here along an area where geological control (presence of bedrock and headlands as attenuation and refraction points), large tidal ranges and strong tidal currents are essential components in explaining sediment dynamics on the shoreface. This provides a novel and updated evaluation of the depth of closure concept emphasizing the role of these in predicting the zone of active sediment transport.

### 2.3 Study area

The North coast of Cornwall and Devon, Southwest England (UK), extends 200 km from Land's End (SW) to Ilfracombe (NE) (Fig. 2.1). The coastline comprises high and hard rock cliffs (up to 120 m above sea level), rocky headlands, small estuaries and relatively short sandy embayed beaches (< 5 km), spanning reflective to dissipative conditions (Scott et al., 2011), often backed by dune systems and/or cliffs. The configuration of the shoreface is highly variable (Scott et al., 2011) and includes: (1) large and deep bays with multiple beaches/embayments of varying west to north orientation; (2) steep and narrow shorefaces with shallow and mainly west-facing embayments separated by headlands; and (3) rocky cliffs fronted by sandy beaches, without clear embayments. The average grain size for this coast is 0.3 mm (Prodger et al., 2017).

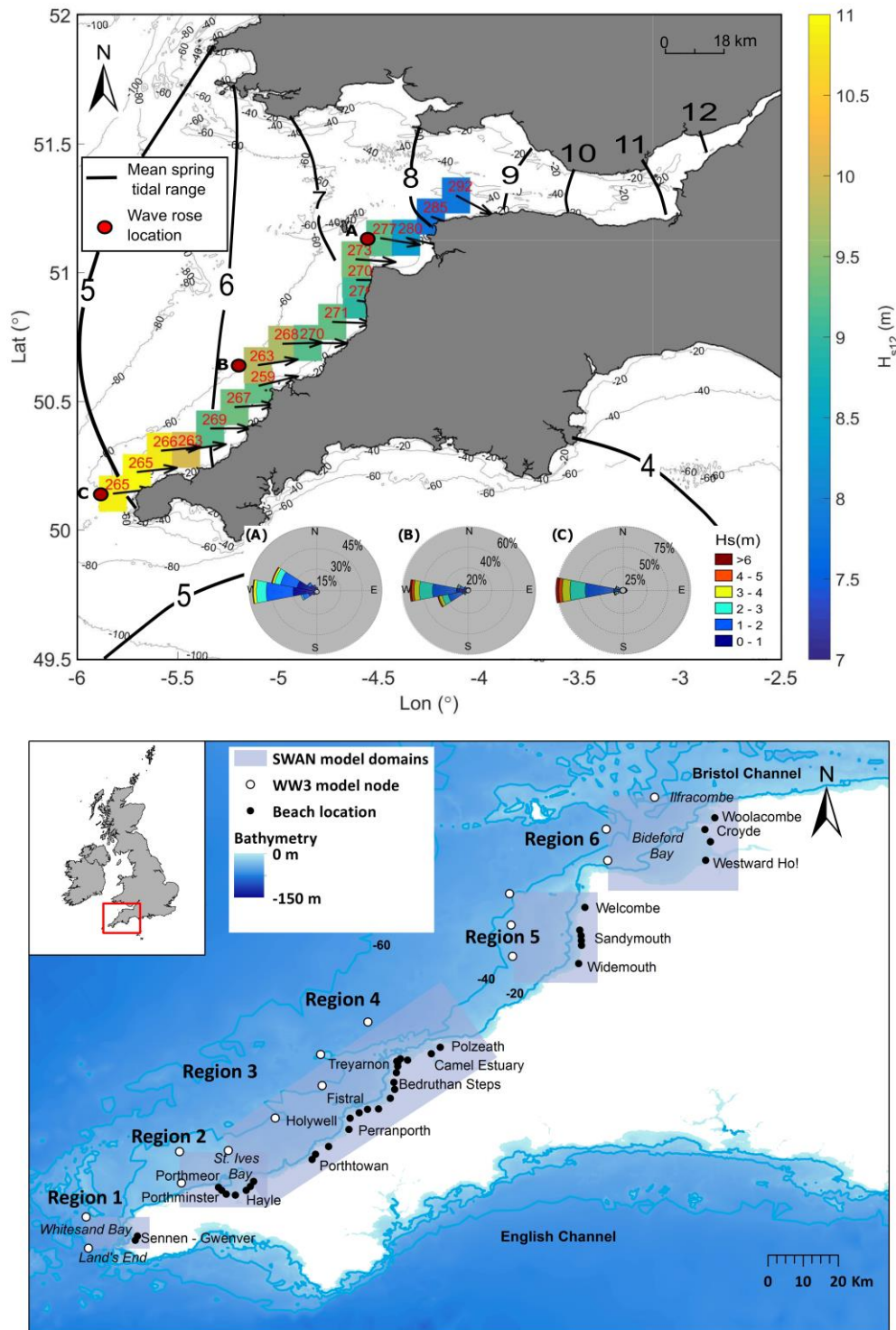


**Fig. 2.1** Study area, SW England. Top panel: wave climate variability and tidal range. Wave climate data represent a 4-year record (2013 – 2016) from the MetOffice WW3 model, with cell colour indicating offshore  $H_s$  exceeded 12 hours per year and associated direction. Red circles (A to C) indicate the locations of wave roses. Black solid lines represent mean spring tidal range, adapted from BERR (2008). Bottom panel: location of study areas along the SW (SWAN model domains for *Regions 1 – 6*). Black dots indicate the studied embayments and white circles are MetOffice UK Waters Wave Model nodes used as SWAN input.

**Table 2.1** Deep-water wave climate statistics for the selected regions using hourly wave model outputs from the MetOffice UK Waters Wave Model, 2013 to 2016. Statistics were computed on each wave model node and averaged over the region.

Region	Hydrodynamics						Morphology		
	$H_s$ (m)	$H_{s99\%}$ (m)	$H_{s12}$ (m)	$T_p$ (s)	$T_{p99\%}$ (s)	$T_{p12}$ (s)	$D_{50}$ (mm)	Slope	Orientation
1	1.9	7.0	10.0	9.8	16.4	18.2	0.49	0.028	NW-W
2	1.7	6.7	9.5	9.8	16.4	18.2	0.37	0.008	NNE-WNW
3	1.6	6.1	9.3	10.2	16.7	18.2	0.37	0.013-0.021	W-NW
4	1.6	5.8	8.8	10.1	16.4	17.9	0.34	0.013	W-NW
5	1.5	5.8	8.4	10.9	17.0	18.5	0.48	0.017	W
6	1.4	5.1	7.3	11.0	16.7	18.5	0.33	0.005	W

$H_s$  – mean significant wave height;  $H_{s99\%}$  – 99<sup>th</sup> percentile;  $H_{s12}$  – significant wave height exceeded 12 hours per year;  $T_p$  – peak period.

This coast receives a combination of Atlantic swell, primarily from the W to WNW, and local wind waves. A wave height gradient exists from SW to NE (Fig. 2.1, top panel), with mean significant wave height ( $H_s$ ) decreasing from 1.9 m at Land’s End (SW, Fig. 2.1b) to 1.0 m in Ilfracombe (NE, Fig. 2.1b), with associated peak periods ( $T_p$ ) of 9.8 s and 11.0 s, respectively. The coastline is macrotidal: the largest tides are experienced in the Bristol Channel where the mean spring tidal range (MSR) is 8 m and the smallest tides in the region occur at Land’s End (MSR = 5 m).

Along most of the coast, the maximum ebb and flood velocity ranges from 0.1 to 0.4 m s<sup>-1</sup> at depths between 10 and 30 m (Fig. 2.2) with the tidal flows predominantly parallel to the shoreline. The strong flood-ebb asymmetry in the current magnitude and direction during a tidal cycle results in a northward tidal net flux along the coast. At depths exceeding 30 m, the maximum tidal current ranges from 0.3 m s<sup>-1</sup> to 0.6 m s<sup>-1</sup> in front of the embayments, and significantly increases around the headlands (Fig. 2.2, right panels), where maximum tidal flows can be of the order of 1 m s<sup>-1</sup> (*Region 1* at 30 m depth; Fig. 2.2, bottom right panel) and even exceed 1.2 m s<sup>-1</sup> in locations close to the Bristol Channel (e.g., in *Region 6* at 30 m depth; Fig. 2.2, upper right panel). Strong tidal velocities are also observed around headlands in central regions (*Regions 3 – 5*) with values of flood current higher than 0.4 m s<sup>-1</sup> at 20 – 30 m depth (Fig. 2.2, middle right panel).

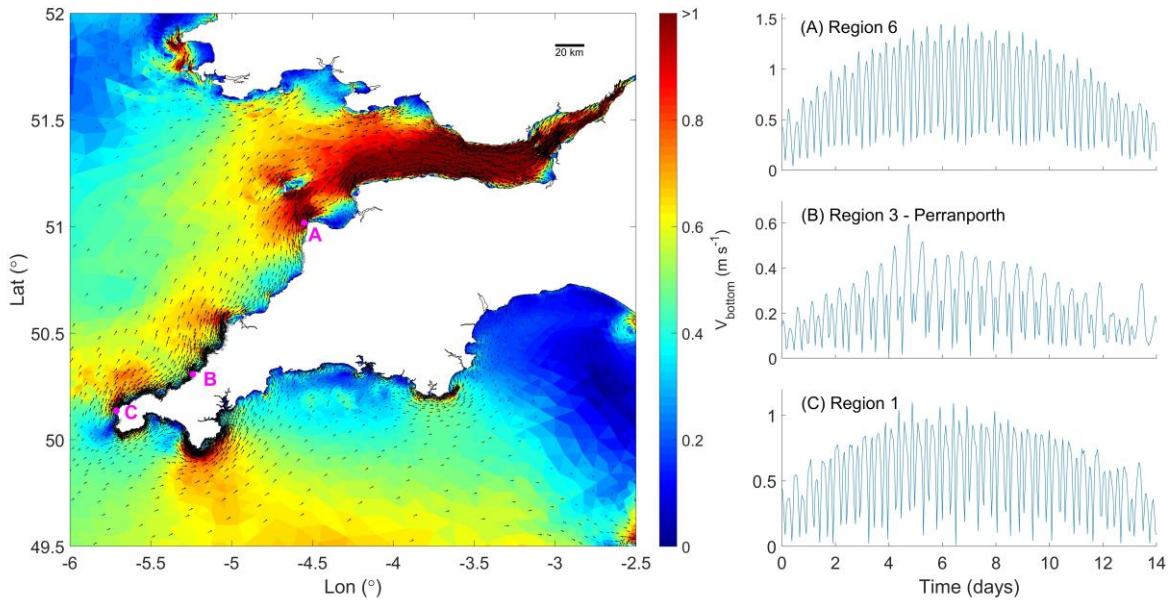


**Fig. 2.2** Left panel: Snapshot of spatial distribution of bottom tidal current velocities and direction during spring tides (flood conditions). Magenta dots with labels (A, B, C) represent locations of speed time series shown in the right panels. Right panels: velocity current time series for a representative neap-spring-neap tidal cycle at the 30-m contour line off the headlands for *Region 6* (upper), *Perranporth-Region 3* (middle) and *Region 1* (lower). Data sourced from FVCOM numerical model (Chen *et al.*, 2003), produced by the UK National Oceanography Centre.

For the analysis, the coastline was divided into six regions (Fig. 2.1, bottom panel) based on geomorphic and hydrodynamic characteristics (Table 2.1), and includes 25 individual low tide embayments (LTEs), which are defined as embayed systems that represent a single embayment at low tide, but may be split up into smaller beaches at high tide. *Region 1* (Fig. 2.3a) represents the southernmost area and covers Whitesand Bay, a concave calcareous-sandy wide bay disrupted by a rocky section at 20 m water depth. This region contains the steep and narrow beaches of Sennen Cove and Gwenver (Fig. 2.3g). *Region 2* covers St. Ives Bay (Fig. 2.3b), a shallow crescentic bay with a wide and flat shoreface (Fig. 2.3g). Three LTEs are present (Porthmeor, Carbis Bay and Godrevy) with sand present up to 25 m depth. *Region 3*, from Porthtowan to Fistral, is characterised by wide dissipative sandy beaches embayed by prominent headlands, backed by large dunes and alternating with stretches of rocky sediment-free areas with 50 – 90 m high cliffs. Six LTEs (including Perranporth, Fig. 2.3c) with steep to moderate shorefaces are present here. *Region 4*, from Newquay to Polzeath, is a relatively straight and exposed section of coast, with a sandy layer covering a partially exposed rock

platform with headlands acting as constraining points, and with cliffs with heights of 40 – 60 m. Two types of LTEs are present in *Region 4*: the first group (Newquay Beaches, Fig. 2.3d) are crescentic sandy bays, while the second group (Bedruthan Steps, Treyarnon) are narrower (Fig. 2.3g), coarser, more exposed and straighter. *Region 5* is relatively straight and embayments are notably absent (Fig. 2.3e). This coastline is characterized by narrow and long patches of coarse sand (to -20 m Ordnance Datum Newlyn, ODN; Fig. 2.3g) constrained by small headlands and a landward cliff. *Region 6*, from Westward Ho! to Woolacombe, is the northern-most region, with sandy beaches embayed by cliffed rocky headlands (Fig. 2.3f). Sediment is finer and the shoreface slope is shallower (Fig. 2.3g) than in the other regions, with sand to -30 m ODN, and with an average distance from the 0 isobath to -30 m ODN of 3600 m for Woolacombe and more than 8000 m for Westward Ho!, Saunton and Croyde.

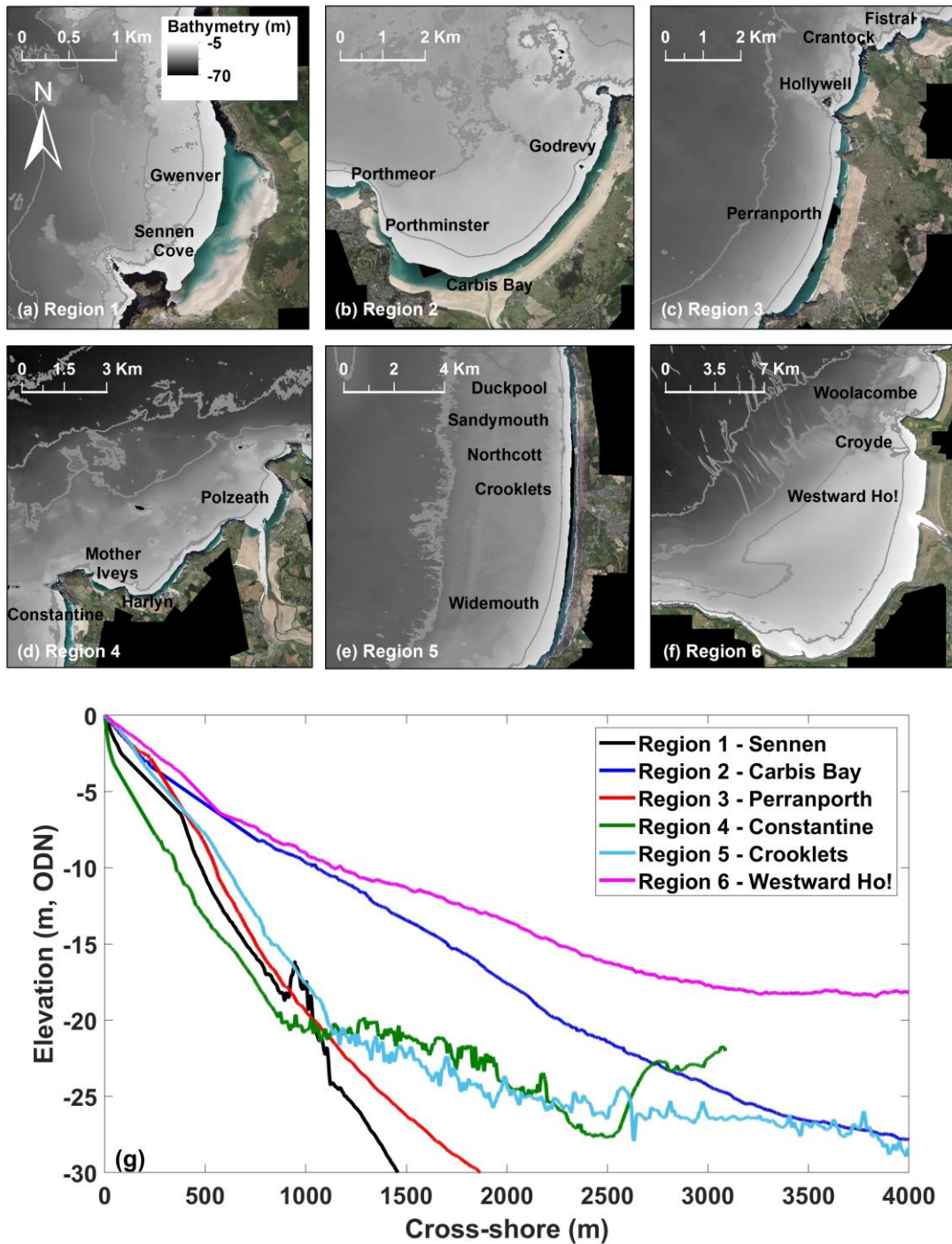


**Fig. 2.3** Upper panel (a–f): aerial photography and bathymetry for the six regions of study. Lower panel (g): representative shoreface profiles extracted from the central part of selected LTEs. Bathymetry data were obtained from United Kingdom Hydrographic Office (2011) and aerial photographs were courtesy of Plymouth Coastal Observatory (available at <https://www.channelcoast.org/southwest/>).

## 2.4 Methodology

Our approach is to compare several criteria for determining the ‘active’ nearshore limits and these are grouped under three methods (Fig. 2.4):  $DoC_{obs,a-c}$  is based on observations,  $DoC_{param,a-b}$  uses wave-based parameterisations and  $DoC_{stress,a-b}$  uses numerical model outputs of bed stress.

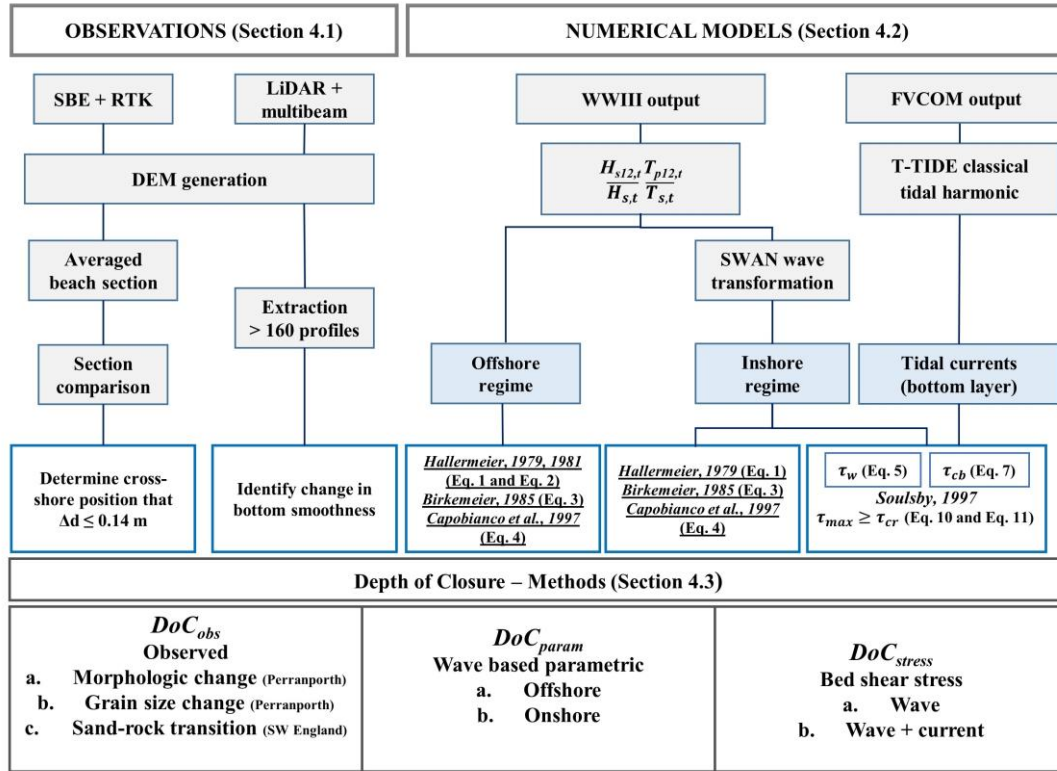


**Fig. 2.4** Flow diagram of research methodology of the  $DoC$  quantification. Underlined criteria correspond with the methods to test.

### 2.4.1 Observational data

A 10-year time series of beach morphology and sub-tidal bathymetry of Perranporth beach (*Region 3*, Fig. 2.3c) was used to determine observed depth of closure ( $DoC_{obs,a}$ , Fig. 2.4). Field data were collected using RTK-GPS for the supra- and inter-tidal beach and single-beam echo-sounder for the sub-tidal area. The uncertainty limit for detecting significant morphologic change was  $\Delta d \leq 0.14$  m ( $\pm 0.14$  m corresponds to the uncertainty associated with the field data collection; RTK-GPS input into Valeport MIDAS Surveyor is accurate to  $\pm 0.02\%$ ). Data were merged and interpolated using the quadratic loess method (Plant et al., 2002) to produce DEMs, providing a time series

sufficiently long to compare observed closure depth with that predicted using wave-based theoretical methods. Complementing the morphological dataset, sediment size distribution ( $DoC_{obs,b}$ , Fig. 2.4) along Perranporth shoreface (from +4 to -30 m) was analysed using sediment samples collected during winter and summer 2016 (Samuel, 2017).

Regional LiDAR (provided by Plymouth Coastal Observatory) and multi-beam bathymetry (United Kingdom Hydrographic Office, 2011) were used to conduct a comparison of shoreface characteristics across the six regions and to determine the sand-rock transition depth of closure ( $DoC_{obs,c}$ , Fig. 2.4). A digital elevation model (DEM) was constructed for the coast of SW England by combining the LiDAR (up to -3 m) and multi-beam bathymetry (to < -50 m), corrected and referenced to Ordnance Datum Newlyn (ODN) using the Vertical Offshore Reference Frame model (VORF) made available by the United Kingdom Hydrographic Office.

## 2.4.2 Numerical modelling data

### 2.4.2.1 Wave models (WW3 and SWAN)

Wave statistics are required to calculate parameterised estimates of depth of closure (Section 2.4.3.2,  $DoC_{param}$ ) and shear stress (Section 2.4.3.3,  $DoC_{stress}$ ). Hindcast wave conditions were obtained from the MetOffice UK Waters WaveWatch III (WW3) Model (Tolman, 2014; Saulter, 2017) for 18 nodes at 8-km resolution across *Regions 1 – 6* (cells in Fig. 2.1, upper panel) over a 4-year period (01/01/2013 – 01/01/2016). This includes the winter of 2013/14, ranked as the most energetic winter in the UK in the last seven decades (Masselink et al., 2016a).

Offshore wave conditions (at > 50 m depth, white circles in Fig. 2.1, bottom panel) may not be representative of inshore conditions (at 15 – 20 m depth) within deep embayments and/or on coastlines that do not face into the prevailing wave direction; therefore, the  $DoC$  computed using offshore conditions may not be appropriate. Accordingly, the third-generation spectral wave model SWAN (Booij et al., 1999) was used to transform wave conditions from offshore to inshore. This model accounts for wind growth, dissipation processes and wave-wave interactions. SWAN was set up for

five domains (one for each region, except *Regions* 3 and 4 which had a shared domain; Fig. 2.1, bottom panel) using a rectangular grid with a resolution of 100×100 m. The dissipation mechanisms considered were bottom friction (with JONSWAP friction coefficient of  $0.067 \text{ m}^2 \text{ s}^{-2}$ ), refraction, whitecapping (Komen et al., 1984) and depth-induced breaking (with ratio of maximum individual wave height over depth equals to 0.73). Non-linear wave-wave interactions were also considered (TRIADS mechanism). SWAN output was validated against wave height observations (wave buoy located in Fig. 2.1, bottom panel) for February 2014 (most energetic month) and the model satisfactorily reproduced wave height, period and direction. Wave height is well predicted and showed a bias of only -0.06 m and a root-mean square error (*RMSE*) of 0.003 m. Peak period prediction is excellent (*bias* = -0.05 s; *RMSE* = 0.02 s).

#### **2.4.2.2 Tide and surge model (FVCOM)**

Data from the finite-volume, three-dimensional (3D) hydrodynamic model FVCOM (Chen et al., 2003) provided by the National Oceanography Centre were used to compute current bed shear stress (Section 2.4.3.2, *DoC<sub>stress</sub>*). The FVCOM domain covers the NW European shelf and the horizontal spatial resolution of the space-varying unstructured cells of the model grid ranges from 2 km offshore to 100 m near the coast. A  $\sigma$  layer (terrain following) coordinate system of 10 uniform layers was used for vertical discretization. Model validation results against tide gauge observations (Ilfracombe and Newlyn) for total water elevation showed a *bias* of -0.002 m and a *RMSE* of 0.26 m. Current meter data collected in 20-m water depth off Perranporth (*Region* 3, Fig. 2.2b) were also compared with FVCOM model data. Recorded maximum current speeds during spring tides at this location were  $0.4 \text{ m s}^{-1}$  and were well reproduced by the numerical model ( $0.42 \text{ m s}^{-1}$ ; *bias* =  $0.09 \text{ m s}^{-1}$ ). FVCOM was run for the year 2008 including full meteorological forcing (tidal, river, surface heat and surface wind forcings). Hourly data of water surface elevation and eastward/northward flow velocity along the SW shelf of England for March 2008 were extracted from the model results. The period used for the hydrodynamic model (2008 in this case) does not represent major implications in our depth of closure computations as the hydrodynamic model output was only used to obtain tidal current velocities for a representative tidal cycle

during spring tides. For a detailed description of a similar FVCOM model set-up and parameterisation refer to De Dominicis et al. (2017).

## 2.4.3 Depth of closure methods

### 2.4.3.1 Observed depth of closure ( $DoC_{obs}$ )

Direct field observations included calculation of the envelope of morphological change ( $DoC_{obs,a}$ ), sediment size distribution ( $DoC_{obs,b}$ ) and sand-rock transition ( $DoC_{obs,c}$ ). Direct morphological change observations and sediment size distribution for one of the study sites (Perranporth, *Region 3*) were used to test the applicability of the parametric wave-based formulations ( $DoC_{param}$ ) and the proposed process-based method ( $DoC_{stress}$ ). The seabed sediment observational dataset was also compared with the presence of sediment (sand-rock transition) in 164 representative cross-shore profiles (covering 25 low tide embayments, LTEs) that were extracted along the six regions.

The Perranporth 10-year time series DEMs (Section 2.4.1) were alongshore-averaged across a 250-m section (black box on Fig. 2.5, left panel) to enable the identification of the point at which morphological change can be considered insignificant ( $\Delta d \leq 0.14$  m;  $DoC_{obs,a}$ ). The observed depth of closure at Perranporth was supplemented by a grain size analysis ( $DoC_{obs,b}$ ) at one representative cross-shore profile. Sediment samples corresponded to winter and summer conditions (March and July 2016), providing a seabed sediment distribution representative of high energy conditions. Depths at which grain size significantly changed were identified (e.g., sand to gravel).

The final observational method for determining depth of closure was to identify the sand-rock transition ( $DoC_{obs,c}$ ) using a regional DEM constructed from LiDAR and multi-beam data (Section 2.4.1). The regional DEM of the SW England was used to compare the shoreface profiles across *Regions 1 – 6*. A total of 164 profiles were extracted (up to -30 m ODN), representative of the different study sites. The profiles were compared to Bruun's equilibrium parametric model (Eq. 2.1; Bruun, 1954; Dean, 1977) using least square fitting to evaluate spatial variability in shoreface configuration within and between the different regions. The depth limit of the fitting was set at 20 m depth;

otherwise, it was determined by the presence of rock. The transition point between sand and rock was manually identified based on a change from smooth to rough bed and/or a break in the shape of the shoreface profiles (e.g., Fig. 2.3g, *Region 1* at 800 m offshore).

#### 2.4.3.2 Wave-based formulations ( $DoC_{param}$ )

The empirically determined wave-based formulations ( $DoC_{param}$ ) based on significant wave height and peak period for a given region were described in Section 2.2 (Eqs. 2.2 – 2.5). First, the offshore wave conditions were used to compute at each WW3 node (Fig. 2.1, top panel) the depth of closure parameters ( $DoC_{param,a}$ ), specifically  $DoC$  (Eqs. 2.2, 2.4, 2.5) and  $DoC-motion$  (Eq. 2.3), and then averaging across all nodes in each of the six regions.  $DoC-motion$  was computed using the median grain size typical from the SW (0.3 mm) for the total time series ( $t = 4$  years), while  $DoC$  was calculated for both the total 4-year time series, as well as independently for each individual year ( $t = 1$  year) and then averaged  $\langle DoC \rangle$ . For clarity, when  $DoC$  is used without chevrons, it is averaged over the full extent of the available data, while  $\langle DoC \rangle$  with chevrons indicates averaging the 1-year results over the 4-year period.

Parameterising depth of closure values for the inshore region ( $DoC_{param,b}$ ) requires wave transformation using SWAN (Section 2.4.2.1). The sediment motion depth of closure  $DoC-motion$  as described by Hallermeier (1981) is not presented for inshore locations, as this depth is commonly located beyond the rocky headlands and falls beyond the regional model domains. Spatially-varying inshore values for the morphological  $DoC$  were determined as follows: (i) for each of the six regions, the offshore modelled wave data were ordered into seven 30°-directional bins with bin centres from 180° to 360°; (ii) for each of these classes, the wave heights were ranked, and the significant wave height exceeded for 12 hours ( $H_{s12,t}$ ) and associated peak period ( $T_{p12,t}$ ) were computed for  $t = 4$  years and  $t = 1$  year; (iii) SWAN models were run for each region using these extreme wave values; (iv) an iterative method (refer to Kraus et al., 1998) was used to extract inshore wave height and associated period at the actual predicted  $DoC$  and  $\langle DoC \rangle$  across each domain, using Eqs. 2.2, 2.4 and 2.5; (v) a representative  $DoC$  and  $\langle DoC \rangle$  value was obtained for each embayment by alongshore-

averaging; and (vi) the depth of closure was calculated relative to MLWS, then corrected to the survey datum (ODN).

### 2.4.3.3 Bed shear stress ( $DoC_{stress}$ )

The approach for estimating the limit of significant sediment transport ( $DoT$ ) under storm conditions and on a macrotidal regime was through analysis of numerically-modelled bed shear stress induced by waves ( $\tau_w$ ) and tidal currents ( $\tau_{cb}$ ), referred to as methods  $DoC_{stress,a}$  and  $DoC_{stress,b}$ , respectively (refer to Fig. 2.4). Bed shear stress was computed following Soulsby (1997) and compared with different thresholds of initiation of motion and bedform activity according to Nielsen (1981).

The bed shear stress produced by waves is generally the main forcing control on sediment transport in shallow water (< 30 m) in exposed (wave-dominated) coastlines. The wave-induced shear stress was computed for the six regions (five SWAN wave model domains) for the extreme wave values ( $H_{s12}$ ,  $T_{p12}$ ). Wave bed shear stress is oscillatory and was obtained using:

$$\tau_w = \frac{1}{2} \rho f_w U_w^2 \quad (2.6)$$

where  $f_w$  is the wave friction factor,  $U_w = \sqrt{2} U_{rms}$ , and  $U_{rms}$  is the root-mean-square wave orbital velocity near the bed. According to Soulsby (1997), the wave friction factor for turbulent flow depends on the bottom roughness parameter ( $z_0 = D_{50}/12$ ) and the semi-orbital excursion ( $A = U_w T / 2\pi$ ) as follows:

$$f_w = 1.39 \left( \frac{A}{z_0} \right)^{-0.52} \quad (2.7)$$

Tidal current bed shear stress was determined using classical tidal harmonic analysis on FVCOM current outputs using T-TIDE (Pawlowicz et al., 2002) for the entire FVCOM domain and at each model node. Tidal currents were resolved using the eight major tidal constituents  $S2$ ,  $M2$ ,  $N2$ ,  $K2$ ,  $K1$ ,  $P1$ ,  $O1$  and  $Q1$ , and the shallow water constituents  $O2$ ,  $N4$ ,  $M4$  and  $S4$ . Current bed shear stress was then computed using only tidal forcing for one representative tidal cycle during spring tides following a quadratic drag law expressed as:

$$\tau_{cb} = \rho C_d \bar{U}_{cb}^2 \quad (2.8)$$

where  $\tau_{cb}$  is the bottom (friction) stress induced by tidal currents,  $\rho$  is the water density,  $\bar{U}_{cb}$  is the maximum near bottom depth-averaged flow velocity for a tidal cycle (during spring tides) in analogy to selecting the maximum wave forcing conditions, and the drag coefficient,  $C_d$ , is determined along the domain by matching a logarithmic bottom layer at a height  $z_{ab}$  above the bottom (see e.g., Young, 1999). Thus:

$$C_d = \max \left[ \frac{k^2}{\ln \left( \frac{z_{ab}}{z_0} \right)^2}, 0.0025 \right] \quad (2.9)$$

with  $k$  being the von Karman constant ( $k = 0.4$ ) and  $z_0$  is the bottom roughness parameter.

The combined wave and current bed shear stress  $\tau_m$  cannot be obtained as a simple linear sum of the separate stresses due to the non-linear interaction between wave and current boundary layers. Soulsby (1995) found a good fit between the observations in the laboratory and a theoretical model based on a two-coefficient optimization of the form:

$$\tau_m = \tau_{cb} \left[ 1 + 1.2 \left( \frac{\tau_w}{\tau_{cb} + \tau_w} \right)^{3.2} \right] \quad (2.10)$$

in which  $\tau_{cb}$  and  $\tau_w$  are the current- and wave-induced shear stresses respectively, computed individually. The corresponding expression for  $\tau_{max}$  is given as follows:

$$\tau_{max} = [(\tau_m + \tau_w |\cos \phi|)^2 + (\tau_w \sin \phi)^2]^{1/2} \quad (2.41)$$

where  $\phi$  is the angle between the direction of wave travel and the current component.

Soulsby (1997) related sediment motion threshold for a specific seabed with the critical Shields parameter  $\theta_{cr}$  through the expression:

$$\tau_{cr} = \theta_{cr} g (\rho_s - \rho) D_{50} \quad (5.12)$$

where  $\rho_s$  is the sediment density and  $g$  is gravitational acceleration. This algorithm calculates critical shear stress ( $\tau_{cr}$ ) for non-cohesive and well-sorted particles using a non-dimensional Shield's curve. Critical shear stresses were calculated using the

average grain size typical of SW England –  $D_{50} = 0.3$  mm, as well as  $D_{50} = 0.15$  and  $0.6$  mm. The use of the different sediment sizes allows analysis of the sensitivity of threshold exceedance of combined wave and current bed shear stress to seabed composition.

According to Eq. 2.22, initiation of motion, as well as sediment transport, will depend on boundary shear stresses and seabed characteristics. Based on laboratory experiments and observations, Nielsen (1981) determined that the occurrence of bedforms is related to the bed shear stress ( $\tau$  or  $\theta$ ) and developed a relation between bedform type and wave energy conditions, expressed as a function of transport stage. Using Grant and Madsen (1982), the following critical values of the Shields number ( $\theta_{cr}$ ) can be identified: (i) initiation of motion  $\theta_{cr} = 0.048$ ; (ii) formation of sharp-crested vortex ripples  $\theta_{cr} = 0.1$ ; (iii) transformation from vortex to post-vortex ripples  $\theta_{cr} = 0.2$ ; and (iv) transition into a plane bed  $\theta_{cr} = 1$ . Following Eq. 2.22, combined wave- and current-induced bed shear stress was computed for each region and compared with the critical shear stresses  $\tau_{cr}$  for the different bedform scenarios.

## 2.5 Results

### 2.5.1 Shoreface shape

Shoreface profile characteristics can provide information on sediment availability, which is of use when analysing depth of closure. Figure 2.5a shows the results of the scale factor  $A$  (Eq. 2.1; Bruun, 1954; Dean, 1977) for the six regions, and Figure 2.5b shows that the root mean square error ( $RMSE$ ) associated with the curve fitting is generally less than 2.5 m. Values for  $A$  range from  $0.06 \text{ m}^{1/3}$  in Saunton (*Region 6*) to  $0.21 \text{ m}^{1/3}$  in Porthtowan (*Region 5*), and are mostly between  $0.11 \text{ m}^{1/3}$  and  $0.18 \text{ m}^{1/3}$  (*Regions 1 to 5*). The shape parameter  $A$  generally decreases with increasing width of the shoreface profile and decreasing slope; hence, the flattest and widest shorefaces are characterized by the smallest  $A$  values (profiles of *Regions 2 and 6*), and the steepest and narrowest shorefaces have the largest  $A$  values (profiles of *Regions 1, 3, 4 and 5*). Most measured profiles present a typical convex shape up to 12 – 15 m water depth relative MSL, and concave shape for the lower shoreface (Figure 2.5c). The shoreface profiles

that are the most poorly fitted by the EP profile are generally characterized by the presence of a wide, flat lower sandy shoreface (mainly in *Region 6*).

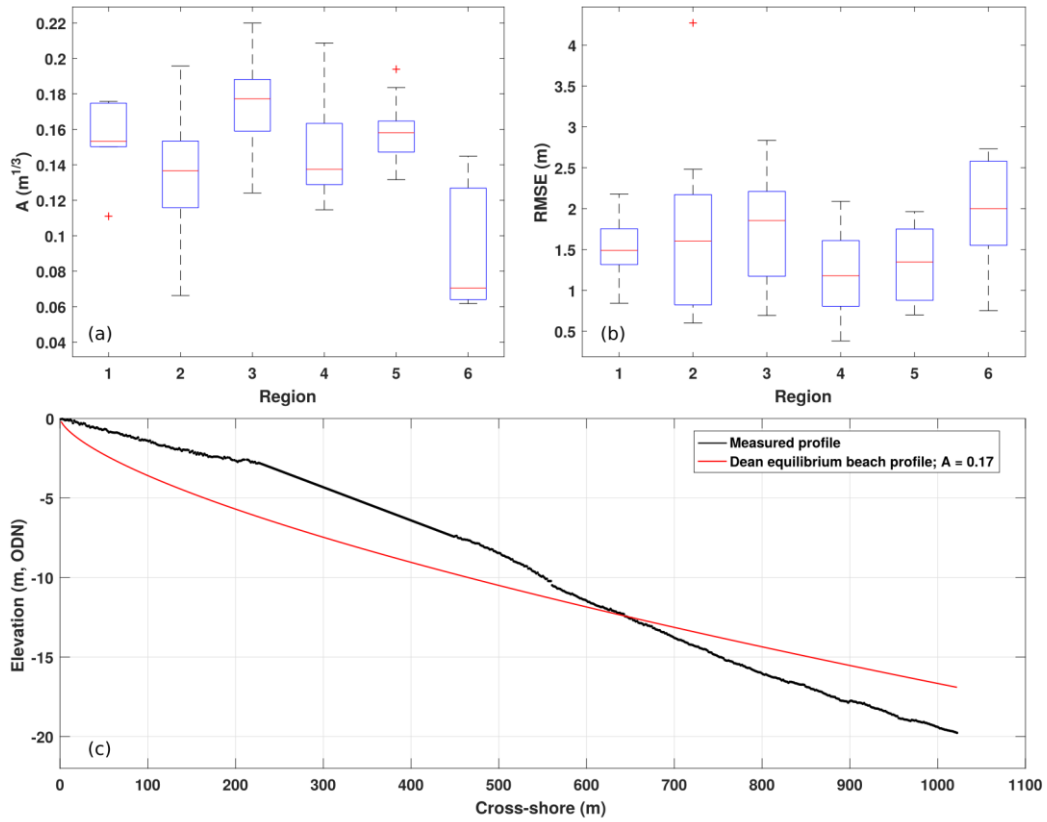


**Figure 2.5** Boxplots representing values of  $A$  (a) and associated  $RMSE$  (b) at central profiles for each of the six regions (excluding profiles located at headlands). (c) Example of fitted profile for *Region 3*.

### 2.5.2 Closure depth based on observations: Perranporth case of study ( $DoC_{obs,a-b}$ )

Survey (beach and bathymetry) data from Perranporth, one of the west-facing embayments of *Region 3* (Fig. 2.1, bottom panel for location), was used to derive the observed closure depth for this location ( $DoC$ ,  $DoC_{obs,a}$ ). Fig. 2.6 shows the mean and the standard deviation ( $SD$ ) associated with all alongshore-averaged shoreface profiles for Perranporth collected over the period 2010 – 2016. The largest bed-level variability ( $SD > 0.5$  m) occurs in the outer bar region ( $x = 700 - 900$  m). This vertical variability decreases offshore to less than 0.14 m at a depth of 14.5 m (ODN), and this depth is considered the morphological depth of closure for this embayment as 0.14 m is the uncertainty associated with the survey data.

Several authors in the literature analyse textural changes in the seabed to determine the boundaries of the active profile (Potter, 1967; Chesher, Smythe and Bishop, 1981; Larson, 1991; Work and Dean, 1991). Following that approach ( $DoC_{obs,b}$ , refer to Fig. 2.4), sediment samples collected during winter and summer 2016 at 13 different locations on the shoreface profile are presented in Fig. 2.6. Supratidal  $D_{50}$  values are relatively constant with a value of 0.33 mm. The coarsest sediments in the upper part of the profile (0.48 mm) are found around the Mean Spring Low Tide level (MSLT). Seaward of this point, sediment size decreases with depth from 0.40 mm at  $z = -3$  m, 0.33 mm at  $z = -18$  m and 0.30 mm between -22 m and -26 m. With increasing depth,  $D_{50}$  abruptly increases to 2.657 mm, representing a transition to gravel. This change in the sediment size is also observed in backscatter data (unpublished data), where the presence of medium sand along the embayment domain is interrupted by gravel patches around the -26 m contour line.

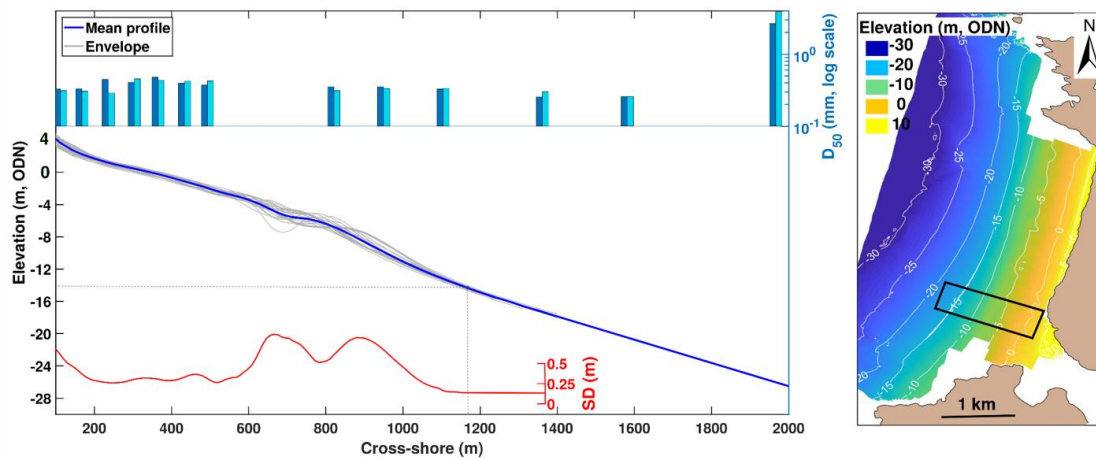


**Fig. 2.6** Left panel: observed  $DoC$  estimated for Perranporth beach, north Cornwall, from the profile envelope ( $DoC_{obs,a}$ ) and from sediment distribution ( $DoC_{obs,b}$ ). Light and dark blue bars represent the median sediment size ( $D_{50}$ ) for winter and summer samples, respectively. The grey lines represent alongshore-average profiles associated with beach survey data collected from 2010 to 2016; the blue line is the mean profile over the survey period; and the red line shows the standard deviation associated with the mean profile. The dashed line represents  $DoC$  based on the morphological observations. Right panel: topographic and bathymetric survey with 250-m wide section of beach (black box) for alongshore-average profile used in left panel.

### 2.5.3 Along-coast variability in depth of closure ( $DoC_{param}$ , $DoC_{obs,c}$ )

The different  $DoC$  measures computed using the various wave formulations  $DoC_{param}$  (Eqs. 2.2 – 2.5) are summarized in Fig. 2.7. The sediment motion depth of closure determined using mean wave characteristics ( $DoC_{motion}$ , Eq. 2.3) was calculated for each of the six regions (Fig. 2.7, upper panel) and decreases from 50 m in the south to 34 m in the north, in response to the associated decrease in wave energy (Fig. 2.1, bottom panel). The morphological depth of closure estimate was calculated over 4-years ( $DoC$ ) and for 1-year averages ( $\langle DoC \rangle$ ) for three different formulations (Eqs. 2.2, 2.4 and 2.5).  $DoC$  decreases from 23 m in the south (*Region 1*) to 19 m in the north (*Region 6*) for Hallermeier (1978), and the corresponding values for the Capobianco et al. (1997) and Birkemeier (1985) formulations are shallower, ranging from 17 m to 14 m, and from 15 to 12 m, respectively. The decrease in  $DoC$  over decreasing time scale is demonstrated through comparison with the  $\langle DoC \rangle$  values (Fig. 2.7, top panel-darkest bars), which are 4 m, 2 m and 1.5 m less than those obtained using the total time series ( $DoC$ , Fig. 2.7, top panel-light bars) for Hallermeier (1978), Capobianco et al. (1997) and Birkemeier (1985), respectively.

Embayment-averaged  $DoC$  results are obtained using wave conditions transformed to the nearshore ( $DoC_{param,b}$ ) and, most significantly, there is no obvious correlation between the  $DoC$  values computed using the offshore (Fig. 2.7, top panel) and inshore (Fig. 2.7, bottom panel) wave formulations. While  $DoC$  computed from offshore wave conditions ( $DoC_{param,a}$ ) decreases from south to north, the value computed using inshore wave conditions increases from *Region 1* to *Region 5*, then decreases for *Region 6*. This emphasizes the very significant role nearshore morphology and embayment orientation play in attenuating wave energy. Clearly, if untransformed wave values are used to estimate  $DoC$  for highly embayed coasts, the results are likely to be significantly overestimated.  $DoC$  values computed using inshore wave conditions using Hallermeier (1978; Eq. 2.2) are in all cases 1 – 2 m larger than results using Capobianco et al. (1997; Eq. 2.5) and Birkemeier (1985; Eq. 2.4). As an example of the results, typical values of  $DoC$  using Hallermeier (1978) ( $DoC_{param,b}$ ) for the most exposed parts of the coast (*Regions 1, 5* and *6*, and the north part of *Regions 3* and *4*) are 12 – 16 m

(relative to ODN), whereas  $DoC$  values for the more sheltered parts (*Regions 2 and the south part of Region 6*) are typically 6 – 10 m.

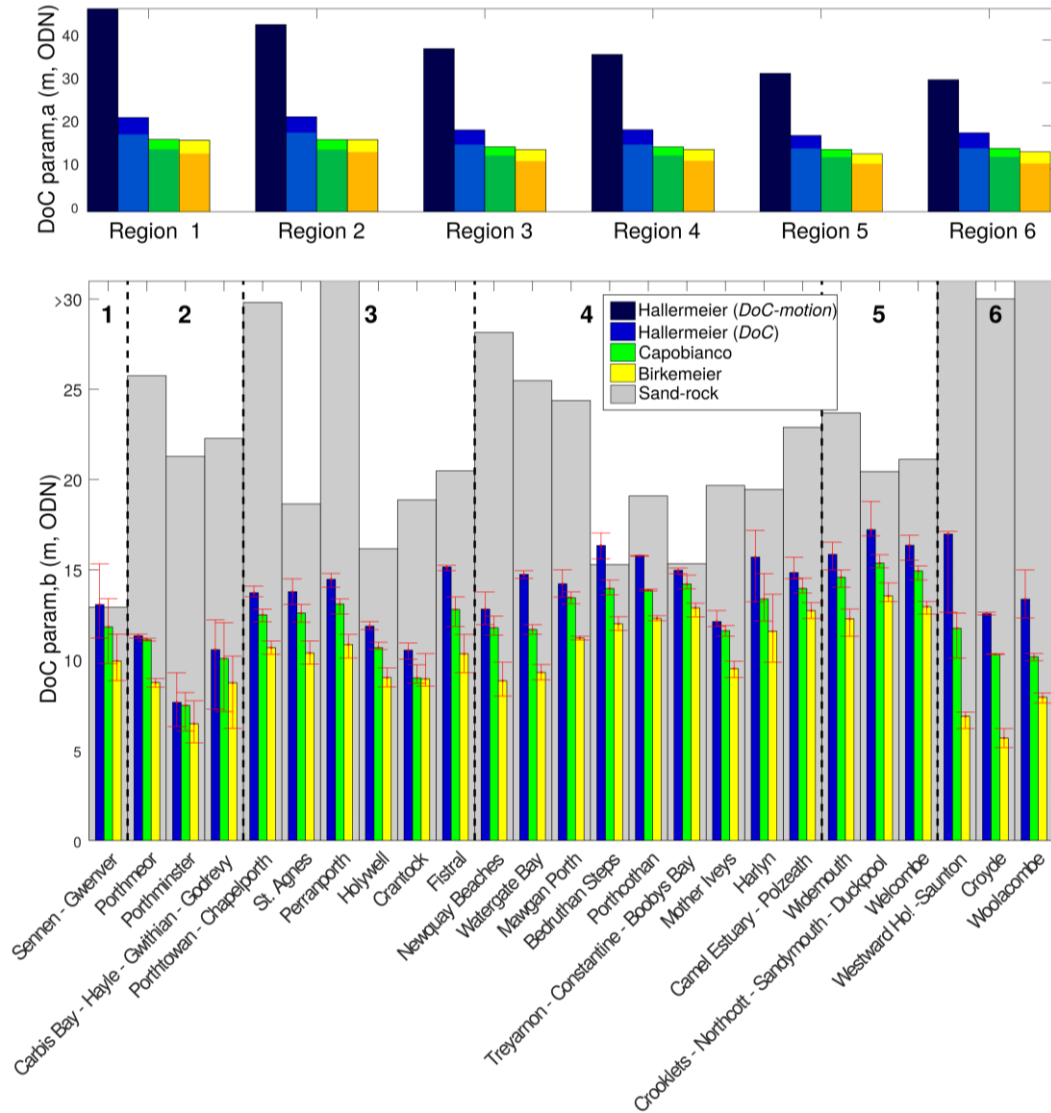


**Fig. 2.7** Along-coast variability in depth of closure obtained by applying the wave-based formulations of Hallermeier for  $DoC$  (light blue) and  $DoC-motion$  (dark blue), Capobianco (green) and Birkemeier (yellow). Upper panel:  $DoC$  at each region computed using offshore WW3 wave conditions ( $DoC_{param,a}$ ). Light bars show  $DoC$  values for  $t = 4$  years and darkest colour bars represent  $DoC$  ( $t = 1$  years). Bottom panel: bars represent the average  $DoC$  for each embayment, computed using the modelled inshore wave conditions and forcing the SWAN wave model with  $H_{s,12}$  and  $T_{p,12}$  derived from the 4-year time series ( $DoC_{param,b}$ ). Minimum and maximum  $DoC$  values for each embayment are represented by the red intervals. Grey bars represent the embayment-averaged depth of the transition between sand and rock. Vertical black dashed lines separate the different regions.

The sand-rock transition depth ( $DoC_{obs,c}$ ) is presented in Fig. 2.7 (bottom panel, grey bars) for comparison with the  $DoC$  estimates obtained using the wave formulations.

There is no obvious alongshore correlation between the sand-rock transition and either the offshore or inshore wave formulations, and this is attributed to sediment availability being a more important factor in determining the sand-rock transition than the hydrodynamic forcing. Additionally, there are no clear alongshore trends in the sand-rock transition. The sand-rock transition ranges from 15 m to > 30 m water depth, which is generally significantly deeper than  $DoC$ , and in some instances double that of the computed  $DoC$  (e.g., Porthmeor, Perranporth, Widemouth, Woolacombe). One exception is Bedruthan Steps, where Eq. 2.2 predicts  $DoC$  at 16 m, while the rocky platform begins at 15 m depth, suggesting this embayment is particularly sediment-starved. At Sennen Cove, the sand and rocky platform transition and  $DoC$  (based on Eq. 2.2) are at a similar depth. Significantly, these results suggest that the upper shoreface active profile for the SW generally has sufficient sediment ( $DoC < \text{sand-rock transition}$ ). However, on the lower shoreface, where sediment transport is more infrequent, there tends to be a lack of available sediment ( $\text{sand-rock transition} < DoC\text{-motion}$ ).

The occurrence of significant along-embayment variability in depth of closure using  $DoC_{param,b}$  (Hallermeier, 1978) is exemplified in Fig. 2.8. Along-embayment variability occurs at locations that display a considerable difference in the shoreline orientation and, therefore, a spatial gradient in the wave conditions. This results in higher  $DoC$  values for more exposed sections (e.g., > 15 m for the W section, Fig. 2.8) compared to more sheltered section (e.g., 5 – 7 m for the NNE section, Fig. 2.8). Such large differences are particularly relevant in *Regions 2, 4 and 6*, which are all sections with considerable variability in shoreline orientation and/or important points of attenuation (refer to Fig. 2.3).

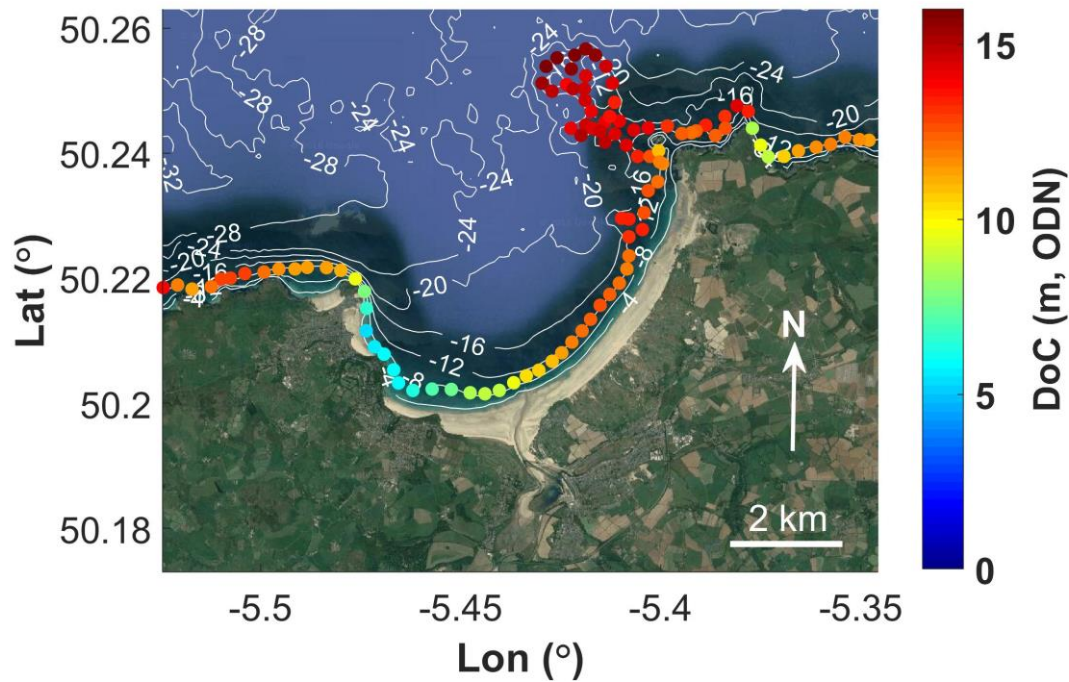


**Fig. 2.8** Example of along-embayment variability in  $DoC$  due to wave transformation for *Region 2* using  $DoC_{param,b}$  (Hallermeier, 1978; Eq. 2.2).

## 2.5.4 $DoC$ determined using bed shear stress maxima ( $DoC_{stress}$ )

### 2.5.4.1 Wave action bed shear stress ( $DoC_{stress,a}$ )

Wave-induced bed shear stress under the most extreme wave conditions ( $H_{s,12}$  and  $T_{p,12}$  for  $t = 4$  years) was computed along the model domains for the six study regions and presented in Fig. 2.9 (left panels). Values of wave-induced shear stress are highly variable along the study sites and these are related to the orientation and configuration of the shoreface. Greater values of  $\tau_w > 5 \text{ N m}^{-2}$  at depths from 10 to 20 m occur in west-facing embayments in *Region 1*, 3, 5 and 6 (Fig. 2.9a, g, m, p), whereas bed shear stresses are significantly less ( $\tau_w < 1 \text{ N m}^{-2}$ ) at similar water depths off NE-facing beaches, such as Porthminster and Carbis Bay in *Region 2* (Fig. 2.9d). Embayments in the north of *Region 4* (e.g., Treyarnon) and many beaches in *Region 5* are very energetic and present values of  $\tau_w = 4.8 \text{ N m}^{-2}$  even in 28 m water depth (Fig. 2.9m). Interestingly, similar values for  $\tau_w$  to the exposed west-facing embayments are registered in 28 m water depth ( $\tau_w \sim 3.5 \text{ N m}^{-2}$ ) in several other NE-facing embayments (e.g., Mother Ives and Harlyn in *Region 4*; Fig. 2.9j). This is attributed to the morphological configuration of these

embayments: they are fronted by a short rocky shelf (c. 700 m) that limits wave energy dissipation during wave transformation and refraction.

**Table 2.2** Dependence of critical shear stress values ( $\text{N m}^{-2}$ ) with sediment size for the considered scenarios: sediment motion, initiation of vortex ripples, initiation of post-vortex ripples and plane bed.

		$D_{50}$ (mm)		
		0.15	0.3	0.6
<b>Bedform activity</b>	Sediment motion	0.17	0.34	0.69
	Initiation of vortex ripples	0.24	0.48	0.95
	Initiation of post-vortex ripples	0.48	0.95	1.91
	Transition to plane bed	2.39	4.78	9.55

Computed wave-induced bed shear stress ( $\tau_w$ ) values are compared to the different case scenarios for sediment transport and bedform activity for the three different sediment sizes (Table 2.2). Wave-induced bed shear stresses exceeding the upper-plane bed transition are presented in Fig. 2.9 (blue line, right panels) as the nearshore sediment transport under such stresses is considered most relevant in shaping the lower shoreface. For *Region 1*, this threshold occurs in depths  $> 30$  m along the exposed northern part of the embayment, but decreases to  $\sim 12$  m at the more sheltered southern end, resulting in an average threshold depth of 19 m (blue line, Fig. 2.9c). In *Region 2*, the location of the upper-plane bed threshold is spatially highly variable with significantly smaller values of 10 m at the southern end, areas where this threshold is not exceeded at all (e.g., Porthminster and Carbis Bay), and a more exposed section with values  $> 28$  m (e.g., Godrevy and Gwithian, blue line, Fig. 2.9f). Embayment-averaged values for the transition depth are generally inflated due to the maximum transition depth values associated with the headlands, which often have values of  $\sim 30$  m. In the more alongshore-uniform *Regions 3* and *4* (blue line, Fig. 2.9i, l), the isobath for the upper-plane bed transition is 22 m and 25 m, respectively. Values for the embayments within these regions are generally around 18 – 20 m for *Region 3* and close to 25 m for *Region 4*, while values are  $> 28$  m around the headlands. In *Region 5*, the depth for the transition to upper-plane bed is largest and is near-constant ( $> 29$  m, Fig. 2.9o). Finally, in *Region 6* (Fig. 2.9r), the transition depth closely follows the 20-m contour line (Saunton, Croyde and Woolacombe), and decreases to 10 m water depth in the south due to wave dissipation by a point of refraction located in the south of the region.

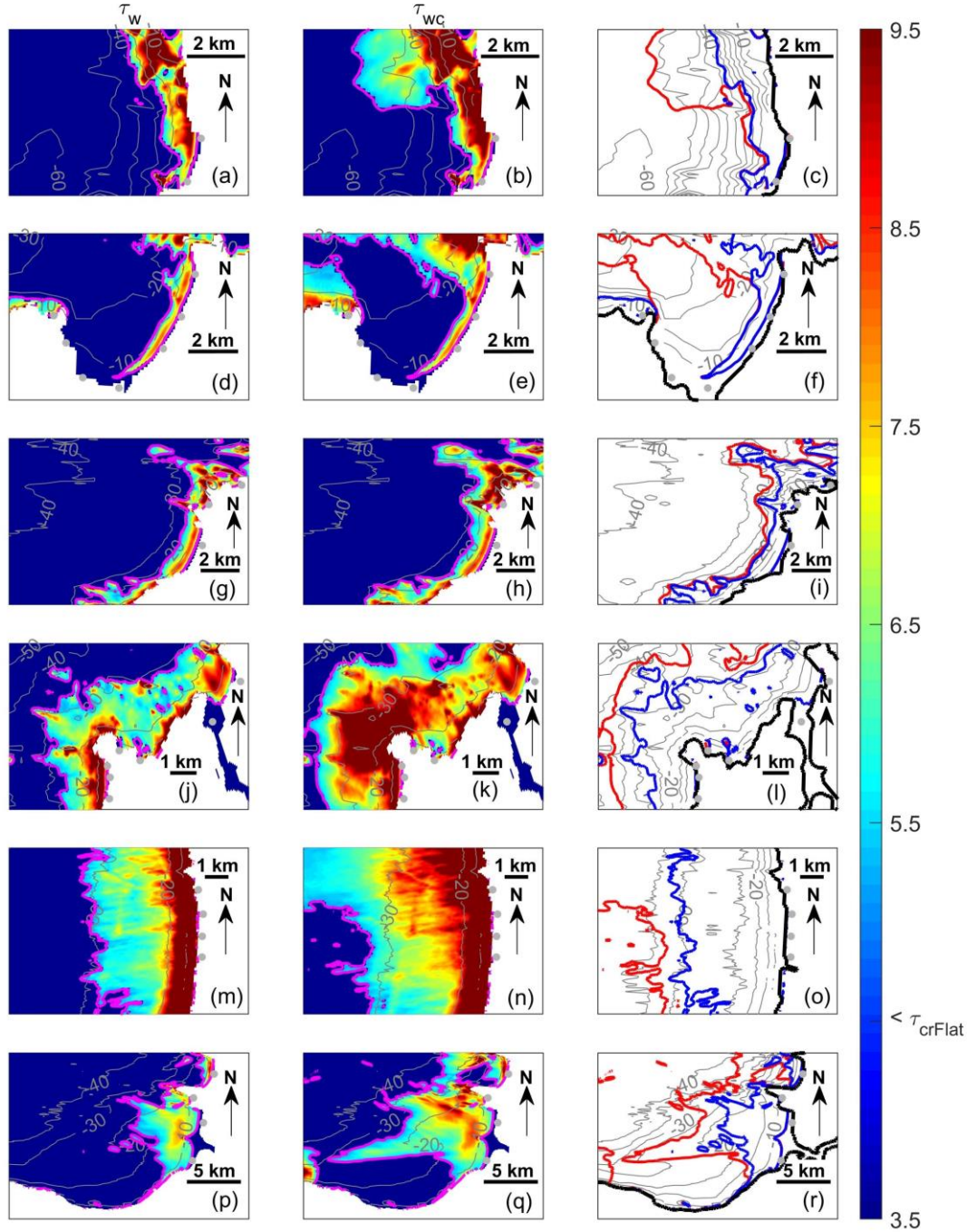


**Fig. 2.9** Left panels show wave-induced bed shear stress ( $\tau_w$ ) computed for extreme wave conditions ( $H_{s,12}$  and  $T_{p,12}$ ) and for *Regions 1 – 6* (a, d, g, j, m, p). Middle panels present combined wave- and current-induced bed shear stress ( $\tau_{wc}$ ) computed for extreme wave conditions ( $H_{s,12}$  and  $T_{p,12}$ ) during maximum values of tidal currents (spring tides) and for *Regions 1 – 6* (b, e, h, k, n, q). Magenta line represents the bed shear stress at the transition to upper-plane bed conditions for medium sand ( $D_{50} = 0.3$  mm,  $\tau_{cr} = 4.77$  N m<sup>-2</sup>). Right panels:  $\tau_w$  (blue) and  $\tau_{wc}$  (red) transition depth to upper-plane bed conditions.

The results are strongly dependent on the sediment size selected for the calculations ( $D_{50} = 0.3$  mm in our case) as shown in Fig. 2.10a. For a sediment size of 0.15 mm the threshold isobaths tend to be > 18 m larger than for medium sand (not shown),

while for the case of the coarser sediment ( $D_{50} = 0.6$  mm), the transition to upper-plane bed is only observed up to 12 m in one of the six domains (*Region 5*, light blue line in Fig. 2.10a). Results for the less energetic scenarios (sediment motion, initiation of vortex ripples and initiation of post-vortex ripples) are not presented as the three associated sediment transport thresholds  $\tau_{cr}$  (for all the considered  $D_{50}$ ) are exceeded throughout all study regions (depths > 50 m).

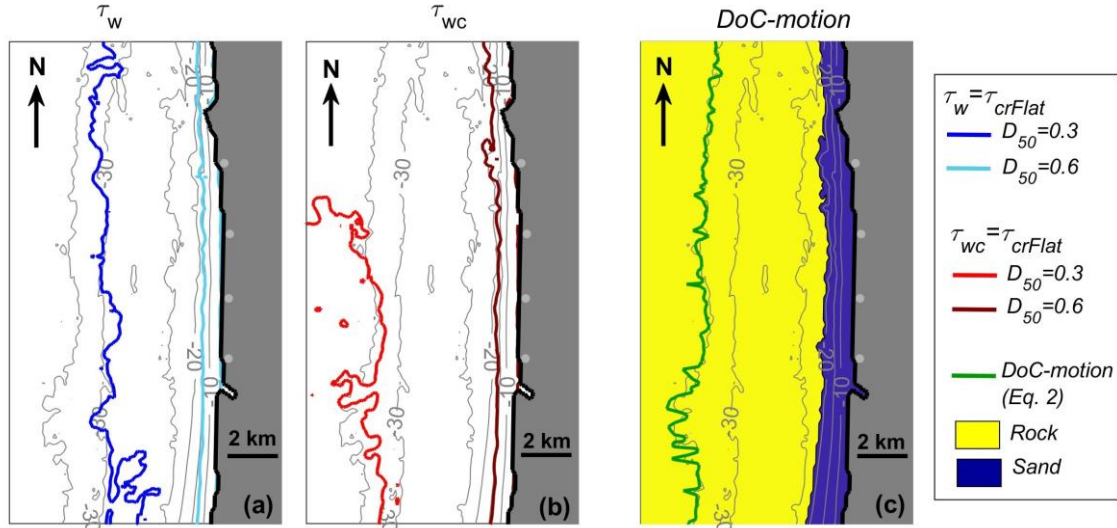


**Fig. 2.10** Bed shear stress at the transition to upper-plane bed conditions for medium and coarse sand ( $D_{50} = 0.3$  and  $0.6$  mm), limit for initiation of motion (*DoC-motion*) and depth between sand and rock for *Region 5*. Bed shear stress transition limit is computed using (a) wave-induced bed shear stress ( $\tau_w$ ) and (b) combined wave- and current-induced bed shear stress ( $\tau_{wc}$ ) computed for extreme wave conditions ( $H_{s,12}$  and  $T_{p,12}$ ) and maximum tidal currents (spring tides). (c) *DoC-motion* is predicted using Hallermeier (1981; Eq. 2.3), and depth between sand-rock is based on observations.

#### 2.5.4.2 Wave and tidal current bed shear stress ( $DoC_{stress,b}$ )

On a high-energy and macrotidal coast, it is important to assess the influence of tidal currents on the bottom stress, in addition to wave agitation, as an additional mobiliser and transporter of sediment. Accounting for the effect of tidal motion on the *DoC* is a prime motivation and novel aspect of this study. The occurrence of combined wave and current bed shear stress ( $\tau_{wc}$ ,  $DoC_{stress,b}$ ) exceeding critical values for transition to upper-plane bed across all study regions is presented in Fig. 2.9 (middle panels). During extreme conditions (storms and spring tides), sheet flow occurs in all the studied LTEs. Maximum depths in the central part of the embayments that register such extreme flows are 20 – 30 m, and these values are very similar to those obtained computing only

wave-induced bed shear stress (red and blue lines in Fig. 2.9, right panels). The contribution of the tidal currents in the computed total shear stresses in the central section of the embayments is small ( $< 0.34 \text{ N m}^{-2}$ ) for the case of *Regions 1 – 3* (Fig. 2.9c, f, i). However, significant increases in  $\tau_{wc}$  relative to  $\tau_w$  are evident around headlands due to stronger tidal currents at these locations (Fig. 2.9c, f, i). Accounting for tidal currents results in an increase of the depth affected by sheet flow of c. 1 m for wide and W-facing LTEs (Fig. 2.9b, h) and in excess of 5 m for short LTEs with variable orientation (Fig. 2.9e, k) as these latter settings are highly influenced by the tidal currents around headlands. Additionally, the maximum limit of sheet flow for combined wave and current bed shear stress increases  $O(10 \text{ m})$  with respect to  $\tau_w$  in embayments affected by large tidal range ( $\text{MSR} = 7 - 8$ , Fig. 2.9q).

The maximum depths of sediment transport (*DoC-motion*, Eq. 2.3) determined for offshore wave values ( $\text{DoC}_{\text{param},a}$ ) are compared with the region-averaged depth values for sediment motion, initiation of vortex ripples, initiation of post-vortex ripples and transition to plane bed ( $\text{DoC}_{\text{stress},b}$ ). The depths of sediment motion, initiation of vortex ripples and initiation of post-vortex ripples under extreme conditions are exceeded across the entire domain for the six regions, and are significantly larger than the parameterized *DoC-motion*. On the other hand, the *DoC-motion* depths correspond closely to the upper-plane bed transition during storm conditions, or the maximum depth of significant potential sediment transport (*DoT*) computed using the process-based method ( $\text{DoC}_{\text{stress},b}$ ), for *Regions 3, 4, 5* and *6* (see Fig. 2.9b,c and Table 2.3). This suggests that *DoC-motion* is more representative of the transition to upper-plane bed conditions than of maximum depth of sediment motion under the influence of maximum wave and tidal shear stresses for highly energetic and macrotidal coastlines.

## 2.6 Discussion

The analysis of the shoreface profile shape (Dean, 1991; Ortiz and Ashton, 2016) linked with the cross-shore distribution of the seabed composition (Roy and Thom, 1981; Thielert et al., 2001; Peters and Loss, 2012) is a useful tool to study sediment availability and beach morphodynamics. The presented analysis of the shoreface shows most likely values of  $A$  between  $0.11 \text{ m}^{1/3}$  and  $0.18 \text{ m}^{1/3}$  for *Regions 1* to *5*, very similar to the

microtidal beaches in the US Atlantic Coast (Dean, 1977) or the mesotidal beaches along the coast of northern Spain (Bernabeu et al., 2003b), characterized by relatively narrow and steep shoreface and high energy regime.  $A$  decreases to  $0.07 \text{ m}^{1/3}$  for embayments in *Regions 2* and *6*. This section presents a steep upper high tide profile similar to tide-modified beaches in Queensland (Dean, 1977; Masselink and Hegge, 1995; Short, 2006), followed by a wide-flat lower shoreface. The shoreface profile shape is representative of macrotidal areas: typically convex up to 12 – 15 m water depth relative MSL, and concave shape for the lower shoreface (Wright and Short, 1984). Additionally, in most of the studied sites, the presence of sand extends from MSL to at least the 20-m depth contour, demonstrating that despite the rocky nature of the coastline of North Cornwall (Leveridge, 2011) there is sufficient sediment present on the shoreface to enable development of an equilibrium shoreface profile.

To facilitate discussion of the different  $DoC$  estimates obtained using the multi-criteria approach, a summary of the results is presented in Table 2.3. Comparing the various applied  $DoC$  formulations provides insights into the usefulness of the different approaches and reinforces the notion that depth of closure is a theoretical concept that will vary according to the used definition. The most widely-used definition for  $DoC$  proposed by Hallermeier (1978), Birkemeier (1985) and Capobianco et al. (1997) is the basal limit of the envelope of profile change or  $DoC$ . When the inshore wave conditions are used ( $DoC_{param,b}$ ), the results correspond with shallow values (10 – 15 m) and are very similar to the limit of significant change using the observational dataset for the case of Perranporth ( $DoC_{obs,a}$ ) for Hallermeier (1978). In contrast,  $DoC$  values computed using Capobianco et al. (1997) and Birkemeier (1985) for inshore wave conditions are always  $O(1 - 2 \text{ m})$  below the observations. Hallermeier (1981) also defined an outer limit ( $DoC_{motion}$ ) as the offshore boundary of the wave-constructed profile. The latter should correspond with the deepest isobath where sediment motion occurs, but analysis of modelled wave and current bed shear stresses ( $DoC_{stress,b}$ ) reveals that this depth corresponds best with the upper-plane bed limit ( $\tau_{wc} > \tau_{crFlat}$ , Table 2.3) under extreme wave conditions, or  $DoT$ . Furthermore, observations of seabed type distribution ( $DoC_{obs,b}$ ) also suggest that significant sediment exchange under high energy conditions (in this case the winter of 2016) is possible at those isobaths. Consequently, some authors

such as Wright (1987, 1995) also considered this deeper limit of extreme motion as a boundary of significant bed-level change, justifying that vertical fluctuations of several cm's (i.e., below the survey accuracy used for defining  $DoC$ ) can represent large volumes of sediment when they are integrated over a wide and gentle-gradient shoreface.

**Table 2.3** Summary of results for the predicted shoreface limits along the SW of England. Region-averaged values of  $DoC$ ,  $DoC$ -motion, sand-rock transition depth,  $DoT$  and associated along-coast standard deviation ( $SD$ ) using the different formulations are presented.

		$DoC_{obs,a}$	$DoC_{obs,b}$	$DoC_{param,a}$				$DoC_{param,b}$					$DoC_{stress}$			
		$DoC$ (m)	Transition depth (m)	$DoC$ - motion (m)	$DoC$ (m)			$DoC$ (m)					$DoT$ (m)			
Region	$SD \leq 0.14$	<i>Sand – rock</i>	Eq. 2.3 <i>Hall.</i>	Eq. 2.2 <i>Hall.</i>	Eq. 2.5 <i>Cap.</i>	Eq. 2.4 <i>Bir.</i>	Eq. 2.3 <i>Hall.</i>	$SD$	Eq. 2.5 <i>Cap.</i>	$SD$	Eq. 2.4 <i>Bir.</i>	$SD$	$\tau_w$ > $\tau_{crFlat}$	$SD$	$\tau_{wc}$ > $\tau_{crFlat}$	$SD$
1	–	12.9	50.1	23.3	17.6	17.5	13.1	1.8	11.8	1.7	9.9	1.3	19	5	22	9.5
2	–	23.1	46.4	21.1	16.2	15.9	9.8	1.6	9.6	1.5	10.1	1.1	0-15	6	0-20	5
3	–	22.5	40.6	20.2	16.3	16.1	13.3	1.6	11.8	1.4	10.0	0.7	22	6	35	5
4	–	21.1	39.4	19.3	15.0	14.6	14.6	1.3	13.1	1	11.1	1.5	28	5	38	5
5	–	21.7	35.2	19.0	14.9	14.2	16.5	0.6	14.9	0.3	12.9	0.3	29	2	35	2
6	–	>30	33.7	18.8	14.8	14.3	14.3	1.9	10.7	0.7	6.8	0.9	19	5	30	4
Perran.	14.5	26*	40.6	20.2	16.3	16.1	14.4	0.4	13.1	0.4	10.8	0.6	22	3	28	5

\*this value corresponds with significant textural change on the seabed.

As identified by Capobianco et al. (1997) and Nicholls et al. (1998b), wave parameterisations ( $DoC_{param}$  methods) are highly dependent on the timescale of interest. We used a 4-year time series of wave conditions, which included the most energetic winter affecting the coast of SW England (winter 2013/14) since at least 1948 (Masselink et al., 2015); this allows a consideration of the predicted  $DoC$  values over at least the decadal time scale. If  $H_{s,12}$  and  $T_{p,12}$  are derived from the complete 4-year time series, the  $DoC$  values are c. 4 m larger than if  $\langle DoC \rangle$  is used (yearly-averaged  $DoC$  computed using  $H_{s,12}$  and  $T_{p,12}$  for each year in the time series). As the concept of depth of closure is generally related to shoreface variability over inter-annual to decadal time scale, it is advisable to select the longest wave time series possible to estimate  $DoC$ . Furthermore,  $DoC$  parameterisations ( $DoC_{param}$ ) suggest that this value will increase over time, moving towards the  $DoT$ .

Previous studies have identified the influence of geological control on the closure depth (Robertson et al., 2008; Ortiz and Ashton, 2016) and, hence, the necessity to use inshore wave conditions when estimating the active shoreface in embayed

coastlines (Kraus et al., 1998). Accordingly, we found that using inshore wave conditions ( $DoC_{param,b}$ ) is more appropriate along embayed coastlines, especially for stretches of coastline not directly facing the prevailing wave direction and/or protected by protruding headlands. However, the closure depth computed using the inshore wave conditions depends on the water depth from which the wave height is extracted: the shallower the depth, the smaller the waves, and the lower the  $DoC$  value. The inshore wave height and associated period extracted at the actual predicted  $DoC$  are used here, obtained through an iterative method, yielding  $DoC$  values that vary along the embayment as a result of the spatial gradient in the wave conditions affecting it.

Similar to the results presented in Robertson et al. (2008), the depth of closure formulation proposed by Hallermeier (1978; Eq. 2.2) provides the best matching with the morphologic observations ( $DoC_{obs,a}$ , and a closure criteria of 014cm defined by the field data collection uncertainty, Table 2.3) and the procedure to compute this depth closure estimate is as follows: (1)  $H_{s,12}$  and  $T_{p,12}$  are computed using the wave time series that encompasses the shoreface monitoring period; (2) the offshore wave conditions are transformed into intermediate/shallow water; (3) the modelled inshore sea state in several representative profiles of the embayment is inserted into Eq. 2.2 and the embayment-averaged closure depth is computed; and (4) the depth of closure value is considered relative to MLWS and then corrected to the survey datum.

As pointed out by Wright (1987), Pilkey et al. (1993), Cowell et al. (2003), and Ortiz and Ashton (2016), the active shoreface is deeper than often predicted using observations and wave-based parameterisations. Recently, Ortiz and Ashton (2016) explored the shoreface dynamics at several locations on the East coast of the U.S. and concluded that  $DoC_{param,b}$  methods under-predict the morphodynamic closure depth. Similarly, our study shows that, in all cases, modelled bed shear stresses for the transitional limits of bedform activity ( $DoC_{stress}$ ) are significantly deeper than those computed using the wave parameterisations ( $DoC_{param,b}$ , Table 2.3). Computed bed shear stresses, reinforced by seabed type distribution observations ( $DoC_{obs,b}$ ), suggest that wave currents during extreme storm events ( $H_{s,12}$  and  $T_{p,12}$ ) can induce energetic sediment transport well seaward of the limit of ‘significant’ morphological change or

$DoC$  (where 'significant' is associated to the minimum detectable limit by the instrumentation) as  $DoT \gg DoC$ . During these events, the wave orbital velocities across the shoreface suggest that under such conditions most of the embayments experience extreme sediment motion, leading to upper-plane bed conditions, up to large depths ( $> 35$  m, Table 3) even when disregarding tidal action. These results are similar to the values for Southeastern Australia (Wright, 1976, Wright, 1995), or the outcomes shown in Wright et al. (1986) and Wright (1987) for the Middle Atlantic Bight, where the limit for on/offshore sediment transport in these microtidal and energetic shelves exceeds the 30-m isobaths. When also considering tidal currents during the maximum flood in a tidal cycle, this transition depth can increase by more than 5 m in areas where coastal geometry and bottom topography (e.g., headlands) induce maximum flow speeds.

Fig. 2.11 synthesises how the maximum depth of sediment transport ( $DoT$ ) varies as a function of wave height and tidal current velocity. The results are obtained using the process-based method (computation of bed shear stresses due to waves and tidal currents,  $DoC_{stress,b}$ ) for transition to upper-plane bed (extreme sediment motion). Traditionally, the  $DoC$  concept is limited to wave-dominated coastlines where tidal currents do not significantly affect sediment transport; however, Fig. 2.11 represents a combined approach to the issue and can be applied to environments where strong tidal currents are important, and waves are not the sole sediment-stirring factor. As can be observed in the figure, whilst keeping  $H_s$  constant,  $DoT$  increases with increasing tidal current velocity and/or increasing wave period. Due to the concurrence of a high-energy wave climate and strong tidal currents,  $DoT$  thresholds along the southwest coast of England (30–50 m) are relatively large compared to most other environments (Fig. 2.11). Moderately energetic shelves (e.g., East coast of England; EE) with large tidal currents can exhibit values for the offshore limit of the active shoreface that are similar to microtidal and more energetic coastlines (Middle Atlantic Bight; MAB). A comparison between the coast of SW England (high energy, macrotidal) to New South Wales, Australia (high energy, microtidal), indicates that  $DoT$  values are c. 10 m deeper in the SW England, due to the presence of greater tidal currents.

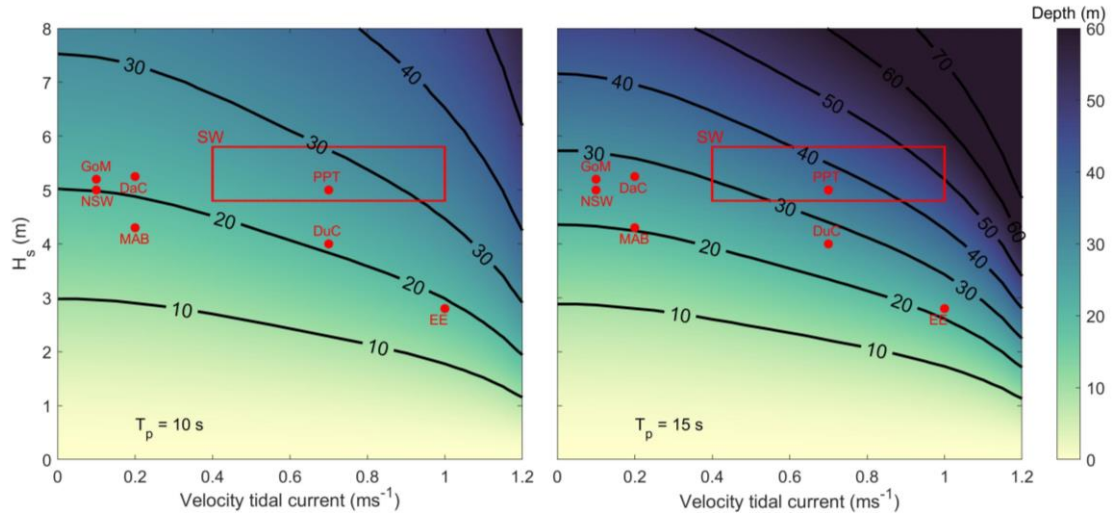


**Fig. 2.11** Variation of  $DoT$  across a broad wave-current parameter space.  $DoT$  is computed using significant wave height ( $H_s$ ) and tidal current speed in the bottom layer ( $\bar{U}$ ) for medium sand ( $D_{50} = 0.3$  mm) and a constant period ( $T_p$ ) of 10 s (left panel) and 15 s (right panel). Examples of computed  $DoT$  values using extreme significant wave height ( $H_{s,99\%}$ ) and maximum tidal current in the bottom layer are shown as red dots: *GoM* – Gulf of Mexico (Pepper and Gregory, 2004; Ortiz and Ashton, 2016); *NSW* – New South Wales (Kulmar et al., 2005); *MAB* – Middle Atlantic Bight (Wright, 1994); *DaC* – Danish Coast (Aagaard et al., 2010); *DuC* – Dutch Coast (Luijendijk et al., 2017); *EE* – East England (Haskoning, 2005; Leonardi and Platter, 2017); and *PPT* – Perranporth. The range of  $H_s - \bar{U}$  combinations estimated for the SW (South West England) is also indicated (red box).

During extreme storm events, exposed embayments can experience cross-shore sediment transport that exceeds the depth of the base of headlands, allowing sediment to move a considerable distance seaward of the beach-constraining headlands. Furthermore, along a macrotidal coast, the shoreface area that is morphodynamically active during these storm events will increase due to the contribution of the tidal currents to the total bottom shear stress, especially during spring tides. A conceptual model of the shoreface dynamics for an idealised high-energy and macrotidal coast that illustrates this situation is presented in Fig. 2.12. The implication is that, even though the headlands that flank many embayed beaches appear sufficiently prominent to suggest that the embayed beach can be considered a closed cell (with restricted sediment transport in/out the cell), significant sediment transport at a short time-scale may take place well beyond the ends of the headland, leading to headland bypassing. Some recent studies also point in this direction, demonstrating that cell compartments often includes several embayed beaches (Kinsela et al., 2017; McCarroll et al., 2018) and that transport

of sediment under extreme events is likely to occur even around headlands with an apex that reaches the 50-m isobath (George et al., 2016). This challenges the notion that embayed beaches are generally closed cells and that headland bypassing may be more widespread than commonly assumed. Accordingly, a re-evaluation of the concept of closed embayments is especially appropriate for the north Cornish coastline, as these embayments can be deemed opened cells, and indeed, the coast of SW England as a whole can perhaps be considered a single sediment cell from Land's End to the Bristol Channel, as previously suggested by May and Hansom (2003). Additional assessment of the nature (open or closed) of the embayments along this coastline is conducted in Chapter 3 using Perranporth beach as a study case.

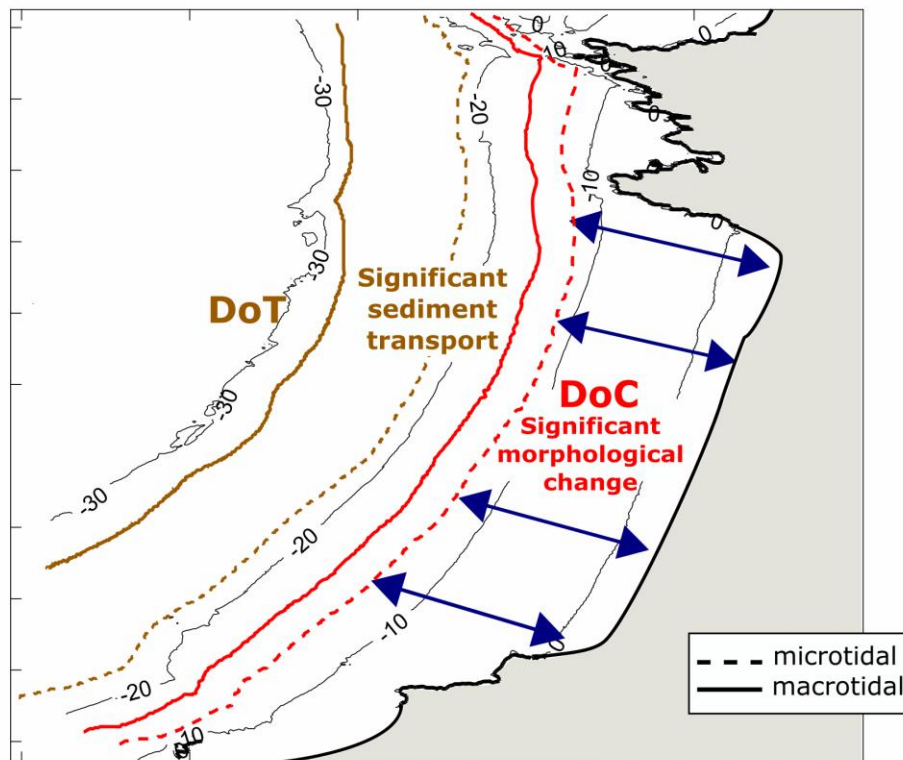


**Fig. 2.12** Plan view of an idealised high-energy and embayed coastline. *DoC* and *DoT* limits are included for both microtidal (dashed lines) and macrotidal settings (solid lines).

## 2.7 Conclusions

This chapter revisits the 'depth of closure' (*DoC*) concept through the study of the predicted zone of significant sediment transport and evaluates its applicability to

the macrotidal and exposed coastline of SW England, discussing the implications for headland bypassing and exploring the open/closed cell concept along embayed coastlines. Two main closure limits based on shoreface morphodynamics and seabed activity are considered: the widely-used morphological depth of closure ( $DoC$ ) defined as the basal limit of the envelope of profile change, and a deeper limit of maximum depth of 'significant' sediment transport ( $DoT$ ) under extreme events, where 'significant' refers to intense bed agitation represented by the upper-plane bed transition. The key findings are:

- $DoT$  is considered a boundary of significant bed level change as up to that water depth intense sediment transport takes place (upper-plane bed transition). Although over the medium-term time scale (years) these morphological changes might not be detectable (below the survey accuracy), they are likely to represent large volumes of sediment when integrated over the shoreface.
- Along embayed coastlines, inshore wave conditions (using the longest time series possible) must be used to compute  $DoC$ , as offshore wave conditions are not representative due to wave transformation processes. Wave attenuation, refraction and diffraction around headlands can result in a large spatial gradient in the inshore wave conditions, and the local embayment geometry can have a greater impact on  $DoC$  values than any regional variability in wave exposure.
- The wave-based parameterization of depth of closure by Hallermeier (1978; Eq. 2.2) provides a good approximation of observed morphological depth of closure (for a minimum detectable limit of 0.14 m) at the medium-term scale for the exposed and macrotidal study area, if calculated relative to MLWS.
- The active shoreface is deeper than often considered by engineering practice. Combined wave-tide bed shear stresses computed following a process-based method, reinforced by seabed type distribution observations, suggest that important sediment transport during extreme conditions occurs well seaward of the limit of 'significant' morphological change.
- $DoT$  is computed across a broad wave height and (tidal) current velocity parameter space to investigate the influence of currents on wave-derived

values for maximum depth of significant transport at a range of contrasting coastal locations. *DoT* depths can be increased by ~10 m  $O(30\%)$  for macrotidal locations compared to microtidal environments with a similar wave climate, highlighting the importance of considering tidal currents in realistic *DoT* calculations.

- The considerable depth ( $\gg 30$  m) at which combined wave- and tide-driven sediment transport can occur under extreme wave conditions along exposed, macrotidal and embayed settings implies that transport of fine and medium sediment under extreme events can exist around headlands with an apex base that surpasses the 30-m isobath. This significantly increases the potential for headland bypassing and challenges the notion that embayments are generally considered closed sediment cells.

## Chapter 3 – New insights into multi-annual embayment scale sediment dynamics

---

This chapter contains work previously presented in the following paper included in Appendix B:

N.G. Valiente, G. Masselink, R.J. McCarroll, T. Scott, M. Wiggins, 2019. Multi-annual embayment sediment dynamics involving headland bypassing and sediment exchange across the depth of closure, *Geomorphology*, 314, 48–64. <https://doi.org/10.1016/j.geomorph.2019.06.020>.

### 3.1 Introduction

Sandy beaches and coastal dunes have significant natural capital through representing efficient and natural coastal defences that can protect the hinterland from coastal flooding. In a context of increasing winter-wave conditions (Castelle et al., 2018a) and an increasing rate of sea-level rise (Church and White, 2011), it is important to understand how coasts respond and evolve as a result of changing boundary conditions, as this significantly affects continued human occupation of the coastal zone. Predicting coastal system behaviour requires an accurate delineation and understanding of coastal cell boundaries, sediment sources and sinks, and transport pathways. The difficulties with identifying these key sediment-related factors, attributed to large uncertainties associated with sediment transport modelling and a paucity of high-quality field datasets extending from the top of the dunes to depths beyond the depth of closure (Aagaard, 2011; Coco et al., 2014), inhibit accurate quantification of sediment fluxes in a particular littoral cell. Moreover, long-term beach response is controlled by the sediment exchanges between the different beach sub-components (e.g., dunes, supratidal beach, inter-tidal zone, and sub-tidal zone), and these sub-components tend to operate over different time scales (Castelle et al., 2017b).

A quantitative understanding of littoral cells and sediment budgets is a fundamental element of coastal sediment studies (Bowen and Inman, 1966; Caldwell,

1966; Komar, 1998; Rosati, 2005). Littoral cell (self-contained or semi-contained; refer to Fig. 3.1) and sediment budget concepts were introduced in the 1960s through several regional studies based upon coastal geology (rocky headlands) and estimates of longshore sand transport along specified sources and sinks (Bowen and Inman, 1966; Caldwell, 1966; Inman and Frautschy, 1966). Littoral cells are essentially defined as self-contained coastal units over a period of time, usually separated by prominent features (often headlands or jetties) that impede transfer of sediment (Kinsela et al., 2017). These cell boundaries delineate the spatial area within which the budget of sediment is known, providing the framework for the quantification of coastal erosion and accretion (CIRIA, 1996). Whether a littoral cell can be considered contained (Fig. 3.1-left panel) or semi-contained (Fig. 3.1-middle and right panels) depends on the timescale of consideration. Often, a compartment or coastal cell may appear closed, but over longer timescales during which long return period events inducing severe sediment transport are included, it may actually be open or semi-contained. Therefore, primary sediment compartments (self-contained/closed) are those that capture the limit in the sediment pathway within a large sediment-sharing area for long timescales ( $10^1$ – $10^2$  years); while sub-cells are usually finer in scale, identify semi-contained/open systems at timescales  $> 10^1$  years and can appear closed in the short-term ( $< 10^1$  years) (Rosati, 2005; Kinsela et al., 2017; Thom et al., 2018).

Highly embayed beaches are often considered closed cells (Fig. 3.1-left panel) with the prominent headlands acting as barriers to littoral drift, such that sediment transport into and/or out of adjacent cells is insignificant. Nevertheless, recent studies show that significant sediment transport offshore and/or beyond these barriers exists under particular conditions, inducing headland bypassing (Short, 1985; Short and Masselink, 1999; Short, 2010; Cudaback et al., 2005; Loureiro et al., 2012; George et al., 2015; Vieira da Silva et al., 2017; McCarroll et al., 2018). Short (1985) suggested that major storm wave events are one of the key drivers of headland-attached bar bypassing, allowing sand to be transported to the morphological depth of closure ( $D_{oC}$ ) and beyond the headland position. Additionally, recent studies of mega-rips and beach response to extreme storm events also reveal important cross-embayment exchanges across the shoreface to deeper water (Short, 2010; Loureiro et al., 2012; McCarroll et al.,

2016) and between adjacent beaches (Cudaback et al., 2005; Vieira da Silva et al., 2017). Furthermore, new research also emphasizes the influence of the strong tidal currents registered around headlands in facilitating bypassing at macrotidal environments (McCarroll et al., 2018; King et al., 2019; Valiente et al., 2019a). All these studies demonstrate that under certain conditions of wave-tidal current interaction, important sediment transport paths occur at depths that well exceed the depth of the base of headlands. This understanding challenges the notion of embayments as closed coastal cells and highlights some limitations to the littoral cell and the depth of closure, critical concepts for long-term coastal evolution studies (e.g., application of the Bruun rule) and shoreline modelling (e.g., one-line models).

A total sediment budget approach to a coastal cell enables derivation of incoming and outgoing sediment fluxes from the rate of sediment volume change within the cell. A significant research gap exists in quantification of sediment budgets, in that many studies examine parts of the budget (e.g., the inter-tidal), while extremely few studies capture the entire system. This information helps with confirming the status of a closed cell and estimating the long-term coastal evolution (Wiggins et al., 2019). For a given coastal cell, the sediment budget ( $dQ_{net}$ ) is expressed by the balance of volumes between sediment supply ( $\Sigma Q_{source}$ ) and sediment losses ( $\Sigma Q_{sink}$ ) in the compartment (Rosati, 2005; Aagaard, 2011). In both closed (Fig. 3.1-left panel) and balanced systems (Fig. 3.1-middle panel)  $dQ_{net} = 0$ ; however, for unbalanced systems (Fig. 3.1-right panel),  $dQ_{net} \neq 0$  and in this case the volume of incoming sediment is not the same as the volume that exits the system. For prograding shorefaces and retrograding shorefaces,  $dQ_{net} > 0$  and  $dQ_{net} < 0$ , respectively. Sediment sources include longshore transport of sediment into the area, cross-shore supply of sediment from offshore (beyond the cell seaward limit), anthropogenic interference (beach nourishment), in-situ production of sediment (Kinsela, 2017) and supply from autochthonous sources, such as rivers and dune and cliff erosion (Aagaard, 2011). Sediment losses from the upper shoreface can be accomplished through longshore and cross-shore processes. Sediment can leave embayments through headland bypassing, onshore aeolian transport beyond the coastal dune region (e.g., into a back-barrier lagoon) and offshore exchange from the upper

shoreface to larger depths, i.e., beyond the *DoC* from where sediment may not be transported back onshore.

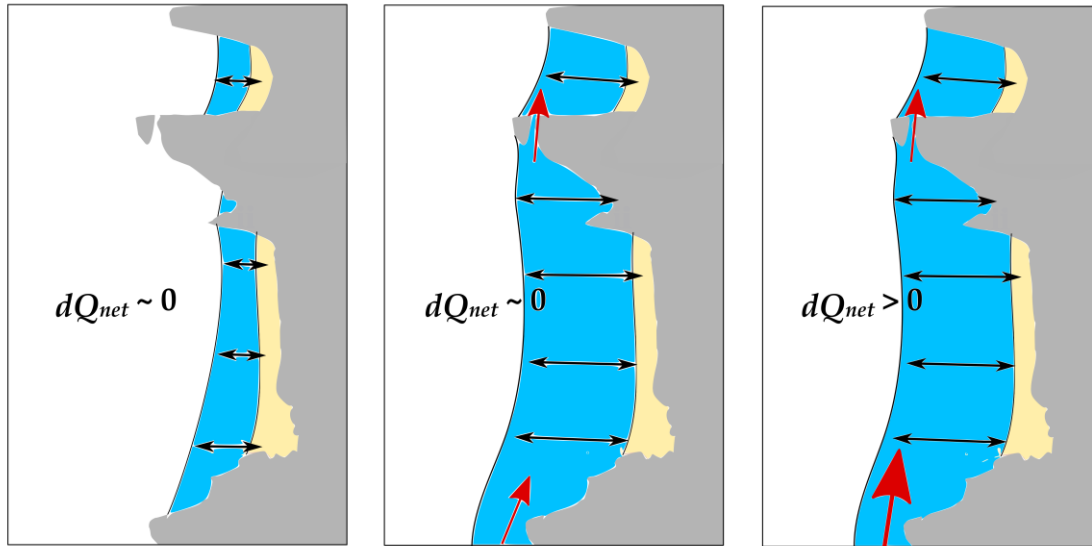


**Fig. 3.1** Plan view of beach-inner shelf dynamics for a closed cell (left panel), a balanced open system (middle panel) and a non-balanced open system (right panel) using an idealized high-energy, cross-shore dominated and embayed coastal cell section. Red arrows depict sediment fluxes in/out of the embayment with size representing magnitude.

Most of current coastal research based on observations lack rigorous uncertainty calculation, potentially identifying measurement artefacts as real morphological changes and consequently, misrepresenting sediment fluxes. For a robust quantification of cross-shore and longshore sediment fluxes within coastal cells, is important to distinguish real changes from noise (Lane et al., 1994; Milne and Sear, 1997; Lane, 1998; Brasington et al., 2000; Lane et al., 2003; Wheaton et al., 2010; Wiggins et al., 2019; Guisado-Pintado and Jackson, 2019). Sandy coastlines commonly exhibit vertical morphological fluctuations of similar magnitude to the uncertainty associated with the measurement. In order to account for this uncertainty, but retain information on real morphological change, effective spatially-variable uncertainty computation techniques are required (Brasington et al., 2003; Lane et al., 2003, Wheaton et al., 2010).

In this study, we apply a total sediment budget approach based on field observations and spatially-variable uncertainty analysis. We evaluate the inter-annual dynamics of Perranporth beach, a sandy, exposed and embayed coastal system located

on the north coast of SW England, over multi-annual time scales. Recent model-based studies investigated the potential for headland bypassing and offshore shoreface limits for significant sediment transport across Perranporth (McCarroll et al., 2018; Valiente et al., 2019a). These indicated that the sub-tidal zone is potentially as dynamic as the rest of the beach system, and that, despite the cross-shore dominated nature of this type of embayment, alongshore processes and sediment fluxes may play an important role in the sediment balance of the system. Hence, we examine: (1) inter-annual morphological evolution of the inner embayment, including cross-shore and longshore sediment exchanges between sub-systems, and outer bar dynamics; (2) multi-annual full embayment morphological response to the 2013/14 winter, which represents the most energetic period along most of the European Atlantic coast since at least 1948 (Masselink et al., 2016b), using a total sediment budget approach;; (3) relationship between wave forcing and embayment response; and (4) the nature of Perranporth's coastal cell (closed or open).

A description of the study area together with the methodology applied to estimate the total sediment budget is presented in Section 3.2. A comprehensive analysis of quasi-full embayment (inter-annual records of dune, inter-tidal and sub-tidal regions) and outer bar beach morphology is presented in Section 3.3. This analysis is extended spatially (for multi-annual epochs) to the full embayment (coastal cell) by including observations offshore ( $> -40$  m Ordnance Data Newlyn, ODN) and beyond the bounding headlands for the years 2011, 2016, 2017 and 2018 in Section 3.4. Links between wave forcing and embayment morphological change are presented in Section 3.5. Section 3.6 presents discussion with a conceptual sediment budget model. Finally, conclusions are presented in Section 3.7.

## **3.2 Study area and methodology**

### **3.2.1 Perranporth beach**

Perran and Penhale Sands beach (hereafter noted as Perranporth beach) is a sandy, exposed, dissipative and macrotidal embayment located on the north coast of Cornwall, SW England (Fig. 3.2a). The configuration of the beach is typical of this

coastline (Burvingt et al., 2018), which is characterized by sandy beaches embayed by sharp headlands (Fig. 3.2b). The site represents a 3.5-km long wide sandy beach facing 290° at the south and 280° at the north, backed by an extensive and high dune system both in the north (Fig. 3.2c, 60 m ODN) and south (Fig. 3.2d, 20 m ODN), divided by a small headland (Cotty's Point). The embayment is delineated by Ligger Point (northern end) and Droskyn Point (southern end), comprised of metamorphic rocks with 40-m high cliffs dropping near vertically (at their most offshore extent) to 2 – 7 m depth ODN at the south and to 5 – 7 m depth ODN at the north. The southern hindshore dune system is the center of numerous anthropogenic interventions that affect the natural morphologic response of that area of the beach, in contrast to the northern dunes where natural processes dominate. The beach presents a relatively featureless upper inter-tidal zone, a three-dimensional lower inter-tidal region (around MLWS), mostly characterized by inner low-tide bar/rip systems (Masselink and Short, 1993; Scott et al, 2011), and a sub-tidal outer bar oscillating between 5 to 7 m depth ODN, which presents two different sequences of transitional states (upstate and downstate) that depend on the wave conditions (Austin et al., 2013; Masselink et al., 2014; Poate et al., 2014). The shoreface is characterized by a low-gradient (mean bed slope of 0.018) with the limit of detectable morphological change or morphological depth of closure ( $D_{oC}$ ) at -14.5 m located 750 – 950 m from the mean sea level (MSL; approximately 0.3 m ODN) and a c. 500-m wide inter-tidal region. Perranporth beach is composed of medium sand with a median grain size ( $D_{50}$ ) of 0.33 – 0.40 mm for the supra- and inter-tidal area (Prodger et al., 2017). The  $D_{50}$  attains a relatively constant value of 0.30 mm for the sub-tidal area with gravel patches ( $D_{50} = 2 – 3$  mm) appearing around 26 m depth ODN (Valiente et al., 2019a).

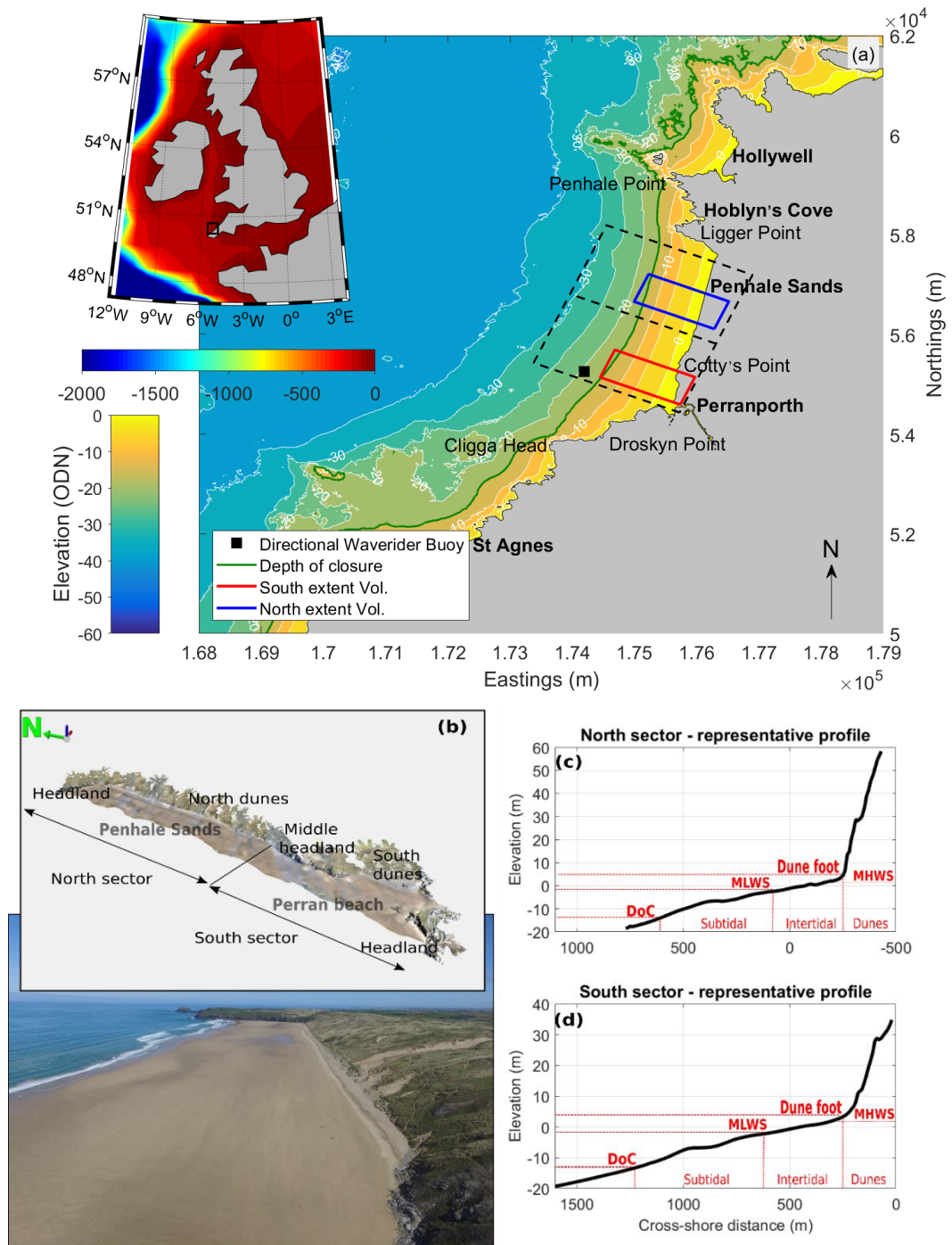


**Fig. 3.2** (a) Location map of Perranporth beach, SW England, physical context and regions used for quasi and full embayment volume time series calculation (red and blue boxes, and black dashed region, respectively). (b) Embayment 3D-view with extension of north and south sectors and aerial photograph of Penhale Sands taken to the north showing north dune system. Bottom right-hand panels show a representation of a vertical profile from the frontal dune system to the inner-shelf for the north (c) and south (d) beach sectors, including the considered sub-systems (sub-tidal, inter-tidal and dunes).

Perranporth is exposed to regular North Atlantic swell with an annual average significant wave height ( $H_s$ ) of 1.6 m and peak period ( $T_p$ ) of 10.2 s, and storm events with a 1% exceedance wave height and associated peak wave period of 4.6 m and 16.7 s, respectively (Fig. 3d). Incoming wave energy displays strong seasonal modulation (Fig. 3a, b) with monthly average  $H_s$  ranging from 1.2 m (June) to 2.3 m (January) over the period 2007 – 2018. Wave approach is typically from the W (0.5 probability) and WNW (0.4 probability), with the larger winter waves also slightly more northerly in direction (WNW:  $H_{s,50\%} = 1.6$  m; W:  $H_{s,50\%} = 1.3$  m; WNW:  $H_{s,1\%} = 5.2$  m; W:  $H_{s,1\%} = 4$  m). Therefore, winters are associated with peaks in southerly-directed (negative) alongshore wave power ( $P_y$ ) (Fig. 3.3f). The tidal regime is semi-diurnal and macrotidal with a mean spring and neap tidal range of 6.3 m and 2.7 m, respectively (Masselink et al., 2014; Scott et al., 2016). Tidal currents with values of c.  $0.7 \text{ m s}^{-1}$  are registered during spring tides near the headlands (Valiente et al., 2019a). The flood-ebb asymmetry in the current magnitude during a tidal cycle results in a northward tidal net residual current along the embayment (McCarroll et al., 2018), in particular near the northern headland. Computed bed shear stresses, reinforced by observations of sediment distribution within the embayment, suggest that wave-driven currents during extreme storm events can induce energetic sediment transport well seaward of the *DoC*, even when disregarding tidal action (Valiente et al., 2019a). When also considering tidal currents during the maximum flood in a tidal cycle, the depth limit for this dynamically active shoreface increases by more than 5 m, reaching 28 m depth ODN (Valiente et al., 2019a; refer to Chapter 2).

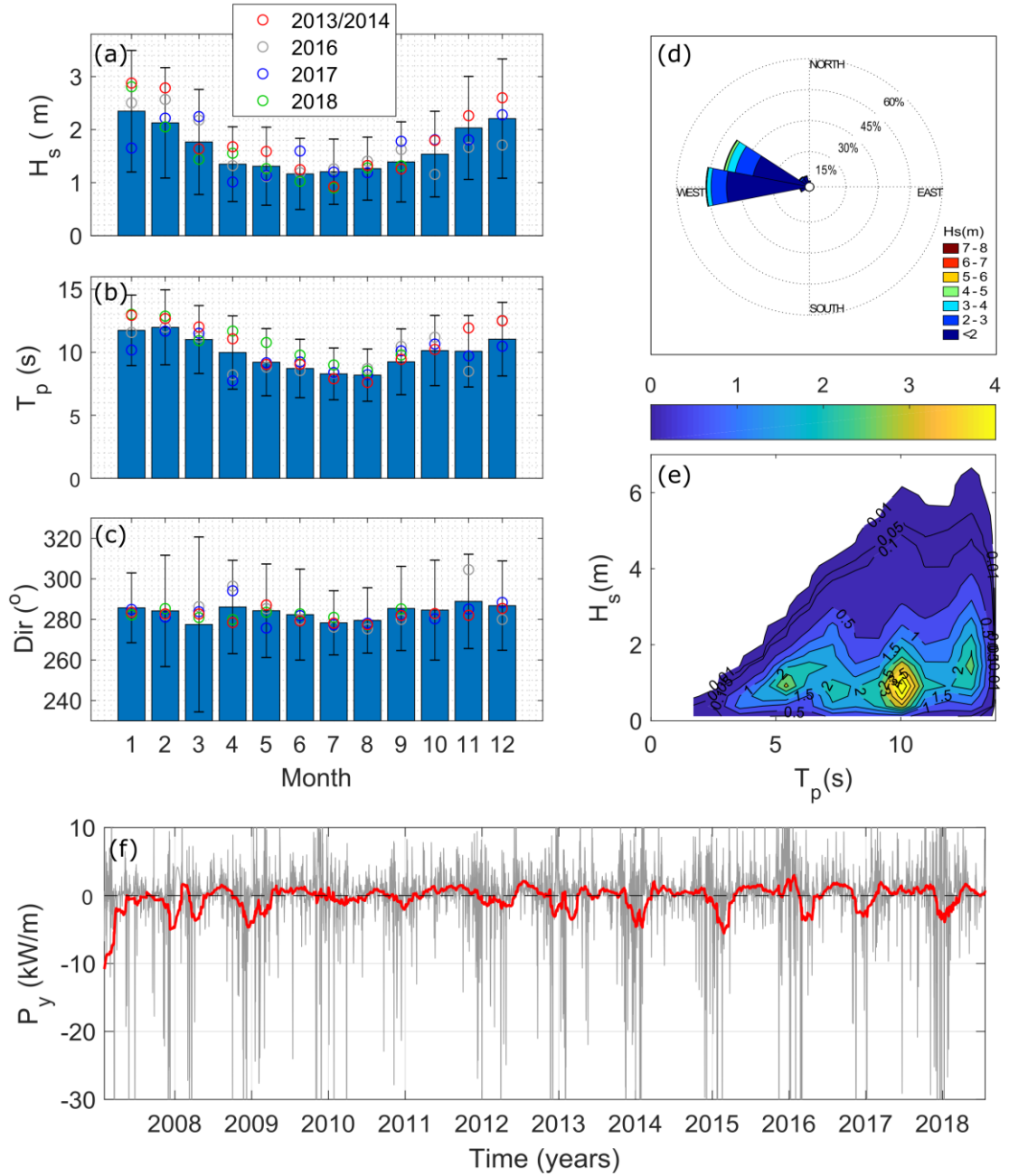


**Fig. 3.3** Monthly statistics of: (a) significant wave height; and (b) peak wave period; and (c) wave direction, computed for the period 2007 – 2018. Wave statistics were derived from the Perranporth directional waverider buoy (refer to Fig. 3.2a for location). In all left panels, bars indicate monthly-averaged values with error bars showing the monthly standard deviation and circles indicating 2013/2014 and years 2016 – 2018 monthly-averaged values. (d) Directional wave rose showing distribution of  $H_s$  and (e) joint probability of  $H_s$  and  $T_p$  with percentage occurrence contours. (f) 11-year time series of alongshore wave power,  $P_y$  (1-day and 8-week running mean) for an averaged orientation of c. 285°. Southward  $P_y$  is negative and northward  $P_y$  is positive.

### 3.2.2 Multimethod morphological surveys

The complete dataset used in this paper is complex as it involves various survey methods at a range of spatial and temporal extents. Fig. 3.4 provides an overview of the coverage of the dataset collected by the Coastal Processes Research Group (CPRG), University of Plymouth, and the Plymouth Coastal Observatory (PCO) since October 2006. The south part of the beach has been monitored for over 10 years, whereas the northern part has only been surveyed since 2016.

Monthly inter-tidal beach surveys covering the south part of the beach (red box; Fig. 3.2a) were conducted since October 2006. Airborne LiDAR datasets that cover the inter-tidal beach and dune system of the whole beach, obtained from PCO, are available for 2008, 2009, 2011, 2012, 2014, 2016 and 2017. The monthly inter-tidal all-terrain vehicle (ATV) based real-time kinematic Global Positioning System (RTK-GPS) surveys of the south area of the beach are complimented with quasi-quarterly single-beam echosounder bathymetric surveys (herein SBE) for the sub-tidal zone during the period 2010 – 2012 and 2014 – 2018. Only since 2016 was the survey program specifically designed to enable quantification of the total sediment budget and net sediment fluxes for Perranporth beach, and multi-method morphological surveys capturing the entire beach (black dashed box; Fig. 3.2a) from May 2016 were performed during spring and autumn. The sub-tidal coverage was extended (down to a depth of -40 m ODN) through conducting yearly (spring/summer) multi-beam echosounder bathymetric surveys (herein MBE). Despite great efforts to collect sub-tidal data, Perranporth is an exposed high-energy environment and areas in close proximity to headlands were too hazardous to survey due to exposed rocks and breaking waves, and hence are not covered in this analysis.

Photogrammetric data of the south and north dunes were collected using an DJI Phantom 4 quadcopter (herein unmanned aerial vehicle; UAV), covering the supratidal up to an elevation of 30 m ODN. Ground control points (GCPs) were vertically and horizontally distributed throughout the survey region at intervals of 100 – 250 m and were surveyed by RTK-GPS for constraining bundle adjustment during Structure-from-Motion post-processing workflow. The inter-tidal and supratidal zone was surveyed

using ATV-based Trimble 5800 RTK-GPS, with line spacing of 20 – 25 m. The shallower sub-tidal data were collected using a Valeport Midas Surveyor single-beam echosounder with a 210 KHz transducer with a sample rate of 6 Hz mounted on an Arancia inshore rescue boat (IRB) and external Trimble 5800 RTK-GPS positioning. These bathymetric surveys were conducted following cross-shore transects at 50-m spacing for inshore lines (< 10 m depth) and 100-m spacing for offshore lines (> 10 m depth). Yearly multi-beam echosounder bathymetric surveys were collected using a pole-mounted 400 kHz R2Sonic 2024 MBES, with motion data provided by a vessel-mounted GNSS-aided Applanix POSMV MRU and primary positioning provided by a Trimble SPS RTK-GPS system.

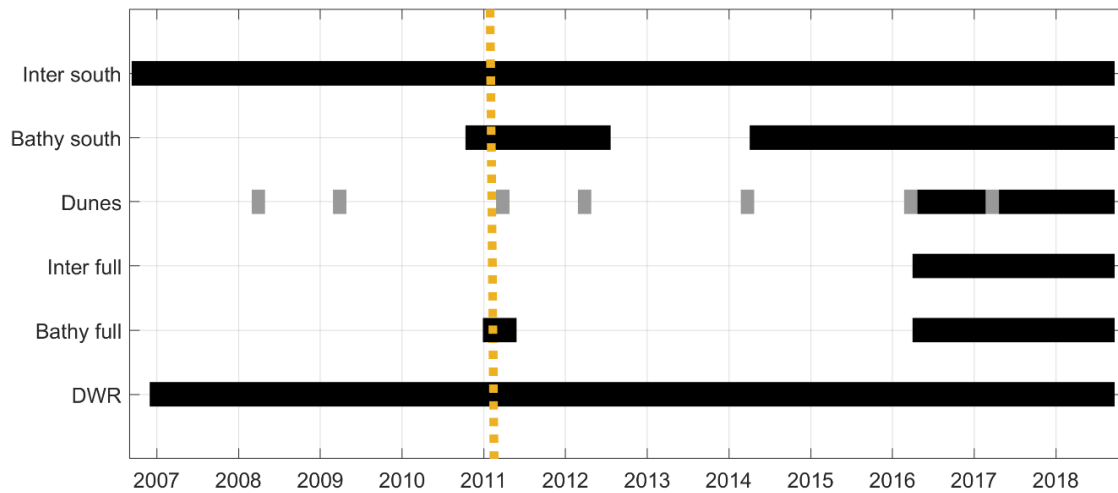


**Fig. 3.4** Timeline of the data sources available for analysis. From top: Perranporth beach inter-tidal beach morphology (Inter south), Perranporth beach sub-tidal bathymetry (Bathy south), full embayment dune morphology from LiDAR and UAV (Dunes), full embayment inter-tidal beach morphology (Inter full), full embayment sub-tidal bathymetry (Bathy full) and directional wave rider buoy (DWR). Grey stripes show years for which LiDAR data are available. Orange dashed line represents winter 2011 reference state.

### 3.2.3 DEM creation

Three sets of 2-m gridded digital elevation models (*DEMs*) were constructed from composite datasets: (1) 27 *DEMs* covering the southern inter- and sub-tidal beach for the period 2010–2018 (red box, Fig 3.2a); (2) 6 seasonal *DEMs* covering the quasi full embayment (black dashed box down to *DoC*, Fig 3.2a) from the sub-tidal to the dunes

(included), hereafter referred to as the ‘inner embayment’, for the period 2016 – 2018; and (3) 3 *DEMs* covering the entire embayment including adjacent areas beyond the bounding inner headlands (including depths > 18 m), hereafter ‘full embayment’, for the years 2011, 2016 and 2018 (Table 3.1). Topographic (RTK-GPS) and bathymetric (SBE) measurements (RTK+SBE; 27 *DEMs*) were combined using a Loess interpolation function (Plant et al., 2002), with variable smoothing scales and maximum permissible interpolation error level of 0.15 m. Individual UAV, RTK+SBE and MBE datasets were combined for the final multimethod full embayment *DEM* construction with natural neighbor interpolation function (Sibson, 1981).

To determine the impacts of the 2013/14 winter storms on the Perranporth beach sediment budget, an additional full embayment dataset for the year 2011 was constructed by combining LiDAR and multi-beam bathymetry, corrected and referenced to ODN using the Vertical Offshore Reference Frame separation model (VORF) facilitated by the United Kingdom Hydrographic Office. 2011 was the closest (and only) year with an available bathymetry useful to reconstruct the pre-2013/14 storm full embayment *DEM*.

**Table 3.1** Component gridded datasets and calculated uncertainty ( $\sigma$ ) included in the 3 full embayment *DEMs*

<i>Name</i>	<i>Method</i>	<i>Date</i>	<i>Coverage</i>	<i>Calculated uncertainty, <math>\sigma</math> (m)</i>
2011 <i>DEM</i>	LiDAR	01/2011	Dunes, supra- and inter-tidal (-2 – >30 m)	0.15
	SBE	01/2011	Sub-tidal (-10 – 2 m)	0.05
	MBE	2011, not specified	Sub-tidal (< -7 m)	0.27
2016 <i>DEM</i>	UAV	04/2016	Dunes (4 – >30 m)	0.06
	RTK	04/2016	Supra- and inter-tidal (-2 – 4 m)	0.04
	SBE	04/2016	Sub-tidal (-18 – 2 m)	0.05
	MBE	08/2016	Sub-tidal (-16 – <-30 m)	0.06 – 0.3 *
2018 <i>DEM</i>	UAV	09/2018	Dunes (4 – >30 m)	0.06
	RTK	09/2018	Supra- and inter-tidal (-2 – 4 m)	0.05
	SBE	09/2018	Sub-tidal (-18 – 2 m)	0.05
	MBE	06/2018	Sub-tidal (-16 – <-30 m)	0.06 – 0.3 *

\*majority of values < 0.15 with maximum values registered around a rocky platform at the northern sector outside the embayment domain

### 3.2.4 Full embayment volume change computation

Full embayment morphological measurements were used to calculate volume change and derive net sediment fluxes following a total sediment approach and accounting for gridded uncertainty through the domains. Several approaches to quantifying the total sediment budget of a coastal cell exist (Van Rijn, 1997; Cowell et al., 2003; Aagaard, 2011; Van Rijn, 2011); however, none of these account for the associated uncertainty ( $\sigma_{DEM}$ ) in the volume computation. Here, we follow the methodology proposed by Wheaton et al. (2010) applied to rivers and later used by Wiggins et al. (2019) for application to gravel beach environments. This methodology consists of three main steps: (1) computing the surface uncertainty associated with the digital elevation model (*DEM*); (2) quantifying the *DEM* of difference ( $DoD = Z_{DEM_1} - Z_{DEM_2}$ ) and the propagated uncertainty or minimum level of detection,  $minLoD = \sqrt{(\sigma_{DEM_1}^2 + \sigma_{DEM_2}^2)}$  for a defined confidence level (95% in this instance); and (3) only considering significant bed-level changes by disregarding elevation changes that are less than the *minLoD* value (herein *LoD*).

Estimates of net morphological change are fundamentally controlled by *DEM* quality, itself largely inherited from the quality of the survey data (Wise, 1998; Wechsler, 2003; Wechsler and Kroll, 2006; Wheaton et al., 2010). We quantify the quality of each *DEM* using a spatially variable uncertainty which is the result of the combination of the spatially uniform (UAV, inter-tidal RTK-GPS and sub-tidal SBE) and spatially variable (MBE) surfaces presented in Table 3.1. Associated uniform uncertainty of the UAV survey technique was extracted from Wiggins et al. (2019), who applies a UAV model comparison to an absolute reference control surface on a gravel beach. Due to the lack of a control surface to compare to RTK and SBE techniques, uncertainty surfaces for these methods were calculated computing instrument and interpolation uncertainties individually and then added using a quadratic sum (Taylor, 1997). RTK instrument error ( $2\sigma$  for 95% confidence level; Brasington et al., 2000) was estimated using the vertical deviation in repeated control points over 3 years (~35 observations); while SBE instrument error was extracted from the standard deviation of the actual SBE measured points with respect to overlapped RTK-GPS topographic points along a testing control

line of 1000 m (facilitated by large tidal range). For both methods, standard deviation values between the raw input data and the resulting interpolated grids within a control region of 50x50 m were used as interpolation error. MBE spatially variable residual uncertainty surface was based on total propagated uncertainty (TPU) values for each individual sounding (generated through QPS QINSy/Qimera hydrographic software) which were then gridded using the Combined Uncertainty and Bathymetric Estimator (CUBE) algorithm (Calder and Mayer, 2003; Calder and Wells, 2007; Schimel et al., 2015). The vertical accuracy of the only externally sourced MBE dataset (for 2011) was based on the known survey specification (International Hydrographic Organization Order 1a). This was relatively large ( $\sigma = 0.27$  m) but provided the only opportunity to obtain a full embayment survey prior to 2013.

Finally, the total volume difference or total sediment budget and associated uncertainty were quantified using the non-discarded  $DoD$  values,  $|Z_{DEM_1} - Z_{DEM_2}| \geq minLoD$  for a 95% confidence level. Sediment volumes (in  $m^3$  per meter width) were computed for different sections of the beach profile: dune (> 30 to 5 m ODN), supra- and inter-tidal (5 to -2 m ODN) and present sub-tidal (beyond -2 m ODN). To avoid errors in the dune volume computation, the vegetated areas not comprising part of the active beach system were discarded. The beach was also divided into northern and southern sections (divided black dashed box, Fig 2a), allowing a full embayment investigation of embayment-scale alongshore variability in volumes. It is noted that alongshore variability refers to volumetric differences between south and north, and not small scale alongshore variability associated with bar/ rip morphology.

### 3.3 Quasi full embayment beach response and evolution

#### 3.3.1 Volume time series

Fig. 3.5 shows beach volumetric time series for each of the sub-systems considered (dunes, inter-tidal and sub-tidal) for the north and south sectors of the beach (red and blue boxes, Fig. 3.2a). Sediment volumes are plotted relative to the reference state, January 2011, as a topographic and bathymetric survey is available for that time for both north and south sectors of the beach. The beach/dune morphology is

significantly different for the two sectors: the inter-tidal beach in the north is narrower than in the south (refer to Fig. 3.2b) and, the front of the northern dune system is characterised by a high and steep ramp, whereas the southern dune system is fronted by a developing fore dune.

The two regions also show markedly contrasting behaviour in terms of dune volumetric change. Over the monitoring period, the southern dune system has progressively accreted 5,550 m<sup>3</sup> (30 m<sup>3</sup> m<sup>-1</sup>), representing 800 m<sup>3</sup> year<sup>-1</sup> (4 m<sup>3</sup> m<sup>-1</sup> year<sup>-1</sup>). The northern dune system, on the other hand, has remained relatively stable over the period 2008 – 2013, but during the 2013/14 winter, 80,000 m<sup>3</sup> was lost (50 m<sup>3</sup> m<sup>-1</sup>, accompanied by total retreat of the dune foot of c. 15 m) with no significant post-event recovery. The dune ramp is still located 7 m landward of the pre-2013/14 dune face 4 years later, without a developing fore dune. The dune volume time series also shows a modest seasonal modulation (amplitude c. 15 m<sup>3</sup> m<sup>-1</sup>), largely due to the advance/retreat of the dune foot during the summer/winter cycle.

Inter-tidal volumetric changes are shown in Fig. 3.5c for the south (11-year time series) and for the north (2.5-year time series) sectors. The southern inter-tidal time series displays both seasonal (amplitude c. 50 m<sup>3</sup> m<sup>-1</sup>, refer to Fig. 3.5c) and multi-annual event response signals (amplitude c. 200 m<sup>3</sup> m<sup>-1</sup>, refer to Fig. 3.5c). Specifically, the southern time series started (October 2006) in a fully accreted state (+50 m<sup>3</sup> m<sup>-1</sup> with respect the reference state), then experienced significant erosion (c. 180 m<sup>3</sup> m<sup>-1</sup>) during the 2006/7 winter ( $H_{s,50\%} = 2.4$  m), followed by a 3 – 5 year recovery (up to October 2010) to a stable fully accreted state. The intense storms during the 2013/14 winter (red circles Fig. 3a,  $H_{s,50\%} = 2.7$  m) resulted in sediment losses in excess of 200 m<sup>3</sup> m<sup>-1</sup> in the south. Following the 2013/14 winter, an increase in alongshore volume standard deviation (Fig. 3.5c) was observed during the 2014 – 2017 recovery period. According to Scott et al. (2016), this is associated with the development of large-scale three-dimensional sandbar morphology in the lower inter-tidal region during beach recovery phases (see also Poate et al., 2014). Post 2013/14 winter, southern and northern beach volumes experienced a multi-annual recovery phase within which significant seasonal variability was observed (for example, an energetic 2015/16 winter ( $H_s = 2.6$  m), resulted in 140 m<sup>3</sup> m<sup>-1</sup> loss in the

south). By autumn 2018 (4.5 years after 2013/14 storms), the south beach had recovered by 88%.

Examining the 10-year time series of beach sediment volume (Fig. 3.5), a surprising observation is that the inter- and sub-tidal volumes do not exhibit the inverse correlation expected for a cross-shore dominated beach, suggesting that alongshore sediment fluxes are significant. Indeed, there appears to be a positive correlation between southern inter-tidal volume and sub-tidal volume, with a time lag of approximately 1-year (e.g., compare the 2013 – 2014 decrease in inter-tidal volume with the 2014 – 2015 decrease in sub-tidal volume). The imbalance in total volume for the south sector was previously alluded to by Scott et al. (2016), who examined the 2013/14 storm response for a 250-m southern sector of Perranporth and found that the inter-tidal zone lost  $> 200 \text{ m}^3 \text{ m}^{-1}$ , while the sub-tidal zone only gained  $110 \text{ m}^3 \text{ m}^{-1}$ . The monthly time series of sediment volume for the southern region (Fig. 3.5c–e) clearly demonstrates that the inter- and sub-tidal volumes do not balance. For example: (1) from October 2010 to July 2012, the sub-tidal gained c.  $200 \text{ m}^3 \text{ m}^{-1}$  of sediment, whereas the inter-tidal sediment volume remained relative constant (ignoring seasonal fluctuations); (2) from May 2014 to February 2015, the sub-tidal lost c.  $300 \text{ m}^3 \text{ m}^{-1}$  of sediment, whereas the inter-tidal gained c.  $100 \text{ m}^3 \text{ m}^{-1}$  of sediment; and (3) from March 2017 to May 2018, the sub-tidal gained c.  $200 \text{ m}^3 \text{ m}^{-1}$  of sediment, whereas the inter-tidal sediment volume lost c.  $30 \text{ m}^3 \text{ m}^{-1}$ . These observations for the southern region strongly point to the presence of significant longshore exchange of sediment, either within the embayment or beyond the southern extend of the region, and/or offshore sediment transport beyond the detectable DoC.

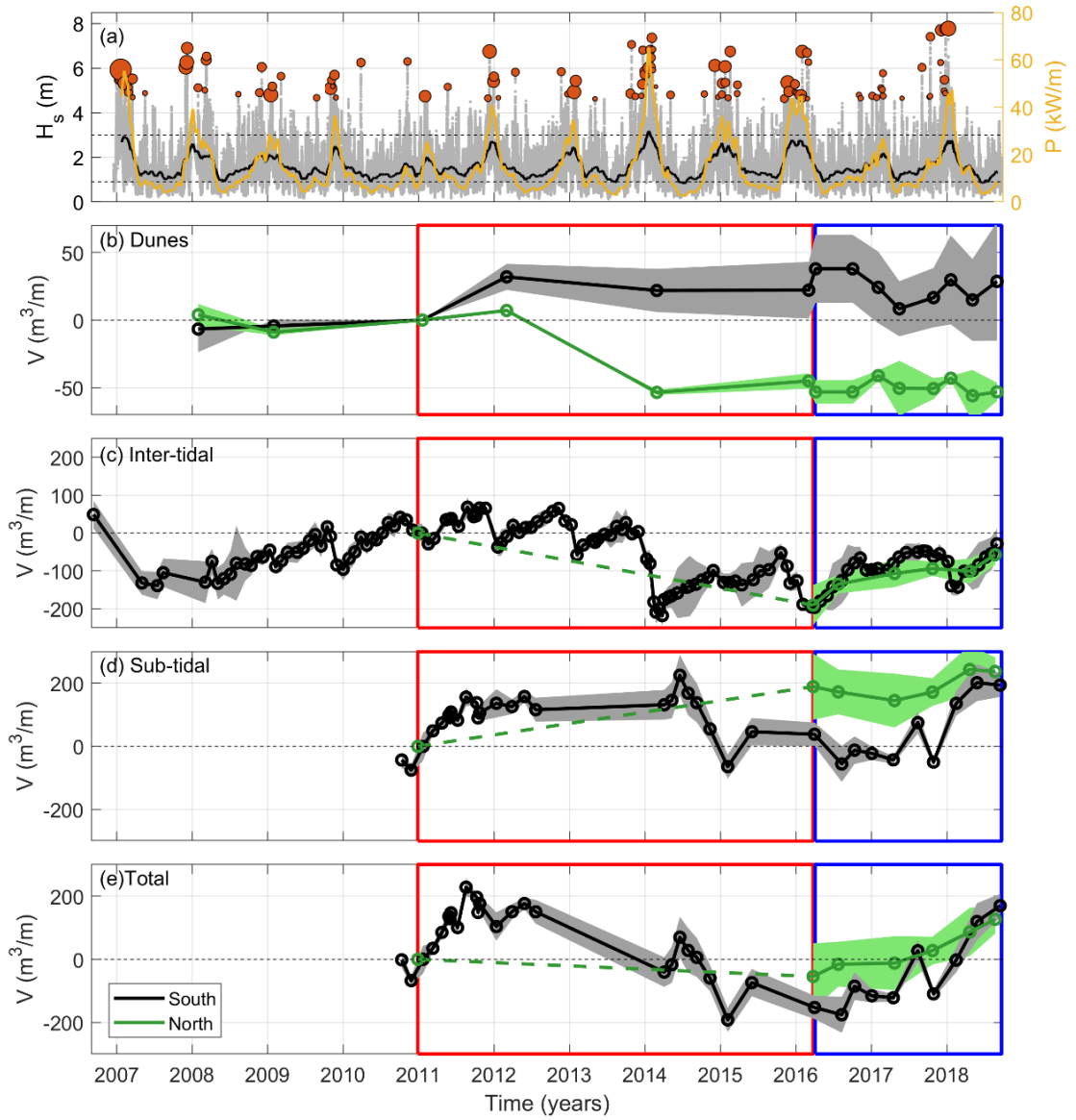


**Fig. 3.5** South (black) and north (green) Perranporth beach response and evolution. (a) 11-year time series of significant wave height measured at Perranporth wave buoy (30-min and 8-week running mean), wave power  $P$  (Herbich, 2000) and storm events (orange bubbles,  $H_s > H_{s,99\%}$ , minimum of 6 hours duration and a meteorological independence criterion of 24 h between peaks). The size of the bubbles is proportional to storm duration based on  $H_{s,95\%}$  cut-off (Ciavola and Coco, 2017). Dune (b), inter-tidal (c) and sub-tidal (d) sediment volume ( $\text{m}^3 \text{m}^{-1}$  alongshore-averaged) and associated alongshore standard deviation (bounded area). (e) Total beach sediment volume ( $\text{m}^3 \text{m}^{-1}$  alongshore-averaged, from dune foot to -14.5 m ODN) and associated alongshore standard deviation (bounded area). Dune volume refers to the area above the dune foot ( $z = 5$ ), inter-tidal volume corresponds with the area from the dune foot to  $z = -2$  m ODN and sub-tidal from  $z = -2$  m to -14.5 m ODN. Red (storm) and blue (recovery) squares represent the considered epochs in Section 3.4.

When the more discontinuous sediment volume time series for the northern region is also considered, an alongshore quasi-coherent response is observed. For the

period 2016 – 2018, the inter-tidal accretion for the northern and southern sectors of the beach are very similar ( $130 - 160 \text{ m}^3 \text{ m}^{-1}$ ). Over that same period, the sub-tidal region also accretes, but the accretion in the northern region (c.  $50 \text{ m}^3 \text{ m}^{-1}$ ) is significantly smaller than in the southern region (c.  $160 \text{ m}^3 \text{ m}^{-1}$ ). Importantly, the total sediment volume for both the southern and northern region increase during this period by a very substantive amount ( $200 - 300 \text{ m}^3 \text{ m}^{-1}$ ). This strongly suggests that the inner embayment is not ‘closed’ (cf. Fig. 3.1) and that sediment may be transported alongshore, potentially around the terminating headlands, and/or offshore beyond the detectable *DoC*, and/or onshore into the vegetated dune area. To robustly examine the sediment fluxes within and beyond the inner embayment and quantify the sediment fluxes between the different sub-systems, it is necessary to take a total sediment budget approach, expanding both the alongshore and cross-shore spatial coverage, and accounting for propagated volumetric uncertainty. The following section examines the two epochs where full embayment coverage is available.

### 3.3.2 Outer bar dynamics

The spatial and temporal variability of sub-tidal fluxes are further explored by analysing outer bar migration and evolution. The residual morphology of the lower part of the inter-tidal and the sub-tidal region (from  $z = 0$  to  $-18 \text{ m ODN}$ ,  $x = 400 - 1500 \text{ m}$ ) was computed to gain both a more visual representation of the inner-outer bar morphology and quantitative measures (bar crest position and depth, and residual bar volume). For each *DEM*, comprising lower inter-tidal and sub-tidal morphology, linear trends (planar gradient) were least-squares-fitted to cross-shore profiles at a 10-m alongshore spacing. These trends were subtracted from the cross-shore profiles and combined to construct the residual morphology. This process was carried out for the 8-year time series of the southern part of the beach, 2011 full embayment and the 2.5-year full embayment survey data that includes the northern part of the beach.

The residual morphologies for seven surveys are presented in Fig. 3.6. Despite a short observational dataset for the full embayment, evident alongshore variability of the outer bar between S and N sectors during the monitoring period is apparent. For both the north and south part of the beach, increased three-dimensionality in sandbar

morphology is observed during accretionary (downstate) conditions and reduced three-dimensionality under erosive conditions (upstate) (Scott et al., 2011; Masselink et al., 2014; Poate et al., 2014; Stokes et al., 2015). For Perranporth, Masselink et al. (2014) identified five bar states: welded bar (W), crescentic attached bar (CA), crescentic bar (C), longshore bar (L) and longshore bar dissected by mega rips (MR).

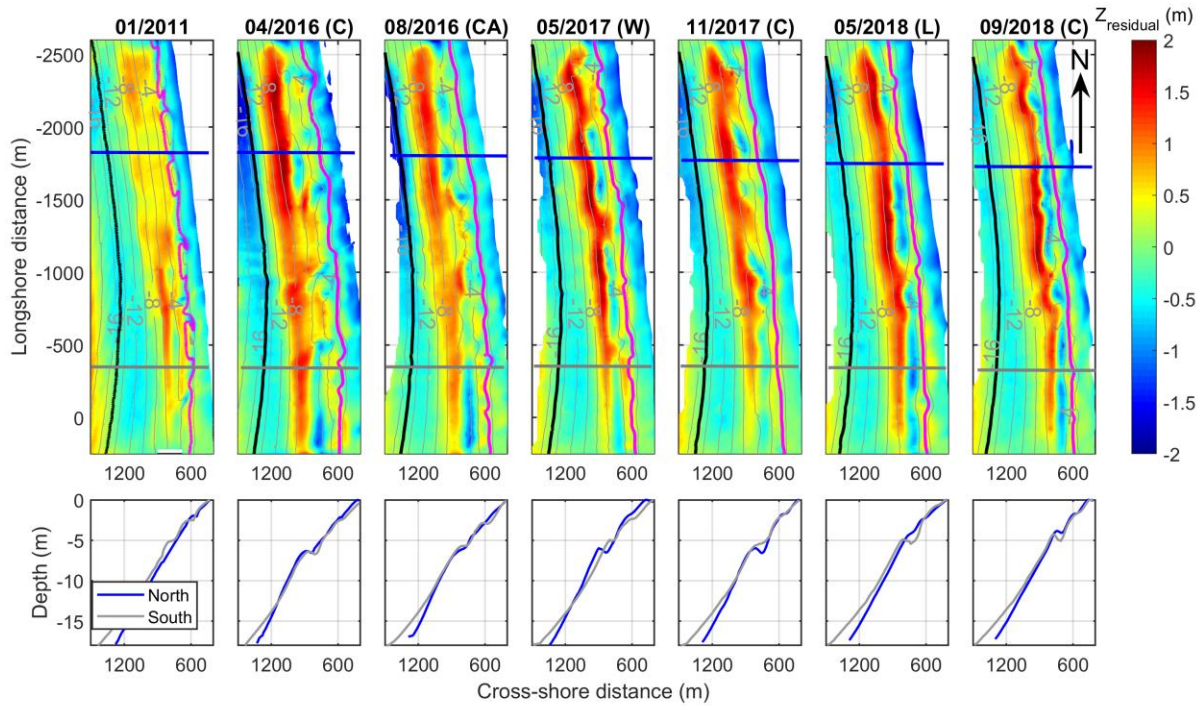


**Fig. 3.6** Upper panels: residual morphology of the full embayment with inner and outer bar systems. Warm colours represent positive values of residual morphology and cool colours represent negative values. The horizontal blue and grey lines show the location of the 2D cross-shore profile (extracted from actual DEMs) presented in bottom panels. Magenta and black contours represent *DoC* and low tide water level, respectively. Bar states are included as welded bar (W), crescentic attached bar (CA), crescentic bar (C) and longshore bar (L).

From April 2016 to May 2017, the sub-tidal bar system increasingly evolved from a crescentic state to a crescentic attached state, especially in the northern part of the beach, where some outer bar segments clearly welded to the inter-tidal beach due to onshore sediment transport and bar migration (downstate). The subsequent summer/autumn period was relatively energetic and by November 2017 the bar system in the north reverted back to crescentic (offshore sediment transport and significant straightening of the outer bar; upstate). Energetic wave conditions during the

subsequent winter/spring period straightened the outer bar systems in the north even more due to crest erosion and trough accretion, whereas a relatively deep and linear trough developed in the southern part of the beach by May 2018 (upstate). After summer 2018, the outer bar continued translating onshore (similar position than during the fully accreted beach states in 2011 – 2012; Masselink et al., 2014) and the inner-outer bar system evolved to a crescentic attached state (downstate).

Fig. 3.7 illustrates the outer bar dynamics for the period 2010 – 2018. For most years, the transition from summer to winter coincides with an offshore bar migration (compare summer/blue with subsequent winter/red profile in Fig. 3.7a,b), whereas onshore bar migration occurs for the transition from winter to summer (compare winter/red with subsequent summer/blue profile in Fig. 3.7a,b). However, onshore outer bar movement also takes place under relatively energetic wave conditions, e.g., from October 2016 to January 2017, the outer bar migrated 75 m onshore, which represents the largest onshore crest translation registered. After the 2013/14 winter, the outer bar was located furthest offshore ( $x_c = 500$  m) in the deepest water ( $z_c = -8$  m ODN) and had the largest size ( $Q_{residual} = 250 \text{ m}^3 \text{ m}^{-1}$ ). In contrast, the outer bar was located closest to the shore ( $x_c = 325$  m) in the shallowest water ( $z_c = -5$  m ODN) and had the smallest size ( $Q_{residual} = 100 \text{ m}^3 \text{ m}^{-1}$ ) at the start of the survey period in 2010, and this is very similar to September 2018. There is a significant relationship between the outer bar size and position, implying that as the outer bar moves offshore (onshore) it increases (decreases) in size, as clearly illustrated in Fig. 3.7c. Additionally, N sub-tidal bar morphology is more pronounced (larger positive bar relief over a wider extent, c. 400 m), residual volumes are larger (larger  $Q_{residual}$ ), bar crest is in deeper water (larger  $z_c$ ) and rip/bar morphology is more three-dimensional (especially May 2017), all of which are a reflection of more energetic wave conditions. In summary, outer bar dynamics respond seasonally but a 4 – 5 year superimposed signal is also evident in both bar position (crest and toe) and relief. Note that bar position always refers to cross-shore translations.

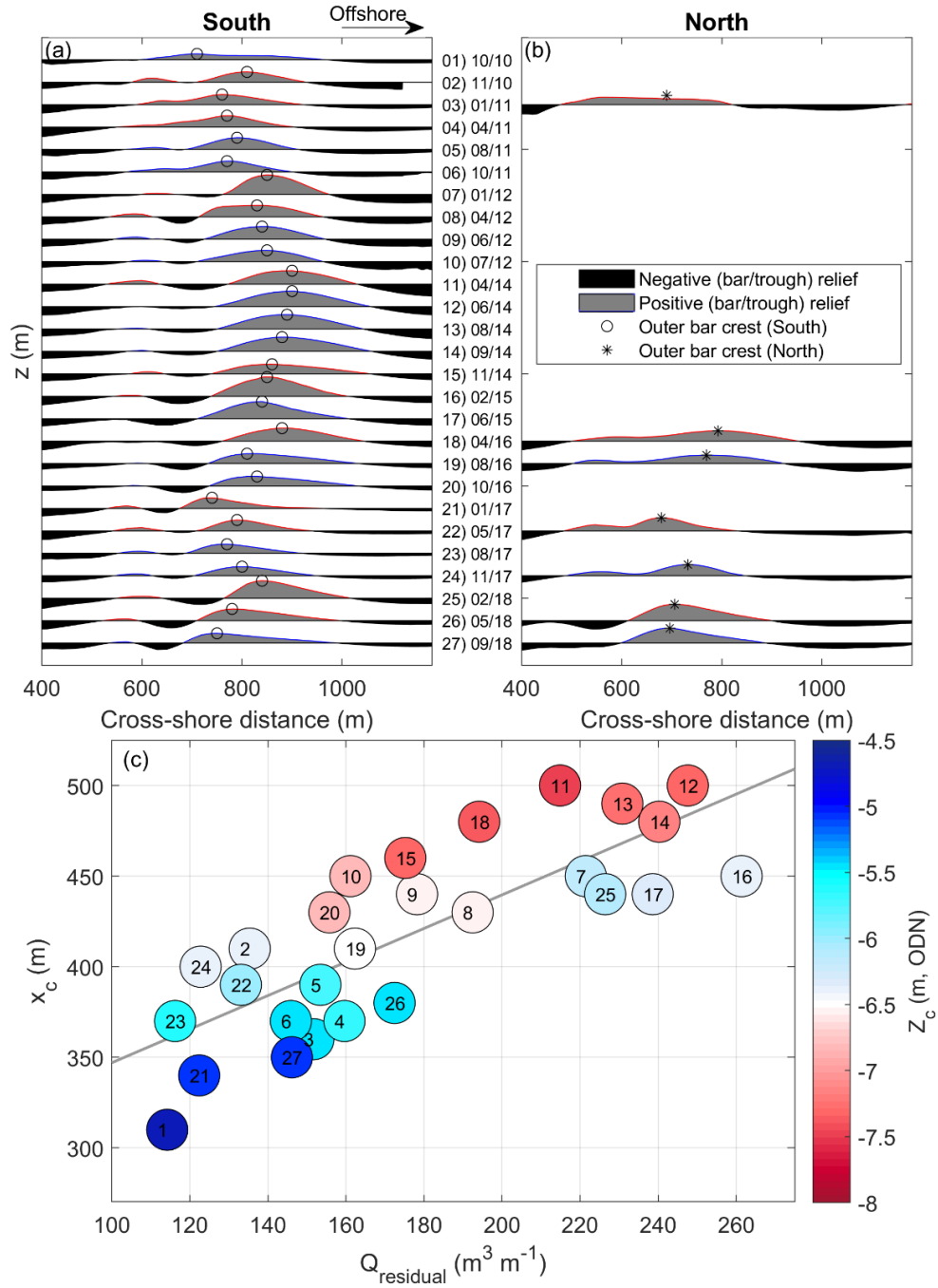


**Fig. 3.7** Alongshore-averaged residual cross-shore profiles for (a) southern and (b) northern part of Perranporth beach. Profile edges are highlighted in blue for summer and red for winter, and circles indicate outer bar crest position. (c) Scatter plot of outer bar volume  $Q_{\text{residual}}$  and bar crest position  $x_c$  for the southern part of Perranporth beach. Colour indicate maximum depth of the bar crest  $z_c$  and numbers represent survey position in the time series (September 2010 to September 2018). Grey line represents the least-squares best fit.

### 3.4 Full embayment total sediment budget

In this section we will present the full embayment analysis for two epochs, representing extreme storm response (Fig. 3.8) and post-storm recovery (Fig. 3.9). The results for both epochs are then summarized in Fig. 3.10 and Table 3.2. It is noted that in the Figures the sediment volume changes are presented in units of  $\text{m}^3$  per unit meter beach width, whereas in the table the total volume changes in  $\text{m}^3$  are listed.

#### 3.4.1 Storm response

Full embayment *DEMs* for the years 2011 and 2016 were used to further investigate cross-shore sub-compartment sediment fluxes and along-coast sediment exchange, within and beyond the inner embayment, surrounding the high energy 2013/14 winter period. The lack of a full embayment morphological dataset bracketing the 2013/14 winter forced us to extend the period from 2011 to 2016. This is considered acceptable in terms of dune and inter-tidal volumetric changes as beach volumes in 2011 were similar to that of 2013, and the volumes for 2014 were similar to that of 2016 (refer to Fig. 3.5b,c). We also acknowledge that total embayment response over this epoch disregards both the dramatic accretion in the southern sub-tidal region during 2011 ( $> 100 \text{ m}^3 \text{ m}^{-1}$ ; Fig. 3.5d) and the significant inter-tidal erosion during winter 2015/16 ( $-150 \text{ m}^3 \text{ m}^{-1}$ ; Fig. 3.5c), meaning that embayment response to the 2013/14 events could potentially have been different than shown.

The difference *DEM*, offshore acoustic backscatter and along-coast variation in sub-compartment sediment volumes are presented in Fig. 3.8. Light colours in the acoustic backscatter image indicate presence of medium sand, interrupted by gravel patches (dark colours) around 26 m depth ODN. It is emphasized that for the sediment volume considerations, only those bed-level changes that exceed the *LoD* (95% uncertainty level) are considered, and a large portion of the deeper sub-tidal is therefore discarded as the measured changes are considered insignificant (uncoloured parts of Fig. 3.8). The salient features of the storm response are: (1) extensive erosion of the front of the dunes in the north part of the beachfront (c.  $50 \text{ m}^3 \text{ m}^{-1}$ ); (2) erosion across the entire supra- and inter-tidal beach (c.  $190 \text{ m}^3 \text{ m}^{-1}$ ); (3) erosion in the shallow sub-tidal zone up

to 6 – 7 m depth ODN; and (4) accretion in the deeper sub-tidal zone up to and even beyond the *DoC* at 14.5 m depth ODN ( $0 - 250 \text{ m}^3 \text{ m}^{-1}$ ).

Integrating the positive and negative sediment volumetric changes across the entire beach to the *DoC* (Fig. 3.10-top panel) robustly demonstrates that the full embayment sediment budget is not balanced: there is a net loss of  $280,000 \text{ m}^3$  and an associated uncertainty of  $206,000 \text{ m}^3$  (Table 3.2). There is also a considerable longshore variability in the morphological response and this is better demonstrated when the sediment volumes are summed across the different sub-compartments for the different sections of the beach (north versus south, Fig. 3.10 and Table 3.2). Over the period 2011–2016, the northern and southern sectors of the beach lost  $50,000 \text{ m}^3$  and  $230,000 \text{ m}^3$  of sediment, respectively. These values represent losses per unit meter beach of  $36 \text{ m}^3 \text{ m}^{-1}$  in the north and  $164 \text{ m}^3 \text{ m}^{-1}$  in the south (although northern volume change is within uncertainty bounds therefore not significant at 95% level).

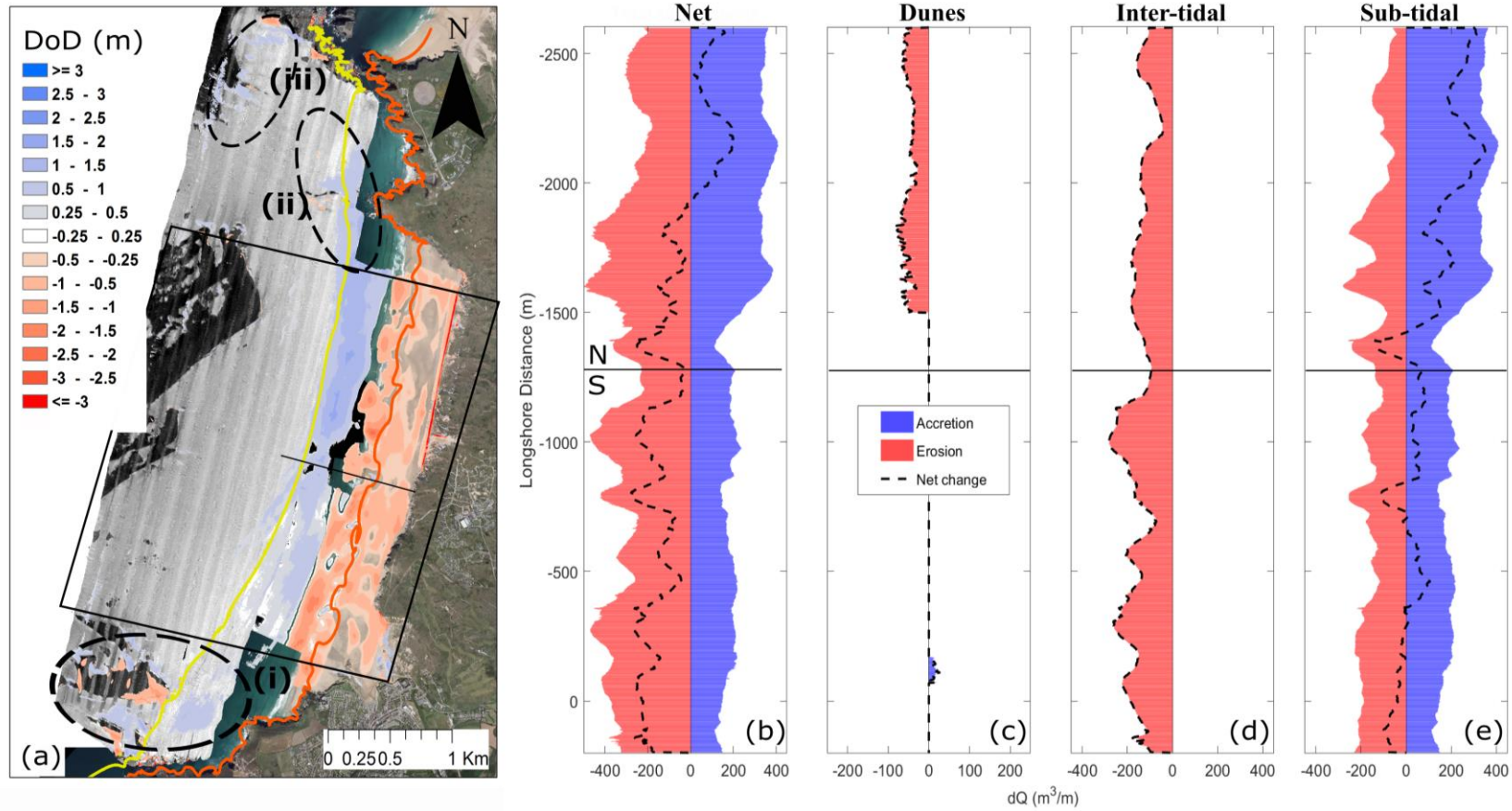


**Fig. 3.8** Storm response total sediment budget. Left panel: full embayment  $DoD$  from 2011 to 2016. Areas where morphological change is not significant ( $|Z_{DEM_1} - Z_{DEM_2}| \geq minLoD_{95\%}$ ) are uncoloured. Orange and yellow contours represent the inter-tidal to sub-tidal limit (-2 m, ODN) and  $DoC$  (-14.5 m, ODN) respectively. Right panels: cross-shore and alongshore variability of volume changes for the complete cross-shore profile and the different sub-systems for the domain comprised inside the black box. i–iii highlight offshore areas where morphological change is within the propagated uncertainty.

Morphological changes beyond the *DoC* and the lateral extent of box (Fig. 3.8a), referred to as ‘outer embayment’, are analysed to investigate possible sediment pathways in/out the inner embayment. The region beyond the *DoC* (within the box, Fig. 3.8) showed a small, but significant gain of 76,000 m<sup>3</sup> (with uncertainty of 50,000 m<sup>3</sup>), and regions beyond the lateral extents of the box (represented by ellipses in Fig. 3.8) indicated significant gains with a combined total of 180,000 m<sup>3</sup> (uncertainty of 120,000 m<sup>3</sup>). The gains beyond the lateral extents of the box are related to three regions. Two are offshore regions at the full embayment extents: one in the south of the study area in proximity to the Cligga Head, the southern embayment boundary (Fig. 3.8a-i), located between 14.5 and 26 m depth ODN; and the second located near Penhale Point, the northern of embayment boundary (Fig. 3.8a-iii), where only accretion occurred. The third region, alongshore to the north of Ligger Point, experienced significant sediment gains offshore of the headland (accretion of 0.6 – 0.8 m) and in the region of Hoblyn’s Cove (Fig. 3.8a-ii) providing a possible sink for sediment lost from the inner embayment. While the total sediment budget cannot be entirely resolved in these regions due to lack of data in the nearshore (data collection too hazardous), these observations suggest major morphological losses from within the inner embayment are linked primarily to inner headland bypassing mechanisms, rather than cross-shore exchange beyond the depth of closure within the inner embayment, suggesting that significant sediment transport occurs seaward of the base of the inner headlands (Ligger and Droskyn) and beyond the morphological depth of closure at the embayment extremities.

### **3.4.2 Multi-annual beach recovery**

Full embayment *DEMs* for the years 2016 and 2018 were compared to further investigate multi-annual sediment fluxes during a recovery period within and beyond the central embayment (black box, Fig. 3.9a). Fig. 3.9a shows the *DoD* for the entire epoch 2016 – 2018. The 2.5 years of recovery show a system that is not balanced but has a net gain of 670,000 m<sup>3</sup> with an associated uncertainty of 180,000 m<sup>3</sup> (Table 3.2). Similar to the storm period, sediment inflows and outflows occur primarily between the inter- and the sub-tidal sub-systems (Fig. 3.10). Overall, both inter- and sub-tidal sub-systems accreted, mostly in the south, and although the dunes continued losing sediment (11,000

m<sup>3</sup> erosion, uncertainty of 3,000 m<sup>3</sup>), the embayment is fully recovered from the 2013/14 winter in terms of net sediment budget (Fig. 3.9).

The key morphological responses over the recovery period are: (1) limited dune recovery; (2) accretion across the entire inter-tidal beach (143 m<sup>3</sup> m<sup>-1</sup>); (3) accretion in the shallow sub-tidal down to 6 m depth ODN; and (4) significant longshore variability in the deeper sub-tidal area down to (and beyond in certain sectors) the *DoC*. The latter observation manifests in an alongshore gradient in the sub-tidal accretionary rates from 50 m<sup>3</sup> m<sup>-1</sup> in the north to 150 m<sup>3</sup> m<sup>-1</sup> in the south. Hence, morphological changes during the 2.5-year period of recovery ( $dQ_{out} \ll dQ_{in}$ ) show an accretion of the supra- and inter-tidal sectors, not matched by sub-tidal erosion.

The influx of sediment into the inner embayment leading to recovery is interpreted as a combined response of entrainment of sediment sourced from greater depths (beyond the morphological *DoC*) and/or outside the headlands that delineate the system (from lateral sub-embayments). This supposition is supported by the recorded loss of sediment (-23,000 m<sup>3</sup>) from within the *DoC* in Hoblyn's Cove sub-embayment (shown in available data to the north of the inner embayment, Fig. 3.9a-ii), where the bed was lowered 0.3 – 0.6 m. While a small proportion of net losses, it provides an indication of possible source regions and transport mechanisms. Additionally, the alongshore continuity of the *DoC* contour located beyond the headland bases (620 m in the south and 170 m in the north), in combination with the morphological change detected beyond the embayment limits, strongly suggests that Perranporth beach is part of an extended coastal cell, not just during high energy events. Despite the large uncertainty associated with offshore areas, localised accumulation patterns similar to those shown in the 2011/16 *DoD*, and located between 14.5 and 26 m depth ODN in the south and far north of the survey area, are also present during the accretionary period (dashed ellipsoids, Fig. 3.9a-i,iii). The possible processes and forcing mechanisms leading to embayment recovery are further examined in Sections 3.5 and 3.6.

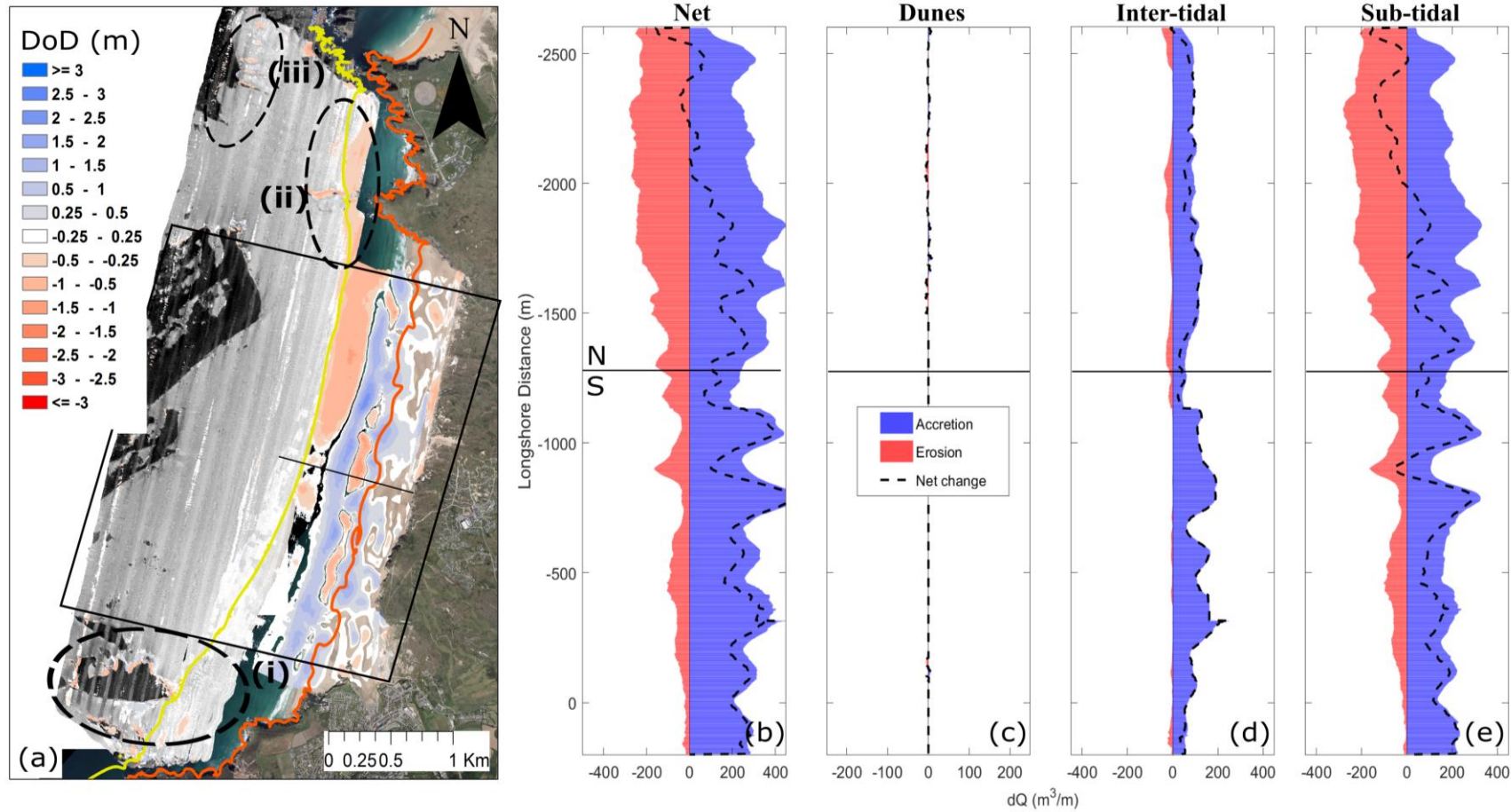


**Fig. 3.9** Multi-annual recovery total sediment budget. Left panel: full embayment  $DoD$  from 2016 to 2018. Areas where morphological change is not significant ( $|Z_{DEM_1} - Z_{DEM_2}| \geq minLoD_{95\%}$ ) are uncoloured. Orange and yellow contours represent the inter-tidal to sub-tidal limit (-2 m, ODN) and  $DoC$  (-14.5 m, ODN) respectively. Right panels: cross-shore and alongshore variability of volume changes for the complete cross-shore profile and the different sub-systems for the domain comprised inside the black box. i-iii highlight offshore areas where morphological change is within the propagated uncertainty.

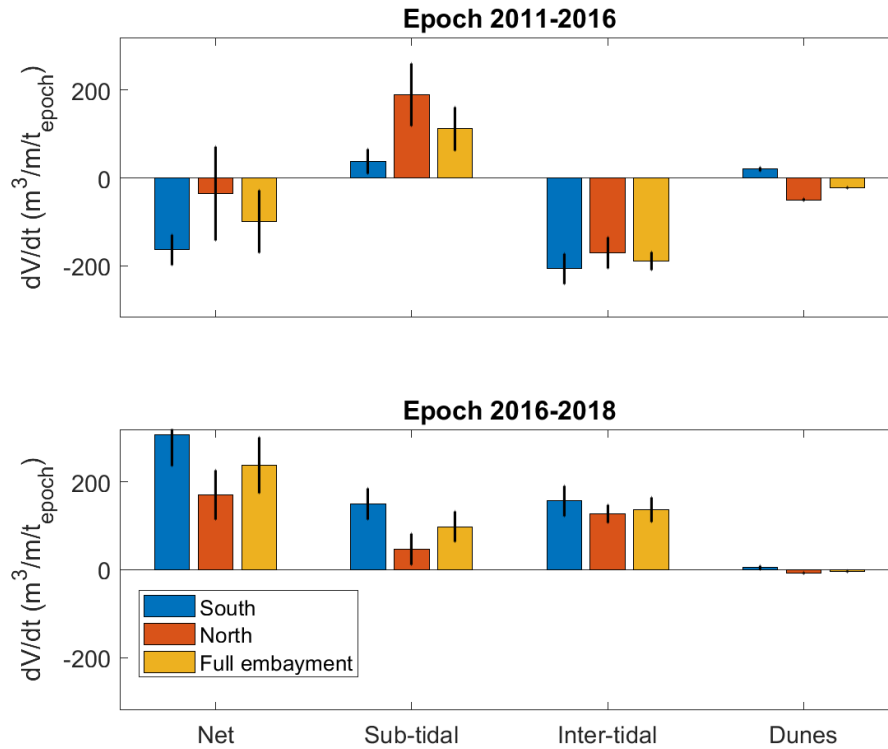


**Fig. 3.10** Averaged sub-tidal, inter-tidal and dune volume per beach width ( $m^3 m^{-1}$  alongshore) and associated uncertainty (error bars) for epochs 2011 – 2016 and 2016 – 2018. Alongshore-averaged volumes are presented for north (1400-m alongshore) and south (1400-m alongshore) domains, except for the case of south dunes (100-m alongshore). Dune volume correspond with regions  $> 5$  m ODN, inter-tidal volume from 5 m to -2 m ODN and sub-tidal volume corresponds with the regions from -2 m to -14.5 m ODN.

**Table 3.2** Net volumetric changes ( $m^3$ ) and associated uncertainty in sub-tidal, inter-tidal and dune sub-systems for epochs 2011 – 2016 and 2016 – 2018. Volumes are presented for north and south domains. Inter-tidal volume corresponds with the area from the dune foot ( $z = 5$  m) to -2 m and sub-tidal volume corresponds with the area from -14.5 to -2 m, inter- and supratidal from -2 to the dune foot ( $z = 5$  m) and dunes beyond  $z = 5$  m

EPOCH	Sector	$\Delta V_{net}$ ( $m^3$ )	$\Delta V_{sub-tidal}$ ( $m^3$ )	$\Delta V_{inter-tidal}$ ( $m^3$ )	$\Delta V_{dunes}$ ( $m^3$ )
2011-2016	Full*		$-2.8 \times 10^5 \pm 2 \times 10^5$		
	Outer**		$2.7 \times 10^5 \pm 2.4 \times 10^5$		
	North	$-5 \times 10^4 \pm 1.5 \times 10^5$	$2.6 \times 10^5 \pm 1 \times 10^5$	$-2.4 \times 10^5 \pm 5 \times 10^4$	$-7 \times 10^4 \pm 3 \times 10^3$
	South	$-2.3 \times 10^5 \pm 5 \times 10^4$	$5.3 \times 10^4 \pm 6 \times 10^4$	$-2.9 \times 10^5 \pm 5 \times 10^4$	$2 \times 10^3 \pm 1 \times 10^3$
2016-2018	Full*		$6.7 \times 10^5 \pm 1.8 \times 10^5$		
	Outer**		$8.7 \times 10^4 \pm 4.5 \times 10^4$		
	North	$2.4 \times 10^5 \pm 8 \times 10^4$	$6.7 \times 10^4 \pm 5 \times 10^4$	$1.8 \times 10^5 \pm 3 \times 10^4$	$-1.1 \times 10^4 \pm 3 \times 10^3$
	South	$4.3 \times 10^5 \pm 1 \times 10^5$	$2.1 \times 10^5 \pm 5 \times 10^4$	$2.2 \times 10^5 \pm 5 \times 10^4$	$1 \times 10^3 \pm 1 \times 10^3$

\*Full is the sum of north and south net volumes (down to DoC, within black box on Fig. 3.8 and 7).

\*\*Outer is the sum of the morphological change beyond the morphological DoC (-14.5 m) and all areas outside of the area of the central embayment (beyond DoC and outside black box on Fig. 3.9 and 3.10).

### 3.4.3 Sub-tidal sediment redistribution

Both storm response and recovery was rather longshore-uniform (disregarding the increase in 3-dimensionality during the accretionary phases) in the inter-tidal zone, but less so in the sub-tidal region, warranting further investigation into the alongshore redistribution of sediment in especially the lower sub-tidal zone. The 6 *DoDs* covering the inner embayment recovery response (black dashed box down to the *DoC*, Fig. 3.2a) for the multi-annual erosive period 2011 – 2016, and inter-annual recovery period 2016 – 2018, are used to compute longshore variability and inter-annual volume change between the north and south (Fig. 3.11). The key finding here is that following the erosion over the 2011 – 2016 epoch, accretion of  $0.5 - 2 \times 10^5$  occurred over each 6-month epoch in the recovery period, with most recovery occurring during the 2017/18 winter, especially in the sub-tidal region of the southern part of the beach.

Burvingt et al. (2017) defined longshore variation in the inter-tidal beach morphological response using the longshore variation index (*LVI*):

$$LVI = Q_{std} / (|Q_{mean}| + Q_{std}) \quad (3.1)$$

where  $Q_{std}$  is the standard deviation of the net volumetric change for cross-shore transects ( $Q_{cross}$ ) and  $|Q_{mean}|$  is the absolute value of the mean of  $Q_{cross}$  values. In order to discriminate between alongshore variability between the north and south sections and variability associated to 3-dimensionality,  $Q_{cross}$  is computed using 2-m alongshore-averaged cross-shore profiles, and is low-pass filtered using a moving averaged filter with a 400-m span. *LVI* index is then computed for the original and the filtered  $Q_{cross}$ . This index is dimensionless and varies between 0 and 1, with zero values implying cross-shore sediment transport is dominant, and  $LVI = 1$  representing both significant alongshore transport and large 3-dimensionality. Hence, by applying the low-pass filter to  $Q_{cross}$ , most of the differences associated to the small-scale morphology are eliminated.

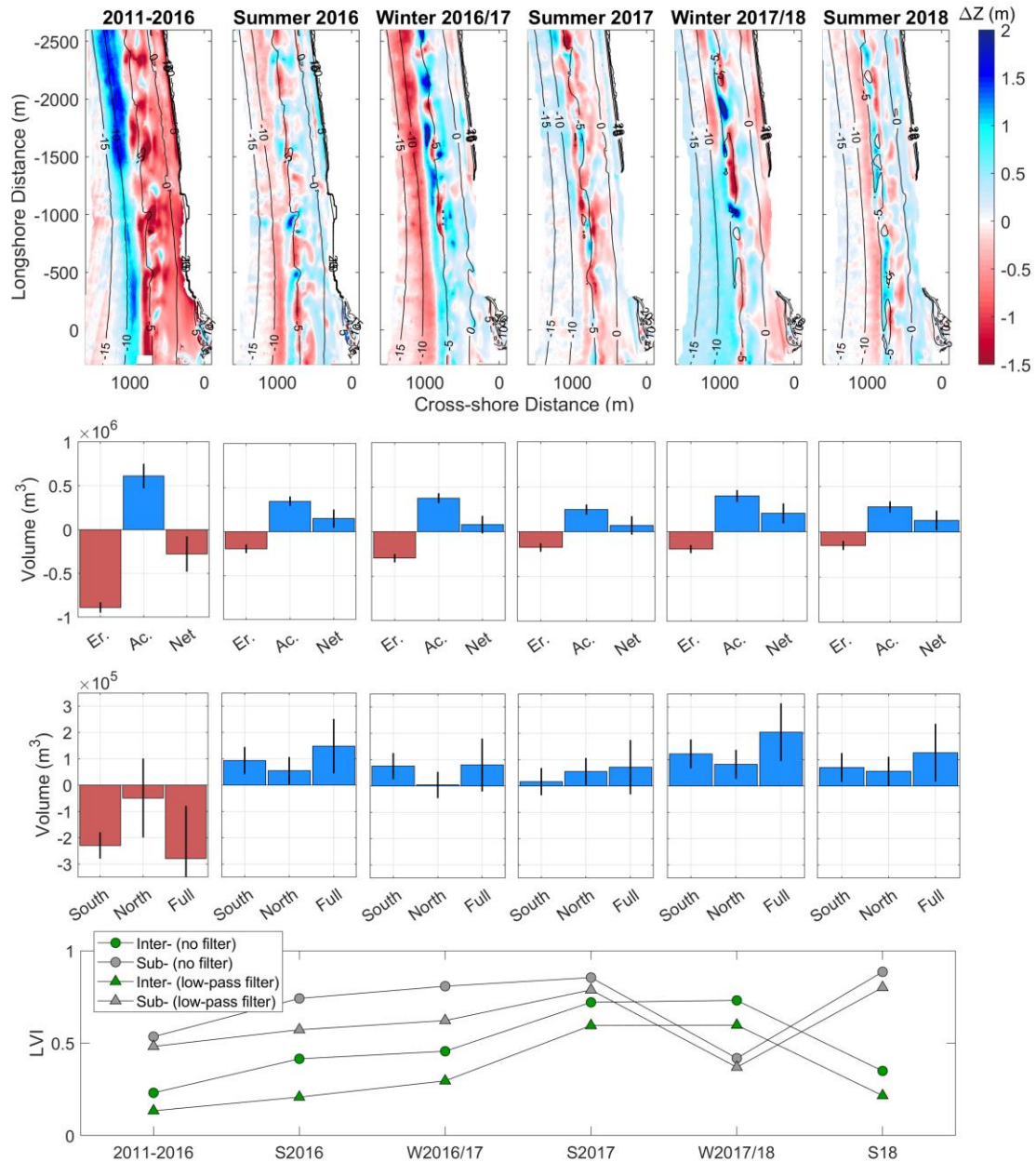


**Fig. 3.11** Upper panels: 3D variability of Perranporth full embayment where red indicates erosion and blue accretion. Contours are from the first of the beach surveys. In order from 2<sup>nd</sup> to 3<sup>rd</sup> row panels: full embayment erosion (Er.), accretion (Ac.) and net (Net) volumetric change; and volumes for north and south sectors. All volumes are for epochs 2011 – 2016 and seasonal 2016 – 2018. Bottom panels: longshore variation index (*LVI*) computed using 2-m alongshore-averaged cross-shore profiles (circle) and a low-pass filter with a 400-m span (triangle).

For 5 of the 6 epochs, *LVI* (both filtered and no filtered) for the sub-tidal region is considerably larger ( $LVI = 0.5 - 0.9$ ) than for the inter-tidal region ( $LVI = 0.1 - 0.7$ ), indicating that the sub-tidal is characterised by a significant longshore variability whereas the inter-tidal is more longshore-uniform. The only exception is the winter

2017/18 period during which the large *LVI* results from very significant changes in the lower inter-tidal/ bar/rip morphology (still present in the filtered signal), which is associated with the positive feedback between rip-cell circulation, sand transport and evolving bathymetry, and not driven by longshore transport processes.

### 3.5 Relating wave forcing and morphological change

To determine the sediment budget for any coastal domain, it is necessary to understand the forcing controls on sediment fluxes within, and in and out of the system, with waves being the primary forcing control in this instance. In the study area, the wave climate is strongly seasonal (Fig. 3.3f), such that the larger waves over winter periods are also slightly more northward in direction. Therefore, winters are associated with greater absolute wave power (forcing offshore transport), but also with greater southward alongshore wave power, likely to result in southward alongshore transport.

The wave parameters we seek to correlate with observed morphological change are the demeaned cumulative total wave power ( $P_{cum}$ ) and the cumulative alongshore wave power ( $P_{y,cum}$ ), computed for the 11-year available time series (2007 – 2018). The wave time series is transformed from the wave buoy location (~20 m depth ODN) to the breaking point using Van Rijn (2014). Assuming that beaches have an equilibrium condition related to the long-term mean wave forcing, total wave power is parameterised using the cumulative integral of the demeaned value (Stokes et al., 2016), denoted  $P_{cum}$ , as:

$$P_{cum}(n) = \int_{t_0}^{t_n} (P - \bar{P})dt \quad (3.2)$$

where  $\bar{P}$  is the long-term mean condition, and  $P$  corresponds to instantaneous wave power at the breakpoint. The assumption of equilibrium (or near-equilibrium) is supported by the morphology observations that show large variations but no clear trend on a decadal timescale (Fig. 3.5).

For alongshore wave power ( $P_{y,cum}$ ), rather than demeaning the signal we select the long-term average power direction as shore-normal (285° in this instance), noting that the average wave direction is 283°, but bigger waves are more northerly. Again, the

assumption here is that a long-term embayment equilibrium exists around variations in longshore forcing. The direction  $285^\circ$  also coincides with the mean orientation of the shoreline near the mid-point of the embayment, but this is not our primary motivation for choosing this angle.

$$P_{y,cum}(n) = \int_{t_0}^{t_n} P_{y,285} dt \quad (3.3)$$

For the purpose of relating wave forcing to morphologic change, only the southern sector observations are sufficiently long to draw statistical correlations (Fig. 3.5), therefore all analyses in this section are restricted to the southern part of the embayment. We seek to differentiate between forcing controls on the inter-tidal and sub-tidal components of the system, as observations suggest these systems behave, to some degree, independently (Fig. 3.5c, d). The morphologic change variables we will use for comparison to wave power are: (i) south-end inter-tidal volume, as it is the longest consistent time series [monthly 2007 – 2018]; (ii) south-end sub-tidal volume [sporadically 2011 – 2016, quarterly 2016 – 2018]; and (iii) total volume for the south end [time points as per sub-tidal volume]. Our preference is for analysis of the longest available dataset in each instance, to avoid misleading correlations with shorter time series'.

An initial examination of the correlations with sub-tidal volumes (Table 3.3,  $V_{S,SUB}$ ) suggest this variable is poorly correlated with wave forcing. This may be due to the sub-tidal being open to flux from the inter-tidal as well as to beyond the outer boundaries, obscuring forcing correlations. What is required is for the exchange with the inter-tidal be offset from the sub-tidal volume. The value we are interested in is flux from the sub-tidal to beyond the outer boundaries (cross- and alongshore) of the southern sector, which is approximated by changes in the total system volume:

$$V_{S,TOTAL} = V_{S,SUB} + V_{S,INTER+DUNES} \quad (3.4)$$

We use the change in total south sector volume ( $\Delta V_{S,TOTAL}$ ) as a proxy indicator for transport in and out of the sub-tidal outer domain boundaries. If we assume that sediment entering and leaving the southern sector primarily passes through the sub-

tidal, then the total volume change ( $\Delta V_{S,TOTAL}$ ) is the flux through the outer boundaries (offshore and lateral) of the sub-tidal region. For example, if over a given period  $\Delta V_{S,INTER+DUNES}$  erode ( $-100 \text{ m}^3/\text{m}$ ) and  $\Delta V_{S,SUB}$  also erodes ( $-100 \text{ m}^3/\text{m}$ ), then we assume that the sub-tidal gained  $+100 \text{ m}^3/\text{m}$  from the inter-supratidal and therefore lost ( $-200 \text{ m}^3/\text{m}$ ) through the outer boundaries. This is not an ideal assumption as some material may be transported alongshore through the inter-tidal, but earlier findings have demonstrated the inter-tidal behaves coherently throughout the embayment and is largely cross-shore dominated (for example see Fig. 3.5c–e).

Considering the relationship between total and alongshore wave power (Fig 3.12a), there is a clear visual inverse correlation between  $P_{cum}$  and  $P_{y,cum}$  at a seasonal time scale i.e., larger waves are more northerly (see also Fig. 3.3f). However, at decadal time scales (2007-2018) there is no clear correlation, in fact the relationship is very weakly positive (Table 3.3;  $r = 0.2$ ), suggesting that decadal trends in wave height are decorrelated from changes in wave direction. Inter-tidal morphological response ( $V_{S,INTER}$ ; Fig. 3.13b) is negatively correlated with  $P_{cum}$  (Table 3.3;  $r = -0.59$ ), indicating that more powerful waves erode the inter-tidal region. This relationship is consistent with the approach of a shoreline prediction model (Davidson et al., 2010; Splinter et al., 2014), which demonstrated a strong relationship at Perranporth between the shoreline position and disequilibrium in the dimensionless fall velocity parameter. Additionally, the seasonal response is also apparent in the outer bar dynamics that show a moderate correlation with  $V_{S,INTER}$  ( $r = -0.6$  for crest position,  $x_c$ , and  $r = 0.58$  for crest depth,  $z_c$ ). This is consistent with the outer bar being primarily forced by cross-shore processes, such that high-energy events will erode the inter-tidal and also translate the outer bar offshore.

The southern total volume ( $V_{S,TOTAL}$ ; red line in Fig. 3.12c-d) is inversely correlated with total wave power ( $r = -0.56$ , Fig. 3.12c) and positively correlated with alongshore wave power ( $r = 0.41$ , Fig. 3.12d). This suggests that as wave power increases overall and becomes cumulatively more negative (southward), the south end erodes, which is primarily attributed to flux through the sub-tidal boundaries. This is counter-intuitive, given that in a closed embayment, we would expect more northerly waves to

drive clock-wise rotation and accrete the southern end of the embayment. Following the discussion by Harley et al. (2015), we also note that it is difficult to differentiate between the influence of total- and alongshore wave power on the total volume, as the wave variables themselves are correlated at short time scales (seasonal), and the strength of the correlations are sensitive to statistical design (e.g., start and end points of wave time series, shore-normal angle chosen). Additionally, low temporal resolution of the survey data aliases the seasonal signal. Taking these caveats into account, there appears to be a weak-moderate relationship where  $V_{S,TOTAL}$  erodes during big, northerly waves (both for individual winters and multiple years above average wave power).

**Table 3.3** Correlation coefficients ( $r$ ) for Perranporth southern sector beach volume and cumulative wave power (total and alongshore). Bold values are significant ( $p$ -value  $< 0.01$ ).

	$P_{cum}$	$P_{y,cum}$	$V_{S,INTER}$	$V_{S,SUB}$	$V_{S,TOTAL}$
$P_{cum}$	1	<b>0.2</b>	<b>-0.59</b>	-0.17	<b>-0.56</b>
$P_{y,cum}$		1	<b>0.24</b>	0.05	<b>0.41</b>
$V_{S,INTER}$			1	0.01	<b>0.66</b>
$V_{S,SUB}$				1	<b>0.70</b>
$V_{S,TOTAL}$					1

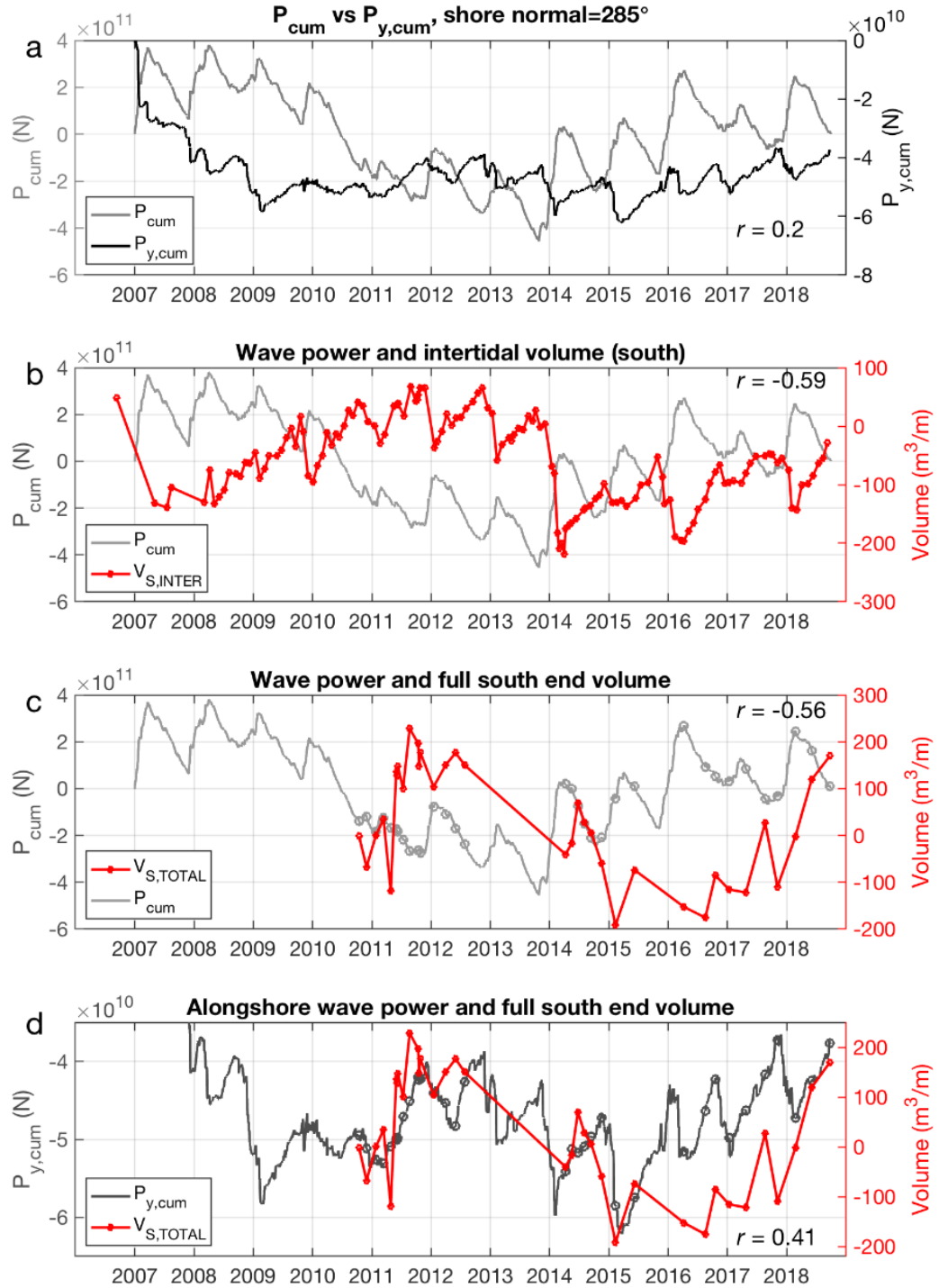


**Fig. 3.12** Time series of wave power and volume observations. (a)  $P_{cum}$  and  $P_{y,cum}$ ; (b)  $P_{cum}$  and  $V_{S,INTER}$ ; (c)  $P_{cum}$  and  $V_{S,TOTAL}$ ; (d)  $P_{y,cum}$  against  $V_{S,TOTAL}$ . For (c, d) grey circles are the points on wave power time series' interpolated to volume. Southward alongshore wave power is negative.

Assessing morphological correlations, it is interesting to note that the total southern system volume ( $V_{S,TOTAL}$ ) is *positively* correlated (Table 3.3) with both  $V_{S,INTER}$  (0.66) and  $V_{S,SUB}$  (0.70), such that each contributes about half the total variance,

indicating that conditions which cause the inter- or sub-tidal to erode (accrete), will also cause the total system to erode (accrete), primarily through transport beyond the outer boundaries. More broadly, the positive correlation between the inter-tidal and total volume suggests that the ability to predict inter-tidal volume change (e.g., using a shoreline prediction model such as Davidson et al., 2010) may also provide some skill in predicting total embayment volume, with the implication that total embayment volume may respond to a disequilibrium in the wave climate, analogous to the inter-tidal. As mentioned in section 3.3, it is surprising to note that the expected inverse correlation between  $V_{S,INTER}$  and  $V_{S,SUB}$  is entirely absent at a time-lag of 0. Instead, it appears that these systems operate with a time-lag of approximately 1-year, with a peak cross-correlation of  $r = 0.67$  found at 11.5-months lag (with the sub-tidal response following the inter-tidal). This suggests that sub-system response occurs at different timescales in reply to different forcing conditions. A hypothesised sequence to explain the lag in response may include: (i) an extreme storm that transports beach material far offshore, beyond the level of detectable change [inter-tidal erodes, sub-tidal is relatively unchanged]; (ii) an initial stage of recovery where sediment is transported mainly from the inner-sub-tidal to the beachface [inter-tidal accretes, sub-tidal erodes]; and (iii) a later phase of gradual transport from the lower-sub-tidal [from beyond the level of detectable change] to the upper-sub-tidal [inter-tidal unchanged, sub-tidal accretes]. The exact nature of this relationship is unclear and will be the target of future work.

## 3.6 Discussion

### 3.6.1 Sediment budget conceptual model

This study has demonstrated that, with reference to Fig. 3.1, Perranporth is an *open* system, that does not have a balanced sediment budget at the short to medium temporal scale (up to 10 years), and displays multi-annual accretional or erosional trends (Fig. 3.5e). Computed *DoDs* based on full embayment observations show significant morphological change in front of the headland bases and beyond the *DoC* in some sectors (Figs. 3.8 and 3.9). The alongshore continuity of the *DoC* contour line off the headland base (620 m in the south and 170 m in the north; refer to Chapter 2), linked

with the detected morphological change beyond the inner embayment limits, suggests that Perranporth beach is part of an extended coastal cell. In line with earlier works (e.g., McCarroll et al., 2018; King et al., 2019; Valiente et al., 2019a), these major morphological changes evidence substantial transport at depths  $> 15$  m that are related to headland bypassing mechanisms.

A semi-quantitative conceptual sediment budget model that is consistent with all observations presented thus far is shown in Fig. 3.13. Volume changes in the north and south sectors ( $\Delta V_N, \Delta V_S$ ) and fluxes within the model domain ( $q_{x,N}, q_{x,S}$ ) are based on observations.  $q_{x,N}$  and  $q_{x,S}$  represent the observed cross-shore fluxes between the upper (inter-, supra-tidal and dunes) and lower shoreface (sub-tidal). We are unable to quantitatively resolve fluxes beyond the survey domain; instead, we refer to a prior numerical modelling study predicting bypass at the northern headland of Perranporth (McCarroll et al., 2018). That study predicted that rapid southward sediment flux occurred at the northern headland during winters (up to  $0.5 \times 10^5 \text{ m}^3$  for a single winter), whilst gradual northward transport ( $\sim 0.2 \times 10^5 \text{ m}^3$ ) occurred during ‘summer’ (spring to autumn). McCarroll et al. (2018) estimated transport through a transect extending off the northern headland, while in the present study the outer boundary for the northern sector extends cross-shore from the shoreline, and alongshore over the northern extent of the bay. Consequently, there are differences between the values inferred here and the values provided in McCarroll et al. (2018). The proposed flux values should be considered as broad estimates, useful for conceptualization and providing hypotheses for future testing in Chapter 4, but they are not definitive. Hence, the direction and approximate magnitude of  $Q_N$  is inferred based on McCarroll et al. (2018), then the budget is balanced (Equations in Fig. 3.13) to calculate fluxes at the mid-point of the embayment ( $Q_M$ ) and the southern boundary ( $Q_S$ ), which are consistent with the observed morphologic change ( $\Delta V_N, \Delta V_S$ ). In other words, based on  $Q_N$  and the observations of from the total sediment budget, values for  $Q_M$  and  $Q_S$  are inferred. Note that fluxes at the outer boundaries ( $Q_N, Q_S$ ) refer to both cross- and alongshore contributions. In summary, major phases of morphologic change include:

1. The **inter-tidal** erodes under energetic (and more northerly) waves and accretes when wave conditions are below average. This process is fairly uniform

alongshore over the multi-year epochs (2011 – 2016; 2016 – 2018), but does vary for individual seasons (e.g., Fig. 3.11, Winter 2017 – 18).

2. During the **storm epoch** (2011 – 2016, Fig. 3.13) two possible scenarios for the northern boundary are presented ( $Q_N$ ): (1) net northward sediment loss of  $3.8 \times 10^5 \text{ m}^3$  with southward sub-tidal bypass and large offshore northward flux; and (2) southward bypass with a net input of  $1 \times 10^5 \text{ m}^3$ . The full embayment erodes, with the south eroding more than the north. Given the orientation of the north coast at a broader scale, the regional transport is expected to be northward for any realistic storm direction as proposed in the first scenario. Hence, northward bypass is also inferred at the southern boundary where a large amount of sediment is transported offshore and towards the north. For the second scenario, the bay does not exhibit the anticipated response of clock-wise rotation, which implies that southward, and potentially offshore, sediment transport is occurring at the south end, exporting sediment beyond the survey region (Fig. 3.8). Both scenarios are not definitive and will be further explored using the model Delft3D in Chapter 4.

3. During the **recovery period** (2016 – 2018), the waves are relatively smaller and more westerly, and the full embayment accretes. The south accretes more than the north, in particular during winter conditions. Northerly transport is inferred to occur during summer periods (Fig. 3.13, Summer 2016), assisted by a northerly residual tidal current (McCarroll et al., 2018). Influx is inferred to occur at both ends of the embayment during ‘recovery winters’ (Fig. 3.13, Winter 2017/18), demonstrating the critical role of winter wave conditions in multi-annual beach recovery (Burvingt et al., 2018; Dodet et al., 2019). This convergent flux is consistent with modelled circulation (McCarroll et al., 2018) for storms from the WNW ( $\sim 285^\circ$ ), that may produce a northward current at the south end, and a southward current at the north end.

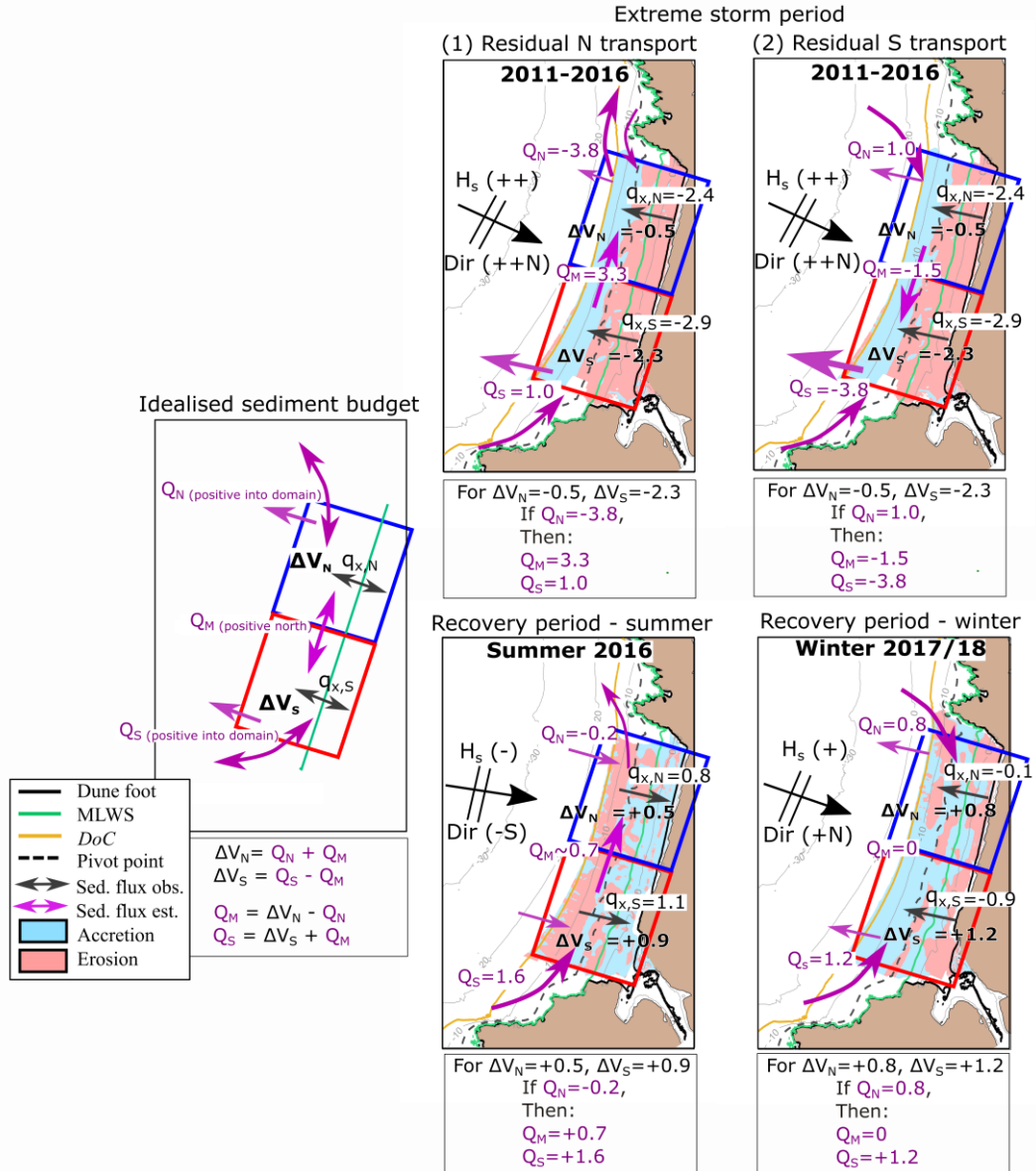


**Fig. 3.13** Semi-quantitative conceptual sediment budget for Perranporth embayment with volume changes ( $\Delta V_N$ ,  $\Delta V_S$ ) and cross-shore flux ( $q_{x,N}$ ,  $q_{x,S}$ ; sed. flux obs.) based on observations. The external flux ( $Q_S$ ,  $Q_N$ ) refer to both cross- and alongshore contributions.  $Q_S$  and  $Q_M$  are estimated using observations and bypass rate in the northern headland (sed. flux est.). Flux and volume change values are  $\times 10^5 \text{ m}^3$ . + and – symbols refer to magnitude of significant wave height ( $H_s$ ) with (++) for large waves, (–) for low energy wave conditions and (+) for moderate to energetic conditions. Direction ( $Dir$ ) refers to shore normal wave direction ( $Dir \sim 283^\circ$ ) with -S for more southward wave approach (W), and +N to ++N for WNW and NW, respectively.

The conceptual model (Fig. 3.13) is useful for explaining the observations, but currently has limited predictive capacity due the complexity of the system response. Further development through numerical modelling approaches are required in order to better predict sediment pathways.

### 3.6.2 Multi-annual embayment scale dynamics

The ‘classic’ characterization of beaches such as Perranporth is that winter storms erode the dunes and the upper part of the beach, depositing the sediment in sub-tidal bar systems, while calmer conditions return the sub-tidal sediment back to the beach (Komar, 1998). This is indeed what our understanding was for the studied beach based on almost a decade of inter-tidal beach surveys and a few sub-tidal surveys (Masselink et al., 2014; Scott et al., 2016), and which has led to the suggestion that Perranporth beach, and similar beaches in the region, are ‘closed systems’ (cf. Fig. 3.1-left panel). However, this characterization has shown to be incorrect as the full sediment budget analysis presented here indicates an ‘open system’ with sediment inputs and outputs in the order of  $300 \text{ m}^3 \text{ m}^{-1}$  over a decadal time period (Fig. 3.5e). The inner embayment region seems therefore connected via sediment pathways to the region beyond the *DoC* and the bounding headlands, which is in line with numerical modelling by Valiente et al. (2019a).

To explain the sediment pathways and close the sediment budget, it is necessary to consider both longshore sediment transport gradients along the embayment (Fig. 3.13) and from adjacent bays through headland bypassing. Importantly, the large sediment volumetric variations across the lower shoreface, which are of the same order of magnitude as those occurring in the inter-tidal region (c.  $200 \text{ m}^3 \text{ m}^{-1}$ ), is suggestive of an energetic longshore transport system across this deeper region, and it is possible that this transport system extends along the whole north coast of SW England as alluded to by May and Hanson (2003) and Valiente et al. (2019a). These findings are critical for informing the next stages of regional scale modelling and observational studies and may lead to a shift in understanding of sediment budgets along exposed and macrotidal embayments globally.

There is an interesting contradiction that, despite the extensive sediment volumetric variations in the sub-tidal region (Fig. 3.5e), a model based solely on inter-tidal beach volume variations such as presented in Fig. 3.5c can be used to predict shoreline position over the 10-year time period (e.g., Davidson et al., 2010). This suggests that the upper part of the beach (supra- inter- and shallow sub-tidal) is partially

decoupled from the deeper sub-tidal region. The vast majority of beach studies in the past (and present) have been (and are) solely based on inter-tidal topographic surveys (e.g., Castelle et al., 2015; Loureiro et al., 2015; Masselink et al., 2016a,b; Harley et al., 2017; Burvingt et al., 2018; Mentaschi et al., 2018); however, full embayment surveys, such as pioneered here, are likely to reveal an additional layer of complexity concerning nearshore sediment transport and beach morphodynamics. Future numerical modelling efforts will be aimed at providing complementary understanding of embayment scale sediment fluxes.

### **3.6.3 Outer bar dynamics**

Onshore/offshore bar migration involves the transfer of sediment from the lower to the upper shoreface and vice versa. Conversely, outer bar dynamics appear decoupled from the sediment fluctuations in the lower shoreface. Along most coasts there are net sediment losses or gains which are reflected on the bar movement (Plant et al., 1999; Shand and Bailey, 1999; Kuriyama, 2002; Aagaard et al., 2010), whereas Perranporth is in long-term equilibrium; hence the bar moves with the variability in the waves. As expected, downstate transitions of the outer bar concur with mild conditions and are characterized by an increase in three-dimensionality, onshore movement of the outer bar and accretion of the lower inter-tidal; while upstate sequences result from energetic periods and can be described by offshore migration of the outer bar, a decrease in three-dimensionality and loss of sediment in the lower inter-tidal (Poate et al., 2014; Masselink et al., 2014). In contrast to the behaviour of the nearshore bars on the Dutch coast, which are characterized by a decay cycle induced by a net offshore/onshore migration and an upper shoreface which decreases/increases in sediment volume (Kroon, 1990; Ruessink and Kroon, 1994; Aagaard et al., 2004; Aagaard et al., 2010), the outer bar at Perranporth does not show a net migration over the decadal scale but also increases in size with depth. Whereas outer bars observed in other multi-barred systems along exposed coasts (e.g., Plant et al., 1999; Shand and Bailey, 1999; Kuriyama, 2002) exhibit a decay (8-year cycle) in water depths of about 4.5 – 6 m (Ruessink et al., 2003; Aagaard et al., 2010), Perranporth outer bar dynamics follow a 4-year cycle (ignoring seasonal signal) that comprises 175 m of onshore (offshore) translation (average

migration rate of 44 m year<sup>-1</sup>) and oscillations from shallower (deeper) to deeper (shallower) position between 5 to 7 m depth ODN, larger depths than those where the bar decay is observed. The implication is that in this type of double-barred environments, cross-shore exchanges (c. 50% of total response) are directly affected by the outer bar dynamics, as it is the bar translation that forces the onshore (offshore) migration of the pivoting interface or point of transfer of sediment between the lower shoreface and the shallower sub-tidal (5 – 7 m depth ODN).

### 3.7 Conclusions

- A total sediment budget approach was implemented across the macrotidal, high energy Perranporth embayment for the period 2011 – 2018, using a multi-method surveying approach and accounting for measurement uncertainties.
- Inter-tidal volumetric changes indicate a longshore coherent, cross-shore dominant behaviour, following a seasonal cycle superimposed by a multi-annual oscillation induced by extremely energetic winter seasons, with full recovery taking at least 5 years.
- Total embayment (combined inter- and sub-tidal) volumes varied by c. 300 m<sup>3</sup> m<sup>-1</sup> over 7-years, indicating that the inner embayment (down to the DoC) is 'open' and 'unbalanced' over multi-annual timescales.
- Sediment volumetric variations in the inter-tidal region are uncorrelated with those in the sub-tidal region at zero time-lag, but a positive correlation is observed at 1-year time-lag. This suggests that the upper and lower shoreface are partially decoupled, responding to different forcing controls.
- The largest dunes system monitored (northern Perranporth) experienced a significant erosion event in 2013/14 (15 m onshore translation of dune foot) with little recovery within 5 years.
- Inter-tidal sediment volume for the long-term southern sector time series was inversely correlated with variations in total wave power ( $r = -0.6$ ), coherent with a cross-shore dominated response. Total sediment volume change (primarily due to flux through the outer sub-tidal boundary) was correlated with both total ( $r = -0.6$ )

and alongshore wave power ( $r = 0.4$ ), suggesting a combined cross- and alongshore dominated response.

- The inter-tidal volume was found to be positively correlated with the total volume (for the south sector), such that when the inter-tidal eroded or accreted, so too did the total system. This was evident for an erosive period of extreme waves (2011 – 2016), followed by a ‘recovery’ period (2016 – 2018), where consistent influxes into the embayment were observed, even during energetic winter periods. This suggests a degree of equilibrium for the total embayment volume.
- A conceptual model was presented that balances the observed volume changes with inferred fluxes, forced by variations in total and alongshore wave power. At present, this model has limited predictive capacity and requires further development through numerical modelling approaches to better predict future sediment budgets on similar coastlines.
- Given the extent of flux through the sub-tidal outer boundaries, it is likely that Perranporth and beaches on similar coastlines form part of an extended coastal cell, with individual embayments linked via a ‘river of sand’ that flows around headlands.



## **Chapter 4 – Numerical modelling of nearshore sediment transport and headland bypassing**

---

This chapter contains work previously presented in the following paper included in Appendix B:

N.G. Valiente, R.J. McCarroll, G. Masselink, T. Scott, D. Conley, E. King. Circulation and sediment fluxes on a macrotidal, exposed and embayed coastline. Proceedings Coastal Sediments, ASCE, Florida, USA, May 2019.

### **4.1 Introduction**

Embayed beaches constitute a large proportion of the world's rocky coastlines. Highly embayed beaches are often considered closed cells with the prominent headlands acting as barriers to littoral drift, such that sediment transport into and/or out of adjacent cells is insignificant. Consequently, there is a paucity of studies focusing on the cross-shore sediment exchange between the upper and the lower shoreface, and the longshore sediment exchange between embayed beaches and the neighboring rocky stretches of coast. Nevertheless, recent studies on sandy beaches show that important sediment transport paths offshore and/or beyond these barriers may occur under particular conditions (Short, 2010; Aagaard, 2011; Goodwin et al., 2013; McCarroll et al., 2018; King et al., 2019; Valiente et al., 2019a).

Sediment transport into and out of embayments are of major interest to coastal researchers, but key processes (e.g., mega-rips, headland bypassing), driving forces, flux rates and local factors influencing it (e.g., headland/embayment morphometric parameters) are still poorly resolved. Recent site-specific observational studies have demonstrated the relevant sediment fluctuations across and along the lower shoreface (George et al., 2018; Valiente et al., 2019b; McCarroll et al., 2019). Several modelling studies have investigated the processes that may induce the significant sediment fluxes beyond the embayment limits through cross-embayment exchanges (Short, 2010; Castelle and Coco, 2013; McCarroll et al., 2016) and between adjacent beaches (McCarroll et al., 2018; Vieira da Silva et al., 2018). Cross-shore sediment fluxes involve

sediment transport between the different sub-systems (dunes, inter- and sub-tidal; Valiente et al., 2019b) or even beyond the morphological *DoC* (Ortiz and Ashton, 2016; Valiente et al., 2019a, mainly due to the presence of megarips. In the alongshore, largest sediment fluxes will occur during large oblique waves (McCarroll et al., 2019). Along rocky coastlines, both transports (cross- and alongshore) may be disrupted and/or altered by the regional topography (e.g., embayment and headland configuration) introducing complexity in the general sediment transport patterns that needs to be better understood. Although substantial research effort has been expended, studies using a combined approach of numerical modelling and high-quality comprehensive field datasets to reduce uncertainty bounds are scarce.

For embayed coastlines, bypassing and embayment-scale cellular circulation (Castelle et al., 2016) are the main mechanisms responsible for sediment exchange between embayments and neighbouring areas. Based on observations, Gallop et al. (2011) and Loureiro et al. (2012a) linked morphological change with embayment-scale circulation (rip and mega-rip formation) on several embayments of varying size and orientation. Additionally, Castelle and Coco (2013) studied the role of embayment morphometry in governing ejection outside the surf zone using simulations of passive tracers. They showed that the surf zone of embayed beaches systematically flushes out more floating material than on open beaches, with most exits occurring through the headland rips, and provide retention rates (in percentage) for varying beach length and constant headland length. More recent studies were more focused on the driving forces for bypass around natural headlands. Vieira da Silva et al. (2018) investigated the influence of wind and waves on headland bypass whereas McCarroll et al. (2018) studied the role of the different embayment-scale circulation modes inducing bypass.

For embayed coastlines, bypassing and embayment-scale circulation are the main mechanisms responsible for sediment exchange between embayments and their neighbouring areas. Based on observations, Gallop et al. (2011) and Loureiro et al. (2012a) linked morphological change with embayment-scale circulation (rip and mega-rip formation) on several embayments of varying size and orientation. Additionally, Castelle and Coco (2013) studied the role of embayments' distal morphology in governing ejection outside the surf zone using simulations of passive tracers. They

showed that the surf zone of embayed beaches systematically flushes out more floating material than on open beaches, with most exits occurring through the headland rips, and provide retention rates (in percentage) for varying beach length and constant headland length. More recent studies were more focused on the driving forces for bypass around natural headlands. Vieira da Silva et al. (2018) investigated the influence of wind and waves on headland bypass whereas McCarroll et al. (2018) studied the role of the different embayment-scale circulation modes inducing this bypass.

Sand bypassing rates are often predicted using simple analytical solutions such as one-line models and straight shorelines (Ab Razak et al., 2013; Brown et al., 2016). More sophisticated approaches include 2D and 3D process-based numerical modelling that is able to simulate horizontal and vertical currents. McCarroll et al. (2018) first introduced a site-specific headland bypass parameter for a multi-year period based on modelled sand bypassing rates on an individual headland. A recent study (George et al., 2019) examined the impact of idealised headlands of varying size and shape on rates of headland bypass and determined that longshore sediment fluxes around headlands are mainly determined by the degree of blockage. However, despite these later efforts, prediction of sediment bypass in embayed beaches of different geometry and complex circulation remains elusive.

A quantitative understanding of littoral cells sediment pathways is fundamental when investigating beach response and evolution along embayed coastlines (Komar, 1998; Rosati, 2006). For open cells, coastal changes cannot only be attributed to a redistribution of the sediment within a single embayment but to sediment exchange within a larger area, hindering a full understanding of embayments individually, while limiting the use of observations in large sediment sharing areas. Imbalance/balance between incoming and outgoing sediment fluxes encompassing several embayments, even when open, can ultimately provide essential information on the major sediment transport pathways as well as help to derive sediment budgets within the inter-connected cells. In Chapter 3, we followed a total sediment budget approach based on morphological observations in an embayed beach concluding that despite the deeply embayed nature of the beach, the system was open. The approach allowed

quantification of sediment gains and losses; however, the understanding of the system was not complete as it lacked complete information on the directional sediment fluxes.

Following the observational study conducted in Chapter 3, the aim of this chapter is to provide a more robust and comprehensive understanding of the complex sediment dynamics driving coastal evolution along embayed coastlines. Here, variable local factors (tidal currents, wave exposure and sheltering, sediment supply, headland bypassing and embayment scale circulation) influencing the inter-annual sediment transport dynamics for 15 km of the macrotidal, exposed and embayed coastline of north Cornwall, SW England (Figure 4.1), are investigated. Numerical simulations are conducted to predict sediment fluxes for a stretch of coast comprising five embayments and six headlands of diverse morphometric characteristics. In particular, we examine: (1) headland bypassing rates; (2) sediment ejection outside the offshore morphological limit of the embayments; and (3) sediment exchanges within Perranporth and adjacent embayments over multi-annual time scales.

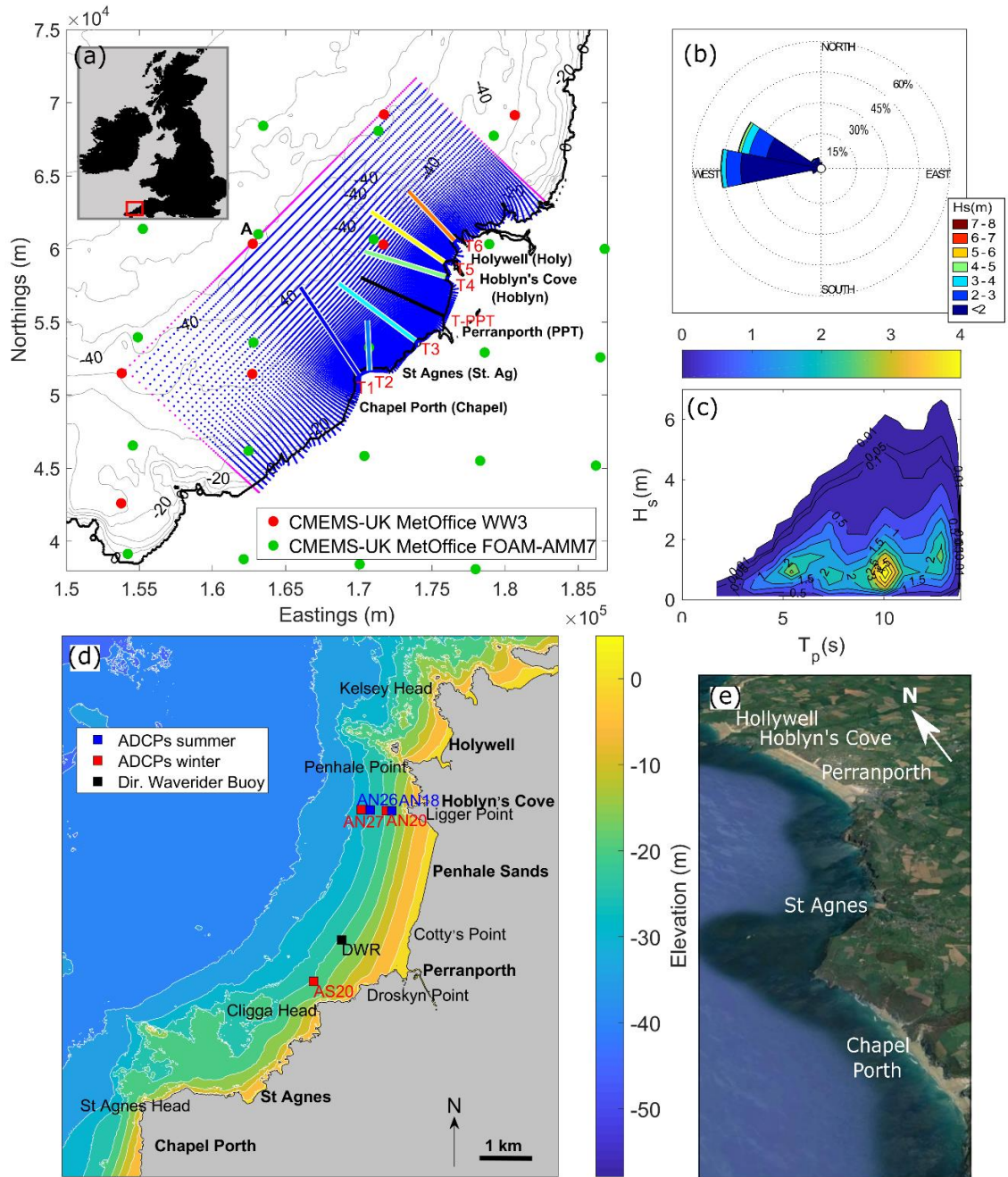


**Fig. 4.1** (a) Delft3D model grid and transects used for the analysis (thick solid lines). Red dots indicate UK MetOffice Wave Watch III 8 km (WW3) model nodes used as wave input and green dots represent Forecasting Ocean Assimilation Model Shelf Seas Atlantic Margin Model 7 km (FOAM-AMM7) hydrodynamic nodes provided by Copernicus Marine Environment Monitoring Service (CMEMS, 2017). Grid nodes are plotted every 2 points in each direction for clarity. Location A was used for examining boundary conditions for simulated sample cases. (b) Wave rose and (c) joint probability for Perranporth using 11 years of wave buoy data (DWR). (d) Physical context of the study site and instrument positions (squares). Instrument name refers to the location and mooring depth relative ODN, respectively, e.g., AS20 was the ADCP deployed in the south of the bay at 20 m water depth. (e) Oblique Google Earth image of headlands and embayments.

## 4.2 Study area

The study encompasses 15 km of the macrotidal, exposed and embayed coastline of north Cornwall from Chapel Porth (Chapel) to Holywell (Holy) (Fig 4.1d). This stretch of coast includes five sandy beaches delineated by sharp headlands of diverse morphometric characteristic (Fig 4.1e) that alternate with rocky sediment-free areas backed by cliffs 50 – 90 m high. The beaches are characterised by a wide low-gradient (mean bed slope ranging 0.018 – 0.021) sandy platform facing W with a slight rotation in the south to the NW ( $280^\circ$  –  $290^\circ$ ), except for St. Agnes (St Ag), which faces N. This beach also differentiates itself from the others in the study through its short length and coarse gravel-sand sediments. The remaining beaches are composed of medium sand with a median grain size ( $D_{50}$ ) of 0.30 – 0.40 mm. For Perranporth (PPT),  $D_{50}$  attains a relatively constant value (0.33 mm) up to 20 – 26 m depth Ordnance Datum Newlyn (Valiente et al., 2019a), which is inferred as the base of the active profile. This coastline is considered cross-shore dominated with the onshore (offshore) point of transfer (pivot point) of sediment between the lower shoreface and the shallower sub-tidal at 5 – 7 m depth ODN (Valiente et al., 2019b). Isolated rocks are present around the apex of most of the headlands at depths of 5 – 10 m Ordnance Datum Newlyn (ODN). Sand is visible around these rocks in aerial imagery (McCarroll et al., 2018) and smooth contours inferred to be sand are found off most of the studied headlands up to 17 – 26 m depth ODN (Valiente et al., 2019a). The averaged morphological depth of closure ( $DoC$ ) along this stretch of coast is c. 15 m depth ODN, and the averaged maximum depth of transport computed using tide- and wave-induced bed shear stresses during extreme conditions is c. 25 – 28 m depth ODN (Valiente et al., 2019a).

This coastline is fully exposed to regular North Atlantic swells, with an annual average significant wave height ( $H_s$ ) of 1.6 m and peak period ( $T_p$ ) of 10 – 11 s. Wave approach is typically from the W and WNW (Fig 4.1b), with largest waves coming from the latter. Wave climate is seasonal with monthly average  $H_s$  ranging from 1.2 m (summer) to 2.3 m (winter), and extreme wave heights can exceed  $H_s = 8$  m and  $T_p = 19$  s (Fig. 4.1c). The tidal regime is semi-diurnal and macrotidal with a mean spring and neap tidal range of 6.3 m and 2.7 m, respectively (Masselink et al., 2014; Scott et al., 2016).

Maximum ebb and flood velocity ranges from 0.1 to 0.4 m s<sup>-1</sup> at depths between 10 and 30 m with the tidal flows predominantly parallel to the shoreline, and with speeds significantly increasing around the headlands (c. 0.7 m s<sup>-1</sup> during spring tides; Valiente et al., 2019a). The strong flood-ebb asymmetry in the current magnitude during a tidal cycle results in a northward residual current along the coast of 0.05 – 0.2 m s<sup>-1</sup> (McCarroll et al., 2018).

### **4.3 Materials and methods**

Sediment fluxes in/out embayment were computed using a coupled Delft3D morphodynamic model for a wide range of representative conditions for the period 2011 – 2018. Based on the hindcast wave data, predictions of sediment fluxes over multi-annual time scales were produced.

#### **4.3.1 Wave and hydrodynamic field observations**

Waves, currents and water levels were measured using three 600 kHz RDI WorkHorse Monitor Acoustic Doppler Current Profilers (ADCPs) deployed during 2 – 3 months in summer 2016 (AN17 and AN25) and winter 2016/17 (AS20, AN20 and AN27) off the two headlands delineating Perranporth beach in 15 – 30 m depth relative ODN (Fig. 1d). Two ADCPs located shore-normal to the apex of the northern headland (same transect, 475 m apart) were moored during summer and winter periods with an extra ADCP located perpendicular to the southern headland during the latter. Waves were also observed by a directional wave buoy (DWR, Fig. 4.1d) located in 20 m depth that recorded every 30-min. Currents and water levels were ensemble averaged at 5-min intervals using 90 pings per averaged ensemble per current profile at 0.33 Hz (over 270 s). The waves were sampled averaged every 2 h, with 20-min bursts of 2400 samples at 2 Hz. Current observations were post-processed and cleaned prior sample averaging to avoid overestimation due to frequent spikes. Surface spikes were removed applying the Return Signal Strength Indicator (RSSI) for bump detection, which conducts a cut-off in the velocity profile where the RSSI is detected. Remaining spikes were cleaned using the phase-space thresholding method by Goring and Nikora (2003) and modified by Mori et al. (2007) (see example in Fig. 4.2). The removed spikes were reconstructed using a

cubic polynomial. Wave and hydrodynamic observations were used to calibrate and validate the numerical model Delft3D. For validation purposes, the currents were averaged using all bins over the water column and smoothed using a 30-min moving average filter.

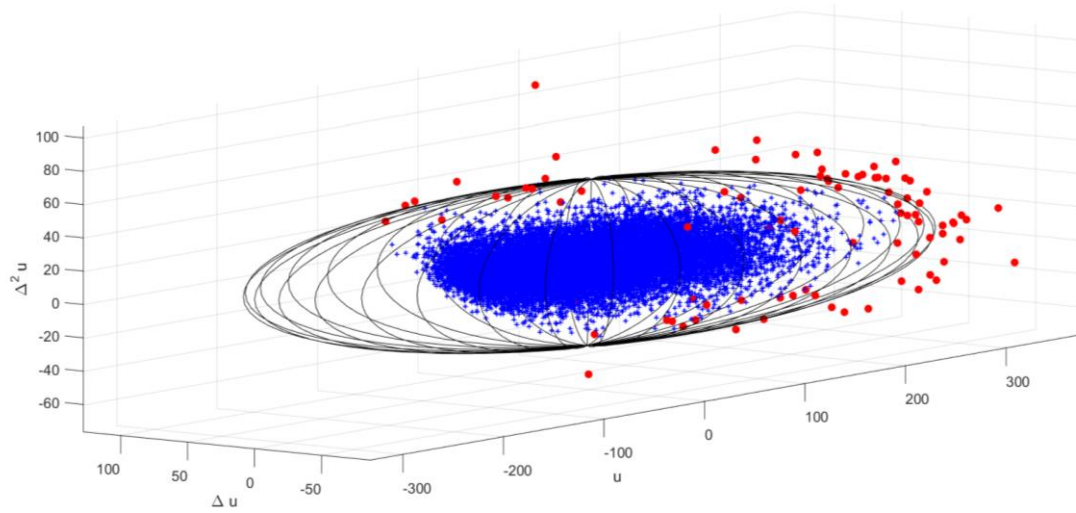


**Fig. 4.2** Example of de-spiking ellipsoid using Goring and Nikora method (2002) for the easting velocity component of the current ( $u$ ) in the bottom bin of AN17.  $\Delta u$  and  $\Delta^2 u$  are the surrogate (not divided by the time step  $\Delta t$ ) of first and second derivative of  $u$  using central differences of  $u$  and  $\Delta u$ , respectively.

### 4.3.2 Numerical model setup

The process-based numerical model Delft3D (Booij et al., 1999) was used for wave transformation (WAVE) and hydrodynamics computation (FLOW). The FLOW module solves the 3D water equations and the WAVE module includes the wave propagation, dissipation, generation by wind and non-linear wave-wave interactions (TRIADS mechanism). Delft3D was run in 2D and online-coupled mode (i.e. two way wave-current interaction).

#### 4.3.2.1 Model forcing datasets

UK MetOffice Wave Watch III 8 km (WW3) model nodes and gridded 7-km hydrodynamic forcing from the Forecasting Ocean Assimilation Model Shelf Seas Atlantic Margin Model 7 km (FOAM-AMM7) were linearly interpolated at intervals to the WAVE model and water level boundaries of the FLOW model, respectively. Both

wave and hydrodynamic model datasets were generated by UK MetOffice and provided by Copernicus Marine Environment Monitoring Service (CMEMS, 2017).

Pressure forcing conditions were obtained from the National Oceanic and Atmospheric Administration (NOAA) Climate Forecast System Version 2 (CFSv2) at  $0.5^\circ$  resolution. Wind forcing data was the L4 dataset CERSAT Global ocean blended wind dataset at  $0.25^\circ$  resolution produced by IFREMER and distributed by the CMEMS Ocean and Sea Ice Thematic Assembly Centre (OSI TAC). Wind and pressure forcing data were linearly interpolated and presented in a spatially-varying separate grid.

#### **4.3.2.2 Bathymetry and model domain**

The high-resolution initial bathymetry was created by combining a multimethod morphological dataset for the year 2011. This bathymetry was constructed by merging Light Detection And Ranging (LiDAR), RTK-GPS aided single-beam survey and multi-beam bathymetry facilitated by the United Kingdom Hydrographic Office. A 2-m spatial resolution digital elevation model (*DEM*) was generated for the entire stretch of coast using Loess (Plant et al., 2002) and natural neighbor (Sibson, 1981) interpolation functions. Due to the resolution of the hydrodynamic forcing conditions (7 km), a transition zone with a smoother bathymetry was implemented to eliminate an inaccurate strong coastal current induced at the cross-shore boundaries (refer to Appendix B). Additionally, a 2-D Gaussian smoothing filter with standard deviation of 2 was exclusively applied along 400 m extent at both ends of the domain (refer to Appendix A). The model domain was large enough to maintain the transition zones far from the area of study.

The model domain encompasses Perranporth beach and adjacent embayments using two orthogonal curvilinear grids (Fig. 4.1a) generated using conformal mapping methods as in Bruciaferri et al. (2020) with an extent of 15 km by 10 km and a space-varying resolution that ranges from 300 m offshore to  $< 20$  m near the coast. These grids are designed to follow the primary morphological features along the study coastline such as headlands and bays, while being able to resolve the coastline with higher resolution. The WAVE grid was a 2-grid cells (0.36 km) halo at the boundaries of the FLOW grid. Sensitivity analysis of this final setup was performed against a WAVE grid

with a halo extension of c. 4.5 km (25-grid cells) at each boundary (not shown) and simulations showed equal performance of the two implementations, discarding the necessity to extend the wave domain more than 2-grid cells.

### 4.3.2.3 Wave model

The third-generation spectral wave model SWAN (Booij et al., 1999), packaged within Delft3D as WAVE, was used to transform wave conditions from offshore to inshore. This model accounts for wind growth, dissipation processes and wave-wave interactions. The dissipation mechanisms considered were bottom friction (with JONSWAP friction coefficient of  $0.067 \text{ m}^2 \text{ s}^{-2}$ ), refraction, whitecapping (Komen et al., 1984) and depth-induced breaking (with ratio of maximum individual wave height over depth equal to 0.7). Non-linear wave-wave interactions were also considered (TRIADS mechanism). Parameterised values of wave characteristics ( $H_s$ ,  $T_p$ ,  $Dir$ , and directional spread) from UK MetOffice Wave Watch III 8 km (WW3) were used as forcing conditions and WAVE was run in stationary mode.

### 4.3.2.4 Hydrodynamic model

Hydrodynamic computations were conducted using the FLOW module. The FLOW model was implemented in 2DH, solving the depth-averaged shallow water equations, and run in hydrostatic mode. Previous coastal studies of similar spatial scale on energetic sandy coastlines (e.g., Luijendijk et al., 2017) have demonstrated that Delft3D run in 2D mode is able to accurately reproduce hydrodynamic behaviour over multi-annual timescales. Other modelling approaches encompassing larger areas of this coast have also shown good replicability of observed hydrodynamic processes in 2D mode (Holt et al., 2001; Bricheno et al., 2015; Lyddon et al., 2018). Additionally, King et al. (2019) studied major sand transport pathways on the SW continental shelf, demonstrating that qualitatively the spatial pattern of net sand transport remained the same after the addition of sigma levels. Consequently, depth-averaged hydrodynamics were considered adequate for this study as sediment fluxes to larger depths will be almost entirely driven by the rip cell circulation that the model in 2D mode is able to reproduce. More details on model limitations are presented in Section 4.3.2.5.

Several methods for open boundary conditions can be implemented for nested modelling on Delft3D. Although traditionally it is recommended to use different boundary conditions for coastal models (Deltares manual, page 46), it is well known that undesired boundary effects can still remain (Qinghua Ye et al., 2011). After several sensitivity analyses (refer to Appendix A.1) using Neumann and water level as cross-shore boundary conditions, the optimal forcing configuration was determined as water level time series at two open boundaries (offshore NW and cross-shore NE) and current time series at the inflow open boundary (cross-shore SW). Additionally, several test cases with a range of boundary reflection parameter *Alfa* values (10 – 200) were set up to assess the best performance. *Alfa* specifies the amount by which the open boundary is less reflective for short wave disturbances that propagate towards the boundary from inside the model and for macro-tidal environments is recommended a value of 50 or 100 (Deltares manual, page 46). A final *Alfa* value of 50 showed the best performance.

Following Luijendijk et al. (2017), bed-load and suspended-load (both current- and wave-related) sand transport rates were computed using the TRANSPOR2004 transport formulation (van Rijn, 2007a, 2007b) with uniform sediment size of 0.33 mm (Prodger et al., 2017) and unlimited sediment availability on areas defined by the sdb file. The FLOW model was run using a 0.05-min time-step to avoid large Courant number values during the simulated periods with extreme wave conditions. The MORPHO module was turned on with update off and transport model settings employed in the model runs were extracted from similar studies (Table 4.1). An additional limiter on the morphological acceleration factor to minimize mass flux was implemented (*Gammax* = 0.7) as suggested by Luijendijk et al. (2017).

**Table 4.1** Delft3D model settings.

Module	Parameter	Value/Setting	Comment
<i>Hydrodynamics</i>	Boundaries	cross-shore SW – current	Different combinations for the cross-shore boundaries (e.g., Neumann) were tested.
		Offshore – WL	
		cross-shore NE – WL	
	Reflection	50	Test from 10 to 200.
	Gammamax	0.7	As per Luijendijk et al. (2017)
<i>Transport</i>	Formulation	Van Rijn (2007b)	‘TRANSPoor2004’, as per Luijendijk et al. (2017).
	D50	0.33 mm	As per Prodger et al. (2016)
	Transport multipliers	Sus (1.4), Bed (0.8), SusW (0.3), BedW (0.3)	Suspended and bed transport multipliers for currents (Sus, Bed) and waves (SusW, BedW). As per Grunnet et al. (2004).
	Update	Off	-
<i>Morphology</i>	ThetSD	1.0	Factor for erosion of adjacent dry cells, as per Luijendijk et al. (2017).
	MORFAC	1.0	Morphological acceleration disabled.
	CaMax	0.05	Limiters to avoid unrealistic suspended sediment transport
	DzMax	0.05	fluxes. As per Elias (2018).

#### 4.3.2.5 Model limitations

Delft3D has been successfully used in a depth-averaged form in studies of wave-current interactions and sediment transport on the inner continental shelf (Hansen et al., 2013; Hopkins et al., 2015; Ridderinkhof et al., 2016; Luijendijk et al., 2017; King et al., 2019). However, offshore (bed return flow) and onshore (wave asymmetry) cross-shore fluxes are poorly resolved in 2D mode, limiting cross-shore sediment transport to the rip circulation in this instance. Other processes such as seasonal stratification (not important in the area of study; unpublished data) or the Ekman spiral are not reproduced in baroclinic mode but these will not affect the sediment fluxes object of this study. Additionally, grid resolution in certain areas might constrain resolution of small-scale eddies (~ 20 m).

#### 4.3.2.6 Model calibration and validation

Model output was calibrated against four points of observations of wave statistics (DWR, AS20, AN20 and AN27), and three of water level and flow velocity and direction (AS20, AN20 and AN27) for March 2017 (refer to Fig. 4.1d for locations). The

model performance was then optimised for the calibration period and then validated against a total of two months observations covering a wide range of summer and winter wave hydrodynamic conditions. Summer and winter validation periods were August 2016 and February 2017, respectively. Model skill was evaluated using root-mean square error (*RMSE*), mean absolute error, *bias* and coefficient of determination ( $R^2$ ). *Bias* was normalised relative to the observed mean, so that the systematic error of the model was expressed in terms of the background observed sample climate.

### 4.3.3 Modelled scenarios

Computational requirements for a 7-year period (2011 – 2018) are excessive; therefore, we opted for shorter model runs (Fig. 4.3a-dashed boxes) covering a wide range of representative wave conditions, namely  $H_s = 0.1 - 8$  m,  $T_p = 4 - 20$  s and  $Dir = 260 - 360^\circ$  (Fig. 4.3e) over different tidal ranges (neap to spring tides, Fig. 4.3f). Frequency distributions of the wave statistics and water-level conditions for the selected model simulations are shown in Fig. 4.3b–d. To facilitate visual comparison with the complete hindcast model forcing time series encompassing 2011 – 2018, the simulated cases are presented using a fitted distribution. Representativeness of the selected periods is demonstrated as all variables follow the distribution of the complete time series (Fig. 4.3b–d). Model simulations were performed over a total of 6 months: (i) a 2-month period over a characteristic summer (2016); (ii) a c. 3-month period over winter (2016/17), both periods also used for validation; and (iii) an extra 1-month of exceptional extreme energy conditions, January 2014 ( $H_s \sim 8$  m; Masselink et al., 2016a,b).

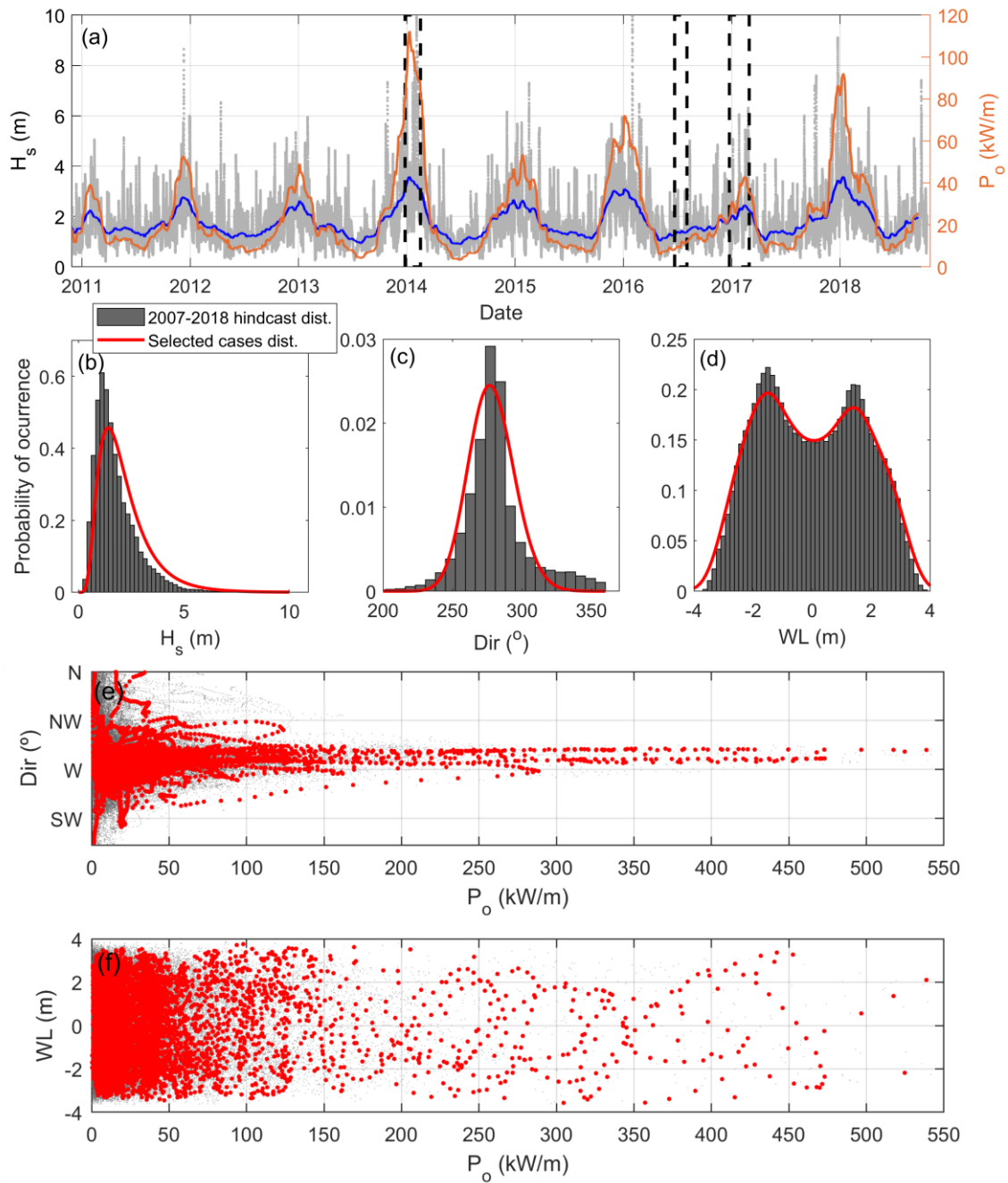


**Fig. 4.3** (a) 8-year time series of significant wave height  $H_s$  (30-min and 4-week running mean) and wave power  $P_o$  (Herbich, 2000). Normalised probability of occurrence for  $H_s$  (a), wave direction  $Dir$  (b) and water level  $WL$  (d) based on the complete hindcast from 2011 – 2018, compared to distribution of the selected cases for model runs (dashed boxes in a). (e, f) Distribution of selected cases for the combinations of  $P_o$ , wave direction ( $Dir$ ) and water level ( $WL$ ). All variables correspond to the CMEMS nodes located at the centre of the offshore boundary of the model domain (Location A, Fig. 4.1a).

#### 4.3.4 Transects for transport rates integration

Six transects (Fig. 4.4) extending from the headland apex to > 35 m ODN were used to compute sediment transport rates between bays. Transects were located at the

primary headlands and drawn perpendicular to the headland apex. Sediment fluxes (sum of bed-load and suspended-load) were integrated over each transect ( $Q_{bypass}$ ) for different range of depths: headland base – 6 m, 6 – 15 m, 15 – 25 m and > 25 m water depth ODN. Alongshore sediment fluxes were also computed across one extra profile located on the middle of Perranporth beach. Longshore drift direction was calculated with respect to the transect orientation in order to discern between inflows and outflows in/out the different embayments, with positive (negative) values indicating northward (southward) flux. Additionally, sediment flux ejected beyond the morphological depth of closure (15 m depth ODN for this particular case) was calculated integrating the fluxes that exit this morphological limit ( $Q_{cross}$ ) with positive (negative) values representing sediment flushed into (ejected out of) the embayment. To facilitate discussion, sediment fluxes were extracted from the 15-m contour line (average *DoC*; Valiente et al., 2019a) from transect to transect and encompassing the 5 embayments (Fig. 4.4). Thus, the computed sediment transport rates will correspond not only to the embayments, but to the entire bays including the subtidal areas within the primary headlands. It is important to note that this is considered a rough estimate of the sediment that is discharged from the beach to larger depths as the sediment fluxes beyond the surf zone are entirely a consequence of the cellular rip-cell circulation.

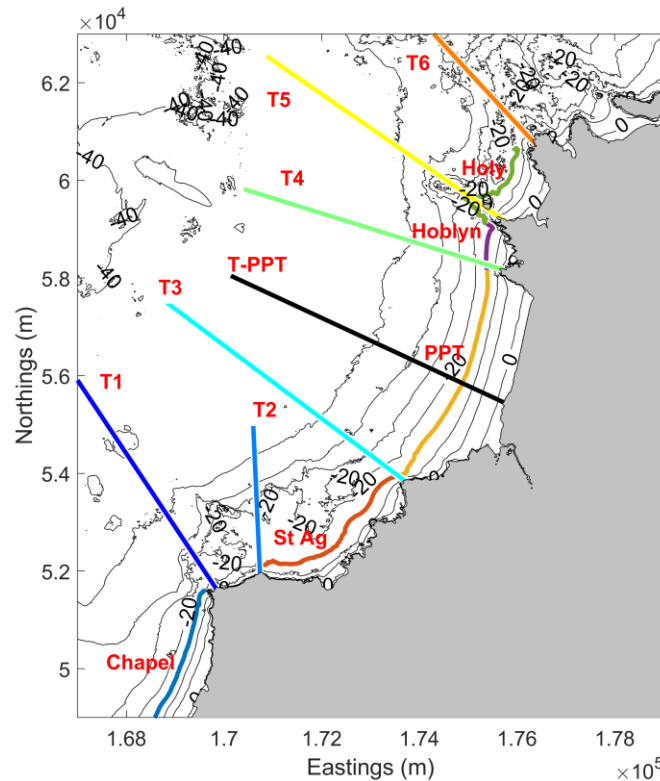


**Fig. 4.4** Transects (thick coloured straight lines) and contour lines (thick coloured contour lines) used to integrate the longshore and cross-shore sediment fluxes, respectively.

## 4.4 Results

#### 4.4.1 Calibration and validation

WAVE output over the validation period compared with observations is presented in Fig. 4.5. Visual inspection indicates that the model correctly reproduced the experienced wave conditions. The model satisfactorily replicated wave height ( $RMSE = 0.40$  m,  $MAE = 0.29$  m,  $R^2 = 0.79$  and  $bias = 0.05$ ; Table 4.2) for both summer and winter validation periods. The peak period prediction was good ( $RMSE = 2.1$  s,  $MAE = 1.3$  s,  $R^2 = 0.65$  and  $bias = 0.01$ ; Table 4.2), with poorer correlations during short periods ( $T_p < 10$  s) when wave period was slightly overestimated. Modelled wave direction oscillated around the prevailing direction ( $\sim 280^\circ$ ) and showed little long-term variation (maximum  $bias = 0.12$ ), therefore  $R^2$  showed poor correlations and is not the best indicators of model performance.  $RMSE$  and  $MAE$  are better indicators in this instance with values for wave direction oscillating between  $9 - 17^\circ$  and  $9 - 11^\circ$ , respectively;

values comparable to those found in similar studies (Vieira da Silva et al., 2016; McCarroll et al., 2018).

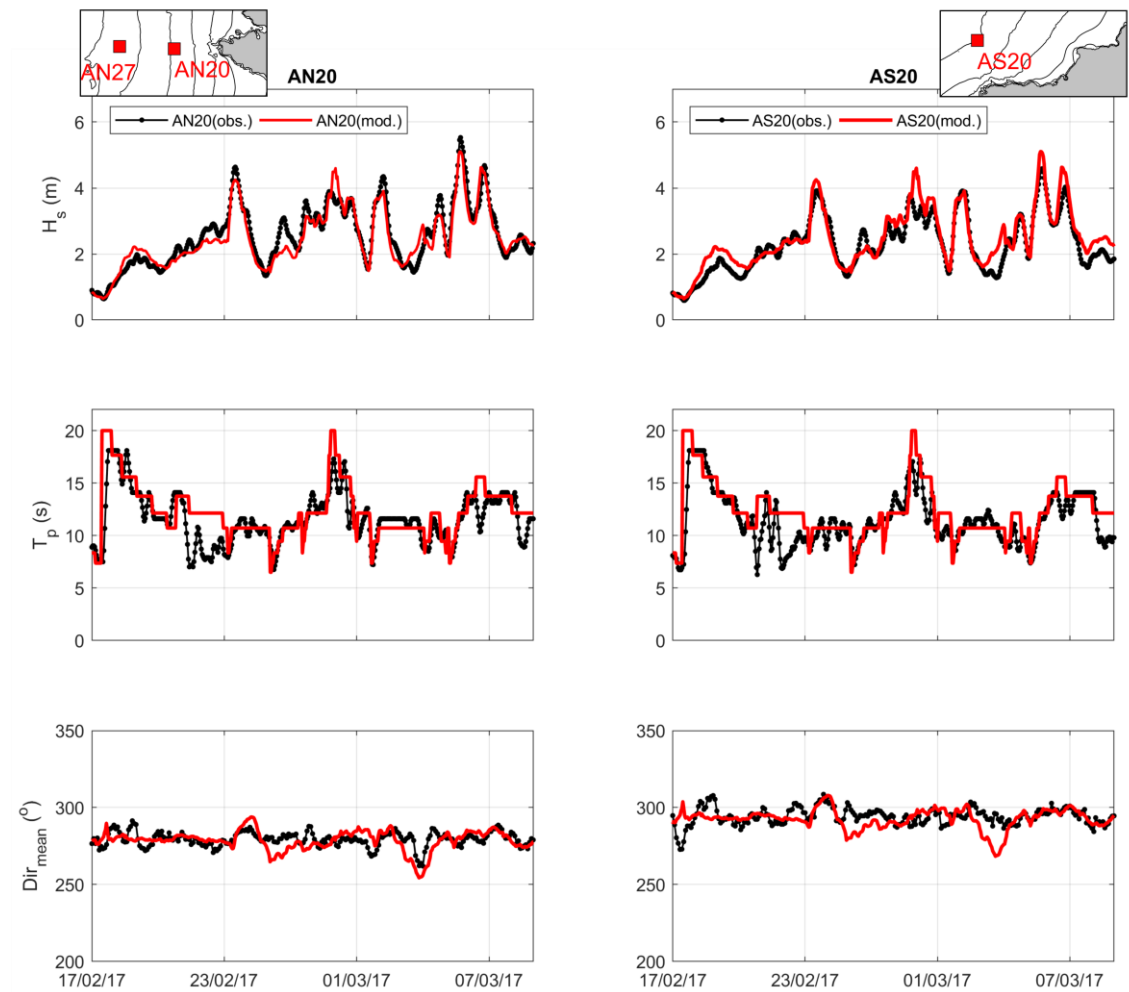


**Fig. 4.5** Wave ADCP observations at AN20 and AS20 compared with Delft3D model output. From top to bottom: significant wave height ( $H_s$ ), peak period ( $T_p$ ), and mean direction ( $Dir_{mean}$ ). Zoomed-in locations of the ADCPs are presented in the small top panels; cf. Fig. 4.1d for large-scale setting of the ADCP locations.

Observed and modelled FLOW output over a month of simulations encompassing two neap and two spring periods are presented in Fig. 4.6 and 4.7. Overall, water level and flow simulations reproduced the observations well. For the northward headland (AN20 and AN27), a residual current of 0.05 and 0.25 m s<sup>-1</sup> (Fig. 4.6c, f) was observed during neap and spring tides, respectively. The flow was mainly explained by the alongshore component ( $v$ , northward current) (Fig. 4.6b, e), with minimal cross-shore flows ( $u$ , eastward current) (refer to Fig. 4.7a). Conversely, AS20 deployed off the southern headland showed a velocity signal that is explained c. 60% by the cross-shore component (-0.4 – 0.5 m s<sup>-1</sup>, Fig. 4.7d) and, although the model is able to

reproduce the cross-shore signal qualitatively (refer to Fig. 4.7a), the cross-shore flow is underestimated during neap tides and overestimated during spring tides (Fig. 4.7d).

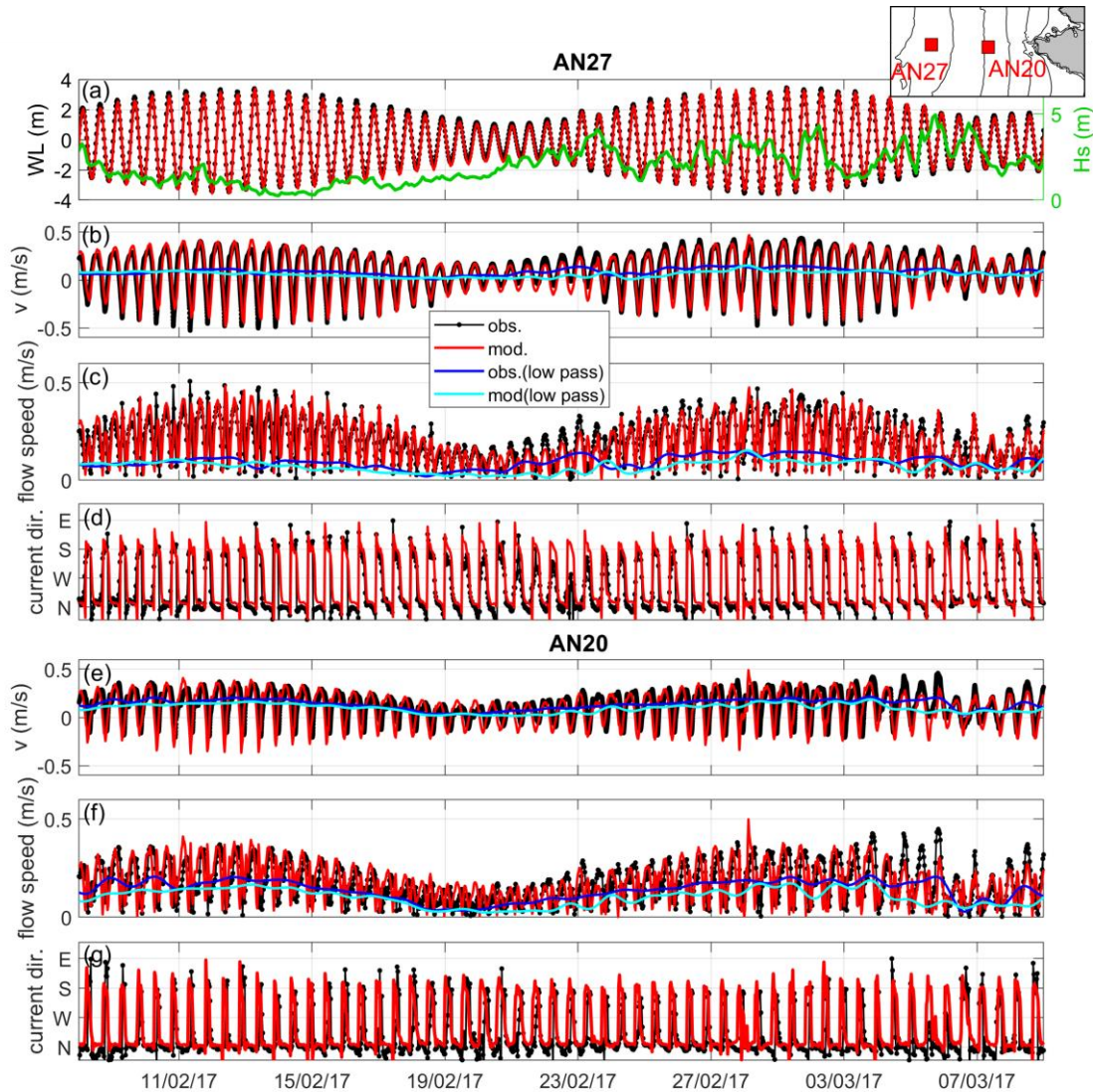


**Fig. 4.6** (a) Water level (WL) and flow observations at ADCPs AN20 (a – d) and AN27 (e – g) compared with Delft3D model output over February 2017. Flow observations include: (b, e) northward current component ( $v$ ), (c, f) flow speed and (d, g) direction (current dir.). Flow variables are 30-min averages whereas WL is 2-hourly. Low-pass flow speed has a 25-h cut-off Fourier transform filter applied. For reference, observed significant wave height at AN27 (green line in top panel) is presented. Zoomed-in locations of the ADCPs are shown in the small top panel; cf. Figure 4.1d for large-scale setting of the ADCP locations.

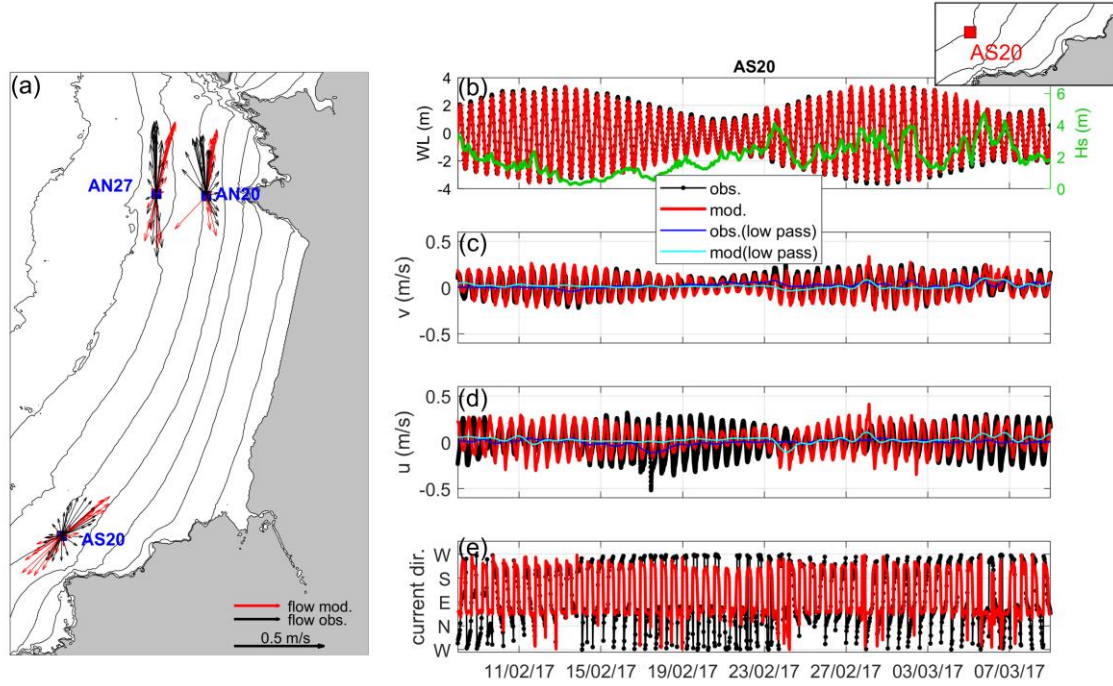


**Fig. 4.7** (a) Flow based on observations (black) and model output (red) for a representative tidal cycle at the ADCPs locations. Observations compared with Delf3D model output over February 2017 for (b) water level (WL), (c) eastward current component ( $u$ ), (d) northward current component ( $v$ ), and (e) direction at ADCP AS20. Flow variables are 30-min averages whereas WL is 2-hourly. Low-pass flow speed has a 25-h cut-off Fourier transform filter applied. For reference, observed significant wave height at AS20 (green line in right top panel) is presented. Zoomed-in location of the ADCP is shown in the small top panel; cf. Figure 4.1d for large-scale setting of the ADCP location.

Water-level prediction was excellent ( $RMSE = 0.20$  m,  $MAE = 0.11$  m,  $R^2 = 0.97$  and  $bias = 0.02$ ; Table 4.2), and velocity currents and flow direction were accurately modelled for the northern ADCPs (averaged  $RMSE = 0.07$  m s<sup>-1</sup> and 51°; averaged  $R^2 = 0.5$  and 0.66, respectively; Table 4.2). The large  $RMSE$  value for direction is related to a time offset in the tidal directional change, such that for short periods the direction is off by ~180°. Skill values showed a better model performance reproducing currents where the flow was primarily alongshore with minimal cross-shore currents (instruments perpendicular to the northern headland). Consequently, velocity magnitude at the AS20 location, where the cross-shore signal was under- or overpredicted, was not well reproduced by the model. The flow at AS20 presented  $RMSE$  values similar to the rest of validation points ( $RMSE = 0.09$  m s<sup>-1</sup> and  $MAE = 0.07$  m s<sup>-1</sup>; Table 4.2), but it showed weak correlation ( $R^2 = 0.17$ , Table 4.2). It is worth noting that the discrepancies between the model data and observations are likely to be related to the presence of a small-scale

eddy that was not captured by the model simulations, possibly due to limitations with the bathymetry, but this should not represent major differences when computing fluxes between the different bays as the longshore component is well reproduced. Overall, the model performance is considered good at predicting wave and hydrodynamic conditions.

**Table 4.2** Model validation coefficients.

	Model	Variable	Location	RMSE	MAE	R <sup>2</sup>	Bias
<i>Summer 2016</i>	WAVE	Significant wave height (m)	AN26	0.32	0.25	0.76	0.03
			AN18	0.31	0.24	0.76	<0.01
			Buoy	0.32	0.24	0.77	<0.01
		Peak period (s)	AN26	1.5	0.95	0.50	0.01
			AN18	1.44	0.94	0.53	0.01
			Buoy	1.62	1.05	0.51	0.02
	FLOW	Mean direction (deg.)	AN26	9.12	8.55	0.09	0.12
			AN18	11.73	9.05	0.03	<-0.01
		Water level (m)	AN26	0.25	0.15	0.97	0.01
			AN18	0.24	0.16	0.97	0.01
		Flow speed (m/s)	AN26	0.06	0.04	0.59	<0.01
			AN18	0.05	0.04	0.58	<0.01
<i>Winter 2017</i>	WAVE	Significant wave height (m)	AN26	41	25.84	0.77	0.38
			AN18	44	27.52	0.70	0.4
			AN27	0.48	0.36	0.7	0.04
			AN20	0.46	0.34	0.81	0.06
		Peak period (s)	AS20	0.48	0.36	0.74	0.09
			Buoy	0.47	0.35	0.81	0.09
			AN27	2.83	2.03	0.27	0.01
			AN20	2.12	1.43	0.51	0.01
			AS20	2.22	1.49	0.50	0.02
			Buoy	2.01	1.34	0.58	0.02
		Mean direction (deg.)	AN27	17.13	11.84	0.44	<0.01
			AN20	10.91	8.04	0.76	<0.01
			AS20	17.31	11.93	0.76	<0.01
	FLOW	Water level (m)	AN27	0.16	0.11	0.97	0.04
			AN20	0.13	0.09	0.97	<0.01
			AS20	0.13	0.09	0.98	<0.01
		Flow speed (m/s)	AN27	0.07	0.05	0.59	<0.01
			AN20	0.09	0.07	0.52	<0.01
			AS20	0.09	0.07	0.17	0.04
		Flow direction (deg.)	AN27	48.49	34.84	0.63	0.39
			AN20	69.00	52.54	0.66	0.35
			AS20	73.53	61.8	0.44	0.82

#### 4.4.2 Numerically modelled circulation

Simulations of coupled wave-driven and tidal currents (tide-averaged) are presented (Figure 4.8) to aid in the interpretation of sediment flux pathways over three embayment-scale circulation modes: moderate-high waves from the W; moderate-high waves from WNW; and extreme waves from W – WNW. The major components of circulation along this coastline include: (1) dominant northward residual tidal current in the vicinity of most of the headlands, (2) northward current in the offshore region ( $> 15$  m), and (3) southward current in the shallow nearshore ( $< 15$  m) within the embayment as a result of the (4) embayment-scale circulation. For shorter embayments, the clockwise circulation is cellular (strong headland control, one circulation cell fills the embayment), while for longer embayments, the circulation is intermediate (moderate headland control, several rip cells may be present along the embayment; Short and Masselink, 1999).

For moderate-high wave forcing ( $H_s \sim 4$  m) from the W (Dir  $\sim 270^\circ$ ; Figure 4.8a, d), clockwise embayment-scale circulation is observed in all the embayments (except St. Agnes). Oblique wave breaking generates a narrow (up to 20 m depth) northward current near the headlands and along the stretch of coast encompassing St. Agnes, with a maximum velocity of  $1 \text{ m s}^{-1}$  near the headlands which decreases to  $0.4 \text{ m s}^{-1}$  around the 20 m contour. This northward flow is diverted offshore in the south of Perranporth and Chapel Porth by a southward current originating at the up-wave northern headland and related to a rip current in the southern part of the embayment. This rip cell circulation associated with the headlands at the north and the subsequent southward current are observed in all the embayments except St. Agnes, where the northward flow is deflected offshore ( $0.4 \text{ m s}^{-1}$  up to 30 m depth) but does not recirculate. A headland rip at the north of Perranporth (up-wave headland) and large headland rips (mega-rip) at the down-wave headlands at the small embayments resulting from the cellular circulation are also evident for moderate to high-energy wave conditions.

For moderate-high wave forcing ( $H_s \sim 4$  m) from the WNW (Dir  $\sim 286^\circ$ ; Figure 4.8b, e), the embayment-scale circulation pattern is still observed, but now a southward flow up to -10 m ODN within the embayment is present. The northward current in the

offshore region is very weak ( $\sim 0.1 \text{ m s}^{-1}$ ) and is only observed beyond the 15 m depth ODN. Headland rips that reach a maximum depth of 12 – 15 m and of smaller magnitude ( $< 0.4 \text{ m s}^{-1}$ ) than those for events from the W are only observed in the short bays (e.g., north of St. Agnes, Hoblyn's Cove and Holywell). It is noteworthy that for only a modest change in wave direction from  $270^\circ$  to  $286^\circ$ , the direction of the nearshore currents along this embayed coast changes considerably.

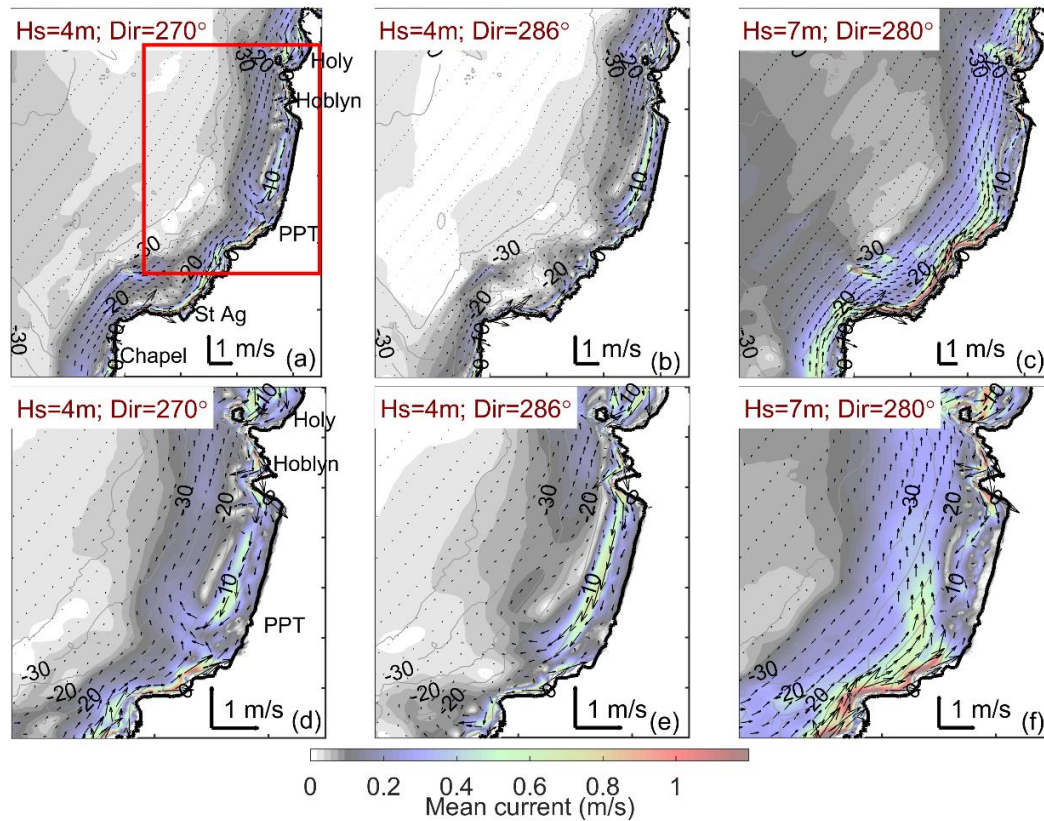


**Fig. 4.8** Time-averaged (12.5 h) currents (top panels) with zoom focused on Perranporth embayment (bottom panels) under storm conditions during spring tides. Circulation under moderate-high waves from the W (a, d), WNW (b, e) and extreme waves during storm Hercules, 2013/14 winter (c, f).  $H_s$  and  $Dir$  presented for each scenario correspond with offshore conditions at location A (Fig. 4.1a). For reference, embayment names abbreviations and bottom panels inset area (red box) are included in first column panels.

For extreme wave forcing ( $H_s \sim 7 \text{ m}$ ) from the W to WNW ( $Dir \sim 280^\circ$ ; Fig. 4.8e, f), a strong northward current of  $\sim 1 \text{ m s}^{-1}$  is predicted along the coast with a surf zone that extends beyond most of the headland apexes ( $> 0.4 \text{ m s}^{-1}$  at 30 m depth). Consequently, the major circulation pattern can encompass several embayments for shallower bounding headlands, with a subsequent flow shift from the prevailing north direction towards the south close to the base of these (e.g., southward bypass between

Hoblyn and Perranporth). During this circulation mode, the northward current is now deflected further offshore in the form of a mega-rip at the longer embayments, Chapel Porth and Perranporth (offshore-directed current of  $0.7 \text{ m s}^{-1}$  up to  $-20 \text{ m ODN}$  in the southern sector of the embayment). A headland rip is only observed in Hoblyn's Cove but this is distorted by the strong northward current that exceeds  $1.2 \text{ m s}^{-1}$  in the stretches of coast highly oblique to wave direction such as the sector from St. Agnes Head to Droskyn Point.

### 4.4.3 Numerically modelled sediment fluxes

#### 4.4.3.1 Gross sediment transport

The gross longshore transport ( $LST_{gross}$ ) is computed as the total transport up (northward) and down (southward) the coast over the six months ( $t = 6 \text{ months}$ ; January 2014, July – Aug 2016 and January – March 2017) of simulation (Fig. 4.9).  $LST_{gross}$  is integrated over the shoreface using the six transects perpendicular to the headlands and one transect located in the center of Perranporth bay (T-PPT) representative of an “open beach” (length of Perranporth beach is  $> 3.5 \text{ km}$ ). Results show that the largest rates of sediment transport occur between the headland apex and the  $20 \text{ m}$  contour line, and these fluxes decay significantly beyond the  $25 \text{ m}$  contour line. Additionally, it is evident that  $LST_{gross}$  greatest values occur around Perranporth beach, and these are 1 to 2 orders of magnitude larger than gross bypass around the other headlands. Examining Perranporth transects individually for the six months simulated, peaks of  $LST_{gross}$  are at  $8 \text{ m}$  ( $1250 \text{ m}^3 \text{ m}^{-1}$  for T3 and  $680 \text{ m}^3 \text{ m}^{-1}$  for T4) and  $5 \text{ m}$  ( $600 \text{ m}^3 \text{ m}^{-1}$  for T-PPT) depth relative to ODN for the headlands (T3 and T4; Fig 4.9d, f) and the center of the beach (Fig 4.9e), respectively.

Sediment transport beyond the  $25 \text{ m}$  contour line is considered insignificant ( $< 5 \text{ m}^3 \text{ m}^{-1} \text{ t}^{-1}$  in all transects) when comparing with the sediment transport at shallower depths (Fig. 4.9b–h). This contour is considered the maximum depth for significant sediment transport and is used as the seaward limit for sediment fluxes computation. The selection of the  $25\text{-m}$  depth contour also responds to seabed textural studies in this area in which  $20 - 26 \text{ m}$  depth is inferred as the base of the active profile (McCarroll et

al., 2018; Valiente et al., 2019a). Moreover, this limit is also close to the average maximum depth of transport or *DoT* (c. 26 – 28 m depth) computed using tide- and wave-induced bed shear stresses during extreme conditions (Valiente et al., 2019a).

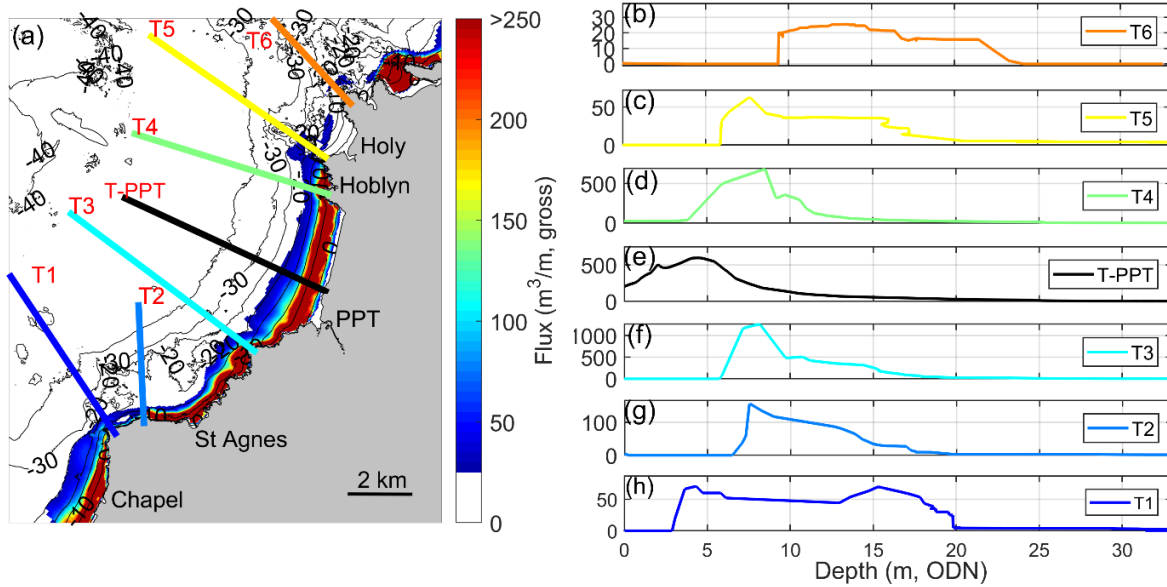


**Fig. 4.9** (a) Gross sediment transport (cumulative flux) for the simulated scenarios (total of 6 months). Gross longshore fluxes as a function of water depth for T1 – T6 (b – d, f – h) and T-PPT (e).

#### 4.4.3.2 Potential sediment transport

Time-averaged (12.5 h) sediment fluxes during moderate to high-energy wave conditions are presented spatially in Fig. 4.10. It is evident that during storm events major sediment fluxes occur inside the surf zone ( $> 8 \text{ m}^3 \text{ m}^{-1} \text{ s}^{-1}$ ). Sediment transport from the beach to the lower shoreface is associated to the presence of mega-rips (Fig. 4.10a,c), generated off the southern to mid sector of all the embayments as a result of the embayment-scale (Fig. 4.10d,e) and multi-embayment scale cellular rip cell circulation (4.10f). The latter occurs in Perranporth-Hoblyn's Cove system as a combined response induced by the strong offshore northward flow developed at the southern headland, high-oblique breaking and deflection of the offshore flow back toward the south at the northern headland of Hoblyn's Cove, and waves breaking beyond Ligger Point headland (northern Perranporth headland) (McCarroll et al., 2018). For moderate-high events, mega-rips induce sediment transport beyond the 15 m contour line ( $> 3 \text{ m}^3 \text{ m}^{-1} \text{ s}^{-1}$ ) and can exceed the 25 m contour line during the extreme wave events. Additionally, in the long embayments, a small rip appears at the northern headlands (4.10d, f);

however, this rip is much smaller ( $\sim 2 \text{ m}^3 \text{ m}^{-1} \text{ s}^{-1}$  around 20 m depth) and tide-dependent, disappearing with the rising tide.

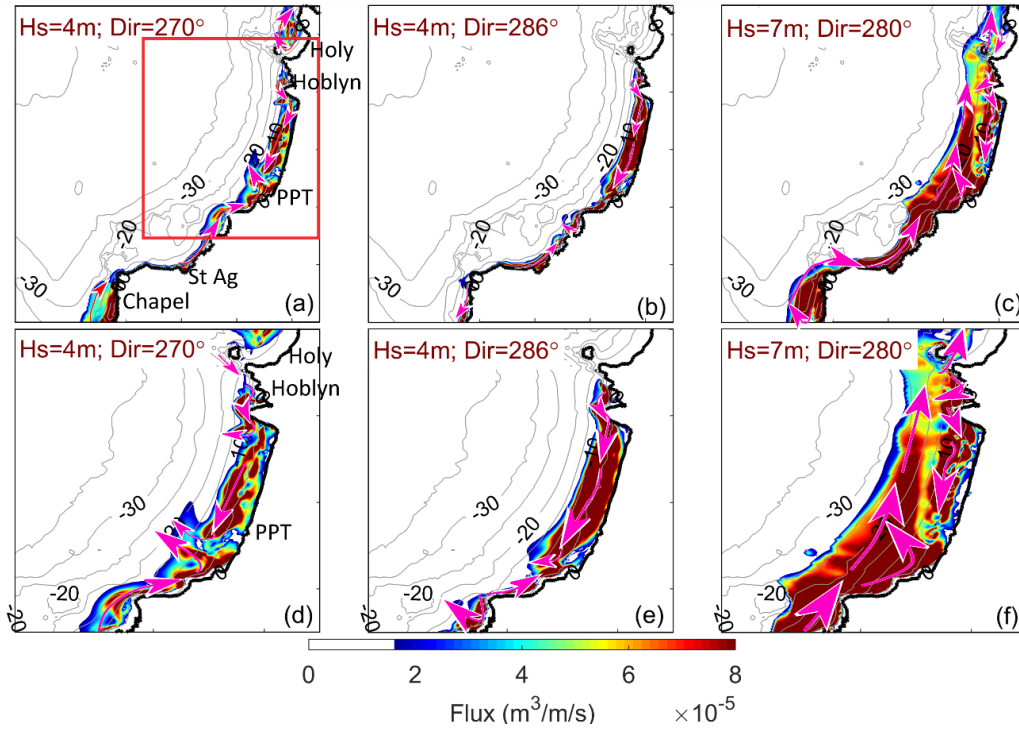


**Figure 4.10** Sediment fluxes and transport pathways during major circulation modes (storm conditions during spring tides). Time-averaged (12.5) fluxes (top panels) with zoom focused on Perranporth embayment (bottom panels) under moderate-high waves from the W (a, d), WNW (b, e) and extreme waves during storm Hercules, 2013/14 winter (c, f).  $H_s$  and  $Dir$  presented for each scenario correspond with offshore conditions. The magenta arrows indicate qualitatively major sediment paths. For reference, embayment names abbreviations and bottom panels inset area (red box) are included in first column panels.

Sediment fluxes during major circulation modes integrated over the shoreface using the 15-m contour line ( $Q_{cross}$ ) are presented in Fig. 4.11. Comparing both shore-normal (W) moderate wave conditions and extreme conditions, it is evident that larger events produce always sediment ejection from the embayment limits, whereas moderate to high energy events seem to vary between sediment inflows/outflows depending on the embayment configuration. For moderate events ( $H_s \sim 4 \text{ m}$ ) from the W, results show significant sediment ejection outside the DoC only occurring at Chapel Porth ( $-5 \text{ m}^3 \text{ m}^{-1}$ ), with some small sediment losses observed at Holywell ( $-1.5 \text{ m}^3 \text{ m}^{-1}$ ) (Fig. 4.11h). It is worth noting that while these moderate-energy wave conditions induce sediment transport outside the embayment limits (negative  $Q_{cross}$ ) in these bays, inflows (positive

$Q_{cross}$ ) of  $1 - 3 \text{ m}^3 \text{ m}^{-1}$  occur at Perranporth and the adjacent bay of St. Agnes as a result of the orientation of the coast (almost perpendicular to wave approach) at the south of both bays (Fig. 4.11h). Conversely, the same moderate-energy wave conditions ( $H_s \sim 4 \text{ m}$ ) from the WNW induce positive  $Q_{cross}$  in all the embayments (except Hoblyn's Cove), ranging from  $0.5 \text{ m}^3 \text{ m}^{-1}$  to  $> 1.5 \text{ m}^3 \text{ m}^{-1}$  (Fig. 4.11h). In this case, the source of sediment for the inflows is the adjacent offshore sectors at the north of the bays, differing from the more westerly events during which fluxes to the embayment mainly occurred at the south. For single extreme events ( $H_s \sim 7 \text{ m}$ ), results show negative  $Q_{cross}$  in all the embayments of the order of  $-10 - -20 \text{ m}^3 \text{ m}^{-1}$ , with larger rates corresponding to the longest embayments ( $> 3.5 \text{ km}$ , Perranporth and Chapel Porth) (Fig. 4.11g).

Headland bypass ( $Q_{bypass}$ ) is computed using the six transects perpendicular to the headlands (T1 – T6) and the extra transect located in the middle of Perranporth embayment (T-PPT). Sediment fluxes present large variability between events c.  $10^2 - 10^4 \text{ m}^3$  and always occur in the direction of the residual flow for this coast (northward) except across T4 and T-PPT. Sediment transport rates across T3 are larger by a factor of 4 respect the other headlands (Fig. 4.11e, f). For moderate-energy and extreme conditions from the W, T3 headland bypass is  $2 \times 10^3$  (Fig. 4.11f) and  $3 \times 10^4$  (Fig. 4.11e), respectively, whereas transport rates are  $< 10^3$  for moderate events coming from the WNW (weaker northward wave-induced current along the headland). In line with McCarroll et al. (2018), T4 greatest bypassing rates are mainly southward of c.  $-1 \times 10^3 - -2 \times 10^4 \text{ m}^3$ . Interestingly, despite the majority of  $Q_{bypass}$  being southward directed as a result of the multi-embayment cellular circulation, during Hercules 2013/14 storm (largest simulated event; Fig. 4.11e) the resultant net northward transport was  $5 \times 10^3 \text{ m}^3$  northward. In this particular case, the southward transport observed between the headland apex and 15 m depth (ODN) was canceled by the northward sediment inflow when integrated up to 25 m. It is worth noting that the specified sediment layer in the model runs provided unlimited sediment supply, therefore, the predicted rates of sediment inflows across the transects are likely to be unrealistic during periods of deficit of sediment in adjacent areas. Despite this limitation, bypassing rates provide an idea of the large sediment inflows to the embayments during storm events when these are not restraint by sediment availability downdrift.

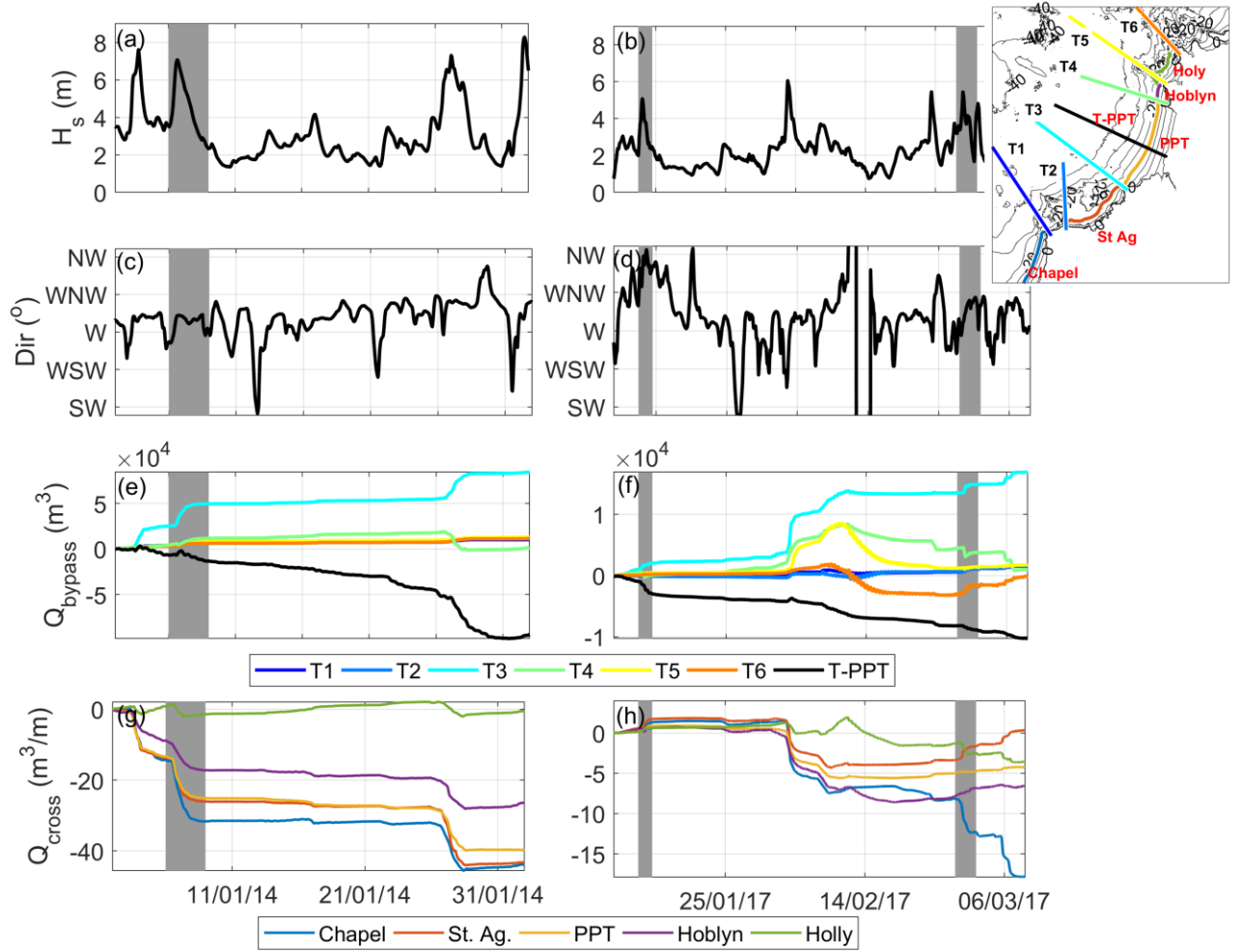


**Fig. 4.11** Sediment fluxes during major circulation modes: moderate-high waves from the W, WNW and extreme waves during storm Hercules, 2013/14 winter (bounded areas). Time series of (a, b) significant wave height ( $H_s$ ); (c, d) direction ( $Dir$ ); and (e, f) fluxes integrated around the headland transects ( $Q_{bypass}$ ) and (g, h) over the morphological DoC per embayment/ bay width ( $Q_{cross}$ ). Positive indicates northward and negative represents southward. Bounded areas represent the time period encompassing the scenarios shown in Fig. 4.10. Inset with location of transects and contours used for  $Q_{bypass}$  and  $Q_{cross}$  integration are presented to facilitate interpretation.

Headland ( $Q_{bypass}$ ) and cross-embayment ( $Q_{cross}$ ) sediment fluxes integrated over two tidal cycles (25 h) respect daily averages of offshore wave forcing parameters ( $P_o$  and  $Dir$ ) are shown in Fig. 4.12. Both processes can be considered the primary mechanisms for sediment exchange on the lower shoreface during conditions of maximum bed shear stress ( $P_o > 200$  kW/m) and to a lesser extent during moderate to high-energy conditions ( $P_o = 75 - 125$  kW/m). Their salient features are: maximum longshore transport rates are  $O(10^4 \text{ day}^{-1})$  and increase with wave power; (2) longshore transport is mostly northward, except at the two southern transects under low-to-

moderate wave conditions ( $P_o < 70 - 80 \text{ kW/m}$ ); (3) cross-shore transport is offshore at all locations under the most energetic conditions (Fig. 4.12c); (4) under moderate-high wave conditions ( $P_o < 125 \text{ kW/m}$ ), cross-shore transport is onshore at Holy and St. Ag, and mostly offshore at the other locations; and (5) wave direction does not seem to play a significant role (Fig. 4.12b, d), meaning that the topography is the main control in the sediment bypassing rates. Hence,  $Q_{bypass}$  appears largely controlled by wave power (Fig. 4.12a), showing a strong positive correlation with Pierson correlation coefficients ( $r > 0.92$  in all instances). It is noted that for the particular case of T4, small variations in wave direction affect the direction of the sediment bypass (Fig. 10e, f) but these appear superimposed by changes in wave power (as per McCarroll et al., 2018).

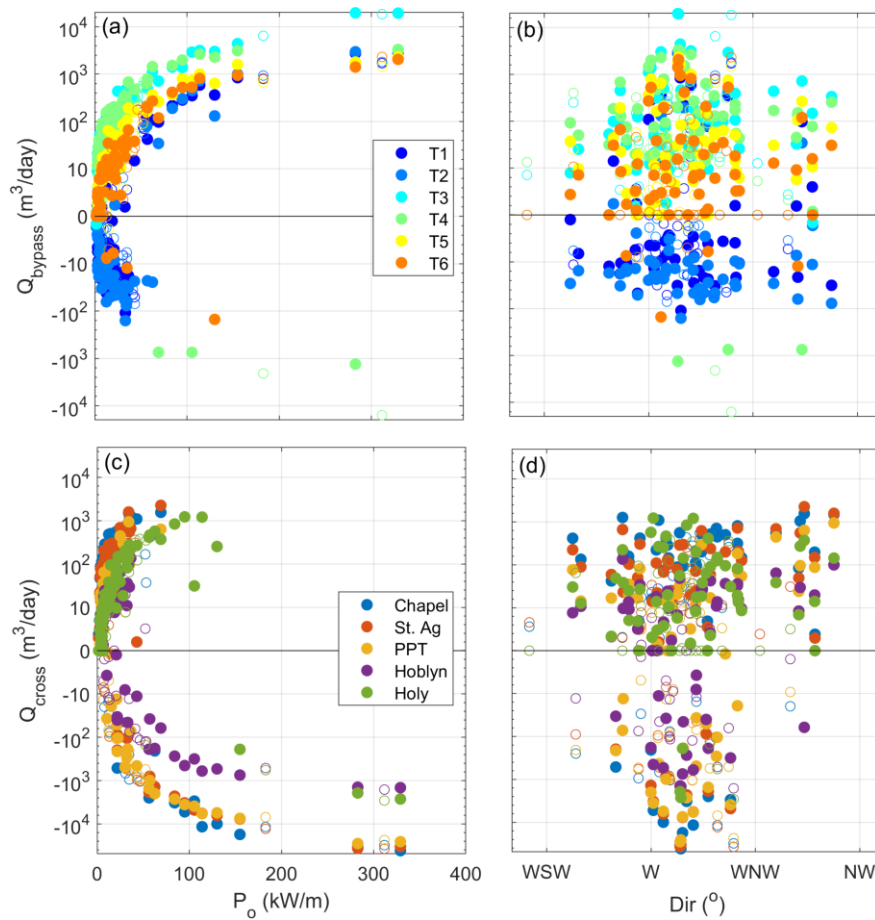


**Fig. 4.12** Daily sediment fluxes integrated over two tidal cycles (25 h) versus daily averages of offshore wave forcing parameters ( $P_o$  and  $Dir$ ). Upper panels: sediment fluxes integrated over the selected transects (refer to Fig. 4.1 for location) with positive values corresponding to northward fluxes and negative to southward. Bottom panels: sediment fluxes integrated over the 15-m contour line (averaged  $DoC$  for the embayments/bays of study). Positive values represent inflows to the embayment and negative values correspond with outflows. Empty circles represent sea states during neap tides whereas filled markers depict spring tides.

## 4.5 Discussion

### 4.5.1 Sediment transport mechanisms

Major mechanisms for redistributing material on the lower shoreface of the macrotidal, exposed and embayed coastline of north Cornwall are the predominant northward longshore flow around headlands, the presence of mega-rips, and the embayment-scale circulation. Both embayment-scale circulation and headland bypass are function of wave obliquity, embayment length and headland configuration (Martens et al., 1999; Short and Masselink, 1999); however, for the cases presented here, wave direction seemed to play a secondary role, and it was the topography what mainly dictated the sediment pathways. Headland bypass was mostly northward except for the case of Ligger Point (Perranporth northern headland). For this particular case, when multi-embayment circulation develops during extreme wave conditions (McCarroll et al., 2018), southward headland bypass from Hoblyn's Cove to Perranporth occurs. Additionally, in all instances, embayment-scale circulation promotes intra-embayment sediment redistribution toward the south along the lower shoreface (6 – 15 m depth, ODN). It is during major events that the southward flow is deflected offshore inducing sediment ejection beyond the 15 m contour line in the southern sector of the short embayments ( $10^3 \text{ m}^3$ ). Sediment losses in the south are one order of magnitude greater ( $\sim 10^4 \text{ m}^3$ ) in the long embayments (e.g., Chapel Porth, Perranporth) due to mega-rip formation. These mega-rips are generated by the confluence of the northward longshore current at the down-wave headland with the southward meandering current generated in the up-wave headland that has enough room to develop, diverting further offshore (c.  $0.7 \text{ m s}^{-1}$  beyond 15 m and up to 20 m depth ODN) the northward current.

### 4.5.2 Prediction of bypassing rates and sediment budgets

This research has shown that substantial sediment transport along the lower shoreface related to headland bypassing mechanisms exists at the N coast of SW England. Furthermore, the modelled sediment bypass fluxes were found to be positively correlated ( $r > 0.92$ ) with offshore wave power ( $P_o$ ), allowing for a simple parameterisation of the headland bypassing rates. The approach followed here to obtain

a daily bypass rate parameterisation ( $Q_{bypass}$ , in  $\text{m}^3 \text{day}^{-1}$ ) is simply based on curve fitting using a second order linear model polynomial of the form:

$$Q_{bypass} = aP_o^2 + bP_o + c \quad (4.1)$$

where  $P_o$  is the daily averaged offshore wave power estimated using Herbich (2000), and  $a$ ,  $b$  and  $c$  (Table 4.3) are the best fitting parameters based on the correlation between model output sediment fluxes and wave power forcing conditions at the offshore boundary of the domain (A nodes, refer to Fig. 4.1a for location). Using Ligger Point as case study, McCarroll et al. (2018) also provided a  $Q_{bypass}$  parameter. This parameter accounted for the tidal residual current while allowing for resolution of changes in wave energy and direction, whereas our approach only relies on total wave energy while addressing the bypass reversal during large energy waves (T4,  $a = -0.2$ ; Table 4.3). By comparison, they predicted maximum bypassing rates around this headland of c.  $10^4 \text{ m}^3 \text{day}^{-1}$  southward, which is comparable to the results of our parameterisation based on curve fitting.

**Table 4.3** Best fitting parameters for Eq. 4.1 based on correlation between modelled sediment fluxes and offshore wave forcing conditions.

Transect	$a$	$b$	$c$
<b>T1 – St. Agnes Head</b>	0.0171	1.85	-40.12
<b>T2 – St. Agnes Head</b>	0.01255	2.54	-26.14
<b>T3 – Cligga Head</b>	0.1883	2.99	-31
<b>T4 – Ligger Point</b>	-0.2009	31.72	-317
<b>T5 – Penhale Point</b>	0.0009	6.06	-62
<b>T6 – Kelsey Head</b>	0.0125	2.54	-26.14

Predicted  $Q_{bypass}$  for the different transects over 2011 – 2018 is presented in Fig. 4.13. In all transects, headland bypass is northward (except for T4) and becomes significant ( $10^3 - 10^5 \text{ m}^3$ ) over winter periods, with maximum predicted values over high energy summer conditions of  $10^3 \text{ m}^3$ . Examining T4 individually, we found that the cumulative  $Q_{bypass}$  is northward, but conversely to the other headlands, the 2013/14 winter storms and to a lesser extent winters 2015/16 and 2017/18 induced a net southward bypass as a result of the multi-embayment circulation. This is consistent with McCarroll et al. (2018), who predicted bypass rates for a transect similar to T4, showing

similar reversals in flux direction at higher wave-energy levels, with net near-zero long-term flux (with wide uncertainty bounds), including gradual northward flux in summer, and brief periods of rapid southward transport in winter.

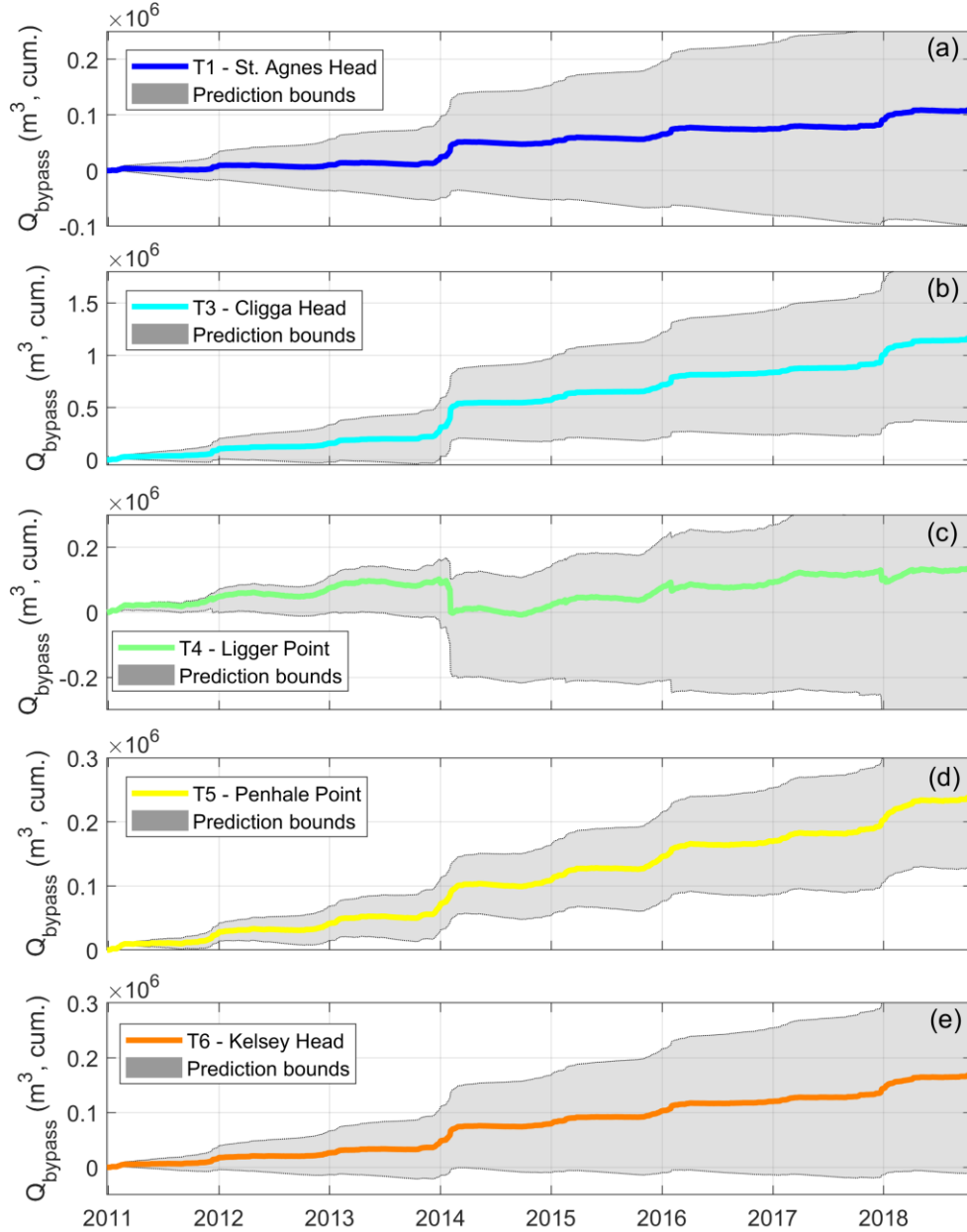


**Fig. 4.13** 8-year cumulative headland bypass volumes ( $Q_{bypass}$ ) for T1 (a) and T3 – T6 (b – e). Positive (negative) values are northward (southward). Grey-patched area indicates cumulative uncertainty bounds (95% confidence based on the statistical model) for the prediction.

The introduction of the  $Q_{bypass}$  parameter allows quantifying sediment bypass over long time scales (multi-annual), and ultimately, can provide of a quick estimate of sediment budgets. Following the proposed parameterisation (Eq. 4.1), a prediction of the

sediment inflows and outflows for the different embayments of study at multi-annual timescales is conducted. For a given coastal cell, the sediment budget ( $dQ_{net}$ ) is expressed by the balance of volumes between sediment supply ( $\Sigma Q_{source}$ ) and sediment losses ( $\Sigma Q_{sink}$ ) in the compartment (Rosati, 2005; Aagaard, 2011). Hence,  $Q_{bypass}$  of a particular headland provides sediment losses (gains) to the downdrift (updrift) bay. For the studied stretch of coast, assuming that  $\Sigma Q_{source}$  through the southern downdrift boundary is equal to zero (virtual zero), and knowing the sediment gains ( $Q_{bypass,up} = \Sigma Q_{source}$ ) and losses ( $Q_{bypass,down} = \Sigma Q_{sink}$ ) of each study bay, we are able to infer the sediment budget over a particular time scale ( $dQ_{net}/dt$ ).

Fig. 4.14 shows the predicted total sediment budgets and net headland bypassing ( $Q_{bypass}$ ) over an 8-year period (2011 – 2018). For two (Perranporth and Holywell) of the five embayments, sediment gains are larger than sediment losses ( $\Sigma Q_{source} > \Sigma Q_{sink}$ ) over multi-annual scales. For the studied 2011 – 2018 epoch, Perranporth embayment sediment budget ( $Q_{bypass,up}$  and  $Q_{bypass,down}$  are c.  $1.2 \times 10^6 \text{ m}^3$  and  $1.3 \times 10^5 \text{ m}^3$ , respectively) is one order of magnitude larger than for Holywell (Fig. 4.14a). Additionally, major circulation paths during large events suggest that the northern headland (Ligger Point) acts as a secondary headland, converting Hoblyn's Cove into an extension of Perranporth beach, and Penhale Point into Perranporth-Hoblyn's Cove major headland. Because northward bypass fluxes at Penhale Point (Fig. 4.14a) are one order of magnitude (c.  $2.4 \times 10^5 \text{ m}^3$ ) smaller than those predicted for Cligga Head (southern downdrift headland), it is suggested that Perranporth-Hoblyn's cove multi-embayment system is in permanent accretion ( $> 1 \times 10^6 \text{ m}^3$  over 8 years) if unlimited supply down-flow exists. For this same epoch (2011 – 2018), in Chapter 3 we demonstrated that Perranporth beach accreted  $> 650,000 \text{ m}^3$  when accounting for changes up to 30-m depth. A comparison against these observations suggest that although Perranporth-Hoblyn's cove may act as a sink for a major coastal cell (Figure 4.14b) over the long term, the predicted total sediment budget based on bypassing rates presented here certainly represents an upper bound. Thus, the sediment budgets estimate is a useful tool for finding hotspots that are more vulnerable to experience lack of sediment supply in the long term, but currently has limited predictive capacity. This sediment budget hindcast assumes unlimited sediment supply downdrift, therefore

results of bypass are likely unrealistic as the cumulative magnitude presented here is not sustainable for a sediment-starved region.

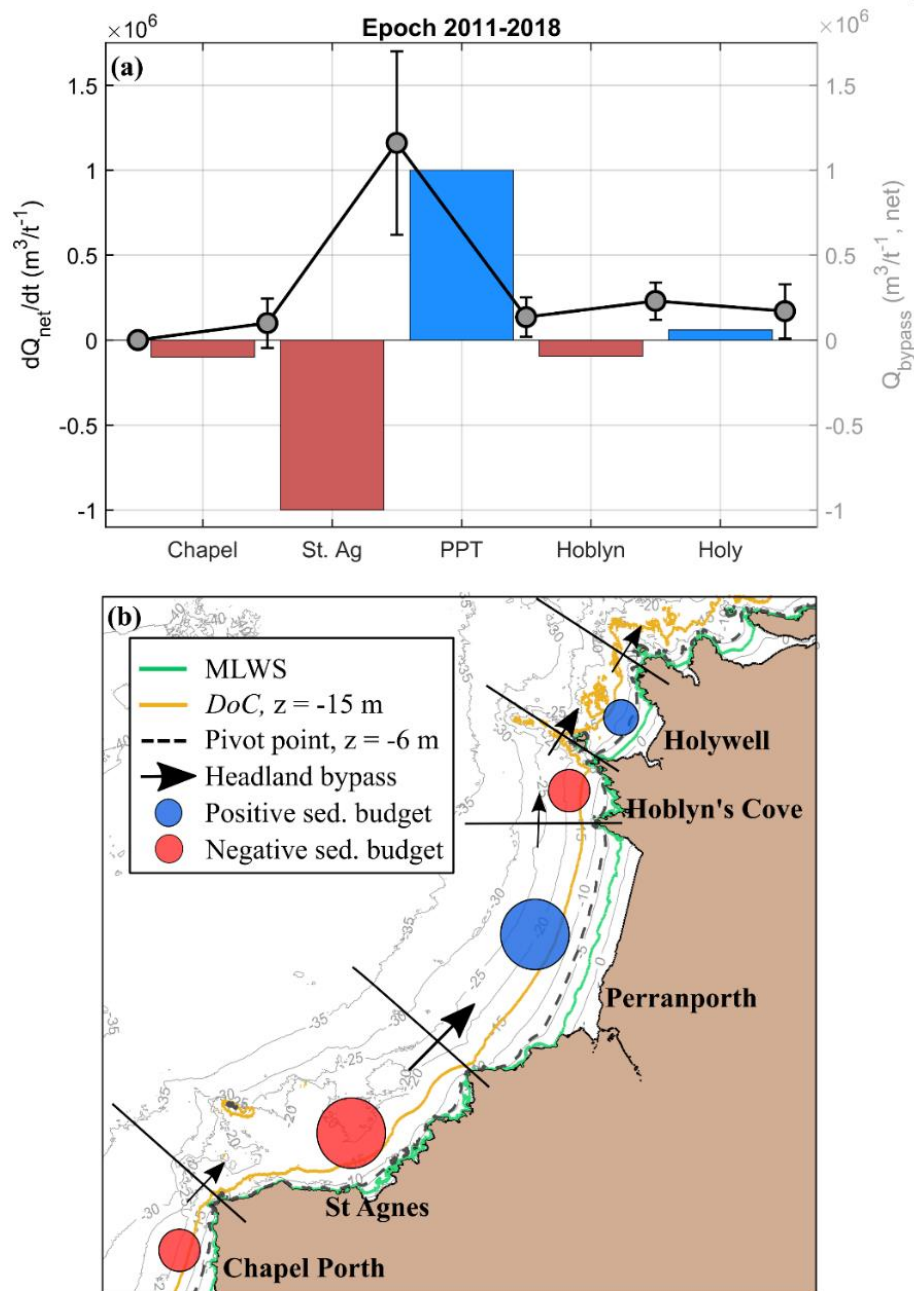


**Figure 4.14** (a) Predicted total sediment budgets ( $dQ_{net}/dt$ ) and net headland bypassing ( $Q_{bypass}$ ) and associated uncertainty bounds (95% confidence based on the statistical model). (b) Planform sediment budget model for Chapel Porth, St. Agnes, Perranporth, Hoblyn's Cove and Holywell over 2011 – 2018. Arrows indicate qualitatively net headland bypassing paths. Arrows and circles size represents magnitude.

Recent modelling studies provided sediment transport prediction around man-made coastal structures (Ab Razak et al., 2013) and natural (Vieira da Silva et al., 2016,

2018; McCarroll et al., 2018, 2019) and idealised (George et al., 2019) headlands. These works predicted and parameterised (e.g., McCarroll et al., 2018; George et al., 2019) bypassing rates around different headlands accounting for certain embayment circulation control. Our study provides similar results in terms of bypassing rates during energetic periods (order of  $10^3 - 10^4 \text{ m}^3 \text{ y}^{-1}$ ); however, we also show possible bypassing rates of  $10^5 \text{ m}^3 \text{ y}^{-1}$  during exceptionally energetic years (e.g., 2014; Masselink et al., 2016a,b), and add a more robust understanding of the embayment- and multi-embayment-scale sediment dynamics and complex circulation for long embayments where cross-shore sediment transport rates into and beyond the morphological limits are of the same order than the largest headland bypassing rates provided by any of the previous investigations.

It is suggested that beaches on this coastline form part of an extended coastal cell, with individual embayments linked via sediment transport around headlands. This study reveals that despite the previously stated cross-shore dominated nature of the embayments in this coastline (Scott et al., 2016; Masselink et al., 2016b; Burvingt et al., 2017), longshore sediment transport rates are of the same order of magnitude (maximum bypassing rates  $10^5 \text{ m}^3 \text{ y}^{-1}$ ) than the observed maximum cross-shore fluxes (Valiente et al., 2019b). Despite having demonstrated in Chapter 3 that upper shoreface sediment fluctuations are uncorrelated to lower shoreface response at short-mid temporal scale, the magnitude of the longshore fluxes presented here will certainly condition the upper shoreface (beach) response at longer time scales ( $> 10$  years). Consequently, lower shoreface alongshore sediment fluctuations seem a critical mechanism which should be considered when studying long-term beach evolution, specifically along high energy and sediment starved coastlines.

## 4.6 Conclusions

This chapter presented a numerical study investigating sediment fluxes and major processes redistributing material along the lower shoreface of a high-energy embayed coastline. Numerical simulations of wave- and tide-induced currents were used to predict the main circulation modes and major sediment transport pathways over multi-annual time scales. This study provides, for the first time, the full picture of

bypassing rates both around headlands, intra- and cross-embayment using real forcing conditions, where:

- Primary mechanisms for redistributing material to and along the lower shoreface for embayed coastlines are longshore residual flow (induced by waves and tide) and headland rip cell circulation, with the latter a function of embayment length and headland configuration with wave obliquity playing a secondary role in this coastline.
- Periods characterized by extreme events ( $H_s \sim 7$  m) involve cross-embayment bypass extending to depths that exceed the base of the headlands and hence constitute multi-embayment circulation. This is associated with large losses of sediment beyond the morphological depth of closure ( $> 3 \times 10^4 \text{ m}^3 \text{ day}^{-1}$ ) mainly in the southern sector (down-wave) of the embayments due to longshore flow to mega-rip formation.
- Sediment gains during accretionary phases mainly occur over moderate-high swell periods ( $H_s \sim 4$  m) and are associated with clockwise intra-embayment circulation with predicted currents inducing redistribution in the long embayments ( $> 10^3 \text{ m}^3 \text{ day}^{-1}$ ) towards the south. The intra-embayment sediment redistribution is combined with significant bypassing rates around the shallower and wider headlands ( $10^2 - 10^3 \text{ m}^3 \text{ day}^{-1}$ ) which compensates sediment losses due to cross-embayment bypass.

A simple parameterisation for sediment bypass based on offshore wave-conditions is presented, allowing prediction of the magnitude of sediment fluxes on the lower shoreface over multi-annual time scales. Hindcast of sediment rates suggested that major sediment fluxes are episodic and occur mainly during high-energy events. During extreme events, cross-embayment rates are of a factor of 4 larger than bypass around the headlands (longshore,  $10^4 \text{ m}^3 \text{ day}^{-1}$ ), whereas for moderate wave conditions, despite that headland bypass is always one order of magnitude smaller ( $10^2 - 10^3 \text{ m}^3 \text{ day}^{-1}$ ) than cross-embayment rates, there is a net positive sediment imbalance (accretion) in the system due to the combined response of both mechanisms. Finally, positive net

sediment rates over 2011 – 2018 suggested that Perranporth-Hoblyn's Cove system acts as a sink for the N coast of SW England.

Our study highlights the importance of sediment transport estimates both across and along the lower shoreface, which remains a poorly resolved area of the coastal system. Additionally, the predicted sediment fluxes in the sub-tidal provide new insights into a type of coastline previously thought to be dominated by cross-shore sediment fluxes. Yearly bypassing rates around the headlands are hindcasted ranging between  $10^3$  and  $10^5 \text{ m}^3 \text{ y}^{-1}$ . The implication is that the magnitude of this bypass will inevitably affect coastal evolution of rocky coastlines over longer temporal scales ( $> 10$  years).

## Chapter 5 – Synthesis and conclusions

---

Embayed beaches occur along rocky shorelines, which make up more than 50% of the world's coasts (Inman and Nordstrom, 1971). Unlike open beaches, embayed beaches are controlled by the three-dimensional geological framework (e.g., bounding headlands, accommodation space; Jackson and Cooper, 2009), and are generally considered relatively stable, closed sediment systems (McNinch, 2004; Jackson et al., 2005). Contrarily to this widely spread idea, recent studies suggest that the inability of certain embayments to recover is a consequence of significant sediment exchange between the beach and neighbouring areas during extreme wave events (Gallop et al., 2011; Loureiro et al, 2012a; Scott et al., 2016); however, research into the magnitude of these exchanges, processes and driving forces remains scarce.

This research aims to improve our understanding of the physical coupling between the surf zone and the inner shelf along embayed coastlines through the study of the sediment dynamics and their linkages and dependency with key forcing conditions. This thesis addresses this aim using different approaches, including: (1) estimating depth of closure in relation to the depth in front of the bounding headlands in Chapter 2; (2) topo-bathymetric surveys to determine the sediment budget for a particular temporal scale in Chapter 3; and (3) numerical modelling to estimate sediment fluxes across and between the bays in Chapter 4. Other approaches available are sedimentological investigation (texture and bedforms) of the seabed, which is also partially covered in Chapter 2, and in-situ measurements of sediment fluxes, not covered in this thesis.

This chapter provides a summary of the key results in relation to the individual aims of the thesis and the major discussion outcomes addressed in the different chapters. Finally, overall conclusions and directions for future work are briefly discussed.

## 5.1 Synthesis and conclusions

The following project objectives were identified in Section 1.5:

- (i) examine the potential for headland bypassing along six regions with different morphometric characteristics using as study site the rocky coastline of SW England.
- (ii) evaluate the inter-annual dynamics of Perranporth beach, a sandy, exposed and macrotidal embayment over multi-annual time scales.
- (iii) investigate the nature (open or closed) of Perranporth beach, for the period 2011 – 2018.
- (iv) investigate major sediment transport pathways between adjacent bays and the embayment of study (Perranporth beach) in order to depict a more complete picture of the complex sediment dynamics in the sub-tidal realm of embayed coastlines and quantification of bypassing rates.

Throughout this thesis, these aims have been satisfied and a number of important findings with regards to processes inducing transport beyond the embayment limits and embayment-scale dynamics over multi-annual time-scales have been revealed. In Chapter 2, a process-based method at regional scale using the computation of bed shear stresses is implemented and a broad parameter-space for the closure limit of sediment transport applicable to embayed beaches globally is developed. In Chapter 3, the spatial scale is reduced to a single embayment where the inter-annual morphodynamics at both embayment- and sub-system-scale (dunes, supra- and inter-tidal, and sub-tidal) are examined. It was then identified that the inter-tidal region is partly uncoupled from the sub-tidal, with the former region dominated by cross-shore sediment fluxes, whereas the sub-tidal is also significantly affected by longshore sediment fluxes. It is also indicated that significant sediment transport occurs seaward of the base of the terminating headlands and beyond the morphological depth of closure at the embayment extremities. In Chapter 4, the study of the inter-annual morphodynamics at embayment-scale was extended to > 15 km of coast using numerical simulations (Delft3D) of real forcing conditions encompassing the monitoring period used in Chapter 3 (2011 – 2018). This part of the study provided new insights into the

linkages between embayment response, circulation modes and bypass in the lower shoreface, aiding to interpret the full picture of the physical coupling between the beaches and the inner shelf in embayed coastlines.

### **5.1.1 Potential for headland bypassing in embayed coastlines**

The estimation of the offshore limit of the morphodynamically active shoreface along embayed coastlines allows questioning whether sediment transport around natural headlands and leakages to the inner shelf are possible under particular wave and tide forcing conditions. Wave-based formulations (Hallermeier, 1978, 1981; Birkemeier, 1985; Capobianco et al., 1997) have been shown to provide reasonable predictions for the morphodynamic closure depth; however, the first part of this thesis (Chapter 2) evaluated their usefulness and provided a novel and updated estimate of the depth of closure concept itself, while emphasizing the role of tidal currents and headlands in predicting the zone of active sediment transport.

The ‘active’ nearshore limits around areas of diverse morphologic configuration and variable forcing conditions (tide and waves) were identified using six regions of the North coast of Cornwall and Devon, Southwest England (UK). We delineated the basal limit of ‘significant’ (i.e., 0.14 m) morphological change (Depth of Closure; *DoC*) and provided a new limit for maximum depth of extreme bed activity and sediment transport (Depth of Transport; *DoT*). The key findings of Chapter 2 were:

- Observations of *DoC* correspond closely to the values predicted by existing formulations based on inshore wave conditions. *DoC* for embayments in the SW varied between 10 and 15 m (relative to mean low water spring water level).
- *DoT* is considered a boundary of significant bed level change as up to that water depth intense sediment transport can take place (upper-plane bed transition) under extreme wave conditions. For the SW, *DoT* varies between 25 and 30 m depth. Over the medium-term time scale (years), morphological changes up to the *DoT* are not detectable (below the

survey accuracy), but they may represent large volumes of sediment when integrated over the shoreface.

- Tidal currents can increase *DoT* estimate by ~10 m along macrotidal coastlines, representing a 30% increase compared to tideless settings.
- The depth of the estimated limits with respect to the bounding headlands suggests that embayments along the SW ‘leak’ during conditions of maximum bed shear stress and may connect through headland bypassing.
- The maximum depth for significant sediment transport was computed across a broad wave-current parameter space and a nomograph is produced that is applicable from micro- to macro-tidal and exposed coastlines globally.

The major implication of these findings is that, even though many headlands appear sufficiently prominent to suggest a closed boundary between adjacent embayments, significant wave- and tide-driven sediment transport is likely to occur beyond the headland base during extreme events, especially at low water levels. Additionally, the importance of tidal currents in *DoC* calculations is illustrated; this is a factor not considered in current coastal engineering practice.

### **5.1.2 Multi-annual embayment-scale sediment dynamics**

Following Chapter 2, which demonstrates that sediment bypass between adjacent embayments is likely, the inter-annual dynamics over multi-annual time scales of Perranporth coastal cell, the embayment used as study case, are evaluated. Although there is a paucity of field measurements on beach and nearshore morphologic change covering the full extension of a coastal cell (Aagaard, 2011; Coco et al., 2014), in Chapter 3 an exceptional dataset that extends fully from the top of the dunes to depths > 40 m is presented to enable quantification of the sediment budget. For the first time on a sandy and embayed beach, a total sediment budget approach is applied to examine inter- and multi-annual embayment scale sediment dynamics over an 8-year period that includes

extreme storm erosion and post-storm recovery. Main findings in regards to this project aim were:

- The very significant net changes in the recorded sediment volume from dune top to depth of closure, representing an embayment-averaged loss of c.  $100 \text{ m}^3 \text{ m}^{-1}$  during the epoch encompassing the extreme 2013/14 storms (2011 – 2016) and a gain of c.  $200 \text{ m}^3 \text{ m}^{-1}$  during the subsequent recovery period (2016 – 2018), indicate that significant sediment transport occurs seaward of the base of the terminating headlands and beyond the morphological *DoC* at the embayment extremities.
- Total sediment volume change was correlated with both total ( $r = -0.6$ ) and alongshore wave power ( $r = 0.4$ ), suggesting that total embayment volumetric changes follow a combined cross- and alongshore dominated response.
- Inter-tidal sediment volume follows a seasonal cycle ( $\pm 75 \text{ m}^3 \text{ m}^{-1}$ ) superimposed by a multi-annual oscillation induced by extremely energetic winter seasons, with full recovery taking at least 5 years. Inter-tidal sub-system response is longshore-coherent and cross-shore sediment transport dominates (inversely correlated with variations in total wave power,  $r = -0.6$ ).
- Dunes at the north of Perranporth embayment experienced a significant erosion event in 2013/14 (15 m onshore translation of dune foot) and little to no recovery in the following 5 years.
- This study contradicts the commonly held understanding that when sediment exits the inter-tidal, it rests undisturbed in the sub-tidal, waiting for a period of low-moderate energy to bring it onshore. The inter-tidal region is partly uncoupled from the sub-tidal region as there is no significant correlation between the two time series. The inter-tidal region is dominated by cross-shore sediment fluxes, whereas the sub-tidal region is also significantly affected by longshore sediment fluxes.

Chapter 3 had limited capacity in predicting sediment pathways due to the complexity of the system response, and some restrictions aroused from the spatial coverage and the temporal resolution of the dataset; therefore, further development through numerical modelling (in Chapter 4) was necessary in order to complete the full picture. Chapter 4 aimed to infer the major sediment transport pathways between adjacent bays and Perranporth beach, and further explain the complex sediment dynamics driving coastal evolution along embayed coastlines over multi-annual time-scales. Using numerically-modelled wave-driven and tidal currents, bypassing rates around headlands, intra- and cross-embayment sediment fluxes were investigated. Major findings were:

- Primary mechanisms for redistributing material to and along the lower shoreface for embayed coastlines are longshore residual flow (induced by waves and tide) and headland rip cell circulation, with the latter a function of wave obliquity, embayment length and headland configuration.
- Multi-embayment circulation dominates during extreme events ( $H_s \sim 7$  m). This circulation mode consists of a strong northward longshore current to mega-rip development at the south of the long embayments which flows offshore (almost parallel to the coast), and can encompass several embayments when bounded by relatively-shallow headlands, until a sharp and deep headland, acting as a (partial) barrier to littoral drift, deflects this current toward the south. This circulation pattern is associated with large losses of sediment ( $> 3 \times 10^4 \text{ m}^3 \text{ day}^{-1}$  for the entire 3.5-km beach) beyond the *DoC* (offshore), mainly in the southern sector (down-wave) of the embayment due to ‘mega-rip’ formation ( $0.7 \text{ m s}^{-1}$  at  $> 20 \text{ m}$  depth).
- Recovery phases are associated with clockwise intra-embayment circulation over moderate events ( $H_s \sim 4 \text{ m}$ ). Predicted currents induce sub-tidal alongshore redistribution within the embayments ( $> 10^3 \text{ m}^3 \text{ day}^{-1}$ ) towards the south, and this is combined with significant bypassing

rates around the shallower and wider headlands ( $10^2 - 10^3 \text{ m}^3 \text{ day}^{-1}$ ) which compensates sediment losses due to cross-embayment bypass.

- Predicted sediment fluxes in the sub-tidal provide new insights into a coast-type previously thought to be dominated by purely cross-shore forcing. Yearly bypassing rates around the headlands ranged  $10^3 - 10^5 \text{ m}^3 \text{ y}^{-1}$  (always function of sediment availability downdrift), and for years with higher than average storms, these are of the same order as maximum cross-shore sediment transport.

The various themes that have been examined are summarised in a conceptual model of embayment-scale dynamics (Fig. 5.1). This conceptual model synthesises embayment response and evolution, including the different areas of the ‘active’ shoreface, spatio-temporal evolution of embayment sub-systems and major sediment fluxes at the decadal scale for high-energy and macrotidal embayed coastlines.

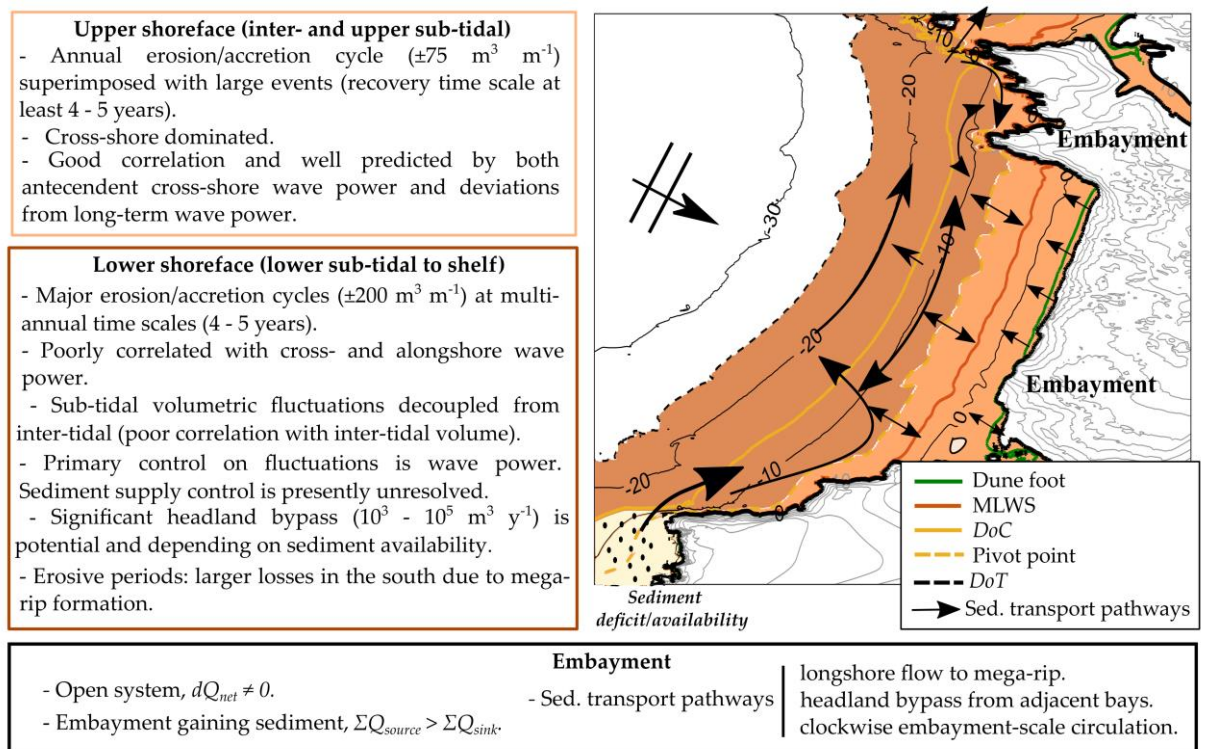


**Fig. 5.1** Embayment-scale sediment dynamics conceptual model for Perranporth beach based on observations and numerical modelling simulations. Light and dark brown coloured areas correspond to the upper and lower shoreface, respectively.

### 5.1.3 Nature of exposed and macrotidal embayments: open or closed?

A quantitative understanding of littoral cells sediment pathways is fundamental when investigating beach response and evolution (Bowen and Inman, 1966; Caldwell, 1966; Komar, 1998; Rosati, 2005). Based on the sediment imbalance or balance between sediment supply ( $\Sigma Q_{source}$ ) and sediment losses ( $\Sigma Q_{sink}$ ), several scenarios can be hypothesised for individual embayments: (1) no sediment exchange beyond the bounding limits or closed system; (2) sediment exchange beyond the bounding limits with  $\Sigma Q_{source} = \Sigma Q_{sink}$ , or open and balanced system,  $dQ_{net} = 0$ ; and (3) sediment exchange beyond the bounding limits with  $\Sigma Q_{source} \neq \Sigma Q_{sink}$  or open and unbalanced system,  $dQ_{net} \neq 0$ . Hence, one of the aims of this thesis was to investigate the nature of Perranporth embayment, concluding that:

- Despite the deeply embayed nature of the beach, the shoreline orientation roughly parallel to the dominant wave direction and the overwhelmingly cross-shore forcing of the inter-tidal beach volume, the system is neither closed, nor balanced, and indeed, total volumetric changes averaged over the embayment (combined inter- and sub-tidal) varied by c. 300 m<sup>3</sup> m<sup>-1</sup> over 8-years.
- A positive net sediment budget for Perranporth-Hoblyn's Cove multi-embayment is observed over 2011 – 2018 (also supported by numerical simulations) suggesting that this system acts as a sink for the N coast of SW England.

This project challenges the notion that embayed beaches are generally closed cells, as headland bypassing is more widespread than commonly assumed, leading to a shift in understanding of sediment budgets along exposed and macrotidal embayments. All three approaches followed in this thesis indicated that Perranporth and beaches on similar coastlines form part of an extended coastal cell, with individual embayments potentially linked via a 'river of sand' that flows around headlands. Furthermore, both the extent of flux and the magnitude of this suggest that sediment transport along and across the lower shoreface should be considered in any study of long-term evolution of headland-bound beaches.

#### 5.1.4 Driving processes and major sediment transport pathways within and between adjacent bays

The main difficulty in fully understanding the sediment dynamics for Perranporth beach arose from the fact that the system is not a closed cell ( $dQ_{net} \neq 0$  with  $\Sigma Q_{source} > \Sigma Q_{sink}$ ). This increases uncertainty in forecasting coastal response (e.g., due to extreme storms) and evolution (e.g., recovery phases) as observed coastal changes cannot only be attributed to a redistribution of sediment within a single system (embayment), but to sediment exchange with a larger area. Hence, to follow a total sediment budget approach allows quantifying sediment gains and losses, while being able to infer flux direction; however, the understanding of the system is not complete, as this approach is not able to provide all the required information on the directional sediment fluxes.

A conceptual model of headland bypassing and major sediment transport pathways for increasing wave forcing conditions ( $H_s = 0 - 2, 2 - 5, > 5$  m) along an idealised embayed coastline with two types of embayment lengths is shown in Fig. 5.2. Three major potential pathways for redistributing material to and along the lower shoreface for embayed coastlines are identified: (1) longshore flow to mega-rip; (2) headland bypass from adjacent bays; and (3) clockwise embayment-scale circulation (intra-embayment circulation) (cf. Fig. 5.1).

##### (i) Sediment Pathway 1: Headland longshore flow to mega-rip

The residual tidal flow, northward for the particular case of the N coast of SW England (Valiente et al., 2019; King et al., 2019) is added to by a strong ( $\sim 1 \text{ m s}^{-1}$ ) wave-induced current produced by oblique wave breaking during high wave conditions. This flow develops in the longer embayments (e.g., Perranporth and Chapel Porth) as an alongshore current at the down-wave headland, and this current is diverted offshore (Fig. 5.2c-i) as a strong mega-rip (c.  $0.7 \text{ m s}^{-1}$  at 20 m depth ODN) in the southern part of the embayment. This mechanism is a pathway for sediment ejection beyond the offshore morphological embayment limit with much larger sediment losses predicted in the southern sectors of the embayments. For moderate-high wave conditions, this mode of

circulation is more subdued (Fig. 5.2b-i), potentially delivering sediment to shallower regions of the sub-tidal (-15 m ODN and shallower). This circulation mode is similar to other swell-dominated headland embayments (Gallop et al., 2011; McCarroll et al., 2014) and consistent with Castelle and Coco (2013), who determined that for obliquely-incident waves, the rip acts as a persistent conduit for transporting floating material into the inner shelf region, and this is more evident for longer beaches in which a longshore current meandering over the bar and rips within the embayment has enough room to develop.

(ii) Sediment Pathway 2: Headland bypass

The tidal residual flow aided by the wave-induced current produced by oblique wave breaking in the vicinity of the headlands forces an important transport (northward for the north coast of SW England) of sand between the different embayments (Fig. 5.2b,c-ii). In line with George et al. (2019), this headland bypass is almost absent at the sharp headlands that act as a semi-blocked barrier to littoral drift. Conversely, in headlands with a wide apex and a down-face almost parallel to the direction of the wave approach (e.g., Cligga Head) important northward headland bypass ( $10^3 - 10^4 \text{ m}^3 \text{ day}^{-1}$ ) during moderate to large waves occurs, and this is similar to other high-energy embayed coastlines (Vieira da Silva et al., 2018). This headland bypass is still present during low-energy wave conditions, but is more subdued ( $< 10^2 \text{ m}^3 \text{ day}^{-1}$ ). Over the long term, this mechanism will cause slow accretion in embayments with an updrift sharp headland, and slow erosion in embayments with an updrift wide headland.

As previously shown by McCarroll et al. (2018), a circulation mode encompassing several embayments (multi-embayment circulation) during extreme events emerged on those embayments bounded by one sharp-deep headland and one wide-shallow headland. For Perranporth beach, this is consequence of the geological configuration of the northern sector and adjacent embayment: a short ( $\sim 100 \text{ m}$ ) embayment (Hoblyn's Cove) bounded by a northern headland-island extending WNW-ESE (Penhale Point) with apex at  $> 20 \text{ m}$  depth, and short southern headland with a shallower apex ( $\sim 7 \text{ m}$  depth). The orientation of the northern headland induces a significant current towards the south ( $> 1 \text{ m s}^{-1}$ ) up to  $12 \text{ m}$  depth that is not deflected

by the shallow southern headland. In line with McCarroll et al. (2018), predicted bypassing rates are c.  $-10^4 \text{ m}^3 \text{ day}^{-1}$  (negative indicates southward) for  $H_s > 5 \text{ m}$  when the predicted offshore northward current is  $< 0.4 \text{ m s}^{-1}$ . Additionally, this southward transport may be cancelled by the northward sediment inflow when integrated up to 25 m during the largest events ( $H_s \sim 7 \text{ m}$ ) and can force a net northward transport of  $5 \times 10^3 \text{ m}^3 \text{ day}^{-1}$ .

(iii) Sediment Pathway 3: Embayment-scale circulation

Clockwise embayment circulation (Fig. 5.2b-iii) is predicted to occur during moderate-high energy conditions that forces a slow transport of sand from the updrift to the downdrift part of all the embayments (cf. Castelle and Coco, 2012). This type of embayed beach circulation arises from the interaction between the wave-driven current and tidal residual flow, and the geometry and orientation of the bounding headlands. Major mechanisms redistributing sediment in the lower shoreface include a northward alongshore current (beyond -10 m ODN) deflected onshore and back toward the south at the north headland, and onshore flow generated by high-oblique breaking waves along the north headland. The combination of both mechanisms is predicted to force a moderate ( $0.4 - 0.5 \text{ m s}^{-1}$ ) flow towards the south below -10 m ODN of c.  $-10^2 - -10^3 \text{ m}^3 \text{ day}^{-1}$ , which induces intra-embayment southward alongshore sediment fluxes over mild winter periods. As a result of this circulation, bypassing at the short headlands (Fig. 5.2b-iii) occurs, although is much weaker than the bypassing rates during extreme events and is also partially conditioned by the direction of the waves. Hence, embayment-cellular circulation at the short embayments may result in a small rate of southward bypass ( $\sim 10^2 - 10^3 \text{ m}^3 \text{ day}^{-1}$ ) around the short headlands, with larger sediment influxes into the embayment at the north mainly during periods with predominant WNW swell events.

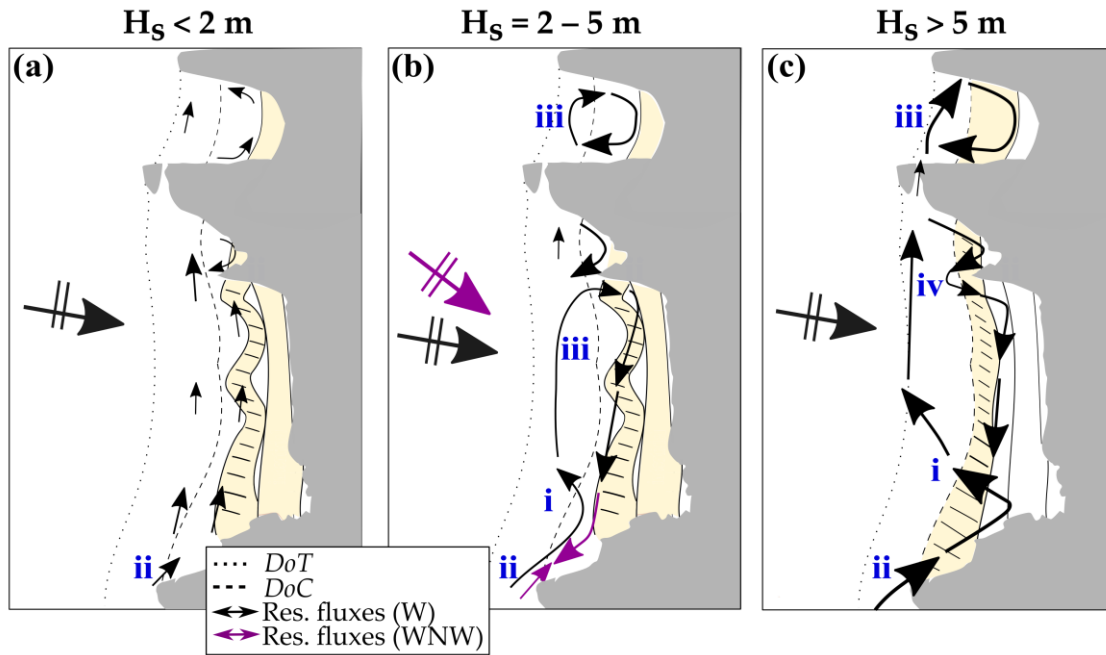


**Fig. 5.2** Conceptual diagram of major alongshore sediment fluxes pathways for a period of (a) mild waves, (b) moderate-high waves and (c) higher than average wave. Arrows (size increases with increasing magnitude) indicate predicted residual fluxes based on model output. Accretion due to gradient in cross-shore fluxes is shown in beige. Idealised limits of the active shoreface Depth of Transport ( $DoT$ ) and Depth of Closure ( $DoC$ ) are presented as dot and dashed lines, respectively.

## 5.2 Future work

Thesis results are based on observations and numerical modelling on Perranporth beach (and adjacent embayments), and although mentioned, the role of the local geology is still poorly resolved as the focus of this research was on a small stretch of coast. Hence, future work should focus on the geological constraints (e.g., embayment and headland configuration; cf. George et al., 2019) influencing the sediment exchange between the beach and the neighbouring areas, as local geology has been demonstrated to be absolutely critical. Particularly, morphometric parameters such as the angle of wave approach (angle between the wave crests and the control line,  $\beta$ , defining the embayment planform shape) or the headland apex angle ( $\alpha_{up}$ ,  $\alpha_{dn}$ ), introduced in Chapter 1, could be incorporated in the formulation proposed in Chapter 4. This addition will help to better parameterise headland and cross-shore bypass for a wider range of headland-bounded locations. Additionally, a novel embayment classification based both on hydrodynamics and morphometric parameters could be implemented. Following Chapter 2, the next step would be to link the morphological characteristics of

the evaluated embayments with the predicted hydrodynamics and sediment fluxes for different levels of exposure.

Another point of future research could be based on adding other research methodologies previously mentioned, but not covered by this thesis: tracer studies, seabed investigation and field measurements of sediment fluxes. Efforts would attempt to extend the sedimentological investigation introduced in Chapter 2 in which the textural changes between sand and rock as well as the sediment size distribution are implemented as indicative of the active profile. Hence, a better interpretation of the nearshore sediment dynamics and bypass could be depicted from a combined approach using tracers, seabed sediment mapping, bedform migration, sediment provenance (mineralogy) and/or in-situ field measurements of sediment fluxes (e.g., using acoustics backscattering data), all conducted as part of the project, with the predicted sediment fluxes and paths. Tracers and measured sediment fluxes (the latter were collected at 20 m depth during 2 weeks over winter 2017) could be used to validate numerical model results. Additionally, seabed sediment mapping and provenance will allow to identify regions with same sediment distribution, providing an extra evidence of the established sediment pathways and/or new insights into the dynamics along embayed coastlines.

### **5.3 Thesis conclusions**

As presented in the review of Chapter 1, few studies have examined the physical coupling between the beach and the inner shelf, as this coupling is generally considered relatively weak. This thesis has demonstrated that along macrotidal high-energy embayed coastlines, sediment exchange between the beach and adjacent areas is significantly more extended and important than commonly assumed. Additionally, the magnitude of the sediment fluxes suggests that these should be considered in long-term coastal evolution studies (> 10 years), particularly along sediment starved coastlines where this major sediment pathways act as an important sediment source. Wave conditions (energy and direction) are the dominant force driving sediment transport outside the embayment limits, with tides playing an important but secondary role. For mid-term temporal scales (< 10 years), fluxes on the lower shoreface do not seem to affect

inter- and supra-tidal beach response; hence, lower and upper shoreface are found not to be correlated, indicating decoupling of these areas. Longshore flow to mega-rip, headland bypass from adjacent bays and clockwise embayment-scale circulation were identified as major processes redistributing material in the lower shoreface. However, as recognised in Chapter 3, to determine the exact sediment dynamics of this type of coastline is complex. We identified a large positive imbalanced (gains) of sediment on Perranporth embayment over the monitoring period (2011 – 2018) as a result of an important recovery (sediment gains of  $6.7 \times 10^5 \text{ m}^3$ ) over the last 2.5 years that well exceeded the sediment losses ( $-2.8 \times 10^5 \text{ m}^3$ ) during the monitoring period encompassing the extreme 2013/14 winter. Despite using a combined approach of observations and numerical modelling simulations, we are not yet fully able to provide a final response to the exact origin of that sediment supply. Nevertheless, thesis findings are informative of the processes involved in the sediment exchange between the beach and the inner-shelf and contribute to better resolve coastal sediment budgets and coastal evolution in general.

## References

---

- Aagaard, T. (2011). Sediment transfer from beach to shoreface: The sediment budget of an accreting beach on the Danish North Sea Coast. *Geomorphology*, 135(1–2), 143–157. <https://doi.org/10.1016/j.geomorph.2011.08.012>
- Aagaard, T., Hughes, M. G. (2017). Equilibrium shoreface profiles: A sediment transport approach. *Marine Geology*, 390, 313–330. DOI: 10.1016/j.margeo.2016.12.013
- Aagaard, T., Kroon, A., Andersen, S., Sørensen, R. M., Quartel, S., Vinther, N. (2005). Intertidal beach change during storm conditions; Egmond, The Netherlands. *Marine Geology*, 218(1–4):65–80.
- Aagaard, T., Kroon, A., Greenwood, B., Hughes, M. G. (2010). Observations of offshore bar decay: Sediment budgets and the role of lower shoreface processes. *Continental Shelf Research*, 30(14), 1497–1510. <https://doi.org/10.1016/j.csr.2010.05.010>
- Ab Razak, M. S., Dastgheib, A., Roelvink, D. (2013). Sand bypassing and shoreline evolution near coastal structure, comparing analytical solution and XBeach numerical modelling. *Journal of Coastal Research*, 65(2), 2083–2088.
- Almeida, L. P., Voutsdoukas, M. V., Ferreira, Ó., Rodrigues, B. A., Matias, A. (2012). Thresholds for storm impacts on an exposed sandy coastal area in southern Portugal. *Geomorphology*, 143–144, 3–12. <https://doi.org/10.1016/j.geomorph.2011.04.047>
- Amoudry, L. O., Souza, A. J. (2011). Deterministic coastal morphological and sediment transport modeling: A review and discussion. *Reviews of Geophysics*, 49(2010):1–21.
- Anon, 2002. Futurecoast: Final Project Report, DEFRA.
- Anthony, E. J. (2008). *Shore Processes and their Palaeoenvironmental Applications*. Elsevier Science.

- Ashton, A., Murray, A. B., Arnault, O. (2001). Formation of coastline features by large-scale instabilities induced by high angle waves. *Nature*, Vol. 414, 296-300.
- A.D. Ashton, A.B. Murray (2006a). High-age wave instability and emergent shoreline shapes: 1. Modeling of sand waves, flying spits, and capes. *J. Geophys. Res. Earth Surf.*, 111, 19 pp.
- A.D. Ashton, A.B. Murray (2006b). High-age wave instability and emergent shoreline shapes: 2. Wave climate analysis and comparisons to nature. *J. Geophys. Res. Earth Surf.*, 111, 17 pp.
- Austin, J. a., Lentz, S. J. (2002). The Inner Shelf Response to Wind- Driven Upwelling and Downwelling. *Journal of Physical Oceanography*, 32(7), 2171–2193.
- Austin, M.J., Scott, T.M., Russell, P.E., Masselink, G. (2013). Rip current prediction: development, validation, and evaluation of an operational tool. *Journal of Coastal Research*, 29, 283–300.
- Aragones, L., Serra, J. C., Villacampa, Y., Saval, J. M., Tinoco, H. (2016). New methodology for describing the equilibrium beach profile applied to the Valencia's beaches. *Geomorphology*, 259, 1–11. <https://doi.org/10.1016/j.geomorph.2015.06.049>
- Backstrom, J. T., Jackson, D. W. T., Cooper, J. A. G. (2009). Shoreface morphodynamics of a high-energy, steep and geologically constrained shoreline segment in Northern Ireland. *Marine Geology*, 257(1-4), 94–106.
- Bagnold, R. A. (1967). An Approach to the Sediment Transport Problem from General Physics. By R. A. Bagnold. U.S. Geological Survey Professional Paper 422-I, pp. v + 37, U.S. Government Printing Office, Washington, D.C.
- Bakker, W. T. (1969). The dynamics of a coast with a groyne system. In *Proceedings of the 11th Coastal Engineering Conference*, ASCE, pages 492– 517.
- Barnard, P. L., Hoover, D., Hubbard, D. M., Snyder, A., Ludka, B. C., Allan, J., Kaminsky, G. M., Ruggiero, P., Gallien, T. W., Gabel, L., McCandless, D., Weiner, H. M., Cohn,

- N., Anderson, D. L., Serafin, K. A. (2017). Extreme oceanographic forcing and coastal response due to the 2015-2016 El Niño. *Nature Communication*. 8, 1–8. <https://doi.org/10.1038/ncomms14365>.
- Bastos, A. C., Paphitis, D., Collins, M. B. (2004). Short-term dynamics and maintenance processes of headland-associated sandbanks: Shambles Bank, English Channel, UK. *Estuarine, Coastal and Shelf Science*, 59(1), 33–47. <https://doi.org/10.1016/j.ecss.2003.07.008>
- Bastos, A. C., Kenyon, N. H., Collins, M. (2002). Sedimentary processes, bedforms and facies, associated with a coastal, headland: Portland Bill, Southern UK. *Marine Geology*, 187, 235–258.
- Bernabeu, A. M., Medina, R., Vidal, C. (2003a). Wave reflection on natural beaches: An equilibrium beach profile model. *Estuarine, Coastal and Shelf Science*, 57, 577–585. [https://doi.org/10.1016/S0272-7714\(02\)00393-1](https://doi.org/10.1016/S0272-7714(02)00393-1)
- Bernabeu, A. M., Medina, R., Vidal, C. (2003b). A morphological model of the beach profile integrating wave and tidal influences. *Marine Geology*, 197 (1-4), 95–116.
- BERR. (2008). Atlas of UK Marine Renewable Energy Resources. Tech. rep.
- Birkemeier, W. (1985). Field data on seaward limit of profile change. *Journal of Waterway, Port, Coastal and Ocean Engineering* *Waterway, Port, Coastal and Ocean Engineering*, 598–602.
- Booij, N., Ris, R. C., Holthuijsen, L. H. (1999). A third-generation wave model for coastal regions: 1. Model description and validation. *Journal of Geophysical Research*, 104(C4), 7649–7666. <https://doi.org/10.1029/98JC02622>
- Bowen, A. J. (1969). Rip currents, part 1: theoretical investigation. *Journal of Geophysical Research*, 74(23), 5467–5478.

- Bowen, A. J., Inman, D. L. (1966). Budget of Littoral Sand in the Vicinity of Point Arguello, California. U.S. Army Coastal Engineering Research Center, Technical Memorandum No. 19, 56p.
- Brasington, J., Langham, J., Rumsby, B. (2003). Methodological sensitivity of morphometric estimates of coarse fluvial sediment transport. *Geomorphology*, 53(3–4), 299–316. [https://doi.org/10.1016/S0169-555X\(02\)00320-3](https://doi.org/10.1016/S0169-555X(02)00320-3)
- Brasington, J., Rumsby, B.T., Mcvey, R.A. (2000). Monitoring and modelling morphological change in a braided gravel-bed river using high resolution GPS-based survey. *Earth Surface Processes and Landforms*, 25(9): 973–990.
- British Geological Survey (2007). Offshore bedrock geology in the UK 1:250000 (DigRock250) - Offshore 1:250000 Sea Bed Sediments Maps DigSBS250). Geological Map Data BGS. NERC.
- Bromirski, P. D., Cayan, D. R. (2015). Wave power variability and trends across the North Atlantic influenced by decadal climate patterns. *J. Geophys. Res. Oceans*, 120, 3419–3443. DOI: 10.1002/2014JC010440.
- Brown, J. M., Davies, A. G. (2009). Methods for medium-term prediction of the net sediment transport by waves and currents in complex coastal regions. *Continental Shelf Research*, 29 (11–12), 1502–1514.
- Brown, J. M., Phelps, J. J. C., Barkwith, A., Hurst, M. D., Ellis, M. A., Plater, A. J. (2016). The effectiveness of beach mega-nourishment, assessed over three management epochs. *Journal of Environmental Management*, 184 (2), 400–408.
- Bruciaferri, D., Shapiro, G., Stanichny, S., Zatsepin, A., Ezer, T., Wobus, F., Francis, X., Hilton, D. (2020). The development of a 3D computational mesh to improve the representation of dynamic processes: the Black Sea test case, *Ocean Modelling*, in press.
- Bruun, P. (1989). Coastal Engineering and Use of the Littoral Zone. *Ocean and Shoreline Management*, 12(5–6), 495–516. [https://doi.org/10.1016/0951-8312\(89\)90027-1](https://doi.org/10.1016/0951-8312(89)90027-1)

- Bruun, P. (1954). *Coast erosion and the development of beach profiles*. Beach Erosion Board Technical Memorandum. Tech. rep., US Army Corps of Engineers, Washington DC.
- Burvingt, O., Masselink, G., Russell, P., Scott, T. (2017). Classification of beach response to extreme storms. *Geomorphology*, 295, 722–737. <https://doi.org/10.1016/j.geomorph.2017.07.022>
- Burvingt, O., Masselink, G., Scott, T., Davidson, M., Russell, P. (2018). Climate forcing of regionally-coherent extreme storm impact and recovery on embayed beaches. *Marine Geology*, 401, 112–128. <https://doi.org/10.1016/j.margeo.2018.04.004>
- Butt, T., Miles, J., Ganderton, P., Russell, P.E. (2002). A simple method for calibrating optical backscatter sensors in high concentrations of non-cohesive sediments. *Marine Geology*, 192, 419–424.
- Butt, T., Russell, P. E. (1999). Sediment transport mechanisms in high energy swash. *Marine Geology*, 161, 361–375.
- Butt, T., Russell, P. E. (2005). Observations of hydraulic jumps in high energy swash. *Journal Coastal Research*, 21, 1219–1227.
- Butt, T., Russell, P.E., Turner, I. (2001). The influence of swash infiltration–exfiltration on beach face sediment transport: onshore or offshore? *Coastal Engineering*, 42, 35–52.
- Butt, T., Russell, P. E., Puleo, J., Masselink, G. (2005). The application of Bagnold-type sediment transport models in the swash zone. *Journal Coastal Research*, 21, 887–895.
- Buscombe, D. D., Scott, T. (2008). The coastal geomorphology of north Cornwall, Wave Hub impact on seabed and shoreline processes. Tech. report.
- Calder, B. R., Mayer, L. A. (2003). Automatic processing of high-rate, high density multi-beam echosounder data. *Geochemistry, Geophysics, Geosystems*, 4(6), 1048. DOI: 10.1029/2002GC000486.

- Calder, B. R., Wells, D. (2007). CUBE User's Manual – Version 1.14. University of New Hampshire, USA.
- Caldwell, J. M. (1966). Coastal processes and beach erosion. *Journal of the Society of Civil Engineers*, 53 (2), 142–157.
- Capobianco, M., Larson, M., Nicholls, R. J., Kraus, N. C. (1997). Depth of Closure: A Contribution to the Reconciliation of Theory, Practise and Evidence. *In: Proceedings of Coastal Dynamics*, ASCE, New York, pp. 506–515.
- Capobianco, M., Hanson, H., Larson, M., Steetzel, H., Stive, M. J. F., Chatelus, Y., Aarninkhof, S., Karambas, T. (2002). Nourishment design and evaluation: applicability of model concepts. *Coastal Engineering*, 47(2), 113–135.
- Castelle, B., Bujan, S., Ferreira, S., Dodet, G. (2017a). Foredune morphological changes and beach recovery from the extreme 2013/2014 winter at a high-energy sandy coast. *Marine Geology*, 385, 41–55. <https://doi.org/10.1016/j.margeo.2016.12.006>
- Castelle, B., Coco, G. (2012). The morphodynamics of rip channels on embayed beaches. *Continental Shelf Research*, 43, 10–23. <https://doi.org/10.1016/j.csr.2012.04.010>
- Castelle, B., Coco, G. (2013). Surf zone flushing on embayed beaches. *Geophysical Research Letters*, 40(10), 2206–2210. <https://doi.org/10.1002/grl.50485>
- Castelle, B., Dodet, G., Masselink, G., Scott, T. (2017b). A new climate index controlling winter wave activity along the Atlantic coast of Europe: The West Europe Pressure Anomaly. *Geophysical Research Letters*, 44(3), 1384–1392. <https://doi.org/10.1002/2016GL072379>
- Castelle, B., Dodet, G., Masselink, G., Scott, T. (2018). Increased Winter-Mean Wave-Height, Variability, and Periodicity in the Northeast Atlantic over 1947-2017. *Geophysical Research Letters*, 45(2). <https://doi.org/10.1002/2017GL076884>
- Castelle, B., Marieu, V., Bujan, S., Splinter, K. D., Robinet, A., Sénéchal, N., Ferreira, S. (2015). Impact of the winter 2013-2014 series of severe Western Europe storms on a

- double-barred sandy coast: Beach and dune erosion and megacusp embayments. *Geomorphology*, 238, 135–148. <https://doi.org/10.1016/j.geomorph.2015.03.006>
- Castelle, B., Ruessink, B.G., Bonneton, P., Marieu, V., Bruneau, N., Price, T. D. (2010a). Coupling mechanisms in double sandbar systems. Part 1: patterns and physical explanation. *Earth Surface Processes and Landforms*, 35, 476–486.
- Castelle, B., Ruessink, B. G., Bonneton, P., Marieu, V., Bruneau, N., Price, T. D. (2010b). Coupling mechanisms in double sandbar systems. Part 2: impact on alongshore variability of inner-bar rip channels. *Earth Surface Processes and Landforms*, 35, 771–781.
- Bricheno, L. M., Wolf, J., Aldridge, J. (2015). Distribution of natural disturbance due to wave and tidal bed currents around the UK. *Continental Shelf Research*, 109, 67–77. <https://doi.org/10.1016/j.csr.2015.09.013>
- Bromirski, P. D., Cayan, D.R. (2015). Wave power variability and trends across the North Atlantic influenced by decadal climate patterns. *Journal of Geophysical Research: Oceans*, 120(5), 1–16.
- CERC (1984). Shore Protection Manual, Volume I. Department of the Army Waterways Experiment Station, Corps of Engineers, Vicksburg, Mississippi, pp. 652.
- CERC (1992). Importance of directional spreading of waves in the nearshore region. Coastal Engineering Technical Note, CETN I-53. Technical report, US Army, Mississippi.
- Chappell, J., Eliot, I. (1979). Surf-beach dynamics in time and space - An Australian case study, and elements of a predictive model. *Marine Geology*, 32(3-4), 231–250.
- Chen, C., Liu, H., Beardsley, R. C., (2003). An unstructured, finite-volume, three-dimensional, primitive equation ocean model: application to coastal ocean and estuaries. *Journal of Atmospheric and Oceanic Technology*, 20(1), 159–186.

- Chesher, J. A., Smythe, D. K., Bishop, P. (1981). The geology of the Minches, Inner Sound and Sound of Raasay, rep. inst. Edition, pp. 41.
- Chu, D. T., Himori, G., Saito, Y., Bui, T. V., Aoki, S. I. (2015). Study of beach erosion and evolution of beach profile due to nearshore bar sand dredging. *Procedia Engineering*, 116(1), 285–292. <https://doi.org/10.1016/j.proeng.2015.08.292>
- Church, J. A. and White, N. J. (2011). Sea-Level Rise from the Late 19th to the Early 21st Century. *Surveys in Geophysics*, 32(4–5), 585–602. <https://doi.org/10.1007/s10712-011-9119-1>
- Ciavola, P, Coco, G., 2017. *Coastal Storms: Processes and Impacts*. Wiley, pp. 1-22.
- CIRIA (1996). Beach management manual. CIRIA Report 153.
- Clayton, K. and Shamoon, N. (1998). New approach to the relief of Great Britain II. A classification of rocks based on relative resistance to denudation. *Geomorphology*, 25, 155-171.
- Coco, G., Senechal, N., Rejas, A., Bryan, K., Capo, S., Parisot, J.P., Brown, J.A., MacMahan, J.H.M. (2014). Beach response to a sequence of extreme storms. *Geomorphology*, 204, 493–501. <https://doi.org/10.1016/j.geomorph.2013.08.028>
- Cooper, J. A. G., Green, A. N., Loureiro, C. (2018). Geological constraints on mesoscale coastal barrier behaviour. *Global and Planetary Change*, 168(March), 15–34. <https://doi.org/10.1016/j.gloplacha.2018.06.006>
- Corbella, S. and Stretch, D. D. (2012). Shoreline recovery from storms on the east coast of Southern Africa. *Natural Hazards and Earth System Science*, 12(1), 11–22. <https://doi.org/10.5194/nhess-12-11-2012>
- Cowell, P.J., Stive, M. J. F., Niedoroda, A. W., de Vriend, H. J., Swift, D. J. P., Kaminsky, G. M., Capobianco, M. (2003). The Coastal-Tract (Part 1): A Conceptual Approach to Aggregated Modeling of Low-Order Coastal Change. *Journal of Coastal Research*, 19(4), 812–827.

- Cudaback, C. N. Washburn, L., Dever, E. (2005). Subtidal inner-shelf circulation near Point Conception, California. *Journal of Geophysical Research*, 110(C10), C10007. <https://doi.org/10.1029/2004JC002608>
- Dally, W. R., Dean, R. G., Dalrymple, R. A. (1985). Wave height variation across beaches of arbitrary profile. *Journal of Geophysical Research*, 90(C6), 11917–11927.
- Davidson, M., Huntley, D., Holman, R., George, K. (1997). The evaluation of large-scale (km) inter-tidal beach morphology on a macrotidal beach using video images. In *Proceedings Coastal Dynamics '97*, ASCE, pp. 385–394.
- Davidson, M.A., Lewis, R.P., Turner, I.L. (2010). Forecasting seasonal to multi-year shoreline change. *Coastal Engineering*, 57, 620-629.
- Davidson, M. A., Splinter, K. D., Turner, I. L. (2013). A simple equilibrium model for predicting shoreline change. *Coastal Engineering*, 73, 191–202. <https://doi.org/10.1016/j.coastaleng.2012.11.002>
- Davidson, M. A., Turner, I. L., Splinter, K. D., Harley, M. D. (2017). Annual prediction of shoreline erosion and subsequent recovery. *Coastal Engineering*, 130(October), 14–25. <https://doi.org/10.1016/j.coastaleng.2017.09.008>
- Davies, J. L. (1958). Wave refraction and the evolution of shoreline curves. *Geographical studies*, 5, 1–14.
- De Dominicis, M., O'Hara Murray, R., Wolf, J. (2017). Multi-scale ocean response to a large tidal stream turbine array. *Renewable Energy*, 114, 1160–1179. <https://doi.org/10.1016/j.renene.2017.07.058>
- Dean, R. G. (1977). Equilibrium Beach Profiles: U.S. Atlantic and Gulf Coasts. Ocean Engineering Technical Report No. 12. Tech. rep.
- Dean, R. G. (1987). Coastal Sediment Processes: Toward Engineering Solutions. In *Proceedings of the Specialty Conference on Coastal Sediments '87*, ASCE, pp. 1-24.

- Dean, R. G. (1991). Equilibrium Beach Profiles : Characteristics and Applications. *Journal of Coastal Research*, 7(1), 53–84. Retrieved from <http://www.jstor.org/stable/4297805>
- Deltares (2014). Delft3D-FLOW User Manual Hydro-Morphodynamics., Pap. 710.
- Denniss, T., Middleton, J. H., Manasseh, R. (1995). Recirculation in the Lee of Complicated Headlands - A Case Study of Bass-Point J -16101. *Journal of Geophysical Research- Oceans Journal of Geophysical Research- Oceans*, 100, 16087–16101.
- Dodet, G., Castelle, B., Masselink, G., Scott, T., Davidson, M., Floc'h, F., Jackson, D., Suanez, S. (2019). Beach recovery from extreme storm activity during the 2013/14 winter along the Atlantic coast of Europe. *Earth Surface Processes and Landforms*, 44(1), 393-401.
- Donnelly, C., Kraus, N., Larson, M. (2006). State of Knowledge on Measurement and Modeling of Coastal Overwash. *Journal of Coastal Research*, 224, 965–991.
- Dott, R. H. and Bourgeois, J. (1982 Hummock stratification: significance of its variable bedding sequences. *Geological Society of America Bulletin*, 93(August), 663–680. [https://doi.org/10.1130/0016-7606\(1982\)93<663:HSSOIV>2.0.CO](https://doi.org/10.1130/0016-7606(1982)93<663:HSSOIV>2.0.CO)
- Duarte, J.; Taborda, R.; Ribeiro, M.; Cascalho, J.; Silva, A.; Bosnic, I. Evidences of sediment bypassing at Nazaré headland revealed by a large scale sand tracer experiment. In *Proceedings of 3rd as Jornadas de Engenharia Hidrográfica*, Lisboa, Portugal, 24–26 June 2014; Volume 2014, pp. 289–292.
- Elias, E. P. L. (2018). Bench-mark morphodynamic model Ameland Inlet – Kustgenese 2.0 (ZG-C2), Deltares, Project 1220339-008, Reference 1220339-008-ZKS-0001, 70 pp.
- Evans, O. F. (1943). The relation of the action of waves and currents on headlands to the control of shore erosion by groynes. *Academy of Science for 1943*, pages 9–13.
- Fellowes, T. E., Vila-Concejo, A., Gallop, S. L. (2019). Morphometric classification of swell-dominated embayed beaches. *Marine Geology*, 411(February), 78–87. <https://doi.org/10.1016/j.margeo.2019.02.004>

- Flather, R. A. (1987). Estimates of extreme conditions of tide and surge using a numerical model of the northwest European continental-shelf. *Estuarine Coastal and Shelf Science*, 24, 69-93.
- Fontan, A., Alcantara-Carrio, J., Correa, I. D. (2012). Combined beach - inner shelf erosion in short and medium term (Maspalomas, Canary Islands). *Geologica Acta*, 10(4), 411-426.
- Fontolan, G., Bezzi, A., Martinucci, D., Pillon, S., Popesso, C., Rizzetto, F. (2015). Sediment budget and management of the Veneto beaches, Italy: an application of the Littoral Cells. *Management System (SICELL)*, 47-50. <https://doi.org/10.5150/cmcm.2015.010>
- Fuller, I. C., Large, A. R. G., Charlton, M. E., Heritage, G. L., Milan, D. J. (2003). Reach-scale sediment transfers: An evaluation of two morphological budgeting approaches. *Earth Surface Processes and Landforms*, 28(8), 889-903. <https://doi.org/10.1002/esp.1011>
- Gallagher, E., Wadman, H., McNinch, J., Reniers, A., Koktas, M. (2016). A Conceptual Model for Spatial Grain Size Variability on the Surface of and within Beaches. *Journal of Marine Science and Engineering*, 4(2), 38. <https://doi.org/10.3390/jmse4020038>
- Gallop, S. L., Bryan, K. R., Coco, G., Stephens, S. A. (2011). Storm-driven changes in rip channel patterns on an embayed beach. *Geomorphology*, 127, 179-188.
- Gao, S., Collins, M. B. (2014). Holocene sedimentary systems on continental shelves. *Marine Geology*, 352, 268-294. <https://doi.org/10.1016/j.margeo.2014.03.021>
- George, D. A., Largier, J. L., Storlazzi, C. D., Barnard, P. L. (2015). Classification of rocky headlands in California with relevance to littoral cell boundary delineation. *Marine Geology*, 369, 137-152. <https://doi.org/10.1016/j.margeo.2015.08.010>
- George, D. A. (2016). Circulation and sediment transport at headlands with implications for littoral cell boundaries. Ph.D. thesis, University of California, Davis.

- George, D. A., Largier, J. L., Storlazzi, C. D., Robart, M. J., and Gaylord, B. (2018). Currents, waves and sediment transport around the headland of Pt. Dume, California. *Continental Shelf Research*, 171, 63–76. <https://doi.org/10.1016/j.csr.2018.10.011>
- George, D.A., Largier, J.L., Pasternack, G. B., Barnard, P. L., Storlazzi, C.D., Erikson, L. H. (2019). Modeling Sediment Bypassing around Idealized Rocky Headlands. *Journal of Marine Science and Engineering*, 7, 40. doi:10.3390/jmse7020040
- Goff, J. A., Allison, M. a., Gulick, S. P. (2010). Offshore transport of sediment during cyclonic storms: Hurricane Ike (2008), Texas Gulf Coast, USA. *Geology*, 38(4), 351–354.
- Goodwin, I. D., Freeman, R., Blackmore, K. (2013). An insight into headland sand bypassing and wave climate variability from shoreface bathymetric change at Byron Bay, New South Wales, Australia. *Marine Geology*, 341, 29–45. <https://doi.org/10.1016/j.margeo.2013.05.005>
- Goring, D. G., Nikora, V. I. (2002). Despiking Acoustic Doppler Velocimeter Data. *Journal of Hydraulic Engineering*, 128(1), 117–126. [https://doi.org/10.1061/\(asce\)0733-9429\(2002\)128:1\(117\)](https://doi.org/10.1061/(asce)0733-9429(2002)128:1(117))
- Grant, W. D., Madsen, O. S. (1982). Movable bed roughness in unsteady oscillatory flow. *Journal of Geophysical Research*, 87, 469–481.
- Green, M. O., Coco, G. (2014). Review of wave driven sediment resuspension and transport in estuaries. *Reviews of Geophysics*, 52(1), 77–117. <https://doi.org/10.1002/2013RG000437>.Received
- Greenwood, B. (1978). Sediment transport by waves. In Fairbridge, editor, *Encyclopedia of Sediments and Sedimentary Rocks*, pages 1016–1028.
- Grunnet, N. M., Walstra, D. J. R., Ruessink, B. G. (2004). Process-based modelling of a shoreface nourishment. *Coastal Engineering*, 51(7), 581–607. <https://doi.org/10.1016/j.coastaleng.2004.07.016>

- Guisado-Pintado, E., Jackson, D.W.T. (2018). Multi-scale variability of storm Ophelia 2017: The importance of synchronised environmental variables in coastal impact. *Science of Total Environment*, 630, 287–301.
- Guza, R. T., Thornton, E. B. (1985). Observations of surf beat. *Journal of Geophysical Research*, 90(C2), 3161. <https://doi.org/10.1029/JC090iC02p03161>
- Halcrow (2007). SMP 7A and 7B/ Volume 1: Land's End to Hartland Point Shoreline Management Plan.
- Hallermeier, R. J. (1978). Uses for a calculated limit depth to beach erosion. In *Proceedings of the 16th Coastal Engineering Conference, ASCE* (pp. 1493–1512). New York.
- Hallermeier, R. J. (1981). A profile zonation for seasonal sand beaches from wave climate. *Coastal Engineering*, 4(C), 253–277. [https://doi.org/10.1016/0378-3839\(80\)90022-8](https://doi.org/10.1016/0378-3839(80)90022-8)
- Hands, E. B., Allison, M. C. (1991). Mound migration in deeper water and methods of categorising active and stable depths. In: *Proceedings of the ASCE Specialty Conference on Quantitative Approaches to Coastal Sediment Processes*, vol. 2, pp. 1985–1999.
- Hanson, H., Kraus, N. C. (1989). GENESIS: generalized model for simulating shoreline change. Tech. rep. 1, Coastal Engineering Research Center, U.S. Army Corps of Engineers, Vicksburg, Mississippi.
- Hansen, J. E., Elias, E., List, J. H., Erikson, L. H., Barnard, P. L. (2013). Tidally influenced alongshore circulation at an inlet-adjacent shoreline. *Continental Shelf Research*, 56, 26–38. <https://doi.org/10.1016/j.csr.2013.01.017>
- Harley, M. D., Turner, I. L., Kinsela, M. A., Middleton, J. H., Mumford, P. J., Splinter, K. D., Phillips, M. S., Simmons, J. A., Hanslow, D. J., Short, A. D. (2017). Extreme coastal erosion enhanced by anomalous extratropical storm wave direction. *Scientific Reports*, 7 (6033). <https://doi.org/10.1038/s41598-017-05792-1>.

- Harley, M. D., Turner, I. L., Short, a D. (2015). New insights into embayed beach rotation: The importance of wave exposure and cross-shore processes. *Journal of Geophysical Research : Earth Surface*, 1–15.
- Harley, M. (2017). Coastal Storm Definition. *Coastal Storms*, 1–21. <https://doi.org/10.1002/9781118937099.ch1>
- Hartman, M., Kennedy, A. B. (2016). Depth of closure over large regions using airborne bathymetric lidar. *Marine Geology*, 379, 52–63. <https://doi.org/10.1016/j.margeo.2016.05.012>
- Haskoning (2005). Suffolk wave and tide analysis report. Final Report 9R0839/R/PBor. Report for the Environment Agency, Anglian Region. Royal Haskoning, Peterborough, December 2005.
- Hendrickson, J., MacMahan, J. (2009). Diurnal sea breeze effects on inner-shelf cross-shore exchange. *Continental Shelf Research*, 29(18), 2195–2206. <https://doi.org/10.1016/j.csr.2009.08.011>
- Herbich, J. B. (2000). *Handbook of Coastal Engineering*. McGraw-Hill Professional, New York City, USA.
- Hinton, C., Nicholls, R. J. (1998). Spatial and Temporal Behaviour of Depth of Closure Along the Holland Coast. In *26th International Conference on Coastal Engineering*, 2913–2925. Retrieved from <http://journals.tdl.org/icce/index.php/icce/article/viewArticle/5812>
- Holman, R. A., Stanley, J. (2007). The history and technical capabilities of Argus. *Coastal Engineering*, 54(6–7), 477–491. <https://doi.org/10.1016/j.coastaleng.2007.01.003>
- Holman, R.A., Symonds, G., Thornton, E.B., Ranasinghe, R. (2006). Rip spacing and persistence on an embayed beach, *Journal Geophysical Research*, 111, pp. C01006.

- Holt, J. T., James, I. D., Jones, E. J. (2001). An s coordinate density evolving model of the northwest European continental shelf: 2. Seasonal currents and tides. *Journal of Geophysical Research*, 106(C7), 14,035–14,053. <https://doi.org/10.1029/2000JC000303>
- Hopkins, J., Elgar, S., Raubenheimer, B. (2015). Observations and model simulations of wave-current interaction on the inner shelf. *Journal of Geophysical Research: Oceans*, 121, 198–208. <https://doi.org/10.1002/2015JC010788>
- Houser, C., Wernette, P., Rentschlar, E., Jones, H., Hammond, B., Trimble, S. (2015). Post-storm beach and dune recovery: Implications for barrier island resilience. *Geomorphology*, 234, 54–63. <https://doi.org/10.1016/j.geomorph.2014.12.044>
- Howie, F. M. P., Ealey, P. J. (2010). An appraisal of Quaternary Calcium Carbonate Deposits in Cornwall. *Geoscience in South-West England*, 12, 233–239.
- Hsu, J., Evans, C. (1989a). Parabolic bay shapes and applications. In *Proceedings Institution Civil Engineers Part 2*, 87, pp. 557-570.
- Hsu, J., Silvester, R., Xia, Y. (1989b). Generalities on static equilibrium bays. *Coastal Engineering*, 12, 353-369.
- Hurst, M. D., A. Barkwith, M. A. Ellis, C. W. Thomas, and A. B. Murray (2015). Exploring the sensitivities of crenulate bay shorelines to wave climates using a new vector-based one-line model. *J. Geo-phys. Res. Earth Surf.*, 120, 2586–2608. doi:10.1002/2015JF003704.
- Inman, D. L., Adams, P. N. (2005). Bedforms and Closure Depth on Equilibrium Beaches. Retrieved from: <http://citeseerx.ist.psu.edu/viewdoc/download?doi=10.1.1.838.7286&rep=rep1&dtype=pdf>
- Inman, D. L., Bagnold, R. A. (1963). Beach and nearshore processes Part II, littoral processes. In M. D. Hill (Ed.), *The Sea: Ideas and Observations on Progress in the Study of the Sea* (pp. 529–553). New York: Interscience Wiley.

- Inman, D. L., Hany, M., Elwany, S., Jenkins, S. C. (1993). Shorerise and Bar-Berm Profiles on Ocean Beaches. *Journal of Geophysical Research*, 98(C10), 18.181–18.199.
- Inman, D. L., Frautschy, J. D. (1966). Littoral processes and the development of shorelines. In *Proceeding Coastal Engineering Specialty Conference*, Reston, VA, ASCE, pp. 511–536.
- Inman, D. L., Nordstrom (1971). On the tectonic and morphologic classification of coasts. *Journal of Geology*, 79, 1–21.
- Inman, D. L., Scott, J., Wasyl, J. (1998). Database for Streamflow and Sediment Flux of California Rivers. SIO Reference Series No. 98-9
- Jackson, D., Cooper, J., Del Rio, L. (2005). Geological control of beach morphodynamic state. *Marine Geology*, 216, 297–314.
- Jayarathne, M. P. R., Rahman, M. R., Shibayama, T. (2014). A Cross-Shore Beach Profile Evolution Model. *Coastal Engineering Journal*, 56(04), 1450020. <https://doi.org/10.1142/S057856341450020X>
- Johnson, D. W. (1919). Shore processes and shoreline development. In M. L. Schwartz (Ed.), *Encyclopedia of Coastal Science* (p. 877). Dordrecht: Springer.
- King, E., Conley, D., Masselink, G., Leonardi, N., McCarroll, R. J., Scott, T. (2019). The Impact of Waves and Tides on Residual Sand Transport on a Sediment-poor, Energetic and Macrotidal Continental Shelf. *Journal Geophysical Research Ocean*, 124, 4974–5002. <https://doi.org/10.1029/2018JC014861>
- Kinsela, M., Morris, B., Linklater, M., Hanslow, D. (2017). Second-Pass Assessment of Potential Exposure to Shoreline Change in New South Wales, Australia, Using a Sediment Compartments Framework. *Journal of Marine Science and Engineering*, 5(4), 61. <https://doi.org/10.3390/jmse5040061>

- Klein, A. H., Ferreira, Ó., Dias, J., Tessler, M. G., Silveira, L. F., Benedet, L., de Menezes, J. T., de Abreu, J. G. (2010). Morphodynamics of structurally controlled headland-bay beaches in southeastern Brazil: A review. *Coastal Engineering*, 57, 98–111.
- Kobayashi, N., Payo, A., Schmied, L. (2008). Cross-shore suspended sand and bed load transport on beaches. *Journal of Geophysical Research: Oceans*, 113(7), 1–17. <https://doi.org/10.1029/2007JC004203>
- Komar, P. D. (1998). Beach processes and sedimentation. Prentice-Hall, Inc., Simon and Schuster, Upper Saddle River, NJ, pp. 66–72.
- Komen, G. J., Hasselmann, S., Hasselmann, K. (1984). On the existence of a fully developed wind-sea spectrum. *Journal of Physical Oceanography*, 14, 1271–1285.
- Kraus, C., Larson, M., Wise, R. (1998). Depth of closure in beach fill design. In *Proceedings 12th National Conference on Beach Preservation Technology, Florida Shore and Beach Preservation Association*, Vol. 40, pp. 271–286.
- Kroon, A. (1990). Three-dimensional morphological changes of a nearshore bar system along the Dutch coast near Egmond aan Zee. *Journal of Coastal Research*, Special Issue 9, 430–451.
- Kulmar, M., Lord, D., Sanderson, B. (2005). Future directions for wave data collection in New South Wales. In: *Proceedings of the 17<sup>th</sup> Australasian Coastal and Ocean Engineering Ports Conference*, Australia, Sidney, pp. 167–172.
- Kuriyama, Y. (2002). Medium-term bar behavior and associated sediment transport at Hasaki, Japan. *Journal of Geophysical Research*, 107 (C9), 3132. doi:10.1029/JCO00899.
- Lanckriet, T., Puleo, J. A., Masselink, G., Turner, I. L., Conley, D., Blenkinsopp, C., Russell, P. E. (2014). Comprehensive field study of swash-zone processes II: Sheet flow sediment concentrations during quasi-steady backwash. *Journal of Waterway, Port, Coastal, and Ocean Engineering*, 140, 29–42.

- Lane S. N. (1998). The use of digital terrain modelling in the understanding of dynamic river channel systems. In *Landform Monitoring, Modelling and Analysis*, Lane SN, Richards K, Chandler J (eds). Wiley: Chichester; 311–342.
- Lane, S. N., Chandler, J. H., Richards, K. S. (1994). Developments in monitoring and modeling small-scale river bed topography. *Earth Surface Processes and Landforms*, 19(4), 349–368. DOI: 10.1002/esp.3290190406.
- Lane, S. N., Westaway, R. M., Hicks, D. M. (2003). Estimation of erosion and deposition volumes in a large, gravel-bed, braided river using synoptic remote sensing. *Earth Surface Processes and Landforms*, 28(3), 249–271. DOI: 10.1002/esp.483.
- Larson, M. (1991). Equilibrium profile of a beach with varying grain size. In: *Proceedings Coastal Sediments 1991*, ASCE, Seattle, pp. 861–874.
- Larson, M., Kraus, N. C. (1992). Dynamics of longshore bars. In: *Proceedings Coastal Engineering*, ASCE, Venice, pp. 2219–2232.
- Larson, M., Hanson, H., Kraus, N. C. (1987). *Analytical solutions of the one-line model of shoreline change. Technical Report CERC-87-15*.
- Larson, M., Hanson, H., Kraus, N. C. (2003). Chapter 12 Numerical modeling of beach topography change. In V. C. Lackhan (Ed.) (pp. 337–365). Elsevier B.V. [https://doi.org/10.1016/S0422-9894\(03\)80129-0](https://doi.org/10.1016/S0422-9894(03)80129-0)
- Larson, M., Kraus, N. C. (1992). Dynamics of Longshore Bars. In *Coastal Engineering 1992* (pp. 2219–2232). New York, NY: American Society of Civil Engineers. <https://doi.org/10.1061/9780872629332.169>
- Lentz, E. E., Hapke, C. J., Stockdon, H. F., Hehre, R. E. (2013). Improving understanding of near-term barrier island evolution through multi-decadal assessment of morphologic change. *Marine Geology*, 337, 125–139. <https://doi.org/10.1016/j.margeo.2013.02.004>

- Lentz, S., Guza, R. T., Elgar, S., Feddersen, F., Herbers, T. H. C. (1999). Momentum balances on the North Carolina inner shelf. *Journal of Geophysical Research*, 104(C8), 18,205–18,226.
- Leonardi, N., Plater, A. J. (2017). Residual flow patterns and morphological changes along macro- and meso-tidal coastline. *Advances in Water Resources*, 109, 290–301.
- Leveridge, B. E., Shail, R. K. (2011). The marine Devonian stratigraphy of Great Britain. *Proceedings of the Geologists' Association*, 122(4), 540–567. <https://doi.org/10.1016/j.pgeola.2011.03.003>
- Liu, S., Qiao, L., Li, G., Li, J., Wang, N., Yang, J. (2015). Distribution and cross-front transport of suspended particulate matter over the inner shelf of the East China Sea. *Continental Shelf Research*, 107, 92–102. <https://doi.org/10.1016/j.csr.2015.07.013>
- Loureiro, C., Ferreira, Ó., Cooper, J. A. G. (2012a). Extreme erosion on high-energy embayed beaches: Influence of megarips and storm grouping. *Geomorphology*, 139–140, 155–171. <https://doi.org/10.1016/j.geomorph.2011.10.013>
- Loureiro, C., Ferreira, Ó., Cooper, J. A. G. (2012b). Geologically constrained morphological variability and boundary effects on embayed beaches. *Marine Geology*, 329–331, 1–15. <https://doi.org/10.1016/j.margeo.2012.09.010>
- Luijendijk, A. P., Ranasinghe, R., de Schipper, M. A., Huisman, B. A., Swinkels, C. M., Walstra, D. J. R., Stive, M. J. F. (2017). The initial morphological response of the Sand Engine: A process-based modelling study. *Coastal Engineering*, 119, 1–14. <https://doi.org/10.1016/j.coastaleng.2016.09.005>
- Lyddon, C., Brown, J. M., Leonardi, N., Plater, A. J. (2018). Flood hazard assessment for a hyper-tidal estuary as a function of tide-surgemorphology interaction. *Estuaries and Coasts*, 41(6), 1565–1586. <https://doi.org/10.1007/s12237-018-0384-9>
- Madsen, O. S. (1991). Mechanistic of cohesionless sediment transport in coastal waters. In *Proceedings of Coastal Sediments 91*, ASCE (pp. 39–64). Seattle.

- Marsh, S. W., Nicholls, R. J., Kroon, a., Hoekstra, P. (1998). Assessment of Depth of Closure on a Nourished Beach: Terschelling, The Netherlands. In *26th International Conference on Coastal Engineering*, 3110–3123.
- Martens, D., Williams, T., Cowell, P. (1999). Mega-rip dimensional analysis on the Sydney coast Australia, and implications for beach-state recognition and prediction. *Journal of Coastal Research*, 17, 34–42.
- Masselink, G., Austin, M., Scott, T., Poate, T., Russell, P. (2014). Role of wave forcing, storms and NAO in outer bar dynamics on a high-energy, macro-tidal beach. *Geomorphology*, 226, 76–93. <https://doi.org/10.1016/j.geomorph.2014.07.025>
- Masselink, G., Black, K. (1995). Magnitude and cross-shore distribution of bed return flow measured on natural beaches. *Coastal Engineering*, 25(3–4), 165–190. [https://doi.org/10.1016/0378-3839\(95\)00002-5](https://doi.org/10.1016/0378-3839(95)00002-5)
- Masselink, G., Castelle, B., Scott, T., Dodet, G., Suanez, S., Jackson, D., Floe, F. (2016a). Extreme wave activity during 2013/2014 winter and morphological impacts along the Atlantic coast of Europe. *Geophysical Research Letters*, 2135–2143.
- Masselink, G., Evans, D., Hughes, M.G., Russell, P. (2005). Suspended sediment transport in the swash zone of a dissipative beach. *Marine Geology*, 216, 169–189.
- Masselink, G., Hughes, M. G. (2003). *Introduction to coastal processes and geomorphology*. (Hodder Education, Ed.). London.
- Masselink, G., Russell, P. (2006). Flow velocities, sediment transport and morphological change in the swash zone of two contrasting beaches. *Marine Geology*, 227, 227–240.
- Masselink, G., Scott, T., Poate, T., Russell, P., Davidson, M., Conley, D. (2016b). The extreme 2013/2014 winter storms: Hydrodynamic forcing and coastal response along the southwest coast of England. *Earth Surface Processes and Landforms*, 41(3), 378–391. <https://doi.org/10.1002/esp.3836>

- Masselink, G., Short, A. D. (1993). The Effect of Tide Range on Beach Morphodynamics and Morphology: A Conceptual Beach Model. *Journal of Coastal Research*, 9(3), 785–800. <https://doi.org/10.2307/4298129>
- Mathew, S., Davidson-Arnott, R. G. D., Ollerhead, J. (2010). Evolution of a beach–dune system following a catastrophic storm overwash event: Greenwich Dunes, Prince Edward Island, 1936–2005. *Canadian Journal of Earth Sciences*, 47(3), 273–290. <https://doi.org/10.1139/e09-078>
- May, V. J., Hansom, J. D. (2003). *Coastal Geomorphology of Great Britain*, geological Edition. Joint Nature Conservation Committee, Peterborough, pp. 754.
- Moore, B. D. (1982). Beach Profile Evolution in Response to Changes in Water Level and Wave Height. Masters Thesis, Department of Civil Engineering, University of Delaware.
- McCarroll, R.J., Brander, R.W., Turner, I.L., Power, H.E., Mortlock, T.R. (2014). Lagrangian observations of circulation on an embayed beach with headland rip currents. *Marine Geology*, 355, 173–188.
- McCarroll, R. J., Brander, R. W., Turner, I. L., Leeuwen, B. Van. (2016). Shoreface storm morphodynamics and mega-rip evolution at an embayed beach: Bondi Beach, NSW, Australia. *Continental Shelf Research*, 116, 74–88. <https://doi.org/10.1016/j.csr.2016.01.013>
- McCarroll, R., Masselink, G., Valiente, N., Scott, T., King, E., Conley, D. (2018). Wave and Tidal Controls on Embayment Circulation and Headland Bypassing for an Exposed, Macrotidal Site. *Journal of Marine Science and Engineering*, 6(3), 94. <https://doi.org/10.3390/jmse6030094>
- McCarroll, R., G. Masselink, G., Wiggins, M., Scott, T., Bilson, O., Conley, D., Valiente, N. G. (2019). High-efficiency longshore gravel transport and headland bypassing over an extreme event, *Earth Surface Processes and Landforms*. DOI: 10.1002/esp.4692

- McNinch, J. E. (2004). Geologic control in the nearshore: Shore-oblique sandbars and shoreline erosional hotspots, Mid Atlantic Bight, USA. *Marine Geology*, 211, 121–141.
- Mentaschi, L., Voudoukas, M. I., Pekel, J., Voukouvalas, E., Feyen, L. (2018). Global long-term observations of coastal erosion and accretion. *Scientific Reports*, 8, 12876.
- Meyer-Peter, E., Müller, R. (1948). Formulas for bed-load transport. In *Proceedings of the 2nd Meeting of the International Association for Hydraulic Structures Research* (pp. 39–64).
- Milne, J.A., Sear, D. (1997). Modelling river channel topography using GIS. *International Journal of Geographical Information Science*, 11(5), 499–519. DOI: 10.1080/136588197242275.
- Morton, R.A., Paine, J.G., Gibeaut, J.C. (1994). Stages and durations of post-storm beach recovery, southeastern Texas coast, USA. *Journal Coastal Research*, 884–908.
- Motyka, J. M. and Brampton, A. H. (1993). Coastal Management: Mapping littoral cells, Tech. report, HR Wallingford.
- Nagai, R. H., Sousa, S. H. M., Burone, L., Mahiques, M. M. (2009). Paleoproductivity changes during the Holocene in the inner shelf of Cabo Frio, southeastern Brazilian continental margin: Benthic foraminifera and sedimentological proxies. *Quaternary International*, 206(1–2), 62–71. <https://doi.org/10.1016/j.quaint.2008.10.014>
- Nicholls, R. J., Larson, M., Capobianco, M., Birkemeier, W. A. (1998). Depth of closure: Improving understanding and prediction. In *Proceedings of the Coastal Engineering Conference, ASCE* (Vol. 3, pp. 2888–2901). New York.
- Nicholls, R. J., Birkemeier, W. A., Lee, G. (1998a). Evaluation of depth of closure using data from Duck, NC, USA. *Marine Geology*, 148(3–4), 179–201. [https://doi.org/10.1016/S0025-3227\(98\)00011-5](https://doi.org/10.1016/S0025-3227(98)00011-5)

- Nicholls, R. J., Larson, M., Capobianco, M., Birkemeier, W. A. (1998b). Depth of closure: Improving understanding and prediction. *In: Proceedings of the Coastal Engineering Conference*, ASCE, New York, vol. 3, pp. 2888–2901.
- Nichols, G. (1999). *Sedimentology and Stratigraphy*, second Edition. John Wiley and Sons, Ltd., Publication, Oxford, pp. 419.
- Niedonora, A. W., Swift, D. J. P. (1981). Maintenance of the shoreface by wave orbital currents and mean flow: observations from the Long Island Coast. *Geophysical Research Letters*, 8(4), 337–340.
- Nielsen, P. (1981). Dynamics and geometry of wave-generated ripples. *Journal of Geophysical Research*, 86, 6467–6472.
- Nielsen, P. (1992). *Coastal Bottom Boundary Layers and Sediment Transport*. World Scientific Publishing Co. Pte. Ltd.
- Okayasu, A., Shibayama, T., Horikawa, K. (1988). Vertical variation of undertow in the surf zone. *In Proceedings 21th Coastal Engineering Conference*, ASCE, pp. 478–491.
- Olabarrieta, M., Warner, J. C., Kumar, N. (2011). Wave-current interaction in Willapa Ba. *Journal of Geophysical Research: Oceans*, 116(C12). <https://doi.org/10.1029/2011JC007387>
- Ollerhead, J., Davidson-Arnott, R., Walker, I.J., Mathew, S. (2013). Annual to decadal morphodynamics of the foredune system at Greenwich Dunes, Prince Edward Island, Canada. *Earth Surface Processes and Landforms*, 38, 284–298.
- Ortiz, A. C., Ashton, A. D. (2016). Exploring shoreface dynamics and a mechanistic explanation for a morphodynamic depth of closure. *Journal of Geophysical Research Earth Surface*, 121(2), 442–464. <https://doi.org/10.1002/2015JF003699>
- Pawlowicz, R., Beardsley, B., Lentz, S. (2002). Classical tidal harmonic analysis including error estimates in MATLAB using TTIDE. *Computers and Geosciences*, 28(8), 929–937. [https://doi.org/10.1016/S0098-3004\(02\)00013-4](https://doi.org/10.1016/S0098-3004(02)00013-4)

- Pazdur, M. F., Bluszcz, A., Pazdur, A., Morawiecka, I. (1995). Radiocarbon and thermoluminescence studies of the karst pipe systems in Southwest England and South Wales.
- Pepper, D. A., Stone, G. W. (2004). Hydrodynamic and sedimentary responses to two contrasting winter storms on the inner shelf of the northern Gulf of Mexico. *Marine Geology*, 210(1–4), 43–62.
- Peters, S. E., Loss, D. P. (2012). Storm and fair-weather wave base: A relevant distinction? *Geology*, 40(6), 511–514. <https://doi.org/10.1130/G32791.1>
- Phillips, M. R., Williams, A. T. (2007). Depth of Closure and Shoreline Indicators: Empirical Formulae for Beach Management. *Journal of Coastal Research*, 232(2001), 487–500. <https://doi.org/10.2112/05-0593.1>
- Pilkey, O. H.; Young, R. S.; Riggs, S. R., Sam Smith, A. W., Wu, H., Pilkey, W. D. (1993). The concept of shoreface profile of equilibrium: a critical review. *Journal of Coastal Research*, 9(1), 255–278.
- Plant, N. G., Holman, R. A., Freilich, M. H., Birkemeier, W. A. (1999). A simple model for interannual sandbar behavior. *Journal of Geophysical Research: Oceans*, 104(C7), 15755–15776. <https://doi.org/10.1029/1999jc900112>
- Plant, N. G., Holland, K. T, Puleo, J. A. (2002). Analysis of the scale errors in nearshore bathymetric data. *Marine Geology*, 191(1–2), 71–86. DOI: 10.1016/S0025-3227(02)00497-8
- Plant, N. G., Holland, K. T., Holman, R. A. (2006). A dynamical attractor governs beach response to storms. *Geophysical Research Letters*, 33(17), 1–6. <https://doi.org/10.1029/2006GL027105>
- Plant, N. G., Holland, K. T., Puleo, J. A. (2002). Analysis of the scale of errors in nearshore bathymetric data. *Marine Geology*, 191(1–2), 71–86. [https://doi.org/10.1016/S0025-3227\(02\)00497-8](https://doi.org/10.1016/S0025-3227(02)00497-8)

- Poate, T., Masselink, G., Russell, P., Austin, M. (2014). Morphodynamic variability of high-energy macrotidal beaches, Cornwall, UK. *Marine Geology*, 350, 97–111. <https://doi.org/10.1016/j.margeo.2014.02.004>
- Potter, P. E. (1967). Sand Bodies and Sedimentary Environments: A Review. *AAPG Bulletin*, 51(3), 337–365.
- Prodger, S., Russell, P., Davidson, M. (2017). Grain-size distributions on high energy sandy beaches and their relation to wave dissipation. *Sedimentology*, 1289–1302. <https://doi.org/10.1111/sed.12353>
- Puleo, J.A., Blenkinsopp, C., Conley, D., Masselink, G. (2014a). Comprehensive field study of swash-zone processes. I: Experimental design with examples of hydrodynamic and sediment transport measurements. *Journal Waterway, Port, Coastal, and Ocean Engineering*, 140(1), 14–28.
- Puleo, J. A., Lanckriet, T., Blenkinsopp, C. (2014b). Bed level fluctuations in the inner surf and swash zone of a dissipative beach. *Marine Geology*, 349, 99–112. <https://doi.org/10.1016/j.margeo.2014.01.006>
- Pye, K. and Blott, S. J. (2016). Assessment of beach and dune erosion and accretion using LiDAR: Impact of the stormy 2013-14 winter and longer term trends on the Sefton Coast, UK. *Geomorphology*, 266, 146–167. <https://doi.org/10.1016/j.geomorph.2016.05.011>
- Qinghua Ye, Morelissen, R., De Goede, E., Van Ormondt, M., Van Kester, J. (2011). A New Technique for Nested Boundary. *Proceedings of the Sixth International Conference on Asian and Pacific Coasts*. <https://doi.org/10.1142/9789814366489>
- Record, N. R., Pershing, A. J., Cropp, R., Norbury, J. (2014). An evaluation of compiled single-beam bathymetry data as a basis for regional sediment and biotope mapping. *Marine Science*, 71, 236–240. <https://doi.org/10.1093/icesjms/fst176>

- Ridderinkhof, W., Swart, H. E., Vegt, M., Hoekstra, P. (2016). Modeling the growth and migration of sandy shoals on ebb-tidal deltas. *Journal of Geophysical Research: Earth Surface*, 121, 1351–1372. <https://doi.org/10.1002/2016JF003823>
- Robertson V, W., Zhang, K., Finkl, C. W., Whitman, D. (2008). Hydrodynamic and geologic influence of event-dependent depth of closure along the South Florida Atlantic Coast. *Marine Geology*, 252(3–4), 156–165. <https://doi.org/10.1016/j.margeo.2008.03.018>
- Robertson V, W., Zhang, K., Whitman, D. (2007). Hurricane-induced beach change derived from airborne laser measurements near Panama City, Florida. *Marine Geology*, 237(3–4), 191–205. <https://doi.org/10.1016/j.margeo.2006.11.003>
- Rosati, J. D., Dean, R. G., Walton, T. L. (2013). The modified Bruun Rule extended for landward transport. *Marine Geology*, 340, 71–81. <https://doi.org/10.1016/j.margeo.2013.04.018>
- Rosati, J. D. (2006). Concepts in Sediment Budgets. *Journal of Coastal Research*, 212(1966), 307–322. <https://doi.org/10.2112/02-475a.1>
- Roy, P. S. and Thom, B. G. (1981). Late Quaternary marine deposition in New South Wales and southern Queensland - an evolutionary model. *Journal of the Geological Society of Australia*, 28, 471–489. <https://doi.org/10.1080/00167618108729182>
- Rubin, D. M. (2004). A simple autocorrelation algorithm for determining grain size from digital images of sediment. *Journal of Sedimentary Research*, 74, 160–165.
- Ruessink, B. G., Kroon, A. (1994). The behaviour of a multiple bar system in the nearshore zone of Terschelling, The Netherlands. *Marine Geology*, 121, 187–197.
- Ruessink, B. G., Wijnberg, K.M., Holman, R. A., Kuriyama, Y., van Enkevort, I. M. J. (2003). Intersite comparison of interannual nearshore bar behaviour. *Journal of Geophysical Research*, 108 (C8), 3249. doi:10.1029/2002JCO01505.

- Ruggiero, P., Kaminsky, G.M., Gelfenbaum, G., Voigt, B. (2005). Seasonal to interannual morphodynamics along a high-energy dissipative littoral cell. *Journal Coastal Research*, 553–578.
- Samuel, R. M. (2017). Seasonal variation of macrobenthos distribution and the biophysical cohesiveness of sediments on a macrotidal, highly exposed sandy beach. Master Thesis, Faculty of Science and Engineering, Plymouth University.
- Saulter, A. (2017). Quality Information Document: North West European Shelf Production Centre. NORTHWESTSHELF\_ANALYSIS\_FORECAST\_WAV\_004\_012. Retrieved from <http://cmems-resources.cls.fr/documents/QUID/CMEMS-NWS-QUID-004-012.pdf>
- Schimmel, A.C.G., Ierodiaconou, D., Hulands, L., Kennedy, D.M. (2015). Accounting for uncertainty in volumes of seabed change measured with repeat multi-beam sonar surveys. *Continental Shelf Research*, 111, 52–68. <https://doi.org/10.1016/j.csr.2015.10.019>.
- Scott, T. M. (2009). Beach morphodynamics and associated hazards in the UK. PhD thesis, University of Plymouth.
- Scott, T., Masselink, G., Russell, P. (2011). Morphodynamic characteristics and classification of beaches in England and Wales. *Marine Geology*, 286(1–4), 1–20. <https://doi.org/10.1016/j.margeo.2011.04.004>
- Scott, T., Masselink, G., Austin, M. J., Russell, P. (2014). Controls on macrotidal rip current circulation and hazard. *Geomorphology*, 214, 198–215. <https://doi.org/10.1016/j.geomorph.2014.02.005>
- Scott, T., Masselink, G., O'Hare, T., Saulter, A., Poate, T., Russell, P., Davidson, M., Conley, D. (2016). The extreme 2013/2014 winter storms: Beach recovery along the southwest coast of England. *Marine Geology*, 382, 224–241. <https://doi.org/10.1016/j.margeo.2016.10.011>

- Shand, R.D., Bailey, D.G. (1999). A review of net offshore bar migration with photographic illustrations from Wanganui, New Zealand. *Journal of Coastal Research*, 15, 365–378.
- Shields, A. (1936). Anwendung der Aehnlichkeitsmechanik und der Turbulenzforschung auf die Geschiebebewegung [Application of similarity mechanics and turbulence research on shear flow]. Preußischen Versuchsanstalt für Wasserbau, vol. 26, Berlin.
- Short, A. D. (1985). Rip-current type, spacing and persistence, Narrabeen Beach, Australia. *Marine Geology*, 65(1–2), 47–71. [https://doi.org/10.1016/0025-3227\(85\)90046-5](https://doi.org/10.1016/0025-3227(85)90046-5)
- Short, A. D., Masselink, G. (1999). Embayed and structurally controlled beaches. In A. D. (Ed. A. Short (Ed.), *Handbook of Beach and Shoreface Morphodynamics* (pp. 230–249). Chichester: John Wiley and Sons.
- Short, A. D. (2006). Australian Beach Systems-Nature and Distribution. *Journal of Coastal Research*, 22 (1), 11–27.
- Short, A. D. (2010). Role of geological inheritance in Australian beach morphodynamics. *Coastal Engineering*, 57(2), 92–97. <https://doi.org/10.1016/j.coastaleng.2009.09.005>
- Sibson, R. (1981). "A Brief Description of Natural Neighbor Interpolation," chapter 2. In *Interpolating Multivariate Data*. New York: John Wiley and Sons, 21–36.
- Soulsby, R. L., Hamm, L., Klopman, G., Alii, E. (1993). Wave- current interaction within and outside the bottom boundary layer. *Coastal Engineering*, 21, 41–69.
- Soulsby, R. (1995). Bed shear-stresses due to combined waves and currents. In M. J. F. Stive and H. H. de Vriend (Eds.), *Advances in Coastal Morphodynamics* (pp. 4–20 to 4–23).
- Soulsby, R. (1997). *Dynamics of Marine Sands: A Manual for Practical Applications*. Thomas Telford Publications, pp. 249.

- Soulsby, R. L., Damgaard, J. S. (2005). Bedload sediment transport in coastal waters. *Coastal Engineering*, 52(8), 673–689. <https://doi.org/10.1016/j.coastaleng.2005.04.003>
- Souto, D. D., de Oliveira Lessa, D. V., Albuquerque, A. L. S., Sifeddine, A., Turcq, B. J., Barbosa, C. F. (2011). Marine sediments from southeastern Brazilian continental shelf: A 1200 year record of upwelling productivity. *Palaeogeography, Palaeoclimatology, Palaeoecology*, 299(1–2), 49–55. <https://doi.org/10.1016/j.palaeo.2010.10.032>
- Splinter, K.D., Turner, I.L., Davidson, M.A., Barnard, P., Castelle, B., Oltman-Shay, J. (2014). A generalized equilibrium model for predicting daily to inter-annual shoreline response. *Journal Geophysical Research Earth Surface*, 1936–1958.
- Stive, M. J. F., de Vriend, H. J. (1995). Modeling Shoreface Profile Evolution. *Marine Geology*, 126(1–4), 235–248. [https://doi.org/10.1016/0025-3227\(95\)00080-I](https://doi.org/10.1016/0025-3227(95)00080-I)
- Stive, M. J. F. and Battjes, J. A. (1984). A Model for Offshore Sediment Transport. *Coastal Engineering Proceedings*, 1420–1436.
- Stive, M. J. F., Nicholls, R. J., de Vriend, H. J. (1991). Sea-level rise and shore nourishment: a discussion. *Coastal Engineering*, 16(1), 147–163. [https://doi.org/10.1016/0378-3839\(91\)90057-N](https://doi.org/10.1016/0378-3839(91)90057-N)
- Stive, M. J., de Vriend, H. J., Nicholls, R. J., Capobianco, M. (1992). Shore nourishment and the active zone: a time scale dependent view. In: *Proceedings of the Twenty-third Coastal Engineering Conference*, ASCE, New York, pp. 2464–2473.
- Stokes, C., Davidson, M., Russell, P. (2015). Observation and prediction of three-dimensional morphology at a high-energy macrotidal beach. *Geomorphology*, 243, 1–13. <https://doi.org/10.1016/j.geomorph.2015.04.024>
- Stokes, C., Russell, P., Davidson, M. (2016). Subtidal and Intertidal Three-Dimensionality at a High Energy Macrotidal Beach. *Journal of Coastal Research*, 75(sp1), 472–476. <https://doi.org/10.2112/si75-095.1>

- Stokes, G. G. (1847). On the Theory of Oscillatory Waves. *Cambridge Philosophical Society*, 8, 197–237. <https://doi.org/10.1017/CBO9780511702242.016>
- Storlazzi, C. D., Ja, B. E. (2002). Flow and sediment suspension events on the inner shelf of central California. *Marine Geology*, 181, 195–213.
- Stride, A. H., Wilson, J. B., Curry, D. (1999). Accumulation of late Pleistocene and Holocene biogenic sands and gravels on the continental shelf between northern Scotland and western France. *Marine Geology*, 159, 273–285. [https://doi.org/10.1016/S0025-3227\(99\)00002-X](https://doi.org/10.1016/S0025-3227(99)00002-X)
- Tanaka, H., Van To, D. (1995). Initial motion of sediment under waves and wave-current combined motions. *Coastal Engineering*, 25(3–4), 153–163. [https://doi.org/10.1016/0378-3839\(94\)00047-2](https://doi.org/10.1016/0378-3839(94)00047-2)
- Taylor, J. (1997). *An Introduction to Error Analysis: the Study of Uncertainties in Physical Measurements*, 2nd eds. University Science Books: Sausalito, CA.
- Thieler, E. R., Pilkey, O. H., Cleary, W. J., Schwab, W. C. (2001). Modern Sedimentation on the Shoreface and Inner Continental Shelf at Wrightsville Beach, North Carolina, U.S.A. *Journal of Sedimentary Research*, 71(6), 958–970. <https://doi.org/10.1306/032101710958>
- Thom, B.G., Eliot, I., Harvey, N., Rissik, D., Sharples, C., Short, A.D., Woodroffe, C.D. (2018). National sediment compartment framework for Australian coastal management. *Ocean and Coastal Management*, 154, 103–120. <https://doi.org/10.1016/j.ocecoaman.2018.01.001>
- Thornton, E. B., Guza, R. T. (1983). Transformation of wave height distribution. *Journal of Geophysical Research*, 88(C10), 5925–5938.
- Thorpe, A., Miles, J., Masselink, G., Russell, P., Scott, T., Austin, M. (2013). Sediment transport in rip currents on a macrotidal beach. 12th International Coastal Symposium, Plymouth, England. *Journal Coastal Research*, SI65, 1880–1885.

- Tilburg, C. E. (2003). Across-Shelf Transport on a Continental Shelf: Do Across-Shelf Winds Matter? *Journal of Physical Oceanography*, 33(12), 2675–2688. [https://doi.org/10.1175/1520-0485\(2003\)033<2675:ATOACS>2.0.CO;2](https://doi.org/10.1175/1520-0485(2003)033<2675:ATOACS>2.0.CO;2)
- Tolman, H. L. (2014). User manual and system documentation of WAVEWATCH III. NOAA. Tech. rep.
- United Kingdom Hydrographic Office (2011). INSPIRE Portal and Bathymetry DAC. Available at <http://aws2.caris.com/ukho/mapViewer/map.action>
- Valiente, N. G., Masselink, G., Scott, T., Conley, D., McCarroll, R. J. (2019a). Role of waves and tides on depth of closure and potential for headland bypassing. *Marine Geology*, 407, 60–75. <https://doi.org/10.1016/j.margeo.2018.10.009>
- Valiente, N.G., Masselink, G., Scott, T., McCarroll, J., Wiggins, M. (2019b). Multi-annual embayment sediment dynamics involving headland bypassing and sediment exchange across the depth of closure. *Geomorphology*, 343, 48–64. <https://doi.org/10.1016/j.geomorph.2019.06.020>.
- van Rijn, L. C. (2007a). Unified view of sediment transport by currents and waves. I: Initiation of motion, bed roughness, and bed-load transport. *Journal of Hydraulic Engineering*, 133(6), 649–667. [https://doi.org/10.1061/\(ASCE\)0733-9429\(2007\)133:6\(649](https://doi.org/10.1061/(ASCE)0733-9429(2007)133:6(649)
- van Rijn, L. C. (2007b). Unified view of sediment transport by currents and waves. II: Suspended transport. *Journal of Hydraulic Engineering*, 133(6), 668–689. [https://doi.org/10.1061/\(ASCE\)0733-9429\(2007\)133:6\(668](https://doi.org/10.1061/(ASCE)0733-9429(2007)133:6(668)
- van Rijn, L.C. (2014). A simple general expression for longshore transport of sand, gravel and shingle. *Coastal Engineering*, 90, 23–39.
- van Rijn, L. C. (2011). Coastal erosion and control. *Ocean and Coastal Management*, 54(12), 867–887. <https://doi.org/10.1016/j.ocecoaman.2011.05.004>

- van Rijn, L. C. (1997). Sediment transport and budget of the central coastal zone of Holland. *Coastal Engineering*, 32(1), 61–90. [https://doi.org/10.1016/S0378-3839\(97\)00021-5](https://doi.org/10.1016/S0378-3839(97)00021-5)
- van Rijn, L. C. (1984). Sediment Transport, Part I: Bed Load Transport. *Journal of Hydraulic Engineering*, 110(10), 1431–1456. [https://doi.org/10.1061/\(ASCE\)0733-9429\(1984\)110:10\(1431\)](https://doi.org/10.1061/(ASCE)0733-9429(1984)110:10(1431))
- Venditti, J. G., Church, M. (2014). Journal of Geophysical Research: Earth Surface. *Journal of Geophysical Research: Earth Surface*, 119(1), 2315–2334. <https://doi.org/10.1002/2014JF003147>.
- Vieira da Silva, G., Toldo, E. E., Klein, A. H. d. F., Short, A. D. (2018). The influence of wave-, wind- and tide-forced currents on headland sand bypassing – Study case: Santa Catarina Island north shore, Brazil. *Geomorphology*, 312, 1–11. <https://doi.org/10.1016/j.geomorph.2018.03.026>
- Vieira da Silva, G., Toldo, E.E., Klein, A.H.F., Short, A.D., Tomlinson, R., Strauss, D. (2017). A comparison between natural and artificial headland sand bypassing in Santa Catarina and the Gold Coast. *Australasian Coasts and Ports 2017: Working with Nature*, 1111.
- Vieira da Silva, G., Toldo, E. E., Klein, A. H. d. F., Short, A. D., Woodroffe, C. D. (2016). Headland sand bypassing - Quantification of net sediment transport in embayed beaches, Santa Catarina Island North Shore, Southern Brazil. *Marine Geology*, 379, 13–27. <https://doi.org/10.1016/j.margeo.2016.05.008>
- Warner, J. C., Armstrong, B., Sylvester, C. S., Voulgaris, G., Nelson, T., Schwab, W. C., Denny, J. F. (2012). Storm-induced inner-continental shelf circulation and sediment transport: Long Bay, South Carolina. *Continental Shelf Research*, 42, 51–63. <https://doi.org/10.1016/j.csr.2012.05.001>
- Watanabe, A. (1982). Numerical model of nearshore currents and beach deformation model. In *Proceedings Coastal Engineering Japan, JSCE* (pp. 147–161).

- Wechsler, S.P. (2003). Perceptions of digital elevation model uncertainty by DEM users. *URISA Journal*, 15(2), 57–64.
- Wechsler, S. P., Kroll, C. N. (2006). Quantifying DEM uncertainty and its effect on topographic parameters. *Photogrammetric Engineering and Remote Sensing*, 72(9), 1081–1090.
- Wheaton, J. M., Brasington, J., Darby, S. E., Sear, D. A. (2010). Accounting for uncertainty in DEMs from repeat topographic surveys: Improved sediment budgets. *Earth Surface Processes and Landforms*, 35(2), 136–156. <https://doi.org/10.1002/esp.1886>
- Wiggins, M., Scott, T., Masselink, G., Russell, P., McCarroll, R. J. (2019). Coastal embayment rotation: Response to extreme events and climate control, using full embayment surveys. *Geomorphology*, 327, 385–403. <https://doi.org/10.1016/j.geomorph.2018.11.014>
- Wijnberg, K. M., Kroon, A. (2002). Barred beaches. *Geomorphology*, 48(1–3), 103–120. [https://doi.org/10.1016/S0169-555X\(02\)00177-0](https://doi.org/10.1016/S0169-555X(02)00177-0)
- Wise, S.M. (1998). The effect of GIS interpolation errors on the use of digital elevation models in geomorphology. In *Landform Monitoring, Modelling and Analysis*, Lane SN, Richards K, Chandler J (eds). Wiley: Chichester; 139–164.
- Work, P. A. and Dean, R. G. (1991). Effect of varying sediment size on equilibrium beach profiles. In: *Proceedings Coastal Sediments*, ASCE, Seattle, pp. 891–904.
- Wright, L. D. (1976). Nearshore wave-power dissipation and the coastal energy regime of the Sydney-Jervis Bay region, New South Wales: a comparison. *Marine and Freshwater Research*, 27, 633–640.
- Wright, L. D. (1987). Shelf-surf zone coupling: diabathic shoreface transport. In: *Proceedings of Coastal Sediments*, ASCE, Washington, D.C., pp. 25–40.
- Wright, L. D. (1995). *Morphodynamics of inner continental shelves*. (L. Donelson Wright, Ed.). CRC Press, Inc.

- Wright, L. D., Boon, J. D., Green, M. O., List, J. H. (1986). Response of the mid shoreface of the southern mid-Atlantic Bight to a “northeaster.” *Geo-Marine Letters*, 6(3), 153–160. <https://doi.org/10.1007/BF02238086>
- Wright, L. D., Boon, J. D., Kim, S. C., List, J. H. (1991). Modes of cross-shore sediment transport on the shoreface of the Middle Atlantic Bight. *Marine Geology*, 96(1–2), 19–51. [https://doi.org/10.1016/0025-3227\(91\)90200-N](https://doi.org/10.1016/0025-3227(91)90200-N)
- Wright, L. D., Xu, J. P., Madsen O. S. (1994). Across-shelf benthic transports on the inner shelf of the Middle Atlantic Bight during the “Halloween storm” of 1991. *Marine Geology*, 118 (1–2), 61–77.
- Wright, L. D., Short, A. D. (1984). Morphodynamic variability of surf zones and beaches: A synthesis. *Marine Geology*, 56(1–4), 93–118. [https://doi.org/10.1016/0025-3227\(84\)90008-2](https://doi.org/10.1016/0025-3227(84)90008-2)
- Yates, M.L., Guza, R.T., O'Reilly, W.C. (2009). Equilibrium shoreline response: observations and modelling. *Journal Geophysical Research*, 114.
- Young, I. R. (1999). *Wind Generated Ocean Waves*, vol. 2, Elsevier Sci., Amsterdam, 287 pp.



## Appendix A – Model sensitivity analysis

---

This appendix includes a brief explanation of the sensitivity analysis conducted during Delft3D model set-up in Chapter 4.

### A.1 Boundary sensitivity analysis

Wave-only model runs combining several boundary conditions including those recommended in the manual for coastal models (water level for offshore boundary and Neumann for x-shore boundaries) and used in several studies (e.g., Roelvink and Walstra, 2004) were conducted to assess the performance of both boundary conditions. Results showed an important instability at the SW boundary (inflow) for all range of wave conditions (Fig. A.1a-red box) with increasing flow speed for higher-energy wave conditions. This instability has been observed previously (e.g., Ye et al., 2011) but no information regarding this issue is available in the manuals. The use of Neumann boundaries was therefore discarded.

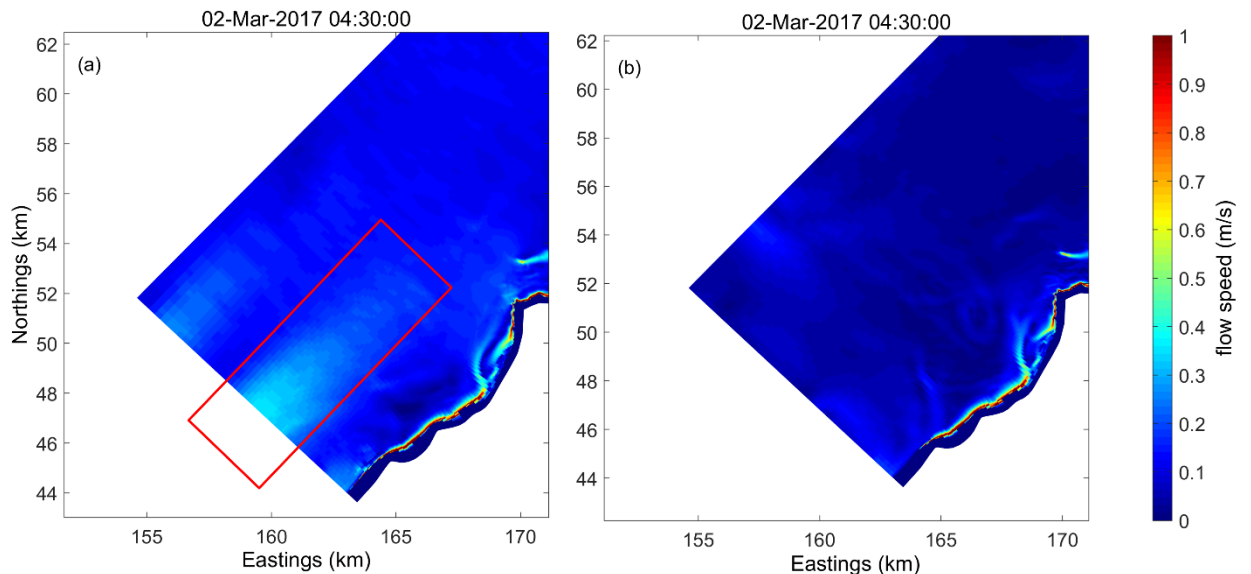


**Fig. A.1** Snapshots of depth averaged wave-induced flow speed during the calibration period with Neumann (a) and current (b) boundary conditions at the SW cross-shore boundary (inflow).

## A.2 Smooth bathymetry

Coupled model runs using the final set-up of current and water level conditions for the inflow (SW) and the outflow (NE) cross-shore boundaries, respectively, were evaluated in order to assess possible additional instabilities caused by the hydrodynamic forcing conditions. Hence, due to the resolution of these (7-km), a transition zone with a smoother bathymetry (Fig. A.2) was implemented to eliminate an inaccurate strong coastal current induced at both cross-shore boundaries (Fig. A.3). Additionally, a 2-D Gaussian smoothing filter ( $G$ , Eq. A.1) with standard deviation ( $\sigma$ ) of 2 was exclusively applied along 400-m (Fig. A.2) at both ends of the domain as follows:

$$G(x, y) = \frac{1}{2\pi\sigma^2} e^{-\frac{x^2+y^2}{2\sigma^2}} \quad (\text{A.1})$$

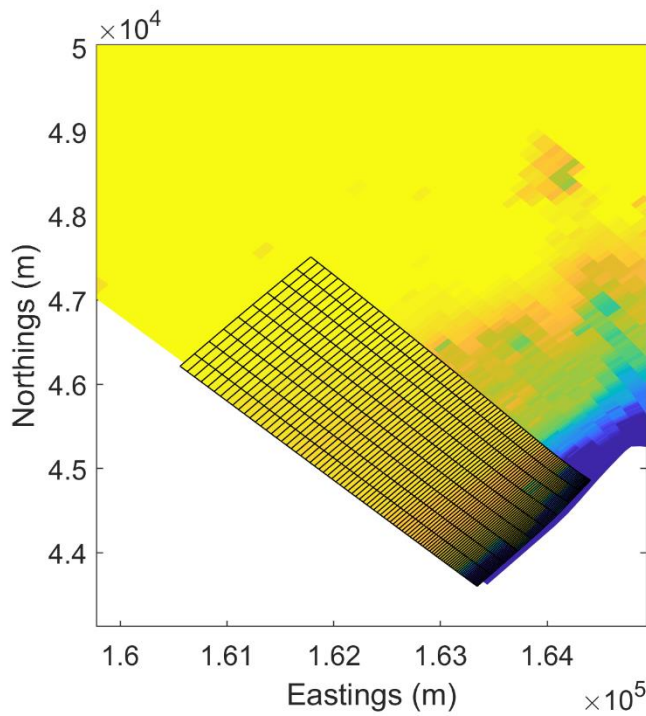


**Fig. A.2** Transition zone at the SW boundary with smooth bathymetry.

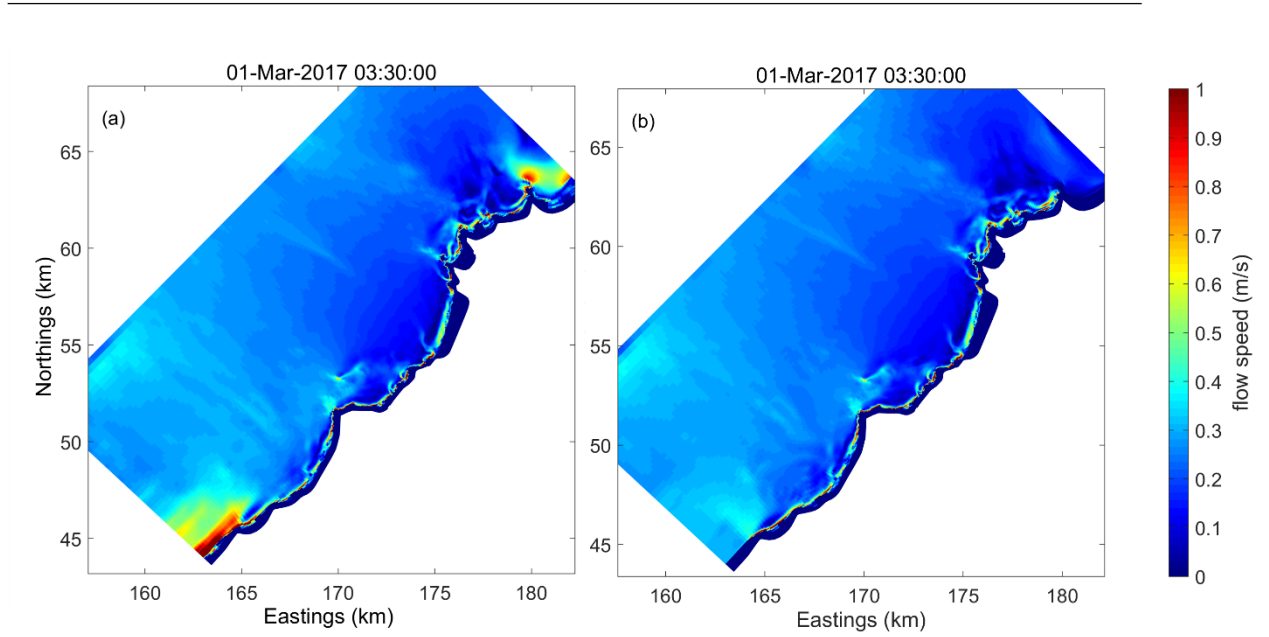


**Fig. A.3** Snapshots of depth averaged wave- and tide-induced flow speed during the calibration period with the initial bathymetry (a) and the bathymetry after the smoothing process (b).



## Appendix B – First author papers

---

This appendix consists of the first author published works related to the content of the thesis. Publications are listed in chronological order and include Refereed Journal papers and Refereed Conference Proceedings.

B1. **N.G. Valiente**, G. Masselink, T. Scott, D. Conley. Depth of Closure Along an Embayed, Macro-Tidal and Exposed Coast: a Multi-Criteria Approach. Proceedings Coastal Dynamics, ASCE, Helsingor, Denmark, Paper No. 185, 1211-1222, June 2017.

B2. **N.G. Valiente**, G. Masselink, T. Scott, D. Conley, R.J. McCarroll, 2019. Role of waves and tides on depth of closure and potential for headland bypassing, *Marine Geology* 407, 60-75. <https://doi.org/10.1016/j.margeo.2018.10.009>.

B3. **N.G. Valiente**, G. Masselink, R.J. McCarroll, T. Scott, M. Wiggins, 2019. Multi-annual embayment sediment dynamics involving headland bypassing and sediment exchange across the depth of closure, *Geomorphology*, 314, 48–64. <https://doi.org/10.1016/j.geomorph.2019.06.020>.

B4. **N.G. Valiente**, R.J. McCarroll, G. Masselink, T. Scott, D. Conley, E. King. Circulation and sediment fluxes on a macrotidal, exposed and embayed coastline. Proceedings Coastal Sediments, ASCE, Florida, USA, May 2019.

## DEPTH OF CLOSURE ALONG AN EMBAYED, MACRO-TIDAL AND EXPOSED COAST: A MULTI-CRITERIA APPROACH

Nieves Garcia Valiente<sup>1</sup>, Gerd Masselink<sup>2</sup>, Tim Scott<sup>3</sup> and Daniel Conley<sup>4</sup>

### Abstract

The concept of depth of closure, denoted by *DoC*, is of fundamental importance in evaluating coastal sediment budgets, investigating shoreface morphodynamics, and in many coastal engineering applications. This key concept has been fully described in the literature, providing several approaches for its identification and parameterisation, but is not straightforward to apply to alongshore non-uniform macro-tidal coastlines. The overall objective of the present research is to apply different criteria to identify the active zone in the nearshore system, using as a study site the embayed, macro-tidal and high-energy coastline of North Cornwall and Devon (United Kingdom). Different approaches are implemented to identify the depth of closure, and theoretical and observational time-dependent interpretations are applied to assess *DoC* at the medium-term and on the regional scale.

**Key words:** depth of closure, shoreface, bed shear stress, extreme storms

### 1. Introduction

The concept of depth of closure (hereafter abbreviated to *DoC*) is of fundamental importance for the coastal engineering and management community. Indeed, the *DoC* is essential in many areas, e.g., for evaluating sediment budgets, investigating shoreface morphodynamics, identification of the active zone for beach nourishment design and dredge disposal, and for modelling coastal evolution. At some point offshore, hydrodynamic processes on the seabed will be sufficiently weak that depth changes over time are insignificant for a given purpose; the depth at this location is denoted as depth of closure (*DoC*), and is the subject of this paper. Of course, the definition of ‘insignificant’ is specific to the purpose, and thus different *DoC* criteria may be used to define the corresponding closure point. Most commonly, *DoC* is considered as the seaward limit of significant depth change for a specific period of time (Nicholls et al., 1998a, b). Thus, *DoC* is a morphodynamic boundary separating a landward active region, from a seaward inactive region (Hinton and Nicholls, 1998). Other authors consider the *DoC* similar to the depth beyond which wave-driven sediment transport is insignificant, and the term ‘depth of no motion’ is more appropriate (Phillips and Williams, 2007).

Several approaches have been pursued during the last four decades to estimate and quantify *DoC*. These can be synthesized in methods based on: wave characteristics (Hallermeier, 1981; Birkemeier, 1985; Capobianco et al., 1997); morphological data defining an envelope of variation that declines with depth (Hinton and Nicholls, 1998; Kraus et al., 1998; Nicholls et al., 1998a, b; Hartman and Kennedy, 2016; Ortiz and Ashton, 2016); and observations of sediment texture in sedimentary sequences (Roy and Thom, 1981; Thielert et al., 2001; Peters and Loss, 2012). Historically, *DoC* was estimated using profile comparisons as this enables direct estimation of the point at which no significant changes on the profile are detected, where ‘significant’ generally relates to bed-level change larger than the detection limit. This traditional method requires an extended dataset which is time-consuming and relatively expensive to obtain; therefore, direct

---

<sup>1</sup>School of Biological and Marine Sciences, Plymouth University, Drake Circus, PL4 8AA, Plymouth, UK.

nieves.garciavaliente@plymouth.ac.uk

<sup>2</sup>g.masselink@plymouth.ac.uk

<sup>3</sup>timothy.scott@plymouth.ac.uk

<sup>4</sup>daniel.conley@plymouth.ac.uk

estimates of *DoC* are only available from a small number of sites. The challenge in accurately quantifying *DoC* motivated the development of formulations to estimate *DoC* based on wave hydrodynamics (and sediment characteristics). Under the assumption that only the most energetic (i.e., largest) waves cause sediment transport out to the closure depth, Hallermeier (1978) developed an empirical approach to define two limits on the beach profile based on the activity experienced by the seabed: an inner and outer *DoC*. The inner limit  $DoC_1$  represents the limit of significant morphological change and is defined as

$$DoC_1 = 2.28 H_{12,t} - 68.5 \left( \frac{H_{12,t}^2}{gT_t^2} \right) \quad (1)$$

where  $DoC_1$  is the predicted depth of closure over  $t$  years referenced to Mean Low Water (Hinton and Nichols, 1998);  $H_{12,t}$  is the non-breaking significant wave height that is exceeded 12 hours over  $t$  years;  $T_t$  is the associated wave period; and  $g$  is the acceleration due to gravity. The outer limit  $DoC_2$  denotes the limit of the shoal zone, representing the depth of no motion, and follows the expression

$$DoC_2 = (\overline{H_{s,t}} - 0.3\sigma_s) \overline{T_{s,t}} \left( \frac{g}{5000D_{50}} \right)^{0.5} \quad (2)$$

where  $\overline{H_s}$  is the annual mean significant wave height,  $\sigma_s$  is the associated standard deviation,  $\overline{T_s}$  is the average significant wave period, and  $D_{50}$  is the grain size (in m). Both Eq. 1 and Eq. 2 have been shown to provide an accurate depth of closure on micro-tidal, wave-dominated, sandy coasts (Nicholls et al., 1996, 1998a, b). In the case of macro-tidal beaches, these depths should be considered relative to the average low spring tide level (Nicholls et al., 1998a, b). Although wave-based formulations are a common and widely-accepted approach to estimate *DoC*, it is appropriate to evaluate their usefulness in areas where geological control, as well as other hydrodynamic processes such as tidal currents, play an important role in terms of sediment dynamics on the shoreface.

Here, we apply a multiple-criteria approach to estimate *DoC* for the embayed, macro-tidal and high-energy coast of North Cornwall and Devon, described in Section 2. In Section 3, we estimate *DoC* based on morphological and sedimentological observations, and relate these to the wave-based theoretical approaches proposed by Hallermeier (1981) and Kraus et al. (1999). As the *DoC* concept aims to provide a limit for the active zone in the nearshore system, we then combine the methods to estimate *DoC* with wave-induced bed shear stresses modelled across our study domain. The modelled bed shear stresses are computed using the extreme wave conditions that define *DoC* to help understand the sediment movement limits (sediment motion, ripple formation and ripple destruction) within our study area. In Section 4, we explore the results of the different *DoC* formulations and discuss its replicability and application for geologically-constrained coastal areas. Finally, conclusions are presented in Section 5.

## 2. Study area

The North coast of Cornwall and Devon is located in the southwest of England (United Kingdom). The physiography of this coast can be considered as highly diverse, combining high hard rock cliffs with relatively short (< 5 km) embayed beaches, often backed by dune systems and cliffs, and separated by rocky headlands and small estuaries (Buscombe and Scott, 2008). The medium resistance to erosion of the cliffs combined with the main phases of transgression have resulted in a large proportion of embayed beaches that cover a wide spectrum from reflective to dissipative morphodynamic conditions. The configuration of the inner shelf is very diverse and includes large and deep bays with several beaches/embayments with varying orientations (Region 1 and 2; Figure 1); stretches of coast characterized by a relatively steep and narrow shoreface with shallow and mainly west-facing embayments separated by headlands (Region 3, 4 and 6; Figure 1); and sections with rocky cliffs fronted by sandy beaches, without any clear embayments (Region 5; Figure 1).

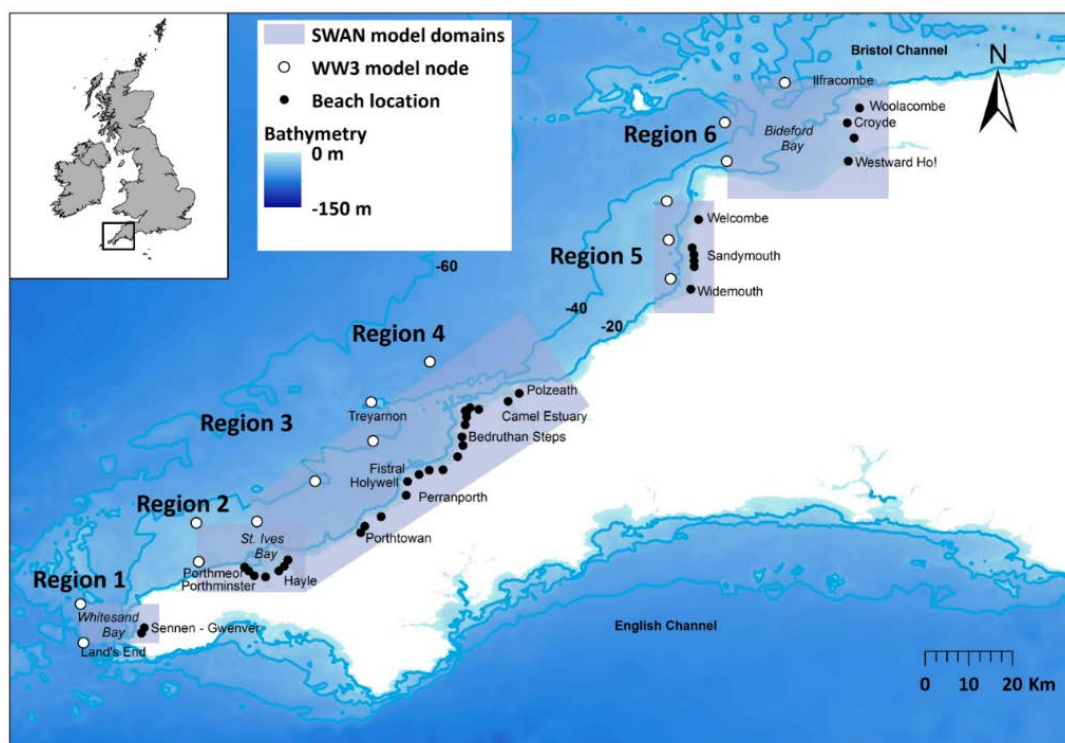


Figure 1. Map of SW England showing location of the six regions (grey shaded rectangles) considered relatively similar in terms of coastal configuration. The black dots in each of the regions represent the different study sites ( $N = 38$ ) and the white circles represent the nodes used for the SWAN wave modelling

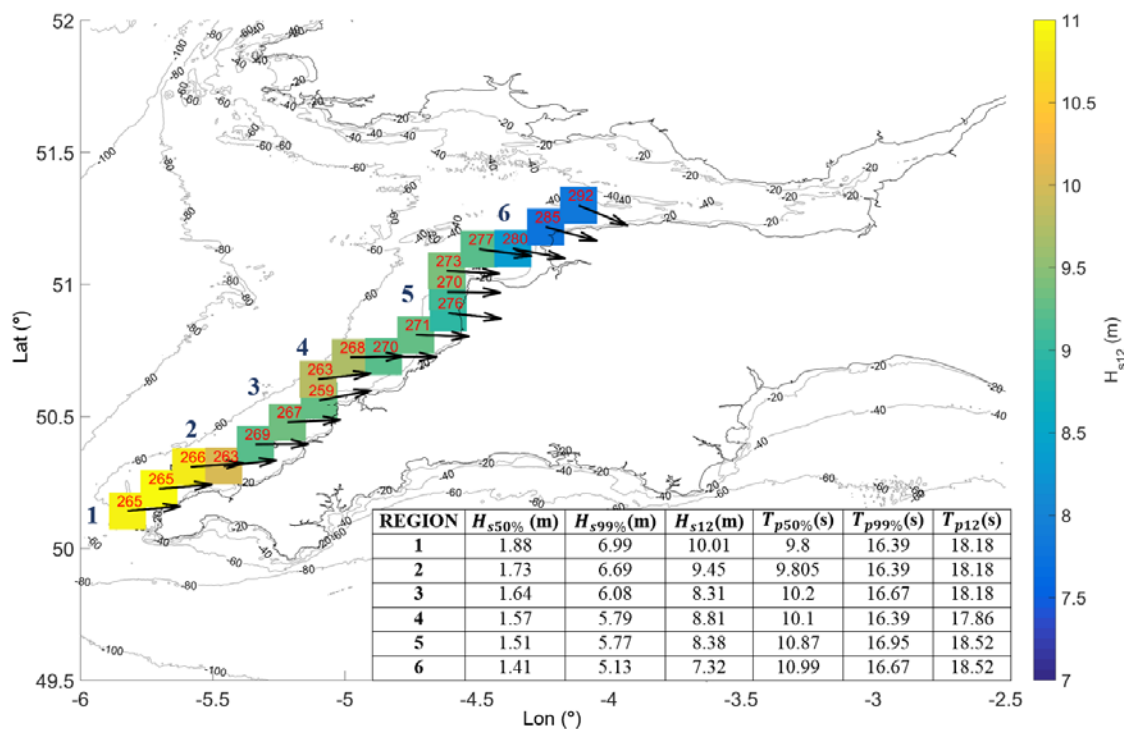


Figure 2. Spatial variability of offshore  $H_s$  exceeded 12 hours a year and direction along the coast of SW England obtained using the Met Office WW3 regional model wave data output from 2012 to 2016. Bottom right table shows deep water wave climate statistics for the selected regions (dark blue numbers indicate regions) from 2012 to 2016

The coastline of SW England is macro-tidal with the mean spring tide range varying between 6 m and 8 m (Scott et al., 2011). Tidal currents with values of  $0.7 \text{ m s}^{-1}$  have been recorded during spring tides near headlands and exceed  $1 \text{ m s}^{-1}$  in the Bristol Channel (unpublished data). Wave statistics for the different regions, based on 4 years (2012–2016) of modelled wave data from the Met Office 8-km WW3 wave model, are summarized in Figure 2. Statistics were computed for each WW3 node and averaged between the relevant nodes for each region of study. Wave conditions along the coast are characterized by energetic waves from the W and WNW quadrants as a result of a combination of Atlantic swell and local wind waves. There is a progressive change in the wave conditions from south to north: modal (50% exceedance) and extreme (99% exceedance) wave heights decrease ( $H_{s50\%}$  from 1.9 m to 1.4 m;  $H_{s99\%}$  from 7.0 m to 5.1 m), and the wave direction changes from W to WNW. The wave period is relatively constant along the coast ( $T_{p50\%} = 10\text{--}11 \text{ s}$ ;  $T_{p99\%} = 16\text{--}17 \text{ s}$ ). For the computation of *DoC*, the wave height that is exceeded 12 hours a year (and its associated period) is required (Eq. 1). These extreme conditions are always associated with W sea states characterized by  $H_{s12}$  from 10.0 m in the south to 7.3 m in the north, with a similar period of  $T_{p12} = 18 \text{ s}$  along the coast (Figure 2).

### 3. *DoC* estimation

There are numerous approaches for estimating *DoC*. Here we focus on those based on wave hydrodynamics as well as morphological observations covering a total of 5 criteria to identify *DoC* (Figure 3). The 4-year modelled wave data time series was used to extract mean and extreme wave conditions to compute inner (Eq. 1) and outer (Eq. 2) *DoC* based on the wave-based formulations of Hallermeier (1979, 1981).  $H_{s,12}$  and its associated  $T_{p,12}$  were transformed to shallow waters using SWAN and  $DoC_1$  was calculated applying Eq. 1. Following Soulsby (1997), the transformed wave conditions were also used to compute the spatial distribution of the bed shear stress induced by the most extreme wave condition ( $H_{s,12}$  and  $T_{p,12}$ ). These were used to identify the depth boundaries where the modelled bed shear stress exceeds critical bed shear stress required for sediment transport and bedform activity. All approaches were applied to the six different regions shown in Figure 1, covering a total of 38 beaches (25 low tide embayments, LTEs) and 164 representative cross-shore profiles.

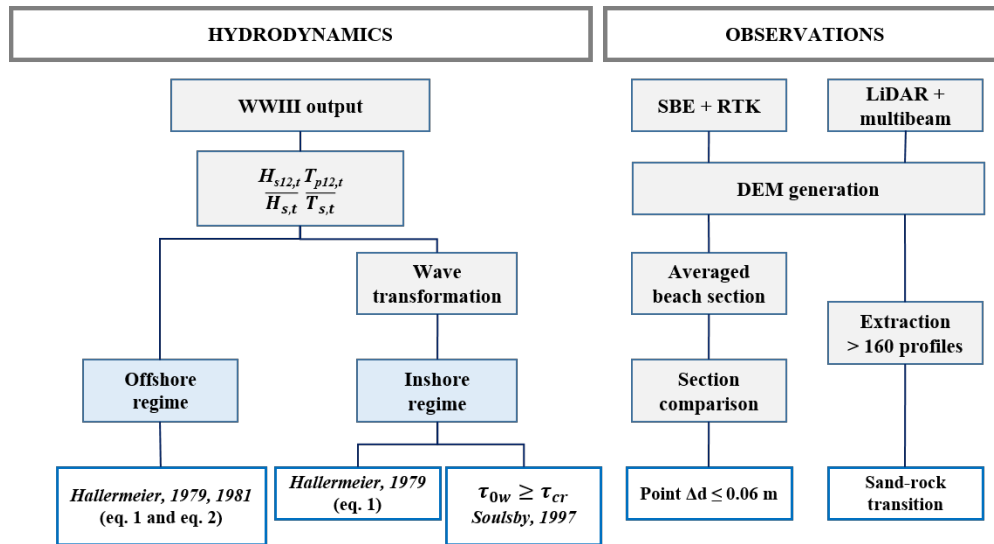


Figure 3. Flow diagram of research methodology of the *DoC* identification

For the application of the observational approaches we use 2 different datasets: (1) bathymetry data (provided by the United Kingdom Hydrographic Office, UKHO) for the offshore profile and LiDAR data (provided by Plymouth Coastal Observatory) for the upper beach covering the entire SW coast; and (2) seasonal single beam and RTK survey datasets from 2007 to 2016 for the beach of Perranporth (Region 3).

In both cases, the datasets were merged to produce different Digital Elevation Models (DEM). The DEM of the SW was used to extract 164 profiles (up to -30 m ODN) representative of the different study sites, where the transition point between sand and rock was identified based on the smoothness and/or the break in the shape of the shoreface profiles. Perranporth DEMs were used to develop profile comparison, to enable identification of the point at which morphological change can be considered insignificant ( $\Delta d \leq 0.06$  m). A flow diagram that synthesizes the methodology followed to develop the study is presented in Figure 3.

Four years (2012–2016) of modelled wave data output from the 8-km resolution regional wave forecast model (based upon the NCEP community model WAVEWATCH III, WW3) (see Figure 1 for WW3 output locations) was used to analyze temporal and spatial variability of wave climate along the coast (presented in Section 2). This wave data series includes the winter of 2013–2014, which represents the most energetic winter over the last 7 decades (Masselink et al., 2015), making the model output suitable to estimate  $DoC$ . Modelled wave data was used to compute Hallermeier's wave-based formulations (Eqs. 1 and 2) applying the extreme (Eq. 1) and mean (Eq. 2) regime statistics extracted from each relevant WW3 node. Both  $DoC_1$  and  $DoC_2$  were computed for the total time series ( $t = 4$  years), as well as independently for each of the years ( $t = 1$  year) and then averaged ( $\langle DoC_1 \rangle$  and  $\langle DoC_2 \rangle$ ).

Offshore wave conditions are not necessarily representative of inshore wave conditions within deep embayments and/or on coastlines that do not face into the prevailing wave direction. Therefore, the  $DoC$  computed using these offshore conditions may not be appropriate and a wave refraction model was used to transform offshore wave conditions to the nearshore. For each of the six regions the modelled wave data were ordered into seven different wave direction classes: 165–195°, 195–225°, 225–255°, 255–285°, 285–315°, 315–345° and 345–15°. For each of these classes, the wave heights were ranked, and the  $H_{s12,t}$  and associated  $T_{p12,t}$  were selected (for  $t = 4$  and  $t = 1$  year). The third-generation spectral wave model SWAN (Booij et al., 1999) was used to transform these extreme wave conditions from offshore to inshore. SWAN was set up for five different domains (one for each region, except Regions 3 and 4 which had a shared domain; refer to Figure 1) with a grid resolution of 100x100 m, so wave height values could be allocated to each embayment in the regions. Following Kraus et al. (1998), wave height and the associated period were determined at a nearshore location (from 20 to 12 m depth) and substituted in the wave empirical formulation of Hallermeier (Eq. 1). Maximum values of the maximum  $DoC_1$  for each of the direction classes were selected at these locations. Finally, to obtain a unique  $DoC_1$  and  $\langle DoC_1 \rangle$  value for each embayment,  $DoC$  was alongshore-averaged. In order to reference to the same datum, a correction from MLWS to ODN was applied (based on MLWS for macro-tidal settings).

A more process-based approach to the  $DoC$  concept, as opposed to the parametric approach of Hallermeier (1978, 1981), is to quantify the bed shear stresses  $\tau_{ow}$  on the sea bed under extreme wave conditions and compare these to sediment motion thresholds  $\tau_{cr}$ . The methodology proposed by Soulsby (1997; see pages 65–110) is used here. To compute the potential for wave-induced sediment resuspension, the root-mean square value of the orbital motion velocity

$$U_{rms} = \left( \sum_{i=1}^N U_i^2 \right)^{1/2} \quad (3)$$

was computed using SWAN through the expression

$$U_{rms}^2 = \int_0^{2\pi} \int_0^\infty \frac{\sigma^2}{\sinh(kd)^2} E(\sigma, \phi) d\sigma d\phi \quad (4)$$

where  $d$  is water depth,  $k$  is the wave number,  $\sigma$  is the angular frequency, and  $E(\sigma, \phi)$  is the spectral density. Wave induced shear stress  $\tau_{ow}$  was obtained using the expression

$$\tau_{ow} = \frac{1}{2} \rho f_w U_w^2 \quad (5)$$

where  $f_w$  is the wave friction factor and  $U_w = \sqrt{2} U_{rms}$ . The wave friction factor for turbulent flow depends on the bed roughness ( $z_0 = D_{50}/12$ ) and the semi-orbital excursion ( $A = U_w T/2\pi$ ) as follows

$$f_{wr} = 1.39 \left( \frac{A}{Z_0} \right)^{-0.52} \quad (6)$$

Soulsby (1997) relates sediment motion threshold for a specific seabed with the critical Shields parameter  $\theta_{cr}$  through the expression

$$\tau_{cr} = \theta_{cr} g (\rho_s - \rho) D_{50} \quad (7)$$

where  $\rho_s$  is the sediment density,  $D_{50}$  is sediment size and  $g$  is the gravitational acceleration.

According to Eqs. 6 and 7, initiation of motion, as well as sediment transport, will depend on boundary shear stresses and seabed characteristics. Based on laboratory experiments and observations, Nielsen (1981) argued that the occurrence of bedforms is related to the bed shear stress ( $\tau_{0w}$  or  $\theta$ ) and developed a relation between bedform type and wave energy conditions, expressed as a function of transport stage. Using Grant and Madsen (1982), and considering a seabed composed by medium sand  $D_{50} = 0.3$  mm, the following critical values of the Shields number ( $\theta_{cr}$ ) can be identified: (1) initiation of motion  $\theta_{cr} = 0.048$ ; (2) formation of sharp-crested vortex ripples  $\theta_{cr} = 0.1$ ; transformation from vortex to post-vortex ripples  $\theta_{cr} = 0.2$ ; and transition into a plane bed  $\theta_{cr} = 1$ . Following Eq. 7, wave-induced bed shear stress was computed for each region, and compared with the critical shear stress  $\tau_{cr}$  for the different scenarios.

The final approach to estimating *DoC* involves the comparison of multiple topographic profiles (alongshore-average of 110-m section) collected over several years for the dissipative sandy beach of Perranporth (located in Region 3; refer to Figure 1). This morphological data was generated using combined field measurements of RTK topographic and single beam datasets from 2007 to 2016, providing a time series long enough to obtain a relevant comparison with the wave-based theoretical methods tested.

## 4. Results

### 4.1 Closure depth computed using offshore wave conditions

All *DoC* results computed using offshore waves have been summarized in Figure 4 with the bars comprising the different regions (refer to Figure 1). To be consistent across the different regions, and other studies, the *DoC* values are related to MLWS (application of Eqs. 1 and 2 for macro-tidal coastlines) and then converted to ODN, which is the vertical datum used in the UK (c. 0.2 m above MSL in the SW of England).  $DoC_1$  values decrease from 23.3 m in the south (Region 1) to 18.8 m in the north (Region 6) when the extreme wave condition ( $H_{s,12}$  and  $T_{p,12}$ ) over the 4-year data set is used, but values are c. 4 m less when  $\langle DoC_1 \rangle$  is computed. Values of the outer depth of closure  $DoC_2$  are c. 50% greater than the inner value  $DoC_1$  for all the regions of study, with values decreasing from 50.1 m in the south to 33.6 m in the north and from 47.2 to 30.7 m for  $\langle DoC_2 \rangle$ . The largest closure depths are registered for the 2014 as the largest wave conditions were experienced during this winter. In all cases, depth of closure values ( $DoC_1$  and  $DoC_2$ ) decrease from south to north in response to the associated decrease in the wave conditions (refer to Figure 2).

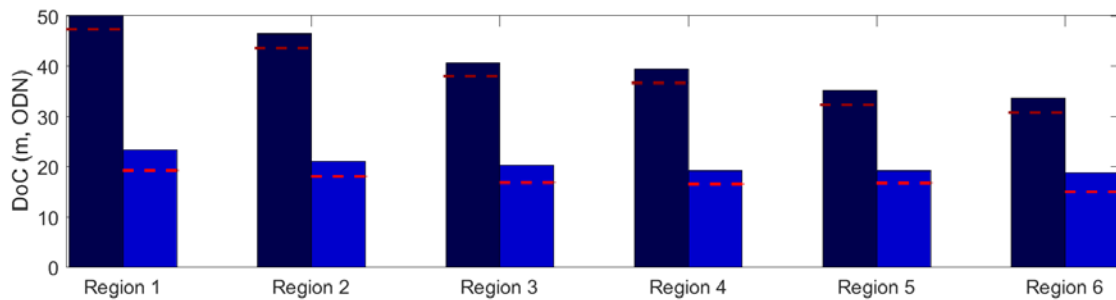


Figure 4. Computed depth of closure at each region obtained by applying the Hallermeier inner and outer *DoC* formulations using offshore WW3 wave conditions. Dark blue bars are  $DoC_2$  values and light blue bars correspond to  $DoC_1$ . Red dashed lines across bars represent  $\langle DoC_2 \rangle$  (dark red) and  $\langle DoC_1 \rangle$  (light red)

#### 4.2 Spatial variability in closure depth due to wave refraction/diffraction in embayments

The offshore wave conditions in c. 40–50 m are not necessarily representative of the inshore wave conditions, particularly for the more embayed locations and/or where the coastline is not directly facing the prevailing wave direction. In this case, wave refraction/diffraction around headlands is likely to generate a significant gradient in the wave height and thus a spatial variability in the depth of closure. The offshore waves were therefore transformed into intermediate and shallow water depth, and, following Kraus et al. (1999), the depth of closure  $DoC_1$  was computed using the wave conditions at different contour lines, in our case for the 12–20 m depth contours (relative to ODN) at 1-m intervals. This yields  $DoC_1$  values that vary both along and across the embayment, and, as an example, the spatial variation in  $DoC_1$  for Region 2 is presented in Figure 5.  $DoC_1$  varies most widely in embayments that display a considerable difference in their orientation and for the case of Region 2 the more exposed sections are characterized by higher  $DoC_1$  values ( $> 10$  m) than the more sheltered sections ( $< 8$  m). The results for Region 2 are representative of other regions with considerable variability in shoreline orientation and/or with important points of refraction (e.g., Regions 4 and 6). Typical values of  $DoC_1$  for the most exposed parts of the coast (Regions 1 and 6, and the north part of Regions 3 and 4) are 12–16 m (relative to ODN), whereas  $DoC_1$  values for the more sheltered parts (Regions 2 and 5, and the south part of Region 6) are typically 6–10 m. Most importantly, the depth of closure values  $DoC_1$  based on inshore wave conditions are significantly smaller than those based on offshore wave conditions.

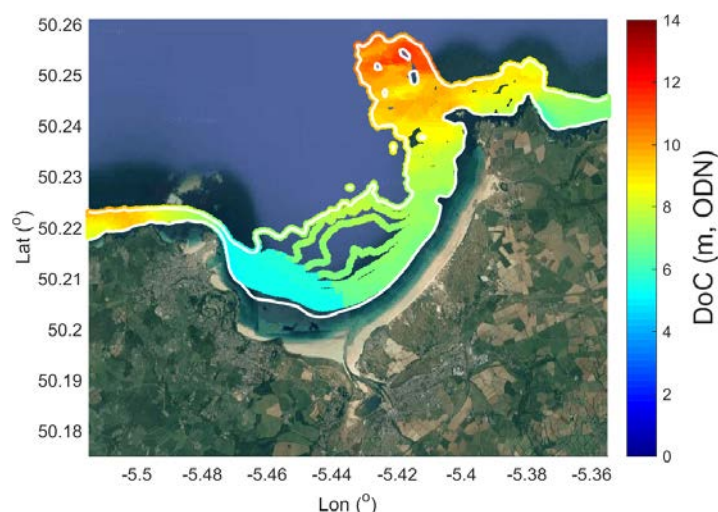


Figure 5. Depth of closure computed following Kraus et al. (1999) in Region 2.  $DoC_1$  has been estimated using the offshore  $H_{s,12}$  and  $T_{p,12}$  propagated to nearshore waters using the SWAN model and subsequently computed at the contour lines from 12 to 20 m depth using the wave-based formulation (Eq. 1) of Hallermeier (1981). The white lines represent the 14- and 20-m contour lines

#### 4.3 Embayment-averaged closure depth

The spatial variability in  $DoC_1$  for each region, such as presented in Figure 5, is considered an improvement to simply using the offshore wave conditions, especially for the more embayed regions. However, having to derive a single depth of closure value from Figure 5 is not practical. To obtain an estimate of the depth of closure for each of the 25 embayments, all  $DoC_1$  estimates along each embayment, computed using Eq. 1 and based on the wave conditions modelled for the 20-m contour line, were averaged and are plotted in Figure 6.  $DoC_1$  values are very variable and range from 8.9 m at Porthmeor and Porthminster (relatively small and NE-facing embayments in Region 2) to 16.2 m in Polzeath and 16.8 m at Bedruthan Steps (larger and W-facing embayments in Region 4). It is evident that exposure plays a key role in explaining the spatial variability in the depth of closure.  $DoC_1$  for the case of Region 3 varies from 13.7 m (embayments in the centre of the region) to 16.8 m in the open W orientated embayments of Region 4. Embayments in Region 2 are affected by an important point of refraction as St. Ives head and present values of  $DoC_1$  increasing from

8.9 to 10.2 m, from W to E, as exposure increases. In Region 5, which is characterised by a relatively straight coastline with no prominent embayments, the closure depth is alongshore uniform and only ranges from 10.4 m to 10.6 m. Generally, the largest within-embayment variability in  $DoC_1$  (length of the red vertical lines in Figure 6) occurs in the larger embayments (e.g., Sennen – Gwenver; Camel Estuary – Polzeath), whereas limited variability in  $DoC_1$  occurs in the smaller embayments (e.g., Porthmeor, Crantock, Porthcothan, most embayments in Region 5).

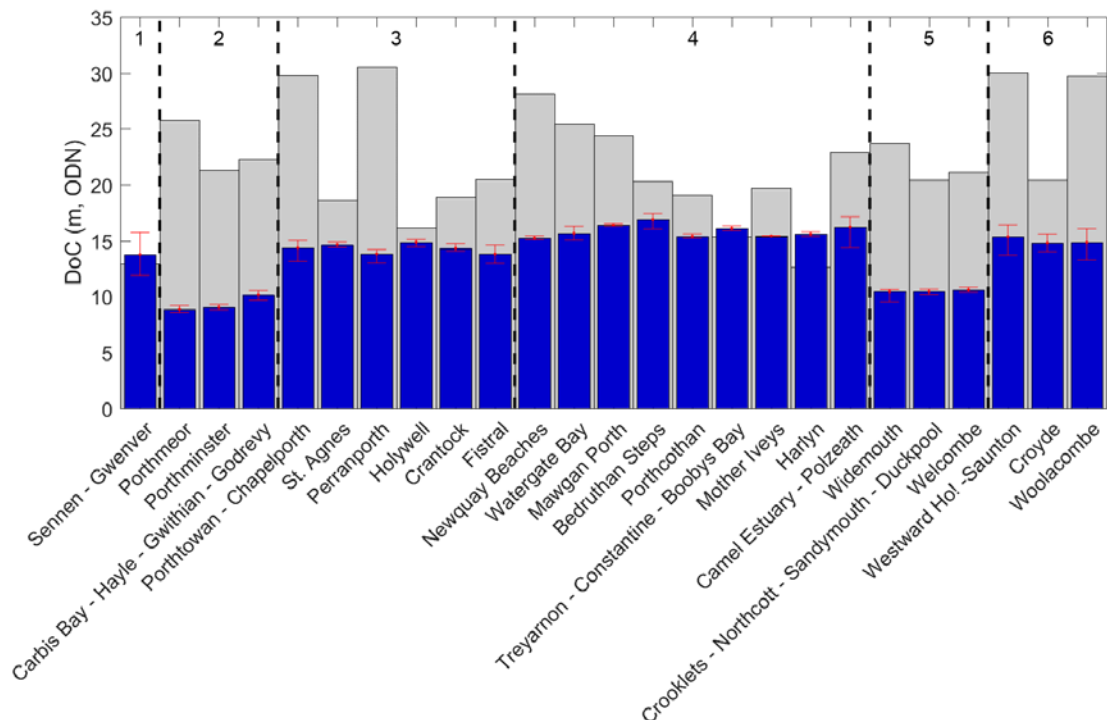


Figure 6. Along-coast variability in depth of closure. Blue bars represent the average  $DoC_1$  for each embayment, computed using the modelled inshore wave conditions at the 20-m contour line and forcing the SWAN wave model with  $H_{s,12}$  and  $T_{p,12}$  derived from the 4-year time-series. Minimum and maximum  $DoC_1$  values for each embayment are represented by the red intervals. Grey bars correspond with the embayment-averaged depth of the transition between sand and rock. Black dashed lines separate the embayments of each region (the number of the corresponding region is indicated in the upper part of the panel)

The average depth of the transition between sand and rock for each of the embayments is also plotted in Figure 6 and comparison between  $DoC_1$  indicates a good correspondence for Sennen Cove, Holywell and Treyarnon; all cases where the rocky platform appears at shallower depths. For the other embayments, the depth of the sand/rock transition, which ranges from 15 m to 30 m, is significantly deeper than the  $DoC_1$ ; frequently more than twice the depth (e.g., for Porthmeor, Perranporth, Widemouth, Woolacombe).

#### 4.4 Observed closure depth at Perranporth

Survey (beach and bathymetry) data from Perranporth (Region 3) is analyzed to derive the actual closure depth for this location. Figure 7 shows the mean and the envelope associated with all alongshore-averaged shoreface profiles for Perranporth collected over the period 2010–2016. The location on the profile with the largest bed-level variability (0.5 m) corresponds with the outer bar region ( $x = 700\text{--}900$  m). The vertical variability decreases to less than 0.06 m (according to Nicholls et al. (1998a) 0.06 m is equivalent to the estimated error in Hallermeier Eq.1) at the depth of -14.8 m (ODN) and this is considered the depth of closure for this embayment.

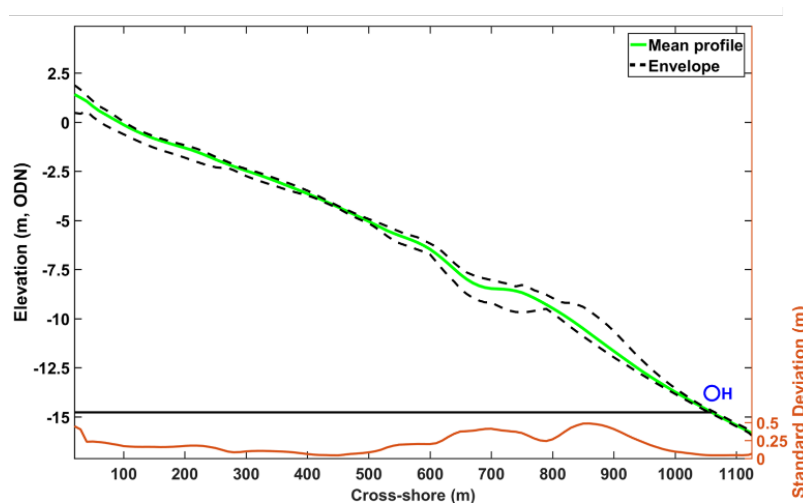


Figure 7. Observed depth of closure estimated for Perranporth beach, north Cornwall, from: (1) the profile envelope (dashed black lines around the mean profile depicted by the green line; brown line representing the width of the envelope) and associated with beach survey data collected from 2010 to 2016. The blue marker 'H' represents the embayment-averaged  $DoC_1$  computed using Hallermeier (1978) at the 20-m contour line and based on the most extreme wave conditions over the 4-year wave time series. The presented profile represents the alongshore-average profile of a 110-m wide section located in the south of the beach

The  $DoC_1$  and  $\langle DoC_1 \rangle$  values based on Eq.1 and offshore wave conditions for Perranporth are 20.2 m and 16.7 m, respectively. When the inshore wave conditions at the 20-m contour are used, the  $DoC_1$  value decreases to 13.8 m, and the  $\langle DoC_1 \rangle$  value to 13.4 m. This suggests that the offshore formulation over-predicts the closure depth.

#### 4.5 Wave-induced bed shear stresses under extreme wave conditions

The output from the SWAN wave modelling for the most extreme wave conditions ( $H_{s,12}$  and  $T_{p,12}$ ) was used to compute the wave-induced bed shear stress  $\tau_{0w}$  across all study regions (Figure 8). Values of  $\tau_{0w} > 5 \text{ N m}^{-2}$  occur at depths between 10 and 20 m in Regions 1, 3 and 6, which are predominantly west-facing embayments with a wide shoreface. Bed shear stress are significantly less ( $\tau_{0w} < 1 \text{ N m}^{-2}$ ) at similar water depth off NE-facing beaches, such as Porthminster and Carbis Bay with a sandy flat shoreface in Region 2 (Figure 8; panel B). Interestingly, there are several other NE-facing embayments (e.g., Mother Ives and Harlyn in Region 4), that have similar values for  $\tau_{0w}$  (c.  $3.5 \text{ N m}^{-2}$  in 28 m water depth) than the exposed west-facing embayments in Regions 1 and 3. This is attributed to the morphological configuration of these embayments, which are fronted by a short rocky shelf (c. 700 m) that limits wave energy dissipation during wave transformation and refraction.

The computed  $\tau_{0w}$  values were compared to the following four sediment transport thresholds: (1) sediment motion  $\tau_{cr} = 0.34 \text{ N m}^{-2}$ ; (2) initiation of vortex ripples  $\tau_{cr} = 0.48 \text{ N m}^{-2}$ ; (3) initiation of post-vortex ripples  $\tau_{cr} = 0.95 \text{ N m}^{-2}$ ; and (4) transition to upper plane bed  $\tau_{cr} = 4.77 \text{ N m}^{-2}$ . As evident from Figure 8, the first three sediment transport thresholds  $\tau_{cr}$  are exceeded in all study region even at depths  $> 50 \text{ m}$ .

The transition to upper plane bed varies considerably across all regions. For Region 1, this threshold occurs in depths  $> 30 \text{ m}$  in the exposed northern part of the embayment, but decreases to c. 12 m at the more sheltered southern end, resulting in an average threshold of 25.5 m (Figure 8, panel A). In Region 2, the location of the upper plane bed threshold is spatially highly variable with significantly smaller values of c. 10 m at the southern end, areas where this threshold is not exceeded (e.g., Porthminster and Carbis Bay) and a more exposed section with values  $> 28 \text{ m}$  (e.g., Godrevy and Gwithian). Embayment-averaged values for the transition depth are generally inflated due to the maximum transition depth values associated with the headlands, which often have values of c. 30 m. In the more alongshore-uniform Regions 3 and 4 (Figure 8, panels c and d, respectively), the isobath for the upper plane bed transition is 23 m and 25 m, respectively. Values for the embayments within these regions are generally around 18–20 m for Region 3 and close to 25 m for Region 4 (similar to the value around headlands), while around the headlands values are  $> 28 \text{ m}$ . In

Region 5, the depth for the transition to upper plane bed is restricted both around headlands and in the beaches to 12 m. Finally, in Region 6 (Figure 8; panel F) the transition depth closely follows the 20-m contour line (Saunton, Croyde and Woolacombe), and decreases to 10 m in the south of the region.

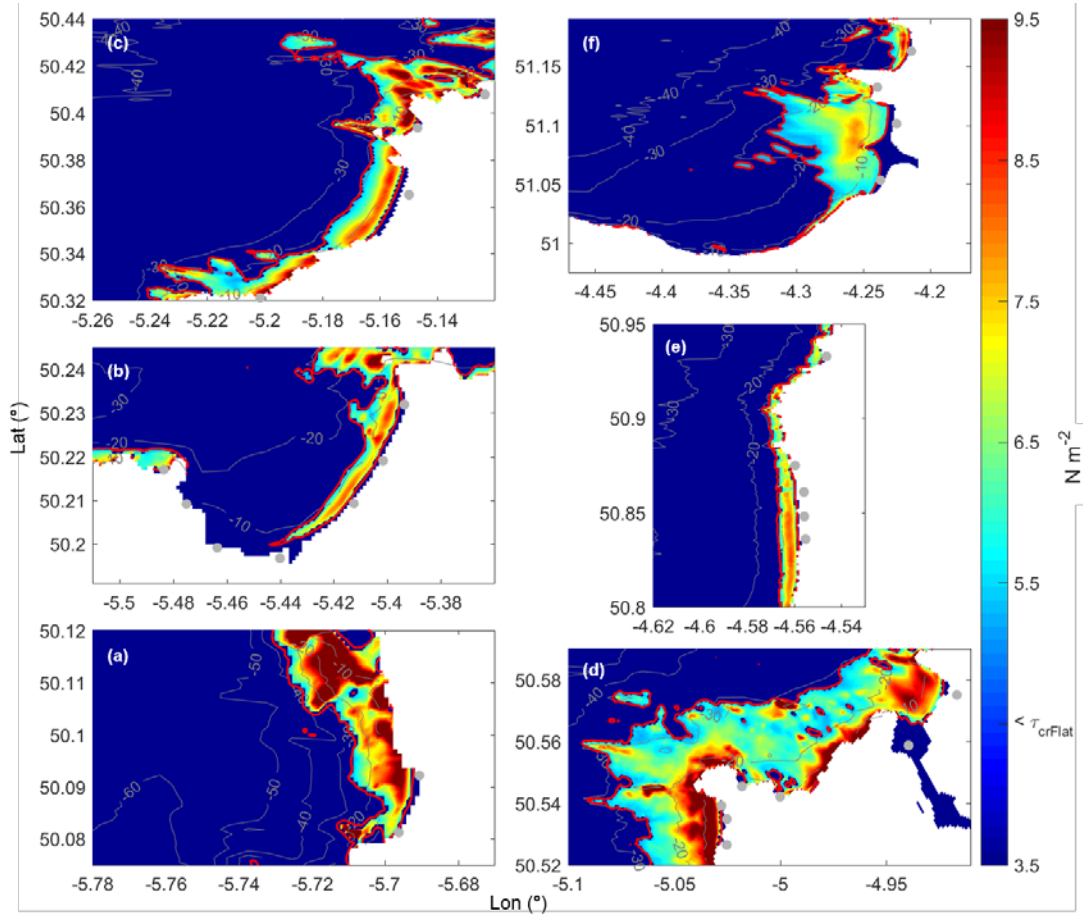


Figure 8. Wave-induced bed shear stress  $\tau_{0w}$  computed for extreme wave conditions ( $H_{s,12}$  and  $T_{p,12}$ ) for all regions: (a)–(f) represents Regions 1–6. The red line represents the bed shear stress at the transition to upper plane bed conditions ( $\tau_{cr} = 4.77 \text{ N m}^{-2}$ )

The  $DoC_2$  values obtained using the offshore wave conditions (refer to Figure 3) are compared with the region-averaged upper plane bed transition depth. This average transition depth is reasonably representative for Regions 3, 4, 5 and 6, but conceals the large variability between headlands and embayments in Regions 1 and 2 (refer to Figure 8).  $DoC_2$  results range from 50 m (southern region) to 34 m in Region 6, and the region-averaged upper plane bed transition depths are c. 40% smaller (decreasing from 25.5 m in Region 1 to 20 m in Region 6) suggesting that  $DoC_2$  is not representative of the transition to upper plane bed conditions. When  $DoC_2$  is compared with the other three sediment transport thresholds (sediment motion, initiation of vortex ripples and initiation of post-vortex ripples), the results indicate that the initiation of post-vortex conditions corresponds to  $DoC_2$  best, whereas the initiation of sediment motion and formation of vortex ripples occurs at significantly larger water depths than  $DoC_2$ . This suggests that, in our study area,  $DoC_2$  corresponds to the depth at which under extreme wave conditions post-vortex ripples develop and such bedform regime is characterised by significant sediment resuspension.

## 5. Discussion and conclusions

Depth of closure is a key concept to describe shoreface morphodynamics. It varies over time and space, and it is widely used to identify the active zone of the beach-shoreface system. Wave-based empirical models

used to estimate closure depth  $DoC$  are highly dependent on the timescale of interest, and are considered to yield good predictions for a medium-term timescale (1 to 4 years) in open, wave-dominated embayments (Nicholls et al., 1998a). In this study, different wave-based methods were used to compute  $DoC$  and compared with observations along the highly diverse and macro-tidal coast of north Cornwall and Devon. We used a 4-year time series of wave conditions, which included the most energetic winter affecting the coast of SW England (winter 2013/14) since at least 1948; therefore, the predicted  $DoC$  values can be considered to represent at least the decadal time scale.

The analytical model of Hallermeier (1991), expressed by Eq. 1, was applied to the six regions comprising 25 embayments on the north coast of Cornwall. Different approaches were followed in obtaining the closure depth  $DoC_1$ . Inserting offshore wave conditions into Eq. 1, as suggested by Kraus et al. (1998), resulted in  $DoC_1$  values that were 20–50% larger than if inshore wave conditions were used. Using the latter is considered more appropriate along embayed coastlines, especially for sites where headlands are a key factor in controlling the inshore wave conditions (e.g., Porthminster and Carbis Bay in Region 2 and Mother Ivey's and Harlyn in Region 4). However, the closure depth computed using the inshore wave conditions depends on the water depth from which the wave height is extracted: the shallower the depth, the smaller the waves, and the lower the  $DoC_1$  value. The inshore wave height at 20 m water depth was used here. Another consideration is the time period over which to determine the extreme wave conditions. If  $H_{s,12}$  and  $T_{p,12}$  are derived from the complete wave time series (4 years in the present case), the  $DoC_1$  values are c. 4 m larger than if  $\langle DoC_1 \rangle$  is used (yearly-averaged  $DoC_1$  computed using  $H_{s,12}$  and  $T_{p,12}$  for each year in the time series). As the depth of closure concept generally related to shoreface variability over inter-annual to decadal time scale, it seems appropriate to select the longest time series possible to estimate  $DoC_1$ .

The cross-shore distribution of the seabed composition can be used to help identify limits of cross-shore sediment exchange (Roy and Thom, 1981; Thielert et al., 2001; Peters and Loss, 2012). For lack of information on the cross-shore variability in sediment characteristics, we focus here on the transition between sand and rock, based on the shape of the shoreface profile (smooth versus rough). The sand-rock transition depth is not necessarily related to the closure depth, but it can add value when following a multi-criteria approach to determine  $DoC$ , especially where the closure depth obtained from analytical methods is located landward of the sand-rock transition depth. As this was only the case in 3 of the 25 embayments, this suggests that despite the rocky nature of the coastline of North Cornwall, there is sufficient sediment present on the shoreface of most embayments to enable development of an equilibrium shoreface profile.

Morphological methods based on observations are the most accurate tool to estimate  $DoC$ ; however, they are logistically demanding to obtain, requiring both time and considerable funding, restricting its application to a reduced number of sites. For the case of Perranporth, our results show a most active zone of up to 14–15 m water depth (relative to ODN). It is concluded that the value for the closure depth for Perranporth is correctly estimated using Hallermeier (1991) Eq. 1 provided: (1)  $H_{s,12}$  and  $T_{p,12}$  are computed using the wave time series that encompasses the shoreface monitoring period; (2) the offshore wave conditions are transformed into intermediate/shallow water; (3) the modelled inshore sea state at the 20-m contour line in several representative profiles of the embayment is inserted into Eq. 1 and the embayment-averaged closure depth is computed; and (4) the depth of closure value is considered relative to MLWS and then corrected to the survey datum (ODN for the case of the UK).

Bed shear stress studies contribute to a better understanding of the depth of closure as a theoretical boundary for sand motion, corresponding to a seaward limit of the 'wave-constructed' profile (Hallermeier, 1981) and thus the outer depth of closure limit  $DoC_2$ . Bed shear stress values at the transition to upper plane bed occur at depths  $> 20$  m in most cases and are c. 40% smaller than the  $DoC_2$  values computed using Eq. 2. The wave orbital velocities across the shoreface computed for most extreme waves suggest that under such conditions most of the embayments experience extreme sediment motion up to large depths. Computed bed shear stresses suggest that along the north coast of Cornwall, extreme wave events induce sediment entrainment, vortex ripple formation and post-vortex ripple formation, and thus sediment resuspension, across the entire study domain at water depths  $> 40$  m. The transition to upper plane bed occurs around the 20–26 m isobaths for the most exposed embayments (e.g., Regions 1 and 3), suggesting that wave currents during an event of the characteristics of the 2013/14 winter storms can induce sediment transport well seaward of the limit where calm conditions will be able to return the sediment as part of the recovery process. Recent research into this topic suggests that some of the embayments along the north coast have recovered  $> 50\%$  since the 2013/2014 storms, while other embayments, such as Sennen (Region 1) and Perranporth (Region 3) have recovered significantly less (Burvingt et al., 2017). The considerable depth at which wave-

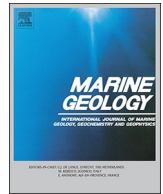
driven sediment transport is likely under extreme wave conditions, easily > 40 m depth and a considerable distance seaward of the headlands, also challenges the notion of embayments being closed sediment cells in the SW of England as suggested by May and Hansom (2003). A re-evaluation of the concept of closed embayments is especially appropriate for the north Cornish coastline as, in addition to the wave-exposed setting, maximum tidal currents around headlands are considerable (c. 0.7 m/s); therefore, wave/current interaction under energetic waves during spring tide conditions are expected to result in significant sediment fluxes at water depths > 20 m.

### Acknowledgements

This work was supported by UK Natural Environment Research Council (NE/M004996/1; BLUE-coast project).

### References

- Birkemeier, W.A., 1985. Field data on seaward limit of profile change, *Journal of Waterway, Port, Coastal and Ocean Engineering*, 111(3): 598-602.
- Booij, N., Ris, R.C. and Holthuijsen, L.H., 1999. A third generation wave model for coastal regions, part I, model description and validation, *Journal of Geophysical Research*, 104(C4): 7649–7666.
- Burvingt, O., Masselink, G., Russell, P., Scott, T., 2017. Beach evolution and recovery from a sequence of extreme storms, *Proceedings Coastal Dynamics*, ASCE, Helsingor, Denmark, this volume.
- Buscombe, D.D. and Scott, T., 2008. The coastal geomorphology of north Cornwall, Wave Hub impact on seabed and shoreline processes report, Tech. rep.
- Capobianco, M., Larson, M., Nicholls, R.J. and Kraus, N.C., 1997. Depth of closure: a contribution to the reconciliation of theory, practice and evidence, *Proc. Coastal Dynamics '97*, Plymouth, ASCE, New York: 506-515.
- Grant, W.D., and Madsen, O.S., 1982. Movable bed roughness in unsteady oscillatory flow, *J. Geoph. Res.*, 87: 469-481.
- Hallermeier, R.J. 1978. Uses for a calculated limit depth to beach erosion, *Proc. 16th Coastal Engineering*, ASCE, Hamburg, 1493–1512.
- Hallermeier, R.J., 1981. A profile zonation for seasonal sand beaches from wave climate, *Coastal Engineering*, 4: 253-277.
- Hartman, M. and Kennedy, A.B., 2016. Depth of closure over large regions using airborne bathymetric lidar, *Marine Geology*, 379: 52-63.
- Hinton, C. and Nicholls, R. J., 1998. Spatial and Temporal Behaviour of Depth of Closure Along the Holland Coast, *26th International Conference on Coastal Engineering*, 2913-2925.
- Kraus, N.C., Larson, M. and Wise, R., 1998. Depth of closure in beach fill design, *Proceedings 12th National Conference on Beach Preservation Technology*, Florida Shore and Beach Preservation Association, 271-286.
- Masselink G., Scott T., Poate T., Russell P., Davidson M. and Conley D., 2015. The extreme 2013/2014 winter storms: hydrodynamic forcing and coastal response along the southwest coast of England, *Earth Surface Processes and Landforms*, n/a-n/a.
- May, V.J. and Hansom, J.D., 2003. *Coastal Geomorphology of Great Britain, geological Edition*, Joint Nature Conservation Committee, Peterborough, U. K.
- Nicholls, R.J., Birkemeier, W.A. and Lee, G., 1998a. Evaluation of depth of closure using data from Duck, NC, USA, *Marine Geology*, 148 (3-4): 179 - 201.
- Nicholls, R.J., Larson, M., Capobianco, M. and Birkemeier, W. A., 1998b. Depth of closure: Improving understanding and prediction, *Proceedings of the Coastal Engineering Conference*, 3: 2888 - 2901.
- Nielsen, P., 1981. Dynamics and geometry of wave-generated ripples, *J. Geophys. Res.*, 86: 6467 – 6472.
- Ortiz, A.C., Ashton and A.D., 2016. Exploring shoreface dynamics and a mechanistic explanation for a morphodynamic depth of closure, *Journal of Geophysical Research F: Earth Surface*, 121 (2): 442-464.
- Peters, S.E. and Loss, D.P., 2012. Storm and fair-weather wave base: A relevant distinction? *Geology*, 40(6): 511 - 514.
- Roy, P.S. and Thorn, B.G., 1981. Late quaternary marine deposition in New South Wales and southern Queensland – An evolutionary model, *Journal of the Geological Society of Australia*, 28: 417-489.
- Scott, T., Masselink, G. and Russell, P., 2011. Morphodynamic characteristics and classification of beaches in England and Wales, *Marine Geology*, 286 (1-4): 1 - 20.
- Soulsby, R.L., 1997. *Dynamics of marine sands: a manual for practical applications*, Thomas Telford, London.
- Thieler, E.R., Pilkey, O.H., Clearly, W.J. and Schwab W.C., 2001. Modern sedimentation on the shoreface and inner continental shelf at Wrightsville Beach, North Carolina, USA, *J. Sediment. Res.*, 71(6): 958-970.



# Role of waves and tides on depth of closure and potential for headland bypassing

Nieves G. Valiente\*, Gerd Masselink, Tim Scott, Daniel Conley, Robert Jak McCarroll

Coastal Processes Research Group, School of Biological and Marine Sciences, Plymouth University, PL4 8AA, UK

## ARTICLE INFO

Editor: Edward Anthony

### Keywords:

Nearshore sediment transport  
Bed shear stress  
Depth of closure  
Headland bypassing  
Macrotidal  
Embayments

## ABSTRACT

Depth of closure is a fundamental concept used to define the seaward extent of a morphodynamically active shoreface at a particular temporal scale. The estimation of this limit in relation to the depth in front of the bounding headlands along embayed coastlines allows questioning whether embayments, often deemed closed sediment cells, experience more headland bypassing than expected. Wave-based parameterisations developed for microtidal beaches are most widely used to estimate closure depth; however, a re-evaluation of the concept for shorefaces influenced by geological control (presence of headlands and/or bedrock) and strong tidal currents is appropriate. Here, we use the macrotidal, embayed and high-energy coastline of SW England to identify the 'active' nearshore limits with a multi-method approach that includes observations of shoreface morphology and sedimentology, offshore/inshore wave formulations and bed shear stress computations. We identify the basal limit of 'significant' (i.e., 0.14 m) morphological change (Depth of Closure; *DoC*) and a maximum depth of extreme bed activity and sediment transport (Depth of Transport; *DoT*). Observations of *DoC* correspond closely to the values predicted by existing formulations based on inshore wave conditions (10–15 m for the study area; relative to mean low water spring water level in this case). The computed *DoT*, represented by the upper-plane bed transition attained under extreme conditions, exceeds 30 m depth in the study area. The significant implication is that, even though many headlands appear sufficiently prominent to suggest a closed boundary between adjacent embayments, significant wave- and tide-driven sediment transport is likely to occur beyond the headland base during extreme events, especially at low water levels. The maximum depth for significant sediment transport (*DoT*) was computed across a broad wave-current parameter space, further highlighting that tidal currents can increase this closure depth estimate by ~10 m along macrotidal coastlines, representing a 30% increase compared to tideless settings. This work illustrates the importance of tidal currents in depth of closure calculations and challenges the notion that embayed beaches are generally closed cells, as headland bypassing may be more wide spread than commonly assumed along exposed coastlines globally.

## 1. Introduction

Delineation of the active shoreface has long been a subject of investigation for coastal scientists and engineers (Hallermeier, 1978; Birkemeier, 1985; Wright et al., 1991; Wright, 1995; Ortiz and Ashton, 2016). The processes leading to sediment exchange across the shoreface, and the estimation of the seaward extent (depth) of those processes, are relevant to a wide range of coastal topics, including evaluation of sediment budgets (Hands and Allison, 1991; Capobianco et al., 2002), investigation of shoreface morphodynamics (Tanaka and Van To, 1995; Ortiz and Ashton, 2016), identification of the active zone for beach nourishment design (Hinton and Nicholls, 1998; Phillips and Williams, 2007; Aragones et al., 2016), computation of the long-term

stability of beaches (Stive et al., 1992; Marsh et al., 1998), modelling coastal evolution (Hanson and Kraus, 1989; Larson and Kraus, 1992) and assessing the impact of sea-level rise on coasts (Stive et al., 1991; Rosati et al., 2013). Recognising the importance of appropriately framing the shoreface extent affected by intense bed activity, this offshore limit, denoted as 'depth of closure', remains a contentious subject in coastal science (Stive et al., 1991; Stive and de Vriend, 1995; Hinton and Nicholls, 1998; Nicholls et al., 1998b; Robertson et al., 2008; Ortiz and Ashton, 2016). Despite the availability of relatively robust near-shore sediment transport models, driven by appropriate hydrodynamic forcing (waves and tides), the concept also remains relevant, especially where resources to develop such numerical models are not available, for example due to lack of reliable bathymetric data.

\* Corresponding author at: Reynolds Building, Drake Circus, Plymouth, Devon PL4 8AA, UK.  
E-mail address: [nieves.garciavaliente@plymouth.ac.uk](mailto:nieves.garciavaliente@plymouth.ac.uk) (N.G. Valiente).

The term ‘depth of closure’, hereafter *DoC*, is a theoretical concept used to limit two zones of different morphodynamic activity along the beach profile at short- and medium-term time scales (1–10 years): the *upper* shoreface is described as the area where significant changes on the beach profile are detected, while the *lower* shoreface is the area extending from the limit of significant change to the wave base where morphological change is negligible (or within the uncertainty limits), but intense bed agitation may occur under energetic wave conditions. The transition between the upper and lower shoreface is known as the morphological depth of closure (*DoC*) and the seaward extent of the lower shoreface is referred to as the maximum depth of significant sediment transport (*DoT*). Hence, *DoC* represents a morphodynamic boundary separating a landward, morphodynamically active region (Hallermeier, 1981; Hinton and Nicholls, 1998; Nicholls et al., 1998b), from a seaward region that is generally considered morphodynamically non-active. Of course, the definition of ‘significant change’ is ambiguous and depends on the time scale of consideration and the methods of morphological change detection; thus, different closure criteria may be used to define the corresponding closure points.

Embayed beaches are often considered closed systems, but even bounding headlands that appear sufficiently prominent to restrict headland bypassing under modal conditions, can ‘leak’ under extreme storms. Estimating the limit of the active shoreface under storm conditions in front of headlands allows identifying whether related embayments are open or closed sediment cells. Additionally, strong tidal currents associated with macrotidal settings are expected to move the closure limit of the active shoreface seaward. Therefore, where geological controls and strong tidal currents influence shoreface configurations, a re-evaluation of the ‘active’ nearshore limit seems appropriate. Here, we use the embayed, macrotidal and high-energy coasts of north Devon and Cornwall (UK) as a natural field laboratory to identify this limit using a multicriteria approach that includes: (1) observations of shoreface topography and sedimentology; (2) classic wave-based *DoC* parameterisations; and (3) bed shear stress computations. We focus on the investigation of the role of headlands in influencing *DoC* and *DoT*, and thus the potential for headland bypassing, thereby improving our understanding of shoreface dynamics on wave- and tide-dominated coasts.

The outline of this paper is as follows. Section 2 contextualizes the depth of closure concept and methods for its estimation employed to date. Section 3 presents a regional description of the North coast of Cornwall and Devon, as well as the prevailing dynamics affecting shoreface configuration along the coast. In Section 4, we present the methods for a multicriteria approach used to estimate *DoC* based on observations (Section 4.3.1), previously established wave-based parameterisations (Section 4.3.2) and modelling of wave- and current-induced bed shear stress (Section 4.3.3). In Section 5, results from the different approaches are explored. A discussion of the replicability and application of the different approaches for geologically-constrained and macrotidal coastal areas is presented in Section 6, followed by the conclusions of this research in Section 7.

## 2. Background

Several approaches have been pursued over the past four decades to estimate the morphological depth of closure. These can be synthesized in: (1) direct methods based on observations of morphological data (Hinton and Nicholls, 1998; Kraus et al., 1998; Nicholls et al., 1998b; Hartman and Kennedy, 2016); and (2) indirect methods that predict this depth based on wave hydrodynamics (Hallermeier, 1978, 1981; Roy and Thom, 1981; Birkemeier, 1985; Capobianco et al., 1997; Peters and Loss, 2012). Direct estimations are based on morphological data defining an envelope of variation that decreases with depth (Hinton and Nicholls, 1998; Kraus et al., 1998; Nicholls et al., 1998b; Hartman and Kennedy, 2016). Historically, *DoC* has been estimated using profile comparison as it is the most reliable method to estimate the point beyond which no significant changes on the profile are detected, where

‘significant’ generally relates to bed-level change larger than the detection limit. This traditional method requires an extended dataset (collected over several years at least) with repeated surveys along cross-shore transects of the beach, which ultimately makes it time-consuming and relatively expensive to obtain; therefore, direct estimates of *DoC* are only available from a small number of sites.

The challenge in accurately quantifying *DoC* motivated the development of indirect methods of prediction based on wave hydrodynamics and sediment characteristics affecting the shoreface. Examples of such indirect methods include wave-based formulations (Hallermeier, 1978, 1981; Birkemeier, 1985; Capobianco et al., 1997), energetics-based sediment transport methods (Ortiz and Ashton, 2016) and identification based on observations of sedimentary sequences (Roy and Thom, 1981; Nichols, 1999; Peters and Loss, 2012), as well as of abrupt changes in the textural composition of the seabed (e.g., Potter, 1967; Chesher et al., 1981; Larson, 1991; Work and Dean, 1991; Thielert et al., 2001).

Sedimentological approaches quantify the transition limit of areas with different wave activity as a particular change in the vertical stratigraphic sequence (sedimentary structures and bedforms); for example, hummocky stratification develops below normal fair-weather wave base during conditions analogous to the transition to upper plane-bed in unidirectional flow (Dott and Bourgeois, 1982). Studies of seabed composition often identify clear variations in texture and/or abrupt differences in sediment size along a beach profile (Potter, 1967; Chesher et al., 1981; Larson, 1991; Work and Dean, 1991). Sedimentological changes are more a reflection of the maximum depth of sediment transport (*DoT*) as both bedforms and sediment texture respond to wave-stirring and tidal current forcing, and they are not necessarily associated with morphological change as delimited by *DoC*.

Wave-based formulations propose different expressions to quantify limits of shoreface activity under the assumption that only the most energetic (i.e., largest) waves cause morphological change out to the closure depth (Hallermeier, 1981; Birkemeier, 1985; Capobianco et al., 1997). Hallermeier (1978, 1981) developed the first empirical approach to estimate the annual depth of closure (*DoC*) and maximum depth of bed activity (*DoC-motion*) on microtidal sandy beaches, based on the activity experienced by the seabed using laboratory experiments. According to these early studies, *DoC* represents the ‘depth of significant morphological change’, and is estimated as:

$$DoC = 2.28 H_{12,t} - 68.5 \left( \frac{H_{12,t}^2}{gT_t^2} \right) \quad (1)$$

where *DoC* is the predicted depth of closure over *t* years referenced to Mean Low Water (Hinton and Nicholls, 1998),  $H_{12,t}$  is the non-breaking significant wave height that is exceeded for 12 h per *t* years,  $T_t$  is the associated wave period and *g* is the acceleration due to gravity. *DoC-motion* (Hallermeier, 1981) represents the limit for sediment motion and follows the expression:

$$DoC - motion = (\overline{H_{s,t}} - 0.3SD_s) \overline{T_{s,t}} \left( \frac{g}{5000D_{50}} \right)^{0.5} \quad (2)$$

where  $\overline{H_{s,t}}$  is the annual mean significant wave height,  $SD_s$  and  $\overline{T_{s,t}}$  are the associated standard deviation and average period of the significant wave height, respectively, and  $D_{50}$  is the median grain size.

Later, Birkemeier (1985), found that the expression for *DoC* (Eq. (1)) proposed by Hallermeier (1978) over-predicted observations by about 25% (Nicholls et al., 1998a) and proposed an adjusted expression for *DoC* of the form:

$$DoC = 1.75 H_{12,t} - 57.9 \left( \frac{H_{12,t}^2}{gT_t^2} \right) \quad (3)$$

Other authors proposed alternative formulations, simplifying the expression proposed by Hallermeier (1978). As an example, Capobianco et al. (1997), suggested an expression for *DoC*, which is

only a function of the non-breaking significant wave height exceeded for 12 h:

$$DoC = KH_{12,t}^{0.67} \quad (4)$$

where the constant  $K$  has value 3.4, 2.8 and 2.1 for a maximum vertical variation in the profile of 0.05, 0.1 and 0.2 m, respectively, over annual to medium temporal scale.

Eqs. (1), (3) and (4) have been shown to provide good predictions of the depth of closure on relatively-exposed, microtidal, sandy coasts. Nicholls et al. (1998a, 1998b) compared 12 years of bathymetric data and nearshore wave statistics from Duck, NC. They showed that Eq. (1) provided conservative estimates of the annual depth of closure values for different closure criteria (maximum vertical variation of 0.06 m, 0.1 m, and 0.15 m), but successfully predicted the closure limit ( $DoC$ ) during erosional events. Later, Robertson et al. (2008) tested Eqs. (2) and (4) using observations of measured changes in the peninsula of Florida and showed that Hallermeier's (1978) wave-based formulation best matched the observations of that area. In all mentioned studies, these formulations were tested on a microtidal coast and they may not necessarily be directly transferable to macrotidal beaches (Nicholls et al., 1998a). According to Hallermeier (1978), the effect of tidal action on Eq. (1) can be accounted for by referencing the depths obtained relative to mean low water (MLW), but this only provides a tidal datum adjustment and does not account for the role of tidal currents.

Although wave-based formulations continue to be a common and widely-accepted approach to predict  $DoC$ , other approaches are appearing in the literature. Robertson et al. (2008) presented the influence of non-erodible beds or hardgrounds on  $DoC$  using airborne bathymetric data, and suggested that this method based on observations is a good approach to follow in areas where the presence of bedrock plays an important role in determining the depth of closure. In addition to the mentioned geological control, other authors have also pointed out to a clear influence of the tidal currents in the estimation of  $DoC$  (Hartman and Kennedy, 2016). Following these more recent suggestions, the usefulness of the wave-based formulations is evaluated here along an area where geological control (presence of bedrock and headlands as attenuation and refraction points), large tidal ranges and strong tidal currents are essential components in explaining sediment dynamics on the shoreface. This provides a novel and updated evaluation of the depth of closure concept emphasizing the role of these in predicting the zone of active sediment transport.

### 3. Study area

The North coast of Cornwall and Devon, Southwest England (UK), extends 200 km from Land's End (SW) to Ilfracombe (NE) (Fig. 1). The coastline comprises high and hard rock cliffs (up to 120 m above sea level), rocky headlands, small estuaries and relatively short sandy embayed beaches (< 5 km), spanning reflective to dissipative conditions (Scott et al., 2011), often backed by dune systems and/or cliffs. The configuration of the shoreface is highly variable (Scott et al., 2011) and includes: (1) large and deep bays with multiple beaches/embayments of varying west to north orientation; (2) steep and narrow shorefaces with shallow and mainly west-facing embayments separated by headlands; and (3) rocky cliffs fronted by sandy beaches, without clear embayments. The average grain size for this coast is 0.3 mm (Prodder et al., 2016). This coast receives a combination of Atlantic swell, primarily from the west to WNW, and local wind waves. A wave height gradient exists from SW to NE (Fig. 1, top panel), with mean significant wave height ( $H_s$ ) decreasing from 1.9 m at Land's End (SW) to 1.0 m in Ilfracombe (NE), with associated peak periods ( $T_p$ ) of 9.8 s and 11.0 s, respectively. The coastline is macrotidal: the largest tides are experienced in the Bristol Channel where the mean spring tidal range (MSR) is 8 m and the smallest tides in the region occur at Land's End (MSR = 5 m).

Along most of the coast, the maximum ebb and flood velocity ranges from 0.1 to 0.4  $\text{ms}^{-1}$  at depths between 10 and 30 m (Fig. 2) with the tidal flows predominantly parallel to the shoreline. The strong flood-ebb asymmetry in the current magnitude during a tidal cycle results in a northward tidal net flux along the coast. At depths exceeding 30 m, the maximum tidal current ranges from 0.3  $\text{ms}^{-1}$  to 0.6  $\text{ms}^{-1}$  in front of the embayments, and significantly increases around the headlands (Fig. 2, right panels), where maximum tidal flows can be of the order of 1  $\text{ms}^{-1}$  (Region 1 at 30 m depth; Fig. 2, bottom right panel) and even exceed 1.2  $\text{ms}^{-1}$  in locations close to the Bristol Channel (e.g., in Region 6 at 30 m depth; Fig. 2, upper right panel). Strong tidal velocities are also observed around headlands in central regions (Region 3–5) with values of flood current higher than 0.4  $\text{ms}^{-1}$  at 20–30 m depth (Fig. 2, middle right panel).

For the analysis, the coastline was divided into six regions (Fig. 1, bottom panel) based on geomorphic and hydrodynamic characteristics (Table 1), and includes 25 individual low tide embayments (LTEs), which are defined as embayed systems that represent a single embayment at low tide, but may be split up into smaller beaches at high tide. Region 1 (Fig. 3a) represents the southernmost area and covers Whitesand Bay, a concave calcareous-sandy wide bay disrupted by a rocky section at 20 m water depth. This region contains the steep and narrow beaches of Sennen Cove and Gwenver (Fig. 3g). Region 2 covers St. Ives Bay (Fig. 3b), a shallow crescentic bay with a wide and flat shoreface (Fig. 3g). Three LTEs are present (Porthmeor, Carbis Bay and Godrevy) with sand present up to 25 m depth. Region 3, from Porthtowan to Fistral, is characterized by wide dissipative sandy beaches embayed by prominent headlands, backed by large dunes and alternating with stretches of rocky sediment-free areas with 50–90 m high cliffs. Six LTEs (including Perranporth, Fig. 3c) with steep to moderate shorefaces are present here. Region 4, from Newquay to Polzeath, is a relatively straight and exposed section of coast, with a sandy layer covering a partially exposed rock platform with headlands acting as constraining points, and with cliffs with heights of 40–60 m. Two types of LTEs are present in Region 4: the first group (Newquay Beaches, Fig. 3d) are crescentic sandy bays, while the second group (Bedruthan Steps, Treyarnon) are narrower (Fig. 3g), coarser, more exposed and straighter. Region 5 is relatively straight and embayments are notably absent (Fig. 3e). This coastline is characterized by narrow and long patches of coarse sand (to –20 m Ordnance Datum Newlyn, ODN; Fig. 3g) constrained by small headlands and a landward cliff. Region 6, from Westward Ho! to Woolacombe, is the northern-most region, with sandy beaches embayed by cliffed rocky headlands (Fig. 3f). Sediment is finer and the shoreface slope is shallower (Fig. 3g) than in the other regions, with sand to –30 m ODN, and with an average distance from the 0 isobath to –30 m ODN of 3600 m for Woolacombe and > 8000 m for Westward Ho!, Saunton and Croyde.

### 4. Methodology

Our approach is to compare several criteria for determining the 'active' nearshore limits and these are grouped under three methods (Fig. 4):  $DoC_{obs,a-c}$  is based on observations,  $DoC_{param,a-b}$  uses wave-based formulations and  $DoC_{stress,a-b}$  uses numerical modelling outputs.

#### 4.1. Observational data

A 10-year time series of beach morphology and subtidal bathymetry of Perranporth beach (Region 3, Fig. 3c) was used to determine observed depth of closure ( $DoC_{obs,a}$ , Fig. 4). Field data were collected using RTK-GPS for the supra- and intertidal beach and single-beam echo-sounder for the subtidal area. The uncertainty limit for detecting significant morphologic change was  $\Delta d \leq 0.14$  m ( $\pm 0.14$  m corresponds to the uncertainty associated with the field data collection; RTK-GPS input into Valeport MIDAS Surveyor is accurate to  $\pm 0.02\%$ ). Data were merged and interpolated using the quadratic loess method (Plant et al.,

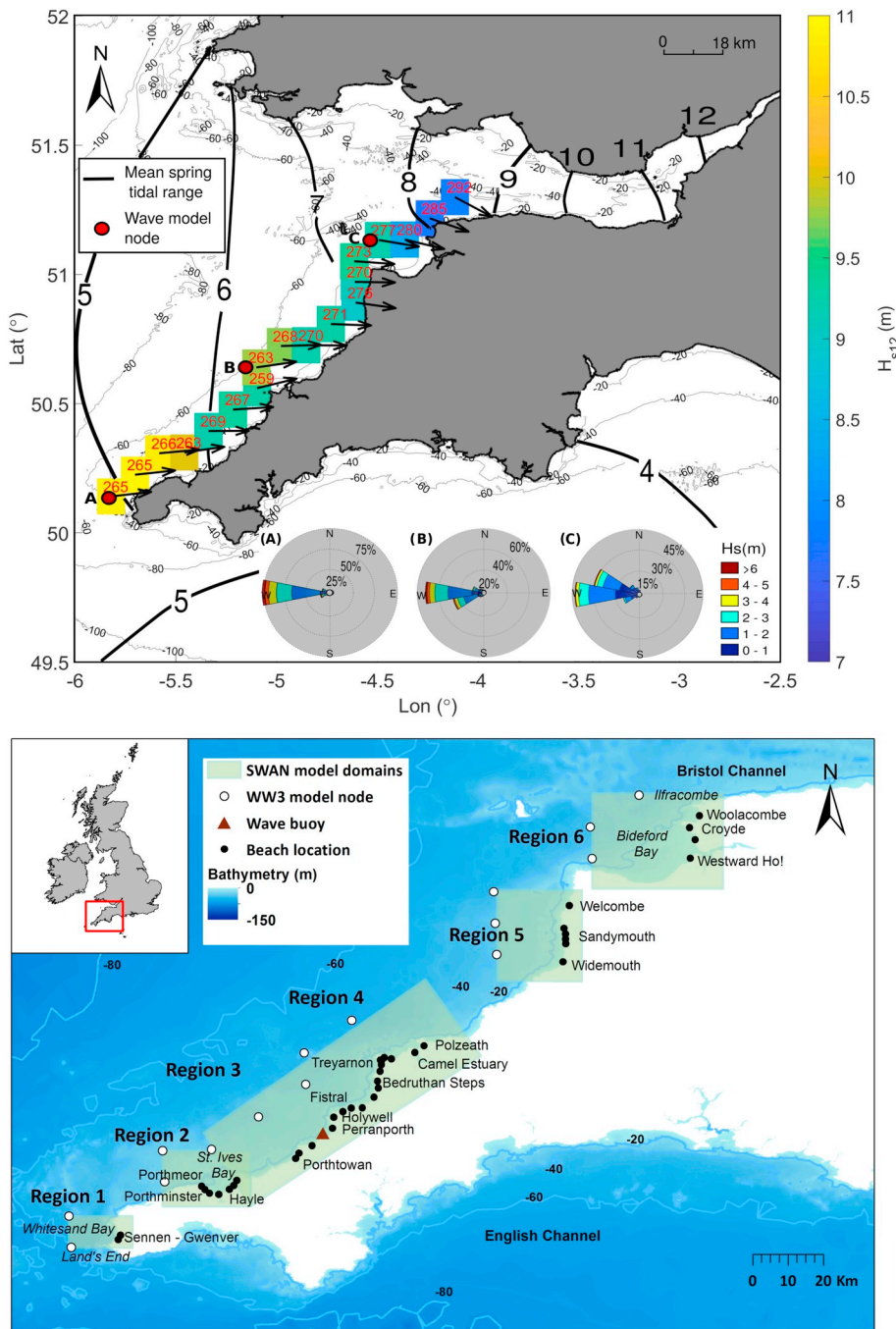


**Fig. 1.** Study area, SW England. Top panel: wave climate variability and tidal range. Wave climate data represent a 4-year record (2013–2016) from the MetOffice WW3 model, with cell colour indicating offshore  $H_s$  exceeded 12 h per year and associated direction of wave roses. Red circles (A to C) indicate the locations of wave roses. Black solid lines represent mean spring tidal range, adapted from BERR (2008). Bottom panel: location of study areas along the SW (SWAN model domains for Regions 1–6). Black dots indicate the studied embayments and white circles are MetOffice UK Waters Wave Model nodes used as SWAN input. (For interpretation of the references to colour in this figure legend, the reader is referred to the web version of this article.)

2002) to produce DEMs, providing a time series sufficiently long to compare observed closure depth with that predicted using wave-based theoretical methods. Complementing the morphological dataset, sediment size distribution ( $DoC_{obs,b}$ , Fig. 4) along Perranporth shoreface (from +4 to –30 m) was analysed using sediment samples collected during winter and summer 2016 (Samuel, 2017).

Regional LiDAR (provided by Plymouth Coastal Observatory) and multi-beam bathymetry (United Kingdom Hydrographic Office, 2011) were used to conduct a comparison of shoreface characteristics across the six regions and to determine the sand-rock transition depth of closure ( $DoC_{obs,c}$ , Fig. 4). A digital elevation model (DEM) was constructed for the coast of SW England by combining the LiDAR (up to –3 m) and multi-beam bathymetry (to < –50 m), corrected and referenced to Ordnance Datum Newlyn (ODN) using the Vertical Offshore Reference Frame model (VORF) made available by the United Kingdom

Hydrographic Office.

## 4.2. Numerical modelling data

### 4.2.1. Wave models (WW3 and SWAN)

Wave statistics are required to calculate parameterised estimates of depth of closure (Section 4.3.2,  $DoC_{param}$ ) and shear stress (Section 4.3.3,  $DoC_{stress}$ ). Hindcast wave conditions were obtained from the MetOffice UK Waters WaveWatch III (WW3) Model (Tolman, 2014; Saulter, 2017) for 18 nodes at 8-km resolution across Regions 1–6 (cells in Fig. 1, upper panel) over a 4-year period (01/01/2013–01/01/2016). This includes the winter of 2013/14, ranked as the most energetic winter under the last seven decades (Masselink et al., 2015).

Offshore wave conditions (at > 50 m depth, white circles in Fig. 1, bottom panel) may not be representative of inshore conditions (at

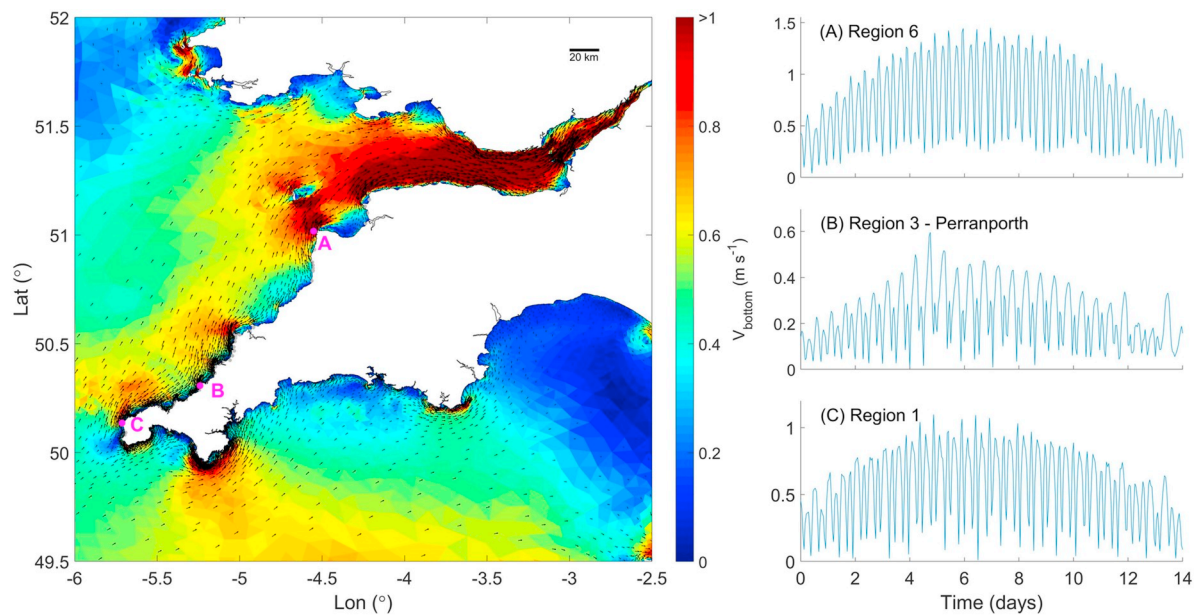


**Fig. 2.** Left panel: Spatial distribution of bottom tidal current velocities and direction during spring tides. Magenta dots with labels (A, B, C) represent locations of velocity time series shown in the right panels. Right panels: velocity current time series for a neap-spring-neap tidal cycle at the 30-m contour line off the headlands for Region 6 (upper), Perranporth-Region 3 (middle) and Region 1 (lower). Data sourced from FVCOM numerical model (Chen et al., 2003), produced by the UK National Oceanography Centre. (For interpretation of the references to colour in this figure legend, the reader is referred to the web version of this article.)

**Table 1**

Deep-water wave climate statistics for the selected regions using hourly wave model outputs from the MetOffice UK Waters Wave Model, 2013 to 2016.

Region	Hydrodynamics						Morphology		
	$H_s$ (m)	$H_{s99\%}$ (m)	$H_{s12}$ (m)	$T_p$ (s)	$T_{p99\%}$ (s)	$T_{p12}$ (s)	$D_{50}$ (mm)	Slope	Orientation
1	1.9	7.0	10.0	9.8	16.4	18.2	0.49	0.028	NW-W
2	1.7	6.7	9.5	9.8	16.4	18.2	0.37	0.008	NNE-WNW
3	1.6	6.1	9.3	10.2	16.7	18.2	0.37	0.013–0.021	W-NW
4	1.6	5.8	8.8	10.1	16.4	17.9	0.34	0.013	W-NW
5	1.5	5.8	8.4	10.9	17.0	18.5	0.48	0.017	W
6	1.4	5.1	7.3	11.0	16.7	18.5	0.33	0.005	W

$H_s$  – significant wave height;  $H_{s99\%}$  – 99th percentile;  $H_{s12}$  – significant wave height exceeded 12 h per year;  $T_p$  – peak period.

15–20 m depth) within deep embayments and/or on coastlines that do not face into the prevailing wave direction; therefore, the DoC computed using offshore conditions may not be appropriate. Accordingly, the third-generation spectral wave model SWAN (Booij et al., 1999) was used to transform wave conditions from offshore to inshore. This model accounts for wind growth, dissipation processes and wave-wave interactions. SWAN was set up for five domains (one for each region, except regions 3 and 4 which had a shared domain; Fig. 1, bottom panel) using a rectangular grid with a resolution of  $100 \times 100$  m. The dissipation mechanisms considered were bottom friction (with JONSWAP friction coefficient of  $0.067 \text{ m}^2 \text{ s}^{-2}$ ), refraction, whitecapping (Komen et al., 1984) and depth-induced breaking (with ratio of maximum individual wave height over depth equals to 0.73). Non-linear wave-wave interactions were also considered (TRIADS mechanism). SWAN output was validated against wave height observations (wave buoy in Fig. 1, bottom panel) for February 2014 and the model satisfactorily reproduced wave height, period and direction. Wave height is well predicted and showed a bias of only  $-0.06$  m and a root-mean square error (RMSE) of  $0.003$  m. Peak period prediction is excellent (bias =  $-0.05$  s; RMSE =  $0.02$  s).

#### 4.2.2. Tide and surge model (FVCOM)

Data from the finite-volume, three-dimensional (3D) hydrodynamic model FVCOM (Chen et al., 2003) provided by the National

Oceanography Centre were used to compute current bed shear stress (Section 4.3.2,  $DoC_{stress}$ ). The FVCOM domain covers the NW European shelf and the horizontal spatial resolution of the space-varying unstructured cells of the model grid ranges from 2 km offshore to 100 m near the coast. A  $\sigma$  layer (terrain following) coordinate system of 10 uniform layers was used for vertical discretization. Model validation results against tide gauge (Ilfracombe and Newlyn) for total water elevation showed a bias of  $-0.002$  m and a RMSE of  $0.26$  m. Current meter data collected in 20-m water depth off Perranporth (Region 3, Fig. 2c) were also compared with FVCOM model data. Recorded maximum current speeds during spring tides at this location were  $0.4 \text{ ms}^{-1}$  and were well reproduced by the numerical model ( $0.42 \text{ ms}^{-1}$ ; bias =  $0.09 \text{ ms}^{-1}$ ). FVCOM was run for the year 2008 including full meteorological forcing (tidal, river, surface heat, surface wind and surface precipitation forcings). Hourly data of water surface elevation and eastward/northward flow velocity along the SW shelf of England for March 2008 were extracted from the model results. The period used for the hydrodynamic model (2008 in this case) does not represent major implications in our depth of closure computations as the hydrodynamic model output was only used to obtain tidal current velocities for a representative tidal cycle during spring tides. For a detailed description of a similar FVCOM model set-up and parameterisation refer to De Dominicis et al. (2017).

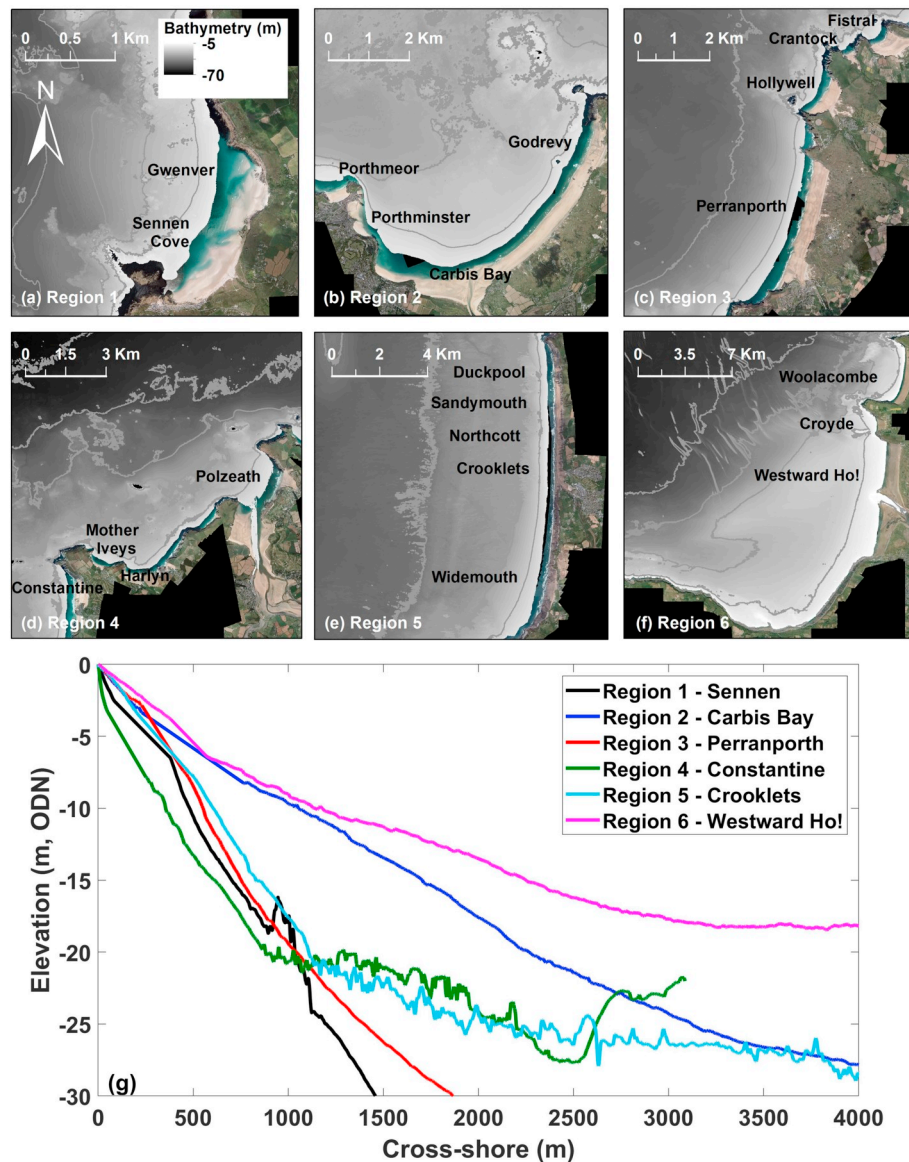


**Fig. 3.** Upper panel (a–f): aerial photography and bathymetry for the six regions of study. Lower panel (g): representative shoreface profiles extracted from the central part of selected LTEs. Bathymetry data were obtained from [United Kingdom Hydrographic Office \(2011\)](https://www.ukho.gov.uk/) and aerial photographs were courtesy of Plymouth Coastal Observatory (available at <https://www.channelcoast.org/southwest/>). (For interpretation of the references to colour in this figure legend, the reader is referred to the web version of this article.)

#### 4.3. Depth of closure methods

##### 4.3.1. Observed depth of closure ( $DoC_{obs}$ )

Direct field observations included calculation of the envelope of morphological change ( $DoC_{obs,a}$ ), sediment size distribution ( $DoC_{obs,b}$ ) and sand-rock transition ( $DoC_{obs,c}$ ). Direct morphological change observations and sediment size distribution for one of the study sites (Perranporth, *Region 3*) were used to test the applicability of the parametric wave-based formulations ( $DoC_{param}$ ) and the proposed process-based method ( $DoC_{stress}$ ). The seabed sediment observational dataset was also compared with the presence of sediment (sand-rock transition) in 164 representative cross-shore profiles (covering 25 low tide embayments, LTEs) that were extracted along the six regions.

The Perranporth 10-year time series DEMs ([Section 4.1](#)) were alongshore-averaged across a 250-m section (black box on [Fig. 5](#), right panel) to enable the identification of the point at which morphological change can be considered insignificant ( $\Delta d \leq 0.14$  m;  $DoC_{obs,a}$ ). The observed depth of closure at Perranporth was supplemented by a grain

size analysis ( $DoC_{obs,b}$ ) at one representative cross-shore profile. Sediment samples corresponded to winter and summer conditions (March and July 2016), providing a seabed sediment distribution representative of high energy conditions. Depths at which grain size significantly changed were identified (e.g., sand to gravel).

The final observational method for determining depth of closure was to identify the sand-rock transition ( $DoC_{obs,c}$ ) using a regional DEM constructed from LiDAR and multi-beam data ([Section 4.1](#)). The regional DEM of the SW England was used to compare the shoreface profiles across *Regions 1–6*. A total of 164 profiles were extracted (up to  $-30$  m ODN), representative of the different study sites. The transition point between sand and rock was manually identified based on a change from smooth to rough bed and/or a break in the shape of the shoreface profiles (e.g., [Fig. 3g](#), *Region 1* at 800 m offshore).

##### 4.3.2. Wave-based formulations ( $DoC_{param}$ )

The empirically determined wave-based formulations ( $DoC_{param}$ ) based on significant wave height and peak period for a given region

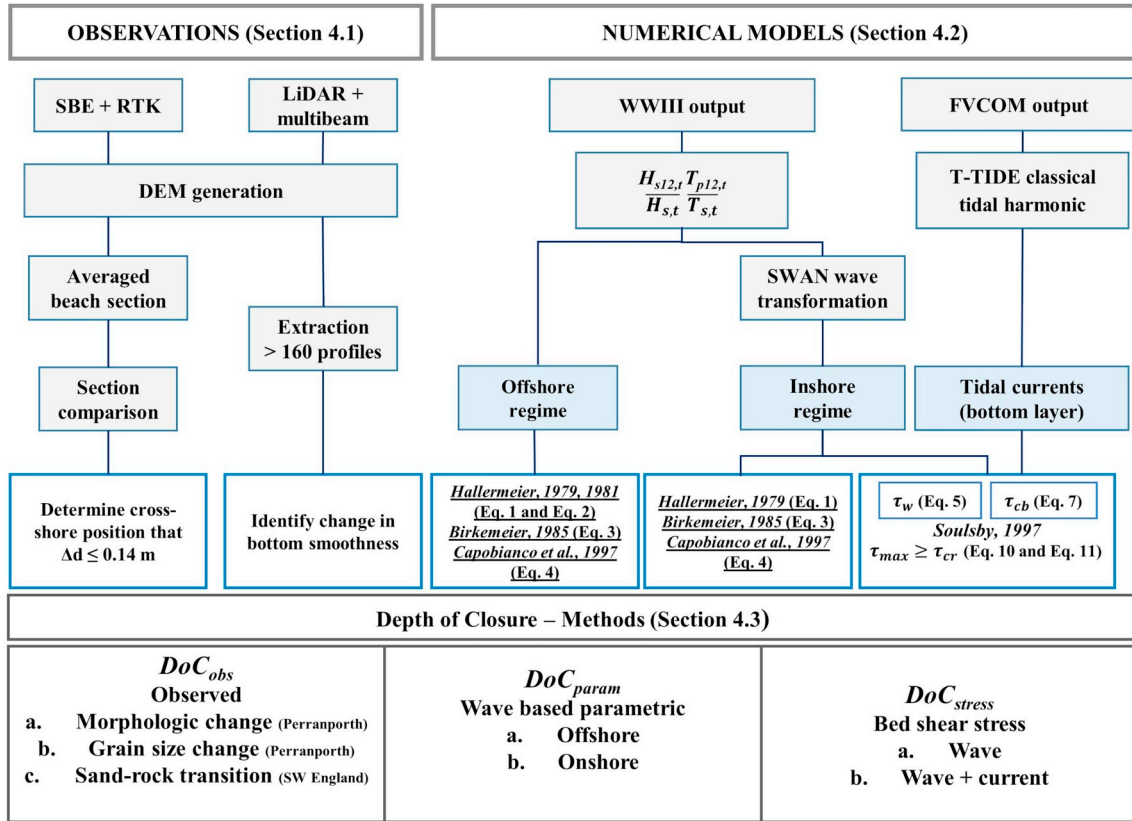


Fig. 4. Flow diagram of research methodology of the DoC quantification. Underlined criteria correspond with the methods to test.

were described in Section 2 (Eqs. (1)–(4)). First, the offshore wave conditions were used to compute at each WW3 node (Fig. 1, bottom panel) the depth of closure parameters ( $DoC_{param,a}$ ), specifically DoC (Eqs. (1), (3), (4)) and  $DoC_{motion}$  (Eq. (2)), and then averaging across all nodes in each of the six regions.  $DoC_{motion}$  was computed using the median grain size typical from the SW (0.3 mm) for the total time series ( $t = 4$  years), while DoC was calculated for both the total 4-year time

series, as well as independently for each individual year ( $t = 1$  year) and then averaged  $\langle DoC \rangle$ . For clarity, when DoC is used without chevrons, it is averaged over the full extent of the available data, while  $\langle DoC \rangle$  with chevrons indicates averaging the 1-year results over the 4-year period.

Parameterising depth of closure values for the inshore region ( $DoC_{param,b}$ ) requires wave transformation using SWAN (Section 4.2.1).

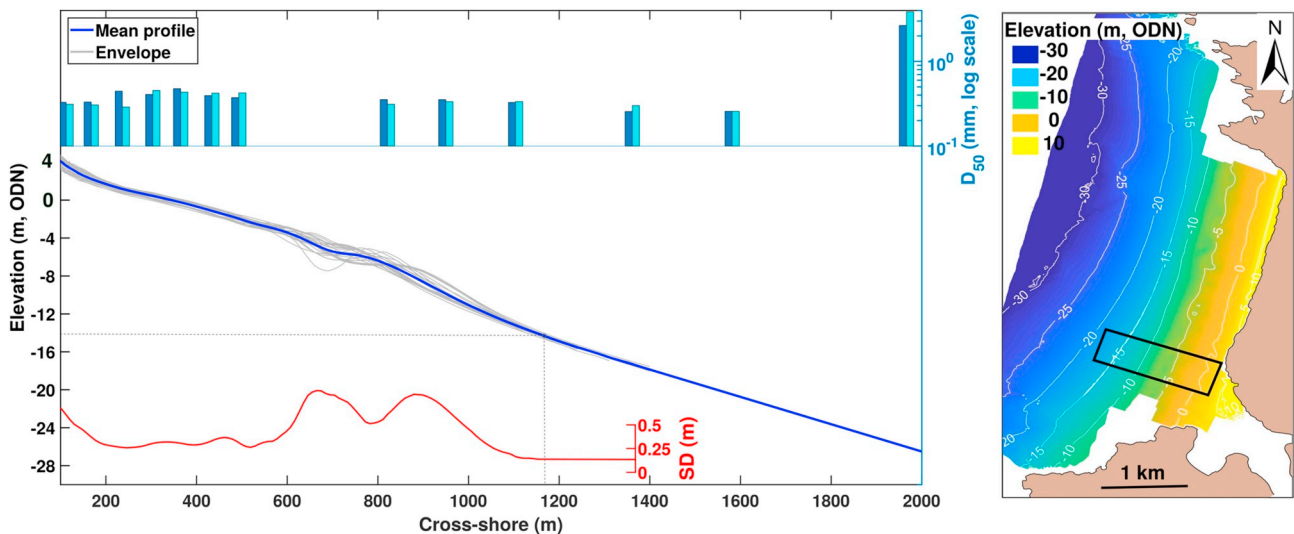


Fig. 5. Left panel: observed depth of closure estimated for Perranporth beach, north Cornwall, from the profile envelope ( $DoC_{obs,a}$ ) and from sediment distribution ( $DoC_{obs,b}$ ). Light and dark blue bars represent the median sediment size ( $D_{50}$ ) for winter and summer samples, respectively. The grey lines represent alongshore-average profiles associated with beach survey data collected from 2010 to 2016; the blue line is the mean profile over the survey period; and the red line shows the standard deviation associated with the mean profile. The dashed line represents DoC based on the morphological observations. Right panel: topographic and bathymetric survey with 250-m wide section of beach (black box) for alongshore-average profile used in left panel. (For interpretation of the references to colour in this figure legend, the reader is referred to the web version of this article.)

The sediment motion depth of closure *DoC-motion* as described by Hallermeier (1981) is not presented for inshore locations, as this depth is commonly located beyond the rocky headlands and falls beyond the regional model domains. Spatially-varying inshore values for the morphological depth of closure were determined as follows: (i) for each of the six regions, the offshore modelled wave data were ordered into seven 30°-directional bins with bin centres from 180° to 360°; (ii) for each of these classes, the wave heights were ranked, and the significant wave height exceeded for 12 h ( $H_{s12,t}$ ) and associated peak period ( $T_{p12,t}$ ) were computed for  $t = 4$  years and  $t = 1$  year; (iii) SWAN models were run for each region using these extreme wave values; (iv) an iterative method (refer to Kraus et al., 1998) was used to extract inshore wave height and associated period at the actual predicted *DoC* and  $\langle DoC \rangle$  across each domain, using Eqs. (1), (3) and (4); (v) a representative *DoC* and  $\langle DoC \rangle$  value was obtained for each embayment by alongshore-averaging; and (vi) the depth of closure was calculated relative to MLWS, then corrected to the survey datum (ODN).

#### 4.3.3. Bed shear stress ( $DoC_{stress}$ )

The approach for estimating the limit of significant sediment transport (*DoT*) under storm conditions and on a macrotidal regime was through analysis of numerically-modelled bed shear stress induced by waves ( $\tau_w$ ) and tidal currents ( $\tau_{cb}$ ), referred to as methods  $DoC_{stress,a}$  and  $DoC_{stress,b}$  respectively (refer to Fig. 4). Bed shear stress was computed following Soulsby (1997) and compared with different thresholds of initiation of motion and bedform activity according to Nielsen (1981).

The bed shear stress produced by waves is generally the main forcing control on sediment transport in shallow water (< 30 m depth) in exposed (wave-dominated) coastlines. The wave-induced shear stress was computed for the six regions (five SWAN wave model domains) for the extreme wave values ( $H_{s12}$ ,  $T_{p12}$ ). Wave bed shear stress is oscillatory and was obtained using:

$$\tau_w = \frac{1}{2} \rho f_w U_w^2 \quad (5)$$

where  $f_w$  is the wave friction factor,  $U_w = \sqrt{2} U_{rms}$ , and  $U_{rms}$  is the root-mean-square wave orbital velocity near the bed. According to Soulsby (1997), the wave friction factor for turbulent flow depends on the bottom roughness parameter ( $z_0 = D_{50}/12$ ) and the semi-orbital excursion ( $A = U_w T/2\pi$ ) as follows:

$$f_w = 1.39 \left( \frac{A}{z_0} \right)^{-0.52} \quad (6)$$

Tidal current bed shear stress was determined using classical tidal harmonic analysis on FVCOM current outputs using T-TIDE (Pawłowicz et al., 2002) for the entire FVCOM domain and at each model node. Tidal currents were resolved using the eight major tidal constituents S2, M2, N2, K2, K1, P1, O1 and Q1, and the shallow water constituents O2, N4, M4 and S4. Current bed shear stress was then computed using only tidal forcing for one representative tidal cycle during spring tides following a quadratic drag law expressed as:

$$\tau_{cb} = \rho C_d \bar{U}_{cb}^2 \quad (7)$$

where  $\tau_{cb}$  is the bottom (friction) stress induced by tidal currents,  $\rho$  is the water density,  $\bar{U}_{cb}$  is the maximum near bottom depth-averaged flow velocity for a tidal cycle (during spring tides) in analogy to selecting the maximum wave forcing conditions, and the drag coefficient,  $C_d$ , is determined along the domain by matching a logarithmic bottom layer at a height  $z_{ab}$  above the bottom (see e.g., Young, 1999). Thus:

$$C_d = \max \left[ \frac{k^2}{\ln \left( \frac{z_{ab}}{z_0} \right)^2}, 0.0025 \right] \quad (8)$$

with  $k$  being the von Karman constant ( $k = 0.4$ ) and  $z_0$  is the bottom roughness parameter.

The combined wave and current bed shear stress  $\tau_m$  cannot be obtained as a simple linear sum of the separate stresses due to the non-linear interaction between wave and current boundary layers. Soulsby (1995) found a good fit between the observations in the laboratory and a theoretical model based on a two-coefficient optimization of the form:

$$\tau_m = \tau_{cb} \left[ 1 + 1.2 \left( \frac{\tau_w}{\tau_{cb} + \tau_w} \right)^{3.2} \right] \quad (9)$$

in which  $\tau_{cb}$  and  $\tau_w$  are the current- and wave-induced shear stresses respectively, computed individually. The corresponding expression for  $\tau_{max}$  is given as follows:

$$\tau_{max} = [(\tau_m + \tau_w |\cos \varnothing|)^2 + (\tau_w \sin \varnothing)^2]^{1/2} \quad (10)$$

where  $\varnothing$  is the angle between the direction of wave travel and the current component.

Soulsby (1997) related sediment motion threshold for a specific seabed with the critical Shields parameter  $\theta_{cr}$  through the expression:

$$\tau_{cr} = \theta_{cr} g (\rho_s - \rho) D_{50} \quad (11)$$

where  $\rho_s$  is the sediment density and  $g$  is gravitational acceleration. This algorithm calculates critical shear stress ( $\tau_{cr}$ ) for non-cohesive and well-sorted particles using a non-dimensional Shield's curve. Critical shear stresses were calculated using the average grain size typical of SW England –  $D_{50} = 0.3$  mm, as well as  $D_{50} = 0.15$  and 0.6 mm. The use of the different sediment sizes allows analysis of the sensitivity of threshold exceedance of combined wave and current bed shear stress to seabed composition.

According to Eq. (11), initiation of motion, as well as sediment transport, will depend on boundary shear stresses and seabed characteristics. Based on laboratory experiments and observations, Nielsen (1981) determined that the occurrence of bedforms is related to the bed shear stress ( $\tau$  or  $\theta$ ) and developed a relation between bedform type and wave energy conditions, expressed as a function of transport stage. Using Grant and Madsen (1982), the following critical values of the Shields number ( $\theta_{cr}$ ) can be identified: (i) initiation of motion  $\theta_{cr} = 0.048$ ; (ii) formation of sharp-crested vortex ripples  $\theta_{cr} = 0.1$ ; (iii) transformation from vortex to post-vortex ripples  $\theta_{cr} = 0.2$ ; and (iv) transition into a plane bed  $\theta_{cr} = 1$ . Following Eq. (11), combined wave- and current-induced bed shear stress was computed for each region and compared with the critical shear stresses  $\tau_{cr}$  for the different bedform scenarios.

## 5. Results

### 5.1. Closure depth based on observations: Perranporth case of study ( $DoC_{obs,a-b}$ )

Survey (beach and bathymetry) data from Perranporth, one of the west-facing embayments of Region 3 (Fig. 1, bottom panel for location), was used to derive the observed closure depth for this location ( $DoC$ ,  $DoC_{obs,a}$ ). Fig. 5 shows the mean and the standard deviation (SD) associated with all alongshore-averaged shoreface profiles for Perranporth collected over the period 2010–2016. The largest bed-level variability ( $SD > 0.5$  m) occurs in the outer bar region ( $x = 700$ – $900$  m). This vertical variability decreases offshore to < 0.14 m at a depth of 14.5 m (ODN), and this depth is considered the morphological depth of closure for this embayment as 0.14 m is the uncertainty associated with the survey data.

Several authors in the literature analyse textural changes in the seabed to determine the boundaries of the active profile (Potter, 1967; Chesher et al., 1981; Larson, 1991; Work and Dean, 1991). Following that approach ( $DoC_{obs,b}$ , refer to Fig. 4), sediment samples collected during winter and summer 2016 at 13 different locations on the shoreface profile are presented in Fig. 5. Supratidal  $D_{50}$  values are relatively constant with a value of 0.33 mm. The coarsest sediments in the

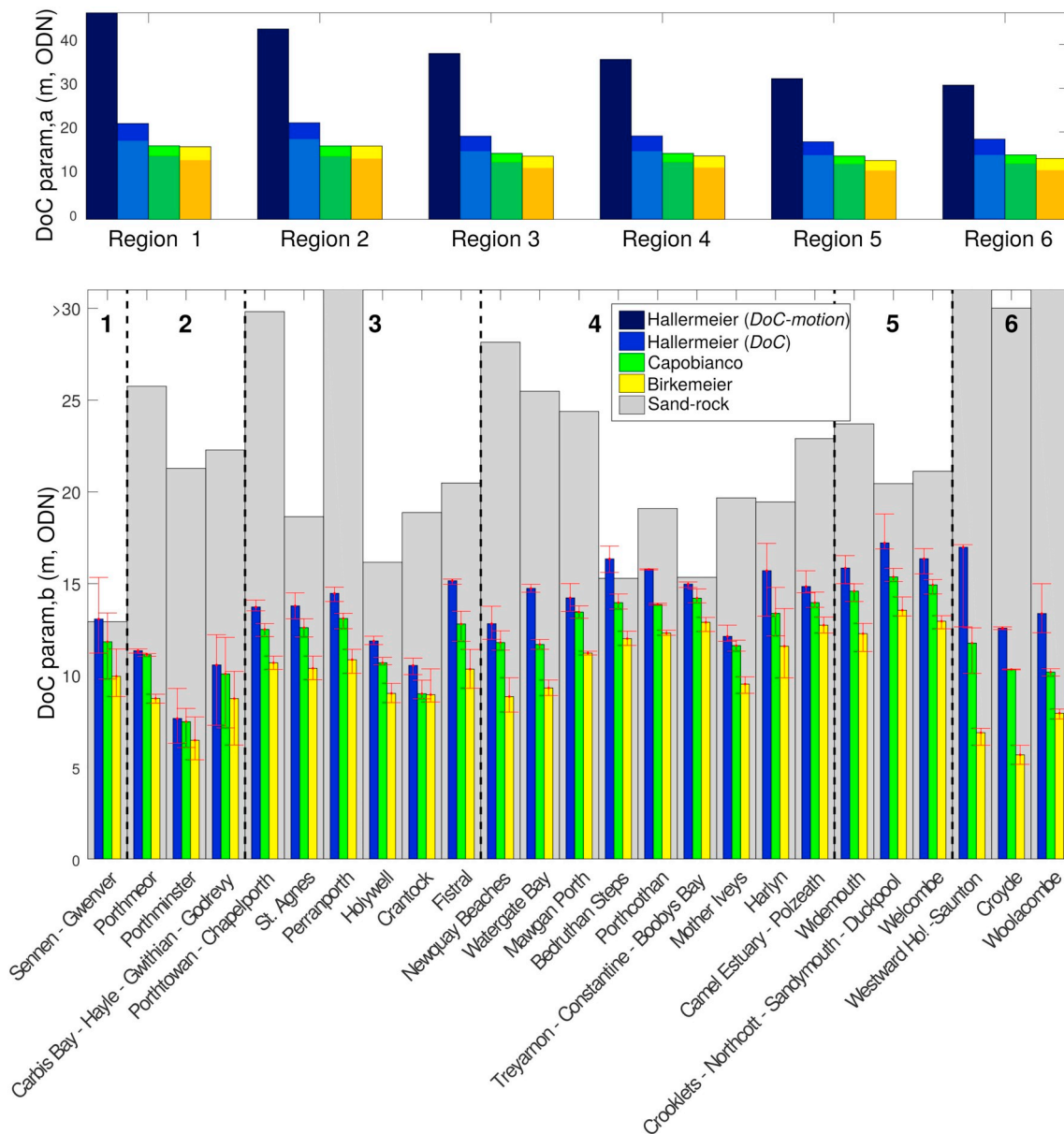


**Fig. 6.** Along-coast variability in depth of closure obtained by applying the wave-based formulations of Hallermeier for  $DoC$  (light blue) and  $DoC-motion$  (dark blue), Capobianco (green) and Birkemeier (yellow). Upper panel:  $DoC$  at each region computed using offshore WW3 wave conditions ( $DoC_{param,a}$ ). Light bars show  $DoC$  values for  $t = 4$  years and darkest colour bars represent  $DoC$  ( $t = 1$  years). Bottom panel: bars represent the average  $DoC$  for each embayment, computed using the modelled inshore wave conditions and forcing the SWAN wave model with  $H_{s,12}$  and  $T_{p,12}$  derived from the 4-year time series ( $DoC_{param,b}$ ). Minimum and maximum  $DoC$  values for each embayment are represented by the red intervals. Grey bars represent the embayment-averaged depth of the transition between sand and rock. Vertical black dashed lines separate the different regions. (For interpretation of the references to colour in this figure legend, the reader is referred to the web version of this article.)

upper part of the profile (0.48 mm) are found around the Mean Spring Low Tide level. Seaward of this point, sediment size decreases with depth from 0.40 mm at  $z = -3$  m, 0.33 mm at  $z = -18$  m and 0.30 mm between  $-22$  m and  $-26$  m. With increasing depth,  $D_{50}$  abruptly increases to 2.657 mm, representing a transition to gravel. This change in the sediment size is also observed in backscatter data (unpublished data), where the presence of medium sand along the embayment domain is interrupted by gravel patches around the  $-26$  m contour line.

## 5.2. Along-coast variability in depth of closure ( $DoC_{param}$ $DoC_{obs,c}$ )

The different depth of closure measures computed using the various wave formulations  $DoC_{param}$  (Eqs. (1)–(4)) are summarized in Fig. 6. The sediment motion depth of closure determined using mean wave

characteristics ( $DoC-motion$ , Eq. (2)) was calculated for each of the six regions (Fig. 6, upper panel) and decreases from 50 m in the south to 34 m in the north, in response to the associated decrease in wave energy (Fig. 1, top panel). The morphological depth of closure estimate was calculated over 4-years ( $DoC$ ) and for 1-year averages ( $\langle DoC \rangle$ ) for three different formulations (Eqs. (1), (3) and (4)).  $DoC$  decreases from 23 m in the south (Region 1) to 19 m in the north (Region 6) for Hallermeier (1978), and the corresponding values for the Capobianco et al. (1997) and Birkemeier (1985) formulations are shallower, ranging from 17 m to 14 m, and from 15 to 12 m, respectively. The decrease in depth of closure over decreasing time scale is demonstrated through comparison with the  $\langle DoC \rangle$  values (Fig. 6, top panel-darkest bars), which are 4 m, 2 m and 1.5 m less than those obtained using the total time series ( $DoC$ , Fig. 6, top panel-light bars) for Hallermeier (1978), Capobianco et al.

(1997) and Birkemeier (1985), respectively.

Embayment-averaged DoC results are obtained using wave conditions transformed to the nearshore ( $DoC_{param,b}$ ) and, most significantly, there is no obvious correlation between the depth of closure values computed using the offshore (Fig. 6, top panel) and inshore (Fig. 6, bottom panel) wave formulations. While DoC computed from offshore wave conditions ( $DoC_{param,a}$ ) decreases from south to north, the value computed using inshore wave conditions increases from Region 1 to Region 5, then decreases for Region 6. This emphasizes the very significant role nearshore morphology and embayment orientation play in attenuating wave energy. Clearly, if untransformed wave values are used to estimate DoC for highly embayed coasts, the results are likely to be significantly overestimated. DoC values computed using inshore wave conditions using Hallermeier (1978) (Eq. (1)) are in all cases 1–2 m larger than results using Capobianco et al. (1997) (Eq. (4)) and Birkemeier (1985) (Eq. (3)). As an example of the results, typical values of DoC using Hallermeier (1978) ( $DoC_{param,b}$ ) for the most exposed parts of the coast (Regions 1, 5 and 6, and the north part of Regions 3 and 4) are 12–16 m (relative to ODN), whereas DoC values for the more sheltered parts (Regions 2 and the south part of Region 6) are typically 6–10 m.

The sand-rock transition depth ( $DoC_{obs,c}$ ) is presented in Fig. 6 (bottom panel, grey bars) for comparison with the depth of closure estimates obtained using the wave formulations. There is no obvious alongshore correlation between the sand-rock transition and either the offshore or inshore wave formulations, and this is attributed to sediment availability being a more important factor in determining the sand-rock transition than the hydrodynamic forcing. Additionally, there are no clear alongshore trends in the sand-rock transition. The sand-rock transition ranges from 15 m to > 30 m water depth, which is generally significantly deeper than DoC, and in some instances double that of the computed DoC (e.g., Porthmeor, Perranporth, Widemouth, Woolacombe). One exception is Bedruthan Steps, where Eq. (1) predicts DoC at 16 m, while the rocky platform begins at 15 m depth, suggesting this embayment is particularly sediment-starved. At Sennen Cove, the sand and rocky platform transition and DoC (based on Eq. (1)) are at a similar depth. Significantly, these results suggest that the upper shoreface active profile for the SW generally has sufficient sediment ( $DoC < \text{sand-rock transition}$ ). However, on the lower shoreface, where sediment transport is more infrequent, there tends to be a lack of available sediment (sand-rock transition <  $DoC\text{-motion}$ ).

The occurrence of significant along-embayment variability in depth of closure using  $DoC_{param,b}$  (Hallermeier, 1978) is exemplified in Fig. 7. Along-embayment variability occurs at locations that display a considerable difference in the shoreline orientation and, therefore, a spatial

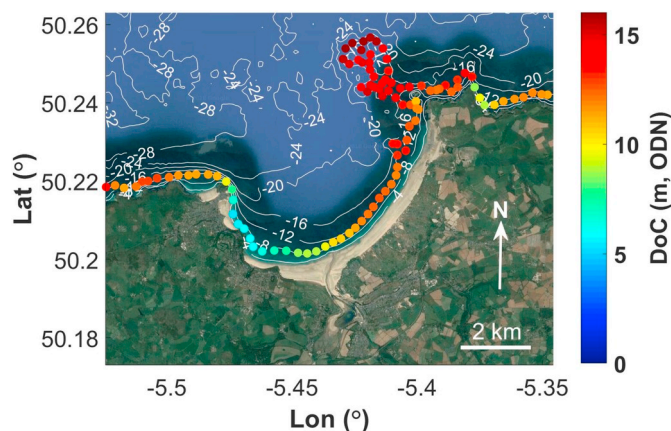


Fig. 7. Example of along-embayment variability in depth of closure due to wave transformation for Region 2 using  $DoC_{param,b}$  (Hallermeier, 1978) (Eq. (1)). (For interpretation of the references to colour in this figure legend, the reader is referred to the web version of this article.)

gradient in the wave conditions. This results in higher DoC values for more exposed sections (e.g., > 15 m for the W section, Fig. 7) compared to more sheltered section (e.g., 5–7 m for the NNE section, Fig. 7). Such large differences are particularly relevant in Regions 2, 4 and 6, which are all sections with considerable variability in shoreline orientation and/or important points of attenuation (refer to Fig. 3).

### 5.3. DoC determined using bed shear stress maxima ( $DoC_{stress}$ )

#### 5.3.1. Wave action bed shear stress ( $DoC_{stress,a}$ )

Wave-induced bed shear stress under the most extreme wave conditions ( $H_{s,12}$  and  $T_{p,12}$  for  $t = 4$  years) was computed along the model domains for the six study regions and presented in Fig. 8 (left panels). Values of wave-induced shear stress are highly variable along the study sites and these are related to the orientation and configuration of the shoreface. Greater values of  $\tau_w > 5 \text{ Nm}^{-2}$  at depths from 10 to 20 m occur in west-facing embayments in Region 1, 3, 5 and 6 (Fig. 8a, g, m, p), whereas bed shear stresses are significantly less ( $\tau_w < 1 \text{ Nm}^{-2}$ ) at similar water depths off NE-facing beaches, such as Porthminster and Carbis Bay in Region 2 (Fig. 8d). Embayments in the north of Region 4 (e.g., Treyarnon) and many beaches in Region 5 are very energetic and present values of  $\tau_w = 4.8 \text{ Nm}^{-2}$  even in 28 m water depth (Fig. 8m). Interestingly, similar values for  $\tau_w$  to the exposed west-facing embayments are registered in 28 m water depth ( $\tau_w \sim 3.5 \text{ Nm}^{-2}$ ) in several other NE-facing embayments (e.g., Mother Ives and Harlyn in Region 4; Fig. 8j). This is attributed to the morphological configuration of these embayments: they are fronted by a short rocky shelf (c. 700 m) that limits wave energy dissipation during wave transformation and refraction.

Computed wave-induced bed shear stress ( $\tau_w$ ) values are compared to the different case scenarios for sediment transport and bedform activity for the three different sediment sizes (Table 2). Wave-induced bed shear stresses exceeding the upper-plane bed transition are presented in Fig. 8 (blue line, right panels) as the nearshore sediment transport under such stresses is considered most relevant in shaping the lower shoreface. For Region 1, this threshold occurs in depths > 30 m along the exposed northern part of the embayment, but decreases to ~12 m at the more sheltered southern end, resulting in an average threshold depth of 19 m (blue line, Fig. 8c). In Region 2, the location of the upper-plane bed threshold is spatially highly variable with significantly smaller values of 10 m at the southern end, areas where this threshold is not exceeded at all (e.g., Porthminster and Carbis Bay), and a more exposed section with values > 28 m (e.g., Godrevy and Gwithian, blue line, Fig. 8f). Embayment-averaged values for the transition depth are generally inflated due to the maximum transition depth values associated with the headlands, which often have values of ~30 m. In the more alongshore-uniform Regions 3 and 4 (blue line, Fig. 8i, l), the isobath for the upper-plane bed transition is 22 m and 25 m, respectively. Values for the embayments within these regions are generally around 18–20 m for Region 3 and close to 25 m for Region 4, while values are > 28 m around the headlands. In Region 5, the depth for the transition to upper-plane bed is largest and is near-constant (> 29 m, Fig. 8o). Finally, in Region 6 (Fig. 8r), the transition depth closely follows the 20-m contour line (Saunton, Croyde and Woolacombe), and decreases to 10 m water depth in the south due to wave dissipation by a point of refraction located in the south of the region.

The results are strongly dependent on the sediment size selected for the calculations ( $D_{50} = 0.3 \text{ mm}$  in our case) as shown in Fig. 9a. For a sediment size of 0.15 mm the threshold isobaths tend to be > 18 m larger than for medium sand (not shown), while for the case of the coarser sediment ( $D_{50} = 0.6 \text{ mm}$ ), the transition to upper-plane bed is only observed up to 12 m in one of the six domains (Region 5, light blue line in Fig. 9a). Results for the less energetic of scenarios (sediment motion, initiation of vortex ripples and initiation of post-vortex ripples) are not presented as the three associated sediment transport thresholds  $\tau_{cr}$  (for all the considered  $D_{50}$ ) are exceeded throughout all study

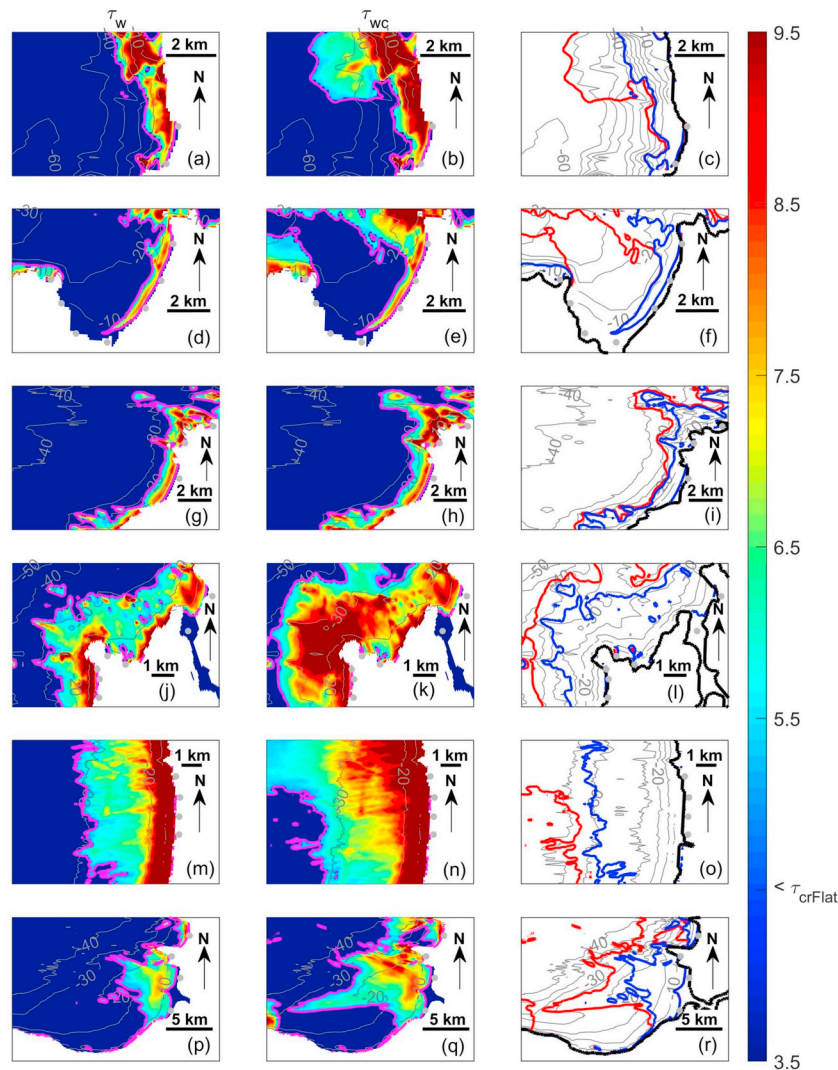


**Fig. 8.** Left panels show wave-induced bed shear stress ( $\tau_w$ ) computed for extreme wave conditions ( $H_{s,12}$  and  $T_{p,12}$ ) and for Regions 1–6 (a, d, g, j, m, p). Middle panels present combined wave- and current-induced bed shear stress ( $\tau_{wc}$ ) computed for extreme wave conditions ( $H_{s,12}$  and  $T_{p,12}$ ) during maximum values of tidal currents (spring tides) and for Regions 1–6 (b, e, h, k, n, q). Magenta line represents the bed shear stress at the transition to upper-plane bed conditions for medium sand ( $D_{50} = 0.3$  mm,  $\tau_{cr} = 4.77$   $\text{Nm}^{-2}$ ). Right panels:  $\tau_w$  (blue) and  $\tau_{wc}$  (red) transition depth to upper-plane bed conditions. (For interpretation of the references to colour in this figure legend, the reader is referred to the web version of this article.)

**Table 2**  
Dependence of critical shear stress values ( $\text{Nm}^{-2}$ ) with sediment size for the considered scenarios: sediment motion, initiation of vortex ripples, initiation of post-vortex ripples and plane bed.

		$D_{50}$ (mm)		
		0.15	0.3	0.6
Bedform activity	Sediment motion	0.17	0.34	0.69
	Initiation of vortex ripples	0.24	0.48	0.95
	Initiation of post-vortex ripples	0.48	0.95	1.91
	Transition to plane bed	2.39	4.78	9.55

regions (depths > 50 m).

5.3.2. Wave and tidal current bed shear stress ( $\text{DoC}_{\text{stress},b}$ )

On a high-energy and macrotidal coast, it is important to assess the influence of tidal currents on the bottom stress, in addition to wave agitation, as an additional mobiliser and transporter of sediment. Accounting for the effect of tidal motion on the depth of closure is a prime motivation and novel aspect of this study. The occurrence of combined wave and current bed shear stress ( $\tau_{wc}$ ,  $\text{DoC}_{\text{stress},b}$ ) exceeding critical values for transition to upper-plane bed across all study regions is presented in Fig. 8 (middle panels). During extreme conditions (storms and spring tides), sheet flow occurs in all the studied LTEs.

Maximum depths in the central part of the embayments that register such extreme flows are 20–30 m, and these values are very similar to those obtained computing only wave-induced bed shear stress (red and blue lines in Fig. 8, right panels). The contribution of the tidal currents in the computed total shear stresses in the central section of the embayments is small ( $< 0.34$   $\text{Nm}^{-2}$ ) for the case of Regions 1–3 (Fig. 8c, f, i). However, significant increases in  $\tau_{wc}$  relative to  $\tau_w$  are evident around headlands due to stronger tidal currents at these locations (Fig. 8c, f, i). Accounting for tidal currents results in an increase of the depth affected by sheet flow of c. 1 m for wide and W-facing LTEs (Fig. 8b, h) and in excess of 5 m for short LTEs with variable orientation (Fig. 8e, k) as these latter settings are highly influenced by the tidal currents around headlands. Additionally, the maximum limit of sheet flow for combined wave and current bed shear stress increases  $O(10$  m) with respect to  $\tau_w$  in embayments affected by large tidal range (MSR = 7–8, Fig. 8q).

The maximum depths of sediment transport ( $\text{DoC}_{\text{motion}}$ , Eq. (2)) determined for offshore wave values ( $\text{DoC}_{\text{param},a}$ ) are compared with the region-averaged depth values for sediment motion, initiation of vortex ripples, initiation of post-vortex ripples and transition to plane bed ( $\text{DoC}_{\text{stress},b}$ ). The depths of sediment motion, initiation of vortex ripples and initiation of post-vortex ripples under extreme conditions are exceeded across the entire domain for the six regions, and are significantly larger than the parameterized  $\text{DoC}_{\text{motion}}$ . On the other hand, the  $\text{DoC}_{\text{motion}}$  depths correspond closely to the upper-plane bed transition

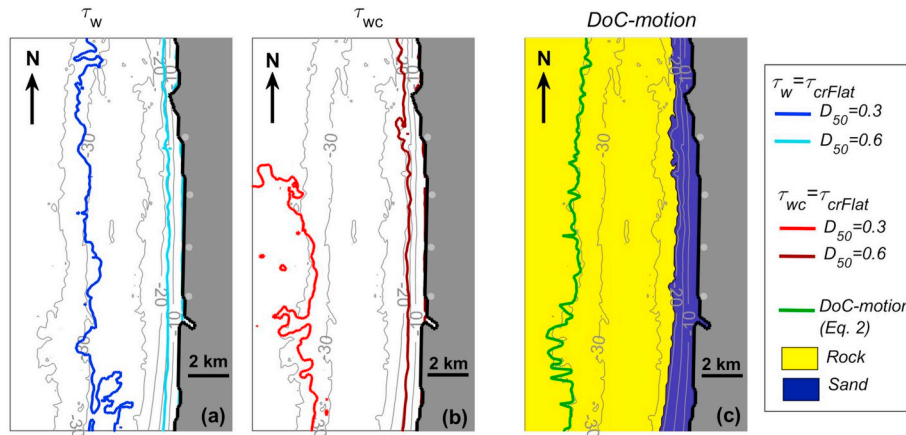


**Fig. 9.** Bed shear stress at the transition to upper-plane bed conditions for medium and coarse sand ( $D_{50} = 0.3$  and  $0.6$  mm), limit for initiation of motion and depth between sand and rock for Region 5. Bed shear stress transition limit is computed using (a) wave-induced bed shear stress ( $\tau_w$ ) and (b) combined wave- and current-induced bed shear stress ( $\tau_{wc}$ ) computed for extreme wave conditions ( $H_{s,12}$  and  $T_{p,12}$ ) and maximum tidal currents (spring tides). (c)  $DoC\text{-}motion$  is predicted using Hallermeier (1981) (Eq. (2)), and depth between sand-rock is based on observations. (For interpretation of the references to colour in this figure legend, the reader is referred to the web version of this article.)

**Table 3**

Summary of results for the predicted shoreface limits along the SW of England. Region-averaged values of  $DoC$ ,  $DoC\text{-}motion$ , sand-rock transition depth,  $DoT$  and associated along-coast standard deviation ( $SD$ ) using the different formulations are presented

Region	$DoC_{obs,a}$		$DoC_{obs,b}$		$DoC_{param,a}$						$DoC_{param,b}$				$DoC_{stress}$			
	$DoC$ (m)		Transition depth (m)		$DoC\text{-}motion$ (m)						$DoC$ (m)				$DoT$ (m)			
	$SD \leq 0.14$		Sand – rock		Eq. 2 Hall.	Eq. 1 Hall.	Eq. 4 Cap.	Eq. 3 Bir.	Eq. 2 Hall.	$SD$	Eq. 4 Cap.	$SD$	Eq. 3 Bir.	$SD$	$\tau_w$ > $\tau_{crFlat}$	$SD$	$\tau_{wc}$ > $\tau_{crFlat}$	$SD$
1	–		12.9		50.1	23.3	17.6	17.5	13.1	1.8	11.8	1.7	9.9	1.3	19	5	22	9.5
2	–		23.1		46.4	21.1	16.2	15.9	9.8	1.6	9.6	1.5	10.1	1.1	0–15	6	0–20	5
3	–		22.5		40.6	20.2	16.3	16.1	13.3	1.6	11.8	1.4	10.0	0.7	22	6	35	5
4	–		21.1		39.4	19.3	15.0	14.6	14.6	1.3	13.1	1	11.1	1.5	28	5	38	5
5	–		21.7		35.2	19.0	14.9	14.2	16.5	0.6	14.9	0.3	12.9	0.3	29	2	35	2
6	–		> 30		33.7	18.8	14.8	14.3	14.3	1.9	10.7	0.7	6.8	0.9	19	5	30	4
Perranporth	14.5		26*		40.6	20.2	16.3	16.1	14.4	0.4	13.1	0.4	10.8	0.6	22	3	28	5

\* This value corresponds with significant textural change on the seabed.

during storm conditions, or the maximum depth of significant potential sediment transport ( $DoT$ ) computed using the process-based method ( $DoC_{stress,b}$ ), for Regions 3, 4, 5 and 6 (see Fig. 9b–c and Table 3). This suggests that  $DoC\text{-}motion$  is more representative of the transition to upper-plane bed conditions than of maximum depth of sediment motion under the influence of maximum wave and tidal shear stresses for highly energetic and macrotidal coastlines.

## 6. Discussion

To facilitate discussion of the different  $DoC$  estimates obtained using the multi-criteria approach, a summary of the results is presented in Table 3. Comparing the various applied  $DoC$  formulations provides insights into the usefulness of the different approaches and reinforces the notion that depth of closure is a theoretical concept that will vary according to the used definition. The most widely-used definition for depth of closure proposed by Hallermeier (1978), Birkemeier (1985) and Capobianco et al. (1997) is the basal limit of the envelope of profile change or  $DoC$ . When the inshore wave conditions are used ( $DoC_{param,a}$ ), the results correspond with shallow values (10–15 m) and are very similar to the limit of significant change using the observational dataset for the case of Perranporth ( $DoC_{obs,a}$ ) for Hallermeier (1978). In contrast,  $DoC$  values computed using Capobianco et al. (1997) and Birkemeier (1985) for inshore wave conditions are always  $O(1\text{--}2\text{ m})$  below the observations. Hallermeier (1981) also defined an outer limit ( $DoC\text{-}motion$ ) as the offshore boundary of the wave-constructed profile. The latter should correspond with the deepest isobath where sediment motion occurs, but analysis of modelled wave and current bed shear stresses ( $DoC_{stress,b}$ ) reveals that this depth corresponds best with the upper-plane bed limit ( $\tau_{wc} > \tau_{crFlat}$ , Table 3) under extreme wave

conditions, or  $DoT$ . Furthermore, observations of seabed type distribution ( $DoC_{obs,b}$ ) also suggest that significant sediment exchange under high energy conditions (in this case the winter of 2016) is possible at those isobaths. Consequently, some authors such as Wright (1987, 1995) also considered this deeper limit of extreme motion as a boundary of significant bed-level change, justifying that vertical fluctuations of several cm's (i.e., below the survey accuracy used for defining  $DoC$ ) can represent large volumes of sediment when they are integrated over a wide and gentle-gradient shoreface.

As identified by Capobianco et al. (1997) and Nicholls et al. (1998b), wave parameterisations ( $DoC_{param}$  methods) are highly dependent on the timescale of interest. We used a 4-year time series of wave conditions, which included the most energetic winter affecting the coast of SW England (winter 2013/14) since at least 1948 (Masselink et al., 2015); this allows a consideration of the predicted  $DoC$  values over at least the decadal time scale. If  $H_{s,12}$  and  $T_{p,12}$  are derived from the complete 4-year time series, the  $DoC$  values are c. 4 m larger than if  $\langle DoC \rangle$  is used (yearly-averaged  $DoC$  computed using  $H_{s,12}$  and  $T_{p,12}$  for each year in the time series). As the concept of depth of closure is generally related to shoreface variability over inter-annual to decadal time scale, it is advisable to select the longest wave time series possible to estimate  $DoC$ . Furthermore,  $DoC$  parameterisations ( $DoC_{param}$ ) suggest that this value will increase over time, moving towards the maximum depth of significant sediment transport, or  $DoT$ .

Previous studies have identified the influence of geological control on the closure depth (Robertson et al., 2008; Ortiz and Ashton, 2016) and, hence, the necessity to use inshore wave conditions when estimating the active shoreface in embayed coastlines (Kraus et al., 1998). Accordingly, we found that using inshore wave conditions ( $DoC_{param,b}$ ) is more appropriate along embayed coastlines, especially for stretches

of coastline not directly facing the prevailing wave direction and/or protected by protruding headlands. However, the closure depth computed using the inshore wave conditions depends on the water depth from which the wave height is extracted: the shallower the depth, the smaller the waves, and the lower the *DoC* value. The inshore wave height and associated period extracted at the actual predicted *DoC* are used here, obtained through an iterative method, yielding *DoC* values that vary along the embayment as a result of the spatial gradient in the wave conditions affecting it.

Similar to the results presented in Robertson et al. (2008), the depth of closure formulation proposed by Hallermeier (1978) (Eq. (1)) provides the best matching with the morphologic observations ( $DoC_{obs,a}$ ) and a closure criteria of 0.14 m defined by the field data collection uncertainty, Table 3) and the procedure to compute this depth closure estimate is as follows: (1)  $H_{s,12}$  and  $T_{p,12}$  are computed using the wave time series that encompasses the shoreface monitoring period; (2) the offshore wave conditions are transformed into intermediate/shallow water; (3) the modelled inshore sea state in several representative profiles of the embayment is inserted into Eq. (1) and the embayment-averaged closure depth is computed; and (4) the depth of closure value is considered relative to MLWS and then corrected to the survey datum.

As pointed out by Wright (1987), Pilkey et al. (1993), Cowell et al. (2003), and Ortiz and Ashton (2016), the active shoreface is deeper than often predicted using observations and wave-based parameterisations. Recently, Ortiz and Ashton (2016) explored the shoreface dynamics at several locations on the East coast of the U.S. and concluded that  $DoC_{param,b}$  methods under-predict the morphodynamic closure depth. Similarly, our study shows that, in all cases, modelled bed shear stresses for the transitional limits of bedform activity ( $DoC_{stress}$ ) are significantly deeper than those computed using the wave parameterisations ( $DoC_{param,b}$ , Table 3). Computed bed shear stresses, reinforced by seabed type distribution observations ( $DoC_{obs,b}$ ), suggest that wave currents during extreme storm events ( $H_{s,12}$  and  $T_{p,12}$ ) can induce energetic sediment transport well seaward of the limit of ‘significant’ morphological change or *DoC* (where ‘significant’ is associated to the minimum detectable limit by the instrumentation) as  $DoT \gg DoC$ . During these events, the wave orbital velocities across the shoreface suggest that under such conditions most of the embayments experience extreme sediment motion, leading to upper-plane bed conditions, up to large depths (> 35 m, Table 3) even when disregarding tidal action. These results are similar to the values for Southeastern Australia (Wright, 1976; Wright, 1995), or the outcomes shown in Wright et al. (1986) and Wright (1987) for the Middle Atlantic Bight, where the limit for on/offshore sediment transport in these microtidal and energetic shelves exceeds the 30-m isobaths. When also considering tidal currents during the maximum flood in a tidal cycle, this transition depth can increase by > 5 m in areas where coastal geometry and bottom topography (e.g., headlands) induce maximum flow speeds.

Fig. 10 synthesises how the maximum depth of sediment transport (*DoT*) varies as a function of wave height and tidal current velocity. The results are obtained using the process-based method (computation of bed shear stresses due to waves and tidal currents,  $DoC_{stress,b}$ ) for transition to upper-plane bed (extreme sediment motion). Traditionally, the *DoC* concept is limited to wave-dominated coastlines where tidal currents do not significantly affect sediment transport; however, Fig. 10 represents a combined approach to the issue and can be applied to environments where strong tidal currents are important and waves are not the sole sediment-stirring factor. As can be observed in the figure, whilst keeping  $H_s$  constant, *DoT* increases with increasing tidal current velocity and/or increasing wave period. Due to the concurrence of a high-energy wave climate and strong tidal currents, *DoT* thresholds along the southwest coast of England (30–50 m) are relatively large compared to most other environments (Fig. 10). Moderately energetic shelves (e.g., East coast of England; EE) with large tidal currents can exhibit values for the offshore limit of the active shoreface that are similar to microtidal and more energetic coastlines (Middle Atlantic

Bight; MAB). A comparison between the coast of SW England (high energy, macrotidal) to New South Wales, Australia (high energy, microtidal), indicates that *DoT* values are c. 10 m deeper in the SW England, due to the presence of greater tidal currents.

During extreme storm events, exposed embayments can experience cross-shore sediment transport that exceeds the depth of the base of headlands, allowing sediment to move a considerable distance seaward of the beach-constraining headlands. Furthermore, along a macrotidal coast, the shoreface area that is morphodynamically active during these storm events will increase due to the contribution of the tidal currents to the total bottom shear stress, especially during spring tides. A conceptual model of the shoreface dynamics for an idealised high-energy and macrotidal coast that illustrates this situation is presented in Fig. 11. The implication is that, even though the headlands that flank many embayed beaches appear sufficiently prominent to suggest that the embayed beach can be considered a closed cell (with restricted sediment transport in/out the cell), significant sediment transport at a short time-scale may take place well beyond the ends of the headland, leading to headland bypassing. Some recent studies also point in this direction, demonstrating that cell compartments often includes several embayed beaches (Kinsela et al., 2017; McCarroll et al., 2018) and that transport of sediment under extreme events is likely to occur even around headlands with an apex that reaches the 50-m isobath (George, 2016). This challenges the notion that embayed beaches are generally closed cells and that headland bypassing may be more widespread than commonly assumed. Accordingly, a re-evaluation of the concept of closed embayments is especially appropriate for the north Cornish coastline, as these embayments can be deemed opened cells, and indeed, the coast of SW England as a whole can perhaps be considered a single sediment cell from Land's End to the Bristol Channel, as previously suggested by May and Hansom (2003).

## 7. Conclusions

This paper revisits the ‘depth of closure’ (*DoC*) concept through the study of the predicted zone of significant sediment transport and evaluates its applicability to the macrotidal and exposed coastline of SW England, discussing the implications for headland bypassing and exploring the open/closed cell concept along embayed coastlines. Two main closure limits based on shoreface morphodynamics and seabed activity are considered: the widely-used morphological depth of closure (*DoC*) defined as the basal limit of the envelope of profile change, and a deeper limit of maximum depth of ‘significant’ sediment transport (*DoT*) under extreme events, where ‘significant’ refers to intense bed agitation represented by the upper-plane bed transition. The key findings are:

1. *DoT* is considered a boundary of significant bed level change as up to that water depth intense sediment transport takes place (upper-plane bed transition). Although over the medium-term time scale (years) these morphological changes might not be detectable (below the survey accuracy), they are likely to represent large volumes of sediment when integrated over the shoreface.
2. Along embayed coastlines, inshore wave conditions (using the longest time series possible) must be used to compute *DoC*, as offshore wave conditions are not representative due to wave transformation processes. Wave attenuation, refraction and diffraction around headlands can result in a large spatial gradient in the inshore wave conditions, and the local embayment geometry can have a greater impact on *DoC* values than any regional variability in wave exposure.
3. The wave-based parameterisation of depth of closure by Hallermeier (1978) (Eq. (1)) provides a good approximation of observed morphological depth of closure (for a minimum detectable limit of 0.14 m) at the medium-term scale for the exposed and macrotidal study area, if calculated relative to MLWS.

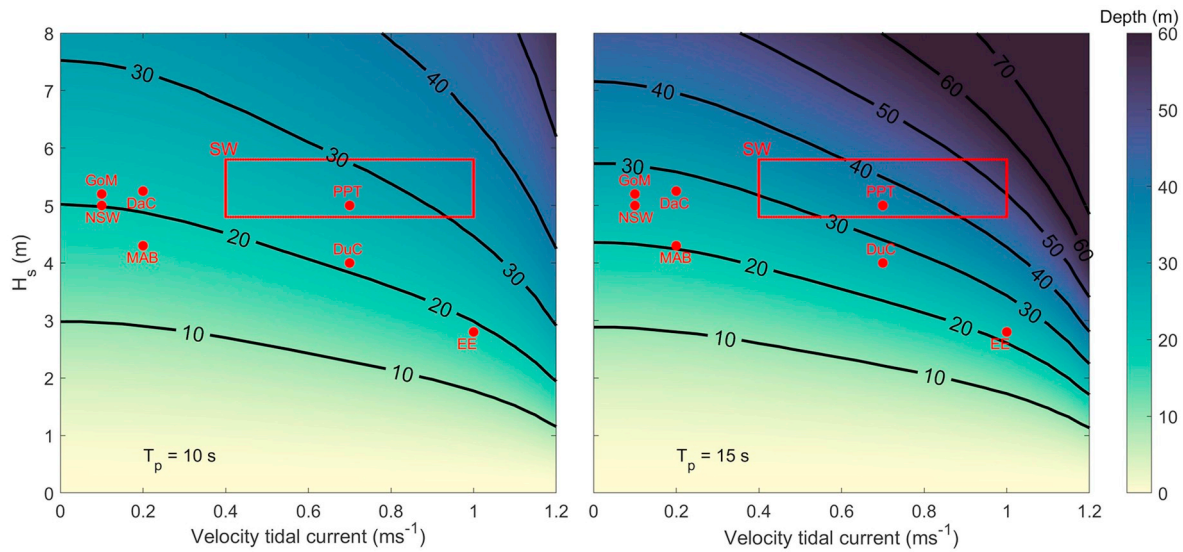


**Fig. 10.** Variation of *DoT* across a broad wave-current parameter space. *DoT* is computed using significant wave height ( $H_s$ ) and tidal current speed ( $\bar{U}$ ) for medium sand ( $D_{50} = 0.3$  mm) and a constant period ( $T_p$ ) of 10 s (left panel) and 15 s (right panel). Examples of computed *DoT* values using extreme significant wave height ( $H_{s,99\%}$ ) and maximum tidal current in the bottom layer are shown as red dots: *GoM* – Gulf of Mexico (Pepper and Stone, 2004; Ortiz and Ashton, 2016); *NSW* – New South Wales (Kulmar et al., 2005); *MAB* – Middle Atlantic Bight (Wright et al., 1994); *DaC* – Danish Coast (Aagaard et al., 2010); *DuC* – Dutch Coast (Luijendijk et al., 2017); *EE* – East England (Haskoning, 2005; Leonardi and Plater, 2017); and *PPT* – Perranporth. The range of  $H_s - \bar{U}$  combinations estimated for the SW (South West England) is also indicated (red box). (For interpretation of the references to colour in this figure legend, the reader is referred to the web version of this article.)

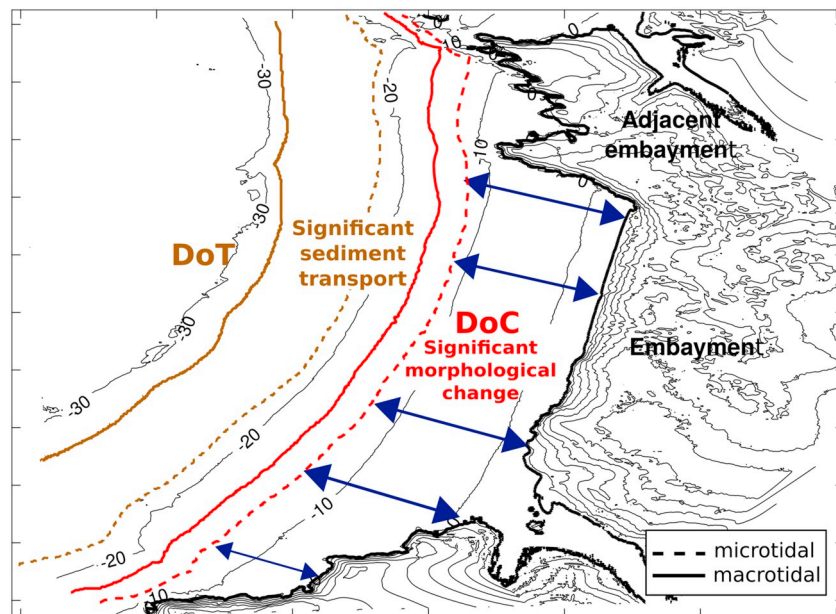


**Fig. 11.** Plan view of an idealised high-energy and embayed coastline. (For interpretation of the references to colour in this figure legend, the reader is referred to the web version of this article.)

4. The active shoreface is deeper than often considered by engineering practice. Combined wave-tide bed shear stresses computed following a process-based method, reinforced by seabed type distribution observations, suggest that important sediment transport during extreme conditions occurs well seaward of the limit of 'significant' morphological change.
5. *DoT* is computed across a broad wave height and (tidal) current velocity parameter space to investigate the influence of currents on wave-derived values for maximum depth of significant transport at a range of contrasting coastal locations. *DoT* depths can be increased by ~10 m  $O(30\%)$  for macrotidal locations compared to microtidal

- environments with a similar wave climate, highlighting the importance of considering tidal currents in realistic *DoT* calculations.
6. The considerable depth ( $\geq 30$  m) at which combined wave- and tide-driven sediment transport can occur under extreme wave conditions along exposed, macrotidal and embayed settings implies that transport of fine and medium sediment under extreme events can exist around headlands with an apex base that surpasses the 30-m isobath. This significantly increases the potential for headland by-passing and challenges the notion that embayments are generally considered closed sediment cells.

## Acknowledgments

This work was supported by UK Natural Environment Research Council grant (NE/M004996/1; BLUE-coast project). This study is only possible thanks to the efforts of the members of the Coastal Process Research Group who have been, and still are, collecting observations at Perranporth. The UK MetOffice (Dr Andy Saulter) and Channel Coast Observatory are project stakeholders and kindly provided modelled wave data and measured topography, respectively. We would also like to acknowledge the EPSRC-funded ARCC “Adaptation and Resilience of Coastal Energy Supply” (ARCoES) project (EPSRC EP/I035390/1) for providing the FVCOM modelled current data.

## References

- Aagaard, T., Kroon, A., Greenwood, B., Hughes, M.G., 2010. Observations of offshore bar decay: sediment budgets and the role of lower shoreface processes. *Cont. Shelf Res.* 30 (14), 1497–1510.
- Aragones, L., Serra, J.C., Villacampa, Y., Saval, J.M., Tinoco, H., 2016. New methodology for describing the equilibrium beach profile applied to the Valencia's beaches. *Geomorphology* 259, 1–11.
- BERR, 2008. Atlas of UK Marine Renewable Energy Resources. Tech. Rep.
- Birkemeier, W., 1985. Field data on seaward limit of profile change. *J. Waterw. Port Coast. Ocean Eng.* 598–602.
- Booij, N., Ris, R.C., Holthuijsen, L.H., 1999. A third-generation wave model for coastal regions: 1. Model description and validation. *J. Geophys. Res.* 104 (C4), 7649–7666.
- Capobianco, M., Larson, M., Nicholls, R.J., Kraus, N.C., 1997. Depth of closure: a contribution to the reconciliation of theory, practise and evidence. In: *Proceedings of Coastal Dynamics*. ASCE, New York, pp. 506–515.
- Capobianco, M., Hanson, H., Larson, M., Steetzel, H., Stive, M.J.F., Chatelus, Y., Aarninkhof, S., Karambas, T., 2002. Nourishment design and evaluation: applicability of model concepts. *Coast. Eng.* 47 (2), 113–135.
- Chen, C., Liu, H., Beardsley, R.C., 2003. An unstructured, finite-volume, three-dimensional, primitive equation ocean model: application to coastal ocean and estuaries. *J. Atmos. Ocean. Technol.* 20 (1), 159–186.
- Chesher, J.A., Smythe, D.K., Bishop, P., 1981. *The Geology of the Minches, Inner Sound and Sound of Raasay*. rep. inst. Edition. pp. 41.
- Cowell, P.J., Stive, M.J.F., Niedoroda, A.W., de Vriend, H.J., Swift, D.J.P., Kaminsky, G.M., Capobianco, M., 2003. The coastal-tract (part 1): a conceptual approach to aggregated modeling of low-order coastal change. *J. Coast. Res.* 19 (4), 812–827.
- De Dominicis, M., O'Hara Murray, R., Wolf, J., 2017. Multi-scale ocean response to a large tidal stream turbine array. *Renew. Energy* 114, 1160–1179. <https://doi.org/10.1016/j.renene.2017.07.058>.
- Dott, R.H., Bourgeois, J., 1982. Hummock stratification: significance of its variable bedding sequences. *Geol. Soc. Am. Bull.* 93 (August), 663–680.
- George, D.A., 2016. Circulation and Sediment Transport at Headlands With Implications for Littoral Cell Boundaries. Ph.D. thesis. University of California, Davis.
- Grant, W.D., Madsen, O., 1982. Movable bed roughness in unsteady oscillatory flow. *J. Geophys. Res.* 87, 469–481.
- Hallermeier, R.J., 1978. Uses for a calculated limit depth to beach erosion. In: *Proceedings of the 16th Coastal Engineering Conference*. ASCE, New York, pp. 1493–1512.
- Hallermeier, R.J., 1981. A profile zonation for seasonal sand beaches from wave climate. *Coast. Eng.* 4 (C), 253–277.
- Hands, E.B., Allison, M.C., 1991. Mound migration in deeper water and methods of categorising active and stable depths. In: *Proceedings of the ASCE Specialty Conference on Quantitative Approaches to Coastal Sediment Processes*. vol. 2. pp. 1985–1999.
- Hanson, H., Kraus, N.C., 1989. GENESIS: Generalized Model for Simulating Shoreline Change. Tech. rep. 1. Coastal Engineering Research Center, U.S. Army Corps of Engineers, Vicksburg, Mississippi.
- Hartman, M., Kennedy, A.B., 2016. Depth of closure over large regions using airborne bathymetric lidar. *Mar. Geol.* 379, 52–63.
- Haskoning, 2005. Suffolk wave and tide analysis report. Final report 9R0839/R/PBor. In: Report for the Environment Agency, Anglian Region. Royal Haskoning, Peterborough (December 2005).
- Hinton, C., Nicholls, R.J., 1998. Spatial and temporal behaviour of depth of closure along the Holland coast. In: *26th International Conference on Coastal Engineering*, pp. 2913–2925.
- Kinsela, M.A., Morris, B.D., Linklater, M., Hanslow, D.J., 2017. Second-pass assessment of potential exposure to shoreline change in New South Wales, Australia, using a sediment compartments framework. *J. Mar. Sci. Eng.* 5 (4), 61. <https://doi.org/10.3390/jmse5040061>.
- Komen, G.J., Hasselmann, S., Hasselmann, K., 1984. On the existence of a fully developed wind-sea spectrum. *J. Phys. Oceanogr.* 14, 1271–1285.
- Kraus, C., Larson, M., Wise, R., 1998. Depth of closure in beach fill design. In: *Proceedings 12th National Conference on Beach Preservation Technology*. vol. 40. Florida Shore and Beach Preservation Association, pp. 271–286.
- Kulmar, M., Lord, D., Sanderson, B., 2005. Future directions for wave data collection in New South Wales. In: *Proceedings of the 17th Australasian Coastal and Ocean Engineering Ports Conference*, pp. 167–172 Australia, Sydney.
- Larson, M., 1991. Equilibrium profile of a beach with varying grain size. In: *Proceedings Coastal Sediments 1991*. ASCE, Seattle, pp. 861–874.
- Larson, M., Kraus, N.C., 1992. Dynamics of longshore bars. In: *Proceedings Coastal Engineering*. ASCE, Venice, pp. 2219–2232.
- Leonardi, N., Plater, A.J., 2017. Residual flow patterns and morphological changes along macro- and meso-tidal coastline. *Adv. Water Resour.* 109, 290–301.
- Luijendijk, A.P., Ranasinghe, R., de Schipper, M.A., Huisman, B.A., Swinkels, C.M., Walstra, D.J.R., Stive, M.J.F., 2017. The initial morphological response of the Sand Engine: a process-based modelling study. *Coast. Eng.* 119, 1–14.
- Marsh, S.W., Nicholls, R.J., Kroon, A., Hoekstra, P., 1998. Assessment of depth of closure on a nourished beach: Terschelling, the Netherlands. In: *26th International Conference on Coastal Engineering*, pp. 3110–3123.
- Masselink, G., Scott, T., Poate, T., Russell, P., Davidson, M., Conley, D., 2015. The extreme 2013/2014 winter storms: hydrodynamic forcing and coastal response along the southwest coast of England. *Earth Surf. Process. Landf.* <https://doi.org/10.1002/esp.3836>. (n/a–n/a).
- May, V.J., Hansom, J.D., 2003. *Coastal Geomorphology of Great Britain*, Geological edition. Joint Nature Conservation Committee, Peterborough, pp. 754.
- McCarroll, J., Masselink, G., Valiente, N.G., Scott, T., King, E., 2018. Wave and tidal controls on headland bypassing and embayment circulation. *J. Mar. Sci. Eng.* 6 (3), 94. <https://doi.org/10.3390/jmse6030094>.
- Nicholls, R.J., Birkemeier, W.A., Lee, G., 1998a. Evaluation of depth of closure using data from Duck, NC, USA. *Mar. Geol.* 148 (3–4), 179–201.
- Nicholls, R.J., Larson, M., Capobianco, M., Birkemeier, W.A., 1998b. Depth of closure: improving understanding and prediction. In: *Proceedings of the Coastal Engineering Conference*. vol. 3. ASCE, New York, pp. 2888–2901.
- Nichols, G., 1999. *Sedimentology and Stratigraphy*, Second edition. John Wiley & Sons, Ltd., Publication, Oxford, pp. 419.
- Nielsen, P., 1981. Dynamics and geometry of wave-generated ripples. *J. Geophys. Res.* 86, 6467–6472.
- Ortiz, A.C., Ashton, A.D., 2016. Exploring shoreface dynamics and a mechanistic explanation for a morphodynamic depth of closure. *J. Geophys. Res. Earth Surf.* 121 (2), 442–464.
- Pawlowicz, R., Beardsley, B., Lentz, S., 2002. Classical tidal harmonic analysis including error estimates in MATLAB using TIDE. *Comput. Geosci.* 28 (8), 929–937.
- Pepper, D.A., Stone, G.W., 2004. Hydrodynamic and sedimentary responses to two contrasting winter storms on the inner shelf of the northern Gulf of Mexico. *Mar. Geol.* 210 (1–4), 43–62.
- Peters, S.E., Loss, D.P., 2012. Storm and fair-weather wave base: a relevant distinction? *Geology* 40 (6), 511–514.
- Phillips, M.R., Williams, A.T., 2007. Depth of closure and shoreline indicators: empirical formulae for beach management. *J. Coast. Res.* 232 (2001), 487–500.
- Pilkey, O.H., Young, R.S., Riggs, S.R., Sam Smith, A.W., Wu, H., Pilkey, W.D., 1993. The concept of shoreface profile of equilibrium: a critical review. *J. Coast. Res.* 9 (1), 255–278.
- Plant, N.G., Holland, K.T., Puleo, J.A., 2002. Analysis of the scale errors in nearshore bathymetric data. *Mar. Geol.* 191 (1–2), 71–86. [https://doi.org/10.1016/S0025-3227\(02\)00497-8](https://doi.org/10.1016/S0025-3227(02)00497-8).
- Potter, P., 1967. Sand bodies and sedimentary environments: a review. *AAPG Bull.* 51 (3), 337–365.
- Prodder, S., Russell, P., Davidson, M., 2016. Grain-size distributions on high-energy sandy beaches and their relation to wave dissipation. *Sedimentology* 64, 1289–1302.
- Robertson, W., Zhang, K., Finkl, C.W., Whitman, D., 2008. Hydrodynamic and geologic influence of event-dependent depth of closure along the South Florida Atlantic Coast. *Mar. Geol.* 252 (3–4), 156–165. <https://doi.org/10.1016/j.margeo.2008.03.018>.
- Rosati, J.D., Dean, R.G., Walton, T.L., 2013. The modified Bruun Rule extended for landward transport. *Mar. Geol.* 340, 71–81. <https://doi.org/10.1016/j.margeo.2013.04.018>.
- Roy, P.S., Thom, B.G., 1981. Late Quaternary marine deposition in New South Wales and southern Queensland - an evolutionary model. *J. Geol. Soc. Aust.* 28 (July), 471–489. <https://doi.org/10.1080/00167618108729182>.
- Samuel, R.M., 2017. Seasonal Variation of Macrobenthos Distribution and the Biophysical Cohesiveness of Sediments on a Macrotidal, Highly Exposed Sandy Beach. Masters Thesis. Faculty of Science and Engineering, Plymouth University.
- Saulter, A.J., 2017. Quality Information Document: North West European Shelf Production Centre. NORTHWEST-SHELF ANALYSIS FORECAST WAV 004 012. Tech. Rep. Available at: <http://cmems-resources.cls.fr/documents/QUID/CMEMS-NWS-QUID-004-012.pdf>.
- Scott, T., Masselink, G., Russell, P., 2011. Morphodynamic characteristics and classification of beaches in England and Wales. *Mar. Geol.* 286 (1–4), 1–20.
- Soulsby, R., 1995. Bed shear-stresses due to combined waves and currents. In: Stive, M., de Vriend, H. (Eds.), *Advances in Coastal Morphodynamics*, (4–20 to 4–23).
- Soulsby, R., 1997. *Dynamics of Marine Sands: A Manual for Practical Applications*. Thomas Telford Publications, pp. 249.
- Stive, M.J.F., de Vriend, H.J., 1995. Modelling shoreface profile evolution. *Mar. Geol.* 126 (1–4), 235–248. [https://doi.org/10.1016/0025-3227\(95\)00080-1](https://doi.org/10.1016/0025-3227(95)00080-1).
- Stive, M.J., Nicholls, R.J., de Vriend, H.J., 1991. Sea-level rise and shore nourishment: a discussion. *Coast. Eng.* 16 (1), 147–163.
- Stive, M.J., de Vriend, H.J., Nicholls, R.J., Capobianco, M., 1992. Shore nourishment and the active zone: a time scale dependent view. In: *Proceedings of the Twenty-Third Coastal Engineering Conference*. ASCE, New York, pp. 2464–2473.
- Tanaka, H., Van To, D., 1995. Initial motion of sediment under waves and wave-current combined motions. *Coast. Eng.* 25 (3–4), 153–163.
- Thieler, E.R., Pilkey, O.H., Cleary, W.J., Schwab, W.C., 2001. Modern sedimentation on

- the shoreface and inner continental shelf at Wrightsville Beach, North Carolina, U.S.A. *J. Sediment. Res.* 71 (6), 958–970.
- Tolman, H.L., 2014. User Manual and System Documentation of WAVE-WATCH III. Tech. Rep.
- United Kingdom Hydrographic Office, 2011. INSPIRE Portal & Bathymetry DAC. Available at: <http://aws2.caris.com/ukho/mapViewer/map.action>.
- Work, P.A., Dean, R.G., 1991. Effect of varying sediment size on equilibrium beach profiles. In: *Proceedings Coastal Sediments*. ASCE, Seattle, pp. 891–904.
- Wright, L.D., 1976. Nearshore wave-power dissipation and the coastal energy regime of the Sydney-Jervis Bay region, New South Wales: a comparison. *Aust. J. Mar. Freshwat. Res.* 27, 633–640.
- Wright, L.D., 1987. Shelf-surf zone coupling: diabathic shoreface transport. In: *Proceedings of Coastal Sediments*. ASCE, Washington, D.C., pp. 25–40.
- Wright, L.D., 1995. *Morphodynamics of Inner Continental Shelves*. CRC Press, Inc.
- Wright, L.D., Boon, J.D., Green, M.O., List, J.H., 1986. Response of the mid-shoreface of the southern Mid-Atlantic Bight to a “northeaster”. *Geo-Mar. Lett.* 6, 153–160.
- Wright, L.D., Boon, J.D., Kim, S.C., List, J.H., 1991. Modes of cross-shore sediment transport on the shoreface of the Middle Atlantic Bight. *Mar. Geol.* 96 (1–2), 19–51.
- Wright, L.D., Xu, J.P., Madsen, O.S., 1994. Across-shelf benthic transports on the inner shelf of the Middle Atlantic Bight during the “Halloween storm” of 1991. *Mar. Geol.* 118 (1–2), 61–77.
- Young, I.R., 1999. *Wind Generated Ocean Waves*. vol. 2 Elsevier Sci, Amsterdam.

# **Multi-annual embayment sediment dynamics involving headland bypassing and sediment exchange across the depth of closure**

**Nieves G. Valiente<sup>1</sup>, Robert Jak McCarroll<sup>1</sup>, Gerd Masselink<sup>1</sup>, Tim Scott<sup>1</sup>, Mark Wiggins<sup>1</sup>**

<sup>1</sup>School of Biological and Marine Sciences, University of Plymouth, PL4 8AA, UK

Corresponding author: Nieves G. Valiente ([nieves.garciavaliente@plymouth.ac.uk](mailto:nieves.garciavaliente@plymouth.ac.uk))

**<https://doi.org/10.1016/j.geomorph.2019.06.020>**

## *Keywords:*

Storm response, sediment budget, beach recovery, sediment dynamics, nearshore sediment transport, beach morphodynamics

## *Highlights:*

- Full sediment budget was produced along an exposed macrotidal embayment and linked to wave forcing
- Inter- and sub-tidal volume are not inversely correlated, indicating decoupling
- Sediment budget suggests significant exchange around headlands and/or across depth of closure
- Beaches on this coast type can be considered part of an extended coastal cell

## Abstract

Predicting the future behavior of beach and nearshore systems requires an accurate delineation and understanding of coastal cell boundaries, sediment transport pathways, and sediment sources and sinks. Unfortunately, there is a paucity of field datasets on beach and nearshore morphological change that extend fully from the top of the dunes to beyond the depth of closure to enable quantification of the sediment budget. Here, for the first time, we employ a total sediment budget approach, examining a sandy and embayed beach located in the north coast of SW England, to investigate inter- and multi-annual embayment scale sediment dynamics over a 10-year period that includes extreme storm erosion and post-storm recovery. We demonstrate that, despite the deeply embayed nature of the beach, the shoreline orientation roughly parallel to the dominant wave direction and the overwhelmingly cross-shore forcing of the inter-tidal beach volume, the system is neither closed, nor balanced. The very significant net changes in the recorded sediment volume from dune top to depth of closure (-14.5 m ODN), representing a loss of c. 100 m<sup>3</sup> m<sup>-1</sup> during the extreme storm period and a gain of c. 200 m<sup>3</sup> m<sup>-1</sup> during the recovery period, indicate that significant sediment transport occurs seaward of the base of the terminating headlands and beyond the morphological depth of closure. The results further indicate that the inter-tidal region is partly uncoupled from the sub-tidal region, with the former region dominated by cross-shore sediment fluxes, whereas the subtidal region is also significantly affected by longshore sediment fluxes. A conceptual model is presented that balances the observed volume changes with inferred fluxes, forced by variations in total and alongshore wave power. This study contradicts the general assumption that when sediment exits the inter-tidal, it rests undisturbed in the sub-tidal, waiting for a period of low-moderate energy to bring it onshore. The large sediment volumetric variations across the lower shoreface (depth of 5–20 m), which are of the same order of magnitude as, but uncorrelated with, those occurring in the inter-tidal region, are suggestive of an energetic longshore transport system across this deeper region. It is possible that this transport system extends along the whole north coast of SW England and this finding may lead to a shift in understanding of sediment budgets along exposed and macrotidal embayments globally.

## 1. Introduction

Sandy beaches and coastal dunes have significant natural capital through representing efficient and natural coastal defenses that can protect the hinterland from coastal flooding. In a context of increasing winter-wave conditions (Castelle et al., 2018) and rate of sea-level rise (Church and White, 2011), it is important to understand how coasts respond and evolve as a result of changing boundary conditions, as this significantly affects continued human occupation of the coastal zone. Predicting coastal system behavior requires an accurate delineation and understanding of coastal cell boundaries, sediment sources and sinks, and transport pathways. The difficulties with identifying these key sediment-related factors, attributed to large uncertainties associated with sediment transport modelling and a paucity of high-quality field datasets extending from the top of the dunes to depths beyond the depth of closure (Aagaard, 2011; Coco et al., 2014), inhibit accurate quantification of sediment fluxes in a particular littoral cell. Moreover, long-term beach response is controlled by the sediment exchanges between the different beach sub-components (e.g., dunes, supratidal beach, inter-tidal zone, and sub-tidal zone), and these sub-components tend to operate over different time scales (Castelle et al., 2017b).

A quantitative understanding of littoral cells and sediment budgets is a fundamental element of coastal sediment studies (Bowen and Inman, 1966; Caldwell, 1966; Komar, 1998; Rosati, 2005). Littoral cell (self-contained or semi-contained; refer to Fig. 1) and sediment budget concepts were introduced in the 1960s through several regional studies based upon coastal geology (rocky headlands) and estimates of longshore sand transport along specified sources and sinks (Bowen and Inman, 1966; Caldwell, 1966; Inman and Frautschy, 1966). Littoral cells are essentially defined as self-contained coastal units over a period of time, usually separated by prominent features (often headlands or jetties) that impede transfer of sediment (Kinsela et al., 2017). These cell boundaries delineate the spatial area within which the budget of sediment is known, providing the framework for the quantification of coastal erosion and accretion (CIRIA, 1996). Whether a littoral cell can be considered contained (Fig. 1-left panel) or semi-contained (Fig. 1-middle and right panels) depends on the timescale of consideration. Often, a compartment or coastal cell may appear closed, but over longer timescales during which long return period events inducing severe sediment transport are included, it may actually be open or semi-contained. Therefore, primary sediment compartments (self-contained/closed) are those that capture the limit in the sediment pathway within a large sediment-sharing area for long timescales ( $10^1$ – $10^2$  years);

while sub-cells are usually finer in scale, identify semi-contained/open systems at timescales  $> 10^1$  years and can appear closed in the short-term ( $< 10^1$  years) (Rosati, 2005; Kinsela et al., 2017; Thom et al., 2018).

Highly embayed beaches are often considered closed cells (Fig. 1-left panel) with the prominent headlands acting as barriers to littoral drift, such that sediment transport into and/or out of adjacent cells is insignificant. Nevertheless, recent studies show that significant sediment transport offshore and/or beyond these barriers exists under particular conditions, inducing headland bypassing (Short, 1985; Short and Masselink, 1999; Short, 2010; Cudaback et al., 2005; Loureiro et al., 2012; George et al., 2015; Vieira da Silva et al., 2017; McCarroll et al., 2018). Short (1985) suggested that major storm wave events are one of the key drivers of headland-attached bar bypassing, allowing sand to be transported to the morphological depth of closure (*DoC*) and beyond the headland position. Additionally, recent studies of mega-rips and beach response to extreme storm events also reveal important cross-embayment exchanges across the shoreface to deeper water (Short, 2010; Loureiro et al., 2012; McCarroll et al., 2016) and between adjacent beaches (Cudaback et al., 2005; Vieira da Silva et al., 2017). Furthermore, new research also emphasizes the influence of the strong tidal currents registered around headlands in facilitating bypassing at macrotidal environments (McCarroll et al., 2018; King et al., 2019; Valiente et al., 2019). All these studies demonstrate that under certain conditions of wave-tidal current interaction, important sediment transport paths occur at depths that well exceed the depth of the base of headlands, challenging the notion of embayments as closed coastal cells and highlighting limitations to the littoral cell and the depth of closure, critical concepts for long-term coastal evolution studies (e.g., application of the Bruun rule) and shoreline modelling (e.g., one-line models).

A total sediment budget approach to a coastal cell enables derivation of incoming and outgoing sediment fluxes from the rate of sediment volume change within the cell. A significant research gap exists in quantification of sediment budgets, in that many studies examine parts of the budget (e.g., the inter-tidal), while extremely few studies capture the entire system. This information helps with confirming the status of a closed cell and estimating the long-term coastal evolution (Wiggins et al., 2019). For a given coastal cell, the sediment budget ( $dQ_{net}$ ) is expressed by the balance of volumes between sediment supply ( $\Sigma Q_{source}$ ) and sediment losses ( $\Sigma Q_{sink}$ ) in the compartment (Rosati, 2005; Aagaard, 2011). In both closed (Fig. 1-left panel) and balanced

systems (Fig. 1-middle panel)  $dQ_{net} = 0$ ; however, for unbalanced systems (Fig. 1-right panel),  $dQ_{net} \neq 0$  and in this case the volume of incoming sediment is not the same as the volume that exits the system. For prograding shorefaces and retrograding shorefaces,  $dQ_{net} > 0$  and  $dQ_{net} < 0$ , respectively. Sediment sources include longshore transport of sediment into the area, cross-shore supply of sediment from offshore (beyond the cell seaward limit), anthropogenic interference (beach nourishment), in-situ production of sediment (Kinsela, 2017) and supply from autochthonous sources, such as rivers and dune and cliff erosion (Aagaard, 2011). Sediment losses from the upper shoreface can be accomplished through longshore and cross-shore processes. Sediment can leave embayments through headland bypassing, onshore aeolian transport beyond the coastal dune region (e.g., into a back-barrier lagoon) and offshore exchange from the upper shoreface to larger depths, i.e., beyond the depth of closure from where sediment may not be transported back onshore.

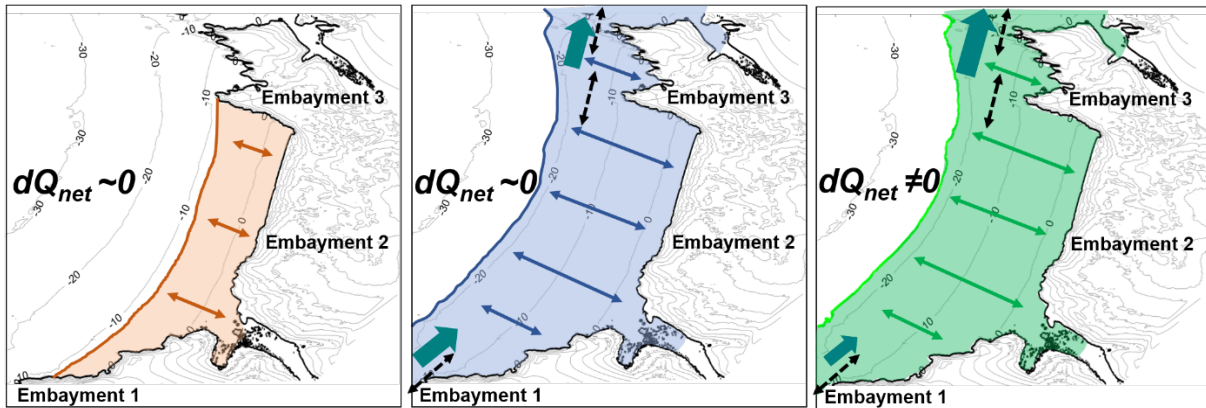


**Fig. 1.** Plan view of beach-inner shelf dynamics for a closed cell (left panel), a balanced open system (middle panel) and a non-balanced open system (right panel) using an idealized high-energy, cross-shore dominated and embayed coastal cell section.

Most of current coastal research based on observations lack rigorous uncertainty calculation, potentially identifying measurement artefacts as real morphological changes and consequently, misrepresenting sediment fluxes. For a robust quantification of cross-shore and longshore sediment fluxes within coastal cells, is important to distinguish real changes from noise (Lane et al., 1994; Milne and Sear, 1997; Lane, 1998; Brasington et al., 2000; Lane et al., 2003; Wheaton et al., 2010; Wiggins et al., 2019; Guisado-Pintado and Jackson, 2019). Sandy coastlines commonly exhibit vertical morphological fluctuations of similar magnitude to the uncertainty

associated with the measurement. In order to account for this uncertainty, but retain information on real morphological change, effective spatially-variable uncertainty computation techniques are required (Brasington et al., 2003; Lane et al., 2003, Wheaton et al., 2010).

In this study, we apply a total sediment budget approach based on field observations and spatially-variable uncertainty analysis. We evaluate the inter-annual dynamics of Perranporth beach, a sandy, exposed and embayed coastal system located on the north coast of SW England, over multi-annual time scales. Recent model-based studies investigated the potential for headland bypassing and offshore shoreface limits for significant sediment transport across Perranporth (McCarroll et al., 2018; Valiente et al., 2019). These indicated that the sub-tidal zone is potentially as dynamic as the rest of the beach system, and that, despite the cross-shore dominated nature of this type of embayment, alongshore processes and sediment fluxes may play an important role in the sediment balance of the system. Hence, we examine: (1) inter-annual morphological evolution of the inner embayment, including cross-shore and longshore sediment exchanges between sub-systems; (2) multi-annual full embayment morphological response to the 2013/14 winter, which represents the most energetic period along most of the European Atlantic coast since at least 1948 (Masselink et al., 2016b), using a total sediment budget approach; (3) relationship between wave forcing and embayment response; and (4) the nature of Perranporth's coastal cell (closed or open).

A description of the study area together with the methodology applied to estimate the total sediment budget is presented in Section 2. A comprehensive analysis of quasi-full embayment beach morphology (inter-annual records of dune, inter-tidal and sub-tidal regions) is presented in Section 3. This analysis is extended spatially (for multi-annual epochs) to the full embayment (coastal cell) by including observations offshore ( $>40$  m Ordnance Data Newlyn, ODN) and beyond the bounding headlands for the years 2011, 2016, 2017 and 2018 in Section 4. Links between wave forcing and embayment morphological change are presented in Section 5. Section 6 presents discussion with a conceptual sediment budget model. Finally, conclusions are presented in Section 7.

## 2. Study area and methodology

### 2.1. Perranporth and Penhale Sands beach

Perran and Penhale Sands beach (hereafter noted as Perranporth beach) is a sandy, exposed, dissipative and macrotidal embayment located on the north coast of Cornwall, SW England (Fig. 2a). The configuration of the beach is typical of this coastline (Burvingt et al., 2018), which is characterized by sandy beaches embayed by sharp headlands (Fig. 2b). The site represents a 3.5-km long wide sandy beach facing  $290^\circ$  at the south and  $280^\circ$  at the north, backed by an extensive and high dune system both in the north (Fig. 2c, 60 m ODN) and south (Fig. 2d, 20 m ODN), divided by a small headland (Cotty's Point). The embayment is delineated by Ligger Point (northern end) and Droskyn Point (southern end), comprised of metamorphic rocks with 40-m high cliffs dropping near vertically (at their most offshore extent) to 2–7 m depth ODN at the south and to 5–7 m depth ODN at the north. The southern hindshore dune system is the center of numerous anthropogenic interventions that affect the natural morphologic response of that area of the beach, in contrast to the northern dunes where natural processes dominate. The beach presents a relatively featureless upper inter-tidal zone, a three-dimensional lower inter-tidal region (around MLWS), mostly characterized by inner low-tide bar/rip systems (Masselink and Short, 1993; Scott et al., 2011), and a sub-tidal outer bar oscillating between 5 to 7 m depth ODN. The shoreface is characterized by a low-gradient (mean bed slope of 0.018) with the limit of detectable morphological change or morphological depth of closure ( $DoC$ ) at -14.5 m located 750–950 m from the mean sea level (MSL; approximately 0.3 m ODN) and a c. 500-m wide inter-tidal region. Perranporth beach is composed of medium sand with a median grain size ( $D_{50}$ ) of 0.33–0.40 mm for the supra- and inter-tidal area (Prodger et al., 2017). The  $D_{50}$  attains a relatively constant value of 0.30 mm for the sub-tidal area with gravel patches ( $D_{50} = 2\text{--}3$  mm) appearing around 26 m depth ODN (Valiente et al., 2019).

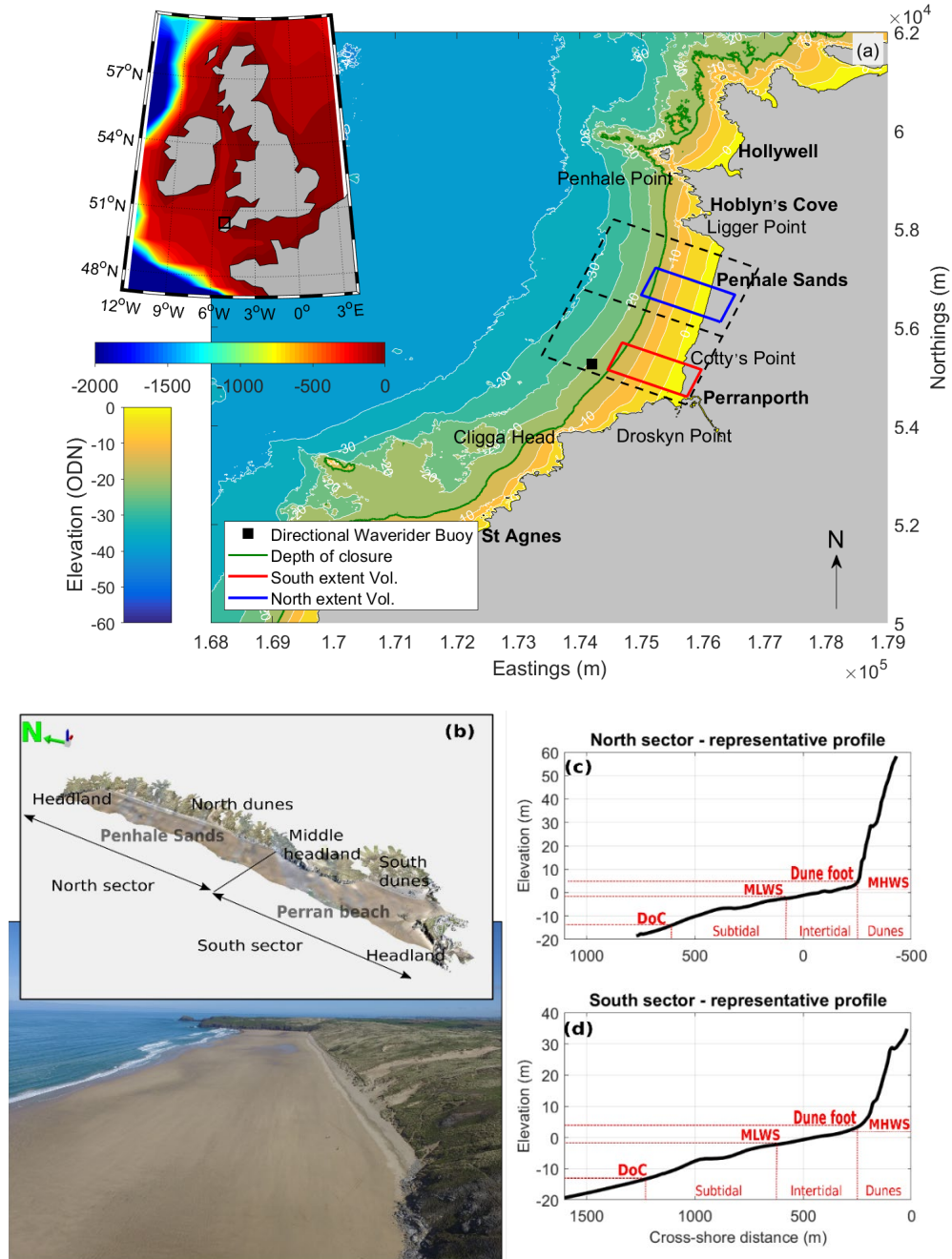


**Fig. 2.** (a) Location map of Perranporth beach, SW England, physical context and regions used for quasi and full embayment volume time series calculation (red and blue boxes, and black dashed region, respectively). (b) Embayment 3D-view with extension of north and south sectors and aerial photograph of Penhale Sands taken to the north showing north dune system. Bottom right-hand panels show a representation of a vertical profile from the frontal dune system to the inner-shelf for the north (c) and south (d) beach sectors, including the considered sub-systems (sub-tidal, inter-tidal and dunes).

Perranporth is exposed to regular North Atlantic swell with an annual average significant wave height ( $H_s$ ) of 1.6 m and peak period ( $T_p$ ) of 10.2 s, and storm events with a 1% exceedance wave height and associated peak wave period of 4.6 m and 16.7 s, respectively (Fig. 3e). Incoming wave energy displays strong seasonal modulation (Fig. 3a-b) with monthly average  $H_s$  ranging from 1.2 m (June) to 2.3 m (January) over the period 2007–2018. Wave approach is typically from the W (0.5 probability) and WNW (0.4 probability), with the larger winter waves also slightly more northerly in direction (WNW:  $H_{s,50\%} = 1.6$  m; W:  $H_{s,50\%} = 1.3$  m; WNW:  $H_{s,1\%} = 5.2$  m; W:  $H_{s,1\%} = 4$  m) (Fig. 3d). Therefore, winters are associated with peaks in southerly-directed (negative) alongshore wave power ( $P_y$ ) (Fig. 3f). The tidal regime is semi-diurnal and macrotidal with a mean spring and neap tidal range of 6.3 m and 2.7 m, respectively (Masselink et al., 2014; Scott et al., 2016). Tidal currents with values of c.  $0.7 \text{ m s}^{-1}$  are registered during spring tides near the headlands (Valiente et al., 2019). The flood-ebb asymmetry in the current magnitude during a tidal cycle results in a northward tidal net residual current along the embayment (McCarroll et al., 2018), in particular near the northern headland. Computed bed shear stresses, reinforced by observations of sediment distribution within the embayment, suggest that wave-driven currents during extreme storm events can induce energetic sediment transport well seaward of the *DoC*, even when disregarding tidal action (Valiente et al., 2019). When also considering tidal currents during the maximum flood in a tidal cycle, the depth limit for this dynamically active shoreface increases by more than 5 m, reaching 28 m depth ODN (Valiente et al., 2019).

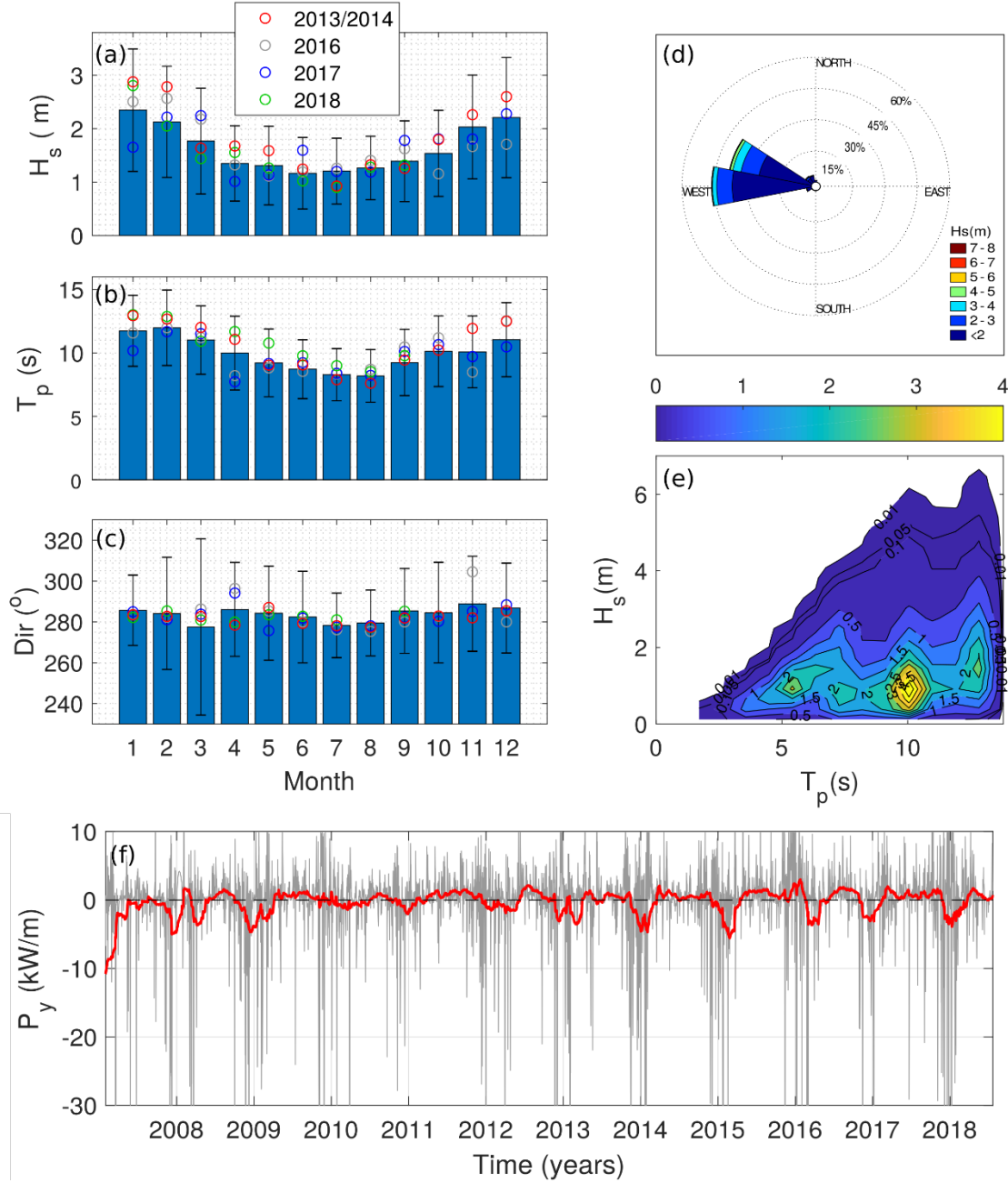


**Fig. 3.** Monthly statistics of: (a) significant wave height; and (b) peak wave period; and (c) wave direction, computed for the period 2007–2018. Wave statistics were derived from the Perranporth directional waverider buoy (refer to Fig. 2a for location). In all left panels, bars indicate monthly-averaged values with error bars showing the monthly standard deviation and circles indicating 2013/2014 and years 2016–2018 monthly-averaged values. (d) Directional wave rose showing distribution of  $H_s$  and (e) joint probability of  $H_s$  and  $T_p$  with percentage occurrence contours. (f) 11-year time series of alongshore wave power,  $P_y$  (1-day and 8-week running mean) for an averaged orientation of c.  $285^\circ$ . Southward  $P_y$  is negative.

## 2.2. Multimethod morphological surveys

The complete dataset used in this paper is complex as it involves various survey methods at a range of spatial and temporal extents. Fig. 4 provides an overview of the coverage of the dataset collected by the Coastal Processes Research Group (CPRG), University of Plymouth, and the Plymouth Coastal Observatory (PCO) since October 2006. The south part of the beach has been monitored for over 11 years, whereas the northern part has only been surveyed since 2016.

Monthly inter-tidal beach surveys covering the south part of the beach (red box; Fig. 2a) were conducted since October 2006. Airborne LiDAR datasets that cover the inter-tidal beach and dune system of the whole beach, obtained from PCO, are available for 2008, 2009, 2011, 2012, 2014, 2016 and 2017. The monthly inter-tidal all-terrain vehicle (ATV) based real-time kinematic Global Positioning System (RTK-GPS) surveys of the south area of the beach are complimented with quasi-quarterly single-beam echosounder bathymetric surveys (herein SBE) for the sub-tidal zone during the period 2010–2012 and 2014–2018. Only since 2016 was the survey program specifically designed to enable quantification of the total sediment budget and net sediment fluxes for Perranporth beach, and multi-method morphological surveys capturing the entire beach (black dashed box; Fig. 2a) from May 2016 were performed during spring and autumn. The sub-tidal coverage was extended (down to a depth of -40 m ODN) through conducting yearly (spring/summer) multi-beam echosounder bathymetric surveys (herein MBE). Despite great efforts to collect sub-tidal data, Perranporth is an exposed high-energy environment and areas in close proximity to headlands were too hazardous to survey due to exposed rocks and breaking waves, and hence are not covered in this analysis.

Photogrammetric data of the south and north dunes were collected using an DJI Phantom 4 quadcopter (herein unmanned aerial vehicle; UAV), covering the supratidal up to an elevation of 30 m ODN. Ground control points (GCPs) were vertically and horizontally distributed throughout the survey region at intervals of 100–250 m and were surveyed by RTK-GPS for constraining bundle adjustment during Structure-from-Motion post-processing workflow. The inter-tidal and supratidal zone was surveyed using ATV-based Trimble 5800 RTK-GPS, with line spacing of 20–25 m. The shallower sub-tidal data were collected using a Valeport Midas Surveyor single-beam echosounder with a 210 KHz transducer with a sample rate of 6 Hz mounted on an Arancia inshore rescue boat (IRB) and external Trimble 5800 RTK-GPS positioning. These

bathymetric surveys were conducted following cross-shore transects at 50-m spacing for inshore lines (< 10 m depth) and 100-m spacing for offshore lines (> 10 m depth). Yearly multi-beam echosounder bathymetric surveys were collected using a pole-mounted 400 kHz R2Sonic 2024 MBES, with motion data provided by a vessel-mounted GNSS-aided Applanix POSMV MRU and primary positioning provided by a Trimble SPS RTK-GPS system.

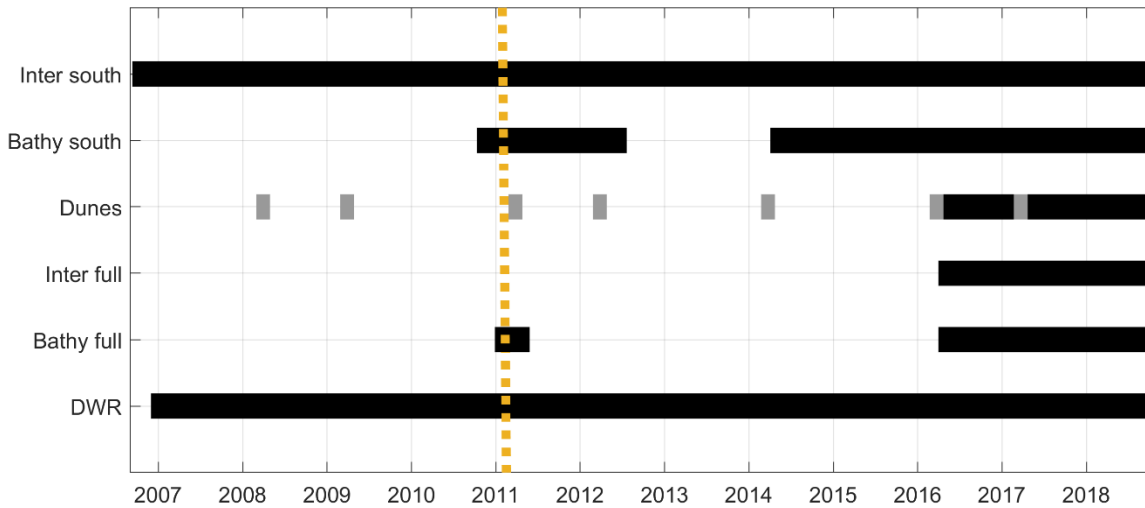


**Fig. 4.** Timeline of the data sources available for analysis. From top: Perranporth beach inter-tidal beach morphology (Inter south), Perranporth beach sub-tidal bathymetry (Bathy south), full embayment dune morphology from LiDAR and UAV (Dunes), full embayment inter-tidal beach morphology (Inter full), full embayment sub-tidal bathymetry (Bathy full) and directional wave rider buoy (DWR). Grey stripes show years for which LiDAR data are available. Orange dashed line represents winter 2011 reference state.

### 2.3. DEM creation

Three sets of 2-m gridded digital elevation models (*DEMs*) were constructed from composite datasets: (1) 27 *DEMs* covering the southern inter- and sub-tidal beach for the period 2010–2018 (red box, Fig 2a); (2) 6 seasonal *DEMs* covering the quasi full embayment (black dashed box down to *DoC*, Fig 2a) from the sub-tidal to the dunes (included), hereafter referred to as the ‘inner embayment’, for the period 2016–2018; and (3) 3 *DEMs* covering the entire embayment including adjacent areas beyond the bounding inner headlands (including depths > 18 m), hereafter ‘full embayment’, for the years 2011, 2016 and 2018 (Table 1). Topographic (RTK-GPS) and bathymetric (SBE) measurements (RTK+SBE; 27 *DEMs*) were combined using a Loess interpolation function (Plant et al., 2002), with variable smoothing scales and maximum

permissible interpolation error level of 0.15 m. Individual UAV, RTK+SBE and MBE datasets were combined for the final multimethod full embayment *DEM* construction with natural neighbor interpolation function (Sibson, 1981).

To determine the impacts of the 2013/14 winter storms on the Perranporth beach sediment budget, an additional full embayment dataset for the year 2011 was constructed by combining LiDAR and multi-beam bathymetry, corrected and referenced to ODN using the Vertical Offshore Reference Frame separation model (VORF) facilitated by the United Kingdom Hydrographic Office.

**Table 1.** Component gridded datasets and calculated uncertainty ( $\sigma$ ) included in the 3 full embayment DEMs

Name	Method	Date	Coverage	Calculated uncertainty, $\sigma$ (m)
2011 DEM	LiDAR	01/2011	Dunes, supra- and inter-tidal (-2→30 m)	0.15
	SBE	01/2011	Sub-tidal (-10→-2 m)	0.05
	MBE	2011, not specified	Sub-tidal (<-7 m)	0.27
2016 DEM	UAV	04/2016	Dunes (4→30 m)	0.06
	RTK	04/2016	Supra- and inter-tidal (-2→4 m)	0.04
	SBE	04/2016	Sub-tidal (-18→-2 m)	0.05
	MBE	08/2016	Sub-tidal (-16→-30 m)	0.06 – 0.3 *
2018 DEM	UAV	09/2018	Dunes (4→30 m)	0.06
	RTK	09/2018	Supra- and inter-tidal (-2→4 m)	0.05
	SBE	09/2018	Sub-tidal (-18→-2 m)	0.05
	MBE	06/2018	Sub-tidal (-16→-30 m)	0.06 – 0.3 *

\*majority of values < 0.15 with maximum values registered around a rocky platform at the northern sector outside the embayment domain

#### 2.4. Full embayment volume change computation

Full embayment morphological measurements were used to calculate volume change and derive net sediment fluxes following a total sediment approach and accounting for gridded uncertainty through the domains. Several approaches to quantifying the total sediment budget of a coastal cell exist (Van Rijn, 1997; Cowell et al., 2003; Aagaard, 2011; Van Rijn, 2011); however, none of these account for the associated uncertainty ( $\sigma_{DEM}$ ) in the volume computation. Here, we follow the methodology proposed by Wheaton et al. (2010) applied to rivers and later used by

Wiggins et al. (2019) for application to gravel beach environments. This methodology consists of three main steps: (1) computing the surface uncertainty associated with the digital elevation model (*DEM*); (2) quantifying the *DEM* of difference ( $DoD = Z_{DEM_1} - Z_{DEM_2}$ ) and the propagated uncertainty or minimum level of detection,  $minLoD = \sqrt{(\sigma_{DEM_1}^2 + \sigma_{DEM_2}^2)}$  for a defined confidence level (95% in this instance); and (3) only considering significant bed-level changes by disregarding elevation changes that are less than the *minLoD* value (herein *LoD*).

Estimates of net morphological change are fundamentally controlled by *DEM* quality, itself largely inherited from the quality of the survey data (Wise, 1998; Wechsler, 2003; Wechsler and Kroll, 2006; Wheaton et al., 2010). We quantify the quality of each *DEM* using a spatially variable uncertainty which is the result of the combination of the spatially uniform (UAV, inter-tidal RTK-GPS and sub-tidal SBE) and spatially variable (MBE) surfaces presented in Table 1. Associated uniform uncertainty of the UAV survey technique was extracted from Wiggins et al. (2019), who applies a UAV model comparison to an absolute reference control surface on a gravel beach. Due to the lack of a control surface to compare to RTK and SBE techniques, uncertainty surfaces for these methods were calculated computing instrument and interpolation uncertainties individually and then added using a quadratic sum (Taylor, 1997). RTK instrument error ( $2\sigma$  for 95% confidence level; Brasington et al., 2000) was estimated using the vertical deviation in repeated control points over 3 years (~35 observations); while SBE instrument error was extracted from the standard deviation of the actual SBE measured points with respect to overlapped RTK-GPS topographic points along a testing control line of 1000 m (facilitated by large tidal range). For both methods, standard deviation values between the raw input data and the resulting interpolated grids within a control region of 50x50 m were used as interpolation error. MBE spatially variable residual uncertainty surface was based on total propagated uncertainty (TPU) values for each individual sounding (generated through QPS QINSy/Quimera hydrographic software) which were then gridded using the Combined Uncertainty and Bathymetric Estimator (CUBE) algorithm (Calder and Mayer, 2003; Calder and Wells, 2007; Schimel et al., 2015). The vertical accuracy of the only externally sourced MBE dataset (for 2011) was based on the known survey specification (International Hydrographic Organization Order 1a). This was relatively large ( $\sigma = 0.27$  m), but provided the only opportunity to obtain a full embayment survey prior to 2013.

Finally, the total volume difference or total sediment budget and associated uncertainty were quantified using the non-discarded *DoD* values,  $|Z_{DEM_1} - Z_{DEM_2}| \geq \text{minLoD}$  for a 95% confidence level. Sediment volumes (in  $\text{m}^3$  per meter width) were computed for different sections of the beach profile: dune ( $> 30$  to  $5$  m ODN), supra- and inter-tidal ( $5$  to  $-2$  m ODN) and present sub-tidal (beyond  $-2$  m ODN). To avoid errors in the dune volume computation, the vegetated areas not comprising part of the active beach system were discarded. The beach was also divided into northern and southern sections (divided black dashed box, Fig 2a), allowing a full embayment investigation of embayment-scale alongshore variability in volumes. It is noted that alongshore variability refers to volumetric differences between south and north, and not small scale alongshore variability associated with bar/ rip morphology.

### 3. Quasi full embayment beach response and evolution (volume time series)

Fig. 5 shows beach volumetric time series for each of the sub-systems considered (dunes, inter-tidal and sub-tidal) for the north and south sectors of the beach (red and blue boxes, Fig. 2a). Sediment volumes are plotted relative to the reference state, January 2011, as a topographic and bathymetric survey is available for that time for both north and south sectors of the beach. The beach/dune morphology is significantly different for the two sectors: the inter-tidal beach in the north is narrower than in the south (refer to Fig. 2c,d) and, the front of the northern dune system is characterised by a high and steep ramp, whereas the southern dune system is fronted by a developing fore dune.

The two regions also show markedly contrasting behavior in terms of dune volumetric change. Over the monitoring period, the southern dune system has progressively accreted  $5,550 \text{ m}^3$  ( $30 \text{ m}^3 \text{ m}^{-1}$ ), representing  $800 \text{ m}^3 \text{ year}^{-1}$  ( $4 \text{ m}^3 \text{ m}^{-1} \text{ year}^{-1}$ ). The northern dune system, on the other hand, has remained relatively stable over the period 2008–2013, but during the 2013/14 winter,  $80,000 \text{ m}^3$  was lost ( $50 \text{ m}^3 \text{ m}^{-1}$ , accompanied by total retreat of the dune foot of c.  $15 \text{ m}$ ) with no significant post-event recovery. The dune ramp is still located  $7 \text{ m}$  landward of the pre-2013/14 dune face 4 years later, without a developing fore dune. The dune volume time series also shows a modest seasonal modulation (amplitude c.  $15 \text{ m}^3 \text{ m}^{-1}$ ), largely due to the advance/retreat of the dune foot during the summer/winter cycle.

Inter-tidal volumetric changes are shown in Fig. 5c for the south (11-year time series) and for the north (2.5-year time series) sectors. The southern inter-tidal time series displays both

seasonal (amplitude c.  $50 \text{ m}^3 \text{ m}^{-1}$ , refer to Fig. 5c) and multi-annual event response signals (amplitude c.  $200 \text{ m}^3 \text{ m}^{-1}$ , refer to Fig. 5c). Specifically, the southern time series started (October 2006) in a fully accreted state ( $+50 \text{ m}^3 \text{ m}^{-1}$  with respect the reference state), then experienced significant erosion (c.  $180 \text{ m}^3 \text{ m}^{-1}$ ) during the 2006/7 winter ( $H_{s,50\%} = 2.4 \text{ m}$ ), followed by a 3–5 year recovery (up to October 2010) to a stable fully accreted state. The intense storms during the 2013/14 winter (red circles Fig. 3a,  $H_{s,50\%} = 2.7 \text{ m}$ ) resulted in sediment losses in excess of  $200 \text{ m}^3 \text{ m}^{-1}$  in the south. Following the 2013/14 winter, an increase in alongshore volume standard deviation (Fig. 5c) was observed during the 2014–2017 recovery period. According to Scott et al. (2016), this is associated with the development of large-scale three-dimensional sandbar morphology in the lower inter-tidal region during beach recovery phases (see also Poate et al., 2014). Post 2013/14 winter, southern and northern beach volumes experienced a multi-annual recovery phase within which significant seasonal variability was observed (for example, an energetic 2015/16 winter ( $H_s = 2.6 \text{ m}$ ), resulted in  $140 \text{ m}^3 \text{ m}^{-1}$  loss in the south). By autumn 2018 (4.5 years after 2013/14 storms), the south beach had recovered by 88%.

Examining the 10-year time series of beach sediment volume (Fig. 5), a surprising observation is that the inter- and sub-tidal volumes do not exhibit the inverse correlation expected for a cross-shore dominated beach, suggesting that alongshore sediment fluxes are significant. Indeed, there appears to be a positive correlation between southern inter-tidal volume and sub-tidal volume, with a time lag of approximately 1-year (e.g., compare the 2013-2014 decrease in inter-tidal volume with the 2014-2015 decrease in sub-tidal volume). The imbalance in total volume for the south sector was previously alluded to by Scott et al. (2016), who examined the 2013/14 storm response for a 250-m southern sector of Perranporth and found that the inter-tidal zone lost  $>200 \text{ m}^3 \text{ m}^{-1}$ , while the sub-tidal zone only gained  $110 \text{ m}^3 \text{ m}^{-1}$ . The monthly time series of sediment volume for the southern region (Fig. 5c-e) clearly demonstrates that the inter- and sub-tidal volumes do not balance. For example: (1) from October 2010 to July 2012, the sub-tidal gained c.  $200 \text{ m}^3 \text{ m}^{-1}$  of sediment, whereas the inter-tidal sediment volume remained relative constant (ignoring seasonal fluctuations); (2) from May 2014 to February 2015, the sub-tidal lost c.  $300 \text{ m}^3 \text{ m}^{-1}$  of sediment, whereas the inter-tidal gained c.  $100 \text{ m}^3 \text{ m}^{-1}$  of sediment; and (3) from March 2017 to May 2018, the sub-tidal gained c.  $200 \text{ m}^3 \text{ m}^{-1}$  of sediment, whereas the inter-tidal sediment volume lost c.  $30 \text{ m}^3 \text{ m}^{-1}$ . These observations for the southern region strongly point to the presence of significant longshore exchange of sediment, either within the embayment or

beyond the southern extend of the region, and/or offshore sediment transport beyond the detectable *DOC*.

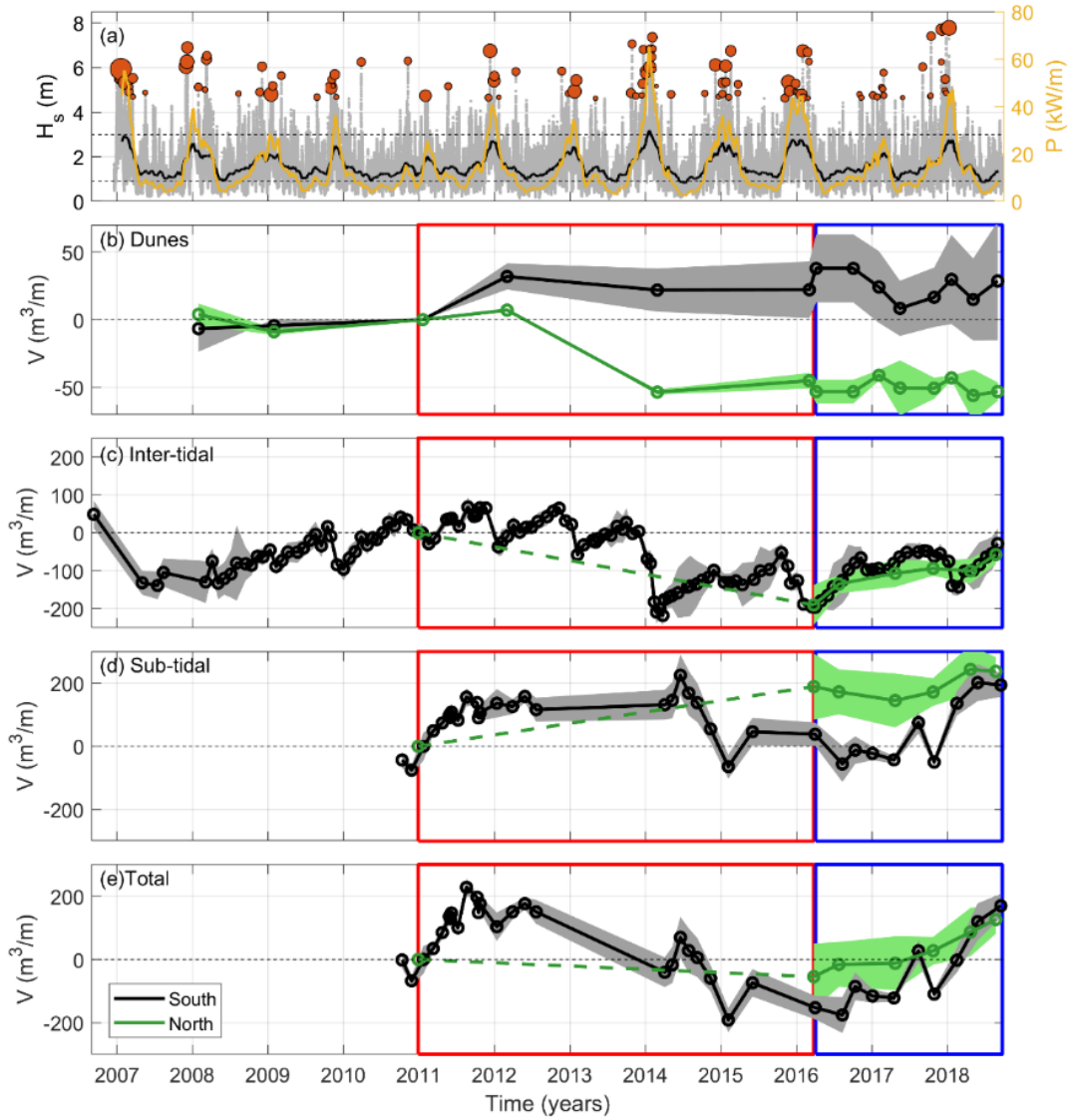


**Fig. 5.** South (black) and north (green) Perranporth beach response and evolution. (a) 11-year time series of significant wave height measured at Perranporth wave buoy (30-min and 8-week running mean), wave power  $P$  (Herbich, 2000) and storm events (orange bubbles,  $H_s > H_{s,99\%}$ , minimum of 6 hours duration and a meteorological independence criterion of 24 h between peaks). The size of the bubbles is proportional to storm duration based on  $H_{s,95\%}$  cut-off. Dune (b), inter-tidal (c) and sub-tidal (d) sediment volume ( $\text{m}^3 \text{m}^{-1}$  alongshore-averaged) and associated alongshore standard deviation (bounded area). (e) Total beach sediment volume ( $\text{m}^3 \text{m}^{-1}$  alongshore-averaged, from dune foot to -14.5 m ODN) and associated alongshore standard deviation (bounded area). Dune volume refers to the area above the dune foot ( $z = 5$ ), inter-tidal volume corresponds with the area from the dune foot to  $z = -2$  m ODN and sub-tidal from  $z = -2$  m to -14.5 m ODN. Red (storm) and blue (recovery) squares represent the considered epochs in Section 4.

When the more discontinuous sediment volume time series for the northern region is also considered, an alongshore quasi-coherent response is observed. For the period 2016–2018, the inter-tidal accretion for the northern and southern sectors of the beach are very similar ( $130\text{--}160\text{ m}^3\text{ m}^{-1}$ ). Over that same period, the sub-tidal region also accretes, but the accretion in the northern region (c.  $50\text{ m}^3\text{ m}^{-1}$ ) is significantly smaller than in the southern region (c.  $160\text{ m}^3\text{ m}^{-1}$ ). Importantly, the total sediment volume for both the southern and northern region increase during this period by a very substantive amount ( $200\text{--}300\text{ m}^3\text{ m}^{-1}$ ). This strongly suggests that the inner embayment is not ‘closed’ (cf. Fig. 1) and that sediment may be transported alongshore, potentially around the terminating headlands, and/or offshore beyond the detectable *DoC*, and/or onshore into the vegetated dune area. To robustly examine the sediment fluxes within and beyond the inner embayment and quantify the sediment fluxes between the different sub-systems, it is necessary to take a total sediment budget approach, expanding both the alongshore and cross-shore spatial coverage, and accounting for propagated volumetric uncertainty. The following section examines the two epochs where full embayment coverage is available.

#### **4. Full embayment total sediment budget**

In this section we will present the full embayment analysis for two epochs, representing extreme storm response (Fig. 6) and post-storm recovery (Fig. 7). The results for both epochs are then summarized in Fig. 8 and Table 2. It is noted that in the figures the sediment volume changes are presented in units of  $\text{m}^3$  per unit meter beach width, whereas in the table the total volume changes in  $\text{m}^3$  are listed.

##### **4.1. Storm response**

Full embayment *DEMs* for the years 2011 and 2016 were used to further investigate cross-shore sub-compartment sediment fluxes and along-coast sediment exchange, within and beyond the inner embayment, surrounding the high energy 2013/14 winter period. The lack of a full embayment morphological dataset bracketing the 2013/14 winter forced us to extend the period from 2011 to 2016. This is considered acceptable in terms of dune and inter-tidal volumetric changes as beach volumes in 2011 were similar to that of 2013, and the volumes for 2014 were similar to that of 2016 (refer to Fig. 5b-c). We also acknowledge that total embayment response over this epoch disregards both the dramatic accretion in the southern sub-tidal region during 2011

(>100 m<sup>3</sup> m<sup>-1</sup>; Fig. 5d) and the significant inter-tidal erosion during winter 2015/16 (-150 m<sup>3</sup> m<sup>-1</sup>; Fig. 5c), meaning that embayment response to the 2013/14 events could potentially have been different than shown.

The difference *DEM*, offshore acoustic backscatter and along-coast variation in sub-compartment sediment volumes are presented in Fig. 6. Light colors in the acoustic backscatter image indicate presence of medium sand, interrupted by gravel patches (dark colors) around 26 m depth ODN. It is emphasized that for the sediment volume considerations, only those bed-level changes that exceed the *LoD* (95% uncertainty level) are considered, and a large portion of the deeper sub-tidal is therefore discarded as the measured changes are considered insignificant (uncoloured parts of Fig. 6). The salient features of the storm response are: (1) extensive erosion of the front of the dunes in the north part of the beachfront (c. 50 m<sup>3</sup> m<sup>-1</sup>); (2) erosion across the entire supra- and inter-tidal beach (c. 190 m<sup>3</sup> m<sup>-1</sup>); (3) erosion in the shallow sub-tidal zone up to 6–7 m depth ODN; and (4) accretion in the deeper sub-tidal zone up to and even beyond the *DoC* at 14.5 m depth ODN (0–250 m<sup>3</sup> m<sup>-1</sup>).

Integrating the positive and negative sediment volumetric changes across the entire beach to the *DoC* (Fig. 8-top panel) robustly demonstrates that the full embayment sediment budget is not balanced: there is a net loss of 280,000 m<sup>3</sup> and an associated uncertainty of 206,000 m<sup>3</sup> (Table 2). There is also a considerable longshore variability in the morphological response and this is better demonstrated when the sediment volumes are summed across the different sub-compartments for the different sections of the beach (north versus south, Fig. 8 and Table 2). Over the period 2011–2016, the northern and southern sectors of the beach lost 50,000 m<sup>3</sup> and 230,000 m<sup>3</sup> of sediment, respectively. These values represent losses per unit meter beach of 36 m<sup>3</sup> m<sup>-1</sup> in the north and 164 m<sup>3</sup> m<sup>-1</sup> in the south (although northern volume change is within uncertainty bounds therefore not significant at 95% level).

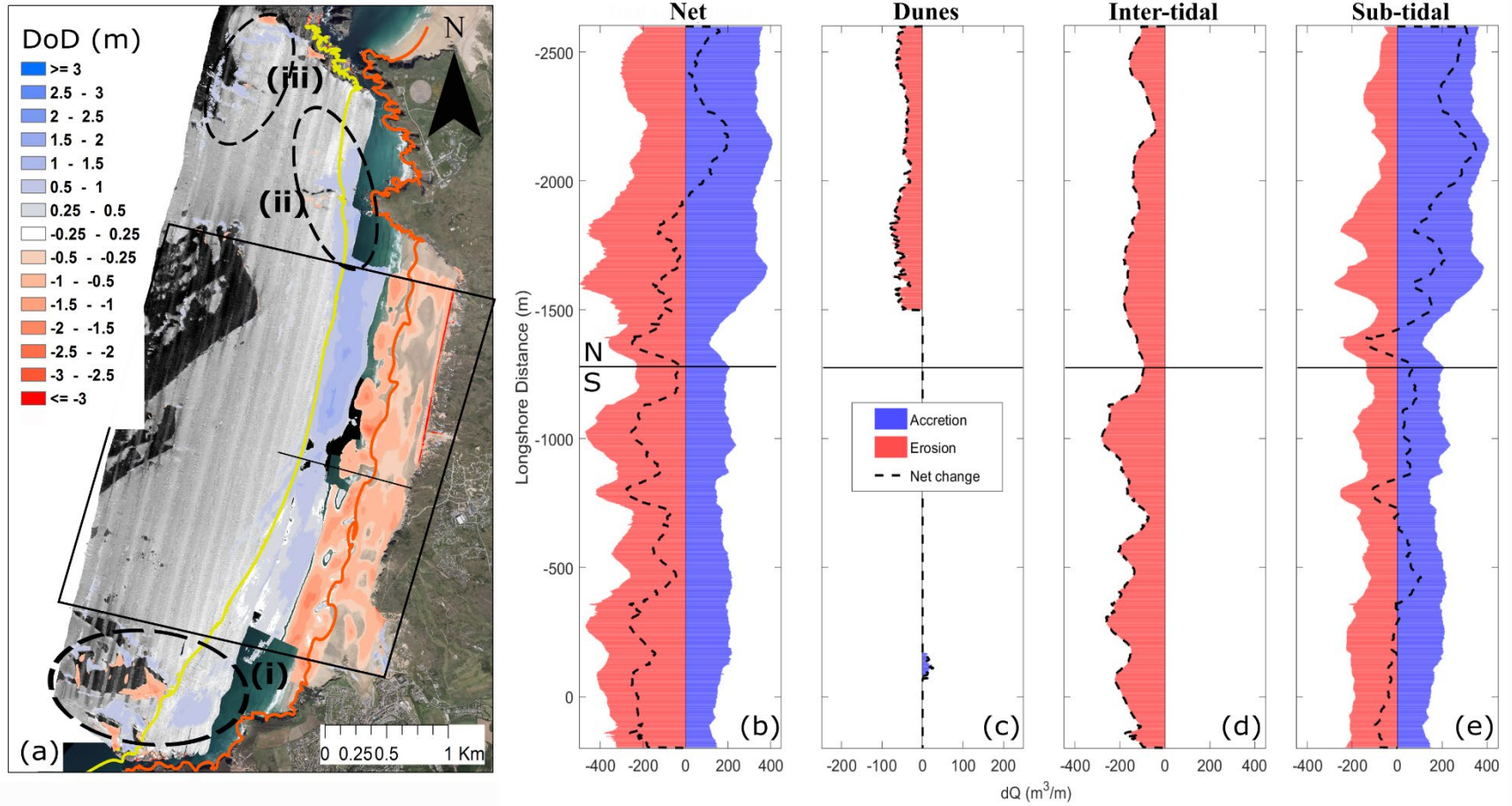


**Fig. 6.** Storm response total sediment budget. Left panel: full embayment *DoD* from 2011 to 2016. Areas where morphological change is not significant ( $|Z_{DEM_1} - Z_{DEM_2}| \geq \min LoD_{95\%}$ ) are uncoloured. Orange and yellow contours represent the inter-tidal to sub-tidal limit (-2 m, ODN) and *DoC* (-14.5 m, ODN) respectively. Right panels: cross-shore and alongshore variability of sediment fluxes for the complete cross-shore profile and the different sub-systems for the domain comprised inside the black box.

Morphological changes beyond the *DoC* and the lateral extent of box (Fig. 6a), referred to as ‘outer embayment’, are analysed to investigate possible sediment pathways in/out the inner embayment. The region beyond the *DoC* (within the box, Fig. 6) showed a small, but significant gain of 76,000 m<sup>3</sup> (with uncertainty of 50,000 m<sup>3</sup>), and regions beyond the lateral extents of the box (represented by ellipses in Fig. 6) indicated significant gains with a combined total of 180,000 m<sup>3</sup> (uncertainty of 120,000 m<sup>3</sup>). The gains beyond the lateral extents of the box are related to three regions. Two are offshore regions at the full embayment extents: one in the south of the study area in proximity to the Cligga Head, the southern embayment boundary (Fig. 6a-i), located between 14.5 and 26 m depth ODN; and the second located near Penhale Point, the northern of embayment boundary (Fig. 6a-iii), where only accretion occurred. The third region, alongshore to the north of Ligger Point, experienced significant sediment gains offshore of the headland (accretion of 0.6–0.8 m) and in the region of Hoblyn’s Cove (Fig. 6a-ii) providing a possible sink for sediment lost from the inner embayment. While the total sediment budget cannot be entirely resolved in these regions due to lack of data in the nearshore (data collection too hazardous), these observations suggest major morphological losses from within the inner embayment are linked primarily to inner headland bypassing mechanisms, rather than cross-shore exchange beyond the depth of closure within the inner embayment, suggesting that significant sediment transport occurs seaward of the base of the inner headlands (Ligger and Droskyn) and beyond the morphological depth of closure at the embayment extremities.

#### 4.2. Multi-annual beach recovery

Full embayment *DEMs* for the years 2016 and 2018 were compared to further investigate multi-annual sediment fluxes during a recovery period within and beyond the central embayment (black box, Fig. 7a). Fig. 7a shows the *DoD* for the entire epoch 2016–2018. The 2.5 years of recovery show a system that is not balanced, but has a net gain of 670,000 m<sup>3</sup> with an associated uncertainty of 180,000 m<sup>3</sup> (Table 2). Similar to the storm period, sediment inflows and outflows occur primarily between the inter- and the sub-tidal sub-systems (Fig. 8). Overall, both inter- and sub-tidal sub-systems accreted, mostly in the south, and although the dunes continued losing sediment (11,000 m<sup>3</sup> erosion, uncertainty of 3,000 m<sup>3</sup>), the embayment is fully recovered from the 2013/14 winter in terms of net sediment budget (Fig. 7).

The key morphological responses over the recovery period are: (1) limited dune recovery; (2) accretion across the entire inter-tidal beach ( $143 \text{ m}^3 \text{ m}^{-1}$ ); (3) accretion in the shallow sub-tidal down to 6 m depth ODN; and (4) significant longshore variability in the deeper sub-tidal area down to (and beyond in certain sectors) the *DoC*. The latter observation manifests in an alongshore gradient in the sub-tidal accretionary rates from  $50 \text{ m}^3 \text{ m}^{-1}$  in the north to  $150 \text{ m}^3 \text{ m}^{-1}$  in the south. Hence, morphological changes during the 2.5-year period of recovery ( $dQ_{out} \ll dQ_{in}$ ) show an accretion of the supra- and inter-tidal sectors, not matched by sub-tidal erosion.

The influx of sediment into the inner embayment leading to recovery is interpreted as a combined response of entrainment of sediment sourced from greater depths (beyond the morphological *DoC*) and/or outside the headlands that delineate the system (from lateral sub-embayments). This supposition is supported by the recorded loss of sediment ( $-23,000 \text{ m}^3$ ) from within the *DoC* in Hoblyn's Cove sub-embayment (shown in available data to the north of the inner embayment, Fig. 7a-ii), where the bed was lowered 0.3–0.6 m. While a small proportion of net losses, it provides an indication of possible source regions and transport mechanisms. Additionally, the alongshore continuity of the *DoC* contour located beyond the headland bases (620 m in the south and 170 m in the north), in combination with the morphological change detected beyond the embayment limits, strongly suggests that Perranporth beach is part of an extended coastal cell, not just during high energy events. Despite the large uncertainty associated with offshore areas, localised accumulation patterns similar to those shown in the 2011/16 *DoD*, and located between 14.5 and 26 m depth ODN in the south and far north of the survey area, are also present during the accretionary period (dashed ellipsoids, Fig. 7a-i,iii). The possible processes and forcing mechanisms leading to embayment recovery are further examined in Sections 5 and 6.

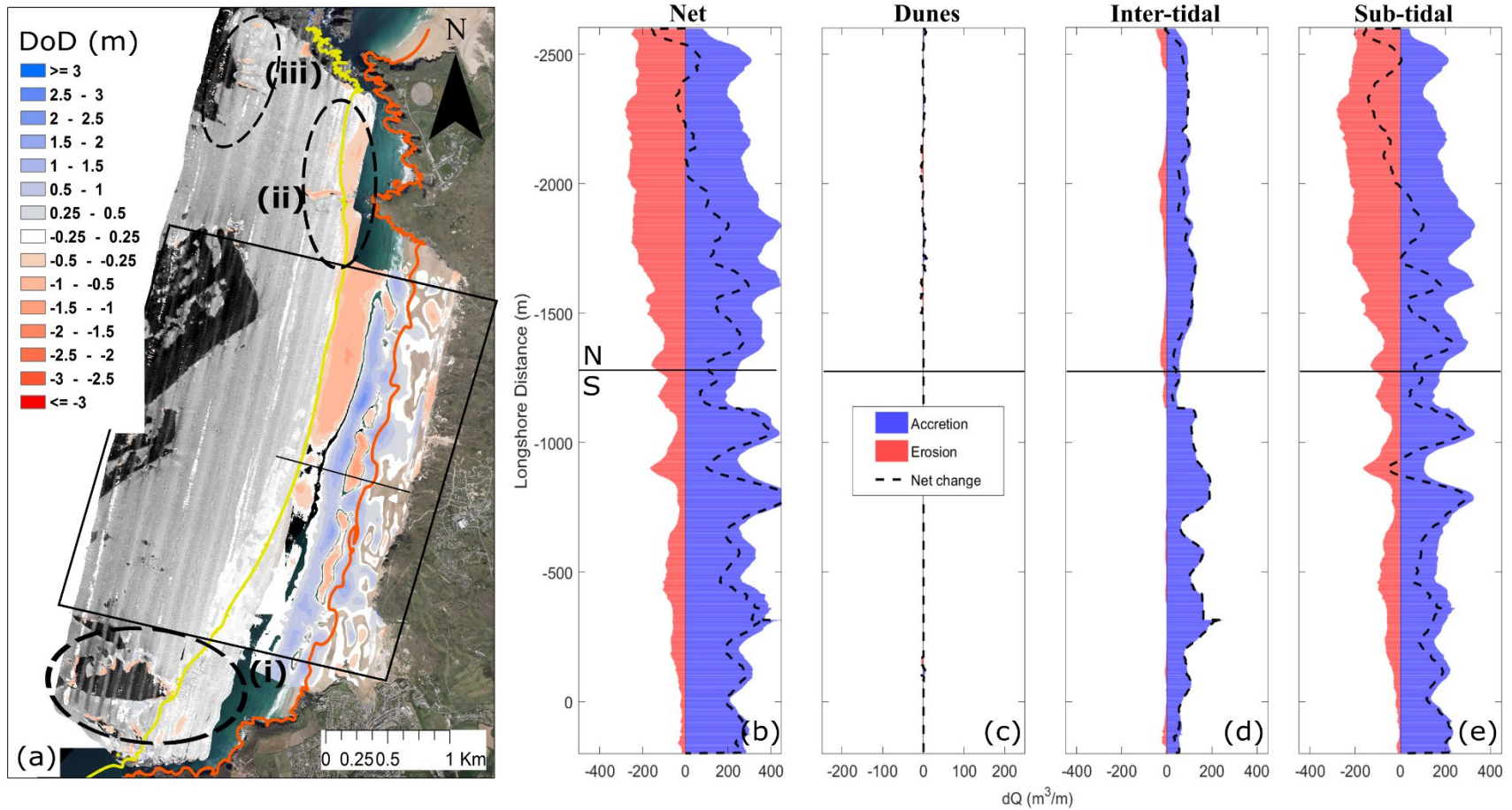


**Fig. 7.** Multi-annual recovery total sediment budget. Left panel: full embayment  $DoD$  from 2016 to 2018. Areas where morphological change is not significant ( $|Z_{DEM_1} - Z_{DEM_2}| \geq minLoD_{95\%}$ ) are uncoloured. Orange and yellow contours represent the inter-tidal to sub-tidal limit (-2 m, ODN) and  $DoC$  (-14.5 m, ODN) respectively. Right panels: cross-shore and alongshore variability of sediment fluxes for the complete cross-shore profile and the different sub-systems for the domain comprised inside the black box.

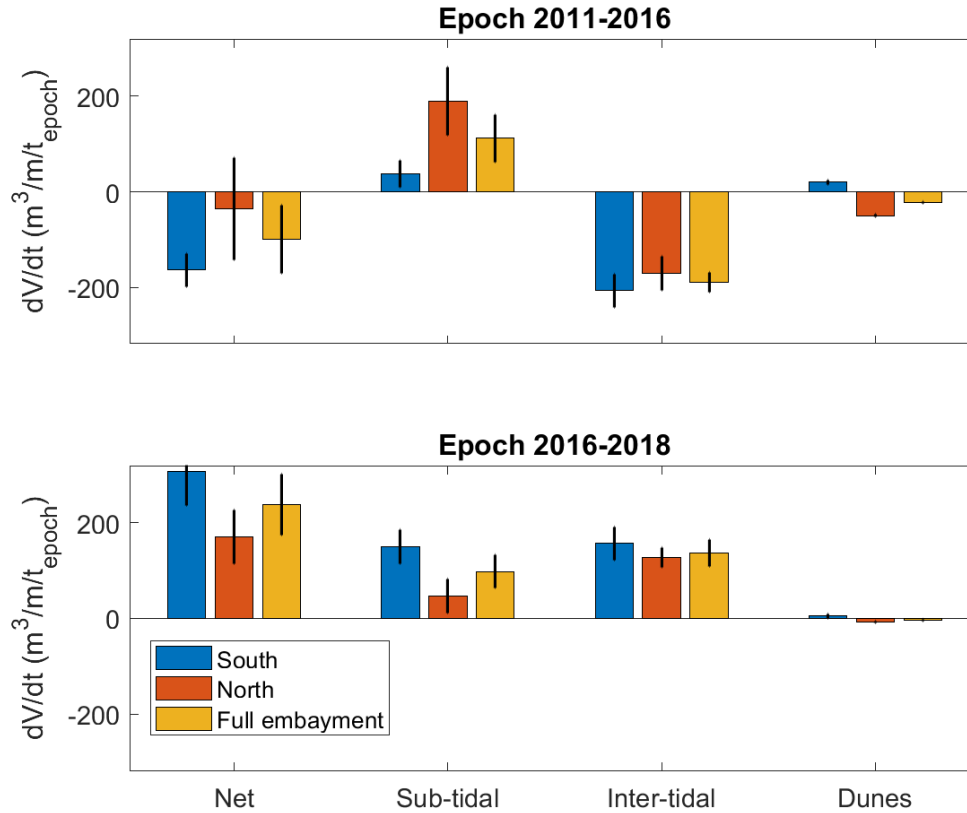


**Fig. 8.** Averaged sub-tidal, inter-tidal and dune volume per beach width ( $\text{m}^3 \text{m}^{-1}$  alongshore) and associated uncertainty (error bars) for epochs 2011–2016 and 2016–2018. Alongshore-averaged volumes are presented for north (1400-m alongshore) and south (1400-m alongshore) domains, except for the case of south dunes (100-m alongshore). Dune volume correspond with regions  $> 5$  m ODN, inter-tidal volume from 5 m to -2 m ODN and sub-tidal volume corresponds with the regions from -2 m to -14.5 m ODN.

**Table 2.** Net volumetric changes ( $\text{m}^3$ ) and associated uncertainty in sub-tidal, inter-tidal and dune sub-systems for epochs 2011–2016 and 2016–2018. Volumes are presented for north and south domains. Inter-tidal volume corresponds with the area from the dune foot ( $z=5$  m) to -2 m and sub-tidal volume corresponds with the area from -14.5 to -2 m, inter- and supratidal from -2 to the dune foot ( $z=5$  m) and dunes beyond  $z=5$  m

<i>EPOCH</i>	<i>Sector</i>	$\Delta V_{net} (\text{m}^3)$	$\Delta V_{sub-tidal} (\text{m}^3)$	$\Delta V_{inter-tidal} (\text{m}^3)$	$\Delta V_{dunes} (\text{m}^3)$
2011-2016	<i>Full*</i>		$-2.8 \times 10^5 \pm 2 \times 10^5$		
	<i>Outer**</i>		$2.7 \times 10^5 \pm 2.4 \times 10^5$		
	<i>North</i>	$-5 \times 10^4 \pm 1.5 \times 10^5$	$2.6 \times 10^5 \pm 1 \times 10^5$	$-2.4 \times 10^5 \pm 5 \times 10^4$	$-7 \times 10^4 \pm 3 \times 10^3$
	<i>South</i>	$-2.3 \times 10^5 \pm 5 \times 10^4$	$5.3 \times 10^4 \pm 6 \times 10^4$	$-2.9 \times 10^5 \pm 5 \times 10^4$	$2 \times 10^3 \pm 1 \times 10^3$
2016-2018	<i>Full*</i>		$6.7 \times 10^5 \pm 1.8 \times 10^5$		
	<i>Outer**</i>		$8.7 \times 10^4 \pm 4.5 \times 10^4$		
	<i>North</i>	$2.4 \times 10^5 \pm 8 \times 10^4$	$6.7 \times 10^4 \pm 5 \times 10^4$	$1.8 \times 10^5 \pm 3 \times 10^4$	$-1.1 \times 10^4 \pm 3 \times 10^3$
	<i>South</i>	$4.3 \times 10^5 \pm 1 \times 10^5$	$2.1 \times 10^5 \pm 5 \times 10^4$	$2.2 \times 10^5 \pm 5 \times 10^4$	$1 \times 10^3 \pm 1 \times 10^3$

\**Full* is the sum of north and south net volumes (down to *DoC*, within black box on Fig. 6 and 7).

\*\**Outer* is the sum of the morphological change beyond the morphological *DoC* (-14.5 m) and all areas outside of the area of the central embayment (beyond *DoC* and outside black box on Fig. 6 and 7).

#### 4.3. Sub-tidal sediment redistribution

Both storm response and recovery was rather longshore-uniform (disregarding the increase in 3-dimensionality during the accretionary phases) in the inter-tidal zone, but less so in the sub-tidal region, warranting further investigation into the alongshore redistribution of sediment in especially the lower sub-tidal zone. The 6 *DoDs* covering the inner embayment recovery response (black dashed box down to the *DoC*, Fig. 2a) for the multi-annual erosive period 2011–2016, and inter-annual recovery period 2016–2018, are used to compute longshore variability and inter-annual volume change between the north and south (Fig. 9). The key finding here is that following the erosion over the 2011–2016 epoch, accretion of  $0.5\text{--}2 \times 10^5$  occurred over each 6-month epoch in the recovery period, with most recovery occurring during the 2017/18 winter, especially in the sub-tidal region of the southern part of the beach.

Burvingt et al. (2017) defined longshore variation in the inter-tidal beach morphological response using the longshore variation index (*LVI*):

$$LVI = Q_{std} / (|Q_{mean}| + Q_{std}) \quad (1)$$

where  $Q_{std}$  is the standard deviation of the net volumetric change for cross-shore transects ( $Q_{cross}$ ) and  $|Q_{mean}|$  is the absolute value of the mean of  $Q_{cross}$  values. In order to discriminate between alongshore variability between the north and south sections and variability associated to 3-dimensionality,  $Q_{cross}$  is computed using 2-m alongshore-averaged cross-shore profiles, and is low-pass filtered using a moving averaged filter with a 400-m span. LVI index is then computed for the original and the filtered  $Q_{cross}$ . This index is dimensionless and varies between 0 and 1, with zero values implying cross-shore sediment transport is dominant, and  $LVI = 1$  representing both significant alongshore transport and large 3-dimensionality. Hence, by applying the low-pass filter to  $Q_{cross}$ , most of the differences associated to the small scale morphology are eliminated. For 5 of the 6 epochs,  $LVI$  (both filtered and no filtered) for the sub-tidal region is considerably larger ( $LVI = 0.5\text{--}0.9$ ) than for the inter-tidal region ( $LVI = 0.1\text{--}0.7$ ), indicating that the sub-tidal is characterised by a significant longshore variability whereas the inter-tidal is more longshore-uniform. The only exception is the winter 2017/18 period during which the large LVI results from very significant changes in the lower inter-tidal bar/rip morphology (still present in the filtered signal), which is associated with the positive feedback between rip-cell circulation, sand transport and evolving bathymetry, and not driven by longshore transport processes.

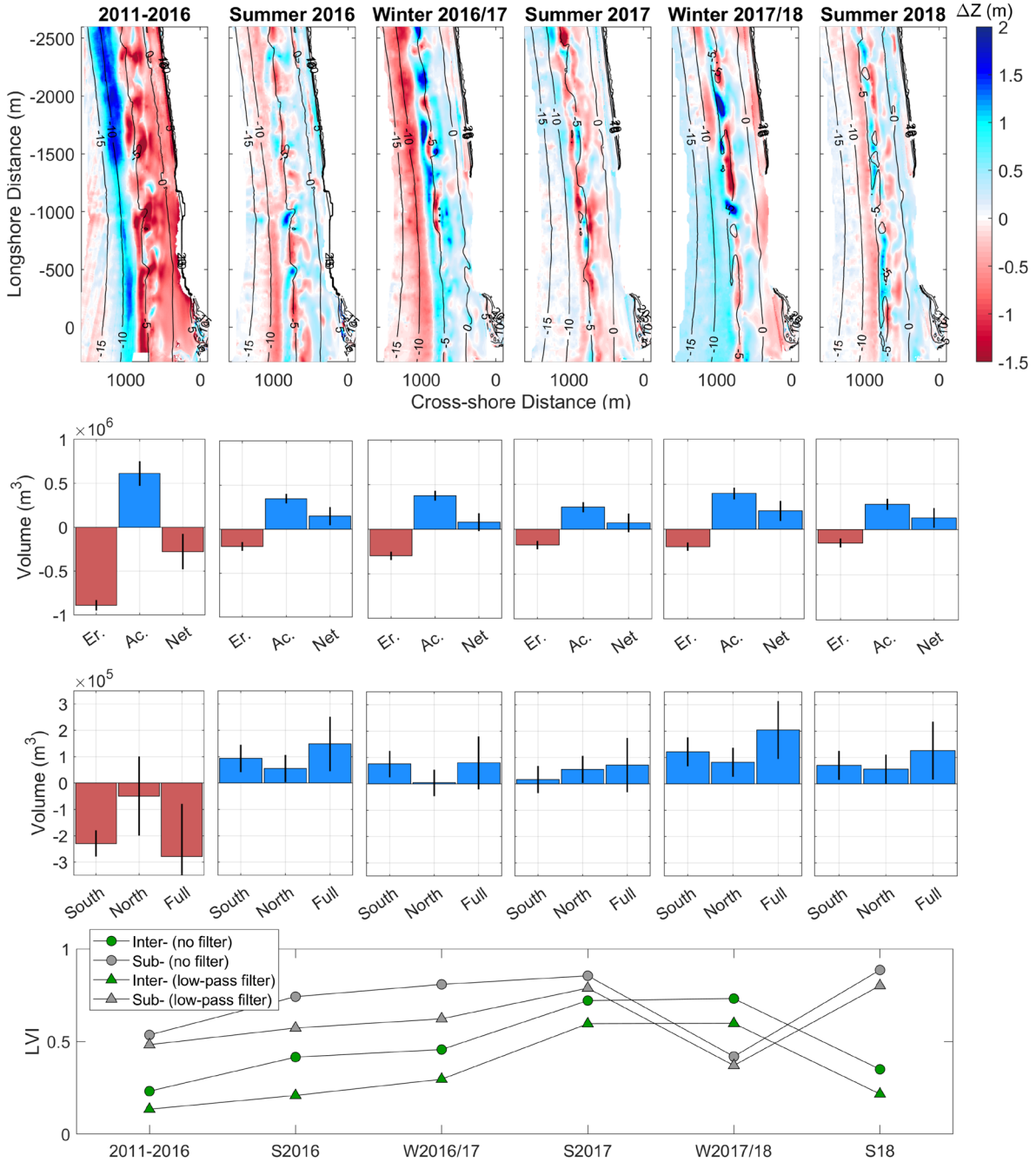


**Fig. 9.** Upper panels: 3D variability of Perranporth full embayment where red indicates erosion and blue erosion. Contours are from the first of the beach surveys. In order from 2<sup>nd</sup> to 3<sup>rd</sup> row panels: full embayment erosion (Er.), accretion (Ac.) and net (Net) volumetric change; and volumes for north and south sectors. All volumes are for epochs 2011–2016 and seasonal 2016–2018. Bottom panels: longshore variation index (*LVI*) computed using 2-m alongshore-averaged cross-shore profiles (circle) and a low-pass filter with a 400-m span (triangle).

## 5. Relating wave forcing and morphological change

To determine the sediment budget for any coastal domain, it is necessary to understand the forcing controls on sediment fluxes within, and in and out of the system, with waves being the primary forcing control in this instance. In the study area, the wave climate is strongly seasonal (Fig. 3f), such that the larger waves over winter periods are also slightly more northward in direction. Therefore, winters are associated with greater absolute wave power (forcing offshore transport), but also with greater southward alongshore wave power, likely to result in southward alongshore transport.

The wave parameters we seek to correlate with observed morphological change are the demeaned cumulative total wave power ( $P_{cum}$ ) and the cumulative alongshore wave power ( $P_{y,cum}$ ), computed for the 11-year available time series (2007–2018). The wave time series is transformed from the wave buoy location (~20 m depth ODN) to the breaking point using Van Rijn (2014). Assuming that beaches have an equilibrium condition related to the long-term mean wave forcing, total wave power is parameterised using the cumulative integral of the demeaned value (Stokes et al., 2016), denoted  $P_{cum}$ , as:

$$P_{cum}(n) = \int_{t_0}^{t_n} (P - \bar{P}) dt \quad (2)$$

where  $\bar{P}$  is the long-term mean condition, and  $P$  corresponds to instantaneous wave power at the breakpoint. The assumption of equilibrium (or near-equilibrium) is supported by the morphology observations that show large variations but no clear trend on a decadal timescale (Fig. 5).

For alongshore wave power ( $P_{y,cum}$ ), rather than demeaning the signal we select the long-term average power direction as shore-normal (285° in this instance), noting that the average wave direction is 283°, but bigger waves are more northerly. Again, the assumption here is that a long-term embayment equilibrium exists around variations in longshore forcing. The direction 285° also coincides with the mean orientation of the shoreline near the mid-point of the embayment, but this is not our primary motivation for choosing this angle.

$$P_{y,cum}(n) = \int_{t_0}^{t_n} P_{y,285} dt \quad (3)$$

For the purpose of relating wave forcing to morphologic change, only the southern sector observations are sufficiently long to draw statistical correlations (Fig. 5), therefore all analyses in this section are restricted to the southern part of the embayment. We seek to differentiate between forcing controls on the inter-tidal and sub-tidal components of the system, as observations suggest these systems behave, to some degree, independently (Fig. 5c-d). The morphologic change variables we will use for comparison to wave power are: (i) south-end inter-tidal volume, as it is the longest consistent time series [monthly 2007-2018]; (ii) south-end sub-tidal volume [sporadically 2011-2016, quarterly 2016-2018]; and (iii) total volume for the south end [time points as per sub-tidal volume]. Our preference is for analysis of the longest available dataset in each instance, to avoid misleading correlations with shorter time series'.

An initial examination of the correlations with sub-tidal volumes (Table 3,  $V_{S,SUB}$ ) suggest this variable is poorly correlated with wave forcing. This may be due to the sub-tidal being open to flux from the inter-tidal as well as to beyond the outer boundaries, obscuring forcing correlations. What is required is for the exchange with the inter-tidal be offset from the sub-tidal volume. The value we are interested in is flux from the sub-tidal to beyond the outer boundaries (cross- and alongshore) of the southern sector, which is approximated by changes in the total system volume:

$$V_{S,TOTAL} = V_{S,SUB} + V_{S,INTER+DUNES} \quad (4)$$

We use the change in total south sector volume ( $\Delta V_{S,TOTAL}$ ) as a proxy indicator for transport in and out of the sub-tidal outer domain boundaries. If we assume that sediment entering and leaving the southern sector primarily passes through the sub-tidal, then the total volume change ( $\Delta V_{S,TOTAL}$ ) is the flux through the outer boundaries (offshore and lateral) of the sub-tidal region. For example, if over a given period  $\Delta V_{S,INTER+DUNES}$  erode ( $-100 \text{ m}^3/\text{m}$ ) and  $\Delta V_{S,SUB}$  also erodes ( $-100 \text{ m}^3/\text{m}$ ), then we assume that the sub-tidal gained  $+100 \text{ m}^3/\text{m}$  from the inter-supratidal and therefore lost ( $-200 \text{ m}^3/\text{m}$ ) through the outer boundaries. This is not an ideal assumption as some material may be transported alongshore through the inter-tidal, but earlier findings have demonstrated the inter-tidal behaves coherently throughout the embayment and is largely cross-shore dominated (for example see Fig. 5c-e).

Considering the relationship between total and alongshore wave power (Fig 10a), there is a clear visual inverse correlation between  $P_{cum}$  and  $P_{y,cum}$  at a seasonal time scale i.e., larger waves

are more northerly (see also Fig. 3f). However, at decadal time scales (2007-2018) there is no clear correlation, in fact the relationship is very weakly positive (Table 3;  $r = 0.2$ ), suggesting that decadal trends in wave height are decorrelated from changes in wave direction. Inter-tidal morphological response ( $V_{S,INTER}$ ; Fig. 10-second row) is negatively correlated with  $P_{cum}$  (Table 3;  $r = -0.59$ ), indicating that more powerful waves erode the inter-tidal region. This relationship is consistent with the approach of a shoreline prediction model (Davidson et al., 2010; Splinter et al., 2014), which demonstrated a strong relationship at Perranporth between the shoreline position and disequilibrium in the dimensionless fall velocity parameter.

The southern total volume ( $V_{S,TOTAL}$ ; red line in Fig. 10c-d) is inversely correlated with total wave power ( $r = -0.56$ , Fig. 10c) and positively correlated with alongshore wave power ( $r = 0.41$ , Fig. 10d). This suggests that as wave power increases overall and becomes cumulatively more negative (southward), the south end erodes, which is primarily attributed to flux through the sub-tidal boundaries. This is counter-intuitive, given that in a closed embayment, we would expect more northerly waves to drive clock-wise rotation and accrete the southern end of the embayment. Following the discussion by Harley et al. (2015), we also note that it is difficult to differentiate between the influence of total- and alongshore wave power on the total volume, as the wave variables themselves are correlated at short time scales (seasonal), and the strength of the correlations are sensitive to statistical design (e.g., start and end points of wave time series, shore-normal angle chosen). Additionally, low temporal resolution of the survey data aliases the seasonal signal. Taking these caveats into account, there appears to be a weak-moderate relationship where  $V_{S,TOTAL}$  erodes during big, northerly waves (both for individual winters and multiple years above average wave power).

Assessing morphological correlations, it is interesting to note that the total southern system volume ( $V_{S,TOTAL}$ ) is *positively* correlated (Table 3) with both  $V_{S,INTER}$  (0.66) and  $V_{S,SUB}$  (0.70), such that each contributes about half the total variance, indicating that conditions which cause the inter- or sub-tidal to erode (accrete), will also cause the total system to erode (accrete), primarily through transport beyond the outer boundaries. More broadly, the positive correlation between the inter-tidal and total volume suggests that the ability to predict inter-tidal volume change (e.g., using a shoreline prediction model such as Davidson et al., 2010) may also provide some skill in predicting total embayment volume, with the implication that total embayment volume may

respond to a disequilibrium in the wave climate, analogous to the inter-tidal. As mentioned in section 3, it is surprising to note that the expected inverse correlation between  $V_{S,INTER}$  and  $V_{S,SUB}$  is entirely absent at a time-lag of 0. Instead, it appears that these systems operate with a time-lag of approximately 1-year, with a peak cross-correlation of  $r = 0.67$  found at 11.5-months lag (with the sub-tidal response following the inter-tidal). This suggests that sub-system response occurs at different timescales in reply to different forcing conditions. A hypothesised sequence to explain the lag in response may include: (i) an extreme storm that transports beach material far offshore, beyond the level of detectable change [inter-tidal erodes, sub-tidal is relatively unchanged]; (ii) an initial stage of recovery where sediment is transported mainly from the inner-sub-tidal to the beachface [inter-tidal accretes, sub-tidal erodes]; and (iii) a later phase of gradual transport from the lower-subtidal [from beyond the level of detectable change] to the upper-sub-tidal [inter-tidal unchanged, sub-tidal accretes]. The exact nature of this relationship is unclear and will be the target of future work.

**Table 3.** Correlation coefficients ( $r$ ) for Perranporth southern sector beach volume and cumulative wave power (total and alongshore). Bold values are significant ( $p\text{-value} < 0.01$ ).

	$P_{cum}$	$P_{y,cum}$	$V_{S, INTER}$	$V_{S, SUB}$	$V_{S, TOTAL}$
$P_{cum}$	1	<b>0.2</b>	<b>-0.59</b>	-0.17	<b>-0.56</b>
$P_{y,cum}$		1	<b>0.24</b>	0.05	<b>0.41</b>
$V_{S, INTER}$			1	0.01	<b>0.66</b>
$V_{S, SUB}$				1	<b>0.70</b>
$V_{S, TOTAL}$					1

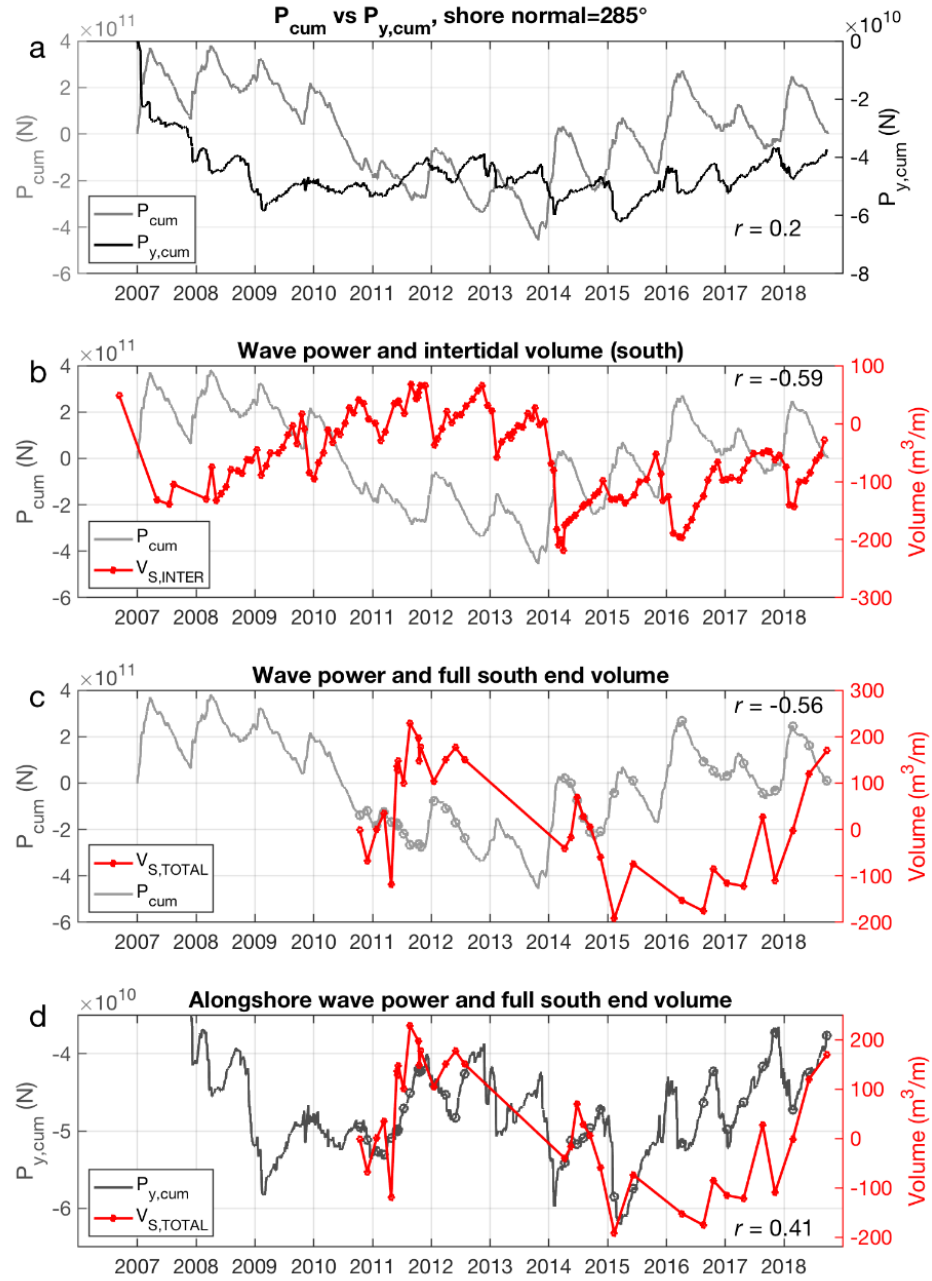


**Fig. 10.** Time series of wave power and volume observations. (a)  $P_{cum}$  and  $P_{y,cum}$ ; (b)  $P_{cum}$  and  $V_{S,INTER}$ ; (c)  $P_{cum}$  and  $V_{S,TOTAL}$ ; (d)  $P_{y,cum}$  against  $V_{S,TOTAL}$ . For (c, d) grey circles are the points on wave power time series' interpolated to volume. Southward alongshore wave power is negative.

## 6. Discussion

### 6.1. Sediment budget conceptual model

This study has demonstrated that, with reference to Fig. 1, Perranporth is an *open* system, that does not have a balanced sediment budget at the short to medium temporal scale (up to 10 years), and displays multi-annual accretional or erosional trends (Fig. 5e). Computed *DoDs* based on full embayment observations show significant morphological change in front of the headland bases and beyond the *DoC* in some sectors (Figs. 8 and 9). The alongshore continuity of the *DoC* contour line off the headland base (620 m in the south and 170 m in the north), linked with the detected morphological change beyond the inner embayment limits, suggests that Perranporth beach is part of an extended coastal cell. In line with earlier works (e.g., McCarroll et al., 2018; King et al., 2019; Valiente et al., 2019), these major morphological changes evidence substantial transport at depths  $> 15$  m that are related to headland bypassing mechanisms.

A semi-quantitative conceptual sediment budget model that is consistent with all observations presented thus far is shown in Fig. 11. Volume changes in the north and south sectors ( $\Delta V_N, \Delta V_S$ ) and fluxes within the model domain ( $q_{x,N}, q_{x,S}$ ) are based on observations. We are unable to quantitatively resolve fluxes beyond the survey domain; instead, we refer to a prior numerical modelling study predicting bypass at the northern headland of Perranporth (McCarroll et al., 2018). That study predicted that rapid southward sediment flux occurred at the northern headland during winters (up to  $0.5 \times 10^5 \text{ m}^3$  for a single winter), whilst gradual northward transport ( $\sim 0.2 \times 10^5 \text{ m}^3$ ) occurred during ‘summer’ (spring to autumn). McCarroll et al. (2018) estimated transport through a transect extending off the northern headland, while in the present study the outer boundary for the northern sector extends cross-shore from the shoreline, and alongshore over the northern extent of the bay. Consequently, there are differences between the values inferred here and the values provided in McCarroll et al. (2018). The proposed flux values should be considered as broad estimates, useful for conceptualization and providing hypotheses for future testing, but they are not definitive. The direction and approximate magnitude of  $Q_N$  is inferred based on McCarroll et al. (2018), then the budget is balanced (Equations in Fig. 11) to calculate fluxes at the mid-point of the embayment ( $Q_M$ ) and the southern boundary ( $Q_S$ ), which are consistent with the observed morphologic change ( $\Delta V_N, \Delta V_S$ ). Note that fluxes at the outer

boundaries ( $Q_N$ ,  $Q_S$ ) refer to both cross- and alongshore contributions. In summary, major phases of morphologic change include:

1. The **inter-tidal** erodes under energetic (and more northerly) waves and accretes when wave conditions are below average. This process is fairly uniform alongshore over the multi-year epochs (2011–2016; 2016–2018), but does vary for individual seasons (e.g., Fig. 11, Winter 2017–18).

2. During the **storm epoch** (2011–2016, Fig. 11), under larger and more northerly waves, the full embayment erodes, with the south eroding more than the north. Evidence is equivocal as to whether net transport is northward or southward, therefore we hypothesise two scenarios, to be resolved by future modelling efforts. In the first scenario (Fig. 11, Residual N transport), a net input of  $1 \times 10^5 \text{ m}^3$  is estimated at the southern boundary ( $Q_N$ ), with the northern sector losing sediment offshore and northward in the outer-subtidal. In the second scenario (Fig. 11, Residual S transport), a net input is estimated at the northern boundary, which implies that offshore sediment transport is occurring at the south end, exporting sediment beyond the survey region (Fig. 6).

3. During the **recovery period** (2016–2018), the waves are relatively smaller and more westerly, and the full embayment accretes. The south accretes more than the north, in particular during winter conditions. Northerly transport is inferred to occur during summer periods (Fig. 11, Summer 2016), assisted by a northerly residual tidal current (McCarroll et al., 2018). Influx is inferred to occur at both ends of the embayment during ‘recovery winters’ (Fig. 11, Winter 2017/18), demonstrating the critical role of winter wave conditions in multi-annual beach recovery (Burvingt et al., 2018; Dodet et al., 2019). This convergent flux is consistent with modelled circulation (McCarroll et al., 2018) for storms from the WNW ( $\sim 285^\circ$ ), that may produce a northward current at the south end, and a southward current at the north end.

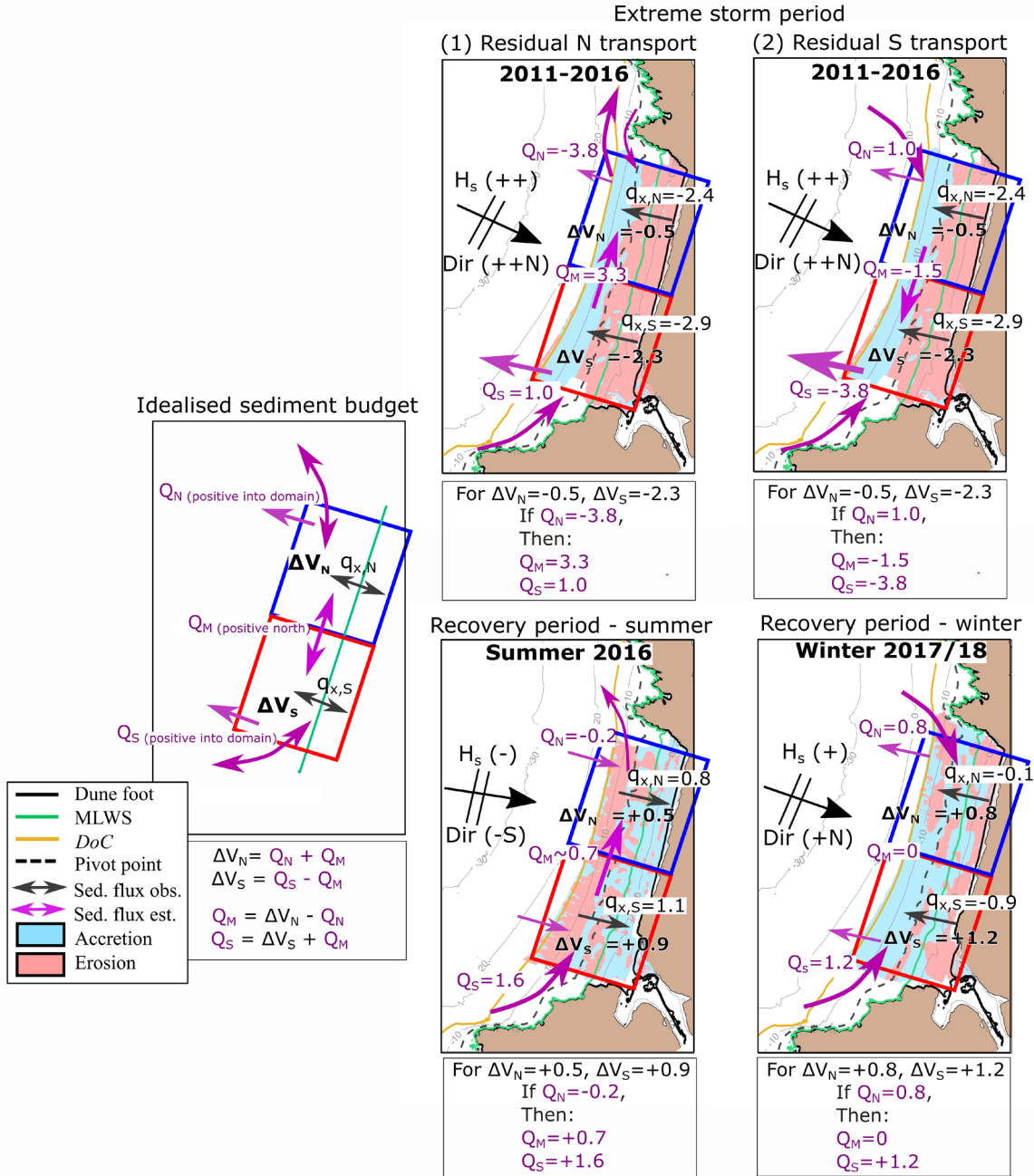


**Fig. 11.** Semi-quantitative conceptual sediment budget for Perranporth embayment with volume changes ( $\Delta V_N, \Delta V_S$ ) and cross-shore flux ( $q_{x,N}, q_{x,S}$ ; sed. flux obs.) based on observations. The external flux ( $Q_S, Q_N$ ) refer to both cross- and alongshore contributions.  $Q_S$  and  $Q_M$  are estimated using observations and bypass rate in the northern headland (sed. flux est.). Flux and volume change values are  $\times 10^5 \text{ m}^3$ . + and – symbols refer to magnitude of significant wave height ( $H_s$ ) with (++) for large waves, (-) for low energy wave conditions and (+) for moderate to energetic conditions. Direction (*Dir*) refers to shore normal wave direction ( $Dir \sim 283^\circ$ ) with -S for more southward wave approach (W), and +N to ++N for WNW and NW, respectively.

The conceptual model (Fig. 11) is useful for explaining the observations, but currently has limited predictive capacity due to the complexity of the system response. Further development through numerical modelling approaches are required in order to better predict sediment pathways.

## 6.2. Multi-annual embayment scale dynamics

The ‘classic’ characterization of beaches such as Perranporth is that winter storms erode the dunes and the upper part of the beach, depositing the sediment in sub-tidal bar systems, while calmer conditions return the sub-tidal sediment back to the beach (Komar, 1998). This is indeed what our understanding was for the studied beach based on almost a decade of inter-tidal beach surveys and a few sub-tidal surveys (Masselink et al., 2014; Scott et al., 2016), and which has led to the suggestion that Perranporth beach, and similar beaches in the region, are ‘closed systems’ (cf. Fig. 1-left panel). However, this characterization has shown to be incorrect as the full sediment budget analysis presented here indicates an ‘open system’ with sediment inputs and outputs in the order of  $300 \text{ m}^3 \text{ m}^{-1}$  over a decadal time period (Fig. 5e). The inner embayment region seems therefore connected via sediment pathways to the region beyond the *DoC* and the bounding headlands, which is in line with numerical modelling by Valiente et al. (2019).

To explain the sediment pathways and close the sediment budget, it is necessary to consider both longshore sediment transport gradients along the embayment (Fig. 11) and from adjacent bays through headland bypassing. Importantly, the large sediment volumetric variations across the lower shoreface, which are of the same order of magnitude as those occurring in the inter-tidal region (c.  $200 \text{ m}^3 \text{ m}^{-1}$ ), is suggestive of an energetic longshore transport system across this deeper region, and it is possible that this transport system extends along the whole north coast of SW England as alluded to by May and Hanson (2003) and Valiente et al. (2019). These findings are critical for informing the next stages of regional scale modelling and observational studies and may lead to a shift in understanding of sediment budgets along exposed and macrotidal embayments globally.

There is an interesting contradiction that, despite the extensive sediment volumetric variations in the sub-tidal region (Fig. 5e), a model based solely on inter-tidal beach volume variations such as presented in Fig. 5c can be used to predict shoreline position over the 10-year time period (e.g., Davidson et al., 2010). This suggests that the upper part of the beach (supra-inter- and shallow sub-tidal) is partially decoupled from the deeper sub-tidal region. The vast

majority of beach studies in the past (and present) have been (and are) solely based on inter-tidal topographic surveys (e.g., Castelle et al., 2015; Loureiro et al., 2015; Masselink et al., 2016a,b; Harley et al., 2017; Burvingt et al., 2018; Mentaschi et al., 2018); however, full embayment surveys, such as pioneered here, are likely to reveal an additional layer of complexity concerning nearshore sediment transport and beach morphodynamics. Future numerical modelling efforts will be aimed at providing complementary understanding of embayment scale sediment fluxes.

## 7. Conclusions

- A total sediment budget approach was implemented across the macrotidal, high energy Perranporth embayment for the period 2011–2018, using a multi-method surveying approach and accounting for measurement uncertainties.
- Inter-tidal volumetric changes indicate a longshore coherent, cross-shore dominant behavior, following a seasonal cycle superimposed by a multi-annual oscillation induced by extremely energetic winter seasons, with full recovery taking at least 5 years.
- Total embayment (combined inter- and sub-tidal) volumes varied by c.  $300 \text{ m}^3 \text{ m}^{-1}$  over 7-years, indicating that the inner embayment (down to the *DoC*) is ‘open’ and ‘unbalanced’ over multi-annual timescales.
- Sediment volumetric variations in the inter-tidal region are uncorrelated with those in the sub-tidal region at zero time-lag, but a positive correlation is observed at 1-year time-lag. This suggests that the upper and lower shoreface are partially decoupled, responding to different forcing controls.
- The largest dunes system monitored (northern Perranporth) experienced a significant erosion event in 2013/14 (15 m onshore translation of dune foot) with little recovery within 5 years.
- Inter-tidal sediment volume for the long-term southern sector time series was inversely correlated with variations in total wave power ( $r = -0.6$ ), coherent with a cross-shore dominated response. Total sediment volume change (primarily due to flux through the outer sub-tidal boundary) was correlated with both total ( $r = -0.6$ ) and alongshore wave power ( $r = 0.4$ ), suggesting a combined cross- and alongshore dominated response.

- The inter-tidal volume was found to be positively correlated with the total volume (for the south sector), such that when the inter-tidal eroded or accreted, so too did the total system. This was evident for an erosive period of extreme waves (2011–2016), followed by a ‘recovery’ period (2016–2018), where consistent influxes into the embayment were observed, even during energetic winter periods. This suggests a degree of equilibrium for the total embayment volume.
- A conceptual model was presented that balances the observed volume changes with inferred fluxes, forced by variations in total and alongshore wave power. At present, this model has limited predictive capacity and requires further development through numerical modelling approaches to better predict future sediment budgets on similar coastlines.
- Given the extent of flux through the sub-tidal outer boundaries, it is likely that Perranporth and beaches on similar coastlines form part of an extended coastal cell, with individual embayments linked via a ‘river of sand’ that flows around headlands.

## **Acknowledgments**

This work was supported by UK Natural Environment Research Council grant (NE/M004996/1; BLUE-coast project). This study is only possible thanks to the efforts of the members of the Coastal Process Research Group who have been, and still are, collecting observations at Perranporth. Special thanks to Aaron Barret, Peter Ganderton, Richard Kenyon, Oliver Bilson, Olivier Burvingt and Erin King for supporting the many field efforts during the last years. The Channel Coastal Observatory is project stakeholder and kindly provided LiDAR data. We would also like to acknowledge QPS for their ongoing support with multi beam software provision (QINSy/Qimera/FMGT).

## **References**

- Aagaard, T. (2011). Sediment transfer from the beach to shoreface: The sediment budget of an accreting beach on the Danish North Sea Coast. *Geomorphology* 135, 143–157.
- Bowen, A.J., Inman, D.L. (1966). Budget of Littoral Sand in the Vicinity of Point Arguello, California. U.S. Army Coastal Engineering Research Center, *Technical Memorandum No. 19*, 56p.

- Brasington J., Langham J., Rumsby B. (2003). Methodological sensitivity of morphometric estimates of coarse fluvial sediment transport. *Geomorphology* 53(3–4), 299–316. DOI: 10.1016/S0169-555X(02)00320-3
- Brasington, J., Rumsby, B.T., Mcvey, R.A. (2000). Monitoring and modelling morphological change in a braided gravel-bed river using high resolution GPS-based survey. *Earth Surface Processes and Landforms* 25(9): 973–990.
- Burvingt, O., Masselink, G., Russell, P., Scott, T. (2017). Classification of beach response to extreme storms. *Geomorphology* 295, 722–737.
- Burvingt, O., Masselink, G., Scott, T., Davidson, M., Russell, P. (2018). Climate forcing of regionally-coherent extreme storm impact and recovery on embayed beaches. *Marine Geology* 401, 112–128.
- Calder, B.R., Mayer, L.A. (2003). Automatic processing of high-rate, high density multi-beam echosounder data. *Geochemistry, Geophysics, Geosystems* 4(6): 1048. DOI: 10.1029/2002GC000486.
- Calder, B.R., Wells, D. (2007). CUBE User's Manual – Version 1.14. University of New Hampshire, USA.
- Caldwell, J.M. (1966). Coastal processes and beach erosion. *Journal of the Society of Civil Engineers*, 53 (2), 142–157.
- Castelle, B., Bujan, S., Ferreira, S., Dodet, G. (2017b). Foredune morphological changes and beach recovery from the extreme 2013/2014 winter at a high-energy sandy coast. *Marine Geology* 385, 41–55.
- Castelle, B., Dodet, G., Masselink, G., Scott, T. (2018). Increased Winter-Mean Wave-Height, Variability, and Periodicity in the Northeast Atlantic over 1947-2017. *Geophysical Research Letters* 45(2). DOI: 10.1002/2017GL076884
- Castelle, B., Marieu, V., Bujan, S., Splinter, K.D., Robinet, A., Sénéchal, N., Ferreira, S. (2015). Impact of the winter 2013–2014 series of severe Western Europe storms on a double-barred sandy coast: beach and dune erosion and megacusps embayments. *Geomorphology* 238, 135–148.

Church, J.A., White, N.J. (2011). Sea-level rise from the late 19th to the early 21st Century. *Surveys in Geophysics* 32, 585–602. DOI: 10.1007/s10712-011-9119-1.

CIRIA (1996). Beach management manual. CIRIA Report 153.

Coastal Engineering Research Center (1984). *Shore Protection Manual, Volume I*. Department of the Army Waterways Experiment Station, Corps of Engineers, Vicksburg, Mississippi, pp. 652.

Coco, G., Senechal, N., Rejas, A., Bryan, K., Capo, S., Parisot, J.P., Brown, J.A., MacMahan, J.H.M. (2014). Beach response to a sequence of extreme storms. *Geomorphology* 204, 493–501.

Cowell, P.J., Stive, M.J.F., Niedoroda, A.W., Swift, D.J.P., de Vriend, H.J., Buijsman, M.C., Nicholls, R.J., Roy, P.S., Kaminsky, G.M., Cleveringa, J., Reed, C.W., de Boer, P.L. (2003). The Coastal-Tract (Part 2): Applications of Aggregated Modeling of Lower-order Coastal Change. *Journal of Coastal Research* 19(4), 828–848.

Cudaback, C.N., Washburn, L., Dever, E. (2005). Sub-tidal inner-shelf circulation near Point Conception, California. *Journal of Geophysical Research: Oceans* 110, C10007. doi:10.1029/2004JC002608

Davidson, M.A., Lewis, R.P., Turner, I.L. (2010). Forecasting seasonal to multi-year shoreline change. *Coastal Engineering* 57, 620–629.

Dodet, G., Castelle, B., Masselink, G., Scott, T., Davidson, M., Floc'h, F., Jackson, D., Suarez, S. (2019). Beach recovery from extreme storm activity during the 2013/14 winter along the Atlantic coast of Europe. *Earth Surface Processes and Landforms*, 44(1), 393–401. George, D.A., Largier, J.L., Storlazzi, C.D., Barnard, P.L. (2015). Classification of rocky headlands in California with relevance to littoral cell boundary delineation. *Marine Geology* 369, 137–152.

Guisado-Pintado, E., Jackson, D.W.T. (2018). Multi-scale variability of storm Ophelia 2017: The importance of synchronised environmental variables in coastal impact. *Science of Total Environment* 630, 287–301.

Harley, M.D., Turner, I.L., Kinsela, M.A., Middleton, J.H., Mumford, P.J., Splinter, K.D., Phillips, M.S., Simmons, J.A., Hanslow, D.J., Short, A.D. (2017). Extreme coastal erosion enhanced by anomalous extratropical storm wave direction. *Sci. Rep.* 7 (6033). <https://doi.org/10.1038/s41598-017-05792-1>.

- Harley, M.D., Turner, I.L., Short, A.D. (2015). New insights into embayed beach rotation: the importance of wave exposure and cross-shore processes. *J. Geophys. Res. Earth Surf* 120, 470-1484. <https://doi.org/10.1002/2014JF003390>.
- Herbich, J.B. (2000). *Handbook of Coastal Engineering*. McGraw-Hill Professional, New York City, USA.
- Inman, D.L., Frautschy, J.D. (1966). Littoral processes and the development of shorelines. *Proceeding Coastal Engineering Specialty Conference*, Reston, VA, ASCE, pp. 511-536.
- King, E., Conley, D., Masselink, G., Leonardi, N., McCarroll, R.J., Scott, T. (2019). The Impact of Waves and Tides on Residual Sand Transport on a Sediment-poor, Energetic and Macrotidal Continental Shelf. *Journal of Geophysical Research Ocean* (in press.).
- Kinsela, M.A., Morris, B.D., Linklater, M., Hanslow, D.J. (2017). Second-pass assessment of potential exposure to shoreline change in New South Wales, Australia, using a sediment compartments framework. *Journal of Marine Science and Engineering* 5, 61. DOI: 10.3390/jmse5040061
- Komar, P.D. (1998). *Beach processes and sedimentation*. Prentice-Hall, Inc., Simon & Schuster, Upper Saddle River, NJ, pp. 66–72.
- Lane S.N. (1998). The use of digital terrain modelling in the understanding of dynamic river channel systems. In *Landform Monitoring, Modelling and Analysis*, Lane SN, Richards K, Chandler J (eds). Wiley: Chichester; 311–342.
- Lane, S.N., Chandler, J.H., Richards, K.S. (1994). Developments in monitoring and modeling small-scale river bed topography. *Earth Surface Processes and Landforms* 19(4): 349–368. DOI: 10.1002/esp.3290190406.
- Lane, S.N., Westaway, R.M., Hicks, D.M. (2003). Estimation of erosion and deposition volumes in a large, gravel-bed, braided river using synoptic remote sensing. *Earth Surface Processes and Landforms* 28(3): 249–271. DOI: 10.1002/esp.483.
- Loureiro, C., Ferreira, Ó., Cooper, J. A. G. (2012). Extreme erosion on high-energy embayed beaches: influence of megarips and storm grouping. *Geomorphology* 139, 155–171.

- Masselink, G., Austin, M., Scott, T., Poate, T., Russell, P. (2014). Role of wave forcing, storms and NAO in outer bar dynamics on a high-energy, macro-tidal beach. *Geomorphology* 226, 76–93.
- Masselink, G., Castelle, B., Scott, T., Dodet, G., Suanez, S., Jackson, D., Floc'h, F. (2016a). Extreme wave activity during 2013/2014 winter and morphological impacts along the Atlantic coast of Europe. *Geophysical Research Letters* 43 (5), 2135–2143.
- Masselink, G., Scott, T., Poate, T., Russell, P., Davidson, M., Conley, D. (2016b). The extreme 2013/2014 winter storms: hydrodynamic forcing and coastal response along the southwest coast of England. *Earth Surface Processes and Landforms* 41 (3), 378–391.
- Masselink, G.; Short, A.D. (1993) The effect of tide range on beach morphodynamics and morphology: A conceptual beach model. *J. Coast. Res.*, 9, 785–800.
- May, V.J., Hansom, J.D. (2003). *Coastal Geomorphology of Great Britain*, Geological edition. Joint Nature Conservation Committee, Peterborough, pp. 754.
- McCarroll, J., Masselink, G., Valiente, N. G., Scott, T., King, E. (2018). Wave and tidal controls on headland bypassing and embayment circulation. *Journal of Marine Science and Engineering* 6 (3), 94. <https://doi.org/10.3390/jmse6030094>.
- Mentaschi, L., Voudoukas, M.I., Pekel, J., Voukouvalas, E., Feyen, L. (2018). Global long-term observations of coastal erosion and accretion. *Scientific Reports* 8, 12876. <https://doi.org/10.1038/s41598-018-30904-w>
- Milne, J.A., Sear, D. (1997). Modelling river channel topography using GIS. *International Journal of Geographical Information Science* 11(5), 499–519. DOI: 10.1080/136588197242275.
- Plant, N.G., Holland, K.T, Puleo, J.A. (2002). Analysis of the scale errors in nearshore bathymetric data. *Marine Geology* 191(1–2), 71–86.
- Poate, T., Masselink, G., Russell, P., Austin, M. (2014). Morphodynamic variability of high-energy macrotidal beaches, Cornwall, UK. *Mar. Geol.* 350, 97–111.
- Prodger, S., Russell, P., Davidson, M. (2017). Grain-size distributions on high-energy sandy beaches and their relation to wave dissipation. *Sedimentology* 64, 1289–1302.
- Rosati, J.D. (2005). Concepts in sediment budgets. *Journal of Coastal Research* 21, 307–322.

- Schimel, A.C.G., Ierodiaconou, D., Hulands, L., Kennedy, D.M. (2015). Accounting for uncertainty in volumes of seabed change measured with repeat multi-beam sonar surveys. *Cont. Shelf Res.* 111, 52–68. <https://doi.org/10.1016/j.csr.2015.10.019>.
- Scott, T., Masselink, G., Austin, M.J., Russell, P.E. (2014). Controls on macrotidal rip current circulation and hazard. *Geomorphology* 214, 198–215 <http://dx.doi.org/10.1016/j.geomorph.2014.02.005>.
- Scott, T., Masselink, G., O'Hare, T., Saulter, A., Poate, T., Russell, P., Davidson, M., Conley, D. (2016). The extreme 2013/2014 winter storms: Beach recovery along southwest coast of England. *Marine Geology* 382, 224–241.
- Scott, T., Masselink, G., Russell, P. (2011). Morphodynamic characteristics and classification of beaches in England and Wales. *Marine Geology* 286 (1-4), 1–20.
- Short, A.D. (1985). Rip-current type, spacing and persistence, Narrabeen Beach, Australia. *Marine Geology* 65(1-2), 47–71.
- Short, A.D. (2010). Role of geological inheritance in Australian beach morphodynamics. *Coastal Engineering*, 57(2), 92–97.
- Short, A., Masselink, G. (1999). Embayed and structurally controlled beaches. In Short, A. E., editor, *Handbook of Beach and Shoreface Morphodynamics*, pp. 230–249. John Wiley & Sons, Chichester.
- Sibson, R. (1981). "A Brief Description of Natural Neighbor Interpolation," chapter 2. In *Interpolating Multivariate Data*. New York: John Wiley & Sons, 21–36.
- Splinter, K.D., Carley, J.T., Golshani, A., Tomlinson, R. (2014). A relationship to describe the cumulative impact of storm clusters on beach erosion. *Coast. Eng.* 83, 49–55.
- Stokes, C., Russell, P., Davidson, M. (2016). Sub-tidal and Inter-tidal Three-Dimensionality at a High Energy Macrotidal Beach. *Journal of Coastal Research* 75, (sp1) 472-476.
- Taylor, J. (1997). *An Introduction to Error Analysis: the Study of Uncertainties in Physical Measurements*, 2<sup>nd</sup> edn. University Science Books: Sausalito, CA.

- Thom, B.G., Eliot, I., Harvey, N., Rissik, D., Sharples, C., Short, A.D., Woodroffe, C.D. (2018). National sediment compartment framework for Australian coastal management. *Ocean and Coastal Management* 154, 103–120.
- United Kingdom Hydrographic Office (2011). INSPIRE Portal & Bathymetry DAC. Available at <http://aws2.caris.com/ukho/mapViewer/map.action>
- Valiente, N.G., Masselink, G., Scott, T., Conley, D., McCarroll, J. (2019). Evaluation of the role of waves and tides on depth of closure and potential for headland bypassing. *Marine Geology* 407, 60-75. <https://doi.org/10.1016/j.margeo.2018.10.009>
- Van Rijn, L.C. (1997). Sediment transport and budget of the central coastal zone of Holland. *Coastal Engineering* 32, 61–90
- Van Rijn, L.C. (2011). Coastal erosion and control. *Ocean & Coastal Management* 54(12), 867-887.
- Van Rijn, L.C. (2014). A simple general expression for longshore transport of sand, gravel and shingle, *Coastal Engineering* 90, 23–39.
- Vieira da Silva, G., Toldo, E.E., Klein, A.H.F., Short, A.D., Tomlinson, R., Strauss, D. (2017). A comparison between natural and artificial headland sand bypassing in Santa Catarina and the Gold Coast. *Australasian Coasts & Ports 2017: Working with Nature*, 1111.
- Wiggins, M., Scott, T., Masselink, G., Russel, P., McCarroll, R.J. (2018). Coastal embayment rotation: response to extreme events and climate control, using full embayment surveys. *Geomorphology* 327, 385–403. <https://doi.org/10.1016/j.geomorph.2018.11.014>
- Wise, S.M. (1998). The effect of GIS interpolation errors on the use of digital elevation models in geomorphology. In *Landform Monitoring, Modelling and Analysis*, Lane SN, Richards K, Chandler J (eds). Wiley: Chichester; 139–164.
- Wechsler, S.P. (2003). Perceptions of digital elevation model uncertainty by DEM users. *URISA Journal* 15(2), 57–64.
- Wechsler, S.P., Kroll, C.N. (2006). Quantifying DEM uncertainty and its effect on topographic parameters. *Photogrammetric Engineering and Remote Sensing* 72(9), 1081–1090.

Wheaton, J.M., Brasington, J., Darby, S.E., Sear, D.A. (2010). Accounting for uncertainty in DEMs from repeat topographic surveys: improved sediment budgets. *Earth Surface Processes and Landforms* 35, 136–156.

# CIRCULATION AND SEDIMENT FLUXES ON A MACROTIDAL, EXPOSED AND EMBAYED COASTLINE

N. G. VALIENTE<sup>1</sup>, J. MCCARROLL<sup>1</sup>, G. MASSELINK<sup>1</sup>, T. SCOTT<sup>1</sup>, D. CONLEY<sup>1</sup>  
AND E. KING<sup>1</sup>

1. School of Biological and Marine Sciences, Plymouth University, Drake Circus, PL4 8AA, Plymouth, UK. [nieves.garciavaliente@plymouth.ac.uk](mailto:nieves.garciavaliente@plymouth.ac.uk).

**Abstract:** We investigate the sediment transport dynamics along a 15-km stretch of embayed coastline in north Cornwall, SW England. Numerically-modelled wave-driven and tidal currents are used to support interpretation of sediment flux pathways inferred from morphological observations. Results for the main embayment (Perranporth) indicate that for an extreme erosive event, sediment ejection beyond the morphological depth of closure (c. -15 m) can exceed  $150 \text{ m}^3 \text{ m}^{-1}$ , related to ‘mega-rip’ formation where an alongshore current is deflected offshore ( $0.7 \text{ m s}^{-1}$  at  $> 20 \text{ m}$  depth). Accretionary phases are characterized by entrainment of sediment from adjacent bays and sub-tidal alongshore redistribution ( $35 \text{ m}^3 \text{ m}^{-1} \text{ year}^{-1}$ ). Our study suggests that major mechanisms for redistributing material to and along the lower shoreface for embayed coastlines are longshore residual flow (induced by waves and tide) and headland rip cell circulation, with the latter a function of wave obliquity, embayment length and headland configuration.

## Introduction

Predicting coastal system behavior requires an accurate delineation and understanding of coastal cell boundaries, sediment sources and sinks, and transport pathways. Highly embayed beaches are often considered closed cells with the prominent headlands acting as barriers to littoral drift, such that sediment transport into and/or out of adjacent cells is insignificant. Nevertheless, recent studies on sandy beaches show that important sediment transport paths offshore and/or beyond these barriers may occur under particular conditions (Short, 2010; Aagaard, 2011; McCarroll et al., 2018; King et al., 2019; Valiente et al., 2019a). Cross-shore sediment fluxes include sediment transport to and from the dunes (Castelle et al, 2017) to the different sub-systems (inter- and sub-tidal), or even beyond the morphological depth of closure (*DoC*) (Ortiz and Ashton, 2014). In the alongshore, sediment transport results from a combination of wave energy and angle (Van Rijn, 2014), with the largest sediment fluxes occurring for large and high-oblique waves.

Sediment transport into and out of embayments is of major interest to coastal researchers, but key processes (e.g., mega-rips, headland bypassing), driving forces, fluxes rates and local factors influencing it (e.g., headland/embayment morphometric parameters) are still poorly resolved. Several site-specific observational studies have demonstrated the relevant sediment fluctuations across

and along the lower shoreface (e.g., George et al., 2018; Valiente et al., 2019b). Additionally, several modelling studies have investigated some of the processes that may induce these significant sediment fluxes beyond the embayment limits through cross-embayment exchanges (Short, 2010; Loureiro et al., 2012; Castelle and Coco, 2013; McCarroll et al., 2016) and between adjacent beaches (McCarroll et al., 2018; Vieira da Silva et al., 2018). In particular, Castelle and Coco (2013) studied the role of embayment size in governing ejection outside the surf zone, with more recent studies focusing on the driving forces (Vieira da Silva et al., 2018) and circulation modes (McCarroll et al., 2018) that induce headland bypassing. Despite these recent efforts to quantify sediment fluxes on the lower shoreface, studies combining high-quality comprehensive morphological datasets with numerical modelling are scarce.

In this study, we investigate nearshore sediment transport dynamics in an embayed setting in north Cornwall, SW England. We combine morphological observations that extend from the coastal dunes to >30 m depth at Perranporth beach with numerical simulations for a 15-km stretch of coast, comprising five embayments and multiple headlands. In particular, we infer sediment exchanges within Perranporth and adjacent embayments based on observations of morphological change, and use numerical modelling of wave-driven and tidal currents to support interpretation of sediment pathways, including the controls imposed by headlands.

## Study area

The study encompasses 15 km of the macrotidal, exposed and embayed coastline of north Cornwall from Chapel Porth to Hollywell, SW England and includes five sandy beaches delineated by sharp headlands of diverse morphometric characteristic (Fig. 1). The sites are characterized by a wide low-gradient (mean bed slope = 0.018–0.021) sandy platform facing W with a slight rotation in the south to the NW (280°–290°), except for St. Agnes, which faces N. The latter beach also differentiates itself from the others in the study through its short length and mixed sand-gravel sediments. The remaining beaches are composed of medium sand with a median grain size ( $D_{50}$ ) of 0.30–0.40 mm. For Perranporth,  $D_{50}$  is relatively constant (0.30 mm) up to 20–26 m depth Ordnance Datum Newlyn. The limit of detectable morphological change or *DoC* at Perranporth is -15 m (Valiente et al., 2019a). Isolated rocks are present around the apex of most of the headlands at depths of 5–10 m Ordnance Datum Newlyn (ODN), transitioning to a sandy bed below this depth.

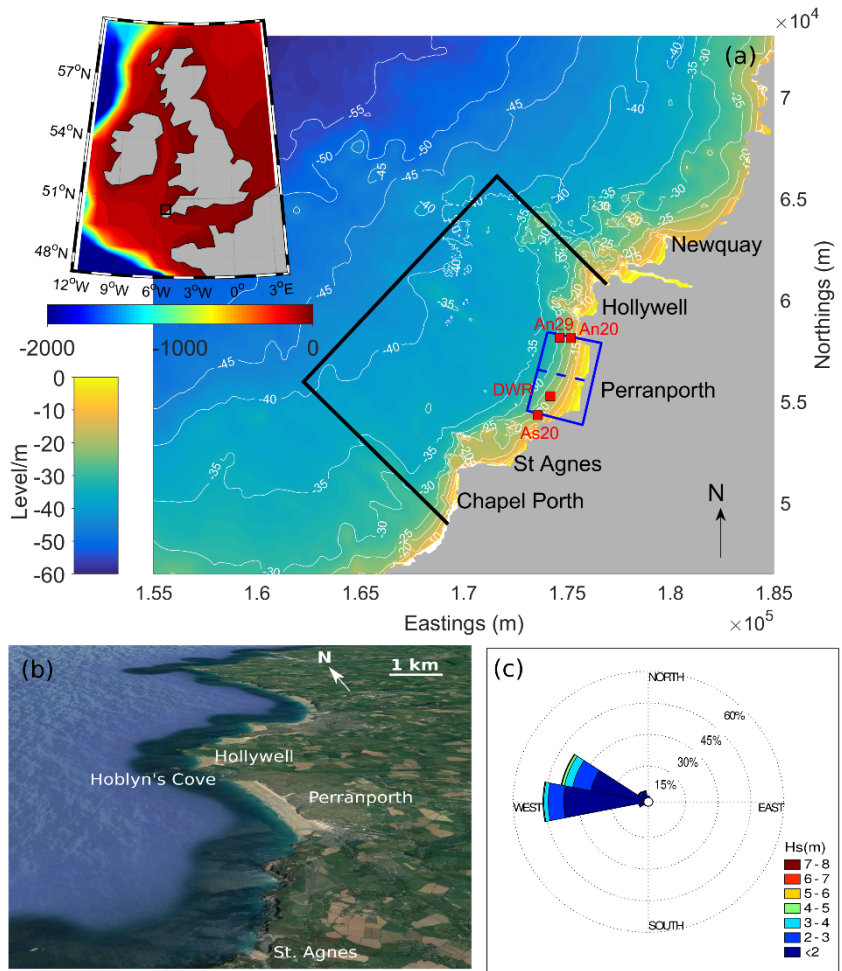


Fig 1. (a) Location map and physical context of the study site. Black box represents the Delft3D model domain, blue box shows coverage of morphological dataset and red squares indicate instrument positions. Dashed blue line depicts Perranporth embayment south and north sectors. (b) Oblique Google Earth image of beach and embayments. (c) Wave rose for Perranporth using 11 years of wave buoy data (DWR).

This coastline is fully exposed to regular North Atlantic swells, with an annual average significant wave height ( $H_s$ ) of 1.6 m and peak period ( $T_p$ ) of 10–11 s. Wave approach is typically from the W and WNW (Fig. 1c), with largest waves coming from the latter. Wave climate is seasonal with monthly average  $H_s$  ranging from 1.2 m (summers) to 2.3 m (winters), and extreme wave heights can exceed  $H_s = 8$  m and  $T_p = 19$  s. The tidal regime is semi-diurnal and macrotidal with a

mean spring and neap tidal range of 6.3 m and 2.7 m, respectively (Masselink et al., 2014; Scott et al., 2016). Maximum ebb and flood velocity ranges from 0.1 to 0.4 m s<sup>-1</sup> at depths between 10 and 30 m with the tidal flows predominantly parallel to the shoreline, and significantly increasing in strength around the headlands, reaching c. 0.7 m s<sup>-1</sup> during spring tides (Valiente et al., 2019a). The strong flood-ebb asymmetry in the current magnitude during a tidal cycle results in a northward tidal net flux along the coast (McCarroll et al., 2018).

## **Materials and methods**

Observed morphological changes from 2011 to 2018 were obtained from differences of digital elevation models (*DEM*) and were used to infer net sediment fluxes. *DEMs* were obtained by merging topographic surveys, and single- and multi-beam echosounder bathymetry. Sediment fluxes in/out embayment were then linked to different circulation paths computed using a coupled Delft3D morphodynamic model which was run for relatively energetic conditions (e.g., sea states of  $H_s \sim 3\text{--}4$  m over winter 2016/17) and extreme wave conditions (storm Hercules over 2013/14 winter). Specifically, we modeled major pathways induced during conditions of maximum bed shear stress (moderate–high and extreme waves, coinciding with tidal currents during spring tides).

## ***Field observations***

### *Multimethod morphological surveys and DEM creation*

Full embayment morphological measurements were collected in spring and autumn from 2016 to 2018 using a combination of: (1) Unmanned Aerial Vehicle (UAV) dune surveys; (2) quad bike mounted RTK-GPS topographic surveys for the inter- and supra-tidal zone; and (3) RTK-GPS aided single-beam (SBE) bathymetric surveys up to c. -18 m ODN. The SBE dataset was complemented by yearly multi-beam bathymetric surveys (MBE) up to c. -40 m ODN. To enable determination of the impacts of the 2013/14 winter storms on the Perranporth beach sediment budget, an extra full embayment dataset for the year 2011 was constructed by combining LiDAR and multi-beam bathymetry facilitated by the United Kingdom Hydrographic Office. Digital elevation models (*DEMs*) with 2-m spatial resolution were constructed by combining the various data sets for the entire embayment (2011, 2016, 2017, 2018) using Loess (Plant et al., 2002) and natural neighbor (Sibson, 1981) interpolation functions. Full embayment morphological measurements were used to infer net sediment fluxes following a total budget sediment approach and accounting for uncertainty.

### *Wave and hydrodynamic observations*

Waves, currents and water levels were measured using three 600 kHz RDI Workhorse acoustic Doppler current profilers (ADCPs) deployed during 2–3 months in winter 2016/17 off the two headlands delineating Perranporth beach in 18–20 m (As20 and An20, Fig. 1a) and 29 m water depth relative to MSL (An29; Fig. 1a). Currents were ensemble-averaged at 5-min intervals, while waves and water levels were sampled every 2 h. Waves were also recorded every 30 min by a directional wave buoy (DWR; Fig. 1a) located in 20 m depth relative to MSL. Wave and hydrodynamic observations were used to calibrate and validate the numerical model Delft3D before using applying the model to extreme conditions.

### *Numerical modelling*

The process-based numerical model Delft3D (Booij et al., 1999) was used for wave (WAVE) transformation and hydrodynamics (FLOW) computation. The FLOW module solves the depth-averaged water equations and the WAVE module is used for wave transformation processes, including wave propagation and dissipation, generation by wind, and non-linear wave-wave interactions (TRIADS mechanism). Delft3D was run in 2D online-coupled mode, including wind forcing. The model was set up for a domain encompassing Perranporth beach and adjacent embayments using two structured curvilinear grids generated using conformal mapping methods as in Bruciaferri et al. (2019) with an extent of 15 km by 10 km and a space-varying resolution that ranges from 300 m offshore to 25 m near the coast. The WAVE grid was a 2-grid cells extension at the boundaries of the FLOW grid.

Model output was calibrated against observations of wave statistics, water level and flow velocity and direction for a 1-week period from 29 January to 04 February 2017 (refer to Fig. 1 for locations). The model performance was optimised for the calibration period and then validated against the observations conducted during winter 2016/17 (Fig. 2). Model skill was evaluated using root-mean square error (*RMSE*) and coefficient of determination ( $R^2$ ). The model satisfactorily reproduced wave height ( $RMSE = 0.32$  m;  $R^2 = 0.90$ ) and period ( $RMSE = 1.5$  s;  $R^2 = 0.71$ ). Velocity currents and flow direction were accurately modelled ( $RMSE = 0.11$  m s<sup>-1</sup> and 60°;  $R^2 = 0.69$  and 0.66, respectively) and water level prediction was excellent ( $RMSE = 0.28$  m;  $R^2 = 0.97$ ). The large *RMSE* value for direction is related to a time offset in the tidal directional change, such that for short periods the direction is off by ~180°. Delft3D was then run for three scenarios: energetic wave conditions for events coming from the W and WNW, and extreme wave conditions (WNW) over the 2013/14 winter. All scenarios were run during spring tides to simulate conditions of maximum bed shear stress leading to the major sediment transport modes along this coast.

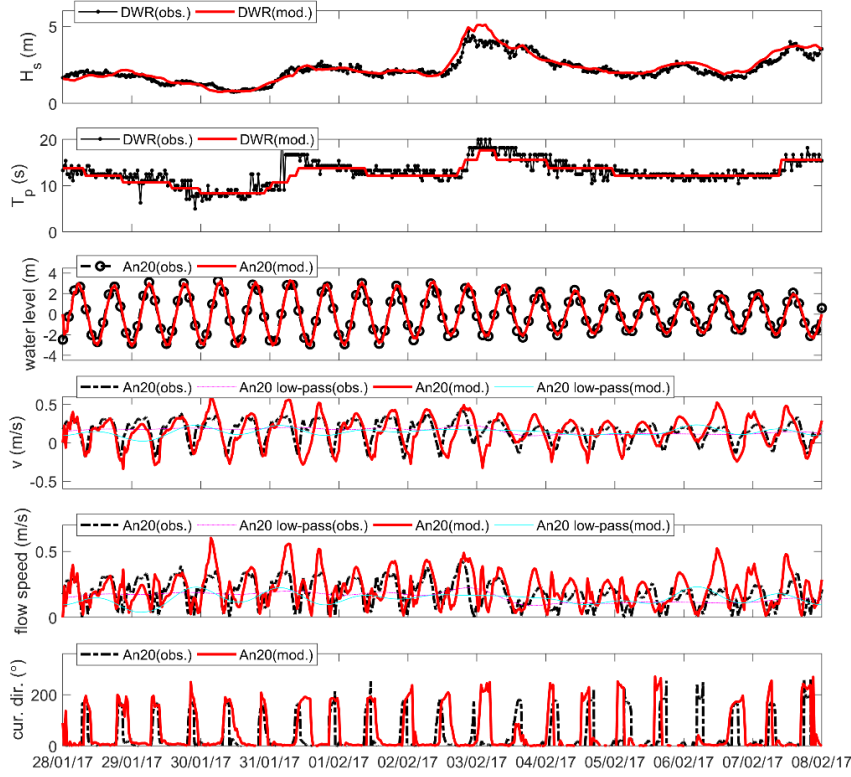


Fig 2. Wave buoy (DWR) and ADCP An20 observations compared with Delft3D model output. From top to bottom: significant wave height ( $H_s$ ), peak period ( $T_p$ ), water level, along-coast current speed ( $v$ ), and flow speed and direction. The observed and modelled current speed and direction are 30-min averages. Low-pass flow speed has a Fourier transform filter applied, with a 25-h cut-off.

## Results

### *Observations of morphological change*

3D variability of the Perranporth full embayment is presented in Fig. 3. Despite being considered a cross-shore dominated embayment with cross-shore fluxes of c.  $90 \text{ m}^3 \text{ m}^{-1} \text{ year}^{-1}$  (Valiente et al., 2019b) as a result of waves approaching predominantly parallel to this stretch of coast, evidence of alongshore sediment transport exists in the lower shoreface (Fig. 3). The storm epoch (2011–2016; Fig. 3a,g) is characterized by large erosion rates in the S ( $-150 \text{ m}^3 \text{ m}^{-1}$ ) and lower rates in the N ( $-50 \text{ m}^3 \text{ m}^{-1}$ ). By contrast, the recovery period (2016–2018) presents larger accretion rates in the S sector of the embayment ( $300 \text{ m}^3 \text{ m}^{-1}$ ) compared to the N ( $170 \text{ m}^3 \text{ m}^{-1}$ ), with maximum sediment gains during winter 2017/18 ( $86 \text{ m}^3$

$\text{m}^{-1}$  in the S compared to  $57 \text{ m}^3 \text{ m}^{-1}$  in the N; Fig. 3e,k). Inter-tidal morphological response can be considered along uniform and cross-shore dominated, while sub-tidal differences between S and N sectors suggest relevant longshore transport and/or along-coast variation in cross-shore fluxes (Fig. 3a–f). This sub-tidal alongshore variability is c.  $35 \text{ m}^3 \text{ m}^{-1}$  on average, but can reach  $50 \text{ m}^3 \text{ m}^{-1}$ .

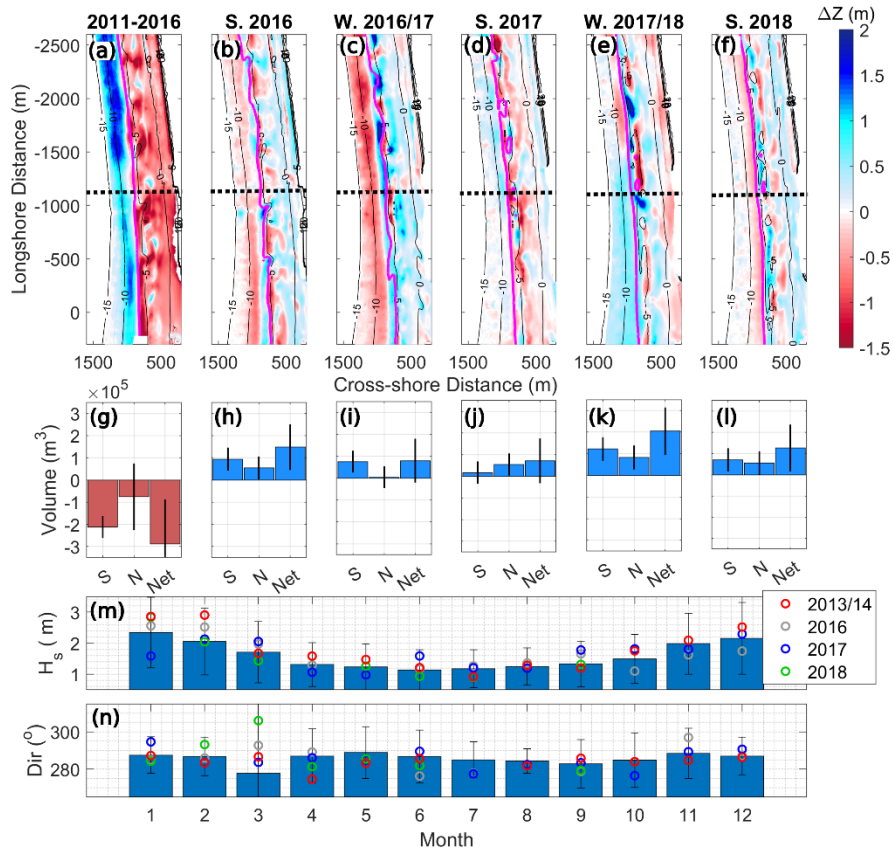


Fig 3. From top to bottom: 3D variability of Perranporth full embayment where red indicates erosion and blue accretion; volumetric changes and associated uncertainty (error bars) for north (N), south (S) sectors (refer to Fig. 1) and full embayment (Net) at Perranporth; monthly statistics of significant wave height ( $H_s$ ) and averaged wave direction ( $Dir$ ) during storm events ( $H_s > H_{s,5\%}$ ) at Perranporth wave buoy. Volumes are for epochs 2011–2016 and winter (W) and summer (S) seasons over 2016–2018. Contours in top panels are from the first of the beach surveys with  $z = -6 \text{ m ODN}$  (pivot point) represented in magenta. Black dot line shows the limit between the volume computation for N and S sectors.

### ***Numerically modelled circulation***

Simulations of coupled wave-driven and tidal currents are now presented to aid in the interpretation of sediment flux pathways. Major circulation patterns along the study site are presented in Fig. 4.

For **moderate-high wave forcing ( $H_s \sim 4$  m) from the W** (Dir  $\sim 270^\circ$ ; Fig. 4a,b), clockwise embayment-scale circulation is observed in all the embayments. Oblique wave breaking generates a northward current near the headlands and along the stretch of coast encompassing St. Agnes, with a maximum velocity of  $0.5 \text{ m s}^{-1}$  that is added to the residual tidal current to the north ( $0.05\text{--}0.2 \text{ m s}^{-1}$ ). This northward flow is diverted offshore in the south of Perranporth and Chapel Porth by a southward current originated by the rip circulation formed at the up-wave northern headlands. This rip cell circulation associated with the headlands at the north and the subsequent southward current is observed in all the embayments except St. Agnes, but it is only strong enough to deflect the northward flow offshore when it develops in the larger embayments.

For **moderate-high wave forcing ( $H_s \sim 4$  m) from the WNW** (Dir  $\sim 286^\circ$ ; Fig. c,d), the embayment-scale circulation pattern is still observed, but now a southward flow up to  $-10 \text{ m ODN}$  is present in front of most of the headlands with a very weak northward current ( $\sim 0.1 \text{ m s}^{-1}$ ) only observed beyond the  $-15 \text{ m ODN}$  depth contour. It is noteworthy that for only a modest change in wave direction from  $270^\circ$  to  $286^\circ$ , the direction of the nearshore currents along this embayed coast changes dramatically.

For **extreme wave forcing ( $H_s \sim 7$  m) from the W to WNW** (Dir  $\sim 280^\circ$ ; Fig. e,f), a strong northward current of  $\sim 1 \text{ m s}^{-1}$  is predicted along the coast with a surf zone that extends beyond most of the headland apexes. Consequently, the major circulation pattern can encompass several embayments for shallower bounding headlands, with a subsequent flow shift from the prevailing north direction towards the south close to the base of these (e.g. southward bypass between Perranporth and northward bay). During this circulation mode, the northward current is now deflected further offshore in the form of a mega-rip at Chapel Porth and Perranporth (offshore-directed current of  $0.7 \text{ m s}^{-1}$  up to  $-20 \text{ m ODN}$  in the southern sector of the embayment).

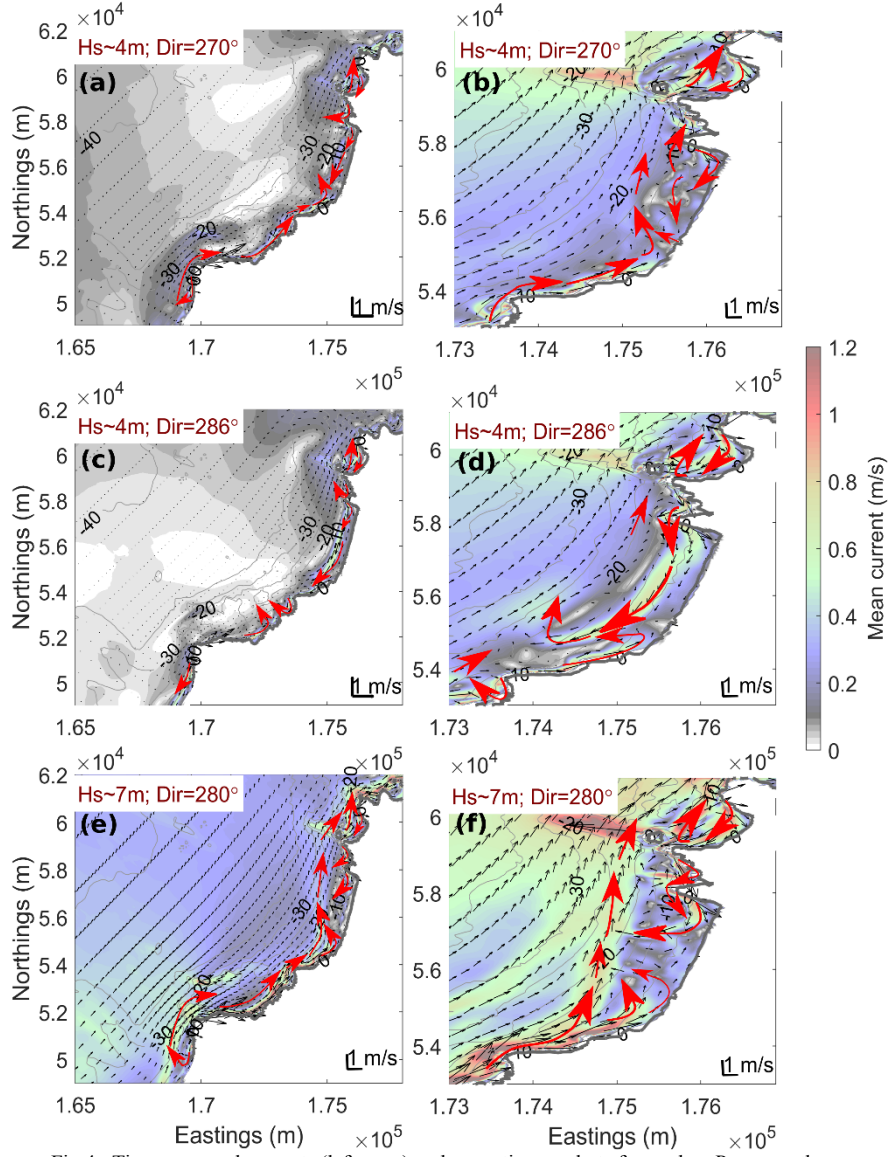


Fig 4. Time-averaged currents (left rows) and synoptic snapshots focused on Perranporth embayment (right rows) under storm conditions during spring tides. All snapshots correspond to maximum bed shear stress conditions over the tidal cycle,  $\sim 2$  h before HT for this particular case. Circulation under moderate-high waves from the W (a,b), WNW (c,d) and extreme waves during storm Hercules, 2013/14 winter (e,f).  $H_s$  and  $Dir$  presented for each scenario correspond with offshore conditions. The red arrows indicate key currents synthesised from the model results.

## Discussion

The combined field observations of morphological change and numerically modelled circulation are now used to infer sediment transport pathways. A conceptual model of headland bypassing and sediment pathways is shown in Fig. 5. Three major potential pathways for redistributing material to and along the lower shoreface for embayed coastlines are identified: (1) longshore flow to mega-rip; (2) headland bypass from adjacent bays; and (3) intra-embayment circulation.

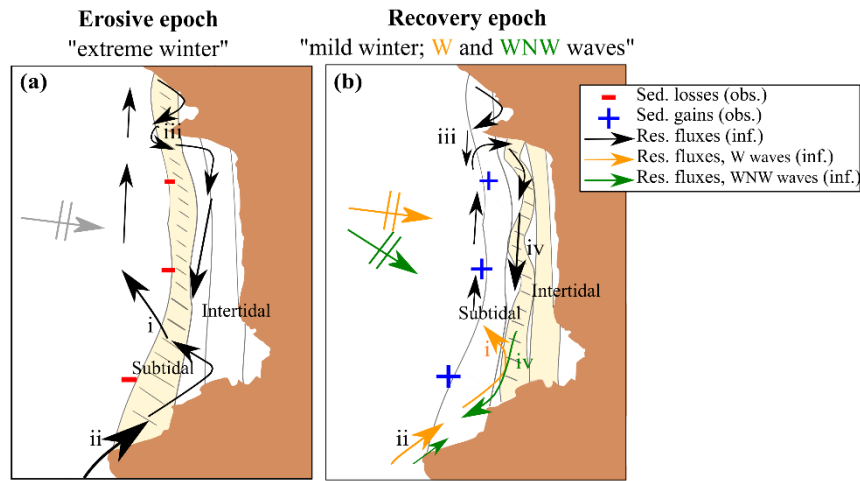


Fig 5. Conceptual diagram of major alongshore sediment fluxes pathways for a period of higher than average winter waves [erosion] (a) and lower than average winter waves [recovery] (b). Outer bar is represented with dashed lines and accretion due to cross-shore fluxes is shown in beige. Arrows indicate observed (obs.) and inferred (inf.) residual fluxes. Red - and blue + symbols indicate embayment alongshore gradient in sediment losses and gains (size increases with increasing magnitude) based on observations (obs.).

### *Sediment Pathway 1: South headland longshore flow to mega-rip*

The northward residual tidal flow along this coastline is added to by a strong ( $\sim 1 \text{ m s}^{-1}$ ) wave-induced current produced by oblique wave breaking during high wave conditions. This flow develops in the longer embayments (e.g., Perranporth and Chapel Porth) as an alongshore current at the down-wave headland, and this current is diverted offshore (Fig. 5a-i) as a strong mega-rip (c.  $0.7 \text{ m s}^{-1}$  at 20 m depth ODN). This mechanism is potentially a pathway for sediment ejection beyond the embayment limits and may be a factor in the observed larger sediment losses in the south sector compared to the north. For example, over the erosive period, Perranporth lost  $150 \text{ m}^3 \text{ m}^{-1}$  in the southern sector and  $50 \text{ m}^3 \text{ m}^{-1}$  in the

north. For moderate-high wave conditions, this mode of circulation is more subdued (Fig. 5b-i), potentially delivering sediment to shallower regions of the subtidal (-15 m ODN and shallower). This circulation mode is similar to other swell-dominated headland embayments (Gallop et al., 2011; McCarroll et al., 2014) and consistent with Castelle and Coco (2013), who determined that for obliquely-incident waves, the rip acts as a persistent conduit for transporting floating material into the inner shelf region, and this is more evident for longer beaches in which a longshore current meandering over the bar and rips within the embayment has enough room to develop.

### ***Sediment Pathway 2: North headland bypassing***

Model results over extreme events indicate southward headland bypass (Fig. 5a-ii) in the north as a result of multi-embayment circulation. McCarroll et al. (2018) predicted bypassing rates up to  $-10^4 \text{ m}^3 \text{ day}^{-1}$  (negative indicates southward) for  $H_s > 5 \text{ m}$ , which may explain the lower erosion rates in the north sector of the embayment. Over accretionary phases with moderate-high energy conditions ( $H_s \sim 4 \text{ m}$ ), bypassing at the north headland (Fig. 5b-ii) is much weaker and is function of the wave angle, directed northward for westerly waves (Fig. 5b-ii, orange arrow) and southward for WNW waves (Fig. 5b-ii, green arrow). Thus, larger sediment influxes into the embayment at the north based on morphologic observations occur mainly during periods with predominant WNW swell events.

### ***Sediment Pathway 3: Embayment circulation***

Clockwise embayment circulation (Fig. 5b-iii) is predicted to occur during moderate-high energy conditions that forces a slow transport of sand from the updrift to the downdrift part of the embayment (Castelle and Coco, 2012). This type of embayed beach circulation arises from the interaction between the wave-driven current and tidal residual flow, and the geometry and orientation of the bounding headlands. Major mechanisms redistributing sediment in the lower shoreface include a northward alongshore current (beyond -10 m ODN) deflected onshore and back toward the south at the north headland, and onshore flow generated by high-oblique breaking waves along the north headland. The combination of both mechanisms is predicted to force a moderate ( $0.4\text{--}0.5 \text{ m s}^{-1}$ ) flow towards the south below -10 m ODN which induces intra-embayment southward alongshore sediment fluxes over mild winter periods. This is supported by observations of morphologic change, where the south accreted  $35 \text{ m}^3 \text{ m}^{-1} \text{ year}^{-1}$  more on average, relative to the north.

## Conclusions

This study investigated sediment fluxes and major processes redistributing material along the lower shoreface of a high-energy embayed coastline. Observations of morphologic change, combined with numerically modelled circulation modes, were used to infer sediment flux pathways over a period of storm and subsequent recovery:

- Periods characterized by extreme events ( $H_s \sim 7$  m, WNW) involve cross-shore exchanges extending to depths that exceed the base of the headlands and hence constitute multi-embayment circulation. This is associated with large losses of sediment ( $>150 \text{ m}^3 \text{ m}^{-1}$ ) in the southern sector (down-wave) of the studied embayment, potentially associated with mega-rip formation.
- Sediment gains during accretionary phases over moderate-high swell periods ( $H_s \sim 4$  m) are highly sensitive to wave angle with inflows that are greater in the south than the north on average (c.  $35 \text{ m}^3 \text{ m}^{-1} \text{ year}^{-1}$ ). This phase is associated with intra-embayment circulation, with predicted currents inducing redistribution towards the south.

These sediment fluxes, especially the subtidal redistribution of sediment, provide new insights into a coast-type previously thought to be dominated by purely cross-shore forcing.

## Acknowledgements

This work was supported by UK Natural Environment Research Council grant (NE/M004996/1; BLUE-coast project). This study is only possible thanks to the efforts of the members of the Coastal Process Research Group who have been, and still are, collecting observations at Perranporth.

## References

- Aagaard, T. (2011). Sediment transfer from the beach to shoreface: The sediment budget of an accreting beach on the Danish North Sea Coast. *Geomorphology*, 135, 143–157.
- Bruciaferri, D., Shapiro, G., Stanichny, S., Zatsepin, A., Ezer, T., Wobus, F., Francis, X., Hilton, D. 2019. Numerical modelling of the Black Sea hydrodynamics using a structured multi-envelope mesh with variable resolution (in prep.).

- Castelle, B., Bujan, S., Ferreira, S., Dodet, G. (2017). Foredune morphological changes and beach recovery from the extreme 2013/2014 winter at a high-energy sandy coast. *Marine Geology* 385, 41–55.
- Castelle, B., Coco, G. (2012). The morphodynamics of rip channels on embayed beaches. *Continental Shelf Research* 43, 10–23.
- Castelle, B., Coco, G. (2013). Surf zone flushing on embayed beaches. *Geophysical Research Letters* 40, 2206–2210.
- Gallop, S.L., Bryan, K.R., Coco, G., Stephens, S.A. (2011). Storm-driven changes in rip channel patterns on an embayed beach. *Geomorphology* 127, 179–188.
- George, D.A., Largier, J.L., Storlazzi, C.D., Robart, M.J., Gaylord, B. (2018). Currents, waves and sediment transport around the headland of Pt. Dume, California. *Continental Shelf Research* 171, 63–76.
- King, E., Conley, D., Masselink, G., Leonardi, N., McCarroll, R.J., Scott, T. (2019). The Impact of Waves and Tides on Residual Sand Transport on a Sediment-poor, Energetic and Macrotidal Continental Shelf (in prep.).
- Loureiro, C., Ferreira, Ó., Cooper, J.A.G. (2012). Extreme erosion on high-energy embayed beaches: influence of mega-rips and storm grouping. *Geomorphology* 139, 155–171.
- Masselink, G., Austin, M., Scott, T., Poate, T., Russell, P. (2014). Role of wave forcing, storms and NAO in outer bar dynamics on a high-energy, macro-tidal beach. *Geomorphology* 226, 76–93.
- McCarroll, R.J., Brander, R.W., Turner, I.L., Power, H.E., Mortlock, T.R. (2014). Lagrangian observations of circulation on an embayed beach with headland rip currents. *Marine Geology*, 355, 173–188.
- McCarroll, R.J., Brander, R. W., Turner, I. L., & Van Leeuwen, B. (2016). Shoreface storm morphodynamics and mega-rip evolution at an embayed beach: Bondi Beach, NSW, Australia. *Continental Shelf Research*, 116, 74–88.
- McCarroll, J., Masselink, G., Valiente, N.G., Scott, T., King, E. (2018). Wave and tidal controls on headland bypassing and embayment circulation. *Journal of Marine Science and Engineering* 6 (3), 94.

- Ortiz, A.C., Ashton, A.D. (2016). Exploring shoreface dynamics and a mechanistic explanation for a morphodynamic depth of closure. *Journal of Geophysical Research: Earth Surface* 121, 442–464.
- Plant, N.G., Holland, K.T, Puleo, J.A. (2002). Analysis of the scale errors in nearshore bathymetric data. *Marine Geology* 191(1–2), 71–86.
- Scott, T., Masselink, G., O'Hare, T., Saulter, A., Poate, T., Russell, P., Davidson, M., Conley, D. (2016). The extreme 2013/2014 winter storms: Beach recovery along southwest coast of England. *Marine Geology* 382, 224–241.
- Short, A.D. (2010). Role of geological inheritance in Australian beach morphodynamics. *Coastal Engineering* 57(2), 92–97.
- Sibson, R. (1981). "A Brief Description of Natural Neighbor Interpolation," chapter 2. In *Interpolating Multivariate Data*. New York: John Wiley & Sons, 21–36.
- Valiente, N.G., Masselink, G., Scott, T., Conley, D., McCarroll, J. (2019a). Evaluation of the role of waves and tides on depth of closure and potential for headland bypassing. *Marine Geology* 407, 60–75.
- Valiente, N.G., Masselink, G., Scott, T., McCarroll, J., Wiggins, M. (2019b). Extreme storm response and recovery of a sandy, exposed and macrotidal embayment using a total sediment approach (in prep.).
- Van Rijn, L.C. (2014). A simple general expression for longshore transport of sand, gravel and shingle. *Coastal Engineering* 90, 23–39.
- Vieira da Silva, G., Toldo, E.E., Klein, A.H.F., Short, A.D., Tomlinson, R., Strauss, D. (2018). The influence of wave–wind– and tide–forced currents on headland sand bypassing – Study case: Santa Catarina Island north shore, Brazil. *Geomorphology* 312, 1–11.